

Vicente Lopes Junior · Valder Steffen Jr.
Marcelo Amorim Savi *Editors*

Dynamics of Smart Systems and Structures

Concepts and Applications

 Springer

Dynamics of Smart Systems and Structures

Vicente Lopes Junior • Valder Steffen Jr.
Marcelo Amorim Savi
Editors

Dynamics of Smart Systems and Structures

Concepts and Applications

 Springer

Editors

Vicente Lopes Junior
Universidade Estadual
Paulista – UNESP
FEIS - Department of Mechanical
Engineering
Ilha Solteira, São Paulo, Brazil

Valder Steffen Jr.
Universidade Federal de Uberlândia – UFU
Faculty of Mechanical Engineering
Uberlândia, Minas Gerais, Brazil

Marcelo Amorim Savi
Universidade Federal do Rio de
Janeiro – UFRJ
COPPE – Department of Mechanical
Engineering
Rio de Janeiro, Brazil

ISBN 978-3-319-29981-5

ISBN 978-3-319-29982-2 (eBook)

DOI 10.1007/978-3-319-29982-2

Library of Congress Control Number: 2016936558

© Springer International Publishing Switzerland 2016

This work is subject to copyright. All rights are reserved by the Publisher, whether the whole or part of the material is concerned, specifically the rights of translation, reprinting, reuse of illustrations, recitation, broadcasting, reproduction on microfilms or in any other physical way, and transmission or information storage and retrieval, electronic adaptation, computer software, or by similar or dissimilar methodology now known or hereafter developed.

The use of general descriptive names, registered names, trademarks, service marks, etc. in this publication does not imply, even in the absence of a specific statement, that such names are exempt from the relevant protective laws and regulations and therefore free for general use.

The publisher, the authors and the editors are safe to assume that the advice and information in this book are believed to be true and accurate at the date of publication. Neither the publisher nor the authors or the editors give a warranty, express or implied, with respect to the material contained herein or for any errors or omissions that may have been made.

Printed on acid-free paper

This Springer imprint is published by Springer Nature
The registered company is Springer International Publishing AG Switzerland

Preface

Dynamics of Smart Systems and Structures presents a general overview of smart material systems and structures. This book represents an effort related to the *First School of Smart Structures in Engineering* that was held at UNESP/Ilha Solteira—SP, Brazil, November 9–13, 2014. The event was an initiative of the *Committee of Smart Materials and Structures* of the *Brazilian Society of Mechanical Sciences and Engineering* (ABCM).

The subject of Smart Materials and Structures in Brazil was related to several disconnected groups. However, in 2008, Brazilian government decided to sponsor thematic projects that would be organized to form *National Institutes of Science and Technology*. One of these projects is the *National Institute for Smart Structures in Engineering (INCT-EIE)* that represents a network that puts together a number of scientists, engineers, and students working collaboratively on a number of topics related to smart structures in cooperation with international groups. This initiative changed the scenario of Smart Structures in Brazil.

Several projects were developed since the beginning of the INCT-EIE activities. This book is one of them, being prepared thinking on the beginner students and engineers interested on Smart Material Systems and Structures. The authors hope that this introductory text may encourage, motivate, and help readers to explore this challenging interdisciplinary area.

Ilha Solteira, SP, Brazil
Uberlândia, MG, Brazil
Rio de Janeiro, RJ, Brazil

Vicente Lopes Jr.
Valder Steffen Jr.
Marcelo Amorim Savi

Contents

Introduction	1
Vicente Lopes Jr., Valder Steffen Jr., and Marcelo A. Savi	
Part I Fundamentals	
Continuum Mechanics	7
Marcelo A. Savi	
Wave Motion in Elastic Structures	41
M.J. Brennan, B. Tang, and F.C.L. Almeida	
Passive and Active Structural Vibration Control	65
Marcelo A. Trindade	
Nonlinear Dynamics and Chaos	93
Marcelo A. Savi	
Part II Smart Materials	
Introduction to Smart Materials and Structures	121
Domingos A. Rade and Valder Steffen Jr.	
Piezoelectric Materials	135
Vicente Lopes Jr. and Clayton Rodrigo Marqui	
Shape Memory Alloys	155
Marcelo A. Savi, Alberto Paiva, Carlos J. de Araujo, and Aline S. de Paula	
Electro- and Magneto-Rheological Materials	189
Gustavo Luiz Chagas Manhães de Abreu, Flávio Donizeti Marques, Fabrício César Lobato de Almeida, Amarildo Tabone Paschoalini, and Felipe Silva Bellucci	

Composite Structures Design and Analysis 217
Volnei Tita

Part III Applications

Piezoelectric Energy Harvesting 267
Carlos De Marqui Jr.

Piezoelectric Structural Vibration Control 289
Marcelo A. Trindade

Impedance-Based Structural Health Monitoring 311
Valder Steffen Jr. and Domingos Alves Rade

Damage Detection Systems for Commercial Aviation 329
Ricardo Pinheiro Rulli, Camila Gianini Gonzalez Bueno,
Fernando Dotta, and Paulo Anchieta da Silva

Introduction

Vicente Lopes Jr., Valder Steffen Jr., and Marcelo A. Savi

Nature should be the essential inspiration for researchers and engineers that try to develop systems and structures. The main inspirational point is certainly the adaptive behavior that provides the self-regulation ability. Through the history, human technology is always related to different materials and it is possible to recognize ages defined by some material invention: stone and metal, for instance. Recently, smart materials should be identified as the stimulus of a new age. Basically, smart materials have a coupling between mechanical and nonmechanical fields that confers the material a special kind of behavior. In this regard, it is possible to imagine numerous applications due to the coupling of fields that usually are not connected. The smart material age tries to exploit the idea to construct systems and structures with adaptive behavior that have the ability to change properties due to environmental changes and repairing themselves when necessary (Oliveira and Savi 2013).

Besides the term smart materials, it is also usually employed intelligent, adaptive, multifunctional, or active materials. Lagoudas (2008) defined active materials as a subgroup of multifunctional materials exhibiting sensing and actuation

V. Lopes Jr. (✉)
Department of Mechanical Engineering, UNESP—Universidade Estadual Paulista,
Ilha Solteira, SP, Brazil
e-mail: vicente@dem.feis.unesp.br

V. Steffen Jr.
School of Mechanical Engineering, Federal University of Uberlândia,
Campus Santa Monica, Uberlândia, MG 38400-892, Brazil
e-mail: vsteffen@ufu.br

M.A. Savi, Ph.D.
COPPE—Department of Mechanical Engineering, Universidade Federal do
Rio de Janeiro, Center for Nonlinear Mechanics, P.O. Box 68.503,
Rio de Janeiro, RJ 21.941.972, Brazil
e-mail: savi@mecanica.ufrj.br

capabilities. However, in general, it is possible to use the term smart or intelligent materials in order to express the materials that present couplings among different physical fields, and therefore, have adaptive characteristics that can be employed to adequate themselves to environmental changes.

Nowadays, the most used smart materials are the shape memory alloys, the piezoelectric materials, the magnetostrictive materials, and the electro- and magneto-rheological fluids (Oliveira and Savi 2013). These materials have the ability of changing their shape, stiffness, among other properties, through the imposition of electrical, electromagnetic, temperature, or stress fields. Variations of this kind of materials have been created, increasing even more the applicability of smart materials. In this regard, one could mention the ferromagnetic shape memory alloys, shape memory polymers, optical activated polymers, and optical fibers. Besides, it should be highlighted the combination of different kinds of materials in hybrid composites, promoting a synergistic use of smart materials. Recently, there is a tendency for the reduction of smart devices to micro- and nanoscales with the so-called MEMS and NEMS (micro-nano-electronic mechanical systems).

Smart materials are usually employed as sensors and actuators in smart structures. The choice of proper material for each application depends on many factors and two design drivers need to be highlighted (Lagoudas 2008): the actuation energy density and the actuation frequency of the material. In addition, smart materials can allow systems and structures to monitor their own integrity while in operation and throughout their lives, in the context of structural health monitoring—SHM—techniques (Park and Inman 2005).

Shape memory alloys (SMAs) present a mechanical-temperature coupling in such a way that they have the ability of recover a shape previously defined, when subjected to an appropriated thermomechanical loading process. When there is a restriction to the shape recovery, these alloys promote high restitution forces. The remarkable properties of SMAs are associated with phase transformations responsible for different thermomechanical behaviors of these alloys. Two different phases are possible in SMAs, namely austenite and martensite. Austenitic phase is stable at high temperatures and stress-free state presenting a single variant. On the other hand, martensitic phase is stable at low temperature in a stress-free state, being related to numerous variants. Phase transformation may be induced either by stress or by temperature.

Piezoelectric materials present a reciprocal electromechanical coupling and, once an electrical field is applied, the material exhibits a mechanical deformation; on the other hand, when the material undergoes a mechanical load, an electrical potential is generated. This reciprocity enables this kind of material to be used either as sensors or actuators in smart structures.

Magnetostrictive materials present a coupling between mechanical and magnetic fields. They can be defined as materials that present a shape change due to an application of a magnetic field. Magnetostriction was originally identified as a length change in an iron sample subjected to a magnetic field. This effect became known as Joule effect, being the most common mechanism employed in

magnetostrictive actuators. The reverse effect, when a mechanical field causes the sample magnetization, is known as Villari effect, being usually employed for sensors.

Electro-rheological (ER) and magneto-rheological (MR) fluids are known as controllable fluids. They present a coupling between mechanical and electro or magneto fields. Therefore, a change in an electro-magneto field causes a change in mechanical rheological behavior. An ER–MR fluid is a solid suspension that presents drastic changes in rheological properties due to structural arrangements in the suspension. Before the application of the electromagnetic field, particles are distributed in a random way, presenting a Newtonian behavior. The application of the electromagnetic field causes an orientation of the particles that changes the fluid viscosity, presenting a nonlinear response.

Dynamics of Smart Systems and Structures presents a general overview of smart material systems and structures. It is split in three parts: I—Fundamentals; II—Smart Materials; III—Applications. In Part I—Fundamentals, several concepts of smart materials are presented. Continuum Mechanics, Wave Motion in Elastic Structures, Passive and Active Structural Vibration Control, and Nonlinear Dynamics and Chaos are the main subjects presented in the first part of the book. Part II presents the Smart Materials: Piezoelectric Materials; Shape Memory Alloys; Electro-Magneto Rheological Materials; and Composite Materials. Part III discusses some applications. It is discussed Piezoelectric Energy Harvesting; Impedance-Based Structural Health Monitoring; and Damage Monitoring in Aircrafts.

This book represents an effort related to the First School of Smart Structures Engineering that was held in UNESP/Ilha Solteira – SP, Brazil, November 9–13, 2014. All the contributions were prepared thinking on the beginner students and engineers interested on Smart Material Systems and Structures. The authors hope that this introductory text may encourage, motivate and help readers to explore the interdisciplinary area of Smart Material Systems and Structures.

References

- D.C. Lagoudas, *Shape Memory Alloys: Modeling and Engineering Applications* (Springer, New York, 2008)
- S.A. Oliveira, M.A. Savi, Os Materiais Inteligentes e suas Aplicações. *Rev. Marít. Bras.* **133** (10–12), 39–56 (2013)
- G. Park, D.J. Inman, Impedance-Based Structural Health Monitoring, in *Damage Prognosis—For Aerospace, Civil and Mechanical Systems*, ed. by D.J. Inman, C.R. Farrar, V. Lopes Jr., V. Steffen Jr. (Wiley, New York, 2005)

Part I

Fundamentals

Continuum Mechanics

Marcelo A. Savi

Abstract This chapter presents an introduction of the fundamentals of continuum mechanics. It starts with a revision of tensor analysis that discusses the definition of tensor and coordinate transformations. In the sequence, continuum motion is treated discussing the kinematics or the geometry of motion. Definitions of strain tensors are of concern. Material derivative and Reynolds transport theorem is also treated. Afterward, a discussion about stress is presented presenting the Cauchy principle. The definition of stress tensors is established presenting Cauchy and Piola-Kirchhoff tensors. Conservation principles are then analyzed: linear and angular momentum; mass; and energy. The principle of entropy is also treated. After these definitions, it is presented a summary of fundamental equations of mechanics, discussing the importance of constitutive equations. The generalized standard material approach is discussed as a framework to elaborate constitutive equations that respect the thermodynamical principles. As examples, it is discussed the elasticity, elastoplasticity, and also smart materials phenomena as piezoelectricity, pseudoelasticity, and shape memory effect.

Keywords Continuum mechanics • Tensor analysis • Indicical notation • Thermodynamics • Conservation principle • Constitutive models • Elasticity

1 Introduction

Mechanics is the science that treats motions and forces, establishing the relations between them. In brief, it is possible to imagine that a body is subjected to external effects that can arise from different sources as forces, movements, interactions with other bodies, gravitational forces, chemical interactions, electromagnetic effects, thermal changes, among other possibilities.

M.A. Savi, Ph.D. (✉)
COPPE—Department of Mechanical Engineering, Center for Nonlinear Mechanics,
Universidade Federal do Rio de Janeiro, P.O. Box 68.503, Rio de Janeiro,
RJ 21.941.972, Brazil
e-mail: savi@mecanica.ufrj.br

Molecules and atoms compose the matter structure and the description of the interactions among them can define the mechanical description of motions and forces. Although appropriate, this point of view has the inconvenience of the huge number of equations to be treated. An alternative approach is to discard the atomistic structure of the matter, representing the physical phenomena by using a macroscopic point of view. This is the main idea of continuum mechanics that is limited to situations where the smallest characteristic length is much larger than the size of an atom.

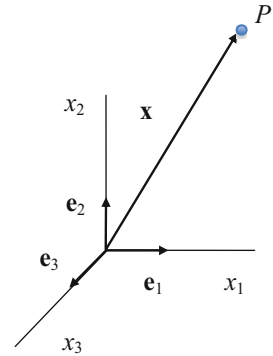
The study of continuum mechanics implies the use of tensor quantities and, because of that, it is important to have a background in tensor analysis. Continuum mechanics can be presented by introducing motion, treating the geometry of the movement, and forces that causes this motion. The conservation principles are the essential part of the mechanics defining the laws of nature. The mechanical problem is a well-posed system if constitutive equations are stated. They are built upon the main features of material behavior, establishing a connection among mechanical quantities based on experimental macroscopic observations.

This chapter presents a general overview of the fundamentals of continuum mechanics. The following references are employed: Borisneko and Tarapov (1968), Crandall et al. (1978), Currie (1974), Ertuk and Inman (2011), Eringen (1967), Fung (1965, 1969), Germain (1962), Gurtin (1981), Malvern (1969), Mase (1970), Reddy (2013), Shames (1992), Sokolnikoff (1956, 1964), Timoshenko and Goodier (1970), Valanis (1972), Ziegler (1977). Initially, it presents a brief overview of tensor analysis, presenting the index notation. The basic notion of motion is then presented, introducing the idea of deformation and strain tensors, material derivative and Reynolds transport theorem. Afterward, the influence of external forces is discussed introducing the concept of stress, presenting different representations. The conservation principles of mechanics are then discussed: linear and angular momenta, mass and energy conservations. The entropy principle is also discussed presenting the second law of thermodynamics. The necessity of the use of constitutive equations is presented and an approach to obtain these equations is shown. Some examples of constitutive models are treated: elasticity, elastoplasticity, piezoelectricity, pseudoelasticity and shape memory effect.

2 Tensor Analysis

Physical entities have different aspects and their mathematical representation needs to reflect their main characteristics. In this regard, an observation of some common mechanical systems allows one to identify scalar and vector quantities. Mass and temperature are typical scalar quantities while force and velocity are typical vector quantities. Observing carefully, it is possible to find other quantities that need a more complex representation. A generalization of physical quantities representation involves the definition of tensors. This generalization defines scalars as zero-order tensors, an entity that needs $1 = 3^0$ components to be represented; vectors are

Fig. 1 Cartesian frame



first-order tensors, an entity that needs $3 = 3^1$ components to be represented; and so on. Hence, an N -order tensor is an entity that needs 3^N components to be represented. Tensor may be understood as a mathematical entity that represents all kinds of physical quantities. In mathematical point of view, its definition is related to the algebra that represents a generalization of scalar and vector algebra.

The nature description usually needs the definition of a coordinate system in a chosen frame. Besides, nature laws should be independent of the choice of a coordinate system. Cartesian coordinate frame is probably the most common reference frame, being close related to our physical intuition. The main idea is to represent a point in an N -dimensional space by a set of N numbers. In the usual 3D (3-dimensional) space, the representation corresponds to (x_1, x_2, x_3) . This representation is similar to consider a position vector, \mathbf{x} , that can be described by using a Cartesian basis (Fig. 1):

$$\mathbf{x} = (x_1, x_2, x_3) = x_1 \mathbf{e}_1 + x_2 \mathbf{e}_2 + x_3 \mathbf{e}_3 \quad (1)$$

where \mathbf{e}_1 , \mathbf{e}_2 , and \mathbf{e}_3 are the basis vectors.

This equation suggests different ways to represent a tensor quantity. Symbolic representation is related to symbols that describe the tensor and all its operations. In this example, \mathbf{x} is a symbolic representation of the vector. On the other hand, it is possible to represent the vector by its components, x_i . In this case, it is implicit that index i varies from 2.1 to 2.3.

Index notation establishes a compact way to deal with tensor calculus. Summation convention is a usual way to facilitate the representation of all tensor operations. Essentially, this convention establishes that the repetition of an index denotes a summation with respect to that index over its range (1, 2, 3 in 3D space). An index that is summed is called *dummy* index. The one that is not summed is called *free* index. Under this assumption, the vector representation is the following:

$$\mathbf{x} \equiv x_i \mathbf{e}_i \quad (2)$$

Note that this is equivalent to: $x_i \mathbf{e}_i = \sum_{i=1}^3 x_i \mathbf{e}_i$.

Since a dummy index just indicates summation, it does not matter what symbol is used. Therefore,

$$\mathbf{x} \equiv x_i \mathbf{e}_i = x_k \mathbf{e}_k = x_j \mathbf{e}_j \quad (3)$$

An important point should be highlighted in terms of summation convention. It is not possible to use more than two dummy indexes since it implies an inconsistent representation.

An N -order tensor can be represented as \mathbf{A} in symbolic notation or as follows, using N indexes:

$$\mathbf{A} \equiv A_{ijkl\dots} \quad (4)$$

It should be pointed out that a tensor is an abstract object whose properties are independent of reference frame used to describe the object. A tensor is represented by its components and therefore, there is a transformation law that connects different frames.

All tensors operations can be represented by the use of index notation. Nevertheless, it is important to define some tensors that help this representation.

2.1 Kronecker Delta Tensor

Kronecker delta is a second-order tensor equivalent to the identity matrix, being defined as follows:

$$\delta_{ij} = \begin{cases} 1, & \text{if } i = j \\ 0, & \text{if } i \neq j \end{cases} \quad (5)$$

An important characteristic of the Kronecker delta is to represent the scalar product of a Cartesian basis vectors:

$$\mathbf{e}_i \cdot \mathbf{e}_j = \delta_{ij} \quad (6)$$

In this regard, observe that the scalar product between two vectors is given by:

$$\mathbf{u} \cdot \mathbf{v} = u_i \mathbf{e}_i \cdot v_j \mathbf{e}_j = u_i v_j (\mathbf{e}_i \cdot \mathbf{e}_j) = u_i v_j \delta_{ij} = u_i v_i \quad (7)$$

Here it is important to highlight a special characteristic of the Kronecker delta tensor—the index change. Since when $i \neq j$ its value vanishes, it is possible to neglect all possibilities different from $i = j$ in the summation. This is equivalent to change the index.

2.2 Permutation Tensor

Permutation tensor is a third-order tensor defined as follows:

$$\xi_{ijk} = \begin{cases} 0, & \text{if there are any equal indexes (112, 121, 233, \dots)} \\ +1, & \text{for even permutation (123, 312, 231, \dots)} \\ -1, & \text{for odd permutation (132, 321, 213, \dots)} \end{cases} \quad (8)$$

An important characteristic of the permutation tensor is to represent the vector product of Cartesian basis vectors:

$$\mathbf{e}_i \times \mathbf{e}_j = \xi_{ijk} \mathbf{e}_k \quad (9)$$

In this regard, observe that the vector product between two vectors is given by:

$$\mathbf{u} \times \mathbf{v} = u_i \mathbf{e}_i \times v_j \mathbf{e}_j = u_i v_j (\mathbf{e}_i \times \mathbf{e}_j) = \xi_{ijk} u_i v_j \mathbf{e}_k \quad (10)$$

The ξ - δ identity establishes a relationship between the permutation symbol and the Kronecker delta:

$$\xi_{miq} \xi_{jkq} = \delta_{mj} \delta_{ik} - \delta_{mk} \delta_{ij} \quad (11)$$

2.3 Coordinate Transformations

Since a physical quantity, as a velocity, is an intrinsic property of the body, it needs to present an invariance related to reference frame. Nevertheless, its representation is dependent of this frame. Therefore, it is important to map the variation between them, defining a proper relationship. In this regard, consider a vector quantity represented by $\mathbf{v} = v_i$. Two different frames are employed to describe this vector: original, X_i , and new, x_i . Figure 2 shows this situation presenting a vector \mathbf{v} and two reference frames.

The representation of the vector can be done as follows:

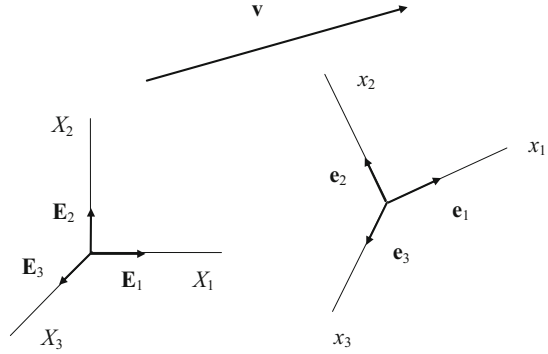
$$\mathbf{v} \equiv V_i \mathbf{E}_i \quad (\text{original frame}) \quad (12)$$

$$\mathbf{v} \equiv v_i \mathbf{e}_i \quad (\text{new frame}) \quad (13)$$

Since the vector is the same, it is possible to write

$$\mathbf{v} \equiv V_i \mathbf{E}_i = v_i \mathbf{e}_i \quad (14)$$

Fig. 2 Vector representation in different frames



Performing a scalar product with \mathbf{E}_j :

$$V_i \mathbf{E}_i \cdot \mathbf{E}_j = v_i \mathbf{e}_i \cdot \mathbf{E}_j \quad (15)$$

Since the following expressions are valid,

$$\mathbf{E}_i \cdot \mathbf{E}_j = \delta_{ij} \quad (16)$$

$$\mathbf{e}_i \cdot \mathbf{E}_j = Q_{ij} = \cos(\mathbf{e}_i, \mathbf{E}_j) \quad (17)$$

the transformation from the new to the original frame is given by

$$V_j = Q_{ij} v_i \quad (18)$$

The inverse transformation, from the original to the new frame, can be obtained in an analogous way by performing the scalar product of \mathbf{e}_j :

$$V_i \mathbf{E}_i \cdot \mathbf{e}_j = v_i \mathbf{e}_i \cdot \mathbf{e}_j \quad (19)$$

since,

$$\mathbf{e}_i \cdot \mathbf{e}_j = \delta_{ij} \quad (20)$$

$$\mathbf{E}_i \cdot \mathbf{e}_j = \cos(\mathbf{E}_i, \mathbf{e}_j) = Q_{ji} \quad (21)$$

the transformation is given by

$$v_j = Q_{ji} V_i \quad (22)$$

Note that, transformation matrices define both operations, being formed by the angles between both frames. Since orthogonal systems are adopted, the inverse is related to the transpose of the transformation matrices. Figure 3 illustrates the transformation between two reference frames.

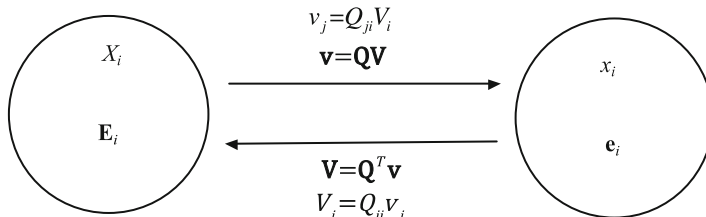


Fig. 3 Transformation between two reference frames

Similar transformations can be defined for higher order tensors. By considering that a second-order tensor is built from vectors, it is possible to write:

$$C_{ij} = A_i B_j = a_i b_j \quad (23)$$

Since,

$$\begin{aligned} A_i &= Q_{ki} a_k \\ B_j &= Q_{mj} b_m \end{aligned} \quad (24)$$

the transformation of the second-order tensor is then given by:

$$C_{ij} = (Q_{ki} a_k) (Q_{mj} b_m) = Q_{ki} Q_{mj} (a_k b_m) = Q_{ki} Q_{mj} c_{km} \quad (25)$$

The generalization for a N -order tensor is automatic:

$$C_{ijk\dots} = Q_{mj} Q_{nj} Q_{ok} \dots c_{mno\dots} \quad (26)$$

3 Motion

The kinematics analysis is related to the geometry of the motion being an essential part of the mechanical modeling. In this regard, consider a continuum body that evolves from an original, initial, or reference configuration to new positions due to the action of some external stimulus. This stimulus does not matter in the geometrical analysis. In order to map the continuum evolution, it is necessary to establish the relationship between its initial and subsequent states. Two frames are considered for this aim (Fig. 4): original or initial and deformed configurations.

In general, the motion can be split into rigid body (translation and rotation) and local strain that represent the relative motion. In order to map the body evolution, consider the position of two points in the original configuration at t_0 , A and B , that evolves to the deformed configuration at instant t_1 , being represented by A' and B' . It should be pointed out that reference frame has an important aspect in the

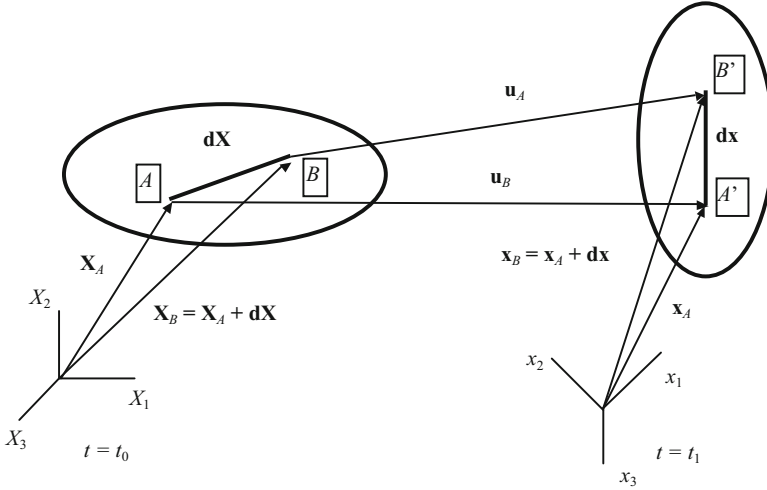


Fig. 4 Continuum motion

description. It is possible to use either original (X_i) or deformed (x_i) frames to describe each quantity involved. Besides, two descriptions are possible: *material* or *Lagrangian* description; and *spatial* or *Eulerian* description.

Material or *Lagrangian* description is essentially based on material points and therefore assumes that initial state is known. The idea is to map a general position of a specific material point from its initial position:

$$x_i = x_i(X_i, t) \quad (27)$$

On the other hand, *spatial* or *Eulerian* description is essentially based on a specific location. Hence, a position is known, and one needs to map the initial configuration of this spatial point. Note that the spatial description is, in general, related to different material points at different times.

$$X_i = X_i(x_i, t) \quad (28)$$

Motion analysis maps the deformed configuration from the original one (or vice-versa) and the description of the segments dX_i and dx_i allows one to evaluate how the motion evolves. The evaluation of this evolution implies the definition of the *material deformation gradient*, F_{ij} :

$$dx_i = \frac{\partial x_i}{\partial X_j} dX_j = F_{ij} dX_j \quad (29)$$

Similar definition is established for the *spatial deformation gradient*, H_{ij} :

$$dX_i = \frac{\partial X_i}{\partial x_j} dx_j = H_{ij} dx_j \quad (30)$$

Note that these tensors define the mapping between the two configurations, and therefore one is the inverse of the other:

$$F_{ik} H_{kj} = \frac{\partial x_i}{\partial X_k} \frac{\partial X_k}{\partial x_j} = \delta_{ij} \quad (31)$$

The Jacobian of the transformation is defined as the determinant of the *material deformation gradient*, F_{ij} :

$$J \equiv \det(F_{ij}) = \xi_{ijk} \frac{\partial x_1}{\partial X_i} \frac{\partial x_2}{\partial X_j} \frac{\partial x_3}{\partial X_k} \quad (32)$$

The Jacobian establishes a relationship between original and deformed volumes.

$$dv = J dV \quad (33)$$

Based on these definitions, it is possible to establish a proper motion description and the definition of deformation and strain are essential. A metric should be used for this aim. Here, two possible situations are treated and each one of them can be described using either the original or the deformed frame. Another important aspect related to the motion description is the definition of the displacement vector:

$$u_i = x_i - X_i \quad (34)$$

The definitions of the displacement gradients are given by the following expressions, being respectively presented with respect to original and deformed configurations:

$$\nabla_x \mathbf{u} = \frac{\partial u_i}{\partial x_j} = \frac{\partial x_i}{\partial x_j} - \frac{\partial X_i}{\partial x_j} = F_{ij} - \delta_{ij} \quad (35)$$

$$\nabla_X \mathbf{u} \equiv \frac{\partial u_i}{\partial X_j} = \frac{\partial x_i}{\partial X_j} - \frac{\partial X_i}{\partial X_j} = \delta_{ij} - H_{ij} \quad (36)$$

3.1 Deformation Tensors

Deformation tensors can be defined from a specific metric. In essence, consider the vector dX_i and dx_j that has, respectively, the magnitudes dS and ds . It is convenient to establish the following definitions:

$$dS^2 = dX_k dX_k = H_{ki} H_{kj} dx_i dx_j = c_{ij} dx_i dx_j \quad (37)$$

$$ds^2 = dx_k dx_k = F_{ki} F_{kj} dX_i dX_j = C_{ij} dX_i dX_j \quad (38)$$

Based on these metrics, two deformation tensors are defined:

$$C_{ij} = F_{ki} F_{kj} \quad \text{Green's deformation tensor} \quad (39)$$

$$c_{ij} = H_{ki} H_{kj} \quad \text{Cauchy's deformation tensor} \quad (40)$$

The displacement vector can be employed to rewrite these tensors as follows:

$$C_{ij} = F_{ki} F_{kj} = \left(\frac{\partial u_k}{\partial X_i} + \delta_{ki} \right) \left(\frac{\partial u_k}{\partial X_j} + \delta_{kj} \right) = \frac{\partial u_i}{\partial X_j} + \frac{\partial u_j}{\partial X_i} + \frac{\partial u_k}{\partial X_i} \frac{\partial u_k}{\partial X_j} + \delta_{ij} \quad (41)$$

$$c_{ij} = H_{ki} H_{kj} = \left(\delta_{ki} - \frac{\partial u_k}{\partial x_i} \right) \left(\delta_{kj} - \frac{\partial u_k}{\partial x_j} \right) = \delta_{ij} - \frac{\partial u_i}{\partial x_j} - \frac{\partial u_j}{\partial x_i} + \frac{\partial u_k}{\partial x_i} \frac{\partial u_k}{\partial x_j} \quad (42)$$

3.2 Strain Tensors

In an analogous way, strain tensors can be defined by using a different metric.

$$ds^2 - dS^2 = dx_i dx_i - dX_i dX_i = (C_{ij} - \delta_{ij}) dX_i dX_j = 2E_{ij} dX_i dX_j \quad (43)$$

$$ds^2 - dS^2 = dx_i dx_i - dX_i dX_i = (\delta_{ij} - c_{ij}) dx_i dx_j = 2e_{ij} dx_i dx_j \quad (44)$$

Based on these metrics, two strain tensors are defined:

$$2E_{ij} = C_{ij} - \delta_{ij} \quad \text{Lagrange's strain tensor} \quad (45)$$

$$2e_{ij} = \delta_{ij} - c_{ij} \quad \text{Euler's deformation tensor} \quad (46)$$

Once again, the displacement vector can be employed to rewrite the strain tensors as follows:

$$E_{ij} = \frac{1}{2} \left(\frac{\partial u_i}{\partial X_j} + \frac{\partial u_j}{\partial X_i} + \frac{\partial u_k}{\partial X_i} \frac{\partial u_k}{\partial X_j} \right) \quad (47)$$

$$c_{ij} = \frac{1}{2} \left(\frac{\partial u_i}{\partial x_j} + \frac{\partial u_j}{\partial x_i} - \frac{\partial u_k}{\partial x_i} \frac{\partial u_k}{\partial x_j} \right) \quad (48)$$

3.3 Infinitesimal Strain Tensors

A usual approximation in terms of strain description is the infinitesimal strains. Basically, two essential simplifications are adopted for this aim. The first one is related to the fact that both configurations (original and deformed) are the same. Hence, X_i and x_i are the same, being represented by x_i . Besides, the nonlinear terms of the strain definitions are neglected. Hence, the following definitions can be presented for the infinitesimal Lagrange-Euler tensor:

$$\hat{E}_{ij} = \hat{e}_{ij} = \frac{1}{2} \left(\frac{\partial u_i}{\partial x_j} + \frac{\partial u_j}{\partial x_i} \right) \quad (49)$$

While the infinitesimal Green and Cauchy's tensors are given by:

$$\hat{C}_{ij} = \frac{\partial u_i}{\partial x_j} + \frac{\partial u_j}{\partial x_i} + \delta_{ij} \quad (50)$$

$$\hat{c}_{ij} = \delta_{ij} - \frac{\partial u_i}{\partial x_j} - \frac{\partial u_j}{\partial x_i} \quad (51)$$

An intuitive form of understanding the consequences of the infinitesimal strain simplification is observing that the displacement gradient, a second-order tensor, can be written as a combination of a symmetric and an anti-symmetric tensor:

$$\frac{\partial u_i}{\partial x_j} = \frac{1}{2} \left(\frac{\partial u_i}{\partial x_j} + \frac{\partial u_j}{\partial x_i} \right) + \frac{1}{2} \left(\frac{\partial u_i}{\partial x_j} - \frac{\partial u_j}{\partial x_i} \right) = \hat{E}_{ij} + \hat{\omega}_{ij} \quad (52)$$

where $\hat{\omega}_{ij}$ is an anti-symmetric tensor related to rotation. Since,

$$\frac{\partial u_j}{\partial x_i} = \hat{E}_{ij} - \hat{\omega}_{ij} \quad (53)$$

the Lagrange's strain tensor can be written in terms of the infinitesimal strains as follows:

$$E_{ij} = \frac{1}{2} [(\hat{E}_{ij} + \hat{\omega}_{ij}) + (\hat{E}_{ij} - \hat{\omega}_{ij}) + (\hat{E}_{ki} + \hat{\omega}_{ki})(\hat{E}_{kj} + \hat{\omega}_{kj})] \quad (54)$$

which results to,

$$E_{ij} = \hat{E}_{ij} + \frac{1}{2} [\hat{E}_{ki}\hat{E}_{kj} + \hat{E}_{ki}\hat{\omega}_{ki} + \hat{E}_{kj}\hat{\omega}_{ki} + \hat{\omega}_{ki}\hat{\omega}_{kj}] \quad (55)$$

Based on that, $E_{ij} = \hat{E}_{ij}$ if there are infinitesimal strains and rotations.

3.4 Principal Strains

All tensors obey the coordinate transformation defined in the previous section. Since strain tensors are second-order tensors, their transformation are represented by:

$$\varepsilon'_{ij} = Q_{ik}Q_{jm}\varepsilon_{km} \quad (56)$$

where the symbol ε'_{ij} represents any strain or deformation tensor at a general configuration while ε_{km} is the same tensor in the initial configuration. There is a special transformation that has as characteristic that the strain vector is aligned with the normal vector. This situation is investigated from the eigenvalue problem. Figure 5 shows a geometrical interpretation of an eigenvalue problem that governs this situation. Note that in 2D space, there are two possible situations for the alignment state.

$$(\varepsilon_{ij} - \lambda\delta_{ij})n_j = 0 \quad (57)$$

The eigenvalue problem is a search for non-trivial situations, established by:

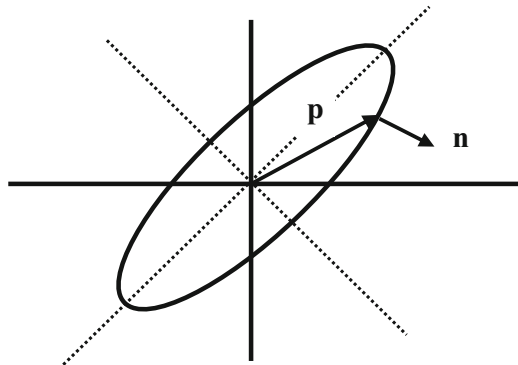
$$\det(\varepsilon_{ij} - \lambda\delta_{ij}) = 0$$

This situation establishes the characteristic polynomial:

$$\lambda^3 - I_\varepsilon\lambda^2 + II_\varepsilon\lambda - III_\varepsilon = 0 \quad (58)$$

where I_ε , II_ε , III_ε are the tensor invariants that are unchanged under coordinate transformation, defined as follows:

Fig. 5 Geometrical interpretation of the eigenvalue problem



$$\begin{aligned}
I_\varepsilon &= \varepsilon_{ii} \\
II_\varepsilon &= \frac{1}{2}(\varepsilon_{ii}\varepsilon_{jj} - \varepsilon_{ij}\varepsilon_{ji}) \\
III_\sigma &= \xi_{ijk}\varepsilon_{1i}\varepsilon_{2j}\varepsilon_{3k} \equiv \det(\varepsilon)
\end{aligned} \tag{59}$$

3.5 Material Derivative and Reynolds Transport Theorem

The physical definition of time derivative is essentially related to the material or Lagrangian description since the time limit of a certain quantity is evaluated at a specific X , being related to the same material point. This is different to evaluate the limit at a spatial point x , since distinct material points are at this point at different times. In this regard, it is essential to establish a proper definition of time derivative that is called *material derivative*. Let $\varphi = \varphi(t)$ be a function of time. Its time derivative is, by definition:

$$\frac{D\varphi}{Dt} = \left. \frac{\partial\varphi}{\partial t} \right|_x \tag{60}$$

which is essentially related to a material description. Nevertheless, by considering spatial description, the time derivative consists of two parts: the local change and the change due to the particle motion. This can be evaluated by considering the chain rule as follows:

$$\frac{D\varphi}{Dt} = \left. \frac{\partial\varphi}{\partial t} \right|_x + \frac{\partial\varphi}{\partial x_i} \frac{\partial x_i}{\partial t} = \frac{\partial\varphi}{\partial t} + v_i \frac{\partial\varphi}{\partial x_i} \tag{61}$$

Note that the first term is a *local or spatial derivative* while the second term is the *convective derivative*, since $v_i = \partial x_i / \partial t$ is the velocity. This term allows one to follow the particle, establishing a proper definition of the time derivative.

Consider a quantity Φ that is represented by its specific value φ in such a way that:

$$\Phi = \int_V \varphi dv \tag{62}$$

The material derivative of this quantity is given by:

$$\frac{D\Phi}{Dt} = \frac{D}{Dt} \left(\int_V \varphi dv \right) = \frac{D}{Dt} \left(\int_V \varphi J dV \right) = \int_V \left(\frac{D\varphi}{Dt} J + \frac{DJ}{Dt} \varphi \right) dV \tag{63}$$

since $\frac{DJ}{Dt} = J \frac{\partial v_k}{\partial x_k}$ the following expression is obtained, being known as the *Reynolds transport theorem*:

$$\frac{D}{Dt} \left(\int_V \varphi dv \right) = \int_V \left(\frac{D\varphi}{Dt} + \varphi \frac{\partial v_i}{\partial x_i} \right) dv \quad (64)$$

By using the definition of material derivative, it is possible to rewrite this equation as follows:

$$\frac{D}{Dt} \left(\int_V \varphi dv \right) = \int_V \left(\frac{\partial \varphi}{\partial t} + \frac{\partial}{\partial x_i} (\varphi v_i) \right) dv \quad (65)$$

4 Stress

The geometry of the continuum motion was mainly discussed until this moment. Now, a different perspective is investigated incorporating the forces that are causing this motion. Basically, contact and body forces can be imagined. Consider a continuum subjected to external forces, $\mathbf{f}^{(k)}$ (Fig. 6). It is important to consider a portion of the continuum body, defined by an arbitrary volume V , surrounded by an area A . As a consequence, forces are transmitted from one portion to another establishing an interaction between internal and external portions.

Hence, consider an arbitrary area that defines two portions. The interaction between them occurs at area A , defined by the unit normal vector, n_i . Then, a generic point P of an area element ΔA of A is subjected to a resultant force Δf_i . The average of the force per unit of area is given by $\Delta f_i / \Delta A$. The *Cauchy's stress principle* establishes that this average tends to a value at P when the area ΔA tends to zero. Based on that, the stress vector t_i at P is defined as follows:

$$t_i = \lim_{\Delta A \rightarrow 0} \frac{\Delta f_i}{\Delta A} \quad (66)$$

At point P , there is a vector t_i associated with a normal vector n_i , $t_i = t_i(n_i)$. Since there are an infinite number of possibilities of the normal vector, there are an infinite

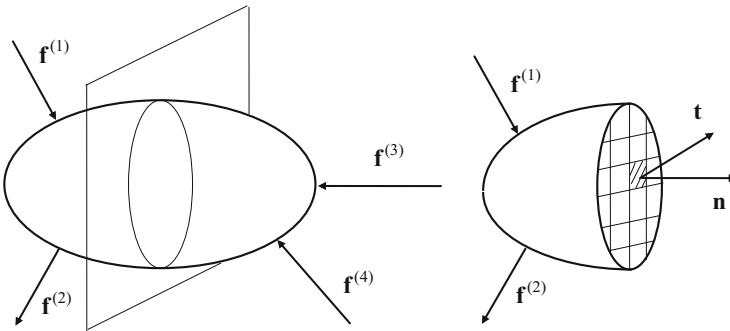


Fig. 6 Continuum media subjected to external forces

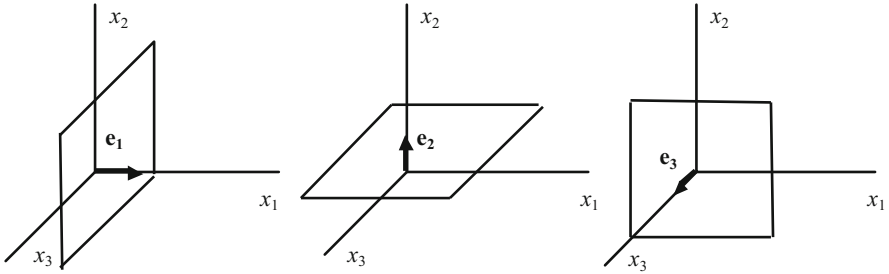


Fig. 7 Three linear independent cuts

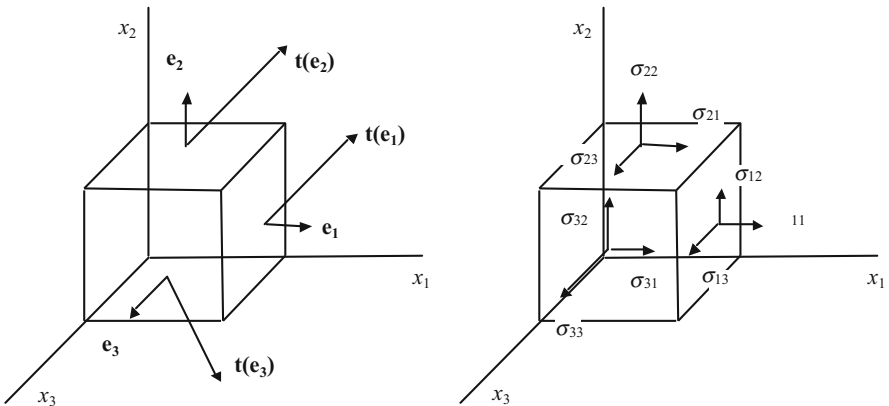


Fig. 8 State of stress

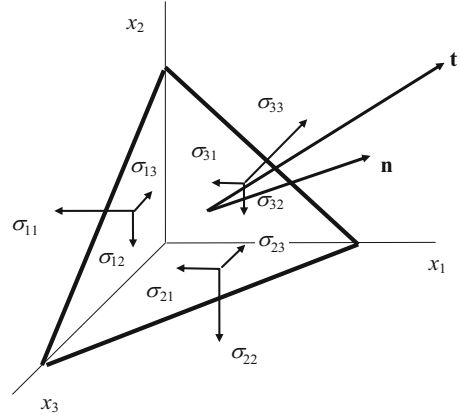
number of stress vector at this point. The totality of possibilities defines a *stress state* that can be completely defined by three normal vectors, evaluated in linear independent directions (Fig. 7). This is equivalent to enclose the point P inside a cubic element (Fig. 8). The projections of each stress vector define the *Cauchy's stress tensor*.

$$\sigma_{ij} = t_j(\mathbf{e}_i) \mathbf{e}_j \tag{67}$$

4.1 Coordinate Transformations

Once the stress state is defined from three different stress vectors, any vector is known by considering coordinate transformations. Hence, consider an arbitrary area, expressed by a normal vector, which defines a tetrahedron that encloses the specific point where the stress state is considered (Fig. 9). By performing the summation of each direction yields to:

Fig. 9 Arbitrary stress vector



$$t_i dA = \sigma_{ji} dA_j \tag{68}$$

since $dA_j = n_j dA$ it is possible to establish a relationship between the stress vector at an arbitrary area and the stress tensor, known as *Cauchy's stress formula*:

$$t_i = \sigma_{ji} n_j \tag{69}$$

4.2 Principal Stress

Since the stress tensor is a second-order tensor, its coordinate change is similar to the one presented for strain tensor. Therefore, similar analysis can be done in terms of principal stress that are defined by the eigenvalue problem,

$$(\sigma_{ij} - \lambda \delta_{ij}) n_j = 0 \tag{70}$$

which establishes the characteristic polynomial,

$$\lambda^3 - I_\sigma \lambda^2 + II_\sigma \lambda - III_\sigma = 0 \tag{71}$$

where $I_\sigma, II_\sigma, III_\sigma$ are the stress invariants.

4.3 Piola-Kirchhoff Tensors

The Cauchy's stress tensor treated until now considers that both the normal vector and the area are evaluated in the deformed configuration. This is a particular situation that can be conveniently changed when necessary. Hence, consider a

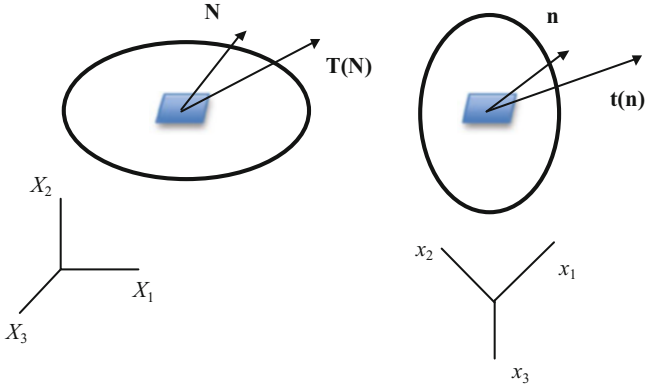


Fig. 10 Different representations of the stress vector

force f_i that can be expressed in terms of the stress vector either of the deformed configuration or of the undeformed configuration. Figure 10 shows this idea considering two different configurations and the definition of stress vectors at both configurations.

Based on that, it is possible to write:

$$f_i = t_i da = T_i dA \tag{72}$$

Each of the stress vectors can be related to stress tensors as follows:

$$t_i = \sigma_{ji} n_j \tag{73}$$

$$T_i = \hat{S}_{ji} N_j \tag{74}$$

where a new stress tensor \hat{S}_{ji} , known as the *first Piola-Kirchhoff tensor*, is defined from the normal vector at the undeformed configuration. On this basis, it is possible to write:

$$\sigma_{ji} n_j da = \hat{S}_{ij} N_j dA \tag{75}$$

Since the relation between areas is given by: $n_j da = JH_{kj} N_k dA$

It follows that:

$$(\sigma_{ji} JH_{kj} - \hat{S}_{ij} \delta_{kj}) N_k dA = 0 \tag{76}$$

and the *first Piola-Kirchhoff stress tensor* is given by

$$\hat{S}_{ij} = J \sigma_{ik} H_{jk} \tag{77}$$

Hence, this tensor is defined at the undeformed configuration from a force at the deformed configuration, having mixture characteristics. In order to use a force at the undeformed configuration, an extra coordinate transformation can be done, defining the *second Piola-Kirchhoff stress tensor*,

$$S_{mk} = H_{mi} \hat{S}_{ki} = JH_{mi} \sigma_{ik} H_{jk} \quad (78)$$

5 Conservation Principles

The conservation principles of mechanics involve laws that govern the general interaction between forces and motions, representing the nature laws. In essence, these principles are:

1. Conservation of linear momentum
2. Conservation of angular momentum
3. Conservation of mass
4. Conservation of energy

The conservation of linear momentum is the Newton's second law while the conservation of energy is the first law of thermodynamics. To these principles, it is important to add the principle of entropy, associated with the second law of thermodynamics, in order to obtain a proper description of mechanical processes. The following sections present these conservation laws.

5.1 Conservation of Linear Momentum

The conservation of linear momentum establishes the balance between linear momentum and external forces acting in a body represented by surface, t_i , and body, b_i , forces. The *Newton's second law* can be written as follows:

$$\frac{D}{Dt}(G_i) = T_i + B_i \quad (79)$$

where

$$G_i = \int_V \rho v_i dv \quad \text{Linear momentum}$$

$$T_i = \int_A t_i da \quad \text{Surface force}$$

$$B_i = \int_V b_i dv \quad \text{Body forces}$$

Using the integral form, the Newton's second law is written as follows:

$$\frac{D}{Dt} \int_V \rho v_i dv = \int_A t_i da + \int_V b_i dv \quad (80)$$

The divergence theorem can be evoked in order to transform the area integral into volume integral,

$$\int_A t_i da = \int_A \sigma_{ji} n_j da = \int_V \frac{\partial \sigma_{ji}}{\partial x_j} dv \quad (81)$$

Based on that, the conservation principle is given by:

$$\int_V \left[\frac{\partial \sigma_{ji}}{\partial x_j} + b_i - \rho \ddot{u}_i \right] dv = 0 \quad (82)$$

The local form of the linear momentum conservation establishes that the principle is valid for arbitrarily small neighborhood, being written as follows:

$$\frac{\partial \sigma_{ji}}{\partial x_j} + b_i - \rho \ddot{u}_i = 0 \quad (83)$$

5.2 Conservation of Angular Momentum

The conservation of angular momentum establishes the balance between angular momentum and external moments acting in a body. From the second Newton's law, it is possible to write the following equation where \mathbf{p} is the position vector with respect to a specific point O .

$$\mathbf{p} \times \frac{D}{Dt} (\mathbf{G}) = \mathbf{p} \times \mathbf{T} + \mathbf{p} \times \mathbf{B} \quad (84)$$

In this regard, it is important to define the angular momentum as follows:

$$\overline{G}_i^0 = \int_V \rho \xi_{ikl} x_k v_l dv \equiv \int_V \mathbf{p} \times \rho \mathbf{v} dv \quad \text{Angular momentum}$$

The balance of angular momentum and external forces are given by:

$$\int_V \xi_{ijk} x_j \rho \ddot{u}_k dv = \int_A \xi_{ijk} x_j t_k da + \int_V \xi_{ijk} x_j b_k dv \quad (85)$$

The divergence theorem is evoked in order to transform the area integral into volume integral:

$$\begin{aligned} \int_A \xi_{ijk} x_j t_k da &= \int_A \xi_{ijk} x_j \sigma_{mk} n_m da = \int_V \frac{\partial}{\partial x_m} (\xi_{ijk} x_j \sigma_{mk}) dv \\ &= \int_V \xi_{ijk} \left(\frac{\partial x_j}{\partial x_m} \sigma_{mk} + \frac{\partial \sigma_{mk}}{\partial x_m} x_j \right) dv = \int_V \xi_{ijk} \left(\sigma_{jk} + \frac{\partial \sigma_{mk}}{\partial x_m} x_j \right) dv \end{aligned} \quad (86)$$

Based on that, the conservation principle is given by:

$$\int_V \left[\xi_{ijk} \sigma_{jk} + \xi_{ijk} x_j \left(\frac{\partial \sigma_{mk}}{\partial x_m} + b_k - \rho \ddot{u}_k \right) \right] dv = 0 \quad (87)$$

This equation contains the conservation of linear momentum. Therefore, the conservation of angular momentum establishes the balance of moments:

$$\int_V \xi_{ijk} \sigma_{jk} dv = 0 \quad (88)$$

The local form of the conservation of angular momentum establishes that:

$$\xi_{ijk} \sigma_{jk} = 0 \quad (89)$$

which means that the Cauchy's tensor is symmetric:

$$\sigma_{jk} = \sigma_{kj} \quad (90)$$

Note that other stress tensors cannot be considered symmetric by definition. By observing the Piola-Kirchhoff tensors, for instance, it is possible to observe that the second tensor is symmetric but the first is not.

5.3 Conservation of Mass

The conservation of mass establishes that the mass of a body, m , is unchanged during the motion. This principle may be expressed by the material derivative as follows:

$$\frac{D}{Dt}(m) = 0 \quad (91)$$

where the mass is defined from the material density:

$$m = \int_V \rho \, dv$$

Using an integral equation,

$$\frac{D}{Dt} \int_V \rho \, dv = 0 \quad (92)$$

This implies a direct application of the Reynolds transport theorem,

$$\frac{D}{Dt} \left(\int_V \rho \, dv \right) = \int_V \left(\frac{\partial \rho}{\partial t} + \frac{\partial}{\partial x_i} (\rho v_i) \right) dv = 0 \quad (93)$$

The local form of the mass conservation establishes that:

$$\frac{\partial \rho}{\partial t} + \frac{\partial}{\partial x_i} (\rho v_i) = 0 \quad (94)$$

5.4 Conservation of Energy

The energy conservation is related to the first law of thermodynamics that establishes that the rate of change of body energy needs to balance with the rate of external work and all other energies that enter or leave the body. In general, assuming that K is the kinetic energy, U is the internal energy, W is the rate of work (power) of external forces, Q is the heat flux, and R is the rate of heat generation, the following balance should be established:

$$\frac{D}{Dt} (K + U) = W + Q + R \quad (95)$$

By defining the energy quantities as integral expressions,

$$K = \int_V \frac{\rho}{2} v_i v_i \, dv \quad \text{Kinetic energy} \quad (96)$$

$$U = \int_V \rho \vartheta \, dv \quad \text{Internal energy} \quad (97)$$

$$W = \int_A t_i v_i \, da + \int_V b_i v_i \, dv \quad \text{Power of external forces} \quad (98)$$

$$Q = - \int_A q_i n_i da \quad \text{Heat flux} \quad (99)$$

$$R = \int_V \rho r dv \quad \text{Heat generation} \quad (100)$$

Using these expressions on the first law of thermodynamics,

$$\frac{D}{Dt} \int_V \rho \left(\frac{v_i v_i}{2} + \vartheta \right) dv = - \int_A q_i n_i da + \int_A t_i v_i da \int_V b_i v_i dv + \int_V \rho r dv \quad (101)$$

The left hand of the equation implies the use of the Reynolds transport theorem:

$$\frac{D}{Dt} \int_V \rho \left(\frac{v_i v_i}{2} + \vartheta \right) dv = \int_V \left[\rho \frac{D}{Dt} \left(\frac{v_i v_i}{2} + \vartheta \right) + \left(\frac{v_i v_i}{2} + \vartheta \right) \left(\frac{D\rho}{Dt} + \rho \frac{\partial v_i}{\partial x_i} \right) \right] dv \quad (102)$$

Since the last term is related to the conservation of mass (needs to vanish), this equation is reduced to:

$$\frac{D}{Dt} \int_V \rho \left(\frac{v_i v_i}{2} + \vartheta \right) dv = \int_V \rho \frac{D}{Dt} \left(\frac{v_i v_i}{2} + \vartheta \right) dv \quad (103)$$

The area integrals need to be transformed into volume integrals with the aid of the divergence theorem. Hence,

$$- \int_A q_i n_i da = - \int_V \frac{\partial q_i}{\partial x_i} dv \quad (104)$$

$$\int_A t_i v_i da = \int_A \sigma_{ji} n_j v_i da = \int_V \frac{\partial (\sigma_{ji} v_i)}{\partial x_j} dv \quad (105)$$

The energy conservation is then rewritten as:

$$\int_V \left[\rho \frac{D}{Dt} \left(\frac{v_i v_i}{2} + \vartheta \right) + \frac{\partial q_i}{\partial x_i} - b_i v_i - \frac{\partial (\sigma_{ji} v_j)}{\partial x_i} - \rho r \right] dv = 0 \quad (106)$$

The local form of the conservation of energy is then given by:

$$\rho \frac{D}{Dt} \left(\frac{v_i v_i}{2} + \vartheta \right) + \frac{\partial q_i}{\partial x_i} - b_i v_i - \frac{\partial (\sigma_{ji} v_j)}{\partial x_i} - \rho r = 0 \quad (107)$$

Since,

$$\rho \frac{D}{Dt} \left(\frac{v_i v_i}{2} + \vartheta \right) = \rho \frac{D\vartheta}{Dt} + \rho \left(v_i \frac{Dv_i}{Dt} \right) \quad (108)$$

$$\frac{\partial(\sigma_{ji} v_j)}{\partial x_i} = \frac{\partial \sigma_{ji}}{\partial x_i} v_j + \sigma_{ji} \frac{\partial v_j}{\partial x_i} \quad (109)$$

the equation can be rewritten and, using the conservation of linear momentum, the new version of the local form of the energy equation is obtained:

$$\rho \frac{D\vartheta}{Dt} = - \frac{\partial q_i}{\partial x_i} + \sigma_{ij} \frac{\partial v_i}{\partial x_j} + \rho r \quad (110)$$

The second-order tensor related to the velocity gradient may be written as a combination of a symmetric and an anti-symmetric tensors:

$$\frac{\partial v_i}{\partial x_j} = D_{ij} + \Omega_{ij} = 0 \quad (111)$$

where

$$D_{ij} = \frac{1}{2} \left(\frac{\partial v_i}{\partial x_j} + \frac{\partial v_j}{\partial x_i} \right) \quad (112)$$

$$\Omega_{ij} = \frac{1}{2} \left(\frac{\partial v_i}{\partial x_j} - \frac{\partial v_j}{\partial x_i} \right) \quad (113)$$

Under this assumption,

$$\sigma_{ji} = \frac{\partial v_j}{\partial x_i} = \sigma_{ji} D_{ji} + \sigma_{ji} \Omega_{ji} = \sigma_{ji} D_{ji} \quad (114)$$

since $\sigma_{ji} \Omega_{ji} = 0$ due to the fact that it represents a product between a symmetric and an anti-symmetric tensors.

Hence, the conservation of energy or the first law of thermodynamics has the following form:

$$\rho \frac{D\vartheta}{Dt} = - \frac{\partial q_i}{\partial x_i} + \sigma_{ij} D_{ij} + \rho r \quad (115)$$

5.5 Principle of Entropy

The principle of entropy introduces the idea of the irreversibility of thermodynamical processes. This is established by the *second law of thermodynamics* with the objective to properly describe the natural processes that obey the first law, but do not occur in nature. In essence, the second law of thermodynamics states that entropy is always greater than or equal to zero. This is expressed by an expression that computes the variation of entropy and the interactions with the neighborhood. The sum of all terms should be always greater than or equal to zero:

$$\frac{D}{Dt}(S) + \Xi \geq 0 \quad (116)$$

where S is the *entropy* and Ξ is the *entropy input rate* that defines the interactions with the neighborhood. The description of this law implies the following definitions:

$$S = \int_V \rho s dv \quad \text{Entropy}$$

$$\Xi = \int_V \frac{\rho r}{T} dv - \int_A \frac{q_i}{T} n_i da \quad \text{Entropy input rate}$$

Using these expressions, an integral expression is obtained:

$$\frac{D}{Dt} \int_V \rho s dv - \int_A \frac{q_i}{T} n_i da + \int_V \frac{\rho r}{T} dv \geq 0 \quad (117)$$

Using the Reynolds transport theorem in the first integral together with the mass conservation:

$$\frac{D}{Dt} \int_V \rho s dv = \int_V \left[\frac{D(\rho s)}{Dt} + \rho s \frac{\partial v_i}{\partial x_i} \right] dv = \int_V \rho \frac{Ds}{Dt} dv \quad (118)$$

The divergence theorem is applied in the second integral, transforming area into volume integral:

$$\int_A \frac{q_i}{T} n_i da = \int_V \frac{\partial}{\partial X_i} \left(\frac{q_i}{T} \right) dv \quad (119)$$

Under these considerations, an expression for the second law of thermodynamics is obtained:

$$\int_V \left[\rho \frac{Ds}{Dt} + \frac{\partial}{\partial x_i} \left(\frac{q_i}{T} \right) - \frac{\rho r}{T} \right] dv \geq 0 \quad (120)$$

The local form of the second law of thermodynamics is known as the *Clausius-Duhem inequality*:

$$\rho \frac{Ds}{Dt} + \frac{\partial}{\partial x_i} \left(\frac{q_i}{T} \right) - \frac{\rho r}{T} \geq 0 \quad (121)$$

By considering that:

$$\frac{\partial}{\partial x_i} \left(\frac{q_i}{T} \right) = \frac{1}{T} \frac{\partial q_i}{\partial x_i} - \frac{1}{T^2} q_i \frac{\partial T}{\partial x_i} = \frac{1}{T} \left(\frac{\partial q_i}{\partial x_i} - q_i g_i \right) \quad (122)$$

where $g_i = -\frac{1}{T} \frac{\partial T}{\partial x_i}$.

It follows that:

$$\rho T \frac{Ds}{Dt} + \frac{\partial q_i}{\partial x_i} - q_i g_i - \rho r \geq 0 \quad (123)$$

Since the first law of thermodynamics is given by:

$$\frac{\partial q_i}{\partial x_i} - \rho r = -\rho \frac{D\vartheta}{Dt} + \sigma_{ij} D_{ij} \quad (124)$$

The second law is rewritten as follows:

$$\sigma_{ij} D_{ij} + \rho (T\dot{s} - \dot{\vartheta}) - q_i g_i \geq 0 \quad (125)$$

By defining the Helmholtz free energy density, $\Psi = \vartheta - Ts$, the second law is rewritten as

$$\sigma_{ji} D_{ji} + \rho (\dot{\Psi} + \dot{T}s) - q_i g_i \geq 0 \quad (126)$$

Similar consideration can be done by the definition of the Gibbs free energy density, $\Gamma = \vartheta - \frac{1}{\rho} \sigma_{ij} \varepsilon_{ij} - \rho T$, resulting in the following form of the inequality:

$$\dot{\sigma}_{ij} \varepsilon_{ij} - \rho (\dot{\Gamma} + s\dot{T}) - q_i g_i \geq 0 \quad (127)$$

5.6 Summary of the Fundamental Equations

Based on the presentation of the conservation principles, it is possible to present the following summary of the essential laws of mechanics.

$$\text{Conservation of linear momentum: } \frac{\partial \sigma_{ij}}{\partial x_j} + b_i - \rho \ddot{u}_i = 0$$

$$\text{Conservation of angular momentum: } \sigma_{jk} = \sigma_{kj}$$

$$\text{Conservation of mass: } \frac{\partial \rho}{\partial t} + \frac{\partial}{\partial x_i}(\rho v_i) = 0$$

$$\text{Conservation of energy: } \rho \frac{D\theta}{Dt} = -\frac{\partial q_i}{\partial x_i} + \sigma_{ij} D_{ij} + \rho r$$

$$\text{Second law of thermodynamics: } \sigma_{ij} D_{ij} + \rho(T\dot{s} - \dot{\theta}) - q_i g_i \geq 0$$

The external forces that cause the motion of a continuum body are related to several sources. They can be mechanical, electrical, magnetic, among other possibilities. Therefore, it is important to understand that the conservation principles have multiphysic characteristics. In this regard, some couplings between usually independent fields are necessary for a general description. Additional conservation laws should also be necessary in these cases. The conservation of electrical charge is an illustrative example. This is of special interest in terms of smart materials that have as an essential property the coupling between different fields.

Note that the fundamental principles furnish a set of 11 equations and 1 inequality that are related to 21 unknown variables. Therefore, there is a need of six extra equations in order to have a well-posed system. This is furnished by constitutive equations that establish a connection between unknown variables of the mechanical problem.

6 Constitutive Equations

Constitutive equations are mathematical models that describe the main features of the material behavior, establishing a connection among mechanical quantities. In general, they are idealized models based on experimental macroscopic observations. The formulation of constitutive equations should follow some cares in order to avoid inconsistent description. *Admissibility* and *objectivity* are some special aspects that need to be observed. Admissibility establishes that constitutive equations must be consistent with fundamental principles. Objectivity defines conditions where the equations must be invariant through rigid motion of the reference frame.

The elaboration of constitutive equations should follow a proper formalism avoiding inconsistent equations that, for instances, disrespect the fundamental principles of mechanics. An interesting procedure is the framework of continuum mechanics employing the generalized standard material approach (Lemaitre and

Chaboche 1990). On this basis, the thermomechanical behavior of a continuum may be modeled from a free energy density (Helmholtz free energy, Ψ , or Gibbs free energy, Γ) and the pseudo-potential of dissipation, Φ , in order to satisfy the second law of thermodynamics. A brief discussion about this procedure is now presented. Consider the Clausius-Duhem inequality, assuming that $D_{ij} = \dot{\varepsilon}_{ij}$:

$$\sigma_{ij}\dot{\varepsilon}_{ij} - \rho(\dot{\Psi} + s\dot{T}) - q_i g_i \geq 0 \quad (128)$$

Stress and strain tensors should be energetically conjugated, meaning that their product defines energy. Hence, it is convenient to use description in the same frame.

As a first hypothesis concerning the constitutive modeling, it is assumed that the Helmholtz free energy density is a function of a finite set of variables:

$$\Psi = \Psi(\varepsilon_{ij}, T, \beta) \quad (129)$$

where β represents a set of internal variables. Since $\dot{\Psi} = \frac{\partial \Psi}{\partial \varepsilon_{ij}} \dot{\varepsilon}_{ij} + \frac{\partial \Psi}{\partial T} \dot{T} + \frac{\partial \Psi}{\partial \beta} \dot{\beta}$, the Clausius-Duhem inequality is rewritten as follows:

$$\left(\sigma_{ij} - \rho \frac{\partial \Psi}{\partial \varepsilon_{ij}} \right) \dot{\varepsilon}_{ij} - \rho \left(s + \frac{\partial \Psi}{\partial T} \right) \dot{T} - \rho \frac{\partial \Psi}{\partial \beta} \dot{\beta} - q_i g_i \geq 0 \quad (130)$$

This form motivates the following definitions of the thermodynamical forces:

$$\sigma_{ij}^R = \rho \frac{\partial \Psi}{\partial \varepsilon_{ij}}; \quad B = -\rho \frac{\partial \Psi}{\partial \beta}; \quad s^R = -\frac{\partial \Psi}{\partial T} \quad (131)$$

In order to describe irreversible processes, complementary laws are defined from a pseudo-potential of dissipation that is a function of internal variables:

$$\Phi = \Phi(\dot{\varepsilon}_{ij}, \dot{\beta}, \dot{T}, q_i) \quad (132)$$

The thermodynamical formalism establishes thermodynamics fluxes as follows (Lemaitre and Chaboche 1990):

$$\sigma_{ij}^I = \frac{\partial \Phi}{\partial \dot{\varepsilon}_{ij}}; \quad B = \frac{\partial \Phi}{\partial \dot{\beta}}; \quad s^I = -\frac{\partial \Phi}{\partial \dot{T}}; \quad g_i = -\frac{\partial \Phi}{\partial q_i} \quad (133)$$

Alternatively, these thermodynamic fluxes may be obtained from the dual of the potential of dissipation $\Phi^*(\sigma_{ij}^I, B, g_i)$ allowing the definitions:

$$\dot{\varepsilon}_{ij}^I = \frac{\partial \Phi^*}{\partial \sigma_{ij}^I}; \quad \dot{\beta} = \frac{\partial \Phi^*}{\partial B}; \quad q_i = -\frac{\partial \Phi^*}{\partial g_i} \quad (134)$$

where ε_{ij}^I is the inelastic strain.

On this basis, a complete set of constitutive equations is defined:

$$\sigma_{ij} = \rho \frac{\partial \Psi}{\partial \varepsilon_{ij}} + \frac{\partial \Phi}{\partial \dot{\varepsilon}_{ij}} \quad (135)$$

$$B = -\rho \frac{\partial \Psi}{\partial \beta} = \frac{\partial \Phi}{\partial \dot{\beta}} \quad (136)$$

$$s = -\frac{\partial \Psi}{\partial T} - \frac{\partial \Phi}{\partial \dot{T}} \quad (137)$$

$$g_i = -\frac{\partial \Phi}{\partial q_i} \quad (138)$$

In general, if the pseudo-potential Φ is a positive convex function that vanishes at the origin, the Clausius-Duhem inequality is automatically satisfied.

The description of thermomechanical couplings must consider the energy conservation equation given by the first law of thermodynamics:

$$\rho \dot{\Psi} = \sigma_{ij} \dot{\varepsilon}_{ij} - \frac{\partial q_i}{\partial x_i} - \rho T \dot{s} - \rho \dot{T} s \quad (139)$$

By considering a single point description, spatial variations are neglected. Besides, a convection boundary condition is assumed. Therefore, the first law of thermodynamics has the following form:

$$\rho c_p \dot{T} = -h(T - T_\infty) + \sigma_{ij} \dot{\varepsilon}_{ij} + B \dot{\beta} + T \left[\frac{\partial \sigma_{ij}}{\partial T} (\dot{\varepsilon}_{ij} - \dot{\varepsilon}_{ij}^I) - \frac{\partial B}{\partial T} \dot{\beta} \right] \quad (140)$$

where c_p is the specific heat at constant pressure, h is the convection coefficient, and T_∞ is the environmental temperature. The first term on the equation right side is the convection term whereas the others are associated with the thermomechanical couplings.

The following sections present basic examples of constitutive equations: elasticity and elastoplasticity. Afterward, piezoelectricity and pseudoelasticity are treated showing examples of smart materials constitutive relations.

6.1 Elasticity

Elastic materials are characterized by reversibility where all effects finish when the stimulus is over. In general, elasticity may have linear or nonlinear behaviors. The general linear constitutive equation for the three-dimensional media establishes that stress components are built from a linear combination of strain components. This is equivalent to consider a quadratic energy function, $\Psi = \frac{1}{2}E_{ijkl}\epsilon_{ij}\epsilon_{kl}$, and the pseudo-potential of dissipation Φ vanishes. Therefore,

$$\sigma_{ij} = E_{ijkl}\epsilon_{kl} \tag{141}$$

or in the inverse form,

$$\epsilon_{ij} = S_{ijkl}\sigma_{kl} \tag{142}$$

where E_{ijkl} is the elastic tensor while S_{ijkl} is the compliance tensor. They are fourth-order tensors that have 81 components. Due to symmetry reasons, it is possible to conclude that only 36 components are independent. Therefore, it is possible to rewrite the equation as follows:

$$\sigma_I = E_{IJ}\epsilon_J \tag{143}$$

or

$$\begin{pmatrix} \sigma_x \\ \sigma_y \\ \sigma_z \\ \tau_{yx} \\ \tau_{xx} \\ \tau_{xy} \end{pmatrix} = \begin{bmatrix} E_{11} & E_{12} & E_{13} & E_{14} & E_{15} & E_{16} \\ E_{21} & E_{22} & E_{23} & E_{24} & E_{25} & E_{26} \\ E_{31} & E_{32} & E_{33} & E_{34} & E_{35} & E_{36} \\ E_{41} & E_{42} & E_{43} & E_{44} & E_{45} & E_{46} \\ E_{51} & E_{52} & E_{53} & E_{54} & E_{55} & E_{56} \\ E_{61} & E_{62} & E_{63} & E_{64} & E_{65} & E_{66} \end{bmatrix} \begin{pmatrix} \epsilon_x \\ \epsilon_y \\ \epsilon_z \\ \epsilon_{yx} \\ \epsilon_{xx} \\ \epsilon_{xy} \end{pmatrix} \tag{144}$$

where the indexes are replaced as presented in Table 1.

Since this elastic matrix is symmetric, there are actually 21 independent components. This general behavior establishes that normal stress causes normal and

Table 1 Index conversion

<i>ij</i>	<i>I</i>
11	1
22	2
33	3
23	4
13	5
12	6

shear strains. This is a typical anisotropic behavior where the material presents different properties for different directions.

By assuming that all material behaviors are the same for all directions, this general anisotropic behavior is reduced to simpler situations. The simplest case is the isotropic media where the stress–strain relation is given by:

$$\sigma_{ij} = 2\mu\varepsilon_{ij} + \lambda\delta_{ij}\varepsilon_{kk} \quad (145)$$

where μ and λ are the Lamé coefficients. Note that there are only two independent coefficients. The inverse equation is given by

$$\varepsilon_{ij} = \frac{(1 + \nu)}{E}\sigma_{ij} - \frac{\nu}{E}\delta_{ij}\sigma_{kk} \quad (146)$$

where E and ν are the engineering constants, together with G , defined as follows:

$$G = \frac{E}{2(1 + \nu)} \quad (147)$$

The relation between the Lamé and engineering coefficients are given by:

$$\begin{aligned} \lambda &= \frac{\nu E}{(1 + \nu)(1 - 2\nu)} \\ \mu &= G = \frac{E}{2(1 + \nu)} \end{aligned} \quad (148)$$

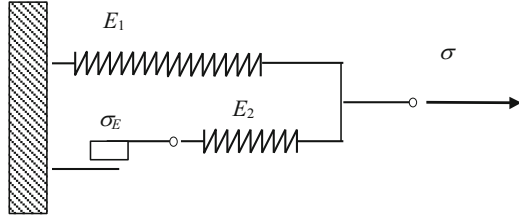
Note that, the use of elastic constitutive equations together with the fundamental principles allows one to completely describe an elastic material system.

6.2 Elastoplasticity

Elastoplastic behavior is an inelastic irreversible process promoted by the discordances movements. This kind of behavior occurs for stress levels over critical values that define the yield surface. There are several idealizations to establish elastoplastic models. Ideal plasticity is the simplest model where yield stress is the maximum limit. A more sophisticated model considers hardening effect, meaning that plastic strains influence the yield surface. The three-dimensional description usually considers an equivalent stress employed to compare the three-dimensional state with an equivalent one-dimensional case, obtained from experimental tests. A one-dimensional version is discussed here.

The elastoplastic model with kinematic and isotropic hardening can be represented by the model presented in Fig. 11. Kinematic hardening is related to

Fig. 11 Elastoplastic model with hardening



the translation of yield surface while isotropic hardening defines the expansion of this surface due to plastic strains.

A simple one-dimensional constitutive model to describe this behavior is written considering the following variables: total strain, ε , and plastic strain, ε^p , isotropic hardening, α , and kinematic hardening, β . Hence, the stress–strain relationship is given by:

$$\sigma = E(\varepsilon - \varepsilon^p) \tag{149}$$

The evolution equations are described by the following equations:

$$\dot{\varepsilon}^p = \dot{\gamma} \text{sign}(\sigma - \beta) \tag{150}$$

$$\dot{\alpha} = |\dot{\varepsilon}^p| \tag{151}$$

$$\dot{\beta} = H\dot{\varepsilon}^p \tag{152}$$

where H is a parameter and $\dot{\gamma}$ represents plastic strain rate.

The yield surface is defined by the function,

$$h(\sigma, \alpha, \beta) = |\sigma - \beta| - (\sigma_E + K\alpha) \tag{153}$$

where K is the plastic parameter. The irreversibility of the plastic flux is represented by the constraints,

$$\begin{aligned} \gamma &\geq 0 \\ \gamma h(\sigma, \alpha, \beta) &= 0 \\ \gamma \dot{h}(\sigma, \alpha, \beta) &= 0 \text{ if } h(\sigma, \alpha, \beta) = 0 \end{aligned} \tag{154}$$

6.3 Piezoelectricity

Piezoelectric materials have a reciprocal electro-mechanical coupling. Hence, once an electrical field is applied, the material exhibits a mechanical deformation; on the other hand, when the material undergoes a mechanical load, an electrical potential is generated.

The description of the three-dimensional behavior of piezoelectric materials involves the connection of both electrical and mechanical quantities. Hence, besides the strain, ϵ_I , and the stress σ_I , it is necessary to consider the electric displacement, D_I , and the applied field, V_I . Therefore, the 3D linear constitutive equation to describe the direct effect, where mechanical loads generates electrical field, is given by:

$$D_M = d_{MI}\sigma_I + \epsilon_{MK}V_K \quad (155)$$

The inverse effect converts electrical field into mechanical energy being described as follows:

$$\epsilon_I = S_{IJ}\sigma_J + d_{MI}V_M \quad (156)$$

where d_{IJ} is the piezoelectric coupling tensor and ϵ_{IJ} is the permittivity tensor. It is essential for a proper description to identify the poling direction, perpendicular to directions 1 and 2. On the other hand, the shear planes are indicated by the subscripts 4, 5, and 6.

6.4 Pseudoelasticity and Shape Memory Effect

Shape memory alloys (SMAs) present a mechanical–temperature coupling motivated by solid phase transformations. These materials have the ability to recover a shape previously defined, when subjected to an appropriate thermomechanical loading process. Besides, they present other phenomena as pseudoelasticity.

The constitutive modeling of SMAs is very complex due to several thermomechanical phenomena involved. Among many alternatives, there is a class known as models with assumed phase transformation kinetics that are popular in the literature (Lagoudas 2008; Paiva and Savi 2006). The main idea related to these models is to consider pre-established mathematical functions to describe the phase transformation kinetics. Here, a one-dimensional version is presented. In this regard, besides strain, ϵ , and temperature, T , an internal variable, β , is used to represent the martensitic volume fraction. The constitutive relation between stress and state variables is considered in the rate form as follows:

$$\dot{\sigma} = E\dot{\epsilon} - \alpha\dot{\beta} - \Omega\dot{T} \quad (157)$$

where E represents the elastic modulus, α corresponds to the phase transformation parameter, and Ω is associated with the thermoelastic expansion. Due to martensitic transformation non-diffusive nature, the martensitic volume fraction can be expressed as function of current values of stress and temperature $\beta = \beta(\sigma, T)$. Brinson (1993) proposed a split of this volume fraction into two distinct martensitic fractions: temperature induced, β_T , and stress induced, β_S , in such a way that

$\beta = \beta_T + \beta_S$. Moreover, different elastic moduli for austenite, E_A , and martensite, E_M , are considered being given by a linear combination such that: $E(\beta) = E_A + \beta(E_M - E_A)$.

The kinetics of the Brinson's model considers that the martensitic transformation evolution is expressed by:

$$\beta_S = \frac{1 - \beta_{S_0}}{2} \cos \left\{ \frac{\pi}{\sigma_s^{\text{CRIT}} - \sigma_f^{\text{CRIT}}} [\sigma - \sigma_f^{\text{CRIT}} - C_M(T - M_s)] \right\} + \frac{1 + \beta_{S_0}}{2}$$

$$\beta_T = \beta_{T_0} - \frac{\beta_{T_0}}{1 - \beta_{S_0}} (\beta_S - \beta_{S_0})$$
(158)

Both equations hold for: $\sigma_s^{\text{CRIT}} + C_M(T - M_s) < \sigma < \sigma_f^{\text{CRIT}} + C_M(T - M_s)$ and $T > M_s$.

For $T < M_s$ and $\sigma_s^{\text{CRIT}} < \sigma < \sigma_f^{\text{CRIT}}$, the martensitic transformation is given by

$$\beta_S = \frac{1 - \beta_{S_0}}{2} \cos \left[\frac{\pi}{\sigma_s^{\text{CRIT}} - \sigma_f^{\text{CRIT}}} (\sigma - \sigma_f^{\text{CRIT}}) \right] + \frac{1 + \beta_{S_0}}{2}$$

$$\beta_T = \beta_{T_0} - \frac{\beta_{T_0}}{1 - \beta_{S_0}} (\beta_S - \beta_{S_0}) + \Delta_T$$
(159)

where $\Delta_T = \begin{cases} \frac{1 - \beta_{T_0}}{2} \{ \cos [a_M(T - M_f)] + 1 \} & \text{if } M_f < T < M_s \text{ and } T < T_0. \\ \text{else :} & 0 \end{cases}$

The reverse transformation holds for $C_A(T - A_f) < \sigma < C_A(T - A_s)$ and $T > A_s$ being defined as:

$$\beta_S = \frac{\beta_{S_0}}{2} \left\{ \cos \left[a_A \left(T - A_s - \frac{\sigma}{C_A} \right) \right] + 1 \right\}$$

$$\beta_T = \frac{\beta_{T_0}}{2} \left\{ \cos \left[a_A \left(T - A_s - \frac{\sigma}{C_A} \right) \right] + 1 \right\}$$
(160)

where a_M and a_A are material coefficients. β_{S_0} and β_{T_0} represent, respectively, the stress induced and the temperature induced martensitic volume fractions immediately before transformations begin.

Acknowledgements The author would also like to acknowledge the support of the Brazilian Research Agencies CNPq, CAPES and FAPERJ and through the INCT-EIE (National Institute of Science and Technology—Smart Structures in Engineering) the CNPq and FAPEMIG. The Air Force Office of Scientific Research (AFOSR) is also acknowledged.

References

- A.I. Borisneko, I.E. Tarapov, *Vector and Tensor Analysis with Applications* (Dover, London, 1968)
- L.C. Brinson, One dimensional constitutive behavior of shape memory alloys: thermomechanical derivation with non-constant material functions and redefined martensite internal variable. *J. Intell. Mater. Syst. Struct.* **4**, 229–242 (1993)
- S.H. Crandall, N.C. Dahl, T.J. Lardner, *An Introduction to the Mechanics of Solids* (McGraw Hill, New York, 1978)
- I.G. Currie, *Fundamental Mechanics of Fluids* (McGraw Hill, New York, 1974)
- A.C. Eringen, *Mechanics of Continua* (Wiley, New York, 1967)
- A. Ertuk, D.J. Inman, *Piezoelectric Energy Harvesting* (Wiley, New York, 2011)
- Y.C. Fung, *Foundations of Solid Mechanics* (Prentice Hall, Englewood Cliffs, 1965)
- Y.C. Fung, *A First Course in Continuum Mechanics* (Prentice Hall, Englewood Cliffs, 1969)
- P. Germain, *Mécanique des Milieux Continus* (Masson et Cie, Paris, 1962)
- M.E. Gurtin, *An Introduction to Continuum Mechanics* (Academic Press, New York, 1981)
- D.C. Lagoudas, *Shape Memory Alloys: Modeling and Engineering Applications* (Springer, New York, 2008)
- J. Lemaitre, J.-L. Chaboche, *Mechanics of Solid Materials* (Cambridge University Press, Cambridge, 1990)
- L.E. Malvern, *Introduction to the Mechanics of a Continuous Medium* (Prentice Hall, Englewood Cliffs, 1969)
- G.E. Mase, *Continuum Mechanics*. Schaum's Outline Series (McGraw Hill, New York, 1970)
- A. Paiva, M.A. Savi, An overview of constitutive models for shape memory alloys. *Math. Probl. Eng.* **2006**, 1–30 (2006). Article ID56876
- J.N. Reddy, *An Introduction to Continuum Mechanics* (Cambridge University Press, Cambridge, 2013)
- I.H. Shames, F.A. Cozzarelli, *Elastic and Inelastic Stress Analysis* (Prentice Hall, Englewood Cliffs, 1992)
- I.S. Sokolnikoff, *Mathematical Theory of Elasticity* (McGraw Hill, New York, 1956)
- I.S. Sokolnikoff, *Tensor Analysis* (Wiley, New York, 1964)
- S.P. Timoshenko, J.N. Goodier, *Theory of Elasticity* (McGraw Hill, New York, 1970)
- K.C. Valanis, *Irreversible Thermodynamics of Continuous Media, Internal Variable Theory* (Springer, New York, 1972)
- H. Ziegler, *Applied Mathematics and Mechanics* (North-Holland, Amsterdam, 1977)

Wave Motion in Elastic Structures

M.J. Brennan, B. Tang, and F.C.L. Almeida

Abstract Describing the dynamic behaviour of structures in terms of waves is particularly useful when high frequency vibration is of interest. This is the case in active and passive vibration control, and in structural health monitoring. In this chapter, the concept of wave motion is introduced and different types of waves are discussed, namely waves in a string, a rod and a beam. Using the wavenumber, the phenomenon of dispersion is introduced as is phase and group velocity, and cut-off. The emphasis is on the physical concepts rather than mathematics, and to this end, the majority of the chapter concentrates on one-dimensional uniform structures.

Keywords Wave motion • Strings • Rods • Beams • Wavenumber • Phase velocity • Group velocity • Cut-off frequency • Dispersion

1 Introduction

Although many mechanical engineers are familiar with the concept of natural frequencies and mode-shapes of structures, very few are familiar with the basic concepts of wave motion. This is probably because most mechanical engineering courses start with static analysis and then move on to dynamic analysis, which leads on naturally to the concept of a finite number of natural frequencies and accompanying mode-shapes. At a high frequency, which is when the dimension of a structure, or part of a structure, is smaller than a structural wavelength, then it can be helpful to think about the structure in terms of waves rather than modes. Indeed, in a structure it is a wave that propagates vibrational energy from one part of a structure to another.

M.J. Brennan, B.A. (Hons.), M.Sc., Ph.D. (✉) • F.C.L. Almeida, B.E., M.Sc., Ph.D.
Departamento de Engenharia Mecânica, UNESP, Ilha Solteira, SP 15385-000, Brazil
e-mail: mjbrennan0@btinternet.com; fabricio@tupa.unesp.br

B. Tang, B.E., M.Sc., Ph.D.
Institute of Internal Combustion Engine, Dalian University of Technology,
Dalian, Liaoning 116023, China
e-mail: btang@dlut.edu.cn

This chapter aims to give an overview of some of the important aspects of structural wave motion. It is not possible in one chapter to give a comprehensive treatment of all types of wave motion, which may be found in complete books on the subject, for example Cremer et al. (2005), Graff (1975), and Hagedorn and DasGupta (2007), so the authors restrict their attention to some basic physics. The notion of a wave is first discussed before specific structural wave-types are examined. To facilitate physical insight without unnecessary mathematical complexity, the focus is on one-dimensional structures, in which three different physical quantities have a dominant influence, namely, tension (as in a string), in-plane compression (as in a rod) and bending (as in a beam). Time harmonic behaviour at low and high frequencies is considered.

2 Some Features of Harmonic Wave Motion

The waves considered in this chapter exist in homogeneous uniform structures (rods, beams, plates, for example), and have displacement v either in-plane or out-of-plane (or both), and the wave (or vibrational energy) propagates in the in-plane direction, x . Examples of waves in a one-dimensional structure are illustrated in Fig. 1. The longitudinal wave is an in-plane wave, but, as shown in the figure, there is some out-of-plane displacement due to the Poisson ratio effect. Shear and bending waves are examples of out-of-plane waves. These waves are discussed later in this chapter.

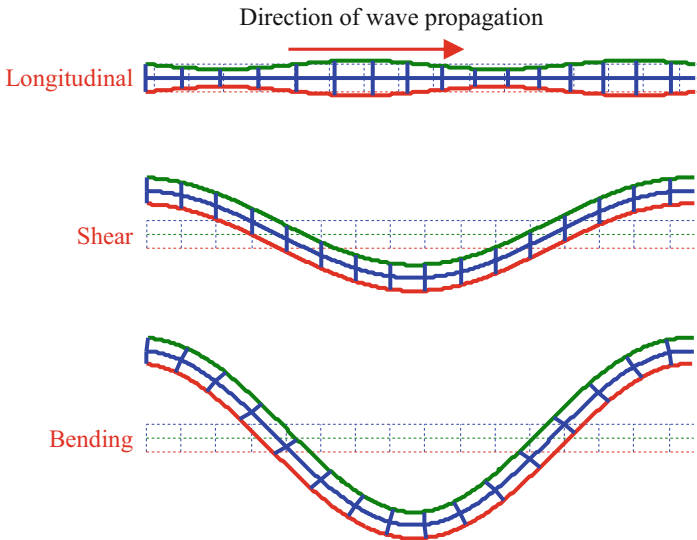


Fig. 1 Illustrations of different types of wave motion in one-dimensional structures. Note that for longitudinal motion, the displacement orthogonal to the direction of wave propagation is exaggerated for clarity

A propagating wave that is harmonic in time and space, can be represented by

$$v(x, t) = V \sin(\omega t \pm kx) \quad (1a)$$

or

$$v(x, t) = V \cos(\omega t \pm kx) \quad (1b)$$

where V is the amplitude of the wave, ω is the angular (or temporal) frequency and k is the wavenumber (or spatial frequency). Note that $-kx$ denotes a wave propagating in the positive x direction and $+kx$ denotes a wave propagating in the negative x direction. Knowing what the wavenumber represents is vital to the understanding of harmonic wave motion. Physically, it is the spatial phase change per unit distance, and is analogous to angular frequency which is the temporal change of phase per unit time. It is related to the wavelength λ , and the spatial phase velocity c , by $k = 2\pi/\lambda = \omega/c$.

To emphasise the physical meaning of the wavenumber, illustrations of a waveform as a function of time and space are given in Fig. 2.

Rather than using trigonometric functions, it is often preferable to use exponential functions by noting that $v(x, t) = V \text{Im}\{e^{j(\omega t \pm kx)}\}$ or $v(x, t) = V \text{Re}\{e^{j(\omega t \pm kx)}\}$ corresponding to Eqs. (1a) and (1b) respectively. Neglecting Re and Im for simplicity (which can be done because the systems considered in this chapter are linear and so the superposition principle applies), the wave motion given in Eqs. (1a) and (1b) can be written as

$$v(x, t) = V e^{\pm jkx} e^{j\omega t} \quad (2)$$

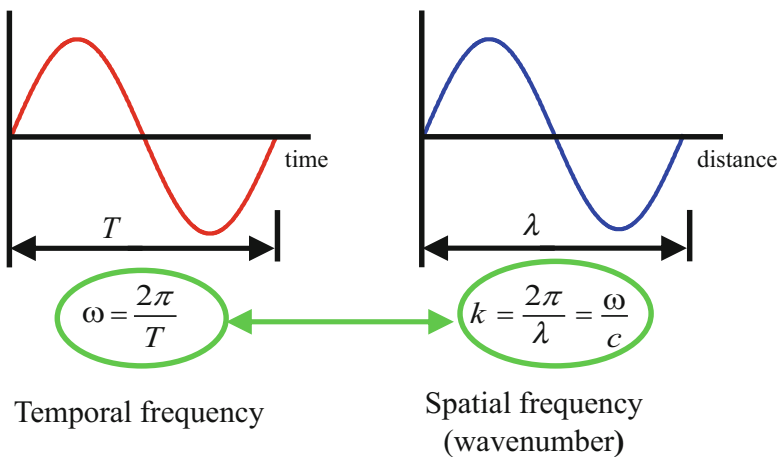
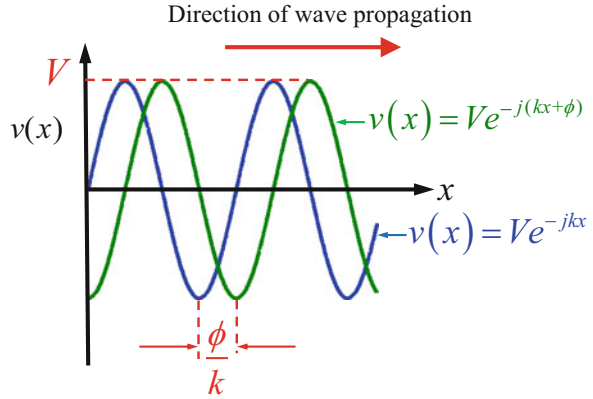


Fig. 2 The analogy between temporal frequency and the wavenumber (spatial frequency)

Fig. 3 An illustration of physical meaning of spatial phase ϕ



where it can be seen that the spatial and temporal variables are separated as $v(x) = Ve^{\pm jkx}$ and $v(t) = e^{j\omega t}$, so that $v(x, t) = v(x)v(t)$. The concept of spatial phase is shown in Fig. 3, where only the spatial variable is considered, and a snapshot of a right-going propagating wave is shown at two distinct times. It can be seen that the distance the wave has travelled between the two snapshots is ϕ/k .

2.1 Interference of Waves

Waves can combine by propagating in the same direction or in opposite directions, both of which are considered in this section. For ease of interpretation, it is convenient here to use trigonometric rather than exponential notation.

2.1.1 Waves Propagating in the Same Direction

Consider two right-going waves propagating at different speeds (consequently with two different wavenumbers). They can be described by

$$v_1(x, t) = V \sin(\omega_1 t - k_1 x) \quad (3a)$$

and

$$v_2(x, t) = V \sin(\omega_2 t - k_2 x) \quad (3b)$$

These can be summed because of the principle of superposition to give

$$v(x, t) = \bar{V} \sin\left(\left(\frac{\omega_1 + \omega_2}{2}\right)t - \left(\frac{k_1 + k_2}{2}\right)x\right) \quad (4)$$

where $\bar{V} = 2V \cos\left(\left(\frac{\omega_1 - \omega_2}{2}\right)t - \left(\frac{k_1 - k_2}{2}\right)x\right)$.

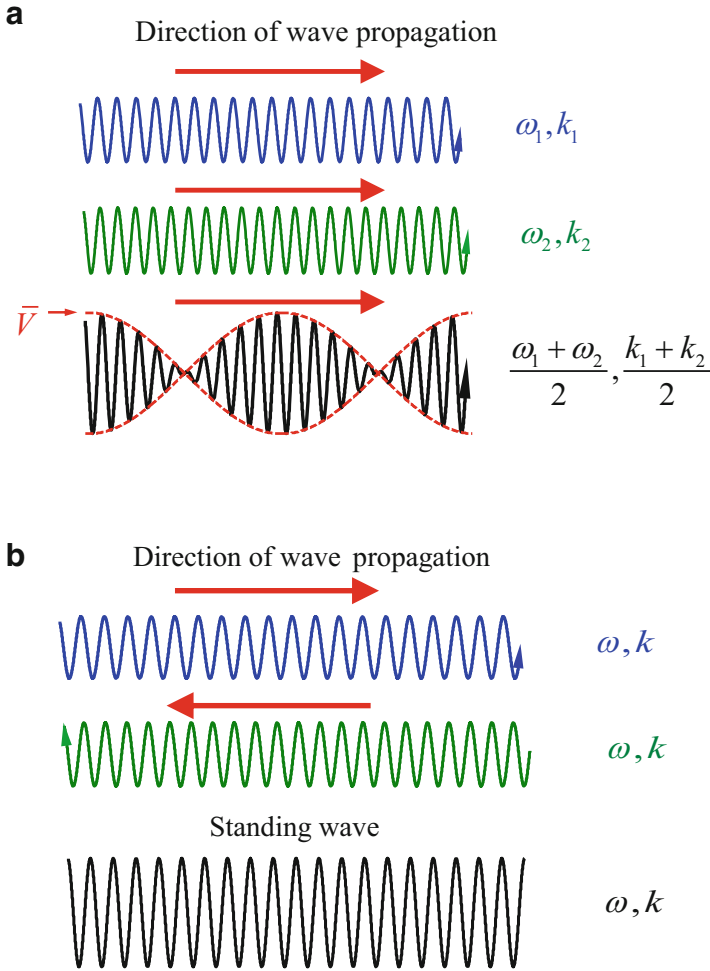


Fig. 4 Illustration of wave interference. (a) The summation of waves propagating in the same direction. (b) The summation of waves propagating in opposite directions to give a standing wave

The waves described in Eqs. (3a), (3b) and (4) are shown in Fig. 4a, where the frequency $\omega_2 = 1.1\omega_1$ and $k_2 = 1.1k_1$. Now, the phase velocity of the two individual waves is $c_1 = \omega_1/k_1$ and $c_2 = \omega_2/k_2$, respectively, and the phase velocity c_P of the combined wave, which has a mean frequency of $(\omega_1 + \omega_2)/2$ and a mean wavenumber of $(k_1 + k_2)/2$, is

$$c_P = \frac{\omega_1 + \omega_2}{k_1 + k_2} \tag{5a}$$

The envelope of the combined waves \bar{V} does not propagate at the phase velocity. It propagates at the group velocity, which is the velocity at which the energy in the combined wave is transported (Cremer et al. 2005). It is given by

$$c_G = \frac{\omega_1 - \omega_2}{k_1 - k_2} = \frac{\Delta\omega}{\Delta k} \quad (5b)$$

In the limiting case, where the frequencies are arbitrarily close to each other, Eq. (5b) becomes $c_G = d\omega/dk$, i.e. the group velocity is the rate of change of frequency with respect to the wavenumber. If the waves have the same phase velocity that is independent of frequency, i.e. they are non-dispersive (such as tension waves in strings and compressional waves in rods (Cremer et al. 2005; Graff 1975; Hagedorn and DasGupta 2007; Kinsler et al. 1982)), then the wavenumbers are proportional to frequency, so that $c_G = c_P = c_1 = c_2$. If the waves have a phase velocity that is dependent on frequency, i.e. they are dispersive (such as bending waves in beams and plates), then this is not the case. In the particular case of bending waves, the wavenumbers are proportional to the square root of frequency. The group velocity is then related to the phase velocity by $c_G = 2c_P$. The terms dispersive/non-dispersive have physical significance. If a structural wave is non-dispersive, then a pulse of vibration generated at a point in the structure will propagate through the structure without distortion. On the contrary, if a wave is dispersive then the pulse changes shape as it propagates through the structure.

2.1.2 Waves Propagating in Opposite Directions

If two waves, with the same amplitude, frequency and wavenumber, are propagating in opposite directions, they can be described by

$$v_1(x, t) = V \sin(\omega t - kx) \quad (6a)$$

and

$$v_2(x, t) = V \sin(\omega t + kx) \quad (6b)$$

They sum to give a standing wave, given by

$$V(x, t) = 2A \sin(\omega t) \cos(kx) \quad (7)$$

in which it can be seen that there is no propagation of energy in either direction. The formation of a standing wave is illustrated in Fig. 4b. An example of a standing wave occurs when a structure vibrates freely at its natural frequency. All points on the structure vibrate either in-phase or in anti-phase with each other. With this kind of wave-field, there are points on the structure that do not vibrate which are called

nodes, and there are points on the structure that vibrate the most, which are called antinodes. If two waves, which are propagating in opposite directions in a structure, have different amplitudes, then the wave-field will consist of both a propagating wave and a standing wave.

3 Basic Wave-Types in One-Dimensional Structures

In this section, three types of waves are considered. These commonly occur in structures and are of fundamental importance in the study of wave propagation in any structure. The equations of motion are derived, as is the impedance of the structures when excited by a force. Note that the equations of motion, which are called wave equations, involve partial differentials in both space and time. This is because the structures are described in terms of distributed mass and stiffness.

3.1 Transverse Waves in a String

Perhaps the simplest structure in which to commence the study of wave propagation is a string. This is an idealised structure in which the bending stiffness is considered to be negligible, so that the elastic force is due only to the tension in the string. To determine the wave equation for this structure, a section of the string of length dx with an in-plane tension T , such as that shown in Fig. 5a, is considered. Summing forces in the y direction gives

$$df_y = (T \sin \theta)_{x+dx} - (T \sin \theta)_x \quad (8)$$

Applying the Taylor series expansion $f(x + dx) = f(x) + \left(\frac{\partial f}{\partial x}\right)_x dx + \dots$ results in

$$df_y = \left[(T \sin \theta)_x + \frac{\partial (T \sin \theta)}{\partial x} dx \right] - (T \sin \theta)_x \quad (9)$$

If $\theta \ll 1$, then $\sin \theta \approx \theta = \partial w / \partial x$ and Eq. (9) reduces to

$$df_y = T \frac{\partial^2 w}{\partial x^2} dx \quad (10)$$

which is the stiffness force (or the restoring force). This is equal to the inertia force, which is the product of the mass and the acceleration in the y direction, and is given by

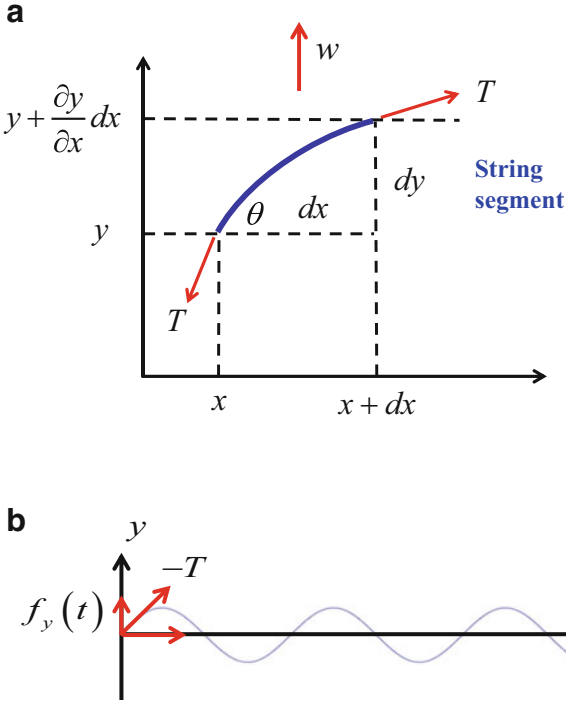


Fig. 5 Vibration of a string in tension. (a) Free vibration of a string. (b) Semi-infinite string excited by a harmonic force

$$df_y = \rho_L dx \frac{\partial^2 w}{\partial t^2} \tag{11}$$

where ρ_L is the mass per unit length. Setting Eq. (10) to be equal to Eq. (11) results in

$$\frac{\partial^2 w}{\partial x^2} - \frac{1}{c_S^2} \frac{\partial^2 w}{\partial t^2} = 0 \tag{12}$$

where $c_S = \sqrt{T/\rho_L}$ is the phase velocity. Equation (12) is the wave equation for a string. Note that the phase velocity is independent of frequency, so that a wave in a string is non-dispersive which means that the group velocity is equal to the phase velocity.

To determine the free-wave behaviour, time harmonic motion of the form $w = w(x)e^{j\omega t}$ is assumed, and the partial differential equation given in Eq. (12) becomes an ordinary differential equation, given by

$$\frac{d^2 w(x)}{dx^2} + k_S^2 w(x) = 0 \quad (13)$$

where $k_S = \omega/c_S$ is the wavenumber. Equation (13) is a second-order ordinary differential equation, the solution of which is $w(x) = Ae^{-jk_S x} + Be^{jk_S x}$. Thus, the solution to Eq. (12) is

$$w(x, t) = (Ae^{-jk_S x} + Be^{jk_S x})e^{j\omega t} \quad (14)$$

Note the similarity between the form of this equation and Eq. (2). There are two propagating waves which are harmonic in space and time, where $Ae^{-jk_S x}e^{j\omega t}$ is a right-going propagating wave with amplitude A , and $Be^{jk_S x}e^{j\omega t}$ is a left-going propagating wave with amplitude B .

One important quantity of interest in the study of wave motion is the mechanical impedance of the structure. One reason for this is that when a wave is incident on a discontinuity, it is the impedance of the discontinuity compared to the impedance of the structure that governs the way in which the wave is reflected and/or transmitted (Fahy and Gardonio 2007).

To determine the impedance of a string, consider the semi-infinite string shown in Fig. 5b. It is excited by the force $f_y(t) = F_y e^{j\omega t}$ at the end of the string, which generates a right-going wave, so that

$$w(x, t) = Ae^{j(\omega t - k_S x)} \quad (15)$$

Differentiating with respect to space and time, respectively, results in

$$\frac{\partial w(x, t)}{\partial x} = -jk_S A e^{j(\omega t - k_S x)}, \quad (16a)$$

$$\frac{\partial w(x, t)}{\partial t} = j\omega A e^{j(\omega t - k_S x)} \quad (16b)$$

Now, the excitation force is $f_y(t) = -T \sin \theta(t) \approx -T \partial y(0, t) / \partial x$. So, from Eq. (16a), $f_y(t) = jTk_S A e^{j\omega t}$ and thus $F_y = jTk_S A$. From Eq. (16b), the velocity in the y direction at $x = 0$ can be written as $v(0, t) = V(0)e^{j\omega t}$, where $V(0) = j\omega A$. The driving point impedance is the ratio of the applied force to the resulting velocity at the point of excitation, and is a frequency domain quantity. It is thus given by

$$Z_S = \frac{F_y}{V(0)} = \frac{jTk_S A}{j\omega A} \quad (17)$$

Noting that $k_S = \omega/c_S$ and $c_S = \sqrt{T/\rho_L}$, Eq. (17) becomes

$$Z_S = \rho_L c_S = \sqrt{T\rho_L} \quad (18)$$

It can be seen that the impedance is a real quantity that does not vary with frequency, which is the characteristic of a viscous damper (Gardonio and Brennan 2004). This means that, as seen by the excitation force, a semi-infinite string behaves as a viscous damper.

3.2 Longitudinal Waves in a Rod

The procedure to derive the wave equation and the wavenumber for a rod is similar to that for a string, in that the inertia force and the stiffness force for a small section are determined and then set to be equal to each other. Consider a section of rod, as shown in Fig. 6. Applying Hooke's law results in

$$\frac{f_x}{S} = E \frac{\partial u}{\partial x} \quad (19)$$

where E and S are the Young's modulus and cross-sectional area of the rod, respectively. Now, the net force on the element (stiffness force) is given by

$$df_x = \left(f_x + \frac{\partial f_x}{\partial x} dx \right) - f_x = \frac{\partial f_x}{\partial x} dx \quad (20)$$

Substituting for f_x from Eq. (19) into Eq. (20) gives the stiffness force

$$df_x = ES \frac{\partial^2 u}{\partial x^2} dx \quad (21)$$

Setting this equal to the inertia force given by $\rho S dx \partial^2 u / \partial t^2$, in which ρ is the density of the rod, results in

$$\frac{\partial^2 u}{\partial x^2} - \frac{1}{c_R^2} \frac{\partial^2 u}{\partial t^2} = 0 \quad (22)$$

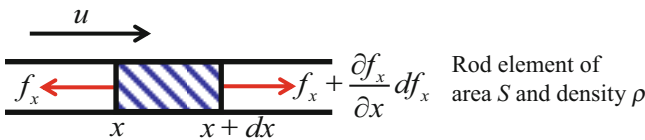


Fig. 6 Free vibration of a rod

where $c_R = \sqrt{E/\rho}$ is the phase velocity. Equation (22) is the wave equation for a rod. Note the similarity between this and the wave equation for a string. The phase velocity is also independent of frequency, so that a wave in a rod is also non-dispersive. Two waves that are harmonic in space and time can exist in the rod, so that the solution to Eq. (22) is

$$u(x, t) = (Ae^{-jk_R x} + Be^{jk_R x})e^{j\omega t} \quad (23)$$

in which $k_R = \omega/c_R$. For a plate, the phase velocity for an in-plane wave is given by $c_P = \sqrt{E/(\rho(1-\nu^2))}$, and for a three-dimensional solid the phase velocity of a compressional wave is given by $c_{3D} = \sqrt{E(1-\nu^2)/(\rho(1+\nu)(1-2\nu))}$ in which ν is Poisson's ratio (Fahy and Gardonio 2007). Note that the phase velocity is greatest in the three-dimensional solid and slowest in the rod, with the phase velocity in the plate being in between the two. The reason for this phenomenon is that the motion orthogonal to the direction of the wave propagation (which is evident in the longitudinal wave shown in Fig. 1) tends to slow down the wave in the in-plane direction. In a three-dimensional solid, there is no motion orthogonal to the direction of wave propagation, so the wave is not slowed by this effect (note that this wave is generally called a compressive wave and has pure longitudinal motion). In the plate, there is out-of-plane motion in one direction only, and in the rod there is out-of-plane motion in two directions, which explains why the wave becomes progressively slower in these two cases.

The impedance for a force-excited rod can be calculated in the same way as that for the string (and so is left as an exercise for the reader). It is given by

$$Z_R = \rho c_R = S\sqrt{E\rho} \quad (24)$$

Note that, as with the string, the impedance is a real quantity which does not vary with frequency. Hence, as seen by the excitation force, a semi-infinite rod also acts as a viscous damper.

3.3 Flexural (Bending) Waves

3.3.1 Beam

In this section, flexural waves in a beam are considered. The behaviour of a beam is much more complicated than the previous cases discussed so far in this chapter. As shown in Fig. 1 there are two types of out-of-plane motion in a beam, one is shear wave motion and the other is bending wave motion. With shear motion, sections of the beam vibrate in the direction of the out-of-plane motion without rotation, as can be seen in the figure. This type of vibration is not discussed in this section, but is discussed in Sect. 5. Of interest here is bending vibration, where sections of beam

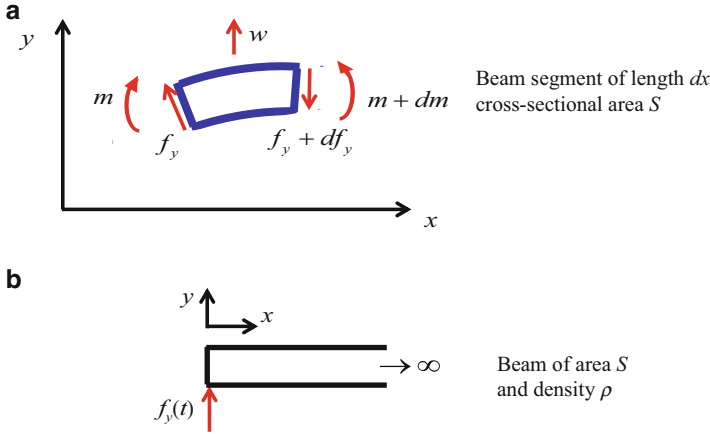


Fig. 7 Vibration of an Euler–Bernoulli beam. (a) Free vibration of an Euler–Bernoulli beam. (b) Forced vibration of a semi-infinite beam

are orthogonal to the neutral axis as can be seen in Fig. 1. They experience both translational displacement and rotation. The reason why this type of vibration is more complicated than longitudinal vibration in a rod, for example, is that both the bending moment and the shear force govern the deformation of the beam and hence the vibration.

Consider a small beam element of length dx as shown in Fig. 7a. The net shear force acting on the element (stiffness force) is given by

$$df_y = f_y - \left(f_y + \frac{\partial f_y}{\partial x} dx \right) = -\frac{\partial f_y}{\partial x} dx \quad (25)$$

Note the similarity between this and Eq. (20). Setting this equal to the inertia force given by $\rho S dx \partial^2 w / \partial t^2$, in which ρ is the density of the beam, results in

$$\frac{\partial f_y}{\partial x} = -\rho S \frac{\partial^2 w}{\partial t^2} \quad (26)$$

Summing the moments about the right-hand edge of the element gives

$$dm = \left(m + \frac{\partial m}{\partial x} dx \right) - m - f_y dx \quad (27)$$

The Euler–Bernoulli assumption is that the rotary inertia is relatively small and can be neglected, which means that $dm = 0$. From Eq. (27) this results in $f_y = \partial m / \partial x$. Combining this with Eq. (26) gives

$$\frac{\partial^2 m}{\partial x^2} + \rho S \frac{\partial^2 w}{\partial t^2} = 0 \quad (28)$$

Now, from basic static beam theory, for example (Hearn 1985), $m = EI \frac{\partial^2 w}{\partial x^2}$, in which I is the second moment of area about the neutral axis. This can be combined with Eq. (28) to give

$$EI \frac{\partial^4 w}{\partial x^4} + \rho S \frac{\partial^2 w}{\partial t^2} = 0 \quad (29)$$

which is the Euler–Bernoulli equation for a beam. Note that this involves a fourth-order spatial derivative rather than a second-order spatial derivative, which is the case for the spring and the rod. If time harmonic motion of the form $w(t) = w(x) e^{j\omega t}$ is assumed, then Eq. (29) becomes

$$\frac{d^4 w(x)}{dx^4} + k_B^4 w(x) = 0 \quad (30)$$

where $k_B = (\rho S / (EI))^{\frac{1}{4}} \omega^{\frac{1}{2}}$ is the wavenumber for the beam. Now, the wavenumber is related to the phase velocity c_B by $k_B = \omega / c_B$, so that $c_B = (EI / (\rho S))^{\frac{1}{4}} \omega^{\frac{1}{2}}$. Thus, it can be seen that a flexural wave is dispersive. A flexural vibration pulse in a structure will consist of several frequency components, and the higher frequency components will propagate at a higher speed than the lower frequency components, with the results that the pulse spreads (or disperses) as it propagates.

Now, Eq. (30) is a fourth-order equation, which means that there are two other solutions in addition to the propagating waves in the left- and right-hand directions. These are nearfield or evanescent waves and are found close to discontinuities. Thus the solution to Eq. (30) is given by

$$w(x, t) = (A_1 e^{k_B x} + A_2 e^{-k_B x} + A_3 e^{jk_B x} + A_4 e^{-jk_B x}) e^{j\omega t} \quad (31)$$

where the A_i 's are the wave amplitudes and $A_1 e^{k_B x}$ and $A_2 e^{-k_B x}$ are the evanescent waves decaying in the left- and right-going directions, respectively. Note that the evanescent waves do not propagate energy unless they interact with each other (Bobrovnikskii 1992). In the majority of textbooks, Eq. (31) is often written in terms of hyperbolic and trigonometric functions. Although this is convenient from the mathematical point of view, it is not so helpful in terms of understanding the physical behaviour, whereas the physical significance of the terms in Eq. (31) is clear.

To determine the impedance of the beam, consider the semi-infinite beam in Fig. 7b, excited by a harmonic force $f_y(t) = F_y e^{j\omega t}$ at the end, which generates right-going evanescent and propagating waves, so that

$$w(x, t) = (A_2 e^{-k_B x} + A_4 e^{-jk_B x}) e^{j\omega t} \quad (32)$$

Now, the two boundary conditions at the end of the beam are (a) that the bending moment is zero, so that $EI \partial^2 w(0, t) / \partial x^2 = 0$ and (b) the shear force is equal to the applied force, so that $EI \partial^3 w(0, t) / \partial x^3 = F e^{j\omega t}$. Applying boundary condition (a) results in $A_2 = A_4$, so that Eq. (32) becomes

$$w(x, t) = (e^{-k_B x} + e^{-jk_B x}) A_4 e^{j\omega t} \quad (33)$$

from which the velocity at $x = 0$ can be calculated. It is given by $v(x, t) = V(0) e^{j\omega t}$, where $V(0) = j\omega 2A_4$. Applying boundary condition (b) results in $F_y = (-1 + j) EI k_B^3 A_4$. The driving point impedance is the ratio of the applied force to the resulting velocity at the point of excitation, and is thus given by

$$Z_B = \frac{F_y}{V(0)} = \frac{(-1 + j) EI k_B^3 A_4}{j\omega 2A_4} = \frac{EI k_B^3 (1 + j)}{2\omega} \quad (34a)$$

Noting that $k_B = (\rho S / (EI))^{1/4} \omega^{1/2}$, Eq. (34a) can be written as

$$Z_B = \frac{(EI)^{1/4} (\rho S)^{3/4}}{2} \omega^{1/2} (1 + j) \quad (34b)$$

This can be interpreted as a frequency dependent damper (related to the real part of the impedance) where the damping coefficient is given by $(EI)^{1/4} (\rho S)^{3/4} \omega^{1/2} / 2$, in parallel with a frequency dependent mass (related to the imaginary part of the impedance which is positive), where the mass is given by $(EI)^{1/4} (\rho S)^{3/4} / (2\omega^{1/2})$ (Gardonio and Brennan 2004). Note that this is different from the string and the rod, where the impedance is damping-like only. The additional mass-like impedance is because the beam has an evanescent wave as well as a propagating wave at the end of the beam.

3.3.2 Plate

The physics governing flexural waves in a uniform flat plate are similar to that in a beam (Cremer et al. 2005). Therefore they are not covered in detail here. The partial differential equation describing the flexural vibration is given by Cremer et al. (2005),

$$D \nabla^4 w + \rho h \frac{\partial^2 w}{\partial t^2} = 0 \quad (35)$$

where $D = \frac{Eh^3}{12(1-\nu^2)}$, $\nabla = \frac{\partial^4}{\partial x^4} + \frac{\partial^4}{\partial x^2 \partial y^2} + \frac{\partial^4}{\partial y^4}$, and h is the thickness of the plate. Note the similarity between Eqs. (29) and (35). Assuming time harmonic motion of the form $w(t) = w(x)e^{j\omega t}$, Eq. (35) becomes

$$\nabla^4 w(x) + k_{\text{PI}} w(x) = 0 \quad (36)$$

where k_{PI} is the wavenumber given by $k_{\text{PI}} = (\rho(1-\nu^2)/(Eh^2))^{\frac{1}{4}} \omega^{\frac{1}{2}}$. Note that for a rectangular beam the wavenumber is given by $k_{\text{B}} = (\rho/(Eh^2))^{\frac{1}{4}} \omega^{\frac{1}{2}}$. It can thus be seen that the plate has a slightly higher bending stiffness compared to a beam due to the Poisson ratio effect, and hence the phase velocity is slightly higher for a given frequency.

4 Dispersion

The aim of this section is to give a physical explanation as to why some waves are non-dispersive and others are dispersive. Two examples are given. First, consider the phase velocity for a rod, which is given by $c_{\text{R}} = \sqrt{E/\rho}$. This can also be written as

$$c_{\text{R}} = \sqrt{\frac{(ES/\lambda_{\text{R}})}{\rho S \lambda_{\text{R}}}} \lambda_{\text{R}} = \frac{\omega_{\lambda}}{2\pi} \lambda_{\text{R}} \quad (37)$$

where $\omega_{\lambda} = 2\pi \sqrt{\frac{\text{stiffness of one wavelength of the structure}}{\text{mass of one wavelength of the structure}}}$, and λ_{R} is the wavelength of a longitudinal wave. In this case, the way in which the stiffness in one wavelength changes with frequency, is inversely proportional to the way in which the mass in one wavelength changes with frequency. Note that Eq. (37) can also be interpreted as $c_{\text{R}} = \sqrt{\frac{\text{stiffness per unit length}}{\text{mass per unit length}}}$, which in this case is constant. In general, if the ratio of the $\frac{\text{stiffness per unit length}}{\text{mass per unit length}}$ does not change with frequency, then the phase velocity is a constant and is hence non-dispersive.

Consider now a flexural or bending wave in which the phase velocity is given by $c_{\text{B}} = (EI/(\rho S))^{\frac{1}{4}} \omega^{\frac{1}{2}}$. Noting that $\omega = k_{\text{B}} c_{\text{B}}$ and that $k_{\text{B}} = 2\pi/\lambda_{\text{B}}$, this can be written as

$$c_{\text{B}} = \sqrt{\frac{EI}{\rho S}} \frac{2\pi}{\lambda_{\text{B}}} \quad (38)$$

where λ_B is the wavelength of a flexural wave. Equation (38) can be further written as

$$c_B = \sqrt{\frac{(4\pi^2 EI / \lambda_B^3)}{\rho S \lambda_B}} \lambda_B = \frac{\omega_B}{2\pi} \lambda_B \tag{39}$$

where $4\pi^2 EI / \lambda_B^3$ is the bending stiffness of a flexural wavelength of the structure and $\rho S \lambda_B$ is the mass of one wavelength of the structure. It can be seen in this case that the stiffness per unit wavelength and mass per unit wavelength are not inversely related as frequency changes. For example, if the wavelength reduces by a factor of 2 (as frequency increases), the stiffness increases by a factor of 8, but the mass only reduces by a factor of 2. Hence ω_B increases by a factor of 4 and the phase velocity increases by a factor of 2. Thus, the wave is dispersive.

In general, if the product of the stiffness per unit wavelength and the mass per unit wavelength is independent of frequency, then the phase velocity is constant, and the wave is non-dispersive. If this is not the case, then the wave is dispersive.

5 Flexural Beam Vibration at High Frequencies

5.1 Wavenumbers

Two fundamental assumptions in Euler–Bernoulli beam theory are (a) that the rotary inertia of the beam can be neglected, and (b) that the shear stiffness is infinite. These assumptions are generally valid for a rectangular beam when $\lambda_B > 10 \times$ depth of the beam. When this is not the case, Timoshenko beam theory has to be used to describe the vibration (Graff 1975; Hagedorn and DasGupta 2007).

Consider a small beam element of length dx as shown in Fig. 8. Note that the element is distorted because of the finite shear stiffness, and that it has a mass moment of inertia $J = \rho I dx$. The net shear force acting on the element is equal to the inertia force so that Eq. (26) still holds, which is repeated here for convenience

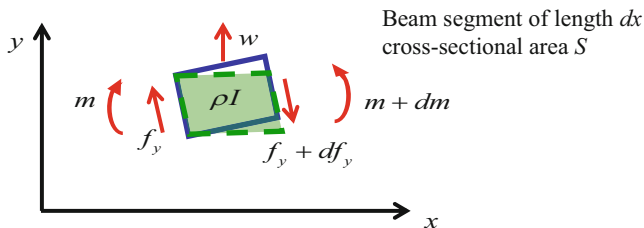


Fig. 8 Free vibration of a Timoshenko beam

$$\frac{\partial f_y}{\partial x} = -\rho S \frac{\partial^2 w}{\partial t^2} \quad (40)$$

Summing the moments about the right-hand edge also results in the same equation as for the Euler–Bernoulli beam, which is given in Eq. (27). However, it is not now set to zero, but is equal to the inertia moment, so that

$$\frac{\partial m}{\partial x} - f_y = \rho I \frac{\partial^2 \psi}{\partial t^2} \quad (41)$$

where ψ is the angular rotation of the element due to the finite shear stiffness. The Hooke's law relationships for the shear force and moment are given by (Graff 1975)

$$f_y = -GS\kappa \left(\frac{\partial w}{\partial x} - \psi \right) \quad (42a)$$

and

$$m = EI \frac{\partial \psi}{\partial x} \quad (42b)$$

where G is the shear modulus and κ is the Timoshenko shear shape factor. Substituting for f_y and m from Eqs. (42a) and (42b) into Eqs. (40) and (41) gives

$$GS\kappa \left(\frac{\partial \psi}{\partial x} - \frac{\partial^2 w}{\partial x^2} \right) + \rho S \frac{\partial^2 w}{\partial t^2} = 0 \quad (43a)$$

$$GS\kappa \left(\frac{\partial w}{\partial x} - \psi \right) + EI \frac{\partial^2 \psi}{\partial x^2} - \rho I \frac{\partial^2 \psi}{\partial t^2} = 0 \quad (43b)$$

Now, Eq. (43a) can be written as

$$\frac{\partial \psi}{\partial x} = \frac{\partial^2 w}{\partial x^2} - \frac{\rho}{G\kappa} \frac{\partial^2 w}{\partial t^2} \quad (44)$$

which can be differentiated twice with respect to x to give

$$\frac{\partial^3 \psi}{\partial x^3} = \frac{\partial^4 w}{\partial x^4} - \frac{\rho}{G\kappa} \frac{\partial^4 w}{\partial x^2 \partial t^2} \quad (45)$$

or differentiated twice with respect to t to give

$$\frac{\partial^3 \psi}{\partial x \partial t^2} = \frac{\partial^4 w}{\partial x^2 \partial t^2} - \frac{\rho}{G\kappa} \frac{\partial^4 w}{\partial t^4} \quad (46)$$

Differentiating Eq. (43b) with respect to x gives

$$GS\kappa \left(\frac{\partial^2 w}{\partial x^2} - \frac{\partial \psi}{\partial x} \right) + EI \frac{\partial^3 \psi}{\partial x^3} - \rho I \frac{\partial^3 \psi}{\partial x \partial t^2} = 0 \quad (47)$$

Substituting Eqs. (44), (45) and (46) into Eq. (47) gives the Timoshenko beam equation, written as

$$\underbrace{EI \frac{\partial^4 w}{\partial x^4} + \rho S \frac{\partial^2 w}{\partial t^2}}_{\text{Euler-Bernoulli equation}} - \underbrace{\rho I \frac{\partial^4 w}{\partial x^2 \partial t^2}}_{\text{rotary inertia}} - \underbrace{\frac{\rho EI}{G\kappa} \frac{\partial^4 w}{\partial x^2 \partial t^2}}_{\text{shear stiffness}} + \underbrace{\frac{\rho^2 I}{G\kappa} \frac{\partial^4 y}{\partial t^4}}_{\text{rotary inertia and shear stiffness}} = 0 \quad (48)$$

where the physical significance is given below each term in the equation. Note that if the shear stiffness is set to be infinite and the rotary inertia is set to zero, then Eq. (48) reduces to the Euler–Bernoulli equation given by Eq. (29). Dividing Eq. (48) by EI and assuming a time harmonic response of $w(t) = w(x)e^{j\omega t}$ as before result in the ordinary differential equation

$$\frac{d^4 w(x)}{dx^4} + \left(k_R^2 + \frac{k_{\text{Sh}}^2}{\kappa} \right) \frac{d^2 w(x)}{dx^2} - \left(k_B^4 - \frac{k_R^2 k_{\text{Sh}}^2}{\kappa} \right) w(x) = 0 \quad (49)$$

where $k_B = (\rho S / (EI))^{\frac{1}{4}} \omega^{\frac{1}{2}}$ is the wavenumber for the Euler–Bernoulli beam, $k_R = \sqrt{\rho / E} \omega$ is the wavenumber for the longitudinal wave, and $k_{\text{Sh}} = \sqrt{\rho / G}$ is the wavenumber for a shear wave (note that this is similar to the longitudinal wavenumber, but is a function of the shear modulus rather than the Young's modulus).

Assuming spatial harmonic dependence of the form $w(x) = W e^{jkx}$, Eq. (49) reduces to the dispersion equation given by

$$k^4 - \left(k_R^2 + \frac{k_{\text{Sh}}^2}{\kappa} \right) k^2 - \left(k_B^4 - \frac{k_R^2 k_{\text{Sh}}^2}{\kappa} \right) = 0 \quad (50)$$

This equation is quadratic in k^2 , so the solution for k is given by

$$k = \pm \sqrt{\frac{1}{2} \left(\frac{k_{\text{Sh}}^2}{\kappa} + k_R^2 \right)} \pm \sqrt{k_B^4 + \frac{1}{4} \left(\frac{k_{\text{Sh}}^2}{\kappa} - k_R^2 \right)^2} \quad (51)$$

At low frequencies, $k_{1,2} \approx \pm j k_B$ and $k_{3,4} \approx \pm k_B$ as a consequence of the rotary inertia being small and the shear stiffness being very large. At high frequencies,

$k_{1,2} \approx \pm k_R$ and $k_{3,4} \approx \pm k_{Sh}/\sqrt{\kappa}$. Noting that $k_{Sh}^2/k_R^2 = E/G = 2(1+\nu)$ and $k_B^4/k_R^4 = 1/4\pi^2(r/\lambda_R)^2$, where $r = \sqrt{I/S}$ is the radius of gyration and $\lambda_R = 2\pi/k_R$, Eq. (51) can be written in non-dimensional form by dividing by k_R to give

$$\hat{k} = \frac{k}{k_R} = \pm \sqrt{\frac{1}{2} \left(\frac{2(1+\nu)}{\kappa} + 1 \right) \pm \frac{1}{2} \sqrt{\frac{1}{\pi^2(r/\lambda_R)^2} + \left(\frac{2(1+\nu)}{\kappa} - 1 \right)^2}} \quad (52)$$

Note that the wavenumbers are dependent on frequency because they are a function of λ_R . It can also be seen that they are dependent on the Timoshenko shear coefficient and Poisson's ratio. To gain physical insight into the wave behaviour at high and low frequencies, the asymptotes of Eq. (52) are examined. At low frequencies when $\lambda_R \gg 1$, the wavenumbers approximate to

$$\hat{k}_{1,2} \approx \pm j \sqrt{\frac{1}{2\pi(r/\lambda_R)}} \quad (53a)$$

and

$$\hat{k}_{3,4} \approx \pm \sqrt{\frac{1}{2\pi(r/\lambda_R)}} \quad (53b)$$

which correspond to normalised Euler–Bernoulli beam wavenumbers. Note that it was assumed that $w(x) = We^{jkx}$ so $\hat{k}_{1,2}$ corresponds to evanescent waves and $\hat{k}_{3,4}$ corresponds to propagating waves. At high frequencies, Eq. (52) approximates to

$$\hat{k} \approx \pm \sqrt{\frac{1}{2} \left(\frac{2(1+\nu)}{\kappa} + 1 \right) \pm \frac{1}{2} \left(\frac{2(1+\nu)}{\kappa} - 1 \right) \left(1 + \frac{1}{2\pi^2 \left(\frac{r}{\lambda_R} \right)^2 \left(\frac{2(1+\nu)}{\kappa} - 1 \right)^2} \right)} \quad (54)$$

which simplifies to

$$\hat{k}_{1,2} \approx \pm \left(1 - \frac{1}{8\pi^2 \left(\frac{r}{\lambda_R} \right)^2 \left(\frac{2(1+\nu)}{\kappa} - 1 \right)} \right) \quad (55a)$$

and

$$\hat{k}_{3,4} \approx \pm \sqrt{\frac{2(1+\nu)}{\kappa} + \frac{1}{4\pi^2 \left(\frac{r}{\lambda_R}\right)^2 \left(\frac{2(1+\nu)}{\kappa} - 1\right)}} \quad (55b)$$

At very high frequencies, these approximate to $\hat{k}_{1,2} = \pm 1$ (a longitudinal wave) and $\hat{k}_{3,4} = \pm \sqrt{2(1+\nu)/\kappa}$ (a shear wave). Note that they are both real and hence they correspond to propagating waves. The frequency at which the wavenumbers that correspond to the nearfield waves become real (which is called the cut-off frequency), and hence the waves start to propagate, can be determined from Eq. (52) by setting $(2(1+\nu)/\kappa + 1) - \sqrt{1/\pi^2(r/\lambda_R)^2 + (2(1+\nu)/\kappa - 1)^2} = 0$, which results in

$$\frac{r}{\lambda_R} \Big|_{\text{cut-off}} = \frac{1}{2\pi} \sqrt{\frac{\kappa}{2(1+\nu)}} \quad (56)$$

In dimensional form, this reduces to $\omega_{\text{cut-off}} = \sqrt{GS\kappa/\rho l}$, which is the square root of the shear stiffness per unit length divided by the rotational inertia per unit length. This can be seen as a type of resonance frequency, in which the rotational stiffness and the rotary inertia interact. Below this frequency the shear stiffness stops the wave from propagating, and above this frequency the rotational inertia overcomes the shear stiffness, allowing the wave to propagate. To illustrate the behaviour of the wavenumbers, the modulus of Eq. (52) is plotted in Fig. 9.

Also plotted are the low and high frequency asymptotes. It can be seen that at low frequencies when $r/\lambda_R \ll 1$, then the beam behaves as an Euler–Bernoulli beam, in which there are two evanescent waves and two propagating waves. As frequency increases, the dispersive propagating bending wave changes to a non-dispersive shear wave. The wavenumber corresponding to the evanescent wave becomes smaller (which means that the phase velocity increases) until it reaches zero at the cut-off frequency. At this frequency, the phase velocity is infinite, which means that the group velocity is zero. Physically, this means that for this wave, every point on the beam is in phase, so there is no phase shift between any points. Above the cut-off frequency, the imaginary wavenumber that corresponds to the evanescent wave below the cut-off frequency, becomes real and hence starts to propagate. Note that above the cut-off frequency, as frequency increases this wavenumber also increases, which means that the phase velocity decreases until it reaches a constant value corresponding to the phase velocity of a longitudinal wave.

It should be noted that, just in the same way that the Euler–Bernoulli beam theory has limitations as frequency increases, so Timoshenko beam theory discussed in this section also has limitations as frequency increases. For very high frequencies, where $r/\lambda_R \gg 1$, then Lamb wave theory has to be used to give an adequate description of the wave behaviour (Doyle 1997). Of course, as the theory takes into account more dynamic features then the mathematical model becomes more complex with a consequent loss of physical insight.

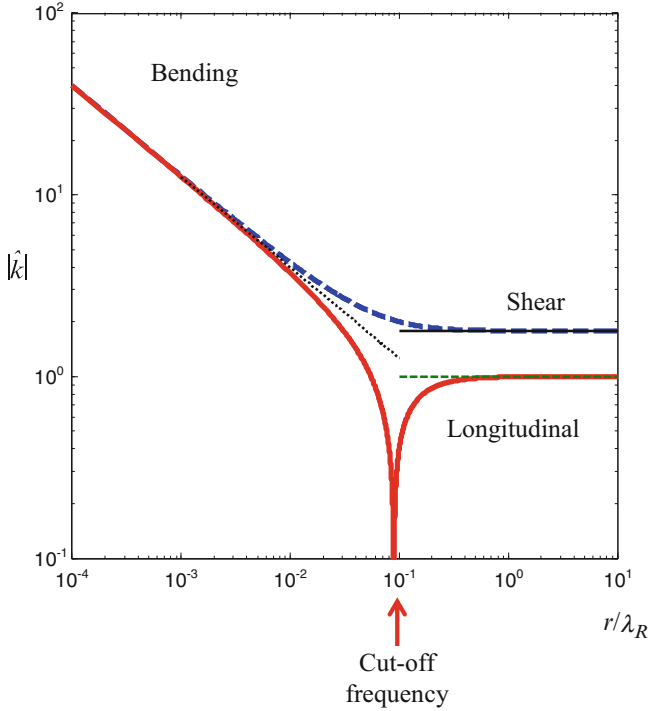


Fig. 9 Normalised wavenumbers for a Timoshenko beam. The shear coefficient is set to 0.833 and Poisson’s ratio is set to 0.33. The *solid red line* is for $\hat{k}_{1,2}$ and the *dashed blue line* is for $\hat{k}_{3,4}$. Below the cut-off frequency $\hat{k}_{1,2}$ is imaginary and above the cut-off frequency $\hat{k}_{1,2}$ is real. The *dotted line* is for the normalised Euler–Bernoulli wavenumber, the thin *dashed green line* is for the longitudinal wavenumber ($\hat{k}_{1,2} = \pm 1$), and the *thin black line* is for the modified shear wavenumber ($\hat{k}_{3,4} = \pm \sqrt{2(1 + \nu)/\kappa}$)

5.2 Wave Mode-Shapes

To gain more information about the waves that propagate at high frequencies, the shape of the wave, which is also called the wave mode-shape, can be determined. To do this, consider Eqs. (43a) and (43b), the solutions of which are given by

$$w(x, t) = B_1 e^{j(\omega t - kx)} \quad \text{and} \quad \psi(x, t) = B_2 e^{j(\omega t - kx)} \tag{57}$$

Substituting these equations into Eqs. (43a) and (43b) gives

$$\begin{bmatrix} GS\kappa k^2 - \rho S\omega^2 & -jGS\kappa k \\ -jGS\kappa k & \rho I\omega^2 - GS\kappa - EI k^2 \end{bmatrix} \begin{Bmatrix} B_1 \\ B_2 \end{Bmatrix} = \begin{Bmatrix} 0 \\ 0 \end{Bmatrix} \tag{58}$$

From Eq. (58), the ratio of the two amplitudes can be written as

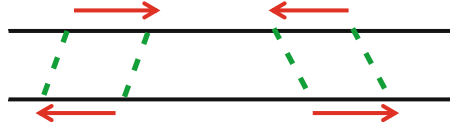


Fig. 10 One of the wave mode-shapes (longitudinal) of a Timoshenko beam at high frequencies

$$\frac{B_2}{B_1} = j \frac{\rho S \omega^2 - G S \kappa k^2}{G S \kappa k} = j \frac{G S \kappa k}{\rho I \omega^2 - G S \kappa - E I k^2} \quad (59)$$

which can be written in non-dimensional form as

$$\frac{B_2 r}{B_1} = j 2\pi \left(\frac{2(1+\nu)}{\hat{k} \kappa} - \hat{k} \right) \left(\frac{r}{\lambda_R} \right) \quad (60)$$

Substituting for $\hat{k} = \pm 1$ from Eq. (55a) results in the mode-shape for the wave that propagates at the phase velocity of a longitudinal wave, which is given by

$$\left. \frac{B_2 r}{B_1} \right|_{\text{Long}} \gg 1 \quad (61)$$

Substituting for $\hat{k} = \pm \sqrt{2(1+\nu)/\kappa}$ results in the mode-shape for the wave governed by the shear phase velocity, which is given by

$$\left. \frac{B_2 r}{B_1} \right|_{\text{Shear}} = 0 \quad (62)$$

Note, that in Eq. (61), the lateral displacement tends to zero, and this corresponds to a rotational wave, which is shown in Fig. 10. In Eq. (62) the rotation tends to zero, and this corresponds to a shear wave.

References

- Y.I. Bobrovnikskii, On the energy flow in evanescent waves. *J. Sound Vib.* **152**(1), 175–176 (1992)
- L. Cremer, M. Heckl, B.A.T. Petersson, *Structure-Borne Sound: Structural Vibration and Sound Radiation at Audio Frequency*, 3rd edn. (Springer, Berlin, 2005)
- J.F. Doyle, *Wave Propagation in Structures: Spectral Analysis Using Fast Discrete Fourier Transform*. Mechanical Engineering Series, 2nd edn. (Springer, New York, 1997)
- F. Fahy, P. Gardonio, *Sound and Structural Vibration: Radiation, Transmission and Response*, 2nd edn. (Academic, Oxford, 2007)
- P. Gardonio, M.J. Brennan, Mobility and impedance methods in structural dynamics, in *Advanced Applications in Acoustics, Noise and Vibration*, ed. by F. Fahy, J. Walker (Spon Press, London, 2004), Ch.9

K.F. Graff, *Wave Motion in Elastic Solids* (Clarendon Press, Oxford, 1975)

P. Hagedorn, A. DasGupta, *Vibrations and Waves in Continuous Mechanical Systems* (Wiley, New York, 2007)

E.J. Hearn, *Mechanics of Materials*. International Series on Materials Science and Technology, 2nd edn. (Pergamon Press, London, 1985)

L.E. Kinsler, A.R. Frey, A.B. Coppens, J.V. Sanders, *Fundamentals of Acoustics*, 3rd edn. (Wiley, New York, 1982)

Passive and Active Structural Vibration Control

Marcelo A. Trindade

Abstract The objective of this chapter is to provide some basic concepts of structural vibration, such as natural frequencies, vibration modes, damping factor, frequency response, among others, and, then, extend these concepts to the design of passive and active vibration control solutions. Well-known passive vibration control solutions such as vibration dampers and absorbers are discussed. Some fundamental aspects related to control theory such as feedforward and feedback strategies and simple control laws well adapted for structural control are also presented and the important effect of sensors and actuators positioning is discussed.

Keywords Structural vibration • Active control • Passive control • Positioning of sensors and actuators

1 Fundamentals of Structural Vibrations

Most mechanical structures are subjected to vibrations coming from different sources. Excessive levels of vibration amplitude may lead to a number of problems such as structural fatigue damage and noise radiation. Therefore, there is great interest in potential solutions that could allow to reduce vibration amplitudes in existing structures.

This chapter aims to present some of these potential solutions involving passive and active strategies. Other textbooks discussing some of the topics presented in this chapter can be recommended (Nashif et al. 1985; Mead 1999; Meirovitch 1990; Miu 1992; Inman 1996; Preumont 1997). The objective of this chapter is to provide some basic concepts of structural vibration, such as natural frequencies, vibration modes, damping factor, frequency response, among others, and, then, extend these concepts to the design of passive and active vibration control solutions. Well-known passive vibration control solutions such as vibration dampers and absorbers are discussed. Some fundamental aspects related to control theory such as

M.A. Trindade (✉)

Department of Mechanical Engineering, São Carlos School of Engineering,
University of São Paulo, Av. Trabalhador São-Carlense, 400, São Carlos, SP 13566-590, Brazil
e-mail: trindade@sc.usp.br

feedforward and feedback strategies and simple control laws well adapted for structural control are also presented and the important effect of sensors and actuators positioning is discussed.

1.1 Basic Concepts on Structural Vibration and Potential Mitigation Solutions

Let us start with a general linear model for a vibrating structure that can be represented by the following system of linear ordinary differential equations

$$\mathbf{M}\ddot{\mathbf{u}} + \mathbf{D}\dot{\mathbf{u}} + \mathbf{K}\mathbf{u} = \mathbf{F}, \quad (1)$$

where \mathbf{M} , \mathbf{D} and \mathbf{K} are matrices representing inertia (mass), damping and stiffness of the structure. \mathbf{u} is a vector of generalized displacements (or the degrees of freedom of the system) and \mathbf{F} is a vector representing all external forces applied to the structure (that is, the applied forces that perturb the structure and thus induce its vibration). Within this general framework, the objective of a structural vibration control solution would be to reduce the vibration amplitude of the structure given its properties (that is, \mathbf{M} , \mathbf{D} and \mathbf{K}) and the external perturbation (that is, \mathbf{F}).

There is a number of possible solutions for such a problem but it will be chosen to classify them in two categories: passive and active solutions. Passive vibration control solutions are those in which a modification of the structure's dynamics is possible without an external power source. Active vibration control solutions, on the other hand, require an external power source to modify the structure's dynamics. As it will be emphasized along this chapter, there is no unique solution for a given problem and it is generally necessary to make an analysis in terms of trade-offs to decide on an optimal solution.

For instance, in many practical cases of structural dynamics, an effective vibration control solution is required only within a given frequency range. Therefore, an analysis in the frequency domain usually applies and, hence, the basic concepts of natural frequencies, vibration modes, modal damping factors and frequency response functions are prerequisites for the design of a control solution.

1.2 Natural Frequencies, Vibration Modes and Damping Factors

Let us consider the free response of an equivalent undamped structure represented by Eq. (1) with $\mathbf{D} = 0$ and $\mathbf{F} = 0$. A harmonic solution of the form $\mathbf{u}(t) = \boldsymbol{\phi}_j e^{i\omega_j t}$ is obtained provided that the following generalized eigenvalue problem is satisfied

$$\left(-\omega_j^2 \mathbf{M} + \mathbf{K}\right) \boldsymbol{\phi}_j = 0. \quad (2)$$

The solution of this eigenvalue problem yields the undamped natural frequencies ω_j and vibration modes $\boldsymbol{\phi}_j$ of the structure. In practice, however, various dissipation mechanisms lead to damped structural responses. The modal damping factor ξ_j associated with each vibration mode can be represented considering a proportional Rayleigh damping, $\mathbf{D} = \beta_1 \mathbf{M} + \beta_2 \mathbf{K}$, such that

$$\xi_j = \frac{1}{2} \left(\frac{\beta_1}{\omega_j} + \beta_2 \omega_j \right). \quad (3)$$

1.3 Principle of Modal Superposition

The generalized displacements vector can then be rewritten as the sum of the harmonic responses such that

$$\mathbf{u}(t) = \sum_j \boldsymbol{\phi}_j \alpha_j(t) = \boldsymbol{\Phi} \boldsymbol{\alpha}(t), \quad (4)$$

and the system matrices can be projected into the modal basis leading to $\boldsymbol{\Phi}^t \mathbf{M} \boldsymbol{\Phi} = \text{diag}(1)$, $\boldsymbol{\Phi}^t \mathbf{D} \boldsymbol{\Phi} = \text{diag}(2\xi_j \omega_j)$ and $\boldsymbol{\Phi}^t \mathbf{K} \boldsymbol{\Phi} = \text{diag}(\omega_j^2)$. The equations of motion are then rewritten as

$$\begin{cases} \ddot{\alpha}_j + 2\xi_j \omega_j \dot{\alpha}_j + \omega_j^2 \alpha_j = f_j, \\ y = \sum_j c_{yj} \alpha_j, \end{cases} \quad (5)$$

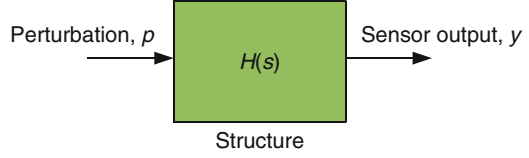
where f_j and c_{yj} provide, respectively, measures of how well the j th vibration mode is excited by the input perturbation force and observed by the output sensor, such that

$$f_j = \boldsymbol{\phi}_j^t \mathbf{F}, \quad c_{yj} = \mathbf{c}_y \boldsymbol{\phi}_j. \quad (6)$$

1.4 Frequency Response Functions and Transfer Functions

A systemic way of analyzing the structure's dynamical response is to evaluate its transfer function $H(s)$ or frequency response function $H(i\omega)$ which are defined as the ratio between an output signal y of the structure and an input signal p either in the Laplace domain or frequency domain, respectively. Then, the input-output

Fig. 1 Structure represented by a single input single output (SISO) linear system



relationship of the structure can be schematically represented as in Fig. 1. For that, the applied force vector \mathbf{F} is written in terms of the input signal p and the output signal is constructed in terms of the structure's generalized displacements,

$$\mathbf{F} = \mathbf{b}_p p, \quad y = \mathbf{c}_y \mathbf{u}. \quad (7)$$

The response of the structure in frequency domain can be obtained considering a harmonic excitation $p = \tilde{p} e^{i\omega t}$, such that $\mathbf{u} = \tilde{\mathbf{u}} e^{i\omega t}$ and $y = \tilde{y} e^{i\omega t}$. Then, the frequency response function $H(i\omega)$ is defined as

$$H(i\omega) = \frac{\tilde{y}}{\tilde{p}} = \mathbf{c}_y (-\omega^2 \mathbf{M} + i\omega \mathbf{D} + \mathbf{K})^{-1} \mathbf{b}_p. \quad (8)$$

In the modal basis, the frequency response function reads

$$H(i\omega) = \sum_j \frac{c_{yj} b_{pj}}{-\omega^2 + \omega_j^2 + i2\xi_j \omega_j \omega}. \quad (9)$$

A reduced model could be constructed by retaining the contribution of only a few N_r vibration modes (modal truncation). The contribution of the remaining $N - N_r$ vibration modes to the FRF is then neglected entirely. Alternatively, only the static contribution of these remaining modes could be accounted for, leading to

$$H(i\omega) \approx \sum_{j=1}^{N_r} \frac{c_{yj} b_{pj}}{-\omega^2 + \omega_j^2 + i2\xi_j \omega_j \omega} + \sum_{j=N_r+1}^N \frac{c_{yj} b_{pj}}{\omega_j^2}. \quad (10)$$

In the Laplace domain, a transfer function $H(s)$ is defined as

$$H(s) = \frac{\tilde{y}}{\tilde{p}} = \mathbf{c}_y (s^2 \mathbf{M} + s \mathbf{D} + \mathbf{K})^{-1} \mathbf{b}_p, \quad (11)$$

or, in modal form,

$$H(s) = \sum_j \frac{c_{yj} b_{pj}}{s^2 + 2\xi_j \omega_j s + \omega_j^2}. \quad (12)$$

It is worthwhile to rewrite the transfer function as the ratio of two functions such that

$$H(s) = \frac{N(s)}{D(s)} \tag{13}$$

with

$$N(s) = \mathbf{c}_y \text{adj} (s^2 \mathbf{M} + s \mathbf{D} + \mathbf{K}) \mathbf{b}_p, \quad D(s) = \det (s^2 \mathbf{M} + s \mathbf{D} + \mathbf{K}). \tag{14}$$

In system and control theories, a transfer function can be also represented by its poles and zeros. The poles are the roots of $D(s) = \prod_j (s - p_j) = 0$, that is $p_j = -\xi_j \omega_j \pm \omega_j (\xi_j^2 - 1)^{1/2}$, which for low values of $\xi_j (\xi_j < 0.5)$ corresponds to resonance peaks in the FRF (at resonance frequencies). The zeros are the roots of $N(s) = \prod_k (s - z_k) = 0$, which could also be written in the form $z_j = -\xi_j \omega_j \pm \omega_j (\xi_j^2 - 1)^{1/2}$ such that for low values of $\xi_j (\xi_j < 0.5)$ corresponds to the anti-resonances in the FRF (at anti-resonance frequencies).

1.5 Analysis of Poles and Zeros for a Simple Spring–Mass Example

Let us consider a simple three degree-of-freedom system composed of lumped masses interconnected by linear springs (Fig. 2). All dissipation mechanisms are represented by a modal damping factor of 0.5 %. Since this is a discrete system, both excitation (input) and measurement (output) can only be done in one of the three lumped masses. However, for each combination of input/output, this system will be represented by different transfer functions $H(s)$ and, thus, will present different responses. In Fig. 3, the pole–zero map (which shows the poles and zeros of the system plotted in the real and imaginary plan, Fig. 3a) and frequency response function amplitude (Fig. 3b) are shown by first considering input and output in the first mass (that is, the excitation is done through a force applied to the

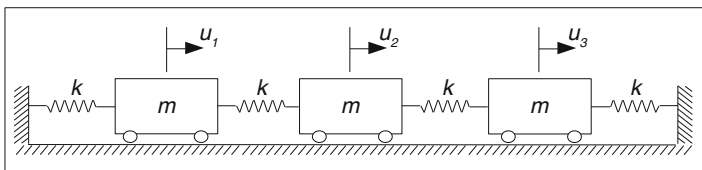


Fig. 2 Schematic representation of a three degree-of-freedom spring–mass system ($m = 2 \text{ kg}$, $k = 1 \text{ kN/m}$, $\xi = 0.5 \%$)

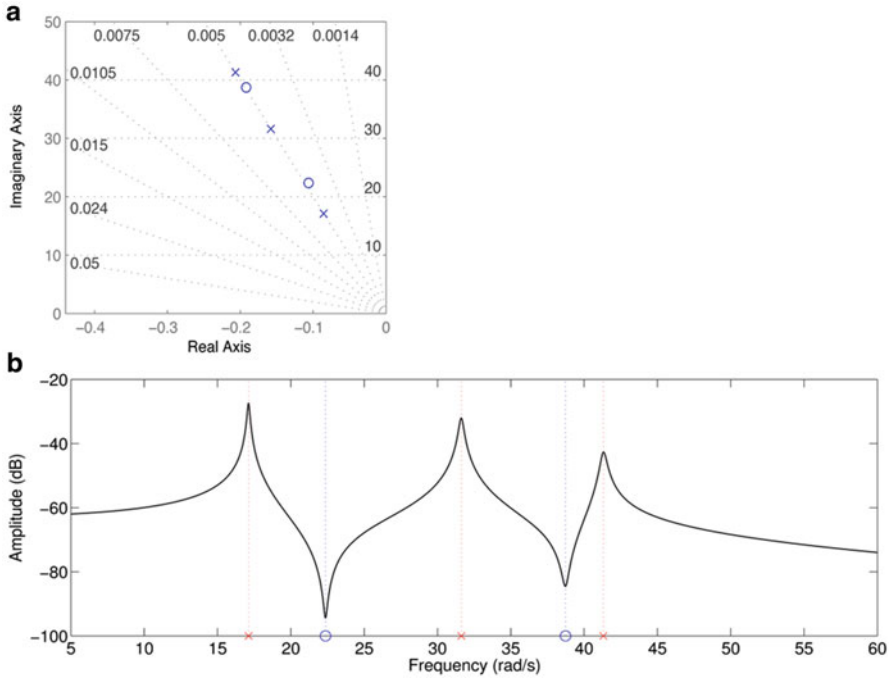


Fig. 3 Equivalence between (a) pole–zero map and (b) frequency response function

first, left, mass and the resulting displacement of the same mass is observed, or measured). They show that, indeed, the poles are associated to resonances while the zeros correspond to anti-resonances of the system.

As predicted in Eq. (14), the poles (and thus resonances) only depend on the system properties (that is, \mathbf{M} , \mathbf{D} and \mathbf{K}) while the zeros (and thus anti-resonances) depend also on the input and output position/configuration (that is, \mathbf{c}_y and \mathbf{b}_p). This can be observed in Fig. 4 that shows the frequency response functions (together with the corresponding poles and zeros in the x -axis) for the same spring–mass system but now with the measurement (output) in the second, center (Fig. 4a) and third, right (Fig. 4b) masses, while the excitation (input) is kept at the first, left, mass.

While the zeros or anti-resonances seem to be less important to the response of the system, they will be very important in the case of feedback control. Thus, it is worthwhile to analyze further the origin and meaning of the system zeros. Indeed, it can be shown that the zeros of the system correspond to the poles of remaining subsystems obtained by excluding the subsystems between the actuator (input) and sensor (output) (Miu 1992). This is represented schematically in Fig. 5.

If the actuator and sensor are collocated, they will be in phase for all vibration modes. In this case, the system is defined as minimum phase system. It can be also observed that, in this case, there is an anti-resonance (or a zero) between each two

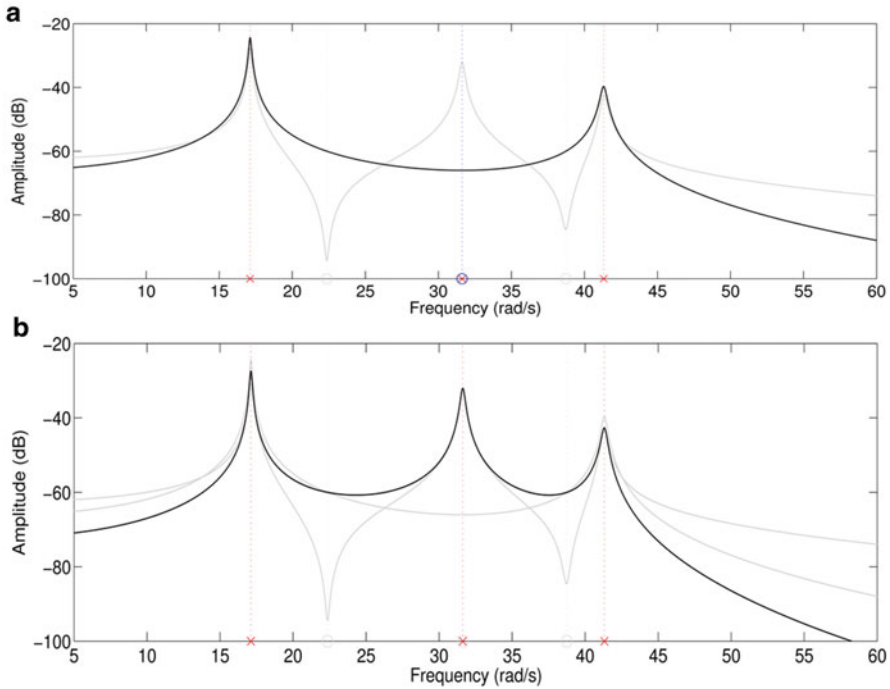


Fig. 4 Zeros depend on actuator and sensor positioning while poles do not

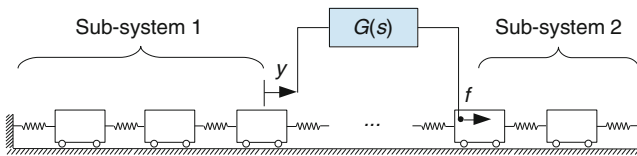


Fig. 5 Transfer function zeros correspond to poles of subsystems excluding the one between actuator and sensor

resonances (or poles). The phase is recovered in the anti-resonances and that is why, in this case, all vibration modes are in phase. This is shown in Fig. 6.

On the other hand, if there are flexible elements between actuator and sensor, it is possible that they will not be in phase for a group of resonant vibration modes. The system is then defined as non-minimum phase system. In this case, there is no guarantee that there will be an anti-resonance (or zero) between any two resonances (or poles) and, thus, the phase may not be recovered. This is shown in Figs. 7 and 8. For the observation in the second mass, there is only one zero which corresponds to a one degree-of-freedom system composed of the third mass and the two connecting springs (leading to a resonance at $\omega = \sqrt{(2k/m)}$) (Fig. 7). This zero coincides with the second resonance (pole) of the original (full) system and, thus, there is a

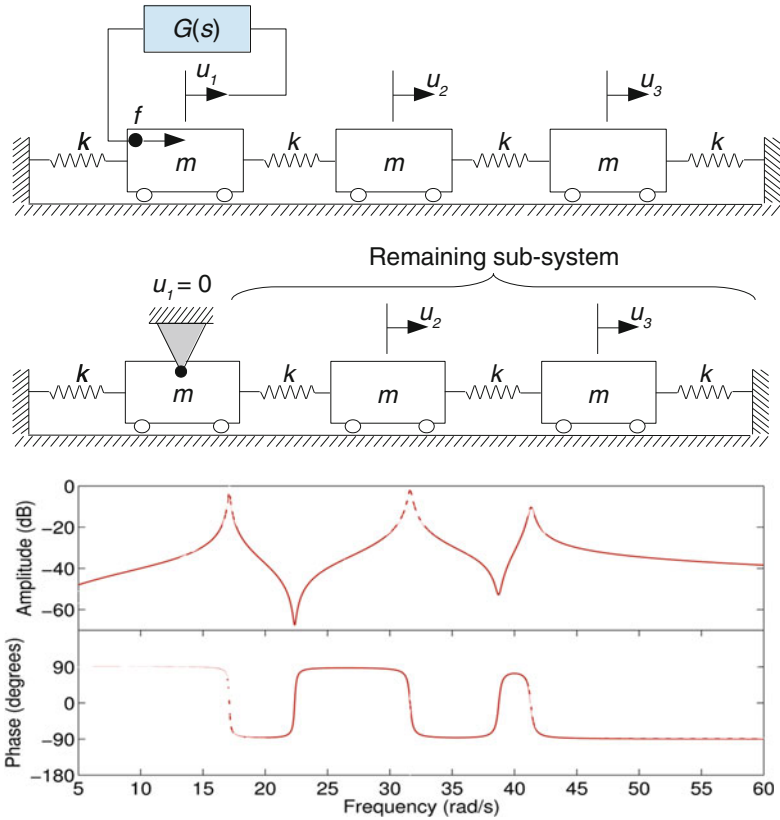


Fig. 6 Collocated actuator and sensor leading to a minimum phase system

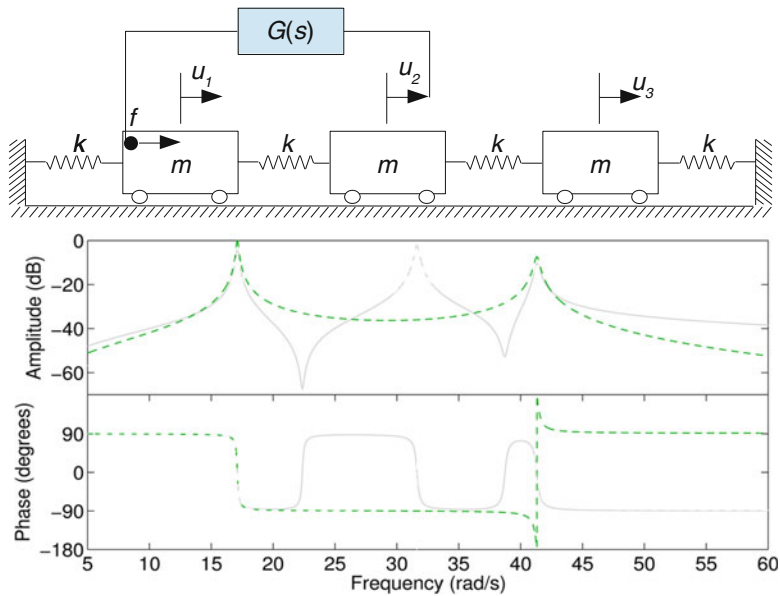


Fig. 7 Flexible elements between actuator and sensor lead to non-minimum phase systems

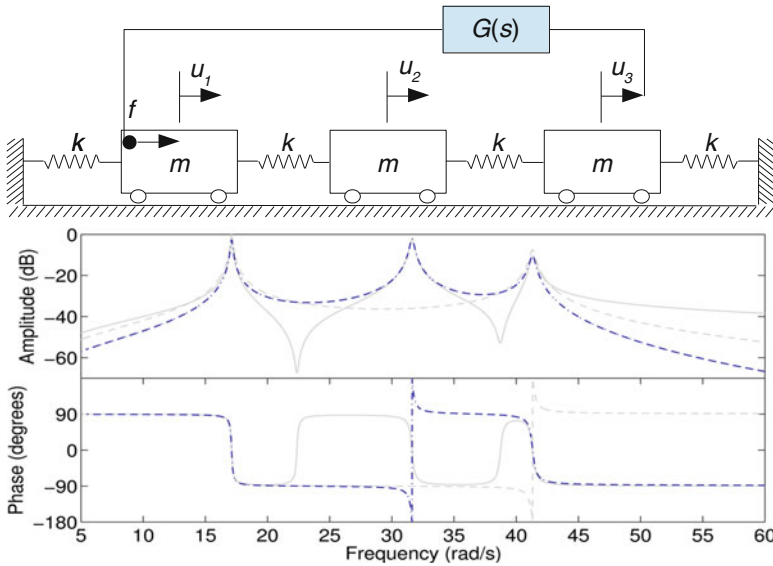


Fig. 8 Flexible elements between actuator and sensor lead to non-minimum phase systems

pole–zero cancellation. This can be also interpreted as being due to the positioning of the sensor in a node of the second vibration mode (for which the second mass does not move). Therefore, there is no phase recovery between first and third resonances and, thus, these modes are out-of-phase (Fig. 7). When the sensor is displaced to the third mass (Fig. 8), there are no longer zeros of the system (there is no remaining resonant subsystem) and, thus, there is no phase recovery between any of the resonances. It is worthwhile to notice, however, that the first and third modes will be in phase (or 360° out-of-phase).

2 Passive Vibration Control

In general terms, passive vibration control can be defined as the modification of the structure’s dynamical behavior such that the vibration amplitude is minimized within a given frequency range and that no substantial external power is required for this modification to occur. The most popular passive vibration control solutions involve the inclusion of dampers and/or absorbers. They both are intended to extract the vibration energy of the host structure leading to smaller vibration amplitudes in the host structure. A generic vibration damper possesses some dissipation mechanism such that when connected to the host structure and, thus, vibrating with it, part of structure’s energy is dissipated in the damper. On the other hand, a generic vibration absorber consists of a resonant vibrating system that is capable of stealing the vibration energy of the primary system (that is, the host

structure). The vibration absorber itself may present high levels of vibration amplitude but from the host structure's viewpoint the vibration amplitude is reduced. The basic component for a successful solution of vibration dampers and absorbers is the mechanical coupling with the host structure such that a significant part of the structure's energy can be transferred to the damper or absorber.

2.1 Passive Vibration Dampers

Vibration dampers differ basically in terms of their dissipation mechanism and their mechanical coupling with the host structure. This section introduces the general concept of two commonly used types of passive vibration dampers: (1) the generic dashpot, for which the resisting force depends on the relative velocity between its two extremities and is based on viscous friction, and (2) viscoelastic dampers, which develop a resisting force that depends on both their mechanical strain and strain rate. Apart from some practical aspects, such as the design of the damper device itself, the main difference between them is that an ideal dashpot is generally represented by its linear viscous damping coefficient whereas viscoelastic dampers are represented by the combination of a spring and a hysteretic damper. Therefore, the second damper type leads also to an overall increase of the stiffness of the original system (besides the increase of damping).

Let us consider a viscous damper added to a generic 3-dof primary system, represented by a spring–mass–damper system as shown in Fig. 9. The original damping of the primary system is considered so that an equal modal damping of 0.5 % for all three vibration modes is obtained and, thus, it is not represented through dashpots in Fig. 9. The other system parameters are: $m = 2\text{kg}$ and $k = 1000\text{N/m}$.

The viscous damper, although representing a localized damping, is intended to increase the modal damping of all vibration modes. Therefore, the location should be chosen such that the damper relative motion is non-null for all modes and maximized for the modes of special interest. In this case, all three vibration modes are affected by the viscous damper. Figure 10 shows the frequency response function between displacement of the first (left) mass and force applied at the same mass for various viscous damping coefficients considered for the added viscous damper. One may observe that indeed all vibration modes are substantially damped. The modal damping factors are shown in Table 1. Notice that the added viscous

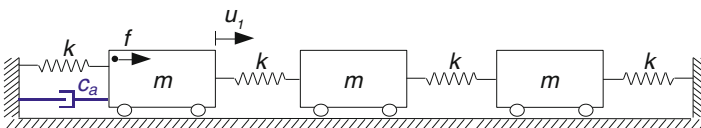


Fig. 9 Viscous damper added to the original structure

Fig. 10 Example of localized viscous damper effect on the vibration amplitude reduction, c_a (Ns/m): 0 (solid), 5 (long dash), 10 (dash-dot), 20 (short dash)

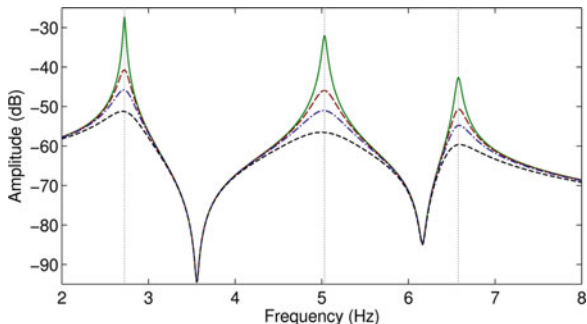


Table 1 Modal damping factors for various localized viscous damping coefficients

c_a (Ns/m)	ξ_1 (%)	ξ_2 (%)	ξ_3 (%)
0	0.5	0.5	0.5
5	2.3	2.5	1.3
10	4.1	4.5	2.0
20	7.8	8.8	3.2

damping coefficient is much higher than the equivalent original one (of about 0.6 Ns/m).

Using the same original spring–mass–damper system, a second analysis is performed considering a viscoelastic damper instead of a viscous damper. The viscoelastic damper is represented by a spring in Fig. 11. However, as it will be shown next, the force developed by the damper is also dependent on the relative velocity between its extremities. Actually, when subjected to a harmonic vibration, a viscoelastic damper presents a hysteretic behavior such that the energy dissipated over one cycle depends on material properties and strain amplitude. One simple way of representing this effect is to consider a complex elastic modulus for the viscoelastic material, which in turn leads to a complex spring coefficient for the viscoelastic damper such that

$$k_a^* = k_a(1 + i\eta), \tag{15}$$

where k_a represents the elastic (or storage) part of the stiffness and η is defined as loss factor. For a 1-dof system with an added viscoelastic damper, the following equation of motion can be written in the frequency domain

$$[-\omega^2 m + i\omega c + (k + k_a^*)] \tilde{u} = \tilde{f}, \tag{16}$$

and, thus,

$$[-\omega^2 m + i(\omega c + k_a \eta) + (k + k_a)] \tilde{u} = \tilde{f}. \tag{17}$$

Hence, for harmonic excitation, an equivalent viscous damping coefficient $c_a = k_a \eta / \omega$ is added to the system besides the increase in the equivalent spring coefficient from k to $k + k_a$.

In the case of the 3-dof system presented in Fig. 11, the effect of the viscoelastic damper in the frequency response function between displacement of the first (left) mass and force applied at the same mass for various storage coefficients considered for the viscoelastic damper is shown in Fig. 12. The loss factor is considered to be equal to 1 in all cases. The results indicate that the modal damping factors of all three vibration modes are increased substantially, but also that this is accompanied by an increase in all resonance frequencies. The resulting modal damping factors are shown in Table 2.

The reader should be aware that the material properties (storage modulus and loss factor) of viscoelastic materials, and thus viscoelastic dampers, normally vary

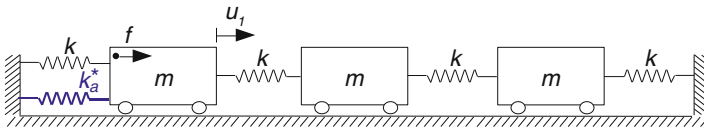


Fig. 11 Viscoelastic damper added to the original structure

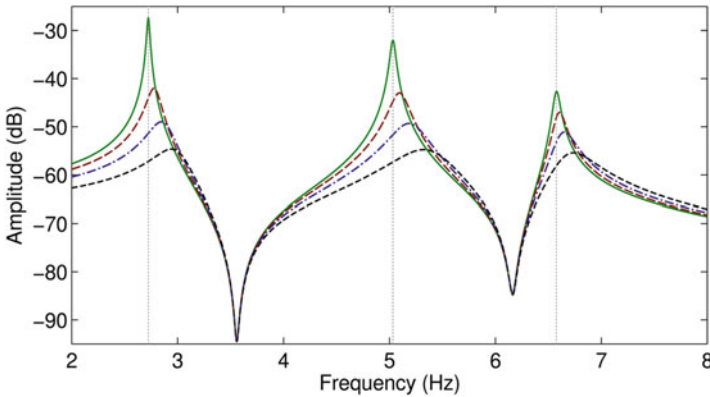


Fig. 12 Example of localized viscoelastic damper effect on the vibration amplitude reduction, k_a/k (%): 0 (solid), 10 (long dash), 25 (dash-dot), 50 (short dash)

Table 2 Modal damping factors for various localized viscoelastic storage stiffnesses

k_a/k (%)	ξ_1 (%)	ξ_2 (%)	ξ_3 (%)
0	0.5	0.5	0.5
10	2.4	1.7	0.9
25	4.3	3.4	1.6
50	6.0	5.6	3.2

with frequency and temperature. Therefore, a more thorough analysis should be carried out to quantify the performance of a viscoelastic damper. For that, the reader may consult several textbooks in the field (Nashif et al. 1985; Mead 1999).

2.2 Passive Dynamic Vibration Absorbers

Dynamic vibration absorbers are subsystems that when connected to the original (or primary) system may “absorb” its vibration energy. This leads to a reduction of the vibration amplitude of the primary system accompanied by potentially high vibration levels in the vibration absorber. This section introduces the fundamental concept of dynamic vibration absorbers and some design criteria based on the effect of their parameters on the vibration amplitude of the primary system.

Let us start with a general primary system represented by a spring–mass–damper system with parameters k_p , m_p and c_p . The dynamic vibration absorber is considered to be another spring–mass–damper system, with parameters k_a , m_a and c_a , connected to the primary system through its spring and damper as shown in Fig. 13.

The equations of motion of the coupled system can be written as

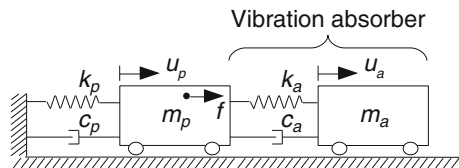
$$\begin{bmatrix} m_p & 0 \\ 0 & m_a \end{bmatrix} \begin{bmatrix} \ddot{u}_p \\ \ddot{u}_a \end{bmatrix} + \begin{bmatrix} c_p + c_a & -c_a \\ -c_a & c_a \end{bmatrix} \begin{bmatrix} \dot{u}_p \\ \dot{u}_a \end{bmatrix} + \begin{bmatrix} k_p + k_a & -k_a \\ -k_a & k_a \end{bmatrix} \begin{bmatrix} u_p \\ u_a \end{bmatrix} = \begin{bmatrix} f \\ 0 \end{bmatrix}. \tag{18}$$

The frequency response function between primary system output u_p and excitation input f can be written in terms of the primary system and absorber parameters such that

$$H(\omega) = \frac{\tilde{u}_p(\omega)}{\tilde{f}(\omega)} = (-\omega^2 m_a + i\omega c_a + k_a) \{ \omega^4 m_a m_p - i\omega^3 [c_a(m_a + m_p) + c_p m_a] - \omega^2 [c_a c_p + k_a(m_a + m_p) + k_p m_a] + i\omega(c_a k_p + c_p k_a) + k_a k_p \}^{-1}, \tag{19}$$

or, for an undamped case,

Fig. 13 Dynamic vibration absorber added to the original structure



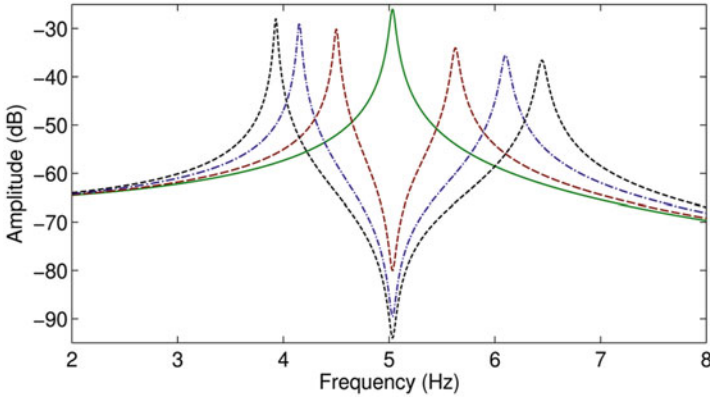


Fig. 14 Effect of absorber mass on the vibration amplitude of the primary system compared to the original response (solid), m_a/m_p (%): 5 (long dash), 15 (dash-dot), 25 (short dash)

$$H(\omega) = \frac{\tilde{u}_p(\omega)}{\tilde{f}(\omega)} = \frac{-\omega^2 m_a + k_a}{\omega^4 m_a m_p - \omega^2 [k_a(m_a + m_p) + k_p m_a] + k_a k_p}. \quad (20)$$

It is possible to observe from Eqs. (19) and (20) that the response amplitude of the primary system at resonance (that is u_p) may be minimized by setting the resonance frequency of the vibration absorber so that it coincides with the primary system (or original) resonance frequency ($\omega_n^2 = k_p/m_p = k_a/m_a$). This leads to a simple design criteria in which the designer has to define the amount of mass that may be considered for the absorber. Therefore, it is worthwhile to analyze the effect of added mass on the vibration absorber performance. This may be observed in Fig. 14, where it is possible to notice that an increase of the added mass yields higher reduction of vibration amplitude at resonance and also wider frequency range for which the vibration amplitude is reduced compared to the original response (that is without the vibration absorber).

It is also clear from Eq. (19), however, that the amount of damping present in the primary system and added through the vibration absorber does affect the reduction in vibration amplitude. Indeed, the effect of an added localized damping (c_a) is to flatten the two resonance peaks but at cost of increasing the amplitude at anti-resonance, leading to a loss of absorption performance in terms of reduction of vibration amplitude at the original resonance. This effect is shown in Fig. 15. Notice however that, in general, the designer should choose a compromise solution between performance at resonance and robustness at frequencies apart from the resonance.

The reader should be aware that there are a number of different techniques to optimize the absorber parameters (m_a , k_a and c_a) depending on the criteria chosen by the designer (Den Hartog 1985).

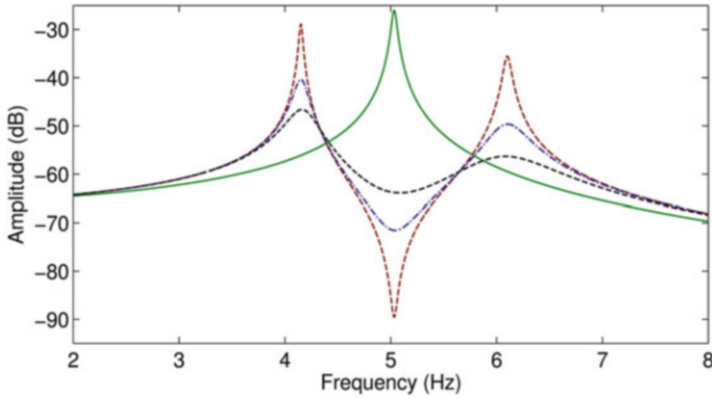
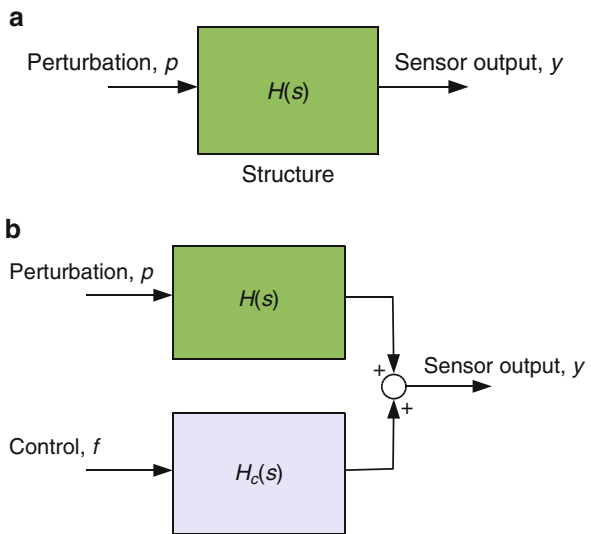


Fig. 15 Effect of absorber damping on the vibration amplitude of the primary system compared to the original response (*solid*), for $m_a/m_p = 15\%$ and ξ_a (%): 0.5 (*long dash*), 4 (*dash-dot*), 10 (*short dash*)

Fig. 16 (a) Open-loop (or original) system and (b) closed-loop system modified by an additional external (control) force



3 Active Vibration Control

Active vibration control can be generally defined as the modification of the dynamic response of the system through the inclusion of an additional external force/input (so-called control force or control input). The response of the structure will then be due to the combined excitations (Fig. 16). The structure’s equations of motion are then rewritten as

$$\begin{cases} \mathbf{M}\ddot{\mathbf{u}} + \mathbf{D}\dot{\mathbf{u}} + \mathbf{K}\mathbf{u} = \mathbf{b}_p p + \mathbf{b}_f f \\ y = \mathbf{c}_y \mathbf{u} \end{cases} \quad (21)$$

The objective of the control design would then be to find the control force f capable of reducing the vibration amplitude (as measured by output y) according to a given set of criteria. Control design strategies may be normally divided into two categories:

- Feedback control (Fig. 17): $f = f(y)$ —The control force f is evaluated based on (or as function of) the measured output y . This generally means that the closed-loop (or controlled) performance is not dependent on the perturbation (or primary excitation). However, in practice, the control force f will depend indirectly on the level of excitation and, thus, the perturbation p must be accounted for.
- Feedforward control (Fig. 18): $f = f(p)$ —The control force f is evaluated based on (or as function of) the perturbation input p . This requires that the perturbation

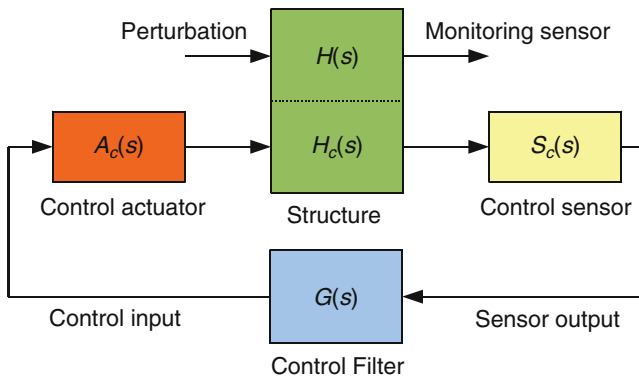


Fig. 17 General active feedback control scheme: control input is dependent on control sensor output

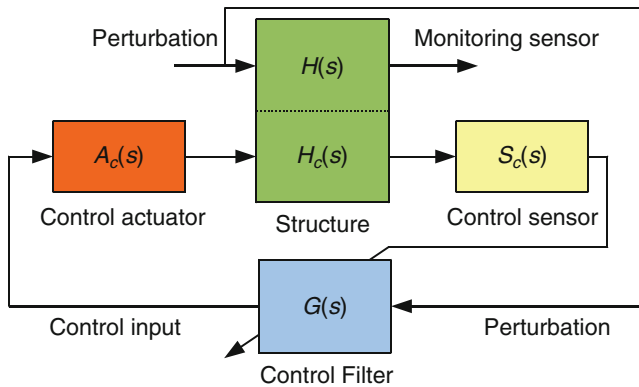


Fig. 18 General active feedforward control scheme: control input is dependent on the perturbation input

input should be known (or measured). In this case, the control force and thus closed-loop performance must be reevaluated (or redesigned) in case of changing perturbation input. Moreover, feedforward control schemes must also account for the measured output in order to quantify/control the performance and, thus, depend indirectly of the output y .

3.1 Feedback Control Strategies

In order to evaluate the closed-loop performance due to a feedback control strategy, let us consider the basic control scheme depicted in Fig. 19. The closed-loop transfer function, denoted as H^* , is then function of the designed control filter $G(s)$, such that

$$\tilde{y} = H\tilde{p} + H_c\tilde{f}, \quad \tilde{f} = -G(s)\tilde{y}. \tag{22}$$

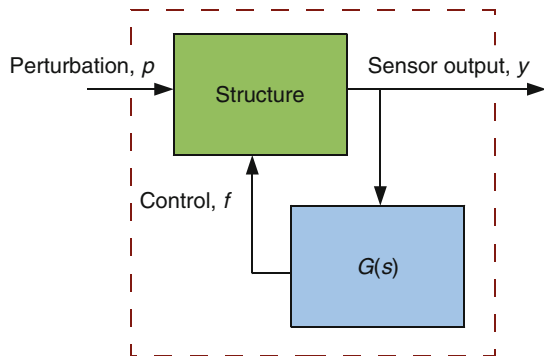
Replacing \tilde{f} , solving for \tilde{y} and defining $H_c = N_c/D$, the closed-loop transfer function reads

$$H^* = \frac{H}{1 + GH_c} = \frac{N_p}{D + GN_c}. \tag{23}$$

This means that, as the control gain is increased, the closed-loop poles of the system move towards the zeros of the transfer function H_c (between output y and control input f). The path followed by the closed-loop poles, for a given open-loop system, depends mainly on two factors: (1) the control law $G(s)$ and (2) the control input positioning which will affect directly the function $N_c(s)$.

In order to analyze the effect of output feedback on a vibrating structure, let us first consider a very simple control law $G(s) = g$, where g is a constant control gain. Then, it is also considered that the displacement or velocity of the structure at some point can be measured. In the case of a direct displacement feedback,

Fig. 19 Basic feedback control scheme



$$y = \mathbf{c}_y \mathbf{u}, \quad f = -gy = -g\mathbf{c}_y \mathbf{u}, \tag{24}$$

and, thus,

$$\mathbf{M}\ddot{\mathbf{u}} + \mathbf{D}\dot{\mathbf{u}} + (\mathbf{K} + g\mathbf{b}_f\mathbf{c}_y)\mathbf{u} = \mathbf{b}_p p. \tag{25}$$

This means that the effect of this control strategy is to modify the stiffness of the structure. On the other hand, if it is considered that velocity is measured and then fed back, defining a direct velocity feedback,

$$y = \mathbf{c}_y \dot{\mathbf{u}}, \quad f = -gy = -g\mathbf{c}_y \dot{\mathbf{u}}, \tag{26}$$

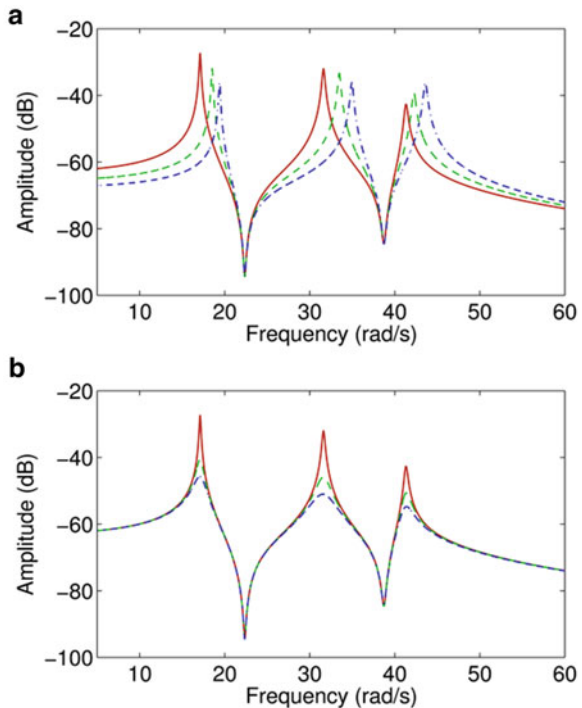
and, thus,

$$\mathbf{M}\ddot{\mathbf{u}} + (\mathbf{D} + g\mathbf{b}_f\mathbf{c}_y)\dot{\mathbf{u}} + \mathbf{K}\mathbf{u} = \mathbf{b}_p p. \tag{27}$$

Thus, the damping of the structure is modified. The way the stiffness and damping of the structure are modified, therefore, depends not only on the control gain g but also on the input and output distribution vectors, \mathbf{c}_y and \mathbf{b}_f , and, hence, in the positioning of sensor and control actuator.

As an example, let us consider the previous 3-dof spring–mass system for which both the sensor and control actuator are positioned at the first mass. Figure 20 shows

Fig. 20 Effect of displacement (**a**, control gains: [0 500 1000] N/m) and velocity (**b**, control gains: [0 5 10] N/(m/s)) feedback on the frequency response function



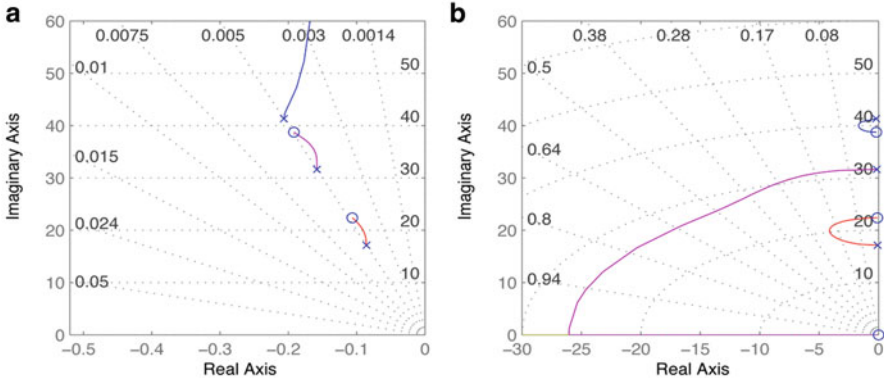


Fig. 21 Effect of displacement (**a**, control gains: [0 500 1000] N/m) and velocity (**b**, control gains: [0 5 10] N/(m/s)) feedback on the pole-zero map

the frequency response function of the closed-loop system considering direct displacement feedback (DDF, Fig. 20a) and direct velocity feedback (DVF, Fig. 20b). It confirms that DDF only modifies structural stiffness (observed through an increase in natural frequencies) while DVF modifies structural damping (observed through a reduction in vibration amplitude). Alternatively, the analysis can be performed observing the root locus (position and path of the closed-loop poles for increasing control gain) of the system which is shown in Fig. 21a, for DDF, and 21b, for DVF. While for DDF the closed-loop poles more or less follow a line of constant damping factor, for DVF the damping of the closed-loop poles is clearly augmented. It is worthwhile to zoom the root locus for DVF (Fig. 22) and notice that, for a given control gain ($g = 10.2\text{Ns/m}$ highlighted in the graph), the amount of added damping (relative to the original damping factor of 0.5 %) is different for each vibration mode. Indeed, in this case, the second vibration mode is the one that is more actively damped (with a closed-loop damping factor of 4.57 %).

Since there is great interest in analyzing the effect of the DVF active control on specific vibration modes, it is worthwhile to rewrite the closed-loop equations of motion projected into the modal basis by considering $\mathbf{u}(t) = \Phi\boldsymbol{\alpha}(t)$ such that

$$\ddot{\boldsymbol{\alpha}} + (\Lambda + g\mathbf{b}_\phi\mathbf{c}_\phi)\dot{\boldsymbol{\alpha}} + \Omega^2\boldsymbol{\alpha} = \Phi^t\mathbf{b}_p p, \tag{28}$$

where the contribution of the velocity feedback to the modal damping factor is mainly due to the vectors of output and input distribution projected into the modal basis,

$$\mathbf{b}_\phi = \Phi^t\mathbf{b}_f, \quad \mathbf{c}_\phi = \mathbf{c}_y\Phi. \tag{29}$$

Notice that the feedback control also couples the original vibration modes since the closed-loop modal damping matrix is no longer diagonal. For the sake of

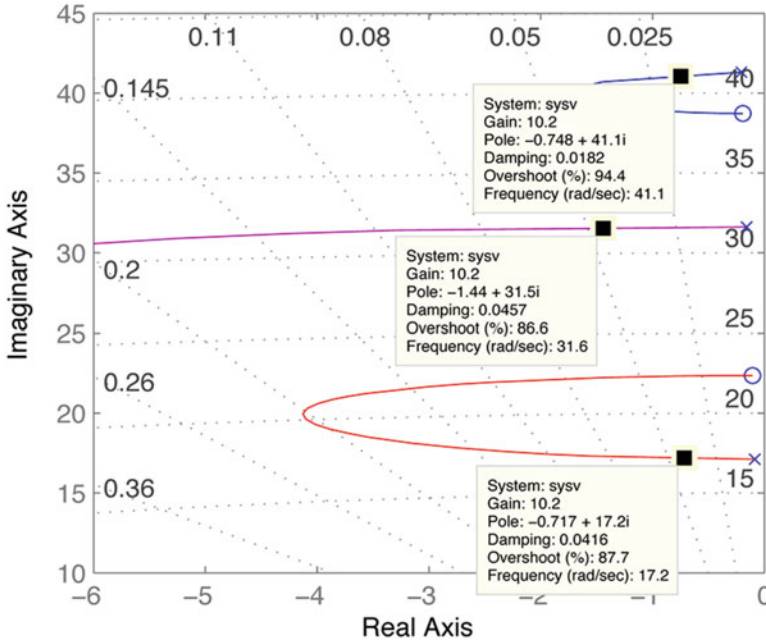


Fig. 22 Effect of velocity (control gains: [0 5 10] N/(m/s)) feedback on the pole–zero map (zoomed)

simplicity, if only the diagonal terms of the added damping matrix are considered, the resulting closed-loop damping factor could be approximated by

$$\lambda_j^* = 2\xi_j^* \omega_j = 2\xi_j \omega_j + g b_j c_j \rightarrow \xi_j^* \approx \xi_j + (g b_j c_j) / (2\omega_j). \quad (30)$$

In the case of the 3-dof spring–mass system, the modal matrix and input and output distribution vectors are

$$\Phi = \begin{bmatrix} -0.3536 & -0.5000 & 0.3536 \\ -0.5000 & 0.0000 & -0.5000 \\ -0.3536 & 0.5000 & 0.3536 \end{bmatrix}, \quad \mathbf{b}_f = \begin{bmatrix} 1 \\ 0 \\ 0 \end{bmatrix}, \quad \mathbf{c}_y = [1 \ 0 \ 0], \quad (31)$$

which leads to the following approximations for the closed-loop damping factors (with control gain $g = 10.2$ Ns/m),

$$\begin{aligned} b_1 c_1 = 0.1250 &\rightarrow \xi_1^* \approx 4.22 \%, \\ b_2 c_2 = 0.2500 &\rightarrow \xi_2^* \approx 4.53 \%, \\ b_3 c_3 = 0.1250 &\rightarrow \xi_3^* \approx 2.04 \%. \end{aligned} \quad (32)$$

This analysis confirms that the second vibration mode is the one that is most affected by the feedback control and this is mainly due to the positioning of the actuator. The analysis also provides a confirmation that for a collocated pair of sensor and actuator, a DVF control may increase all modal damping factors simultaneously. Notice that this is not the case for non-collocated pairs. This is illustrated here by changing the position of the sensor and leaving the actuator at the first mass. For the sensor at the second mass and same control gain, the closed-loop damping factors are approximated as $\xi_1^* = 5.77\%$, $\xi_2^* = 0.50\%$ and $\xi_3^* = -1.68\%$, meaning that as expected the first mode is controlled, the second mode is not modified (since sensor is in a second mode node) and the third mode is destabilized. Indeed, since first and third modes are out-of-phase it is not possible to control both at the same time. For the sensor at the third mass and same control gain, the closed-loop damping factors are approximated as $\xi_1^* = 4.22\%$, $\xi_2^* = -3.53\%$ and $\xi_3^* = 2.04\%$. In this case, the first and third modes are in-phase but the second mode is out-of-phase. Thus, first and third modes are controlled but the second mode is destabilized.

A root locus analysis provides a more precise information about the feedback control effect on each closed-loop pole. This is shown in Fig. 23 for the three possible sensor positions while the actuator is kept at the first mass.

It is also possible to evaluate the natural frequency and modal damping factor of each vibration mode for increasing DVF control gain values (Fig. 24).

3.2 Positioning of Sensors and Actuators

From the previous section, it is noticeable that the positioning of sensors and actuators has a great importance in the performance of feedback control schemes. It was also observed that for a simple control law, such as DVF, the projections of

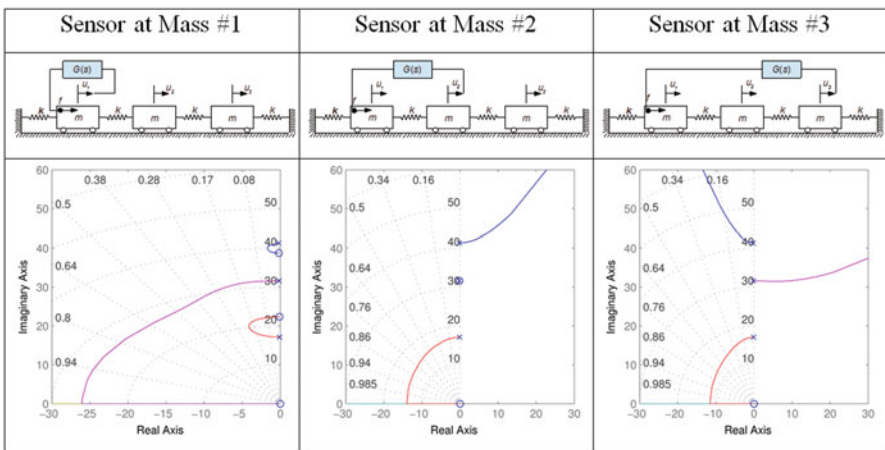


Fig. 23 Effect of non-minimum phase on the control of first three vibration modes

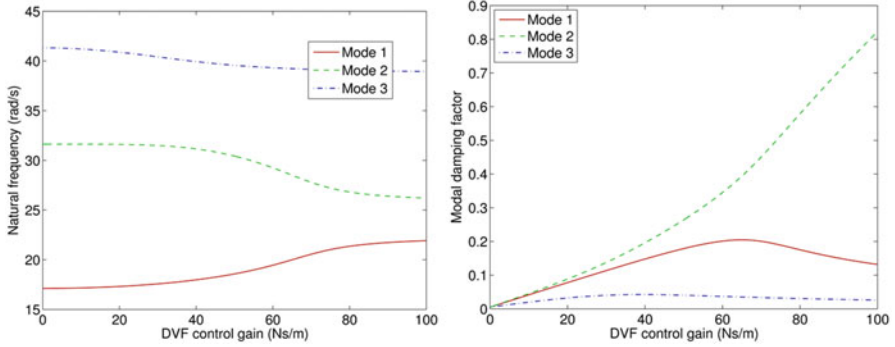


Fig. 24 Closed-loop frequency and damping due to output feedback control (collocated sensor/actuator pair in the first mass)

the input and output distribution vectors onto the modal basis are the main performance factors. Therefore, this information could be used to optimize the positioning of sensors and actuators for better control performance. One possible objective could be to maximize b_j and c_j for a given j th vibration mode.

To this end, the Popov–Belevitch–Hautus (PBH) test could be used to choose from a set of possible locations for sensors and actuators. For each k th mode of interest, a matrix may be constructed considering a sensor i and an actuator j , leading to

$$R_k(i, j) = \mathbf{c}_i \boldsymbol{\phi}_k \boldsymbol{\phi}_k^t \mathbf{b}_j. \quad (33)$$

For the 3-dof spring–mass example, this leads to

$$\mathbf{R}_1 = \begin{bmatrix} 0.125 & 0.177 & 0.125 \\ 0.177 & 0.250 & 0.177 \\ 0.125 & 0.177 & 0.125 \end{bmatrix}, \quad \mathbf{R}_2 = \begin{bmatrix} 0.250 & 0 & -0.250 \\ 0 & 0 & 0 \\ -0.250 & 0 & 0.250 \end{bmatrix}, \quad (34)$$

$$\mathbf{R}_3 = \begin{bmatrix} 0.125 & -0.177 & 0.125 \\ -0.177 & 0.250 & -0.177 \\ 0.125 & -0.177 & 0.125 \end{bmatrix}.$$

This analysis shows that the best solution to control the first and third modes is to place actuator and sensor (collocated) in the second mass, although this leads to no control of the second mode. On the other hand, the best solution to control the second mode is to place actuator and sensor (collocated) in the first or third masses. Indeed, the root locus plots of the three possible collocated solutions, using DDF or DVF, presented in Fig. 25 show that the amount of added damping to the first and third modes can be substantially higher placing the sensor/actuator pair in the second mass, if compared with the added damping that can be obtained for the sensor/actuator pair placed in the first and third masses.

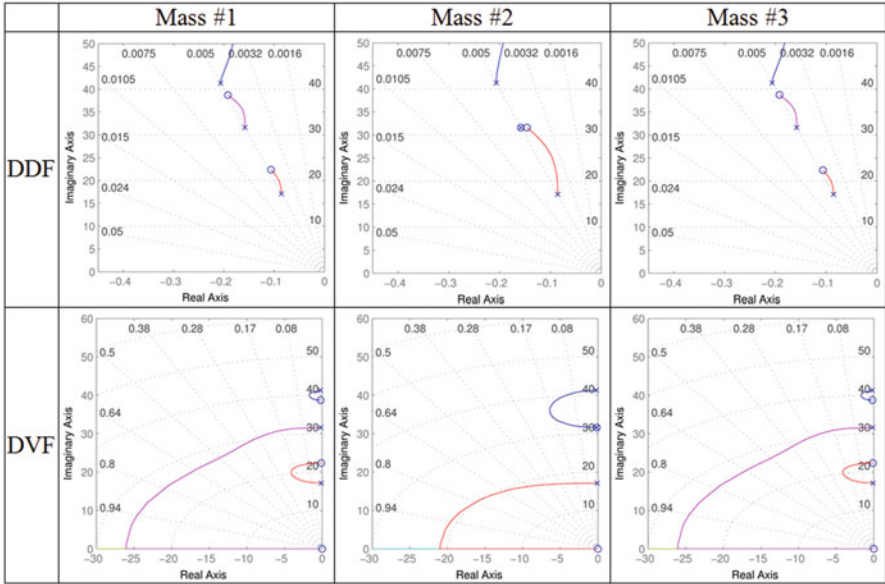


Fig. 25 Root Locus for the three possible positions of a collocated sensor/actuator pair



Fig. 26 Schematic representation of the vibration modes of the 3-dof spring–mass system

Notice that the PBH test also shows the combinations of non-collocated sensor and actuator positions that may lead to destabilization. This can be observed by the difference in sign between different modes for a given sensor/actuator pair.

It is also worthwhile to point out that the vibration modes of the structure provide substantial information about the optimal placement for sensors and actuators. In the case of the spring–mass system with point sensors and actuators, the projection of the input and output distribution vectors is proportional to the modal displacement. Therefore, actuator and sensor should be placed where the modal displacement is higher for the mode of interest (Fig. 26).

3.3 Simple Control Laws Using Output Feedback

Once the optimal location for sensor and actuator is found, it is possible to focus on the design of a proper output feedback control law $G(s)$ (see Fig. 19). First, it should be stated that the control law design depends heavily on the practical application,

since a number of different criteria could be used leading to different optimal solutions. In the present analysis, it is chosen to focus on control laws that allow to increase the structural damping of selected vibration modes.

Let us start by writing $G(s)$ as the following transfer function

$$G(s) = g \frac{N_c(s)}{D_c(s)} \quad (35)$$

Since $\tilde{f} = -G(s)\tilde{y}$, the control force $f(t)$ is to be found in real time by solution of a differential equation that is also function of the measurement $y(t)$,

$$D_c(s)\tilde{f} = -gN_c(s)\tilde{y}, \quad (36)$$

therefore, the order of $G(s)$ should be small enough so that the control processing unit is able to evaluate $f(t)$ in real time.

Previously, it was stated that a velocity feedback (DVF) can be useful for increasing structural damping. However, in some practical applications, the point velocity may not be measured directly. In this case, even for such a simple control law, some additional signal processing may be necessary. For instance, if only the point displacement is available for measurement, the control unit should first differentiate the displacement signal and then feed it back after multiplying it by a control gain. However, if the displacement signal provided by the sensor contains noise, it will also be differentiated. Thus, in this case, a low pass filter should be included. In terms of the control transfer function, this could be achieved by

$$G(s) = g \frac{s}{1} \rightarrow G(s) = g \frac{s}{s+a}, \quad (37)$$

where a is a parameter to be set depending on the frequency range to be filtered. It is easy to see that for higher frequencies ($s \gg a$), the control signal tends to be proportional to the displacement measured signal so that the high frequency noise is not differentiated. For low frequencies ($s \ll a$), the control signal tends to be proportional to the time derivative of the displacement measured signal. The parameter a should be large enough in order not to interfere in the frequency range of interest. Figure 27 shows the importance of the low pass filtering for different noise-to-signal ratios.

In the case where only a point acceleration can be measured, the control unit should integrate the acceleration signal to obtain the corresponding velocity signal to be fed back. However, a low frequency noise or DC value should be filtered before integrating the signal. This could be achieved using the following control transfer function

$$G(s) = g \frac{1}{s} \rightarrow G(s) = g \frac{1}{s+a} \quad (38)$$

which, for low frequencies ($s \ll a$), leads to the feedback of the acceleration signal while, for higher frequencies ($s \gg a$), is equivalent to time integration. The parameter a should be small enough in order not to interfere in the frequency

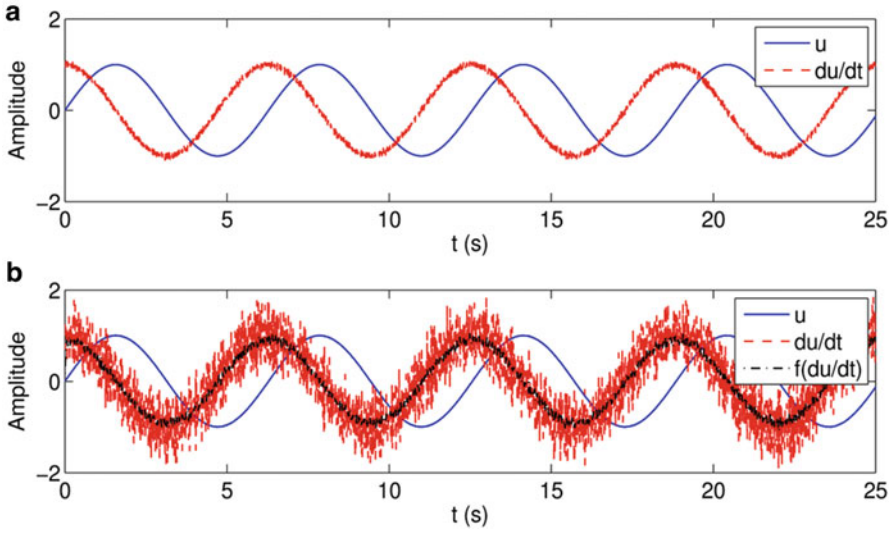


Fig. 27 Effect of noise-to-signal ratio (**a**: $N/S = 1/1000$, **b**: $N/S = 1/100$) in a derivative feedback control

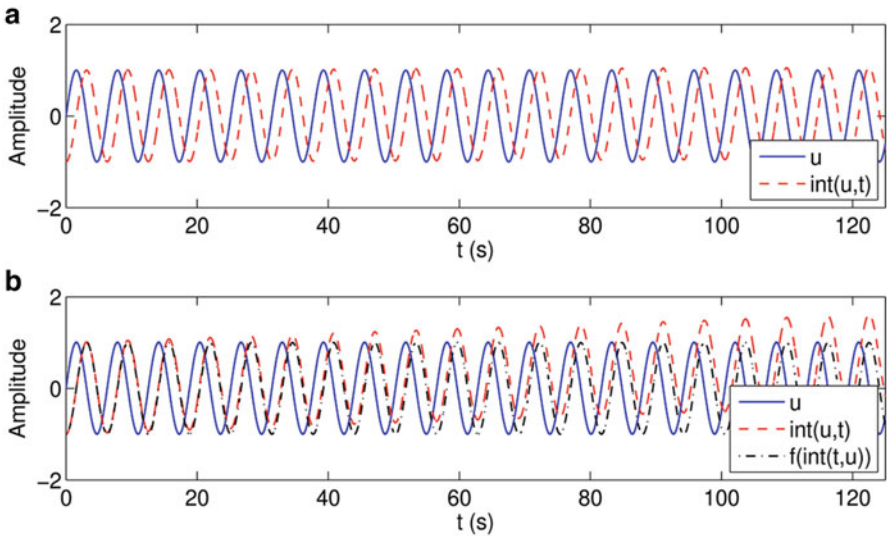


Fig. 28 Effect of noise-to-signal ratio (**a**: $N/S = 1/1000$, **b**: $N/S = 1/100$) in an integral feedback control

range of interest. Figure 28 shows the importance of the high pass filtering for different noise-to-signal ratios.

Sometimes it is interesting to increase both damping factors and natural frequencies of the system. In this case, a combination of velocity and displacement feedback could be used. When displacement is measured, this is equivalent to a PD

(proportional-derivative) control law. This can be achieved by the following control transfer function

$$G(s) = g \frac{1 + Ts}{1}, \tag{39}$$

in which the control parameter T establishes the relative importance of displacement and velocity feedback. Since there is a differentiation of a displacement signal, this control law could also be combined to a low pass filter to minimize noise problems, leading to

$$G(s) = g \frac{1 + Ts}{s + a}, \tag{40}$$

where a should be large enough not to interfere in the control performance.

Figure 29 shows the root locus for a PD control law using a measured displacement.

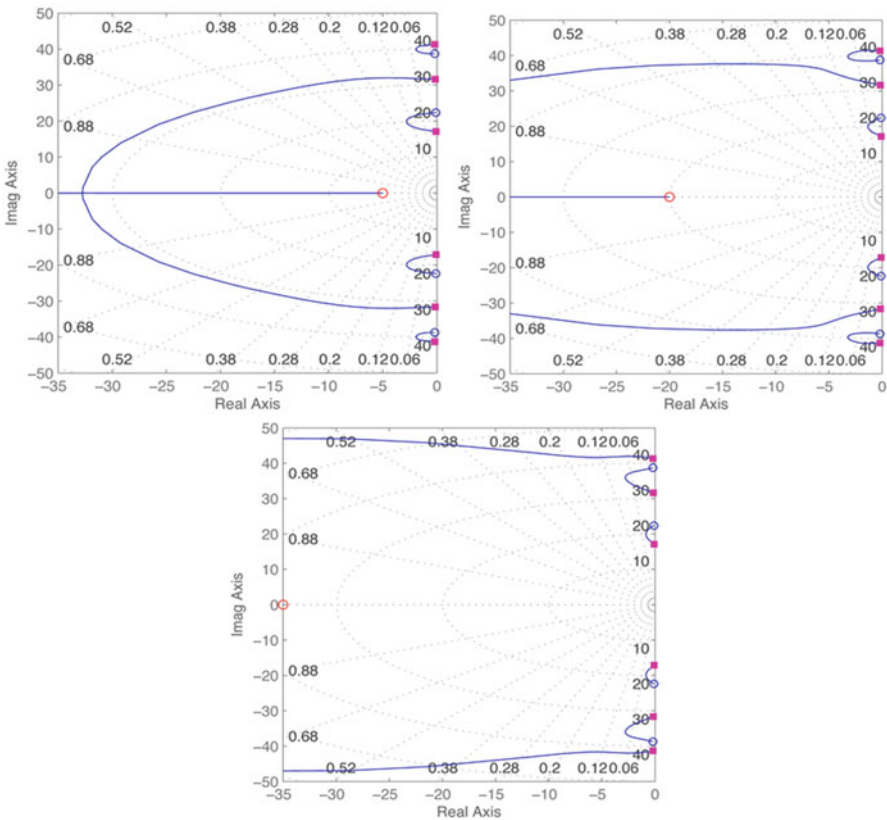


Fig. 29 Root locus for combined velocity and displacement feedback control $G(s) = g(1 + Ts)$

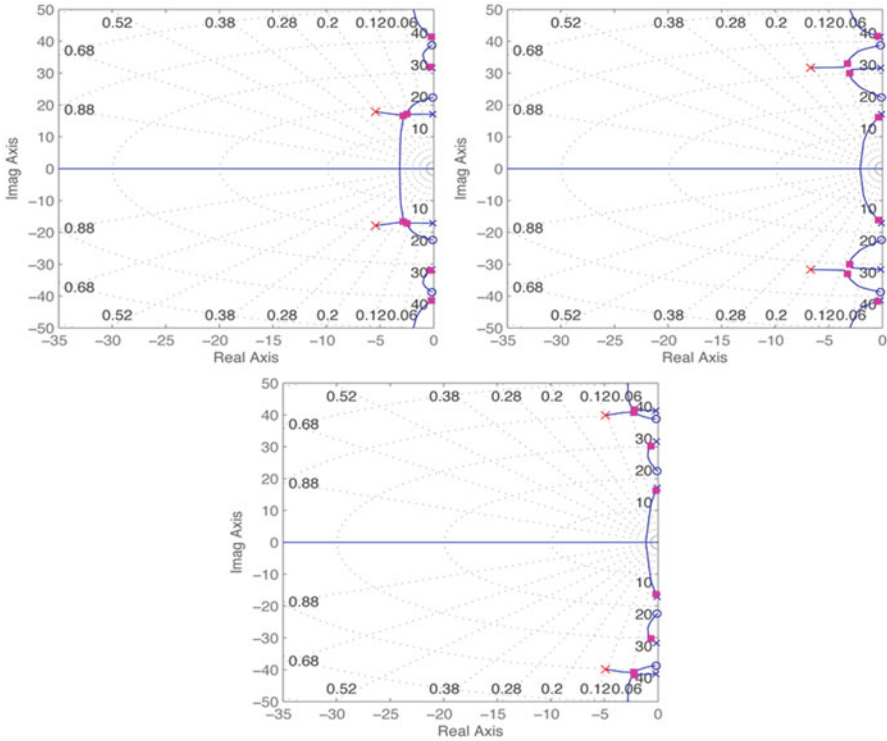


Fig. 30 Root locus for positive position feedback (PPF) control $G(s) = -g \omega_f^2 / (s^2 + 2\xi_f \omega_f s + \omega_f^2)$

Another interesting control law that allows to focus on one specific vibration mode is the Positive Position Feedback (PPF). The control transfer function simulates a resonant system, such that

$$G(s) = -g \frac{\omega_f^2}{s^2 + 2\xi_f \omega_f s + \omega_f^2} \tag{41}$$

where the parameters ω_f and ξ_f correspond to natural frequency and damping factor of an attached subsystem which poles should be close to the original system poles that one wants to modify. Figure 30 shows the root locus of PPF control strategies focusing on each one of the vibration modes of the spring–mass system.

References

J.P. Den Hartog, *Mechanical Vibrations*, 4th edn. (Dover, New York, 1985)
 D.J. Inman, *Engineering Vibration* (Prentice-Hall, New Jersey, 1996)

- D.J. Mead, *Passive Vibration Control* (Wiley, Chichester, 1999)
- L. Meirovitch, *Dynamics and Control of Structures* (Wiley, New York, 1990)
- D.K. Miu, *Mechatronics: Electromechanics and Contromechanics* (Springer, New York, 1992)
- A.D. Nashif, D.I.G. Jones, J.P. Henderson, *Vibration Damping* (Wiley, New York, 1985)
- A. Preumont, *Vibration Control of Active Structures: An Introduction* (Kluwer Academic Publishers, Dordrecht, 1997)

Nonlinear Dynamics and Chaos

Marcelo A. Savi

Abstract This chapter presents an overview of nonlinear dynamics and chaos. It starts with a background revision of dynamical systems. Concepts of equilibrium points, linearization, stability, and Poincaré maps are treated. Afterward, chaotic dynamics is explored. Horseshoe transformation is discussed in order to define the main aspects of chaos. Fractal characteristics are presented and discussed. Routes to chaos are investigated showing some definitions of bifurcation. Lyapunov exponents are defined presenting a diagnostic tool for chaos. The main concepts and tools are then presented by considering a case study related to a shape memory alloy system. Single and two degrees of freedom systems are treated using a polynomial constitutive model to describe the restitution forces.

Keywords Nonlinear dynamics • Chaos • Dynamical systems • Stability • Bifurcation • Horseshoe transformation • Shape memory alloy

1 Introduction

Nature is essentially nonlinear and this characteristic is responsible for a great variety of possibilities of natural systems. Natural rhythms can be understood as a manifestation of dynamical behavior englobing all distinct aspects of system dynamics. In brief, these rhythms could be either regular or irregular over time and space. Each kind of dynamical behavior may be related to both normal and pathological functioning.

Nature-inspired behavior motivates several engineering systems and instigates researches to develop proper tools to treat nonlinear systems. Historically, nonlinear systems were usually avoided creating a linear paradigm that limited the comprehension of natural processes. One of these paradigms is the strict determinism, clearly illustrated by the Laplace thinking: “*If we conceive of an*

M.A. Savi, Ph.D. (✉)
COPPE—Department of Mechanical Engineering, Universidade Federal do
Rio de Janeiro, Center for Nonlinear Mechanics, P.O. Box 68.503,
Rio de Janeiro, RJ 21.941.972, Brazil
e-mail: savi@mecanica.ufrj.br

intelligence which at a given instant comprehends of all the relations of the entities of this universe, it could state the respect positions, motions, and general effects of all these entities at any time in the past or future."

Only in the end of the nineteenth century the linear paradigm started to be broken. Motivated by the stability analysis of the universe, Poincaré studied the dynamical response of the three-body problem. Poincaré presented a counterpoint for the strict determinism of Laplace and its idea is clearly represented by its famous phrase: *"Even if the case that the natural laws had no longer secret for us, . . . it may happen that small differences in initial conditions produce very great ones in the final phenomena."* This is the essential characteristic of nonlinearity meaning that small causes may generate great effects.

Nonlinear systems have a great variety of responses, and chaos is one of these possibilities being characterized by sensitive dependence on initial conditions. Although Poincaré has an absolutely clear vision with respect to chaos (as it is understood nowadays), only in 1963, when Lorenz developed meteorology studies, this idea came back to the scientific scenario again (Lorenz 1963). The Lorenz's analysis established the colloquial understanding that became famous as the *butterfly effect*, which means that if a butterfly flaps its wings in China it may cause a hurricane in Brazil.

This chapter presents a general overview of the fundamentals of nonlinear dynamics and chaos. The following references can be indicated: Hilborn (1994), Kapitaniak (1991), Moon (1992), Monteiro (2002), Mullin (1993), Ott (1993), Thompsom and Stewart (1986), Savi (2006) and Strogatz (1994). Initially, fundamental background is provided. The mathematical representation of dynamical systems is discussed presenting concepts as state variables and phase space. Stability analysis and linearization approaches are then discussed together with some important tools for the nonlinear analysis. The formal definition of chaos is treated in the sequence introducing Lyapunov exponents as an important diagnostic tool of chaos. A case study of shape memory alloy systems is presented as a general application of the discussed background material.

2 Dynamical Systems: Background

A dynamical system may be understood as a transformation f that is imposed to a vector field x , that represents state variables used to describe the system dynamics. This idea represents a frame-by-frame description of reality that can be mathematically represented by a set of differential equations as follows:

$$\dot{x} = f(x), \quad x \in \mathbb{R}^n \tag{1}$$

This kind of system is called autonomous since it does not have an explicit dependence on time. On the other hand, it is possible to consider a non-autonomous system that has an explicit time dependence as follows:

$$\dot{x} = f(x, t), \quad x \in R^n \quad (2)$$

The space of dependent variables, x , is called *state space* or *phase space*. It has different topologies that characterize several aspects of system dynamics. A geometrical approach to understand system dynamics is related to the investigation of how objects in the phase space respond under transformations imposed by f . In this regard, it is interesting to imagine an object in phase space representing a set of initial conditions. Each one of these points is the starting point of a trajectory. After a time interval, they form a new object and the transformation between these two objects is imposed by f that defines the kind of behavior of the system. This geometrical approach allows one to establish an interesting comprehension of the dynamical behavior, being usually called *topology* that studies continuous transformations.

Usually, nonlinear systems do not have analytical solution and, therefore, different tools need to be employed. Numerical simulation is one of the most important tools for this aim but there are also hybrid tools as perturbation methods (Nayfeh and Mook 1979). In general, it is important to understand that dynamical systems have trajectories that represent the system response. These trajectories are obtained by some technique as numerical methods. In this regard, it is also important to highlight the existence and uniqueness of the solution of the nonlinear dynamical system.

2.1 Equilibrium Points and Linearization

An *equilibrium point* (or *fixed point*) is a special point of the state space where the system may stay stationary, which means that the solution does not vary with time. Therefore, if $\bar{x} \in R^n$ is an equilibrium point of the system, hence $f(\bar{x}) = 0$. Usually, nonlinear systems have several equilibrium points and system response can visit all of them, which confer flexibility and complexity to the system behavior.

A useful form to investigate dynamics of nonlinear system is to linearize its response around a solution. In particular, one can consider an equilibrium point. In this regard, consider a coordinate change of the form:

$$x = \bar{x} + \eta \quad (3)$$

where η is perturbation of the solution. Using Taylor series,

$$f(x) = f(\bar{x} + \eta) = f(\bar{x}) + Df(\bar{x})\eta + \dots \quad (4)$$

$Df(\bar{x}) = A$ is the Jacobian matrix evaluated at the equilibrium point. Hence, assuming just the linear part of the series, the dynamics around the equilibrium point is given by:

$$\dot{\eta} = A\eta \quad (5)$$

This linear system has analytical solution and for its analysis it is convenient to perform a coordinate change as follows:

$$\eta = \Gamma \xi \quad (6)$$

where Γ is the modal matrix, built with the eigenvectors of the Jacobian matrix. Under this assumption, the equivalent system is defined:

$$\dot{\xi} = B \xi \quad (7)$$

where $B = \Gamma^{-1}A\Gamma = \text{diag}(\lambda_i)$, and λ_i are the eigenvalues of the Jacobian matrix. Hence, the system response is given by:

$$\xi = e^{tB} \xi_0 = \text{diag} \left(\sum_{k=0}^{\infty} \frac{t^k}{k!} \lambda_i^k \right) \xi_0 = \text{diag} (e^{t\lambda_i}) \xi_0 \quad (8)$$

Therefore, the dynamical characteristics of the system in the neighborhood of the equilibrium points are defined from the eigenvalues of the Jacobian matrix A . In this regard, stability issues can be evaluated splitting the eigenvalues in three different groups: ϑ^s , ϑ^u , and ϑ^c , respectively, representing stable, unstable, and central sets. Each one of these groups is defined from the real part of the eigenvalues as follows:

$$\begin{aligned} \vartheta^s &= \{\lambda \text{ such that } \text{Re}(\lambda) < 0\} \\ \vartheta^u &= \{\lambda \text{ such that } \text{Re}(\lambda) > 0\} \\ \vartheta^c &= \{\lambda \text{ such that } \text{Re}(\lambda) = 0\} \end{aligned} \quad (9)$$

The linearized system has similar response of the nonlinear system in the neighborhood of hyperbolic equilibrium points. A hyperbolic point is defined such that the real part of the eigenvalues of the Jacobian matrix does not vanish ($\text{Re}(\lambda_k) \neq 0 \forall k$). This conclusion is the essence of the Hartman-Grobman theorem (Savi 2006) that establishes the relation between the nonlinear and linearized solution of a dynamical system in the neighborhood of an equilibrium point.

Therefore, the dynamics of the nonlinear system can be locally evaluated from the eigenvalues of the Jacobian matrix. In order to visualize different types of equilibrium points, it is useful to observe a two-dimensional system (2-Dim). Figure 1 shows different types of equilibrium points for 2-Dim systems, defined from the eigenvalues of A .

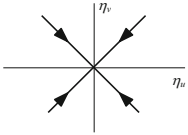
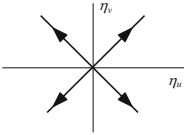
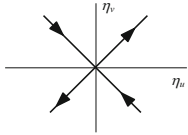
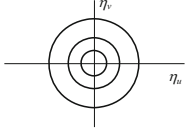
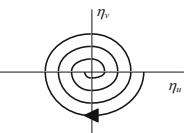
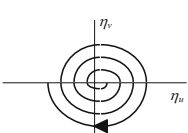
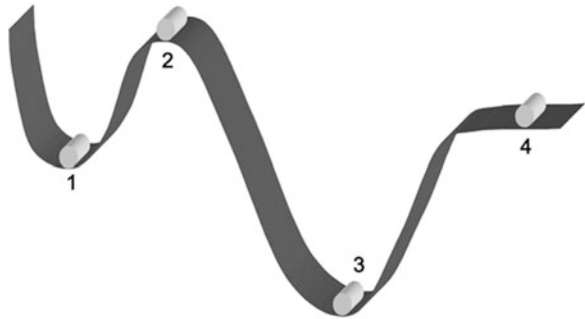
<p style="text-align: center;">Sink (Stable node)</p> <div style="border: 1px solid black; padding: 5px; margin-bottom: 10px;"> $\text{Re}(\lambda_1) = -b_1 < 0, \text{Im}(\lambda_1) = 0$ $\text{Re}(\lambda_2) = -b_2 < 0, \text{Im}(\lambda_2) = 0$ </div> 	<p style="text-align: center;">Source (Unstable node)</p> <div style="border: 1px solid black; padding: 5px; margin-bottom: 10px;"> $\text{Re}(\lambda_1) = +b_1 > 0, \text{Im}(\lambda_1) = 0$ $\text{Re}(\lambda_2) = +b_2 > 0, \text{Im}(\lambda_2) = 0$ </div> 	<p style="text-align: center;">Saddle</p> <div style="border: 1px solid black; padding: 5px; margin-bottom: 10px;"> $\text{Re}(\lambda_1) = +b_1 > 0, \text{Im}(\lambda_1) = 0$ $\text{Re}(\lambda_2) = -b_2 < 0, \text{Im}(\lambda_2) = 0$ </div> 
<p style="text-align: center;">Center</p> <div style="border: 1px solid black; padding: 5px; margin-bottom: 10px;"> $\text{Re}(\lambda_1) = 0, \text{Im}(\lambda_1) = +b$ $\text{Re}(\lambda_2) = 0, \text{Im}(\lambda_2) = -b$ </div> 	<p style="text-align: center;">Stable spiral (Stable focus)</p> <div style="border: 1px solid black; padding: 5px; margin-bottom: 10px;"> $\text{Re}(\lambda_1) = -b_1 < 0, \text{Im}(\lambda_1) = +b_2$ $\text{Re}(\lambda_2) = -b_1 < 0, \text{Im}(\lambda_2) = -b_2$ </div> 	<p style="text-align: center;">Unstable spiral (Unstable focus)</p> <div style="border: 1px solid black; padding: 5px; margin-bottom: 10px;"> $\text{Re}(\lambda_1) = +b_1 > 0, \text{Im}(\lambda_1) = +b_2$ $\text{Re}(\lambda_2) = +b_1 > 0, \text{Im}(\lambda_2) = -b_2$ </div> 

Fig. 1 Equilibrium points for 2-Dim systems

Fig. 2 Stability



2.2 Stability

Stability is an essential issue of nonlinear dynamical systems being associated with characteristics of a solution subjected to perturbations. If a perturbation does not affect a system response in a significant way, the system is stable. Otherwise, the system is unstable. Figure 2 illustrates stability concept considering the movement of a body in three distinct situations.

1. Meta-stable equilibrium—After the perturbation, the body returns to its initial configuration. Nevertheless, there is another possible situation, more stable than the original one. Hence, the influence depends on the perturbation level.

2. Unstable equilibrium—After the perturbation, the body does not return to its original configuration, assuming a new position far from the original one.
3. Stable equilibrium—After the perturbation, the body returns to its initial configuration.
4. Neutral equilibrium—After the perturbation, the body stays at the new configuration.

The idea of stability can be extended to dynamical behavior. The local analysis of linearized system around equilibrium points is an example. Another possibility is the Lyapunov criterion that analyzes the effect of a perturbation in a specific system solution. Hence, it establishes a relationship between a specific orbit or solution of the dynamical system and its perturbation, represented by a nearby orbit associated with a different initial condition in the neighborhood of the original one.

The stability concept of Lyapunov defines a stable system in such a way that two nearby orbits remain close to each other with the evolution of time. Figure 3a shows this behavior. On the other hand, the system is asymptotically stable if these orbits tend to converge to each other when time tends to infinity (Fig. 3b).

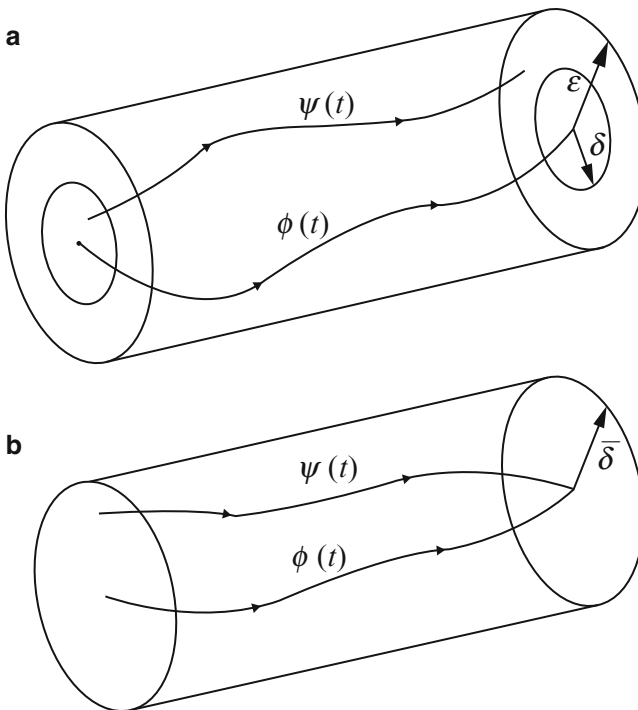


Fig. 3 Stability concept of Lyapunov. (a) Stable; (b) asymptotically stable

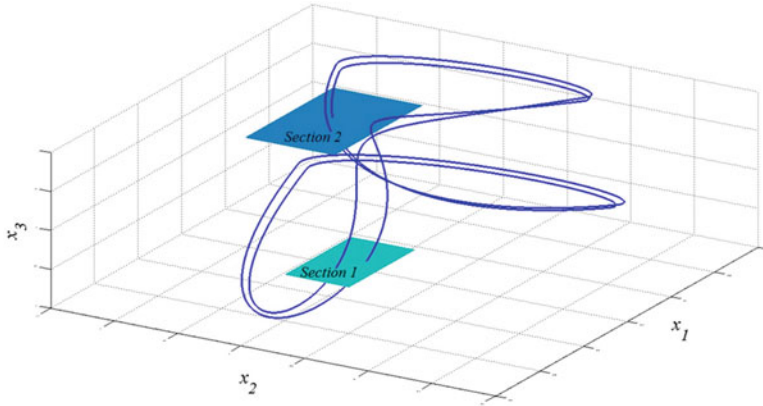


Fig. 4 Poincaré map

2.3 Poincaré Maps

Poincaré map constitutes a procedure employed to eliminate a dimension of the system and, therefore, a continuous system is transformed into a discrete one. There are many forms to define a Poincaré map, but in general, it is considered as a surface that transversely intersects a given orbit. For systems subjected to periodic forcing, Poincaré section may be represented by a surface that corresponds to a specific phase of the driving force. On this basis, one has a stroboscopically sample of the system response. Figure 4 illustrates the idea of Poincaré map showing two different surfaces transversely crossed by a specific orbit.

3 Chaos

Nonlinear dynamical systems present a great variety of responses. This can be understood as a system freedom, associated with alternative behaviors. Chaos is one of these possibilities related to richness and unpredictability. In brief, chaos may be defined as the apparent stochastic behavior of deterministic systems.

Since a dynamical system may be understood as a transformation f that is imposed to a vector field x , it is interesting to imagine a special type of transformation characterized by a sequence of contraction–expansion–folder process. This process represents an archetypal behavior of the system being called horseshoe transformation. By considering a unitary square in phase space, two different transformations can be imagined: a positive part of transformation, f , and a negative part, f^{-1} , both represented in Fig. 5. The limit as the number of interactions of these transformations tend to infinity, the positive part of transformation tends to form a set of vertical lines. On the other hand, the inverse function tends to form a set of

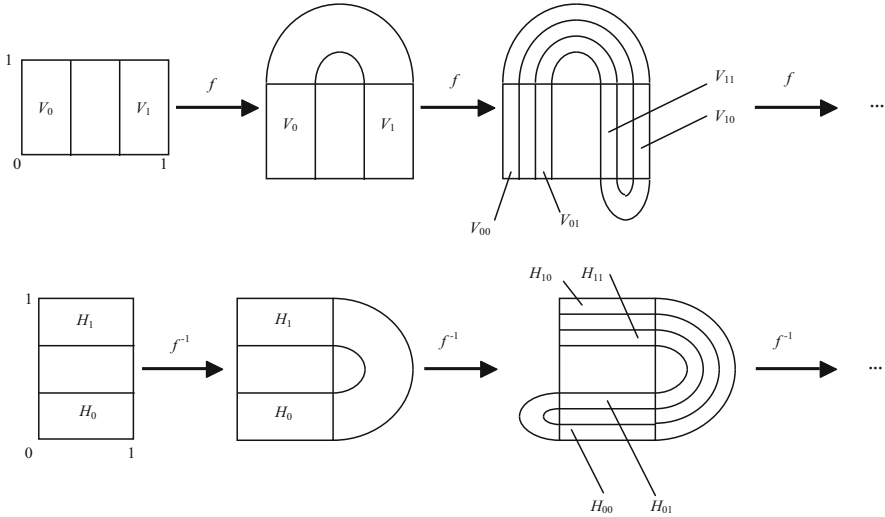


Fig. 5 Contraction–expansion–folder transformation known as horseshoe

horizontal lines. Hence, the intersections of positive and negative parts form an invariant set of disconnected points that have the structure of a *Cantor set*. This set is closed, disconnected, and has an uncountable infinity of points. Examples of this set are shown in Fig. 6. Basically, a line is split in three equal parts and the center part is discarded. This process is repeated tending to infinity. An analogous situation is related to an area or to a volume. Line is a typical 1-Dim structure and the set related to this has a fractional dimension, between 1 and 0. The area results in a structure with dimension between 2 and 1. The cube produces a structure with dimension between 3 and 2. Line and volume structures are shown in Fig. 6, constructed from a repetition of a simple rule. This kind of structure has a *fractal* characteristic as a reference of the non-integer, fractional nature of its dimension.

The contraction–expansion–folder process has become famous as horseshoe transformation because of the form of the transformed square. It was originally proposed by the mathematician Steve Smale, and because of that became known as the *Smale horseshoe*. A dynamical system subjected to this kind of transformation has some special characteristics.

A generic point of the invariant set of points constructed by the horseshoe transformation may be identified by a sequence of 0’s and 1’s and, because of that, it is possible to construct a structure that represents orbits of dynamical systems from these sequences. This approach is called *symbolic dynamics* and since it is based on sequences of integer numbers, it is not associated with floating point errors, being useful in several situations. On this basis, consider two generic points, p and \tilde{p} , that belong to a small neighborhood, ε . It does not matter the size of the neighborhood ε , there is a number of iterations imposed by f such these points are separated by a finite distance. Therefore, the system presents a sensitive

Fig. 6 Cantor set (modified from Gleick 1987)

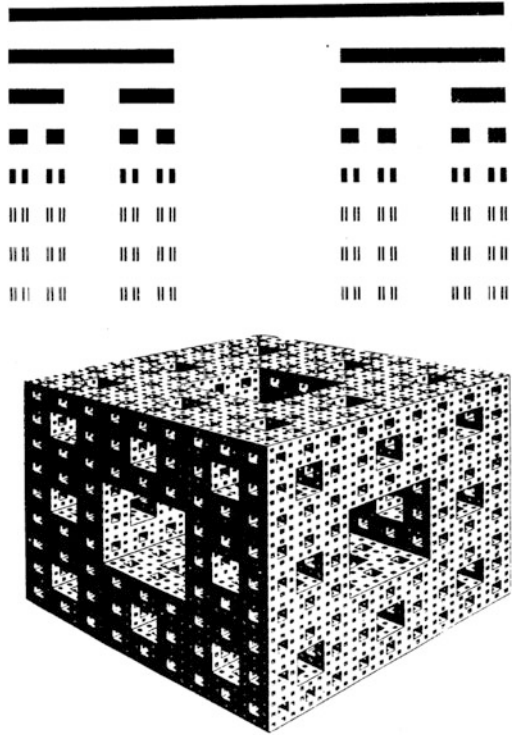
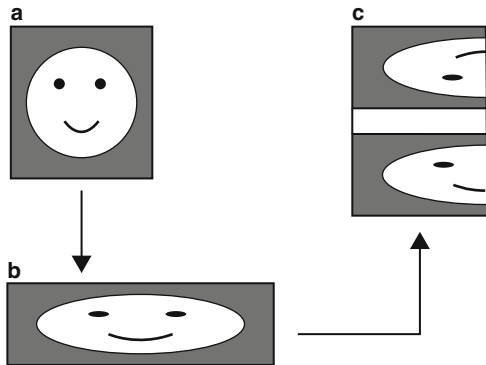


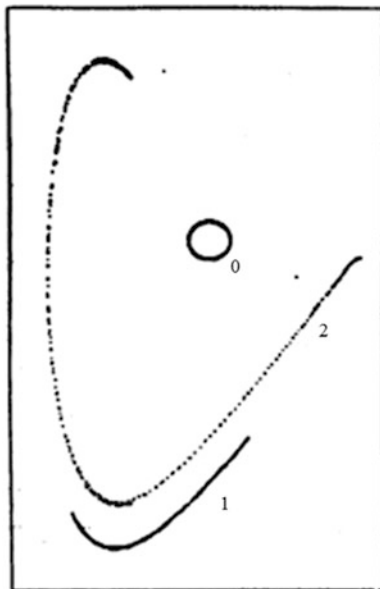
Fig. 7 Schematic representation of the sensitive dependence of initial conditions associated with horseshoe transformation



dependence on initial condition, as shown in Fig. 7 (Wiggins 1990; Strogatz 1994). This property characterizes the chaotic behavior of a dynamical system. This sensitive dependence represents the butterfly effect described in Lorenz’s work.

Chaotic behavior is intrinsically related to the existence of the horseshoe transformation. As a consequence, chaos is associated with nonlinear systems with, at least, three distinct directions: one related to expansion, one related to contraction, and a neutral one, where folder occurs. This means that a dynamical system may

Fig. 8 Evolution of a circle of initial conditions in a chaotic behavior



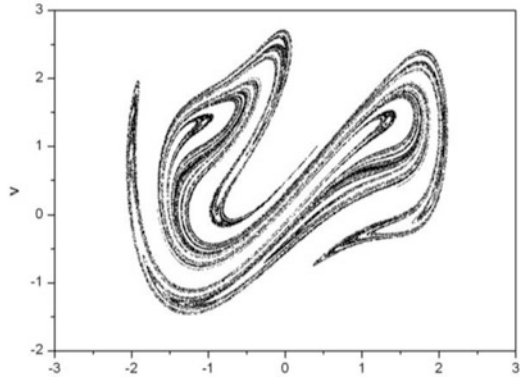
have at least three dimensions in order to exhibit chaotic behavior (Savi 2006; Wiggins 1990; Guckenheimer and Holmes 1983). Many authors refer to the horseshoe transformation as the baker transformation, as a reference of the process of bread paste. An original paste (related to the square of initial conditions) is prepared by a sequence of contraction–expansion–folder (Savi 2014; Gleick 1987; Stewart 1991).

In order to illustrate the physical behavior of the horseshoe transformation, consider an object represented by a circle of initial conditions. After some interactions, it is evaluated the intersection of the orbits on a Poincaré section. If the system presents a chaotic behavior, there is a horseshoe transformation characterized by expansion–contraction–folder process. Figure 8 shows the original circle and two other instants (Savi and Braga 1993).

Another characteristic of chaos is the richness that can be associated with the existence of an infinite number of unstable periodic orbits embedded in the chaotic behavior. These orbits represent the essential structure of chaos conferring richness and flexibility to this kind of behavior.

Dissipative dynamical systems are characterized by the asymptotic behavior associated with attractors. Several types of attractors can be observed in dynamical system. A stable equilibrium point can be understood as a 0-Dim attractor. A limit-cycle is another possibility. Chaotic behavior is also related to an attractor that represents a preferred region of the phase space where orbits converge. Special characteristics of this kind of attractor are related to the horseshoe transformation. Usually, it has a Cantor set aspect with a fractal structure associated with a non-integer dimension. Due to that, the name *strange attractor* is usually employed.

Fig. 9 Chaotic strange attractor



It represents a collection of points, organized in lamellas, with voids. Note that this is the same structure of the invariant set described for horseshoe transformation (Fig. 5).

The strangeness of an attractor is related to a geometrical aspect, essentially fractal, with non-integer dimension. Chaoticity, on the other hand, is a dynamical aspect. Therefore, although not usual, it is possible to have different situations in dynamical systems: chaotic strange attractor; chaotic non-strange attractor; strange non-chaotic attractor (Grebogi et al. 1984). A typical chaotic, strange attractor is shown in Fig. 9 (Savi 2006).

3.1 Routes to Chaos

The different responses of a dynamical system are defined by parameters and initial conditions. Each set of parameter produces a specific response. Multistability is a nonlinear characteristic where a specific set can be associated with more than one stable solution. In these cases, initial conditions define the system behavior.

A proper comprehension of system dynamics includes the form of how system behavior is altered by parameter changes. In this regard, it is important to identify qualitative changes on system behavior. Poincaré introduced the idea of qualitative changes in solution structure using the term *bifurcation*.

Bifurcation analysis is useful to identify these qualitative changes, defining the routes to chaos. In general, two types of bifurcation can be imagined: local and global. Local bifurcations are restricted to regions of phase space. On the other hand, global bifurcations are non-local. Local bifurcation analysis is usually employed considering *normal forms* that represent prototypes of bifurcations. Figure 10 shows some classical forms of bifurcations being related to the creation and destruction of solutions or equilibrium points.

Global bifurcations are related to qualitative changes in global system aspects and cannot be observed from local analysis. In essence, a parameter change can cause a

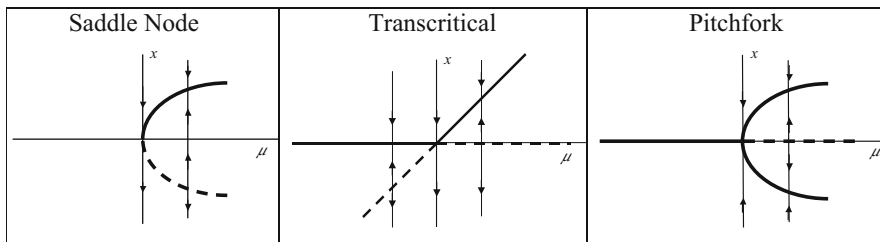


Fig. 10 Some bifurcations observed in dynamical systems

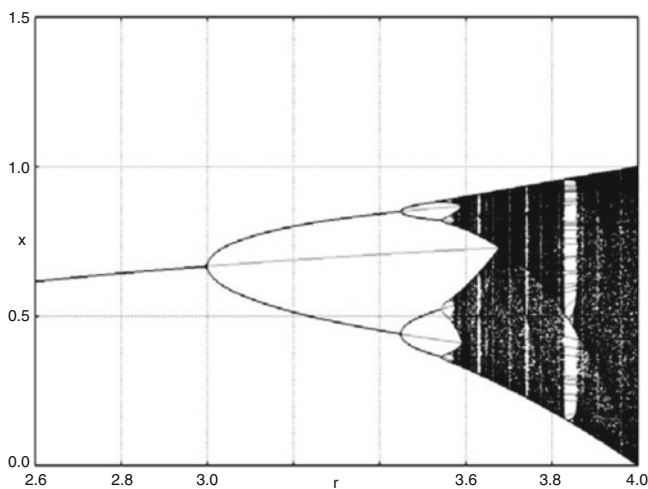


Fig. 11 Bifurcation diagram

global change in the orbit structure. This type of bifurcation can explain the birth of chaos due to some orbit collision, for instance. For more details, see Hirsch et al. (2004), Strogatz (1994), Wiggins (1990), and Guckenheimer and Holmes (1983).

Bifurcation diagrams constitute an important tool to identify the influence of parameter changes in system response. It represents a stroboscopically sampled of a system variable under the slow quasi-static change of a system parameter. A typical bifurcation diagram is presented in Fig. 11 (Savi 2006).

3.2 Lyapunov Exponents

Chaotic behavior needs to be properly identified in dynamical systems. In this regard, diagnostic tools are essential and system invariants are good alternative for this aim. Attractor dimension and Lyapunov exponent are usually employed to identify chaos.

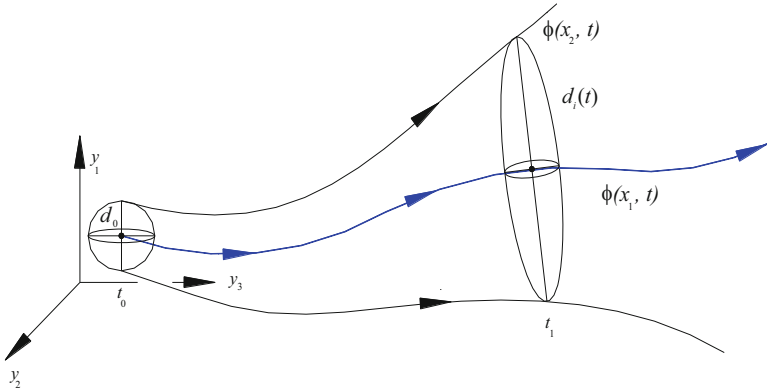


Fig. 12 Lyapunov exponents

Lyapunov exponent evaluates the sensitive dependence on initial conditions estimating the exponential divergence of nearby orbits. These exponents have been used as the most useful diagnostic tool for chaotic system analysis and can also be used for the calculation of other invariant quantities as the attractor dimension. The signs of these exponents provide a qualitative picture of the system’s dynamics. The existence of positive Lyapunov exponents defines directions of local instabilities in the system dynamics and any system containing at least one positive exponent presents chaotic behavior. A response with more than one positive exponent is called hyperchaos (Savi and Pacheco 2002; Franca and Savi 2003; Machado et al. 2003).

In order to understand the idea related to the determination of Lyapunov exponents consider a D -sphere of states that is transformed by the system dynamics in a D -ellipsoid. Lyapunov exponents are related to the expanding and contracting nature of different directions in phase space. The evaluation of the divergence of two nearby orbits is done considering the relation between the initial D -sphere and the D -ellipsoid (Fig. 12). This variation may be expressed by:

$$d(t) = d_0 b^{\lambda t} \tag{10}$$

where d is the diameter, b is a reference basis, and λ is called Lyapunov exponent. Hence, there is a Lyapunov spectrum given by,

$$\lambda = \frac{1}{t} \log_b \left(\frac{d(t)}{d_0} \right) \tag{11}$$

When Lyapunov exponent is negative or vanishes, trajectories do not diverge. On the other hand, when the exponent is positive, indicates that trajectories diverge, characterizing chaos. In addition to the signs of the Lyapunov exponents, their values also bring important information related to system dynamics. Since the

exponents evaluate the average divergence of nearby orbits, dissipative systems have a negative sum of the whole Lyapunov spectrum.

The determination of Lyapunov exponents of dynamical system with an explicitly mathematical model, which can be linearized, is well established from the algorithm proposed by Wolf et al. (1985). On the other hand, the determination of these exponents from time series is quite more complex. In essence, there are two different classes of algorithms: Trajectories, real space or direct method; and perturbation, tangent space or Jacobian matrix method (Wolf et al. 1985; Kantz and Schreiber 1997; Franca and Savi 2003; Savi 2006).

In chaotic situations, there is a local exponential divergence of nearby orbits and hence, it is necessary proper algorithms in order to evaluate Lyapunov exponents (Wolf et al. 1985; Parker and Chua 1989). These algorithms evaluate the average of this divergence considered in different points of the trajectory. Hence, when the distance $d(t)$ becomes large, it is defined a new $d_0(t)$ in order to evaluate the divergence, as follows:

$$\lambda = \frac{1}{t_n - t_0} \sum_{k=1}^n \log_b \left(\frac{d(t_k)}{d_0(t_{k-1})} \right) \quad (12)$$

Lyapunov exponents can be employed to calculate other system invariants as attractor dimension. The Kaplan–Yorke conjecture establishes a way to calculate attractor dimension from the spectrum of Lyapunov exponents (Savi 2006).

4 Shape Memory Alloy System

The analysis of smart systems and structures involves nonlinear dynamics of multi-degrees of freedom systems. As an illustrative example of some of the concepts presented in this chapter, one presents the nonlinear dynamics analysis of shape memory systems considering single and two degree of freedom oscillators. Equations of motion are formulated using polynomial constitutive model to describe the restitution force of the oscillator. Despite the deceiving simplicity of the model, its analysis contributes to the understanding of the nonlinear dynamics of shape memory alloy systems. Paiva and Savi (2006) presented a general overview about constitutive models to describe the thermomechanical behavior of SMAs. The prospect of chaotic behavior is of concerned and the existence of hyperchaos is an interesting characteristic of these systems.

Numerical simulations are performed employing a fourth order Runge-Kutta method for numerical integration and time steps less than $\Delta\tau = 2\pi/200\omega$ present good results. The characterization of chaotic motion is done employing Lyapunov exponents, and its estimation employs the algorithm proposed by Wolf et al. (1985). A collection of results from Savi and Pacheco (2002) is presented. Savi (2015) presented a general overview of nonlinear dynamics and chaos in system with SMA

elements. Savi and Braga (1993) and Machado et al. (2003, 2004) discussed some other aspects related to oscillators where the restitution force is described by the polynomial model.

4.1 Polynomial Constitutive Model

Polynomial constitutive model is a one-dimensional model that describes the SMA behavior considering a polynomial free energy that depends on the temperature, T , and on the one-dimensional strain, E . The form of the free energy is chosen in such a way that the minima and maxima points represent stability and instability of each phase of the SMA. As it is usual on one-dimensional models proposed for SMAs (Savi and Braga 1993; Paiva and Savi 2006), three phases are considered: Austenite (A) and two variants of martensite ($M+$, $M-$). Hence, the free energy is chosen such that for high temperatures it has only one minimum at vanishing strain, representing the equilibrium of the austenitic phase. At low temperatures, martensite is stable, and the free energy must have two minima at non-vanishing strains. At intermediate temperatures, the free energy must have equilibrium points corresponding to both phases. Under these assumptions, the stress–strain–temperature relation is given by:

$$\sigma = a(T - T_M)E - bE^3 + eE^5 \quad (13)$$

where a , b , and e are positive constants, while T_M is the temperature below which the martensitic phase is stable. If T_A is defined as the temperature above which the austenite is stable, and the free energy has only one minimum at zero strains, it is possible to write the following condition,

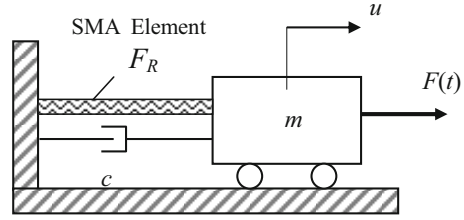
$$T_A = T_M + \frac{1}{4} \frac{b^2}{ae} \quad (14)$$

4.2 Single Degree of Freedom System

Initially, a single degree of freedom oscillator, which consists of a mass m attached to a shape memory element of length l and cross-sectional area A , and restitution force F_R , is treated. A linear viscous damper, characterized by a viscous coefficient c , is also considered in order to represent dissipations. Moreover, the system is harmonically excited by a force $F(t) = F_0 \sin(\omega t)$. Figure 13 presents an oscillator where the restitution force, F_R , is provided by a general SMA element.

The equation of motion of this oscillator may be formulated by considering the balance of forces acting on the mass as follows.

Fig. 13 Single degree of freedom oscillator



$$m\ddot{u} + c\dot{u} + F_R = F_0 \sin(\Omega t) \quad (15)$$

where $F_R = \sigma A$. Using the polynomial model to represent the restitution force, the non-dimensional equations of motion are given by (Savi and Pacheco 2002):

$$\begin{aligned} y_0' &= y_1 \\ y_1' &= \delta \sin(\varpi \tau) - \xi y_1 - (\theta - 1)y_0 + \beta y_0^3 - \varepsilon y_0^5 \end{aligned} \quad (16)$$

where ξ , β , and ε are material parameters; δ and ϖ are external force parameters; and θ represents non-dimensional temperature.

In all simulations one considers a unitary mass and $\varpi = 1$, $\xi = 0.1$, $\beta = 1.3 \times 10^3$, and $\varepsilon = 4.7 \times 10^5$. Note that $\theta_A = 1 + \frac{\beta^2}{4\varepsilon}$, and therefore, $\theta_A = 1.9$.

In order to illustrate the free response of the oscillator, a non-dissipative system ($\xi = 0$) is considered. Results from simulations are presented in the form of phase portraits. Figure 14 presents the free response of the system at different temperatures. Figure 14a shows the case where the martensitic phase is stable ($\theta = 0.7$). In this case, there are three equilibrium points where two are stable while the other one is unstable. Figure 14b considers a higher temperature, where austenitic phase is stable ($\theta = 3.5$). Under this condition, the system presents only one stable equilibrium point.

Forced vibrations are now in focus. In order to start the analysis, bifurcation diagrams are presented (Fig. 15), showing the stroboscopically sampled displacement values, y_0 , under the slow quasi-static increase of the driving force amplitude, δ , and different temperatures. Note that there are parameter values associated with a cloud of points, which is related to chaotic motion.

Different responses are now contemplated. Assuming $\theta = 3.5$ and $\delta = 0.06$, the system presents a period-1 motion. Figure 16 shows the phase space and the Poincaré section associated with this motion. Regarding the same forcing parameter and a lower temperature, $\theta = 0.7$, where the martensitic phase is stable, the motion becomes chaotic. The phase space and the Poincaré section associated with this motion are presented in Fig. 17. Under this condition, a strange attractor is identified and Lyapunov spectrum estimated by the algorithm due to Wolf et al. (1985) is $\lambda_i \equiv (+0.28, -0.42)$, presenting one positive exponent.

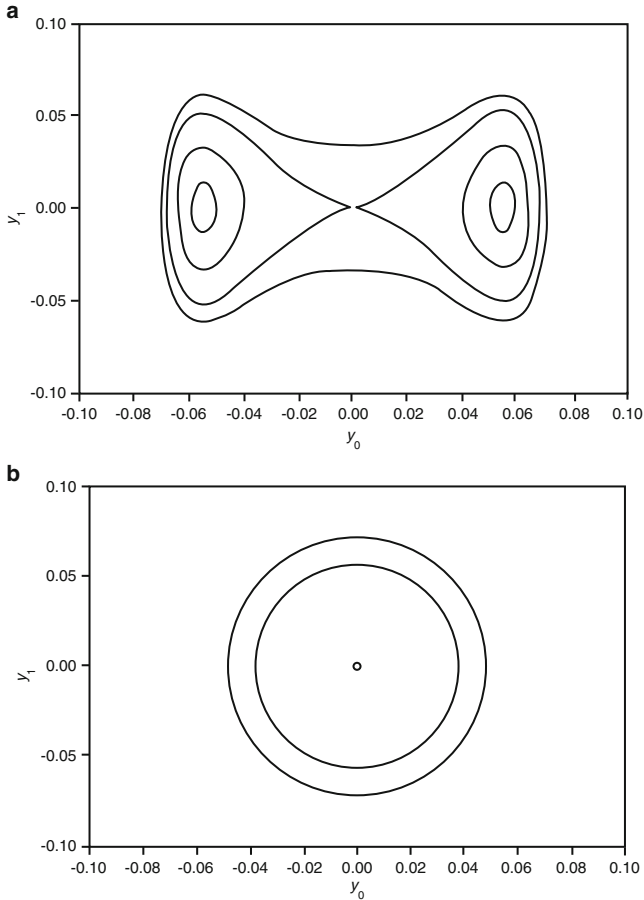


Fig. 14 Phase portrait. (a) $\theta = 0.7$; (b) $\theta = 3.5$

4.3 Two Degree of Freedom System

A two degree of freedom SMA oscillator, depicted in Fig. 18, is now considered. It consists of two masses, m_i ($i = 1, 2$), supported by SMA elements and linear dampers with coefficient c_i ($i = 1, 2, 3$). The system is harmonically excited by two forces $F_i = \bar{F}_i \sin(\Omega_i t)$ ($i = 1, 2$).

Using the polynomial constitutive model, the non-dimensional equations of motion is written as follows (Savi and Pacheco 2002):

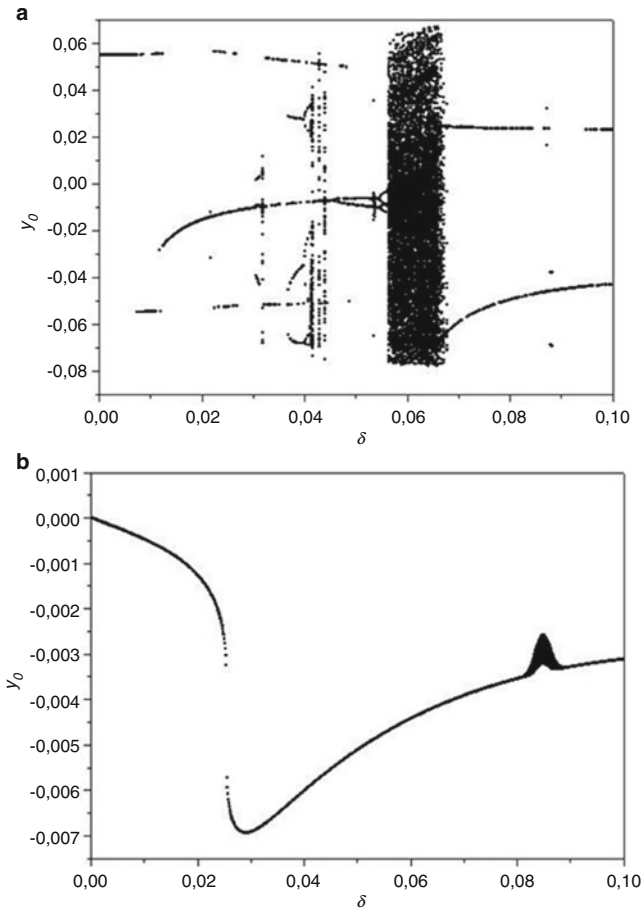


Fig. 15 Bifurcation diagrams. (a) $\theta = 0.7$; (b) $\theta = 3.5$

$$\begin{aligned}
 y_0' &= y_1 \\
 y_1' &= \delta_1 \sin(\varpi_1 \tau) - (\xi_1 + \xi_2 \alpha_{21} \mu) y_1 + \xi_2 \alpha_{21} \mu y_3 - [(\theta_1 - 1) + \alpha_{21}^2 \mu (\theta_2 - 1)] y_0 \\
 &\quad + \alpha_{21}^2 \mu (\theta_2 - 1) y_2 + \beta_1 y_0^3 - \varepsilon_1 y_0^5 - \beta_2 \alpha_{21}^2 \mu (y_2 - y_0)^3 + \varepsilon_2 \alpha_{21}^2 \mu (y_2 - y_0)^5 \\
 y_2' &= y_3 \\
 y_3' &= \alpha_{21}^2 \delta_2 \sin(\varpi_2 \tau) + \xi_2 \alpha_{21} y_1 - (\xi_2 \alpha_{21} + \xi_3 \alpha_{21} \alpha_{32}) y_3 + \alpha_{21}^2 (\theta_2 - 1) y_0 \\
 &\quad - [\alpha_{21}^2 (\theta_2 - 1) + \alpha_{21}^2 \alpha_{32}^2 (\theta_3 - 1)] y_2 + \beta_2 \alpha_{21}^2 (y_2 - y_0)^3 - \varepsilon_2 \alpha_{21}^2 (y_2 - y_0)^5 \\
 &\quad + \beta_3 \alpha_{21}^2 \alpha_{32}^2 y_2^3 - \varepsilon_3 \alpha_{21}^2 \alpha_{32}^2 y_2^5
 \end{aligned} \tag{17}$$

Again, numerical simulations are performed employing a fourth order Runge-Kutta method for numerical integration and time steps less than $\Delta\tau = 2\pi/200\varpi_1$

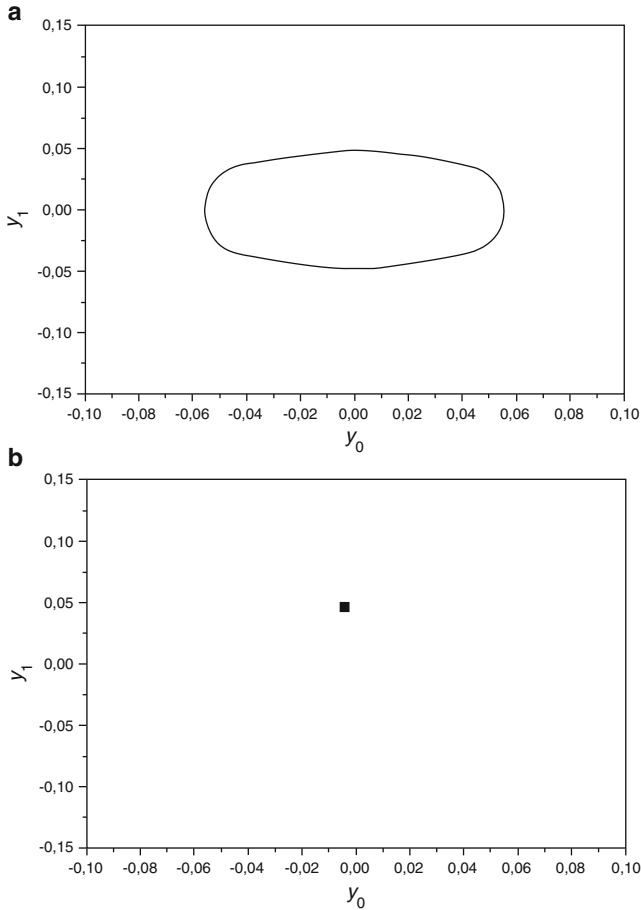


Fig. 16 Periodic motion: $\theta = 3.5$ and $\delta = 0.06$. (a) Phase space; (b) Poincaré section

present good results. In all simulations, similar mechanical properties are regarded for the three spring-dashpot systems. It is assumed a unitary mass and $\varpi_1 = \varpi_2 = 1$, $\xi_1 = \xi_2 = \xi_3 = 0.1$, $\beta_1 = \beta_2 = \beta_3 = 1.3 \times 10^3$, and $\varepsilon_1 = \varepsilon_2 = \varepsilon_3 = 4.7 \times 10^5$. These information allow one to conclude that $\alpha_{21} = \alpha_{32} = \mu = 1$ and $\theta_{A1} = \theta_{A2} = \theta_{A3} = 1.9$.

Since equations of motion are associated with a five-dimensional system, the phase space is split into projections. The analysis is performed by considering two oscillators, both with single degree of freedom, connected by a spring-dashpot system. Under this assumption, it is possible to analyze the transmissibility of motion between the two oscillators, constructing a phase subspace for each mass. This transmissibility is evaluated studying different temperatures on the connection system, which causes different patterns on each phase subspace.

Consider an excitation that causes chaotic motion on both oscillators ($\delta_1 = \delta_2 = 0.06$ and $\theta_1 = \theta_3 = 0.7$) of two uncoupled systems. Therefore, Poincaré

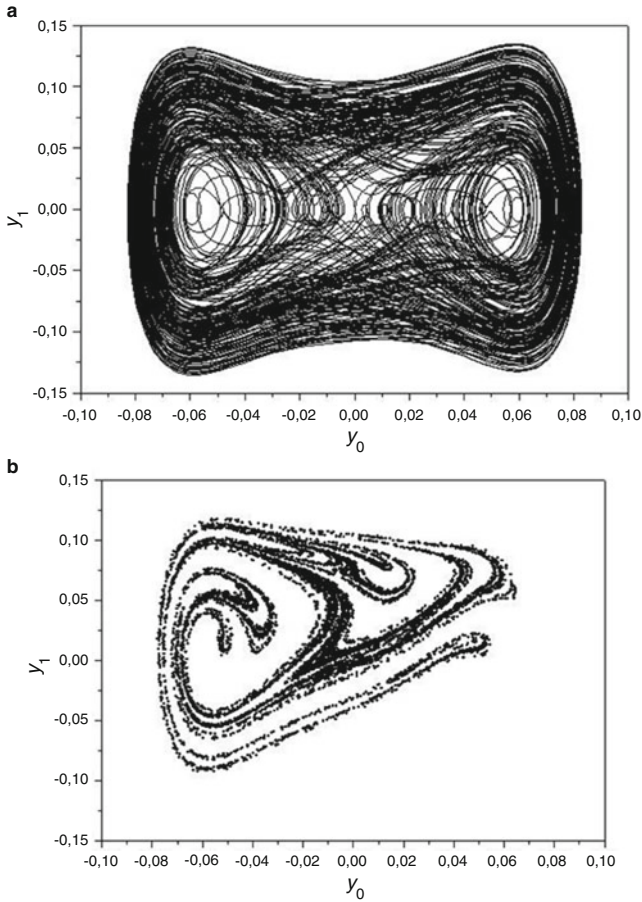


Fig. 17 Chaotic motion: $\theta = 0.7$ and $\delta = 0.06$. (a) Phase space; (b) strange attractor

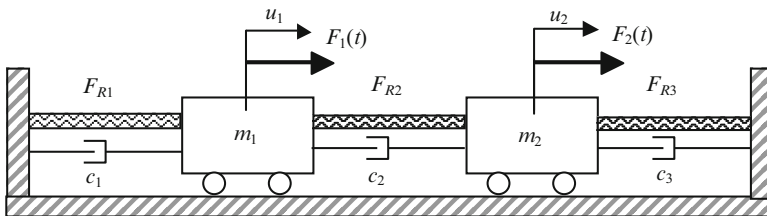


Fig. 18 Two degree of freedom oscillator

sections related to mass m_1 (subspace y_0-y_1) and m_2 (subspace y_2-y_3) present strange attractors similar to the one presented in Fig. 17. By introducing a connection with $\theta_2=0.7$, martensitic phase is stable and strange attractors associated with both masses change their patterns (Fig. 19). Lyapunov spectrum

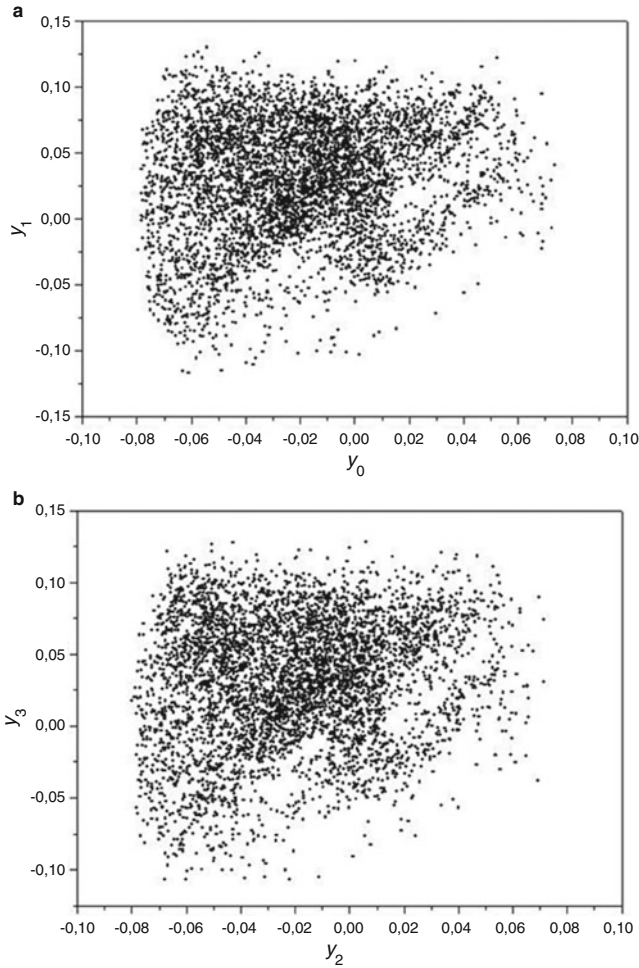


Fig. 19 Phase space. $\delta_1 = 0.06, \delta_2 = 0.06; \theta_1 = \theta_2 = \theta_3 = 0.7$

is $\lambda_i \equiv (+0.54, +0.17, -0.37, -0.92)$ presenting two positive exponents, characterizing the hyperchaos. This means that two directions in the phase space suffer expansion under the dynamical process. This scenario is changed if connection temperature is in austenitic phase, $\theta_2 = 3.5$. Under this new condition, the transmissibility is quite different from the previous one (Fig. 20). Now, there are strange attractors related to both masses and Lyapunov spectrum is $\lambda_i \equiv (+0.30, -0.14, -0.29, -0.45)$, which presents only one positive exponent, characterizing chaos.

Different subspaces can be employed for a better comprehension of these behaviors. Hence, consider a 3D projection ($y_0-y_1-y_2$) of the five-dimensional phase space. Figure 21 shows the hyperchaotic behavior associated with the

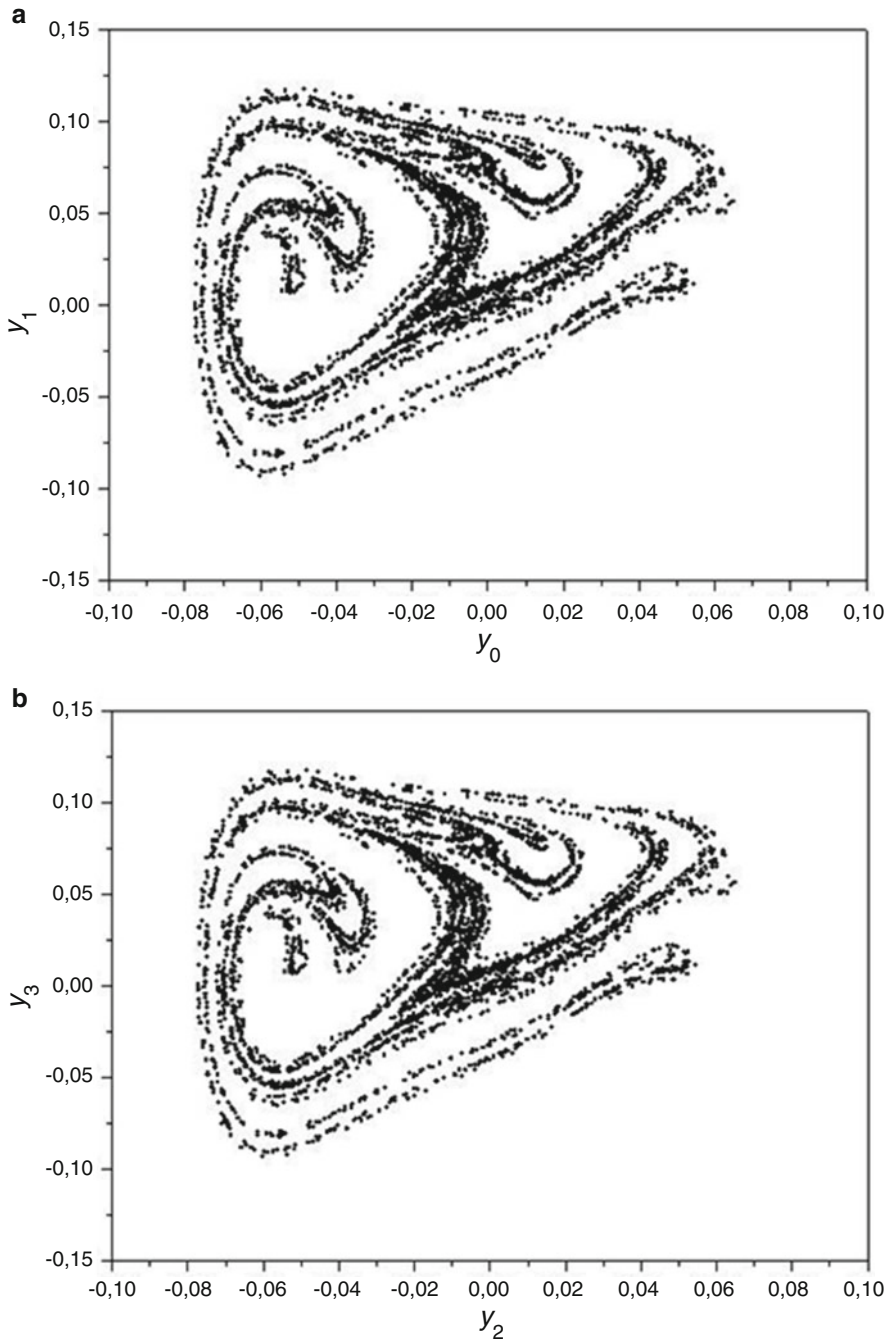


Fig. 20 Phase space. $\delta_1 = 0.06$, $\delta_2 = 0.06$; $\theta_1 = \theta_3 = 0.7$; $\theta_2 = 3.5$

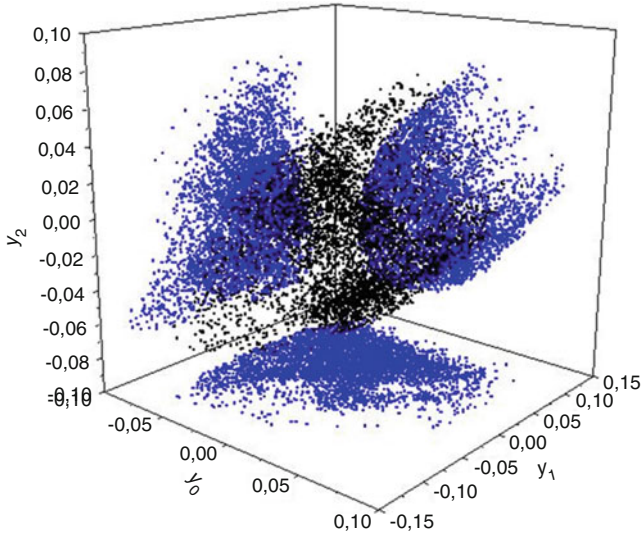


Fig. 21 Poincaré section in the space y_0 - y_1 - y_2 for $\delta_1 = \delta_2 = 0.06$, and $\theta_1 = \theta_2 = \theta_3 = 0.7$

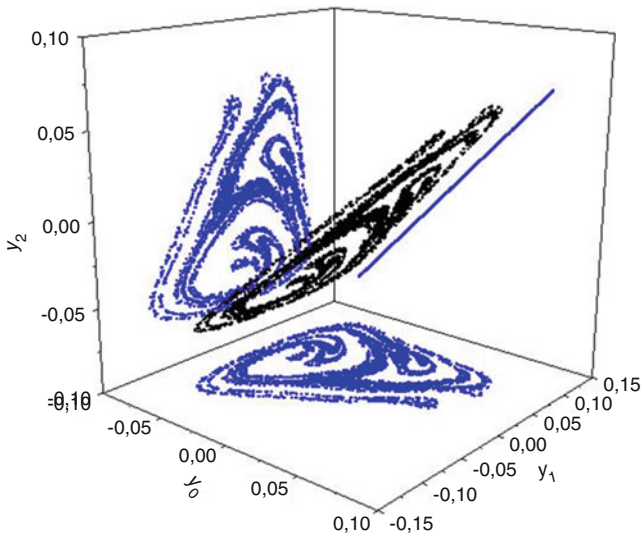


Fig. 22 Poincaré section in the space y_0 - y_1 - y_2 for $\delta_1 = \delta_2 = 0.06$, $\theta_1 = \theta_3 = 0.7$, and $\theta_2 = 3.5$

martensitic connection. This 3D projection shows a cloud of points and allows one to observe the phase subspace of mass m_1 (Fig. 19) projected on the y_0 - y_1 plane. Note that it is not possible to see a cantor-like structure of the chaotic attractor. The same 3D projection of the case with austenitic connection shows a strange attractor with a typical structure (Fig. 22).

These results show that austenitic connection, which occurs at higher temperatures ($\theta_2 = 3.5$, for example), tends to preserve order in contrast of the situation where a martensitic connection is considered ($\theta_2 = 0.7$, for example). This conclusion passes from the understanding that there is an inherent order associated with the pattern of the strange attractor.

Acknowledgements The author would also like to acknowledge the support of the Brazilian Research Agencies CNPq, CAPES and FAPERJ and through the INCT-EIE (National Institute of Science and Technology—Smart Structures in Engineering) the CNPq and FAPEMIG. The Air Force Office of Scientific Research (AFOSR) is also acknowledged.

References

- L.F.P. Franca, M.A. Savi, Evaluating noise sensitivity on the time series determination of Lyapunov exponents applied to the nonlinear pendulum. *Shock Vib.* **10**(1), 37–50 (2003)
- J. Gleick, *Chaos* (Heinemann, London, 1987)
- C. Grebogi, E. Ott, S. Pelikan, J. Yorke, Strange attractors that are not chaotic. *Phys. D* **13**, 261–268 (1984)
- J. Guckenheimer, P. Holmes, *Nonlinear Oscillations, Dynamical Systems, and Bifurcations of Vector Fields* (Springer, New York, 1983)
- R.C. Hilborn, *Chaos and Nonlinear Dynamics* (Oxford Press, Oxford, 1994)
- M.W. Hirsch, S. Smale, R.L. Devaney, *Differential Equations, Dynamical Systems & An Introduction to Chaos* (Elsevier, Amsterdam, 2004)
- H. Kantz, T. Schreiber, *Nonlinear Time Series Analysis* (Cambridge University Press, Cambridge, 1997)
- T. Kapitaniak, *Chaotic Oscillations in Mechanical Systems* (Manchester University Press, Manchester, 1991)
- E. Lorenz, Deterministic nonperiodic flow. *J. Atmos. Sci.* **20**, 130–141 (1963)
- L.G. Machado, M.A. Savi, P.M.C.L. Pacheco, Nonlinear dynamics and chaos in coupled shape memory oscillators. *Int. J. Solids Struct.* **40**(19), 5139–5156 (2003)
- L.G. Machado, M.A. Savi, P.M.C.L. Pacheco, Bifurcations and crises in a shape memory oscillator. *Shock Vib.* **11**(2), 67–80 (2004)
- F.C. Moon, *Chaotic and Fractal Dynamics* (Wiley, New York, 1992)
- L.H.A. Monteiro, *Dynamical Systems*. Editora Livraria da Física (in Portuguese) (2002)
- T. Mullin, *The Nature of Chaos* (Oxford University Press, Oxford, 1993)
- A.H. Nayfeh, D.T. Mook, *Nonlinear Oscillations* (Wiley, New York, 1979)
- E. Ott, *Chaos in Dynamical Systems* (Cambridge University Press, Cambridge, 1993)
- A. Paiva, M.A. Savi, An overview of constitutive models for shape memory alloys. *Math. Probl. Eng.* **2006**, 1–30 (2006), ID56876
- T.S. Parker, L.O. Chua, *Practical Numerical Algorithms for Chaotic Systems* (Springer, New York, 1989)
- M.A. Savi, *Nonlinear Dynamics and Chaos*. Editora E-papers (in Portuguese) (2006)
- M.A. Savi, *Rhythms of Nature*. Editora E-papers (in Portuguese) (2014)
- M.A. Savi, Nonlinear dynamics and chaos in shape memory alloy systems. *Int. J. Non Linear Mech.* **70**, 2–19 (2015). doi:10.1016/j.ijnonlinmec.2014.06.001
- M.A. Savi, A.M.B. Braga, Chaotic vibration of an oscillator with shape memory. *J. Braz. Soc. Mech. Sci.* **15**(1), 1–20 (1993)
- M.A. Savi, P.M.C.L. Pacheco, Chaos and hyperchaos in shape memory systems. *Int. J. Bifurcat. Chaos* **12**(3), 645–657 (2002)

- I. Stewart, *Does God Play Dice?* Jorge Zahar Editor (in Portuguese) (1991)
- S.H. Strogatz, *Nonlinear Dynamics and Chaos* (Perseus, Cambridge, 1994)
- J.M.T. Thompson, H.B. Stewart, *Nonlinear Dynamics and Chaos* (Wiley, Chichester, 1986)
- S. Wiggins, *Introduction to Applied Nonlinear Dynamical Systems and Chaos* (Springer, New York, 1990)
- A. Wolf, J.B. Swift, H.L. Swinney, J.A. Vastano, Determining Lyapunov exponents from a time series. *Phys. D* **16**, 285–317 (1985)

Part II

Smart Materials

Introduction to Smart Materials and Structures

Domingos A. Rade and Valder Steffen Jr.

Abstract This chapter first introduces the basic definitions and concepts related to smart materials and structures. Then, the underlying physical principles and main operational features of some of the smart materials most widely used in engineering applications are described. The potential of the technology of smart materials and structures for innovative solutions of practical problems is put in evidence by the description of some relevant research studies and engineering applications, with the support of relevant bibliographic references. The concepts introduced in this chapter are further developed in the other chapters of the book.

Keywords Smart materials • Smart structures • Smart material systems • Intelligent materials • Intelligent structures

1 Introduction

Recent advances in material sciences enabled the exploration of novel types of materials, favoring innovative solutions to a number of engineering problems. Among these materials, the so-called *smart materials* have deserved a great deal of attention. According to Leo (2006), these materials are characterized by the existence of coupling between two or more physical domains (mechanical, electrical, thermal, chemical, optical), in such a way that modifications of the state variables related to a given domain lead to changes of the state variables related to another domain. This coupling is illustrated in Fig. 1 considering mechanical, electrical, and thermal domains. Also indicated are the most important effects associated to the coupling between each pair.

D.A. Rade (✉)

Division of Mechanical Engineering, Technological Institute of Aeronautics,
São José dos Campos, SP 12228-900, Brazil
e-mail: rade@ita.br

V. Steffen Jr.

School of Mechanical Engineering, Federal University of Uberlândia,
Uberlândia, MG 38408-100, Brazil
e-mail: vsteffen@ufu.br

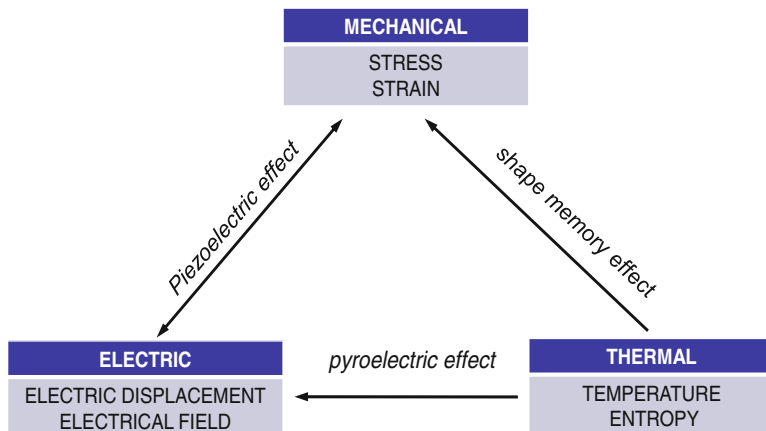


Fig. 1 Illustration of coupling of physical domains, typical of smart materials (adapted from Leo 2006)

In the field of mechanical systems, the existence of the aforementioned coupling has enabled the use of smart materials under the form of sensors and actuators which, once integrated to a system, can provide unusual capabilities to it. In this sense, *smart structures* or, more generally, *smart material systems* are understood as engineering systems (civil engineering structures, vehicles, household appliances, industrial equipment, for example), to which smart materials are integrated aiming at improving their functionalities with respect to traditional versions.

In their more advanced conceptions, smart materials systems are designed to mimic certain functionalities of living beings, by using sensors to detect modifications of the operational and/or environmental features, and promote, by means of actuators, the necessary corrective actions in order to keep a satisfactory performance of the system. This process is controlled by software running in microprocessors, which are responsible for signal processing and command of the actuators. This description makes clear that one of the main characteristics of smart material systems is the high level of integration of sensors, actuators, and electronic processors into them.

The relevance and maturity of the technology of smart material systems is confirmed by the large number of existing patents and innovative products. However, the subject remains an important scientific topic as searching for improved performance and bridging technological gaps are still necessary. Due to its nature, the field of smart structures is inherently interdisciplinary. As a result, expertise in numerous disciplines (e.g., material science, applied mechanics, electronics, control theory, and computer science) is necessary for the conception and design of new solutions.

In this sense, the future evolution of this field highly depends on the education of engineers and scientists with the necessary knowledge and skills. For this purpose, much effort has been made to popularize this technology and provide didactic

material for students (Banks et al. 1996; Clark et al. 1998; Srinivasan and McFarland 2000; Leo 2006). Moreover, many review papers have been published, which provide the reader with a sense of underlying principles, potential for applications and research needs and perspectives (Chee et al. 1998; Frecker 2003; Hurlbaeus and Gaul 2006).

From the industrial/commercial standpoint, many companies now produce and commercialize smart materials and appliances containing them.

In this introductory chapter the main characteristics of some of the most widely used intelligent materials are presented. Also, their potential for the solution of practical engineering problems is put in evidence by the description of some relevant research studies and practical applications, with the support of some relevant bibliographic references. In the chapters that follow, more detailed descriptions and analyses are provided by experts, for each of those materials.

2 Piezoelectric Materials

Piezoelectricity, discovered in 1880 by French physicists Jacques and Pierre Curie, is the property exhibited by certain natural or synthetic solids (quartz, tourmaline, ceramics, polymers), and biological tissues (bone, skin, dentin) that cumulate electric charge in response to the application of mechanical loads (direct piezoelectric effect). Conversely, they undergo geometric deformations (elongations, contractions, or distortions) when submitted to external electric fields (inverse piezoelectric effect). The fundamentals of piezoelectricity have been presented in a number of books (Cady 1964; Jaffe et al. 1971).

Most piezoelectric materials have crystalline structures, which means that their atoms are arranged with a certain degree of regularity in such a way that one can identify fundamental arrangements of atoms, called unit cells, that make up the whole volume of the material. According to the geometric arrangement of the atoms, the unit cells can be assimilated to electric dipoles, meaning that they present net separations of positive and negative electric charges. This is a necessary condition for the existence of the piezoelectric effect. A similar principle applies to piezoelectric polymers in which the dipoles are associated to molecular chains.

Confining the focus on crystalline piezoelectric ceramics, which are widely used in smart structure applications, Fig. 2 illustrates one of the phases of their manufacturing process, called *poling*. As can be seen in Fig. 2a, within the raw material the electric dipoles are oriented randomly. As a result, the material does not exhibit significant piezoelectric features at the macroscopic level. After being heated, the material is subjected to an intense electric field, in such a way that the combination of heating and electric field enables the individual dipoles to be reoriented in the direction of the electrical field, due to the action of electrostatic forces (Fig. 2b). After removing the electrical field and lowering the temperature, the electric dipoles come to a preferred orientation in the direction of the poling field and the material exhibits macroscopic piezoelectric properties.

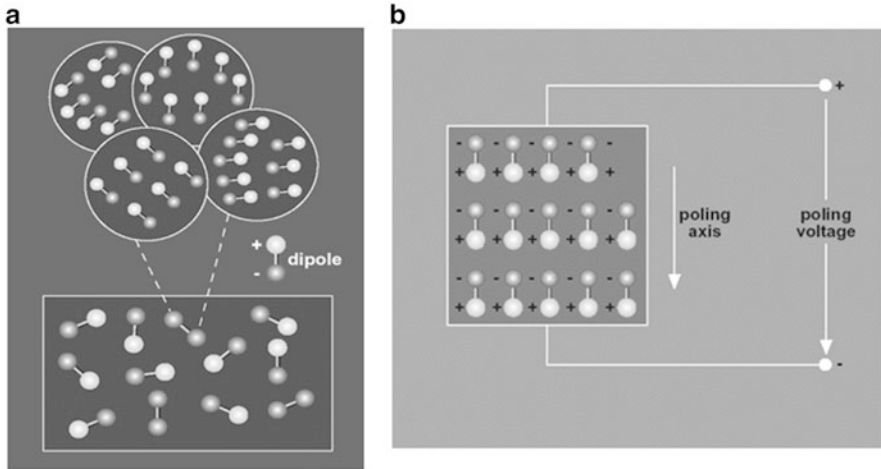


Fig. 2 Illustration of the poling process of piezoelectric ceramics. (a) Randomly oriented electric dipoles; (b) reoriented dipoles under poling electric field

When using piezoelectric materials, care should be exercised to avoid that temperature exceeds the so-called *Curie temperature*, above which the material loses its piezoelectric properties. The same happens when the material is subjected to strong electric fields with signal opposite to that of the original poling field.

Figure 3 illustrates the direct and inverse piezoelectric effects. According to the first, when subjected to a mechanical stress T , the material develops electric charges that are accumulated in the metallic electrodes deposited on the surface of the material. The surface charge density, named *electric displacement*, is denoted by D . The signal of the charge depends on the signal of the applied stress (tension or compression). As illustrated in Fig. 3a, for relatively low applied stress, the relation between D and T is linear.

Regarding the inverse piezoelectric effect, the material presents deformations when an electric field E is applied across the electrodes. In Fig. 3b, the deformation is represented in terms of the strain S . For relatively low intensities of the electrical field, a linear relation between S and E is observed.

Exploring the direct and inverse piezoelectric effects, piezoelectric materials can be used either as sensors or actuators, respectively. In the first case, as illustrated in Fig. 4a, a piezoelectric element is bonded to the surface of a host structure, in such a way that, when the structure deforms, either statically or dynamically, part of the surface strain is transmitted to the piezoelectric element. As a result, this latter generates electric charges that, by using appropriate electronics, can be converted into a voltage signal proportional to the strain.

In the second case (Fig. 4b), when a voltage signal is applied to the piezoelectric element, it tends to deform; as this deformation is counteracted by the mechanical impedance of the structure, forces are developed on the interface, which make the structure to deform, statically or dynamically, according to the nature of the input voltage signal.

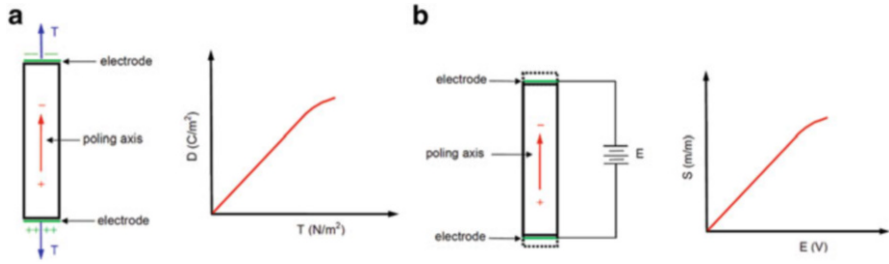


Fig. 3 Illustration of the piezoelectric effect. (a) Direct effect; (b) inverse effect

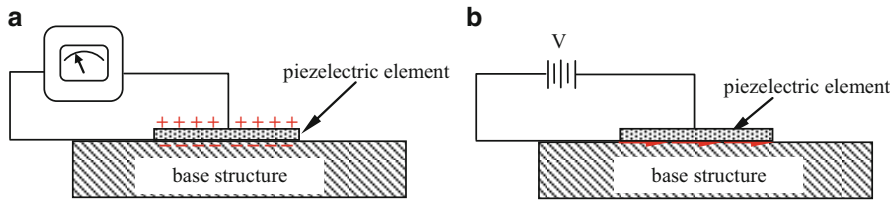


Fig. 4 Illustration of the use of piezoelectric materials as: (a) sensor; (b) actuator

Piezoelectric materials have been extensively used in various engineering applications, either as sensors or actuators, based on the principles previously described. Some of the most relevant applications, from the perspective of smart structures technology, are exemplified next.

2.1 Active Vibration, Aeroelastic and Noise Control

In the context of active noise and vibration control of mechanical systems, the use of piezoelectric materials provides many advantages, as compared to traditional sensors (e.g., inertial accelerometers, inductive proximity sensors) and actuators (e.g., electromagnetic, hydraulic, pneumatic). As a matter of fact, piezoelectric materials can be used as distributed sensors or actuators, at moderate added weight and can exhibit sufficient sensing capacity and control effectiveness, this latter in terms of both force magnitude and frequency bandwidth. Moreover, piezoelectric sensors and actuators can be arbitrarily shaped in such a way to enable full integration to the mechanical systems.

Many applications related to the use of piezoelectric materials for active noise and vibration control, and also for the control of aeroelastic phenomena, such as buffeting and flutter, have been reported in the literature. For example, Giurgiutiu (2000) provides a comprehensive review of achievements in the application of smart materials actuation to counteract aeroelastic and vibration effects in rotary and fixed wing aircraft. Nitzsche (2012) reports the challenging use of piezoelectric

actuators as part of a Buffeting Loading Alleviation (BLA) system applied to the vertical fin of a F-18 fighter. A comprehensive review of active vibration and noise suppression of plate-like structures with piezoelectric sensors and actuators, considering various boundary conditions and controller architecture has been recently presented by Aridogan and Basdogan (2015).

2.2 *Passive Noise and Vibration Control Based on Shunted Piezoelectric Transducers*

In a pioneering research work, Forward (1979) suggested the use of piezoelectric elements associated to electric circuits (named *shunt circuits*) for the purpose of passive vibration control. The basic idea, illustrated in Fig. 5, consists in converting the dynamic strain energy of the host structure into electric energy by exploring the direct piezoelectric effect, and transferring this energy to the circuit of impedance $Z(\omega)$, in which it can be partially dissipated.

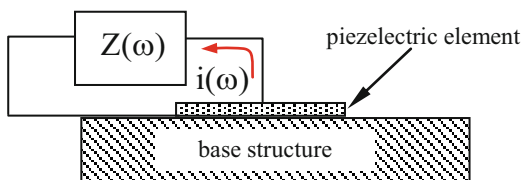
It is important to point out that, from the perspective of the dynamic behavior, some types of shunt circuits exhibit close similarity to other types of vibration control devices. Indeed, as demonstrated by Hagood and Flotow (1991), Wu (1996), and Lesieutre (1998), if the shunt circuit is a pure resistance, R , the dynamic behavior is similar to that exhibited by viscoelastic materials, characterized by a frequency-dependent complex material modulus. On the other hand, if the shunt circuit is a resistive–inductive (RL) circuit, its influence is analogous to that of a viscously damped dynamic vibration absorber (Viana and Steffen 2006).

More recently, more sophisticated electronic circuits have been suggested for improved performance, such as switched shunts (Richard et al. 2000; Ducarne et al. 2010) and negative capacitance (Marneffe and Preumont 2008). A recent study devoted to vibroacoustic control is presented by Rocha and Dias (2014).

2.3 *Piezoelectric Energy Harvesting*

The possibility of generating electric energy from vibratory motion by exploring the direct piezoelectric effect has been intensively investigated lately (Erturk and Inman 2011). This concept is known as *piezoelectric energy harvesting* or

Fig. 5 Scheme of a piezoelectric element connected to a shunt circuit



piezoelectric energy scavenging. It should be clear, however, that, as compared to other traditional sources of energy, this technology is capable of producing relatively small amounts of energy, which can, nonetheless, be used to feed low power devices. As an example, some applications involve the use of piezoelectric energy harvesting to feed remote sensing devices and wireless transmission systems (Zhou and Zuo 2015).

Studies reported in the literature associate the concept of piezoelectric energy harvesting with a variety of vibration sources, such as machinery and structure vibrations (Kim 2015), ocean wave motions (Wu et al. 2015), aeroelastic oscillations (Rocha Vieira and De Marqui 2013), air flow (Zou et al. 2015), and human motion (Shukla and Bell 2015).

2.4 Structural Health Monitoring

The technology of structural health monitoring (SHM) addresses the problem of identifying damage by processing structural response signals, and includes the tasks of damage detection, location, evaluation of extent, and prognosis (Inman et al. 2005; Adams 2007; Farrar and Worden 2012). Among the different strategies conceived for SHM, the use of piezoelectric materials has received a great deal of attention, particularly due to the possibility of deep integration of these materials into the monitored structures. In this context, piezoelectric transducers are used either as sensors or actuators in the process of capturing the influence of damage on the structural response, with the advantage that those transducers can operate in very broad frequency bands. The operation in the high-frequency domain makes it possible to identify the presence of incipient damage.

Examples of SHM techniques based on piezoelectric materials are those based on electromechanical impedance (Annamdas and Soh 2010) and Lamb waves (Raghavan and Cesnik 2005; Su et al. 2006). In the first, a single piezoelectric transducer is bonded to the surface of the structure. Special electronics and software are used to drive the transducer with a voltage signal which excites the structure dynamically in a high-frequency range (of the order of tens or hundreds of kHz). The response of the structure is measured by using the same transducer as a sensor, in terms of the output electrical current. The ratio of the input voltage and output current defines the electromechanical impedance function, which is a complex function of frequency and depends on the physical features of both the monitored structure and piezoelectric transducer. Hence, the occurrence of damage provokes changes in the electromechanical impedance function and the observed variations are used to infer the presence, location, and extent of damage. Since the same transducer is used for excitation and response measurement, this technique is classified as a *pitch-echo* method.

Piezoelectric transducers can also be used to generate Lamb waves, which exist in thin plate-like components, and are guided by the parallel free boundaries. The interesting feature of Lamb waves is that they interfere with damages, generating

reflections that can be detected. SHM methods based on Lamb waves can be implemented either as pulse-echo, when a single transducer is used to generate and measure the reflected waves, or *pitch-catch*, when these functions is performed by different transducers.

3 Shape Memory Alloys

Shape memory alloys (SMAs) is a class of metallic materials which exhibit the capacity of developing and recovering large strains (of the order of 8 %), in response to combination of thermal and mechanical activation. This behavior is due to transformations between two solid phases: martensite, which is stable at lower temperatures, and austenite, stable at higher temperatures. For a given alloy composition, the temperatures of transition from one phase to the other depend on the stress state.

Among the SMAs, Ni–Ti alloys, known commercially under the name “Nitinol,” are the most popular.

The phenomenology of SMAs is relatively well known. Starting from the material in the austenitic phase, free of mechanical load at high temperature, upon cooling, a gradual transformation from austenite to martensite takes place. In this process, different variants of martensite are obtained, which are distinguished from each other by the orientation of their crystallographic structures. In this state, the martensite is called the *twinned martensite*. Upon heating the martensite, the reverse transformation to austenite occurs.

In these transformations, an important variable is the martensite fraction ξ ($0 \leq \xi \leq 1$), defined in such a way that $\xi = 1$ and $\xi = 0$ correspond to the states of full martensite and full austenite, respectively.

For a given alloy, the thermally induced transformations are characterized by four values of temperature, namely:

- M_s : temperature at which the transformation from austenite to martensite starts
- M_f : temperature at which the transformation from austenite to martensite finishes
- A_s : temperature at which the transformation from martensite to austenite starts
- A_f : temperature at which the transformation from martensite to austenite finishes

A schematic representation of the temperature-induced transformations between the two phases is depicted in Fig. 6.

Regarding the thermomechanical behavior, SMAs exhibit two distinct phenomena, namely, *shape memory effect* and *superelastic effect*. The shape memory effect is the property by which large strains undergone by the material in response mechanical loading can be recovered by heating above a certain temperature, as indicated in Fig. 7a. On the other hand, the superelastic effect is the property by which the material exhibits a very large strain upon loading, which is fully recovered when the material is unloaded, without any temperature variation. In this process, a very large hysteresis loop in the stress–strain curve takes place, as show in Fig. 7b.

Fig. 6 Temperature-induced phase transformations in SMAs

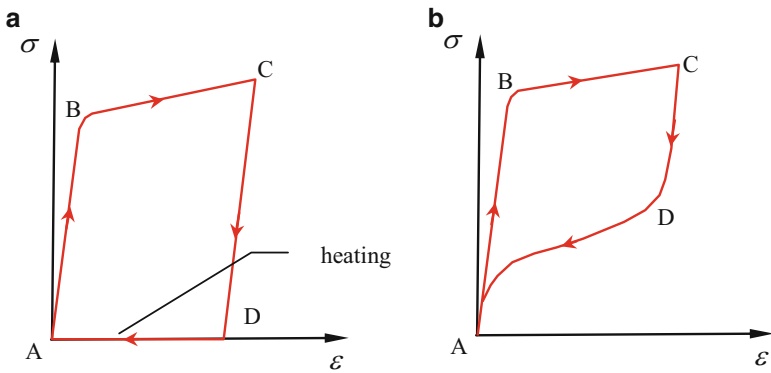
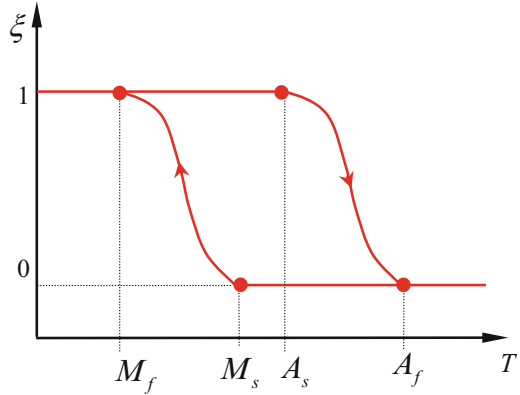


Fig. 7 (a) Representation of the shape memory effect; (b) representation of the superelastic effect

In Fig. 7a, at point A, at a sufficient low temperature, with no mechanical load, the only phase present in the material is twinned martensite. Upon loading, detwinning of the martensite occurs, so that, for sufficiently high load, at point C only detwinned martensite exists in the material. Detwinning is the process of reorientation of the martensite variants induced by the load, which is accompanied by large deformation. Upon unloading, at point D the specimen exhibits a remaining strain. If the specimen is heated in the load-free state, the remaining strain is fully recovered, and the original state of detwinned martensite is obtained at point A.

Regarding Fig. 7b, for the superelastic effect to take place, at point A the material must be fully austenitic, which means that the temperature must be sufficiently high for this phase to be stable. As the result of mechanical loading, the austenite ceases to be stable and is transformed to martensite, which is simultaneously detwinned by the load action. This process is accompanied by large deformation (branch B–C). When the specimen is unloaded, the martensite is transformed back to austenite, and the strain is fully recovered (path C–D–A). It should be noticed that, as opposed to the shape memory effect, which involves temperature increase, the superelastic effect occurs under isothermal condition.

By exploring the shape memory effect, SMAs have been used for the conception of thermally activated actuators (motion or force generators) in a number of applications, among which one can mention aircraft engines (Lagoudas and Hartl 2007), medical devices (Machado and Savi 2003; Silva et al. 2013), robotics (Yan et al. 2012), aeroelastic control (Giurgutiu 2000, Abreu et al. 2014), and morphing aircraft structures (Barbarino et al. 2011).

On the other hand, the superelastic effect has been explored in various applications in which large recoverable strains are required. Moreover, as the loop in the strain–strain is associated to energy dissipation, this effect has also been explored for increasing damping in vibratory systems, in the scope of passive vibration control (Han et al. 2003; Song et al. 2006). Also, superelastic SMAs have found a number of applications in medical and dental devices (Machado and Savi 2003; Jania et al. 2014).

Very useful review papers and books devoted to the fundamentals and applications of SMA can be found in the literature (Lagoudas 2008; Jania et al. 2014).

4 Magneto-Rheological and Electro-Rheological Fluids

Magneto-rheological fluids (designated herein as MR) are those which exhibit significant reversible modifications of their rheological properties (those related to the flow behavior), when they are submitted to external magnetic fields. Likewise, electro-rheological fluids (ER) exhibit similar dependence with respect to electric field.

Physically, MR fluids are stable suspensions of magnetically polarizable micron-sized particles suspended in a low-volatility carrier fluid, usually a synthetic hydrocarbon. The order of the dimension of the particles can vary from 1 to hundreds of μm . Surfactants are added to favor the dispersion of the particles in the fluid. As to ER fluids, the particles must be made of dielectric (insulating) materials.

To illustrate the underlying phenomenology, Fig. 8 shows a MR fluid between two plates which can be slipped with respect to the other, so that the fluid is

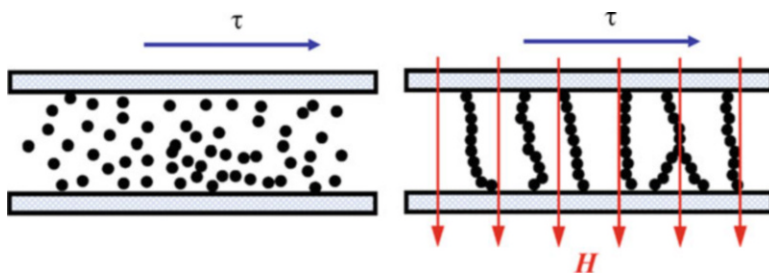


Fig. 8 Illustration of the formation of magnetized particle clusters in a MR fluid

deformed in shear. In the absence of magnetic field, the particles are evenly dispersed in the volume of the fluid, which behaves essentially as a Newtonian fluid (the shear stress is proportional to the shear strain rate). However, upon the application of a magnetic field H , the particles become magnetically polarized and are gathered in clusters. Under this condition, the MR fluid exhibits a yield shear stress, which depends on the intensity of the magnetic field. As a result, there is a minimum value of shear stress necessary for the onset of the flow.

Similar principle applies to electro-rheological fluids, for which the formation of clusters can be interpreted as the result of electrostatic polarization.

A model often used to describe the behavior of MR fluids is the Bingham plastic model, for which the constitutive relation is written as:

$$\tau = \tau_y + \mu \frac{d\gamma}{dt},$$

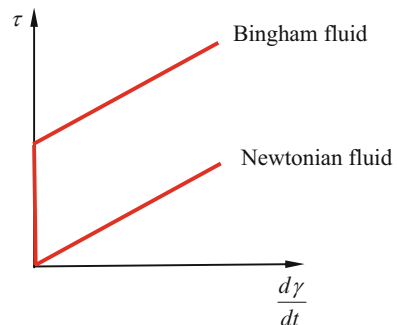
where τ is the shear stress, τ_y is the yield shear stress, μ is the viscosity, and $d\gamma/dt$ is the shear strain rate. As discussed above, the flow does not occur as long as the applied shear stress is smaller than the yield stress. Figure 9 illustrates the Bingham constitutive model, compared to the Newtonian fluid model.

In most applications, the main rheological property of interest is the viscosity, which determines the damping capacity of the fluid. Hence, in the scope of smart structures, electro-rheological and magneto-rheological fluids have been explored for the purpose of achieving controllable damping.

Confronting MR and ER fluids, it has been recognized that ER fluids have some inherent drawbacks, which make MR fluids preferable in a number of applications. Such shortcomings include the tendency of permanent polarization of the ER fluid particles and the necessity of application of relatively high voltages.

MR fluids can currently be found in a number of commercial products, including clutches, brakes, dampers, mounts, bushings, and haptic devices (Jolly et al. 1999). One of the most mature fields of applications is the automotive industry, which has explored MR fluids for the conception of semi-active dampers, integrated in car suspensions and truck driver seats (McManus et al. 2002). Also, some promising studies have been conducted for civil engineering structures (Dyke et al. 1998).

Fig. 9 Illustration of the constitutive laws for Bingham and Newtonian fluids



5 Electroactive Polymers

The category of electroactive polymers comprises a wide range of materials that exhibit a variety of coupling mechanisms. Those which exhibit electromechanical coupling are functionally similar to piezoelectric materials in that they produce mechanical strain under the application of electric fields and produce electrical signals when subjected to mechanical stresses. However, as opposed to piezoelectric ceramics, which are characterized by small free strains and high blocked stresses, electroactive polymers, which are very soft, can develop high strains (on the order of 50–100 %), but have little load capacity.

Electromechanical electroactive polymers can be classified in two main types: electronic and ionic materials. The mechanism behind the behavior of electronic electroactive polymers is associated to polarization or electrostatic effects. The electrical properties of these materials are very similar to those of piezoelectric materials since they are dielectric materials that contain electric charges forming electric dipoles. On the other hand, ionic electroactive polymers exhibit electromechanical coupling due to the diffusion, or conduction, of charged species within the polymer network, which produce the accumulation of charge within the material.

Electroactive polymers have been considered in a variety of applications, such as artificial muscles (Shahinpoor 2003), robotics (Mutlu et al. 2014), and micropumps (Xia et al. 2006).

In spite of being an emerging technology, electroactive polymers have been the subject of rich literature, including books (Bar-Cohen 2004) and review papers (Shahinpoor 2003).

6 Final Remarks

Smart Materials and Structures is one of the most active and promising research fields in Engineering, having much potential for novel solutions and incremental improvement of existing solutions to a range of problems.

In the forthcoming years, many new achievements are expected to occur as the result of the consolidation of research groups worldwide, the emergence of improved materials, and the incorporation of the advances into industrial products. To sustain this trend, it is of utmost importance to educate researchers and engineering students, and make practitioners convinced of the potential of smart materials.

References

- G.L.C.M. Abreu, M.F. Maesta, V. Lopes Jr., C. De Marqui Jr., C.T. Faria, D.J. Inman, Active angular control of a sectioned airfoil using shape memory alloys and fuzzy controller. *J. Braz. Soc. Mech. Sci. Eng.* **1**, 1–13 (2014)

- D.E. Adams, *Health Monitoring of Structural Materials and Components* (Wiley, Chichester, 2007)
- V.G.M. Annamdas, C.K. Soh, Application of electromechanical impedance technique for engineering structures: review and future issues. *J. Intell. Mater. Syst. Struct.* **21**, 41–59 (2010)
- U. Aridogan, I. Basdogan, A review of active vibration and noise suppression of plate-like structures with piezoelectric transducers. *J. Intell. Mater. Syst. Struct.* **26**, 1455–1476 (2015)
- H.T. Banks, C. Smith, Y. Wang, *Smart Material Structures. Modeling, Estimation and Control* (Wiley, New York, 1996)
- S. Barbarino, O. Bilgen, R.M. Ajaj, M.I. Friswell, D.J. Inman, A review of morphing aircraft. *J. Intell. Mater. Syst. Struct.* **22**, 823–977 (2011)
- Y. Bar-Cohen, *Electroactive Polymer (EAP) Actuators as Artificial Muscles: Reality, Potential, and Challenges*, vol. PM136, 2nd edn. (SPIE Press Monograph, 2004)
- W. Cady, *Piezoelectricity: An Introduction to the Theory and Applications of Electromechanical Phenomena in Crystals*, vol. I, 2nd edn. (Dover, New York, 1964)
- C.Y.K. Chee, L. Tong, G.P. Steven, A review on the modelling of piezoelectric sensors and actuators incorporated in intelligent structures. *J. Intell. Mater. Syst. Struct.* **9**, 3–19 (1998)
- R.L. Clark, W.R. Saunders, G.P. Gibbs, *Adaptive Structures: Dynamics and Control* (Wiley, New York, 1998)
- L. Ducarne, O. Thomas, J.-F. Deü, Structural vibration reduction by switch shunting of piezoelectric elements: modeling and optimization. *J. Intell. Mater. Syst. Struct.* **21**(8), 797–816 (2010)
- S.J. Dyke, B.F. Spencer Jr., M.K. Sain, J.D. Carlson, An experimental study of MR dampers for seismic protection. *Smart Mater. Struct.* **7**(5), 693–703 (1998)
- A. Erturk, D.J. Inman, *Piezoelectric Energy Harvesting* (Wiley, Chichester, 2011)
- C.R. Farrar, K. Worden, *Structural Health Monitoring: A Machine Learning Perspective* (Wiley, Chichester, 2012)
- R.L. Forward, Electronic damping of vibrations in optical structures. *J. Appl. Opt.* **18**, 690–697 (1979)
- M.I. Frecker, Recent advances in optimization of smart structures and actuators. *J. Intell. Mater. Syst. Struct.* **14**, 207–216 (2003)
- V. Giurgiutiu, Review of smart-materials actuation solutions for aeroelastic and vibration control. *J. Intell. Mater. Syst. Struct.* **11**(8), 525–544 (2000)
- N.W. Hagood, A.V. Flotow, Damping of structural vibrations with piezoelectric materials and passive electrical networks. *J. Sound Vib.* **146**, 243–268 (1991)
- Y.-L. Han, Q.S. Li, A.-Q. Li, Y.T. Leung, P.-H. Lin, Structural vibration control by shape memory alloy damper. *Earthquake Eng. Struct. Dynam.* **32**, 483–494 (2003)
- S. Hurlbaeus, L. Gaul, Smart structure dynamics. *Mech. Syst. Signal Process.* **20**, 255–281 (2006)
- D.J. Inman, C.R. Farrar, V. Lopes Jr., V. Steffen Jr. (ed.), *Damage Prognosis: For Aerospace, Civil and Mechanical Systems* (Wiley, Chichester, 2005)
- F. Jaffe, W.R. Cook Jr., H. Jaffe, *Piezoelectric Ceramics* (Academic, London, 1971)
- J.M. Jania, M. Learya, A. Subic, M.A. Gibson, A review of shape memory alloy research, applications and opportunities. *Mater. Des.* **56**, 1078–1113 (2014)
- M.R. Jolly, J.W. Bender, J.D. Carlson, Properties and applications of commercial magnetorheological fluids. *J. Intell. Mater. Syst. Struct.* **10**(1), 5 (1999)
- G.W. Kim, Piezoelectric energy harvesting from torsional vibration in internal combustion engines. *Int. J. Autom. Technol.* **16**, 645–651 (2015)
- D.I. Lagoudas (ed.), *Shape Memory Alloys Modeling and Engineering Applications* (Springer, New York, 2008)
- D. Lagoudas, D. Hartl, Aerospace applications of shape memory alloys. Proceedings of the institution of mechanical engineers, part G. *J. Aerosp. Eng.* **221**(Special Issue), 535–552 (2007)
- D. Leo, *Engineering Analysis of Smart Material Systems* (Wiley, Hoboken, 2006)
- G.A. Lesieutre, Vibration damping and control using shunted piezoelectric materials. *Shock Vib. Digest* **30**, 181–190 (1998)

- L.G. Machado, M.A. Savi, Medical applications of shape memory alloys. *Braz. J. Med. Biol. Res.* **36**, 683–691 (2003)
- F. Marneffe, A. Preumont, Vibration damping with negative capacitance shunts: theory and experiment. *Smart Mater. Struct.* **17**, 1–8 (2008)
- S.J. McManus, K.A. St. Clair, P.E. Boileau, J. Boutin, Evaluation of vibration and shock attenuation performance of a suspension seat with a semi-active magnetorheological fluid damper. *J. Sound Vib.* **253**(1), 313–327 (2002)
- R. Mutlu, G. Alici, X. Xiang, W. Li, Electro-mechanical modelling and identification of electroactive polymer actuators as smart robotic manipulators. *Mechatronics* **24**, 241–251 (2014)
- F. Nitzsche, The use of smart structures in the realization of effective semi-active control systems for vibration reduction. *J. Braz. Soc. Mech. Sci. Eng.* **XXXIV**(Special Issue), 371–377 (2012)
- A. Raghavan, C.E.S. Cesnik, Lamb wave-based structural health monitoring, in Book Chapter: *Damage Prognosis*, ed. by D.J. Inman, C.R. Farrar, V. Lopes Jr., V. Steffen Jr. (Wiley, New York, 2005)
- C. Richard, D. Guyomar, D. Audigier, H. Bassaler, Enhanced semi-passive damping using continuous switching of a piezoelectric device on an inductor. *Proc. SPIE Smart Struct. Mater. Conf. Passive Damping Isolation* **3989**, 288–299 (2000)
- T.L. Rocha, M. Dias, Improved sound transmission loss in an automotive component using piezoceramic patches and dissipative shunt circuits. *J. Intell. Mater. Syst. Struct.* **26**(4), 476–786 (2014)
- W.G. Rocha Vieira, C. De Marqui Jr. Piezoelectric energy harvesting from nonlinear aeroelastic, *Proceedings of the ASME Conference on Smart Materials, Adaptive Structures and Intelligent Systems*, Snowbird, UT, USA
- M. Shahinpoor, Ionic polymer–conductor composites as biomimetic sensors, robotic actuators and artificial muscles—a review. *Electrochim. Acta* **48**, 2343–2353 (2003)
- R. Shukla, A.J. Bell, PENDEXE: a novel energy harvesting concept for low frequency human waistline. *Sens. Actuators A Phys.* **222**, 39–47 (2015)
- A.F.C. Silva, A.J.V. Dos Santos, C.R. Souto, C.J. De Araújo, S.A. Da Silva, Artificial biometric finger driven by shape-memory alloy wires. *Artif. Organs* **37**, 965–972 (2013)
- G. Song, N. Ma, H.-N. Li, Applications of shape memory alloys in civil structures. *Eng Struct.* **28**, 1266–1274 (2006)
- A.V. Srinivasan, D.M. McFarland, *Smart Structures: Analysis and Design* (Cambridge University Press, Cambridge, 2000)
- Z. Su, L. Ye, Y. Lu, Guided Lamb waves for identification of damage in composite structures: a review. *J. Sound Vib.* **295**, 753–780 (2006)
- F.A.C. Viana, V. Steffen Jr., Multimodal vibration damping through piezoelectric patches and optimal resonant shunt circuits. *J. Braz. Soc. Mech. Sci. Eng.* **XXVIII**(3), 293–310 (2006)
- S.Y. Wu, Piezoelectric shunts with a parallel R-L circuit for structural damping and vibration control. *SPIE Proc.* **2720**, 259–269 (1996)
- N. Wu, Q. Wang, X.D. Xie, Ocean wave energy harvesting with a piezoelectric coupled buoy structure. *Appl. Ocean Res.* **50**, 110–118 (2015)
- F. Xia, S. Tadigadapa, Q.M. Zhang, Electroactive polymer based microfluidic pump. *Sens. Actuators A Phys.* **125**, 346–352 (2006)
- Q. Yan, L. Wang, B. Liu, J. Yang, S. Zhang, A novel implementation of a flexible robotic fin actuated by shape memory alloy. *J. Bionic Eng.* **9**, 156–165 (2012)
- W. Zhou, L. Zuo, A self-powered piezoelectric vibration control system with switch precharged inductor (SPCI) method. *IEEE ASME Trans. Mech.* **20**, 773–781 (2015)
- H. Zou, H. Chen, X. Zhu, Piezoelectric energy harvesting from vibrations induced by jet-resonator system. *Mechatronics* **26**, 29–35 (2015)

Piezoelectric Materials

Vicente Lopes Jr. and Clayton Rodrigo Marqui

Abstract Piezoelectricity is a phenomenon in which certain crystalline substances develop an electric field when subjected to pressure force, or conversely, exhibit a mechanical deformation when subjected to an electric field. This reciprocal coupling between mechanical and electrical energy provides useful features for these materials. The dynamics of the piezoelectric sensor/actuator plays an increasing importance when higher performance from closed loop systems or damage monitoring is required for strategic applications. This chapter focuses on the development of the constitutive equations of smart structures. The incorporation of mass, stiffness, and electromechanical coupling of the piezoceramic patches has a significant influence on the dynamics properties of the system.

Keywords Electromechanical coupling • Piezoelectric material • Smart structure

1 Introduction

The dynamics of the piezoelectric sensor/actuator plays an increasing importance when higher performance from closed loop systems or damage monitoring is required for strategic applications. For a piezoceramic, the three direction (z -axis) is usually associated with the direction of poling and the material is approximately isotropic in the other two directions.

Materials that become electrically polarized when they are deformed present the direct piezoelectric effect, producing an electrical charge at the surface of the material. The converse piezoelectric effect results in a strain in the material when placed within an electric field. The direct and converse effects result an electromechanical coupling. While piezoelectric elements exhibit nonlinear hysteresis at high excitation levels, the response required in the current typical structural applications

V. Lopes Jr. (✉)

Mechanical Engineering Department, Universidade Estadual Paulista, UNESP,
Campus Ilha Solteira, Ilha Solteira, SP, Brazil
e-mail: vicente@dem.feis.unesp.br

C.R. Marqui

EMBRAER, São José dos Campos, SP, Brazil

is approximately linear. The linear constitutive relations for piezoelectric materials are given by Leo (2007):

$$\mathbf{T} = [c^E]\{\mathbf{S}\} - [e]\{\mathbf{E}\} \quad (1)$$

$$\mathbf{D} = [e]^T\{\mathbf{S}\} + [\varepsilon^S]\{\mathbf{E}\} \quad (2)$$

where the superscript (^S) means that the values are measured at constant strain, the superscript (^E) means that the values are measured at constant electric field, \mathbf{T} is the stress tensor [N/m²], \mathbf{D} is the electric displacement vector [C/m²], $\{\mathbf{S}\}$ is the strain tensor [m/m], $\{\mathbf{E}\}$ is the electric field [V/m = N/C], $[c^E]$ is the elasticity tensor at constant electric field [N/m²], $[e]$ is the dielectric permittivity tensor [N m/V m² = C/m²], and $[\varepsilon^S]$ is the dielectric tensor at constant mechanical strain (permittivity matrix) [N m/V² m]. The letters in brackets indicate the units of the variables (in the SI system of units) with N, m, V, and C denoting Newton, meter, Volts, and Coulomb, respectively.

$$\mathbf{T} = [T_{11} \quad T_{22} \quad T_{33} \quad T_{23} \quad T_{13} \quad T_{12}]^T$$

$$\mathbf{S} = [S_{11} \quad S_{22} \quad S_{33} \quad S_{23} \quad S_{13} \quad S_{12}]^T$$

$$\mathbf{D} = [D_1 \quad D_2 \quad D_3]^T; \quad \mathbf{E} = [E_1 \quad E_2 \quad E_3]^T$$

$$[e^S] = \begin{bmatrix} \varepsilon_1^S & 0 & 0 \\ 0 & \varepsilon_2^S & 0 \\ 0 & 0 & \varepsilon_3^S \end{bmatrix}; \quad [e] = \begin{bmatrix} 0 & 0 & e_{13} \\ 0 & 0 & e_{31} \\ 0 & 0 & e_{33} \\ 0 & e_{15} & 0 \\ 0 & e_{15} & 0 \end{bmatrix};$$

$$[c^E] = \begin{bmatrix} c_{11}^E & c_{12}^E & c_{13}^E & 0 & 0 & 0 \\ c_{12}^E & c_{22}^E & c_{23}^E & 0 & 0 & 0 \\ c_{13}^E & c_{23}^E & c_{33}^E & 0 & 0 & 0 \\ 0 & 0 & 0 & c_{44}^E & 0 & 0 \\ 0 & 0 & 0 & 0 & c_{55}^E & 0 \\ 0 & 0 & 0 & 0 & 0 & c_{66}^E \end{bmatrix}$$

If each element of the matrix of piezoelectric material constant, $[e]$, is designed by e_{ij} where i corresponds to the row and j corresponds to the column of the matrix, then e_{ij} corresponds to the stress developed in the j 'th direction due to an electric field applied in the i 'th direction. The piezoelectric strain constants d_{ij} , relating the

voltage applied in the i th direction to a strain developed in j th direction, are provided more often than the stress constants. However, the piezoelectric stress constants can be obtained from the strain constants since the constitutive equation can also be written as:

$$\mathbf{S} = [\mathbf{s}^E]\{\mathbf{T}\} + [\mathbf{d}]\{\mathbf{E}\} \quad (3)$$

$$\mathbf{D} = [\mathbf{d}]^T\{\mathbf{T}\} + [\boldsymbol{\varepsilon}^T]\{\mathbf{E}\} \quad (4)$$

where $\boldsymbol{\varepsilon}^T$ is the dielectric tensor at constant stress. The relative dielectric constant, K^T , is the ratio of the permittivity of the material, $\boldsymbol{\varepsilon}^T$, to the permittivity of the free space, ε_0 , ($\varepsilon_0 = 8.9 \times 10^{-12}$ F/m or A s/V m). Then,

$$[\mathbf{c}^E] = [\mathbf{s}^E]^{-1}; \quad [\mathbf{e}] = [\mathbf{c}^E][\mathbf{d}]$$

$$[\boldsymbol{\varepsilon}^S] = [\boldsymbol{\varepsilon}^T] - [\mathbf{d}]^T[\mathbf{c}^E][\mathbf{d}]; \quad K^T = \frac{\boldsymbol{\varepsilon}^T}{\varepsilon_0}$$

with

$$[\mathbf{d}] = \begin{bmatrix} 0 & 0 & d_{31} \\ 0 & 0 & d_{31} \\ 0 & 0 & d_{33} \\ 0 & d_{15} & 0 \\ 0 & 0 & d_{15} \end{bmatrix}$$

2 Finite Element Formulation of Electromechanical Systems

Finite Element Method (FEM) is widely used in engineering problems allowing to obtain approximate solutions to differential equations that describe the dynamics of a system. Other methods for obtaining electromechanical models may be used as the assumed modes method. However, the biggest advantage of FEM is to model structures with complex geometry. The basic idea is to divide the region into a finite number of elements and assume that these elements are interconnected by nodes (Bathe and Wilson 1976).

The pioneers in the development of dynamic models for smart structures are the work Allik and Hughes (1970). They use the mechanical stress induced by the piezoelectric to contribute with the total mechanical stress of the host structure. However, the first research work that has developed a rigorous system for the design of electromechanical coupled structure was presented by Hagood

et al. (1990), who applied the generalized Hamilton's principle, also known as variational principle applied to piezoelectric systems (Allik and Hughes 1970). The great contribution of Hagood et al. (1990) was formulated more clearly the electromechanical coupling.

The FEM is a method of transformation and approximation of an integral formulation, by an approximation linear algebraic formulation, where the coefficients are integral evaluations on the subarea of the area of resolution. The Rayleigh–Ritz formulation is used to derive the equations of motion of the electroelastic beam. The assumed displacement field shapes within the elastic body and electric potential field shapes will be combined through the piezoelectric properties to form a set of coupled electromechanical equations of motion. The generalized form of Hamilton's principle for a coupled electromechanical system is (Hagood et al. 1990)

$$\int_{t_1}^{t_2} [\delta(T - U + W_e - W_m) + \delta W] dt = 0 \quad (5)$$

where t_1 and t_2 are two arbitrary instants, T is the Kinetic energy, U is the potential energy, W_e is the work done by electrical energy, and W_m is the work done by magnetic energy, which is negligible for piezoceramic material.

$$T = T_S + T_P = \int_{V_S} \frac{1}{2} \rho_S \dot{\mathbf{u}}^T \dot{\mathbf{u}} dV + \int_{V_P} \frac{1}{2} \rho_P \dot{\mathbf{u}}^T \dot{\mathbf{u}} dV \quad (6)$$

$$U = U_S + U_P = \int_{V_S} \frac{1}{2} \mathbf{S}^T \mathbf{T} dV + \int_{V_P} \frac{1}{2} \mathbf{S}^T \mathbf{T} dV \quad (7)$$

$$W_e = \int_{V_P} \frac{1}{2} \mathbf{E}^T \mathbf{D} dV \quad (8)$$

where ρ is the mass density and the subscript s and p refer to the structure and piezoelectric material, respectively. The virtual work, δW , done by external forces and the prescribed surface charge, Q , is,

$$\delta W = \int_{V_S} \delta \mathbf{u}^T P_b dV + \int_{S_S} \delta \mathbf{u}^T P_S ds_S + \delta \mathbf{u}^T P_C - \int_{S_P} \delta \Phi Q ds_P \quad (9)$$

where P_b is the body force, P_S is the surface force, P_C is the concentrated load, and Q is the surface charge. To formulate the matrix of the electromechanical coupling using FEM, the displacement vector, u , and the electric potential, ϕ , must be expressed in terms of nodal value, i , via the interpolation function

$$\mathbf{u}(x) = [\mathbf{N}_u]\{\mathbf{u}_i\} \quad (10)$$

$$\Phi(x) = [\mathbf{N}_\phi]\{\phi_i\} \quad (11)$$

Substituting Eq. (10) into Eq. (6) yields

$$T = \iiint_{V_s} \frac{1}{2} \rho_s \dot{\mathbf{u}}^T \dot{\mathbf{u}} dV_s + \iiint_{V_p} \frac{1}{2} \rho_p \dot{\mathbf{u}}^T \dot{\mathbf{u}} dV_p \frac{1}{2} \quad (12)$$

The potential energy is the sum of the potential energy of the structure and of the piezoelectric material. The constitutive relation of the structure in matrix form is given by:

$$\mathbf{T}_s = \mathbf{G}_s \mathbf{S} \quad \text{and} \quad \mathbf{G}_s$$

$$= \frac{E_s}{(1+\nu)(1-2\nu)} \begin{bmatrix} 1-\nu & \nu & \nu & 0 & 0 & 0 \\ \nu & 1-\nu & \nu & 0 & 0 & 0 \\ \nu & \nu & 1-\nu & 0 & 0 & 0 \\ 0 & 0 & 0 & \frac{1-2\nu}{2} & 0 & 0 \\ 0 & 0 & 0 & 0 & \frac{1-2\nu}{2} & 0 \\ 0 & 0 & 0 & 0 & 0 & \frac{1-2\nu}{2} \end{bmatrix} \quad (13)$$

\mathbf{G}_s is the matrix containing the elastic coefficients of the material. E_s is the Young's modulus and ν is the Poisson ratio. The strain can be represented in matrix form by:

$$\mathbf{S} = \mathbf{L}_u \mathbf{u}; \quad \begin{Bmatrix} S_x \\ S_y \\ S_z \\ S_{xy} \\ S_{xz} \\ S_{yz} \end{Bmatrix} = \begin{bmatrix} \frac{\partial}{\partial x} & 0 & 0 \\ 0 & \frac{\partial}{\partial y} & 0 \\ 0 & 0 & \frac{\partial}{\partial z} \\ \frac{\partial}{\partial y} & \frac{\partial}{\partial x} & 0 \\ \frac{\partial}{\partial z} & 0 & \frac{\partial}{\partial x} \\ 0 & \frac{\partial}{\partial z} & \frac{\partial}{\partial y} \end{bmatrix} \begin{Bmatrix} u_x \\ u_y \\ u_z \end{Bmatrix}; \quad \mathbf{S} = \mathbf{L}_u \mathbf{N}_u \mathbf{u}_i \quad (14)$$

or

$$\mathbf{S} = \mathbf{B}_u \mathbf{u}_i \quad (15)$$

and

$$\mathbf{B}_u = \mathbf{L}_u \mathbf{N}_u \quad (16)$$

Substituting (15) in (13), one obtains the stress tensor in the host structure

$$\mathbf{T}_s = \mathbf{G}_s \mathbf{S} = \mathbf{G}_s \mathbf{B}_u \mathbf{u}_i \quad (17)$$

Solving (7) in the structural domain, V_s , yields

$$\mathbf{U}_s = \iiint_{V_s} \frac{1}{2} \mathbf{u}_i^T \mathbf{B}_u^T \mathbf{G}_s \mathbf{B}_u \mathbf{u}_i dV_s \quad (18)$$

Similarly from the mechanical strain, the electric field is described by

$$\mathbf{E} = \mathbf{L}_\phi \Phi \quad (19)$$

or

$$\mathbf{E} = \mathbf{L}_\phi \mathbf{N}_\phi \phi_i = \mathbf{B}_\phi \phi_i \quad (20)$$

where

$$\mathbf{B}_\phi = \mathbf{L}_\phi \mathbf{N}_\phi \quad (21)$$

and \mathbf{L}_ϕ is the matrix containing the differential operators. Substituting (1) into (7) and using (20), the potential energy in the piezoelectric domain, V_p , yields

$$\mathbf{U}_p = \iiint_{V_p} \frac{1}{2} \mathbf{u}_i^T \mathbf{B}_u^T \mathbf{c}^E \mathbf{B}_u \mathbf{u}_i dV_p - \iiint_{V_p} \frac{1}{2} \mathbf{u}_i^T \mathbf{B}_u^T \mathbf{e} \mathbf{B}_\phi \phi_i dV_p \quad (22)$$

The potential energy of the piezostructure is obtained by adding (18) and (22)

$$\mathbf{U} = \iiint_{V_s} \frac{1}{2} \mathbf{u}_i^T \mathbf{B}_u^T \mathbf{G}_s \mathbf{B}_u \mathbf{u}_i dV_s + \iiint_{V_p} \frac{1}{2} \mathbf{u}_i^T \mathbf{B}_u^T \mathbf{c}^E \mathbf{B}_u \mathbf{u}_i dV_p - \iiint_{V_p} \frac{1}{2} \mathbf{u}_i^T \mathbf{B}_u^T \mathbf{e} \mathbf{B}_\phi \phi_i dV_p \quad (23)$$

The work done by electrical energy is

$$\mathbf{W}_e = \iiint_{V_p} \frac{1}{2} \mathbf{E}^T \mathbf{D} dV_p \quad (24)$$

Using the constitutive relations yields

$$\mathbf{W}_e = \iiint_{V_p} \frac{1}{2} \phi_i^T \mathbf{B}_\phi^T \mathbf{e}^T \mathbf{B}_u \mathbf{u}_i dV_p + \iiint_{V_p} \frac{1}{2} \phi_i^T \mathbf{B}_\phi^T \epsilon^S \mathbf{B}_\phi \phi_i dV_p \quad (25)$$

At this point, the coupled electromechanical system equation can be derived from the generalized form of Hamilton's principle. Allowing arbitrary variations of $\{\mathbf{u}_i\}$ and $\{\Phi_i\}$, two equilibrium matrix equations, in generalized coordinates, are obtained.

$$([\mathbf{M}_S^e] + [\mathbf{M}_P^e])\{u_i\} + ([\mathbf{K}_S^e] + [\mathbf{K}_P^e])\{u_i\} - [\mathbf{K}_{u\phi}^e]\{\Phi_i\} = \{F^e\} \quad (26)$$

$$[\mathbf{K}_{\phi u}^e]\{u_i\} - [\mathbf{K}_{\phi\phi}^e]\{\Phi_i\} = \{Q^e\} \quad (27)$$

where \mathbf{M}_S^e and \mathbf{M}_P^e are the local matrix of mass for the host structure and the PZT, respectively:

$$\mathbf{M}_S^e = \iiint_{V_s} \rho_s \mathbf{N}_u^T \mathbf{N}_u dV_s \quad (28)$$

$$\mathbf{M}_P^e = \iiint_{V_p} \rho_p \mathbf{N}_u^T \mathbf{N}_u dV_p \quad (29)$$

and \mathbf{K}_S^e and \mathbf{K}_P^e are the local matrix of stiffness for the host structure and the PZT, respectively:

$$\mathbf{K}_S^e = \iiint_{V_s} \mathbf{B}_u^T \mathbf{G}_s \mathbf{B}_u dV_s \quad (30)$$

$$\mathbf{K}_P^e = \iiint_{V_p} \mathbf{B}_u^T \mathbf{c}^E \mathbf{B}_u dV_p \quad (31)$$

The electromechanical coupling matrix, $\mathbf{K}_{u\phi}^e$, and the piezoelectric capacitance matrix, $\mathbf{K}_{\phi\phi}^e$, are

$$\mathbf{K}_{u\phi}^e = \iiint_{V_p} \mathbf{B}_u^T \mathbf{e} \mathbf{B}_\phi dV_p \quad (32)$$

$$\mathbf{K}_{\phi\phi}^e = \iiint_{V_p} \mathbf{B}_\phi^T \boldsymbol{\epsilon}^S \mathbf{B}_\phi dV_p \quad (33)$$

with $[\mathbf{K}_{\phi u}^e] = [\mathbf{K}_{u\phi}^e]^T$. The force vectors are given by:

$$\{F^e\} = \int_{V_s} [N_u]^T \{P_B\} dV_s + \int_{S_s} [N_u]^T \{P_S\} dS_s + [N_u]^T \{P_c\} \quad (34)$$

$$\{Q^e\} = - \int_{S_p} [N_\phi]^T Q dS_p \quad (35)$$

For the entire structure, using the standard assembly technique for the FEM, we obtain the complete equation for a coupled electromechanical system as

$$\begin{bmatrix} \mathbf{M} & 0 \\ 0 & 0 \end{bmatrix} \begin{Bmatrix} \ddot{\mathbf{u}} \\ \ddot{\boldsymbol{\phi}} \end{Bmatrix} + \begin{bmatrix} \mathbf{K}_{uu} & \mathbf{K}_{u\phi} \\ \mathbf{K}_{\phi u} & \mathbf{K}_{\phi\phi} \end{bmatrix} \begin{Bmatrix} \mathbf{u} \\ \boldsymbol{\phi} \end{Bmatrix} = \begin{Bmatrix} \mathbf{F} \\ \mathbf{Q} \end{Bmatrix} \quad (36)$$

where the global matrices are defined by

$$\mathbf{M} = \sum_{i=1}^{ne} (\mathbf{M}_s^e)_i + \sum_{j=1}^{np} (\mathbf{M}_p^e)_j \quad (37)$$

$$\mathbf{K}_{uu} = \sum_{i=1}^{ne} (\mathbf{K}_s^e)_i + \sum_{j=1}^{np} (\mathbf{K}_p^e)_j \quad (38)$$

$$\mathbf{K}_{u\phi} = \mathbf{K}_{\phi u}^T = - \sum_{j=1}^{np} (\mathbf{K}_{u\phi}^e)_j \quad (39)$$

$$\mathbf{K}_{\phi\phi} = - \sum_{j=1}^{np} (\mathbf{K}_{\phi\phi}^e)_j \quad (40)$$

where ne is the number of structural elements and np is the number of piezoelectric patches in the structure. The symbol summation, in the above equations, means finite element assembling matrices. At this point, it is important to note that the

mass and stiffness matrices for a finite element and therefore for the complete structure are not positive definite.

The sensor equation is:

$$\mathbf{K}_{\phi u} \mathbf{u} + \mathbf{K}_{\phi\phi} \Phi_s = \mathbf{Q} \quad (41)$$

Making the electric charge Q to zero since there is no electric potential applied to the sensor, yields

$$\Phi_s = -\mathbf{K}_{\phi\phi}^{-1} \mathbf{K}_{\phi u} \mathbf{u} \quad (42)$$

To find the force generated in the actuator, one must consider the charge Q nonzero, then we can rewrite equation (41) as follows:

$$\mathbf{K}_{\phi u} \mathbf{u} + \mathbf{K}_{\phi\phi} \Phi_a = \mathbf{Q} \quad (43)$$

or

$$\Phi_a = \mathbf{K}_{\phi\phi}^{-1} (\mathbf{Q} - \mathbf{K}_{\phi u} \mathbf{u}) \quad (44)$$

Replacing the electric potential (44) in the global equation (36) yields

$$\mathbf{M}\ddot{\mathbf{u}} + \mathbf{K}\mathbf{u} = \mathbf{F} + \mathbf{F}_{el} \quad (45)$$

where

$$\mathbf{K} = \mathbf{K}_{uu} - \mathbf{K}_{u\phi} \mathbf{K}_{\phi\phi}^{-1} \mathbf{K}_{\phi u} \quad (46)$$

$$\mathbf{F}_{el} = -\mathbf{K}_{u\phi} \mathbf{K}_{\phi\phi}^{-1} \mathbf{Q} \quad (47)$$

where \mathbf{F}_{el} is the electric force generated in the actuator by applying an electrical charge.

The term $\mathbf{K}_{u\phi} \Phi$ can be divided in two parts dependent on the electric potential, one referring to the piezoelectric material used as sensor and the other for the piezoelectric material used as actuator.

$$\mathbf{K}_{u\phi} \Phi = \mathbf{K}_{u\phi} \Phi_s + \mathbf{K}_{u\phi} \Phi_a \quad (48)$$

Substituting in the motion equation (36)

$$\mathbf{M}\ddot{\mathbf{u}} + \mathbf{K}_{uu} \mathbf{u} + \mathbf{K}_{u\phi} \left(-\mathbf{K}_{\phi\phi}^{-1} \mathbf{K}_{\phi u} \mathbf{u} \right) = \mathbf{F} - \mathbf{K}_{u\phi} \Phi_a \quad (49)$$

or

$$\mathbf{M}\ddot{\mathbf{u}} + \mathbf{K}\mathbf{u} = \mathbf{F} - \mathbf{K}_{u\phi} \Phi_a \quad (50)$$

where

$$\mathbf{K} = \mathbf{K}_{uu} - \mathbf{K}_{u\phi} \mathbf{K}_{\phi\phi}^{-1} \mathbf{K}_{\phi u} \quad (51)$$

Every structure has some damping effect. Usually, this value is difficult to be defined precisely, but can be predicted. A practical approach is considering proportional damping, to the mass and stiffness.

$$\mathbf{D}_a = \alpha \mathbf{M} + \beta \mathbf{K} \quad (52)$$

The global equation of motion, considering damping matrix, is given by

$$\mathbf{M}\ddot{\mathbf{u}} + \mathbf{D}_a\dot{\mathbf{u}} + \mathbf{K}\mathbf{u} = \mathbf{F} - \mathbf{K}_{u\phi} \mathbf{K}_{\phi\phi}^{-1} \mathbf{Q} \quad (53)$$

where \mathbf{M} , \mathbf{D}_a , and \mathbf{K} are the global matrices of mass, damping, and stiffness, respectively.

3 Eigenvalue Problem for the Short Circuit Case

Natural frequencies and mode shapes can be obtained by reducing the assembled global matrices to a standard eigenvalue form. It can be done by suitable grounding the structure by specifying one or more nodal value of electrical potential. Then the new piezoelectric capacitance matrix, $\mathbf{K}_{\phi\phi}^*$ is non-singular and the eigenvalue problem, for the undamped homogeneous system, can be written as (Lopes Jr. et al. 2000)

$$([\mathbf{K}] - \omega^2 [\mathbf{M}]) \{\mathbf{u}\} = \{0\} \quad (54)$$

where

$$[\mathbf{M}] = [\mathbf{M}_{uu}] \quad (55)$$

$$[\mathbf{K}] = [\mathbf{K}_{uu}] - [\mathbf{K}_{u\phi}] [\mathbf{K}_{\phi\phi}^*]^{-1} [\mathbf{K}_{\phi u}] \quad (56)$$

and $[\circ]^{-1}$ indicates the inverse of the matrix.

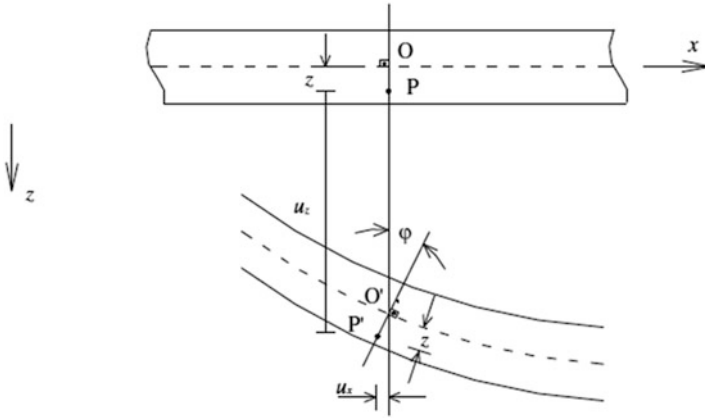


Fig. 1 Displacement of a point P at a distance z from the median line of the beam

4 Application: Clamped-Free Beam with Bonded PZT

The general equations from the previous section will be applied for the case of a clamped-free beam with a pair of bonded PZT (bimorph case). Different numbers and locations of PZTs can be considered.

The poling of the piezoelectric is in the z -direction. Figure 1 shows an Euler-Bernoulli beam, where the displacement of a point on a normal plane of the beam at a distance “ z ” from the median line in the direction “ x ” is

$$u_x = -z\theta = -z \frac{\partial u_z}{\partial x} \tag{57}$$

The state of plane strain is given by

$$S_x = \frac{\partial u_x}{\partial x} = -z \frac{\partial^2 u_z}{\partial x^2} \tag{58}$$

Equation (14) can be rewritten as

$$\mathbf{S} = \mathbf{L}_u u_z \tag{59}$$

where

$$\mathbf{L}_u = \left[-z \frac{\partial^2}{\partial x^2} \right] \tag{60}$$

The stress is also rewritten as

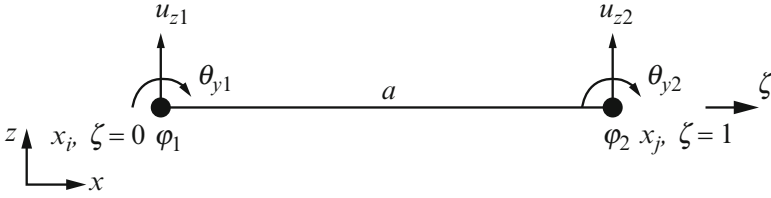


Fig. 2 Structural element with electromechanical coupling

$$\mathbf{T}_x = \mathbf{E}_s \mathbf{S}_x \quad (61)$$

Considering that the piezoelectric material is being modeled as Euler–Bernoulli beam element, their constitutive relations can be summarized as:

$$D_3 = e_{31} S_{11} + \epsilon_{33}^S E_3 \quad \text{sensor equation} \quad (62)$$

$$T_{11} = c_{11}^E S_{11} - e_{31} E_3 \quad \text{actuator equation} \quad (63)$$

The goal is to obtain the interpolation function on the basis of generalized coordinates for the degrees of freedom of displacement and electrical potential. With these functions, one can determine the elementary matrices of electromechanical coupled system. Initially, it is considered the electromechanical coupling between the host structure and the piezo element, as shown in Fig. 2.

The element is composed by two nodes, with two structural degrees of freedom per node, translation denoted by “ u_{zi} ” in direction “ z ” and rotation in the plane “ yz ” denoted by “ θ_{yi} ,” and one electric potential degree of freedom per node “ ϕ_i .” Considering x_i the point localized in the node i and ξ the generalized coordinate in function of x , as

$$\xi = \frac{x}{a} \quad (64)$$

One can rewrite the displacement vector of the i th element as

$$\mathbf{u}_i = [u_{z1} \quad \theta_{y1} \quad u_{z2} \quad \theta_{y2}]^T \quad (65)$$

and the electric potential is

$$\Phi_i = [\phi_1 \quad \phi_2]^T \quad (66)$$

or

$$\mathbf{u}(\xi) = \mathbf{N}_{u1}(\xi)u_{z1} + \mathbf{N}_{u2}(\xi)\theta_{y1} + \mathbf{N}_{u3}(\xi)u_{z2} + \mathbf{N}_{u4}(\xi)\theta_{y2} \quad (67)$$

and

$$\Phi(\xi) = \mathbf{N}_{\phi_1}(\xi)\phi_1 + \mathbf{N}_{\phi_2}(\xi)\phi_2 \quad (68)$$

Initially, one can find the interpolation functions of the mechanical displacements. For this, it is observed that the element is analyzed in only one dimension (ξ) and has four degrees of freedom. Therefore, one obtains the following interpolating function for displacement in the z -direction.

$$u_z(\xi) = \alpha_1 + \alpha_2\xi + \alpha_3\xi^2 + \alpha_4\xi^3 \quad (69)$$

or

$$u = \mathbf{P}\alpha \quad (70)$$

where

$$\mathbf{P} = [1 \quad \xi \quad \xi^2 \quad \xi^3] \quad (71)$$

$$\alpha = [\alpha_1 \quad \alpha_2 \quad \alpha_3 \quad \alpha_4]^T \quad (72)$$

Considering small angles

$$\theta_\eta(\xi) = -\frac{\partial u_z(\xi)}{\partial \xi} = -\alpha_2 - 2\alpha_3\xi - 3\alpha_4\xi^2 \quad (73)$$

The values of the generalized coordinates for each element node can be obtained in matrix form as Eq. (74). The columns of the inverse matrix $\mathbf{P}n$ contain the interpolation functions. The values of the generalized coordinates for node 1 ($\xi = 0$) and node 2 ($\xi = 1$) yield

$$\begin{Bmatrix} u_{z1} \\ \theta_{\eta1} \\ u_{z2} \\ \theta_{\eta2} \end{Bmatrix} = \begin{bmatrix} 1 & 0 & 0 & 0 \\ 0 & -1 & 0 & 0 \\ 1 & 1 & 1 & 1 \\ 0 & -1 & -2 & -3 \end{bmatrix} \begin{Bmatrix} \alpha_1 \\ \alpha_2 \\ \alpha_3 \\ \alpha_4 \end{Bmatrix} \quad (74)$$

or

$$\delta = \mathbf{P}n \alpha \quad (75)$$

and,

$$\alpha = [\mathbf{P}n]^{-1} \delta \quad (76)$$

One can also write

$$\theta_y = -\frac{\partial u_z}{\partial x} = -\left(\frac{\partial u_z}{\partial \xi} \frac{\partial \xi}{\partial x}\right) = \frac{1}{a}\theta_\eta \rightarrow \theta_\eta = a\theta_y, \quad (77)$$

where $\frac{\partial u_z}{\partial \xi} = -\theta_\eta$ and $\frac{\partial \xi}{\partial x} = \frac{1}{a}$, then

$$\begin{Bmatrix} u_{z1} \\ \theta_{\eta1} \\ u_{z2} \\ \theta_{\eta2} \end{Bmatrix} = \begin{bmatrix} 1 & 0 & 0 & 0 \\ 0 & a & 0 & 0 \\ 0 & 0 & 1 & 0 \\ 0 & 0 & 0 & a \end{bmatrix} \begin{Bmatrix} u_{z1} \\ \theta_{y1} \\ u_{z2} \\ \theta_{y2} \end{Bmatrix} \quad (78)$$

or

$$\delta = \mathbf{Z}\mathbf{u}_i \quad (79)$$

Substituting equation (79) into (76) and after that into (70) yields

$$\mathbf{u} = \mathbf{P}[\mathbf{P}n]^{-1}\mathbf{Z}\mathbf{u}_i \quad (80)$$

One knows that $\mathbf{u} = \mathbf{N}_u\mathbf{u}_i$, then

$$\mathbf{N}_u = \mathbf{P}[\mathbf{P}n]^{-1}\mathbf{Z} \quad (81)$$

and

$$\mathbf{N}_u = \begin{bmatrix} 1 - 3\xi^2 + 2\xi^3 \\ -a\xi + 2a\xi^2 - a\xi^3 \\ 3\xi^2 - 2\xi^3 \\ a\xi^2 - a\xi^3 \end{bmatrix}^T \quad (82)$$

In order to find the matrix \mathbf{B}_u , one considers

$$\mathbf{L}_u = \begin{bmatrix} z \\ -\frac{z}{a^2} \frac{\partial^2}{\partial \xi^2} \end{bmatrix} \quad (83)$$

then

$$\mathbf{B}_u^T = -\frac{z}{a^2} \frac{\partial^2 \mathbf{N}_u^T}{\partial \xi^2} \quad (84)$$

and

$$\mathbf{B}_u = -\frac{z}{a^2} \begin{bmatrix} -6 + 12\xi \\ 4a - 6\xi \\ 6 - 12\xi \\ 2a - 6a\xi \end{bmatrix}^T \quad (85)$$

Similarly, one can find the interpolation functions of the electric potential. The element has one dimension (ξ) and two electric degrees of freedom, thus one obtains the following polynomial basis to obtain the interpolation functions.

$$\mathbf{P} = [1 \quad \xi] \quad (86)$$

The values of the generalized coordinates for each element node, $\mathbf{P}n$, are given in equation (87). The columns of the inverse matrix $\mathbf{P}n$ contain the indices of the interpolation functions. The values of the generalized coordinate for the node 1 ($\xi = 0$) and node 2 ($\xi = 1$) yield

$$\mathbf{P}n = \begin{bmatrix} 1 & 0 \\ 1 & 1 \end{bmatrix} \quad (87)$$

and

$$[\mathbf{P}n]^{-1} = \begin{bmatrix} 1 & 0 \\ -1 & 1 \end{bmatrix} \quad (88)$$

The interpolation functions are given by multiplying equations (86) and (88)

$$\mathbf{N}_\phi = \mathbf{P}[\mathbf{P}n]^{-1} = \begin{bmatrix} 1 - \xi \\ \xi \end{bmatrix}^T \quad (89)$$

Whereas the electric field can be written directly proportional to the difference of the electric potential and inversely proportional to the distance of these potentials, then

$$\Phi = \mathbf{E}\delta \rightarrow \mathbf{E} = \frac{d\Phi}{d\delta} \quad (90)$$

where δ is the distance between the potentials, so $\phi = \phi(x) \rightarrow \delta = \delta(x)$, then

$$\mathbf{E} = \frac{\partial \Phi}{\partial x} \quad (91)$$

Rewritten in the matrix form

$$\mathbf{E}(x) = \left[\frac{\partial}{\partial x} \right] \Phi(x) \quad (92)$$

Comparing (92) with (19)

$$\mathbf{L}_\phi = \left[\frac{\partial}{\partial x} \right] \quad (93)$$

Considering the generalized coordinate $\xi = \frac{x}{a} \rightarrow \partial x = a \partial \xi$, one can rewrite (93) as

$$\mathbf{L}_\phi = \left[\frac{1}{a} \frac{\partial}{\partial \xi} \right] \quad (94)$$

then,

$$\mathbf{B}_\phi^T = \left[\frac{1}{a} \frac{\partial \mathbf{N}_\phi^T}{\partial \xi} \right] \quad (95)$$

$$\mathbf{B}_\phi = \frac{1}{a} \begin{bmatrix} -1 \\ 1 \end{bmatrix}^T \quad (96)$$

The interpolation functions of the mechanical displacement and electric potential can now be used in equations from (28) to (33) in order to find the electromechanical coupled elementary matrices. The differential volume of the host structure element is

$$dV_S = dz \, dx \, dy \quad (97)$$

Considering the generalized coordinates $\eta = \frac{y}{b}$, one can write the differential volume as

$$dV_s = dz \, ab \, d\xi \, d\eta \quad (98)$$

Substituting (98), equations (28) and (29) are rewritten as:

$$\mathbf{M}_s^e = \int_0^1 \int_0^1 \int_{-t_s/2}^{t_s/2} dz \rho_s \, ab \, \mathbf{N}_u^T \mathbf{N}_u \, d\xi \, d\eta \quad (99)$$

where a is the length, b the width, and t_s the thickness of the element. Integrating in z - and η -directions yields

$$\mathbf{M}_s^e = \rho_s t_s ab \int_0^1 \mathbf{N}_u^T \mathbf{N}_u d\xi \quad (100)$$

similarly,

$$\mathbf{M}_p^e = \rho_p t_p ab \int_0^1 \mathbf{N}_u^T \mathbf{N}_u d\xi \quad (101)$$

The local matrix of stiffness for the host structure and the PZT, Eqs. (30) and (31), are obtained by substituting the differential volume

$$\mathbf{K}_s^e = \frac{E_s t_s^3 b}{12a^3} \int_0^1 \mathbf{B}_u^T \mathbf{B}_u d\xi \quad (102)$$

$$\mathbf{K}_p^e = \frac{c_{11}^E t_p^3 b}{12a^3} \int_0^1 \mathbf{B}_u^T \mathbf{B}_u d\xi \quad (103)$$

The electromechanical coupling matrix and the piezoelectric capacitance matrix, Eqs. (32) and (33), are

$$\mathbf{K}_{u\phi}^e = \frac{e_{31} t_p^2 ab}{2} \int_0^1 \mathbf{B}_u^T \mathbf{B}_\phi d\xi \quad (104)$$

and

$$\mathbf{K}_{\phi\phi}^e = \varepsilon_{33}^S t_p ab \int_0^1 \mathbf{B}_\phi^T \mathbf{B}_\phi d\xi \quad (105)$$

where $[\mathbf{K}_{u\phi}^e]^T = \mathbf{K}_{\phi u}^e$

The general equations from the previous sections are applied for the case of an aluminum clamped-free beam, as shown in Fig. 3. The beam is modeled with 20 elements with 2 mechanical and 1 electrical DOF per node. Different numbers and locations of PZTs can be considered. The poling of the piezoelectric patches is in the z -direction. The geometrics and physics features of the beam are Young

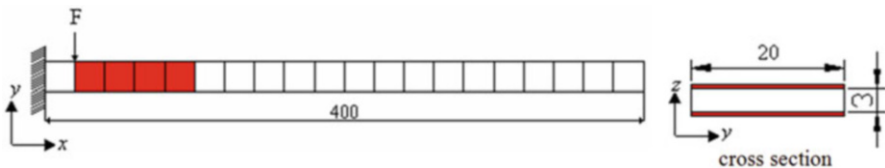
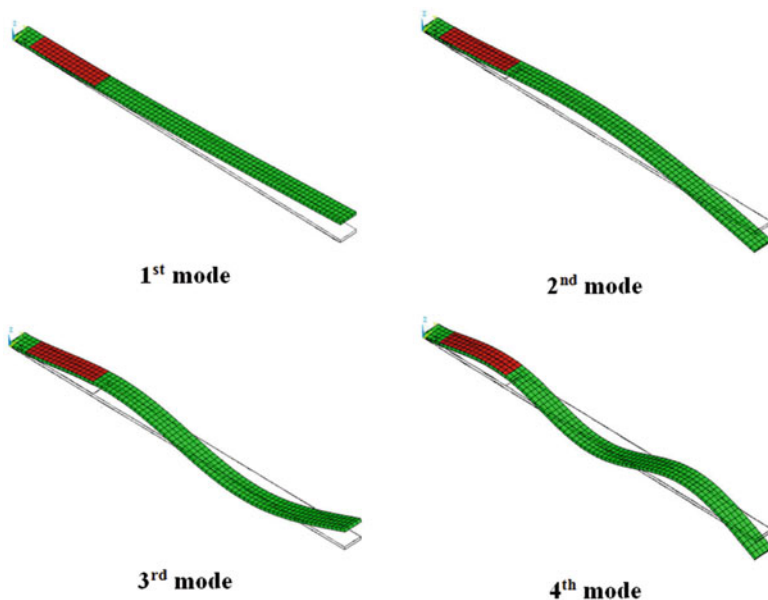


Fig. 3 Schematic drawing of the beam with PZT patches

Table 1 Six first natural frequencies for the aluminum clamped-free beam

Modes	Analytics f_n (Hz)	SMARTSYS f_n (Hz)	Difference (%)
1	15.47	15.39	0.52
2	96.98	96.47	0.52
3	271.56	270.13	0.53
4	532.14	529.36	0.52
5	879.67	875.17	0.51
6	1314.07	1307.62	0.49

**Fig. 4** Four first vibration modes for the electromechanical-coupled beam

modulus 70 GPa; Poisson coefficient 0.31; mass density 2710 kg/m³; length 400 mm; width 20 mm; and thickness 3 mm.

A finite element code was developed using the previous equations, called SmartSys. Table 1 shows the six first natural frequencies obtained with the SmartSys code and analytically (INMAN 2013) for the case without PZT patches.

The incorporation of mass, stiffness, capacitance, and coupling matrix of the piezoelectric patch has a significant influence on the dynamic properties of the system. The disregarding of these terms may cause errors in many applications. In order to verify the influence of the electromechanical coupling, four pairs of PZT patches were bonded on both sides of the beam, as shown in Fig. 3. The beam is discretized with 20 beam elements, 21 nodes with two mechanical and 1 electrical DOF per node. The geometrics and physics features of the PZT patches are Young modulus 62 GPa; mass density 7500 kg/m³; length of each PZT patch 20 mm; width 20 mm; thickness 3 mm; strain constant d_{31} 320e-12; dielectric tensor at constant

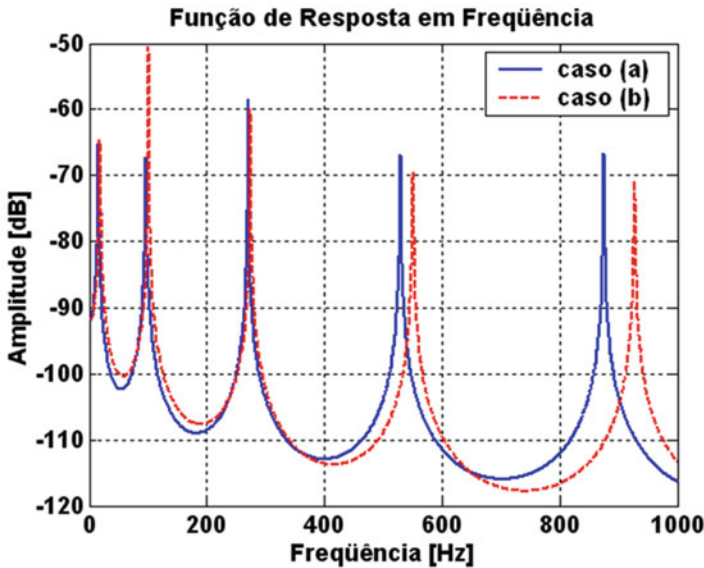


Fig. 5 FRF of the beam; (a) without PZTs and, (b) four pairs of PZT patches as shown in Fig. 3

Table 2 Five first natural frequencies for the beam without PZT patch and for the beam with four pairs of PZT patches

Modes	Case (a)	Case (b)	
	f_n (Hz)	f_n (Hz)	Difference (%)
1	15.39	18.45	19.88
2	96.47	101.02	4.72
3	270.13	274.18	1.50
4	529.36	550.53	4.00
5	875.17	927.39	5.97

mechanical strain ϵ_{33}^S $3.363e-8$ F/m; elasticity constant c_{11} $92.3e9$ N/m²; and dielectric permittivity ϵ_{31} 16.27 C/m²

Figure 4 shows the four first vibration modes for the electromechanical-coupled beam.

Figure 5 shows the Frequency Response Functions, FRF, for an impulsive excitation ($F = 1$ N) in node 2 and response in the free end of the beam, node 21. There were considered two cases: (a) beam without PZT patch, and (b) beam with four pairs of PZT patches as shown in Fig. 3.

The five first natural frequencies are shown in Table 2 for both cases, beam without PZT patch and beam with four pairs of PZT patches

The analytical model of a beam with piezoelectric material coupling the electrical and mechanical coordinates was derived using a generalized Hamilton's principle. It was found that the incorporation of mass, stiffness, capacitance, and coupling matrix of the piezoelectric patch has a significant influence on the dynamic properties of the system. This model of smart structure contains additional

degrees of freedom at each node, the electrical potential, and it makes the global mass and stiffness matrices non-positive definite, which require special numerical preparation to solve the eigenvalue problem.

References

- H. Allik, T.J.R. Hughes, Finite method for piezoelectric vibration. *Int. J. Numer. Methods Eng.* **2**, 151–157 (1970)
- K.J. Bathe, E.L. Wilson, *Numerical Methods in Finite Element Analysis* (Prentice Hall, New Jersey, 1976)
- N.W. Hagood, W.H. Chung, A. von Flotow, Modeling of piezoelectric actuator dynamics for active structural control. *J. Intell. Mater. Syst. Struct.* **1**, 4–25 (1990)
- D.J. Inman, *Engineering Vibration*, 4th edn. (Prentice Hall, Upper Saddle River, 2013)
- D. Leo, *Engineering Analysis of Smart Material Systems* (Wiley, New York, 2007)
- V. Lopes Jr, J.A. Pereira, D.J. Inman, Structural FRF acquisition via electric impedance measurement applied to damage location, in *IMAC*, 2000

Shape Memory Alloys

Marcelo A. Savi, Alberto Paiva, Carlos J. de Araujo, and Aline S. de Paula

Abstract This chapter presents a general overview of shape memory alloys (SMAs). A discussion about thermomechanical behaviors is carried out establishing the most important characteristics of these alloys. Applications of SMAs in different areas of human knowledge are explained. Thermomechanical characterization is discussed considering different experimental procedures. Afterward, a brief review of constitutive models is presented. A model with assumed transformation kinetics is explored showing some numerical simulations.

Keywords Shape memory alloys • Pseudoelasticity • Shape memory effect • Characterization • Constitutive models • Numerical simulations

1 Introduction

Shape Memory Alloys (SMAs) belong to smart materials class, presenting thermomechanical coupling associated with solid phase transformations. SMA undergoes a reversible phase transformation in the solid state, assuming different crystalline structures at different temperatures. This phase transformation is similar

M.A. Savi, Ph.D. (✉)

COPPE—Department of Mechanical Engineering, Center for Nonlinear Mechanics, Universidade Federal do Rio de Janeiro, Rio de Janeiro, RJ 21.941.972, Brazil
e-mail: savi@mecanica.ufrj.br

A. Paiva

Department of Mechanical Engineering, Universidade Federal Fluminense, Escola de Engenharia de Volta Redonda, Volta Redonda, RJ 27.255.250, Brazil
e-mail: paiva@puvr.uff.br

C.J. de Araujo

Department of Mechanical Engineering, Universidade Federal de Campina Grande, Campina Grande, PB 58.109.970, Brazil
e-mail: carlos.araujo@ufcg.edu.br

A.S. de Paula

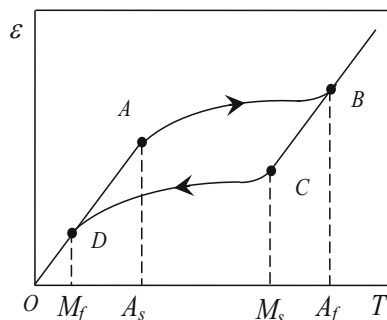
Department of Mechanical Engineering, Universidade de Brasília, Brasília, DF 70.910.900, Brazil
e-mail: alinedepaula@unb.br

to that observed in the carbon steels, also being called the martensitic transformation. The main difference is that SMA transformation is reversible, with thermoelastic characteristics. Besides, phase transformation can be induced either by temperature or by stress. The unique characteristics of SMAs motivate several applications in different areas of the human knowledge, such as robotics, aerospace, biomedical, shape, and vibration control (Lagoudas 2008; Machado and Savi 2002, 2003; Paiva and Savi 2006).

The main phenomena responsible for the cited characteristics are the typical SMAs thermomechanical behaviors: pseudoelasticity or superelasticity, shape memory effect (SME) (one-way and two-way), and phase transformation due to temperature variation. In order to introduce these behaviors, it is worthwhile to define some characteristic temperatures of SMAs. Essentially, two different phases are possible: austenite and martensite. Martensitic phase has several variants while austenite has only one. Considering a stress-free state, A_s and A_f are the starting and finishing temperatures for austenite formation, respectively, while M_s and M_f are the starting and finishing temperatures for martensite formation, respectively. Therefore, if a stress-free sample is subjected to temperature variations, phase transformations occur defined by these temperatures. Figure 1 presents a typical curve in a strain–temperature space ($\epsilon \times T$). For low temperatures, below M_f , the sample is at martensitic state, actually, twinned martensite, composed by several variants. By increasing the temperature, martensite \Rightarrow austenite phase transformation begins to take place at A_s , point A, finishing at A_f , point B. By decreasing the temperature, the reverse transformation takes place, starting at M_s , point C, and finishing at M_f , point D. Since phase transformation temperatures for each phase have different values, the sample presents a dissipative hysteretic behavior.

Pseudoelasticity or superelasticity happens whenever an SMA sample is in a temperature above A_f , which is considered a high temperature. In this situation, under a constant temperature, Fig. 2a shows the typical stress–strain curve (σ – ϵ), expressing the macroscopic behavior of SMAs. A mechanical loading causes an elastic response until a critical value is reached, point A, when the martensitic transformation (austenite \Rightarrow martensite) arises, finishing at point B. At this point, the crystal structure of the sample is totally composed of detwinned (single variant) martensite. For higher stress values, SMA presents a linear elastic response. During unloading process, the sample presents an elastic recovery ($B \Rightarrow C$). From

Fig. 1 Phase transformation due to temperature variation



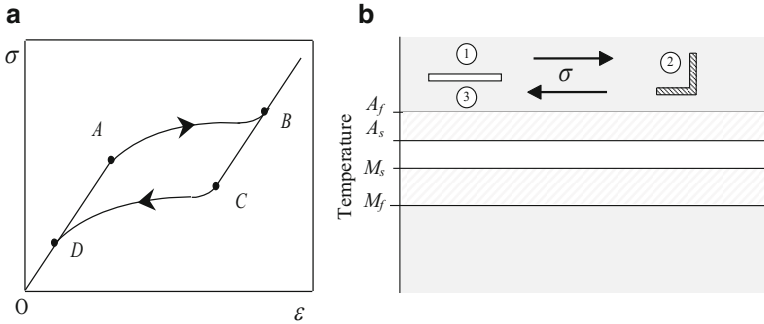


Fig. 2 Pseudoelasticity

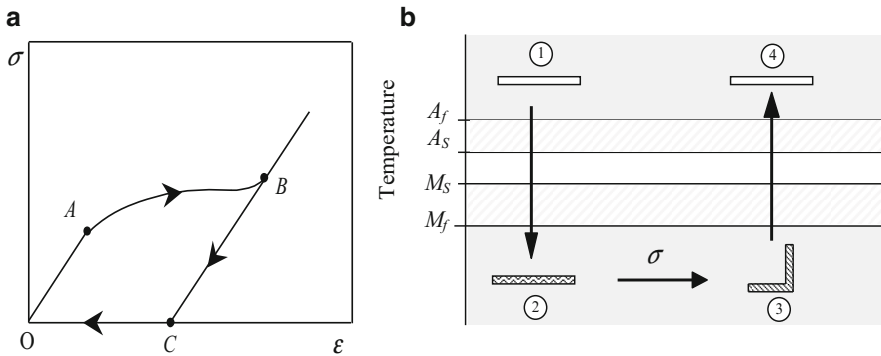


Fig. 3 Shape memory effect

point C to D, one can note the reverse martensitic transformation (martensite \Rightarrow austenite). After that, the sample presents an elastic behavior during discharge. When the loading–unloading process is finished, SMA has no residual strain. However, since the path of the forward martensitic transformation does not coincide with the reverse transformation path, there is a hysteresis loop associated with energy dissipation. Another way to observe pseudoelastic effect is pointed out in Fig. 2b. At first, considering a temperature above A_f , there is only one phase: austenite ①. Under a constant temperature, a mechanical loading is applied promoting the appearance of the detwinned martensite, ②. During unloading process, reverse transformation takes place (detwinned martensite \Rightarrow austenite) and when load vanishes, ③, the sample presents no residual strain.

The SME happens at temperatures below A_s . The typical macroscopic behavior of SMAs during SME can be observed in the stress–strain curve (σ - ϵ) presented in Fig. 3a, for $T < M_f$. When the sample is subjected to a mechanical loading, the stress reaches a critical value, point A, starting the reorientation process from twinned martensite to the detwinned martensite, ending at point B. When the mechanical loading–unloading process is finished, SMA sample presents a residual strain (point C). This residual strain can be recovered through a sample’s heating, which induces

the reverse phase transformation (detwinned martensite \Rightarrow austenite). This is the SME, also known as one-way SME. This phenomenon can be understood from a motion of the hysteresis loop shown on the stress–strain curve of Fig. 2a. Since the temperature goes down, the hysteresis loop moves down as well. Figure 3b presents an alternative way to observe SME. At first, the SMA sample is at a temperature above A_f , ①. At this temperature, the sample has only the austenitic phase. When the temperature of SMA sample goes down and crosses the line related to M_s , the phase transformation begins to take place and the twinned martensite replaces the austenite. This transformation is concluded when the sample temperature is below M_f , ②. Under a constant temperature, a mechanical loading is applied (② \rightarrow ③), promoting the appearance of detwinned martensite. When this load vanishes, the sample presents a residual strain, ③. The former shape of the sample can be recovered through a heating process (③ \rightarrow ④), which causes the reverse martensitic transformation (detwinned martensite \Rightarrow austenite).

The two-way SME is obtained after a training process that makes the sample has a shape in the austenitic state and another in the martensitic state. The change of temperature produces a change in the sample shape without any mechanical loading. Typically, there are two training procedures (Zhang et al. 1991): SME cycling (*cycles of SME*) and the training through the appearance of the detwinned martensite, the stress-induced martensite training, or *SIM training*. Both of them induce considerable plastic strains.

This chapter presents a general overview of SMAs. Initially, applications are discussed, showing the great potential of these alloys in distinct areas. The characterization of SMAs is then discussed, presenting some basic procedures to experimentally characterize the thermomechanical behavior of these alloys. Finally, the constitutive modeling is discussed. Specifically, the model proposed by Brinson (1993) is presented together with some numerical results. It is important to mention that constitutive modeling and thermomechanical characterization are essential tools for the design of SMA devices.

2 Applications

The remarkable properties of SMAs are attracting significant technological interest in several fields of sciences and engineering, from biomedical to aerospace applications.

Biomedical applications with SMAs have become successful due to the characteristic of noninvasive devices and also due to its excellent biocompatibility. SMAs are usually used in surgical instruments, cardiovascular mechanisms, orthopedic and orthodontic appliances, among other applications. Self-erectable structures are typical applications of SMA devices and biomedical devices also exploit this aspect in different ways. Simon filter has as main function to filter blood clots that exist in the bloodstream (Duerig et al. 1990). Self-expandable stents (Ahlhelm et al. 2009) have the main function of supporting any tubular passage as, for example, blood vessels.

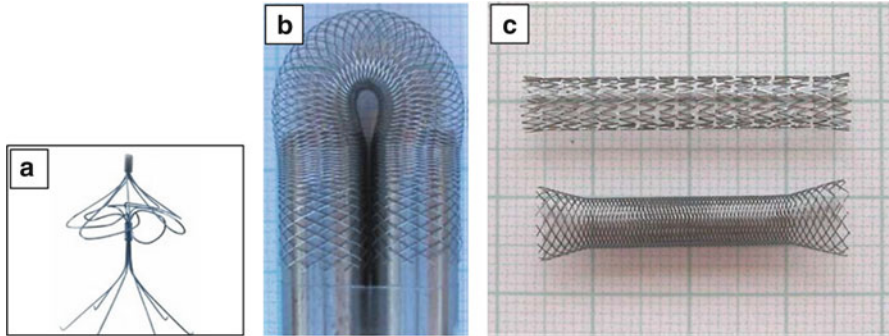


Fig. 4 Medical components manufactured with SMA. (a) Nitinol Simon filter (taken from <http://www.whichmedicaldevice.com>); (b, c) shape memory self-expanding stents (Ahlhelm et al. 2009)



Fig. 5 SMA multi-actuated hydrofoil prototype (Rediniotis et al. 2002)

Both applications can be observed in Fig. 4. Duerig et al. (1999), Reynaerls et al. (1997) and Machado and Savi (2002, 2003) discussed different biomedical applications that include orthopedic and orthodontics ones.

Besides medical applications, SMAs are widely exploited in engineering fields. In this regard, references related to applications of SMAs in naval industry, vibration control, robotics, and aerospace engineering are discussed in this text. Coupling and joints of pipes and the use of SMAs as sensor and/or actuators are also treated. It is important to mention that a limiting factor to the design of new applications is SMA's slow rate of response—their main drawback.

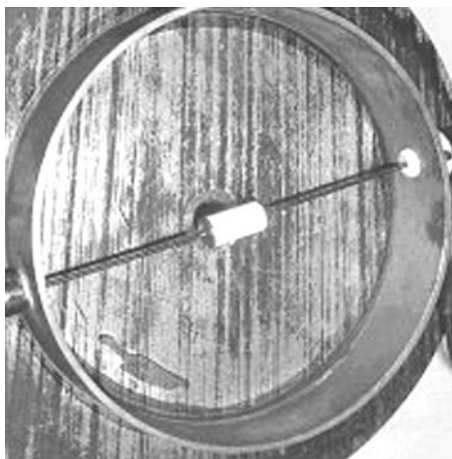
The use of SMAs to promote movement to intelligent structures has a great potential. Naval industry is one of the areas that is investing in the development of this kind of system. As an illustrative example, one can cite an SMA multi-actuated flexible hydrofoil prototype, which simulates fishtail swimming dynamics, through hydrodynamic propulsion study (Rediniotis et al. 2002). The SMA wires are externally actuated by electrical heating source. Figure 5 presents a picture of the

hydrofoil prototype in a water tunnel. A hydrostatic robot is another application of SMAs in the naval industry, reported by Vaidyanathan et al. (2000). The use of SMA springs in the robot provides a waving motion that makes it able to overlap obstacles under high depth pressures.

Vibration control is an important field within mechanical engineering. SMAs are employed for the passive control of structures due to their high dissipation capacity, which is related to their hysteretic behavior. The great advantage concerning this type of behavior is that the higher the vibration amplitude, the higher the dissipation is (Savi et al. 2011; van Humbeeck 1999). An alternative for vibration control is the use of SMA wires embedded in composite matrices that modify the mechanical properties of slender structures (Birman 1997; Rogers 1995). Sitnikova et al. (2009), Savi et al. (2011), McCormick et al. (2006), Tuissi et al. (2009) and Oberaigner et al. (2002) also deal with vibration reduction using SMA elements.

A classical passive control device is known as *Tuned Vibration Absorber*—TVA, which consists of a secondary oscillator connected to a primary system. By adjusting the TVA's natural frequency to the primary system excitation frequency, it is possible to attenuate primary system vibrations. Williams et al. (2002, 2005) and Tiseo et al. (2010) present an adaptive TVA (ATVA) device using SMA elements. This type of control is suitable for systems where frequencies vary or are unknown. SMA ATVAs are able to adjust their stiffness according to SMA temperature (Savi et al. 2011; Aguiar et al. 2013). This feature allows SMA ATVAs to attenuate primary system vibrations within a given frequency range. The ATVA design proposed by Tiseo et al. (2010) is presented in Fig. 6. The adaptive absorber consists of a pre-stressed Ni–Ti wire, clamped at the edges, with a concentrated mass placed in its geometric center. It is heated by an electrical current (Joule effect), so that the internal stress field is forced to change (strain is inhibited), attaining a large controlled eigenfrequency shift. A sustaining frame that hosts the wire completes the assembling design.

Fig. 6 SMA adaptive tuned vibration absorber (Tiseo et al. 2010)



Robotics is another area where SMA applications find a great potential. Basically, it can be used as an actuator, trying to mimic the muscles actuation. Many efforts have been made to reproduce the natural movement of the muscles of animals in robots using characteristics of locomotion in rugged environments or difficult to access, such as at the bottom of rivers and oceans (Safak et al. 2002). Choi et al. (2001) presented a flexible claw that consists of two flexible beams connected to a gripper base. Each beam is connected to two springs. An SMA spring is used as an actuator, while a conventional spring is responsible for the beam position restoring. There is also a coil spring linking the two beams' free edges. Strain gages are responsible for monitoring the beams' deflection. The SMA springs should be externally actuated.

In many situations, humans need to rely on the aid of autonomous systems to perform risky activities and thus many researches have been conducted to develop robots that combine mobility and accuracy in operations such as, for example, disabling bombs and landmines. Dilibal and Dilibal (2002) present a prototype of a robot hand, ITU Hand, composed of shape memory material in the region of the fingers coupled to a flexible tube through which passes a fluid. The actuator uses the reversible SME and the finger movement is controlled by the temperature of the fluid that heats or cools the SMA. The major advantages of this system compared to pneumatic and hydraulic systems are greater control of the force applied to the hand reducing the risks in their use and a decrease in the total weight of the equipment making it more versatile.

Figure 7 shows a robot composed of eight legs, with three degrees of freedom per leg and a set of SMA actuators that are activated by the passage of electric current and make use of the SME to promote the rotational motion of the joints of the robot (Safak et al. 2002).

The use of SMAs in aerospace applications covers fixed-wing aircraft, spacecraft, and solar panels, among others. Researches are conducted to implement active materials in the optimization of lifting performance of rigid bodies. This represents an important step in the development and application of smart materials and active control technologies.

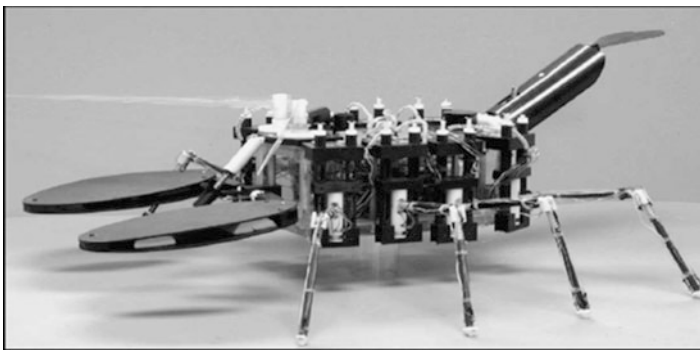


Fig. 7 Lobster Robot (Safak et al. 2002)

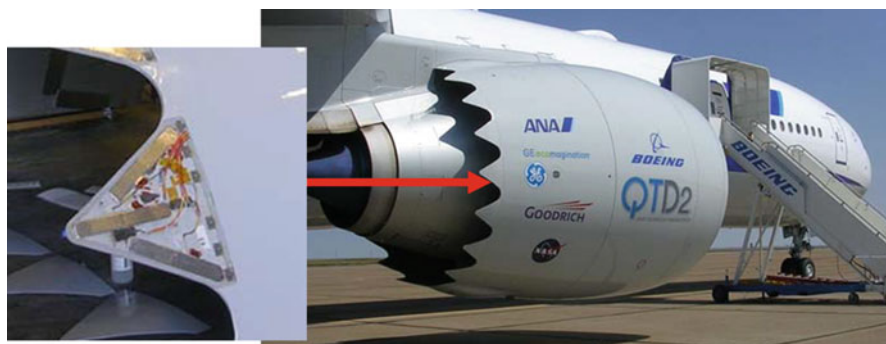


Fig. 8 Installation of chevrons in the output of the turbines (Hartl and Lagoudas 2007)

One of the most popular programs was the “Smart Wing Program” conducted by a research group, with support from NASA, AFOSR, and AFRC. The goal was the development of smart technologies to improve the aerodynamic performance of military aircraft. The work team developed an adaptive wing with integrated actuation mechanisms to adjust the standard surface of the wing and provide an aerodynamic shape for a great variety of flight regimes (Kudva et al. 1999). The model of smart wing incorporated hinged flap and aileron format using SMA cables. With these improvements, a control surface deflection by 10° was obtained. With the use of torque tubes, the wing structure enabled a twist of 5° improving the performance of 8–12 % compared to conventional wing surface (Hartl and Lagoudas 2007).

The worldwide increase in the flow of aircraft and the proximity of airports with major urban centers has created a new challenge to be solved by engineering: the reduction of airport noise. The permissible level of noise during takeoff and landing has been increasingly controlled in all countries. SMAs provide an alternative solution to reduce this noise. Chevrons are installed with SMA elements in the outputs of the turbines to mix the flow of exhaust gases and reduce noise generated (Fig. 8). SMA bars bend chevrons on the flow of combustion gases during flight at low altitude or at low speeds, increasing the mixture of gases and thus reducing the noise generated. In the case of aircraft being under high speed or high altitude, SMA bars are cooled and returned to the martensitic phase. This phase transformation changes the shape of chevrons, increasing the performance of the turbine. The phase transformation is given by the electrical system that, passing an electric current in SMAs, promotes the phase transformation induced by temperature.

Another SMA use is the spatial actuating in solar panels. These devices are used as thin strips of SMA elements such as hinges to open the panels when heated by electrical stimulus. The use of SMAs is interesting due to less weight than the set that are used in conventional hinges, favoring the power to weight ratio (Carpenter and Lyons 2001).

A device successfully employed by the U.S. Air Force in an F-14 chaser (used for the first time in the 1970s) motivates other interesting application of SMAs

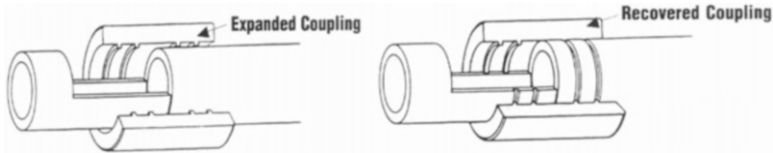


Fig. 9 *CryOfit* SMA coupling (Hodgson and Brown 2000)

related to pipes assemblage. This device is known as *CryOfit*, being developed by Raychem (2001) (Fig. 9). In order to assemble the two parts, the SMA coupling should be immersed in a liquid Nitrogen bath ($\cong -196^\circ\text{C}$). Afterward, its diameter is mechanically enlarged and remains immersed in the Nitrogen bath. After being removed from bath, it is quickly assembled to the two pipes to be connected. As the SMA coupling returns to room temperature, it assumes its former contracted shape, connecting the pipes. In some cases, the adhesion is better than the one obtained by welded joints, without the inconvenience of the inherent residual stress (Hodgson and Brown 2000).

Similar situation can be found in the coupling and joints often employed in oil industry, where an SMA device is employed in pipe flanges (SINTEF 2002). A pre-compressed cylindrical SMA washer is placed between the flange and the nut. When it is heated, it returns to its former shape and promotes an axial restitution force on the bolt, connecting the two parts. This procedure avoids the application of torques, which induces shear stress on the bolt. La Cava et al. (2000) present modeling and simulations related to this device and conclude that this form of assembling offers about 20 % of equivalent stress reduction on the bolt as compared to the traditional procedure.

The last category of SMAs applications cited in this chapter is its use as sensors and/or actuators. In this regard, the device developed by Nagnuma et al. (1998), presented in Fig. 10, uses SMA as both sensor and actuator in a hydrothermal fluid sampler. The sampler senses hot fluid and generates pumping power from the heat energy of the fluid. The functioning is explained as follows. Initially, the SMA suction spring is first compressed at low temperature (point A). At this point, the suction force is smaller than the friction force due to push the piston. Exposed to hot fluid the suction spring immediately extends and generates larger force, enough to intake the fluid (point B). The suction force decreases with the increase of the spring length, and the suction stops at the end of the stroke (point C). The SMA spring is cooled, and suction does not occur (point D). The idea of this device can be employed in different situations related to deployment. Solar panels and fire systems are some examples.

Jun et al. (2007) presented an analysis of a fuel-powered shape memory alloy actuator system (FPSMAAS) that uses fuels with high energy densities, such as propane, as its energy source. The benefits of this high energy density are evident in the efficiency activation cycles (heating and cooling). The heat generated by the combustion can be controlled by forced convection transferred to a fluid and,

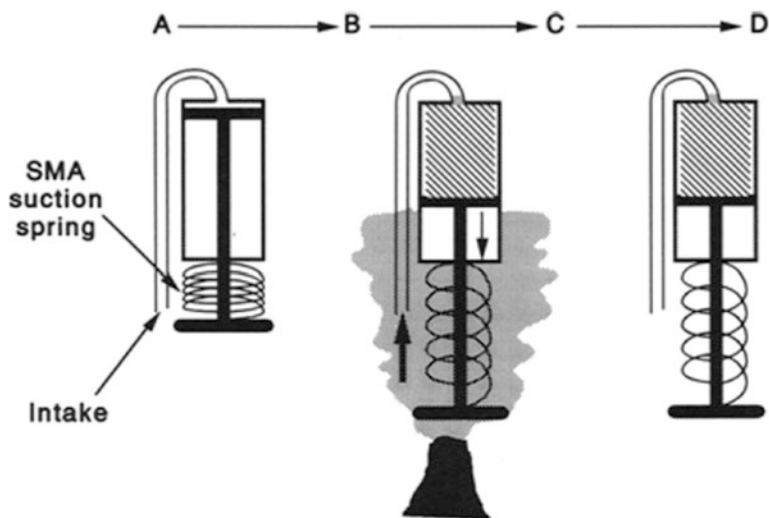


Fig. 10 Tube sampler hydrothermal

thereafter, to the element of shape memory actuator, until it reaches the temperature phase transformation. With the high speed which the fluid temperature can reach and a relatively large surface area of the actuator element, the process activation can be obtained rapidly. The cycle ends with the process of cooling also using forced convection, which prevents overheating the element, a common occurrence in actuators that use electricity as an activation mechanism, which may result in the loss of ability to performance. In the analyzed FPSMAAS, the main component of the actuator, an SMA element, operates as a heat engine and converts the thermal energy of fuel combustion into mechanical energy. Due to the relatively high recovery stress and strain of SMAs, the compact actuator can provide significant force and stroke. Convection heating and cooling of the SMA also results in relatively high actuation frequencies.

SMA actuators for automotive applications are also considering the use of SMAs for different purposes. Czechowicz (2013) pointed out the main reason for application of SMA actuators in automotive systems: its high working capacity with a force range up to 80 N and a stroke range up to 30 mm; the possibility of weight, cost and complexity reduction once the number of actuator parts decreases and external sensors can be eliminated as they can be replaced by a single SMA wire; SMA actuators are corrosion resistant; additionally, SMA actuator presents noiseless actuation. Based on these points, three conceptual adaptive SMA actuators are proposed by Czechowicz (2013) and the most promising concept is experimentally validated. The actuator works against a conventional spring, which is attached in parallel to a pseudoelastic device. This additional pseudoelastic element is responsible for an additional mechanical stress at varying ambient temperatures. Two SMA elements are used, one as actuator and the other one as the pseudoelastic device.

An alternative for shape memory actuators where there is a need for a large actuation force is to use a set of wires attached to a device type tendon. The use of this device was developed by Mosley et al. (1999) that present the design, the constructed prototype, and the experimental evaluation of the dynamic characteristics of an SMA actuator, which is composed of 48 SMA wires mechanically bundled in parallel forming one powerful muscle. The actuator is able to lift 100 lb, which is approximately 300 times its weight. The aim of the authors is to develop a new generation of large-scale robotic manipulators that are lightweight, compact, dexterous and able to produce high actuation forces.

Recently, shape memory thin films have been recognized as a great promise for high-performance materials in the application of micro-electro-mechanical MEMS (Micro-Electro-Mechanic Systems) by standardizing fabrication processes by lithography. They possess small quantities of mass for heating or cooling, resulting in rapid responses in the cycles of activation. The work (energy) per unit volume of these devices overcomes any other device performance. The application of these films allows further simplification of the mechanisms with a great flexibility of design and production of friction-free movement and vibration. The phase transformation that occurs in the SMA thin film substantially modifies the mechanical, physical, chemical, electrical, and optical properties such as yield stress, elastic modulus, hardness, electrical resistivity and conductivity, thermal expansion coefficient, among other properties. Such changes can be used to create a sensor or actuator different characteristics. These devices can be applied in severe environments such as radioactive, corrosive, or aerospace, which require large actuation force, low operating voltage, and resistance. An example of this kind of application can be found in Nakatani et al. (2003), which present the development of a 3D display created from small shape memory actuators.

3 Thermomechanical Characterization

This section presents an explanation about how to characterize some quasi-static thermomechanical behaviors of SMAs through experimental procedures. The presented procedures are stress-free thermal analysis; isothermal stress-strain test; and isobaric strain-temperature test.

3.1 *Stress-Free Thermal Analysis*

Temperature plays an essential role in the thermoelastic martensitic phase transformation experienced by SMA. Therefore, most of the physical properties, such as the electrical resistivity and elastic modulus, change with temperature. This change is commonly used to determine the temperatures of phase transformation and thermal hysteresis of SMAs. The determination of these specific thermal properties

is fundamental to the design of actuators based on SMAs, targeting advanced applications.

The two main techniques for determining transformation temperatures and thermal hysteresis in SMA are differential scanning calorimetry (DSC) and the electrical resistance measured as a function of temperature (ERT). In both techniques, there is no need for the application of mechanical loading. While DSC is popular with several commercial calorimeters available for this aim, ERT is simple to be implemented without the need of sophisticated equipment.

3.1.1 DSC Analysis

Figure 11 shows a typical DSC calorimeter for stress-free thermal analysis of SMA, as well as the arrangement of samples in the equipment. In the DSC test, the temperature of SMA sample is continuously varied with a constant heating and cooling rate. In general, for SMA, rates of 5 or 10 °C/min are used for thermal characterization. The SMA sample is placed in a small pot, while another sample is used as a reference in the second pot. The second reference sample can be a stable metal without phase transformation in the temperature range examined. The calorimeter is microcontrolled and makes automated measurements of temperature and energy occurring in the furnace containing the two samples. If the equipment allows the use of liquid nitrogen for helping cooling and the sample pans are in aluminum, tests between -150 and 500 °C can be achieved.

Figure 12 shows a typical result of an SMA DSC analysis. In general, there are peaks related to phase transformations. During cooling, there is a sample energy release that corresponds to thermoelastic transformation from austenite, at high temperature, to twinned martensite, at low temperature. Applying tangent lines to the peak region, it is possible to determine the start and finish temperatures of martensite phase formation, M_s and M_f , respectively. Typically, the DSC has a software that automatically determines these temperatures. This peak is the energy

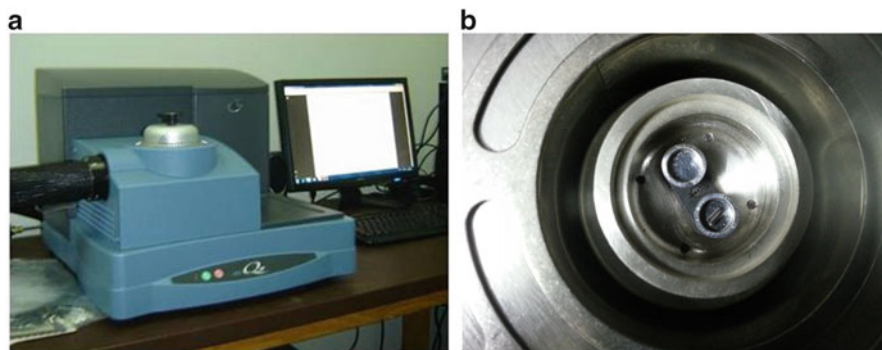
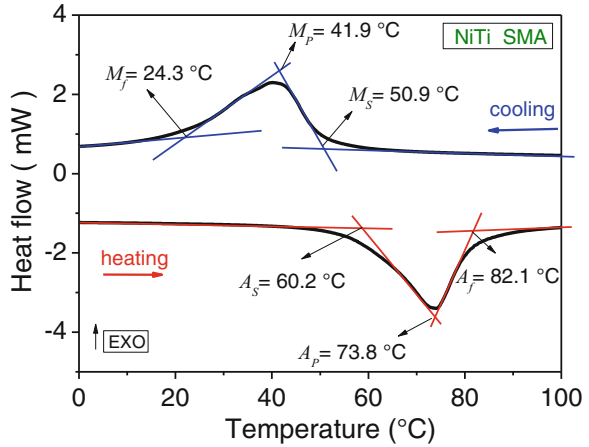


Fig. 11 Stress-free thermal analysis by DSC. (a) DSC apparatus from TA Instruments (model Q20). (b) NiTi SMA sample into DSC furnace

Fig. 12 Typical DSC result for thermal analysis in a SMA

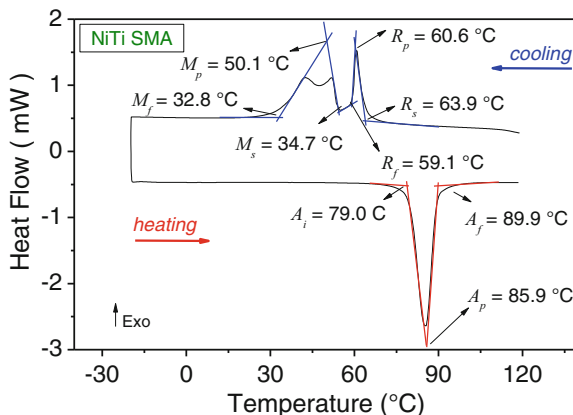


released for this phase change, which corresponds to an exothermic reaction. Once achieved the lowest temperature programmed for cooling, the reverse phase transformation, from twinned martensite to austenite, is performed during heating. At this stage, a peak corresponding to the reverse transformation appears in the DSC curve. Now, the peak is the energy absorption by the material for this phase change, which corresponds to an endothermic reaction. Once again, the tangent procedure allows one to determine the start and finish temperatures of reverse transformation from austenite to twinned martensite, A_s and A_f , respectively.

From a typical SMA DSC curve, as the one presented in Fig. 12, it is also possible to determine the thermal hysteresis (H_T) of the phase transformation: forward, during cooling (M_p); and reverse, during heating (A_p). In addition to these thermal properties related to the phase transformation temperatures, DSC apparatus are also used to determine the enthalpies of transformation (ΔH) through the peak area of forward transformation (austenite–martensite, ΔH_{A-M}) during cooling, and reverse (martensite–austenite, ΔH_{M-A}) during heating.

It is noteworthy to observe the possibility to appear extra peaks in an SMA DSC test, during either cooling or heating. In case of Nickel–Titanium (NiTi) alloys, it is very common to detect a phase transformation occurring in two stages during cooling. First, the austenite transforms to a twinned martensite with a rhombohedral structure, known as *R*-phase and, afterward, this first martensite transforms into a second martensite, which has a monoclinic structure. Figure 13 shows a DSC result considering this behavior in a NiTi SMA. In this case, two new temperatures are defined, indicating the start and finish of *R*-phase formation from austenite during cooling, called R_s and R_f , respectively. Similarly, it may be also established a new hysteresis in temperature corresponding to the temperature difference between the peaks of the austenite phase (A_p) and *R*-phase (R_p).

Fig. 13 DSC result for thermal analysis in a NiTi SMA with two-stage transformation during cooling



As previously mentioned, the phase transformation temperatures of SMA can also be determined by techniques that are not commercially available. In this case, the most frequently used method consists of monitoring the change in electrical resistance (ER) of SMA as a function of temperature.

3.1.2 ERT Analysis

Basically, the technique of measuring the electrical resistance as a function of temperature (ERT) to monitor the reversible phase transformation in SMA consists of attaching four electrical terminals in a sample (two external and two inner positions). This technique is known as the 4-wire method, as shown in Fig. 14. The SMA sample is immersed in an environment where it can be continuously cooled and heated. The thermo-controlled environment can be provided by a thermal bath, Peltier cell, or liquid nitrogen with heating system. This type of environment defines the temperature range of heating and cooling, which is usually between -100 and $200\text{ }^\circ\text{C}$. A power supply allows one to select and maintain a constant electrical current passing through the SMA sample. Then, a constant electrical current is passed through the two external terminals, while the voltage drop is monitored in the inner terminals. The corresponding voltage drop and the temperature values, which are measured using a micro thermocouple attached to the SMA sample, are obtained and stored by a data acquisition system connected to a computer.

Figure 15 shows some typical results of an ERT analysis in a NiTi SMA with the system of Fig. 14. In general, for conventional stable metals, there is a linear relationship between electrical resistance and temperature, and hysteresis is not observed. In the case of SMAs, this linear relationship exists only in the temperature ranges at which the phases, martensite and austenite, are stable. In the temperature range of phase transformation region, during cooling and heating, there is an increase and decrease of electrical resistance, which causes a hysteretic behavior of

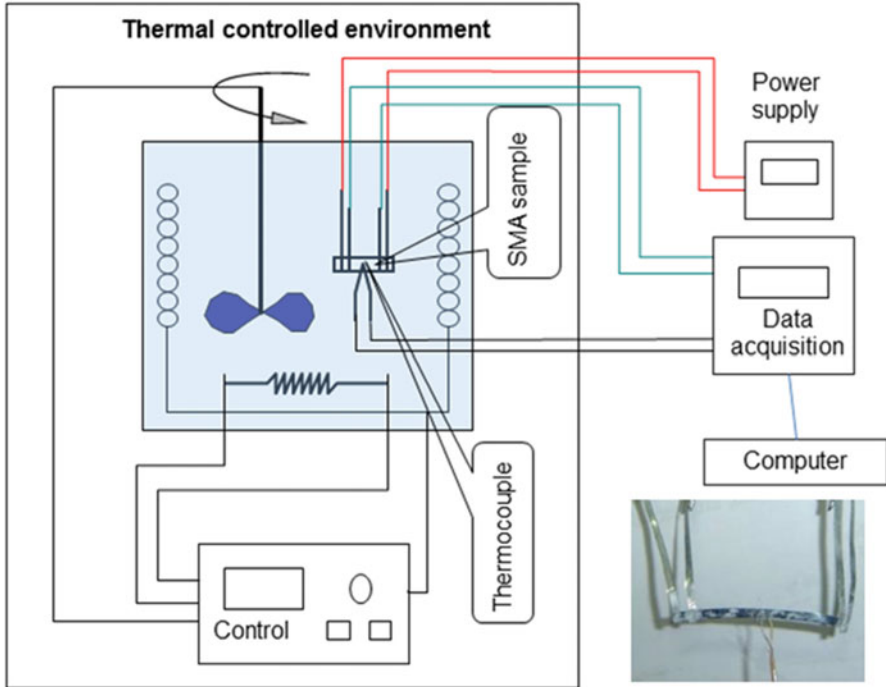


Fig. 14 Schematic picture of an ERT measurement system using the 4-wire method. The depicted photo shows a typical NiTi SMA sample with welded thermocouple

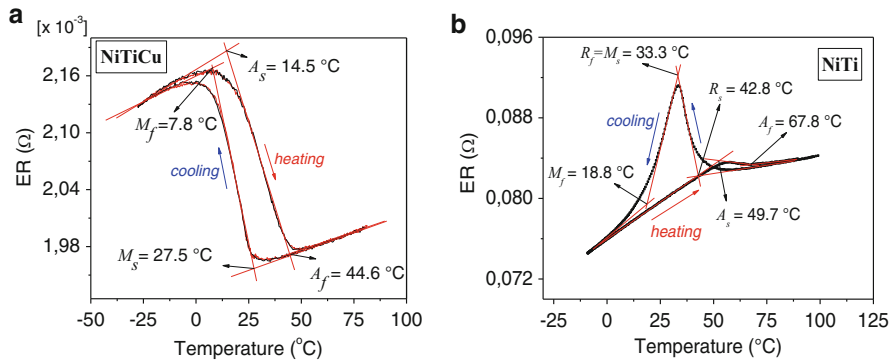


Fig. 15 ERT results for some SMA. (a) NiTiCu. (b) NiTi

ERT, as shown in Fig. 15a. Similarly to the case of DSC, the temperatures of phase transformation from ERT curves are measured by the method of tangent lines, as shown in Fig. 15. The tangents are applied to straight sections of ERT curves, so that each transformation temperature is defined by the intersection of these lines at inflection points for cooling and heating, respectively.

Specifically for the binary NiTi SMA, the presence of a two-stage phase transformation alters the behavior of ERT curve with respect to that shown in Fig. 15a. Figure 15b shows that the cooling from austenite transforms, firstly, into a rhombohedral twinned martensite (R -phase, in the range of temperatures R_s and R_f) and, then, transforms to monoclinic martensite (between M_s and M_f). The result of this phenomenon is the formation of a peak of ERT in the range of temperature corresponding to this double phase transformation. In many cases, this peak is sharp because the temperatures M_s and R_f are coincident, as shown in Fig. 15b. During heating, all the formed martensite reverts to austenite causing a deviation from linearity that determines the A_s and A_f temperatures, previously defined.

The major advantage of this ERT technique, compared to other methods of commercial thermal analysis, is that it can be directly applied to measure phase transformation temperatures of mechanical elements made from SMA, such as coil springs, pins, screws, and several others.

3.2 Isothermal Stress–Strain Tests

The thermomechanical characterization of SMAs passes through a proper comprehension of pseudoelasticity, defined in section 1 (Fig. 2). Therefore, an experimental infrastructure for applying controlled mechanical loading and unloading at different levels of constant temperature (isothermal) is required. Figure 16 shows a universal testing machine with a heating chamber used in LaMMEA/UFCG (Brazil) for thermomechanical characterization of SMA in pseudoelastic regime.

An important issue related to the SMA characterization is the Clausius–Clapeyron law, established by the following equation:

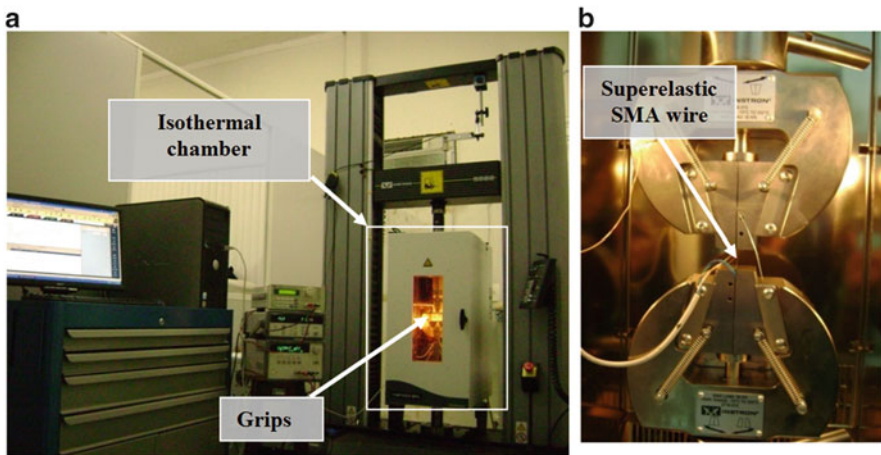


Fig. 16 Experimental test bench to evaluate the pseudoelastic behavior of a NiTi SMA wire. (a) Instron 5582 universal testing machine. (b) NiTi SMA wire installed in the grips

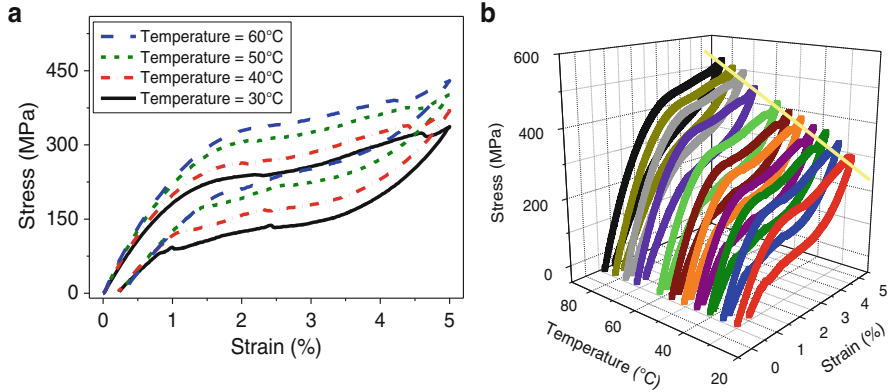


Fig. 17 Experimental pseudoelastic behavior of a NiTi SMA wire. **(a)** Behavior in the stress–strain plane for four different temperatures. **(b)** Three-dimensional stress–strain–temperature behavior between 30 and 90 °C

$$\frac{d\sigma}{dT} = \frac{\Delta H^{A-M}}{T_0 \cdot \varepsilon_{tr}} \quad (1)$$

where $d\sigma/dT$ may be used as the coefficient C_s^{AM} , T_0 can be calculated as $(M_s + A_s)/2$, ε_{tr} is the SIM strain, and ΔH^{A-M} is the enthalpy change of the phase transformation. Thus, the enthalpy of phase transformation (ΔH^{A-M}), typically determined by DSC analysis, can also be estimated by thermomechanical characterization in pseudoelastic regime.

Figure 17 shows a series of stress–strain curves for different temperatures during loading and unloading until a maximum strain of 5 % in a pseudoelastic NiTi SMA wire. The yellow line in Fig. 17b shows that the maximum stresses (at 5 % of strain) have a linear increase with temperature, following the Clausius–Clapeyron law for SMAs.

The critical stresses for formation and reversion of the stress-induced martensite (SIM, detwinned martensite) can be determined, again, by applying tangent lines in the stress–strain curves of Fig. 17. Figure 18a illustrates the determination of these critical stresses for start and finish of SIM during mechanical loading, σ_{Ms} and σ_{Mf} , respectively. During mechanical unloading, it is possible to determine the critical stresses for start and finish for reversal SIM, which are σ_{As} and σ_{Af} , respectively. If these critical stresses are plotted as a function of temperature, a linear behavior arises as shown in Fig. 18b, confirming the Clausius–Clapeyron behavior.

The mechanical characterization can be defined from the treatment of the data shown in Fig. 18b. Based on that, the following slopes for the C_s^{AM} and C_f^{MA} coefficients are determined: $C_s^{AM} = d\sigma/M_s = 4.6 \text{ MPa}/^\circ\text{C}$, $C_f^{AM} = d\sigma/M_f = 3.8 \text{ MPa}/^\circ\text{C}$, $C_s^{MA} = d\sigma/A_s = 5.0 \text{ MPa}/^\circ\text{C}$, and $C_f^{MA} = d\sigma/A_f = 3.0 \text{ MPa}/^\circ\text{C}$. Some theoretical models consider the parallelism between these coefficients (C_s^{AM} , C_f^{AM} and C_s^{MA} , C_f^{MA}). However, experimental results rarely confirm this hypothesis, as revealed in Fig. 18b.

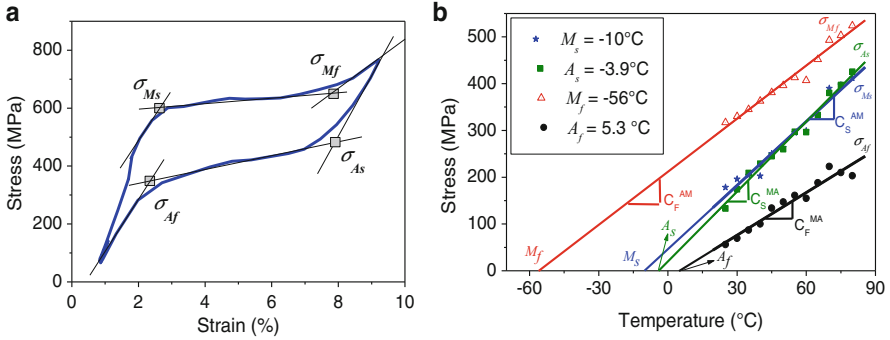


Fig. 18 Critical stresses for SIM. (a) Identification and definition of stresses from a superelastic loop. (b) Relationship between critical stresses and test temperatures

The hysteretic behavior of pseudoelastic stress–strain curves indicates that the SMA can dissipate energy during the stress-induced phase transformation. This behavior can be interesting for the development of applications for mitigation and control of mechanical vibrations. The dissipated energy per unity volume (E_D), in J/m^3 , corresponds to the area inside the stress–strain loop, calculated by Eq. (2).

$$E_D = \oint \sigma d\varepsilon \tag{2}$$

For a first cycle reaching maximum strains of the order of 10 %, without considering the effects of fatigue, this dissipated energy can reach values as high as 24 MJ/m^3 .

3.3 Isobaric Strain–Temperature Tests

Another way to carry out the thermomechanical characterization of SMA is to perform cycles of SME under constant load. Figure 19 shows a schematic picture of an experimental apparatus designed in LaMMEA laboratory from UFCG (Brazil) especially to apply a constant load (using a dead weight) in SMA wires and strips and carry out controlled heating and cooling of the material, monitoring the temperature and strain during thermal cycling under constant stress (isobaric).

This apparatus is basically composed of a mechanical structure composed by a drawbar with mobile and fixed clamps to hold the SMA sample and apply the desired constant load. This structure is immersed in a thermal bath that can continuously vary temperature between -80 and 200°C by using special silicone oil. A micro thermocouple ($100 \mu\text{m}$ in diameter) of K-type is attached to the SMA sample, while an LVDT displacement sensor is installed on the draw bar to measure the displacement during heating and cooling. A data acquisition system connected

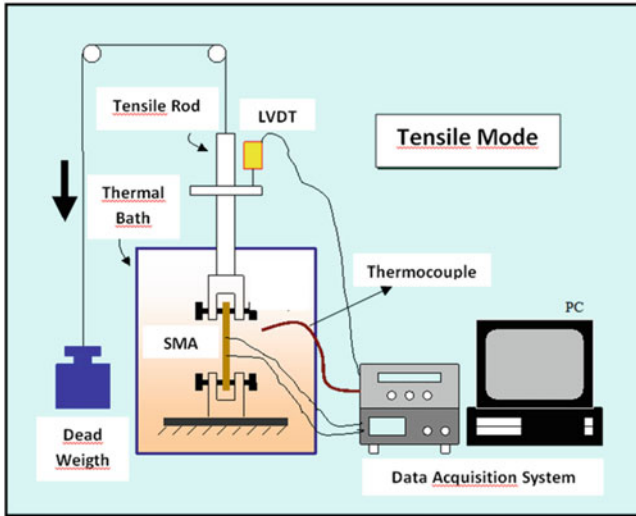
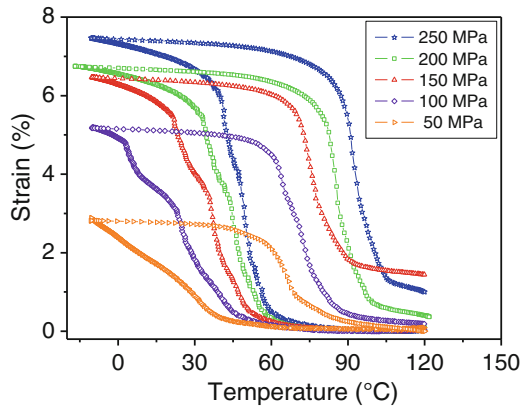


Fig. 19 Schematic picture of an experimental apparatus for testing shape memory effect under constant load (tensile mode)

Fig. 20 Hysteretic strain–temperature curves under constant stresses obtained with the apparatus shown in Fig. 19



to a computer stores the values of temperature and displacement for further analysis.

Figure 20 shows a series of strain–temperature curves for various levels of applied stress in a NiTi SMA wire with 1.5 mm in diameter. Qualitatively, results show that the transformation temperatures and strain increase with the applied stress. It is also observed that for limited stresses, up to 100 MPa, strain–temperature loops are closed, without any residual strain under load at the end of heating (120 °C). Note that it is possible to obtain the four characteristic phase transformation temperatures as a function of applied load. Figure 21 illustrates this determination for each value of stress by applying the method of tangent lines.

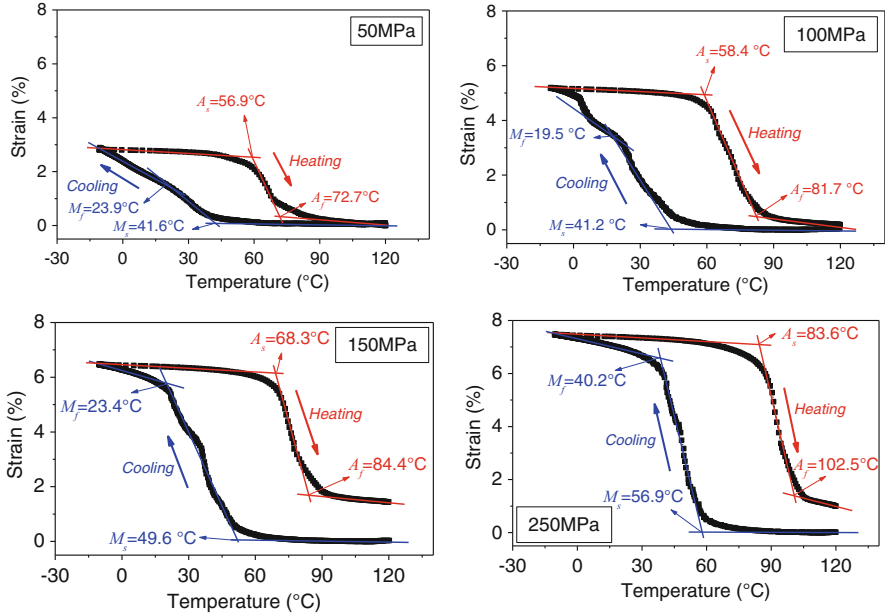
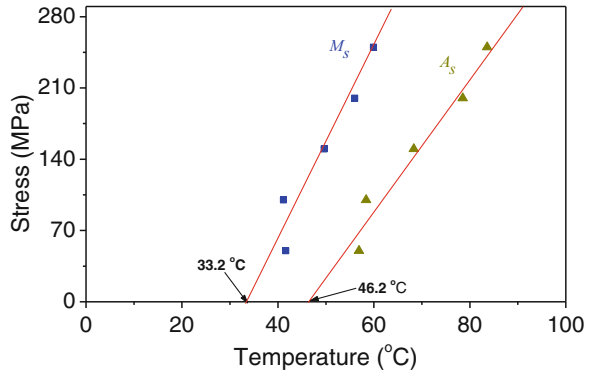


Fig. 21 Strain–temperature curves for four levels of constant applied stress on a NiTi SMA wire

Fig. 22 Linear relationship between the applied stress and the M_s and A_s temperatures



Figures 20 and 21 show that the strains related to the SME after heating vary from 3 to 7.5 % for applied stress levels between 50 and 250 MPa, with residual strains limited to less than 1.5 %.

If the temperatures obtained from Fig. 21 are plotted as functions of applied stress, we can also get the linear coefficients ($C = d\sigma/dT$) corresponding to the Clausius–Clapeyron law for SMA discussed in the previous section. Figure 22 shows this result for M_s and A_s temperatures. The values of M_s and A_s extrapolated to zero-stress case are similar to those obtained by DSC for Ni–Ti, with differences generally limited to ± 10 °C.

3.4 Final Remarks

In this section, the most important procedures for thermomechanical characterization of SMAs are presented considering an experimental approach. Characterization techniques consider methods that do not use commercial devices.

Two alternatives are presented for determining transformation temperatures in stress-free situations: electrical resistance versus temperature (ERT) and DSC analysis. Contrary to DSC, the ERT technique is cheaper and can be applied to various mechanical components made of SMA, such as coil springs; pins; screws; and others.

Tests with application of mechanical loading, isothermal (pseudoelasticity), or isobaric (SME under constant load) lead to the coefficients of stress increase with temperature ($C = d\sigma/dT$) that allows one to obtain transformation temperatures by extrapolation to zero stress, as well as the enthalpy of transformation via the Clausius–Clapeyron law.

All these experimental thermomechanical characteristics are very important for the development of applications for SMA, as well as for modeling and simulation of the behavior of these smart materials.

4 Constitutive Modeling

The mathematical modeling of SMAs is essential for the proper development of SMA applications. Constitutive models are, usually, based on macroscopic features and the *standard generalized material* approach is a suitable choice for their formulation. Accordingly, the thermodynamic state of a given continuum in a specific position at a certain time may be completely defined if a finite number of variables are known. These variables are called state variables and may be classified into observable and internal variables. For typical material's behavior, the observable variables are the absolute scalar temperature (T) and the strain tensor (ϵ_{ij}) (Eringen 1967; Mase and Mase 1999; Gurtin et al. 2010). For reversible phenomena, the material thermodynamic state depends solely upon observable variables; on the other hand, if any dissipation mechanism is present, internal variables are required to help describing these irreversible processes evolution, which may depend on variables time rate.

SMAs behavior is intrinsically non-diffusive, nonlinear, and dissipative. There are several attempts towards SMA thermomechanical constitutive modeling (Paiva and Savi 2006; Lagoudas 2008). The macroscopic theories may be classified based on the original concept they are built upon. Some examples are plasticity-based models, internal restrictions models, assumed transformation kinetics, among others.

The assumed *Phase Transformation Kinetics* (PTK) approach considers preestablished mathematical functions to describe the phase transformation.

This theory is widely explored in the literature due to its simplicity and, therefore, presents plenty of experimental verification. The first attempt to use this concept to model the SMA behavior was proposed by Tanaka and Nagaki (1982), by introducing algebraic exponential equations to describe martensitic and reverse transformations. The original model considered two volume fractions as internal variables, associated with the austenite (A) and detwinned martensite ($M+$) and, thus, was neither able to capture the reorientation process, nor to represent the compressive behavior. This work motivated other researchers (Liang and Rogers 1990; Brinson 1993; Boyd and Lagoudas 1996, among others) that used the same constitutive formulation except for the evolution equations adopted for the internal variables. Liang and Rogers (1990) proposed a cossenoidal evolution law, which was able to better-fit experimental results. These cossenoidal equations were refined by Brinson (1993) to take into account a new volume fraction associated with the twinned martensite (M) but still did not capture the compressive behavior. For further details about PTK formulation, please see the aforementioned references.

In general, the PTK models consider the following constitutive equation, expressed in terms of time rate of the involved variables:

$$\dot{\sigma}_{ij} = E_{ijkl} \dot{\varepsilon}_{kl} - \alpha_{ij} \dot{\beta} - \Theta_{ij} \dot{T} \quad (3)$$

where σ_{ij} is the stress tensor; ε_{kl} is the strain tensor; and T is the scalar absolute temperature. Concerning the material properties, E_{ijkl} is the elastic tensor; α_{ij} is the phase transformation tensor; and Θ_{ij} is associated with thermal dilatation/contraction. Along this work, all parameters are considered constants.

The model proposed by Brinson (1993) is reduced to one-dimensional context, where the stress tensor becomes the axial stress σ ; the strain tensor becomes the axial strain ε ; β and T remains scalars, the elastic tensor becomes the *Young* modulus (E), the phase transformation tensor becomes the scalar parameter α that controls the vertical size of the hysteresis loop, while the thermal tensor becomes the scalar thermal expansion coefficient (Θ). Integrating Eq. (3), admitting constant material properties, the one-dimensional constitutive relation remains:

$$\sigma - \sigma_0 = E(\varepsilon - \varepsilon_0) + \alpha(\beta - \beta_0) - \Theta(T - T_0) \quad (4)$$

where the quantities $()_0$ may be understood either as the initial conditions or the past instant values of the respective quantities.

Brinson's model splits the volume fraction β into two new internal variables, being one of them related to twinned martensite (M) named β_T and the other one associated with detwinned martensite ($M+$), β_S , such that $\beta = \beta_S + \beta_T$. Considering the non-diffusive characteristic of the martensitic transformation, the volume fractions β_S and β_T are considered to depend on the instantaneous values of stress and temperature: $\beta_{S,T} = \beta_{S,T}(\sigma, T)$. In addition to that, the elastic modulus, during phase transformations, may be assumed as a linear combination of the austenitic elastic modulus (E_A) and the martensitic elastic modulus (E_M), varying linearly with the total volume fraction β , such that $E(\beta) = E_A + \beta(E_M - E_A)$.

As an extra consideration, regarding the maximum residual strain, namely ϵ_R , is defined as the accumulated deformation after being mechanically loaded until complete phase transformation is reached and, subsequently, unloaded for a constant temperature. Admitting as initial conditions: $\sigma_0 = \epsilon_0 = \beta_0 = 0$; as final conditions: $\sigma = 0$; $\epsilon = \epsilon_R$; $\beta = 1$; constant temperature $T \leq A_S$ and substituting these information into Eq. (4), result in $\alpha = -\epsilon_R E$. As a consequence, the parameter α , from now on, is a linear implicit function of β . After these considerations, it is possible to rewrite the constitutive relation in its final form as:

$$\sigma - \sigma_0 = E(\beta)\epsilon - E(\beta_0)\epsilon_0 + \alpha(\beta)\beta_S - \alpha(\beta_0)\beta_{S_0} - \Theta(T - T_0) \tag{5}$$

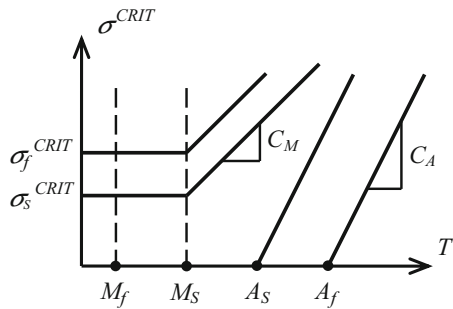
The model evolution laws are set to be cossenoidal equations for both internal variables β_S and β_T . For $T > M_S$, the direct martensitic transformation ($A \Rightarrow M+$) is given by:

$$\beta_S = \frac{1 - \beta_{S_0}}{2} \cos \left\{ \frac{\pi}{\sigma_S^{CRIT} - \sigma_f^{CRIT}} [\sigma - \sigma_f^{CRIT} - C_M(T - M_S)] \right\} + \frac{1 + \beta_{S_0}}{2} \tag{6}$$

$$\beta_T = \beta_{T_0} - \frac{\beta_{T_0}}{1 - \beta_{S_0}} (\beta_S - \beta_{S_0})$$

Equation (6) must be applied when: $\sigma_S^{CRIT} + C_M(T - M_S) < \sigma < \sigma_f^{CRIT} + C_M(T - M_S)$, where, for cyclic tests, β_{S_0} , β_{T_0} , and β_0 correspond to stress-induced, temperature-induced and total martensitic volume fractions' amount prior to the present transformation (remaining from previous transformations), respectively, in order to adequately describe the subloops due to incomplete phase transformations. σ_S^{CRIT} and σ_f^{CRIT} represent the critical stresses for beginning and finishing direct martensitic phase transformations, respectively. In this model, according to Fig. 23, for $T < M_S$, these stress levels remain constant, while the material parameter C_M corresponds to the slope of the straight line, representing the linear critical stress increasing for martensitic transformation for $T > M_S$.

Fig. 23 Temperature dependence of phase transformation critical stress (Brinson 1993)



For $T \leq M_S$, the following equations hold:

$$\beta_S = \frac{1 - \beta_{S_0}}{2} \cos \left[\frac{\pi}{\sigma_S^{\text{CRIT}} - \sigma_f^{\text{CRIT}}} (\sigma - \sigma_f^{\text{CRIT}}) \right] + \frac{1 + \beta_{S_0}}{2} \quad (7)$$

$$\beta_T = \beta_{T_0} - \frac{\beta_{T_0}}{1 - \beta_{S_0}} (\beta_S - \beta_{S_0}) + \Delta_T$$

Equation (7) must be applied when: $\sigma_S^{\text{CRIT}} < \sigma < \sigma_f^{\text{CRIT}}$, where:

$$\Delta_T = \frac{1 - \beta_0}{2} \{ \cos [A_M(T - M_f)] + 1 \} \quad \text{if } M_f < T < M_S \text{ and } T < T_0 \quad (8)$$

$$\Delta_T = 0 \quad \text{else}$$

where A_M is a material parameter obtained by: $A_M = \pi/M_S - M_f$.

The reverse transformation $M \leftrightarrow A$ is given by:

$$\beta_S = \frac{\beta_{S_0}}{2} \left\{ \cos \left[A_A \left(T - A_S - \frac{\sigma}{C_A} \right) \right] + 1 \right\} \quad (9)$$

$$\beta_T = \frac{\beta_{T_0}}{2} \left\{ \cos \left[A_A \left(T - A_S - \frac{\sigma}{C_A} \right) \right] + 1 \right\}$$

Equations (9) hold for: $T > A_S$ and $C_A(T - A_f) < \sigma < C_A(T - A_S)$, where, according to Fig. 23, C_A corresponds to the slope of the straight line, representing the linear critical stress increasing for reverse transformation for $T > A_S$ and A_A is a material parameter obtained by: $A_A = \pi/A_f - A_S$.

From the numerical point of view, the implementation is quite simple, since all equations (not only the constitutive one but also the evolution laws) are algebraic. The evolution laws are stress-dependent; therefore, for the sake of simplicity, the algorithm considers prescribed stress. Concerning the compressive behavior inclusion in the original Brinson's model, the stress-induced volume fraction originally varies in the interval $[0, 1]$. Instead of that, it may now vary from $[-1, 1]$; thus, all the limit conditions to apply the evolution laws should be redefined as their modulus. Besides that, in every step, it is necessary to evaluate the sign of stress rate ($\dot{\sigma}$) to verify whether the prescription is a tensile loading or a compressive loading. While conceiving the algorithm, special attention should be devoted for stress-free thermal tests.

4.1 Numerical Simulations

This section presents numerical simulations obtained by the modified algorithm based on Brinson's (1993) model. Initially, the comparison between numerical and

Table 1 SMA properties and parameters identified for Brinson (1993) constitutive model through comparison with the experimental results obtained by Tobushi et al. (1991)

Material properties	Transformation temperatures	Model parameters
$E_A = 57$ GPa	$M_f = 285$ K	$C_M = 9$ MPa/K
$E_M = 42$ GPa	$M_s = 295$ K	$C_A = 8.5$ MPa/K
$\theta = 0.55$ MPa/K	$A_s = 320$ K	$\sigma_s^{\text{CRIT}} = 90$ MPa
$\epsilon_R = 0.0555$	$A_f = 333$ K	$\sigma_f^{\text{CRIT}} = 170$ MPa

experimental results found in the literature enables the model parameters' identification. Then, qualitative results are presented for different typical SMA tests, including internal subloops due to incomplete phase transformation.

4.1.1 Model Calibration

This subsection presents the comparison between the numerical results obtained by the implemented constitutive model and experimental results obtained by Tobushi et al. (1991) for one-dimensional, isothermal, pseudoelastic tests for three different temperatures, aiming the identification of the model parameters presented in Table 1.

In Fig. 24, the experimental results are monotonic and, thus, exhibit a residual strain after unloading due to the *Transformation Induced Plasticity* (TRIP) effect that is out of this model's scope. It is worthwhile to distinguish that, after a "training" cyclic process, this effect becomes saturated (resulting in a complete residual strain recovery) and, therefore, the present model is able to capture the correct pseudoelastic behavior. The numerical results are in good agreement with the experimental results, except for $T = 333$ K (Fig. 24a); nevertheless, the experimental result does not present a complete phase transformation, which may justify the softening effect at the end of the direct transformation $A \Rightarrow M+$, where the numerical result deviates from the experimental result.

4.1.2 Qualitative Results

This subsection presents some qualitative results that attest the model capability to describe the temperature-induced phase transformation, the pseudoelastic behavior, and the SME.

Figure 25 illustrates the phase transformation phenomenon due to temperature variation for a free-stress state. Figure 25a presents the thermomechanical time prescriptions; Fig. 25b shows the volume fractions' time evolution; and Fig. 25c exhibits the temperature–strain diagram.

In Fig. 25a, for a free-stress ($\sigma = 0$), the thermal loading involves two-and-a-half heating/cooling cycles, being the first cycle ($0 \text{ s} < t < 4 \text{ s}$) such that the maximum/minimum temperature levels overlap the limiting transformation temperatures A_f and M_f , inducing complete phase transformations. The other one cycle and a half

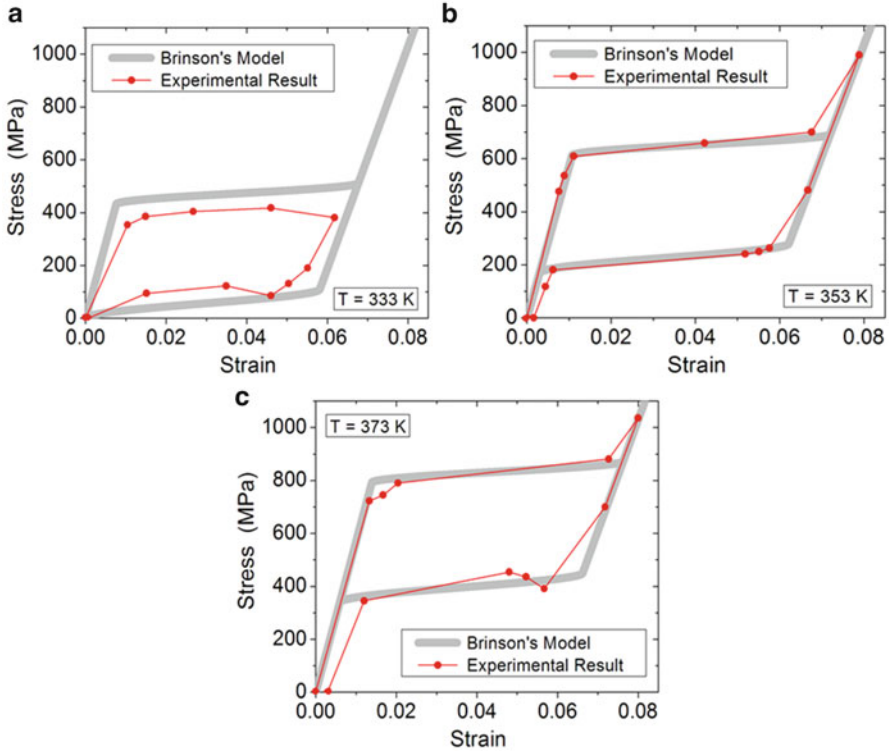


Fig. 24 Comparison between numerical results obtained by the Brinson (1993) constitutive model and experimental results obtained by Tobushi et al. (1991) for different temperature pseudoelastic tensile tests. (a) $T = 333$ K; (b) $T = 353$ K; (c) $T = 373$ K

($4 \text{ s} < t < 10 \text{ s}$) have maximum/minimum temperature levels within the transformation temperatures' range, inducing subloops.

Considering Fig. 25b, initially, at a low temperature ($T < M_f$), twinned martensite is the stable phase, thus $\beta_T = 1$. While heating the material ($0 \text{ s} < t < 2 \text{ s}$) above A_f , a complete $M \Rightarrow A$ austenitic transformation takes place and β_T becomes null. When the material is cooled back to a low temperature ($2 \text{ s} < t < 4 \text{ s}$), an $A \Rightarrow M$ martensitic transformation occurs and, as a consequence, $\beta_T = 1$ again. This first cycle is responsible for the external (envelope) thermal loop in Fig. 25c. Then, the subsequent partial heating below A_f ($4 \text{ s} < t < 6 \text{ s}$) reduces β_T , inducing a partial austenitic transformation (between points A and B). The next partial cooling above M_f ($6 \text{ s} < t < 8 \text{ s}$) increases β_T , inducing a partial martensitic transformation (between points C and D). At last, another heating process ($6 \text{ s} < t < 8 \text{ s}$), but this time above A_f , reduces β_T , inducing a complete austenitic transformation (between points E and F). The resulting structure, after the test, is fully austenitic with $\beta_T = 0$. The intermediate plateaus for $0 < \beta_T < 1$ (between points B and C and points

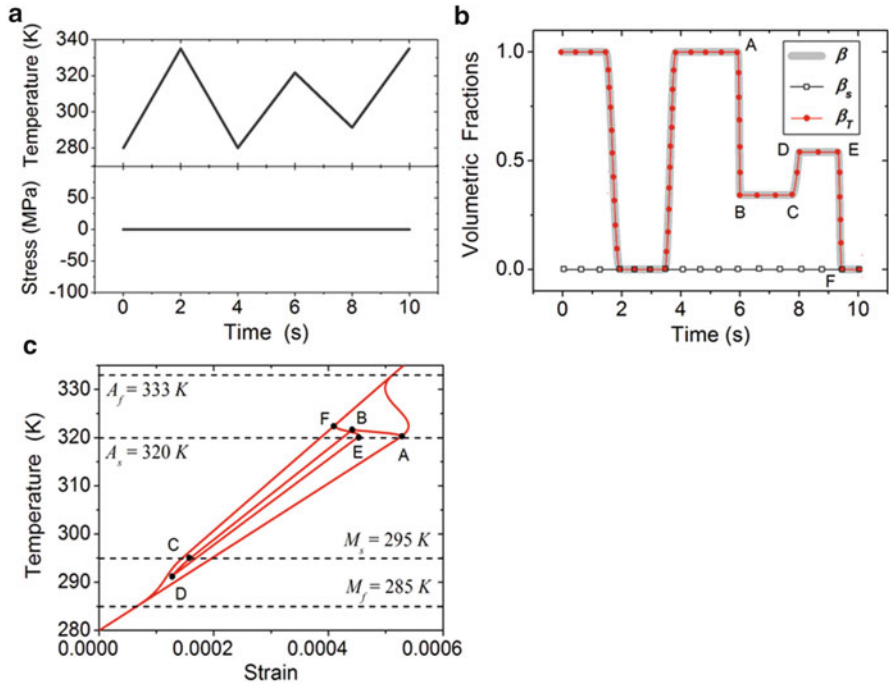


Fig. 25 Free-stress phase transformation due to temperature variation. (a) Thermomechanical loading; (b) volume fractions’ evolution; (c) temperature–strain diagram

D and *E* in Fig. 25b, are associated to linear thermal contraction/expansion paths in Fig. 25c, respectively.

In Fig. 25c, it is possible to observe the thermal subloops due to incomplete phase transformations, together with the characteristic transformation temperatures: $M_f = 285\text{ K}$; $M_s = 295\text{ K}$; $A_s = 320\text{ K}$; and $A_f = 333\text{ K}$.

Figure 26 presents the isothermal tensile response for five different temperatures. Each temperature considered is within one specific temperature range, according to Fig. 25c; i.e., $T = 335\text{ K} > A_f$; $A_f > T = 327\text{ K} > A_s$; $A_s > T = 310\text{ K} > M_s$; $M_s > T = 290\text{ K} > M_f$; $T = 280\text{ K} < M_f$.

In Fig. 26, for $T = 335\text{ K} > A_f$, it is possible to identify the pseudoelastic behavior. The original free-stress stable phase is austenite. During mechanical loading, there is an $A \Rightarrow M+$ transformation, while, during unloading, a reverse transformation $M+ \Rightarrow A$ takes place, since $M+$ becomes an unstable phase for low stress levels, such that: $\sigma < C_A(T - A_s)$. In this case, after the test, the sample completely recovers its original austenitic shape.

In Fig. 26, for $A_f > T = 327\text{ K} > A_s$, the original free-stress stable phase is, again, austenite. During mechanical loading, there is an $A \Rightarrow M+$ transformation, as well as for $T = 335\text{ K} > A_f$. Nevertheless, during unloading, the reverse transformation $M+ \Rightarrow A$ is partial, since $A_f > T > A_s$. As a consequence, a partial residual strain

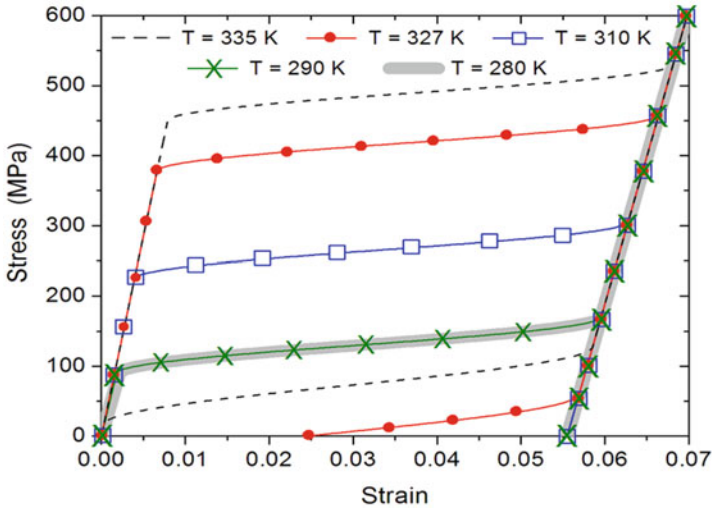


Fig. 26 Isothermal Tensile tests for different temperatures

($\epsilon_R \cong 0.025$) remains and the sample does not completely recover its former shape. After the test is complete, a mixed resulting structure takes place, where phases A and M+ coexist.

In Fig. 26, for $A_s > T = 310 \text{ K} > M_s$, the original free-stress stable phase is, still, austenite. During mechanical loading, there is an $A \Rightarrow M+$ transformation, as well as for the two previous cases. This time, during unloading, only an elastic recovery with no reverse transformation takes place and the maximum residual strain ($\epsilon_R = 0.0555$) arises. The resulting structure, for this test, is fully M+.

In Fig. 26, for $M_s > T = 290 \text{ K} > M_f$, the original free-stress stable phase is a mixture of austenite (A) and twinned martensite (M). During mechanical loading, there are two simultaneous processes as follows: the austenitic fraction experiments a phase transformation into detwinned martensite M+, while the twinned martensite (M) fraction undergoes a reorientation (detwinning) process, converting M into M+. Therefore, after complete loading, the uniform resulting structure is fully M+. During unloading, again, as in the previous case for $A_s > T = 310 \text{ K} > M_s$, there is only an elastic recovery with no reverse transformation. After that, detwinned martensite M+ remains stable, accompanied with the maximum residual strain ($\epsilon_R = 0.0555$).

In Fig. 26, for $T = 280 \text{ K} < M_f$, the original free-stress stable phase is fully twinned martensite (M). During mechanical loading, a reorientation process $M \Rightarrow M+$ occurs. During unloading, again, as in the two previous situations, there is only an elastic recovery with no reverse transformation. Thus, after the test, detwinned martensite M+ remains stable, accompanied with the maximum residual strain ($\epsilon_R = 0.0555$).

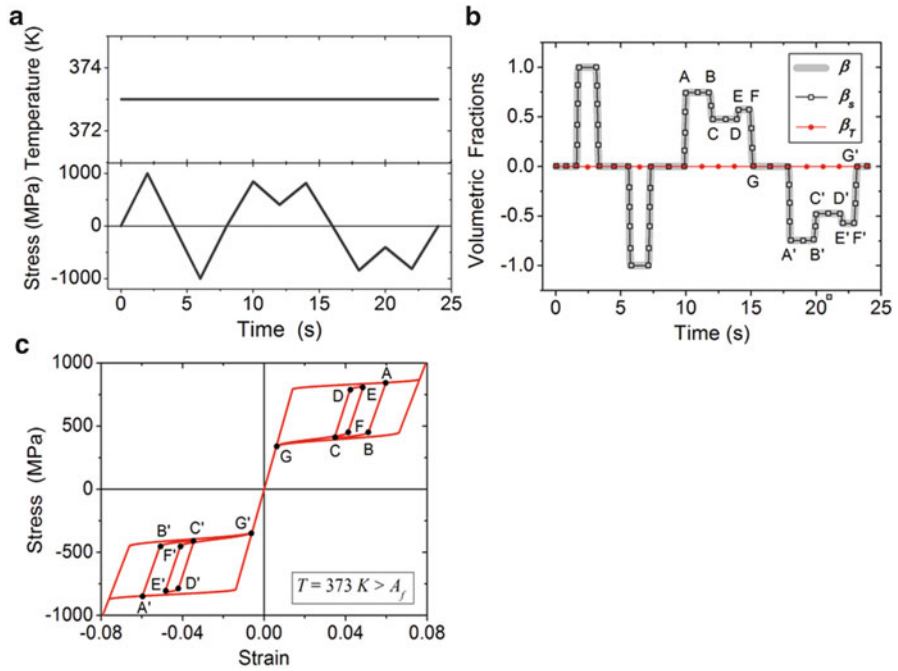


Fig. 27 Tension-compression isothermal pseudoelastic test with subloops for $T = 373\text{ K} > A_f$. (a) Thermomechanical loading; (b) volume fractions' evolution; (c) stress–strain diagram

Observing Fig. 26, it is possible to take some conclusions as follows:

- For isothermal tensile tests, as the temperature is lowered, the hysteresis loop is shifted downward; i.e., all critical stresses for beginning and finishing transformations are reduced
- A necessary condition for the complete reverse transformation requires that the test should be performed at a temperature $T \geq A_f$. For $A_f > T > A_s$, the reverse transformation is partial, while, for $T \leq A_s$, there is no reverse transformation
- For $T \leq M_s$, the critical stresses for beginning and finishing transformations are always the same

Figure 27 considers the pseudoelastic behavior. Figure 27a presents the thermomechanical time prescription for this test; Fig. 27b shows the volume fractions' time evolution; and Fig. 27c exhibits the stress–strain diagram.

Observing Fig. 27a, there is no temperature variation, while the mechanical loading is composed of a loading/unloading tensile cycle ($0\text{ s} < t < 4\text{ s}$), where the maximum stress level during loading overlaps the critical stress for finishing martensitic transformation, inducing complete transformation. After that, a similar compressive cycle is imposed ($4\text{ s} < t < 8\text{ s}$). Then, two subsequent partial loading/unloading tensile mechanical cycles are imposed ($8\text{ s} < t < 16\text{ s}$), inducing

subloops. Finally, two analogous compressive partial cycles are performed ($16 \text{ s} < t < 24 \text{ s}$).

Concerning Fig. 27b, this test is performed at a constant high temperature ($T = 373 \text{ K} > A_f$), therefore, $\beta_T = 0$ during all the test (since, at no time, there will be temperature-induced martensite M). At first, the fully austenitic phase is stable ($\beta_S = 0$). Along with the applied tensile loading ($0 \text{ s} < t < 2 \text{ s}$), an $A \Rightarrow M+$ transformation takes place ($0 < \beta_S < +1$). After unloading ($t = 4 \text{ s}$), the structure returns back to the austenitic phase ($\beta_S = 0$). When a compressive loading is applied, an $A \Rightarrow M-$ transformation occurs ($0 < \beta_S < -1$). These loading/unloading processes for tensile ($0 \text{ s} < t < 4 \text{ s}$) and compressive stress ($4 \text{ s} < t < 8 \text{ s}$) induce complete phase transformations that are responsible for the external (envelope) loops in Fig. 27c. Then, the subsequent partial loading ($8 \text{ s} < t < 10 \text{ s}$) induces β_S . Before the martensitic transformation finishes, the sample is unloaded, reducing β_S , inducing a partial reverse transformation (between points B and C). The next partial loading ($12 \text{ s} < t < 14 \text{ s}$) increases β_S , inducing a partial martensitic transformation (between points D and E). At last, a complete mechanical unloading ($14 \text{ s} < t < 16 \text{ s}$) turns β_S null, inducing a complete reverse transformation (between points F and G). The resulting structure, after the test, is fully austenitic with $\beta_S = 0$. The intermediate plateaus for $0 < \beta_S < +1$ (between points A and B , points C and D , and points E and F in Fig. 27b) are associated to linear elastic behavior in Fig. 27c. An analogous process occurs for the compressive behavior.

Figure 27c exhibits the stress–strain diagram for a high temperature $T > A_f$, where the austenite is the stable phase for a stress-free state. This result also demonstrates the model capability to describe both tensile and compressive subloops due to incomplete phase transformations.

Figure 28 presents the SME effect for a low-temperature situation ($T = 280 \text{ K} < M_f$). Figure 28a shows the thermomechanical time prescription for this test; Fig. 28b exhibits the volume fractions' time evolution; and Fig. 28c shows the stress–strain–temperature diagram.

According to Fig. 28a, initially, a loading/unloading isothermal mechanical tensile cycle is imposed ($0 \text{ s} < t < 4 \text{ s}$). Then, for a free-stress condition ($\sigma = 0$), a subsequent heating/cooling thermal cycle, from $T < M_f$ to $T > A_f$ and vice versa, is imposed ($4 \text{ s} < t < 8 \text{ s}$), bringing the structure back to its initial twinned martensitic stable state. Then, the same procedure is conducted for compressive behavior.

In Fig. 28b, firstly, twinned martensite is the only stable phase ($\beta_T = 1$ at point A). During the first isothermal mechanical tensile loading ($0 \text{ s} < t < 2 \text{ s}$), the sample exhibits an elastic behavior (between points A and B), until a martensitic reorientation process $M \Rightarrow M+$ occurs (between points B and C), converting β_T into β_S . After the martensitic transformation finishes (point C), the sample behaves elastically again until the maximum prescribed stress (point D). Then, the sample is unloaded ($2 \text{ s} < t < 4 \text{ s}$), presenting an elastic recovery with no reverse transformation (between points D and E); thus, $\beta_S = +1$ (at point E) and the maximum residual strain ($\epsilon_R = 0.0555$) remains. From this point on, the sample is heated ($4 \text{ s} < t < 6 \text{ s}$) such that $T > A_f$. There is a linear thermal expansion (between points E and F), until

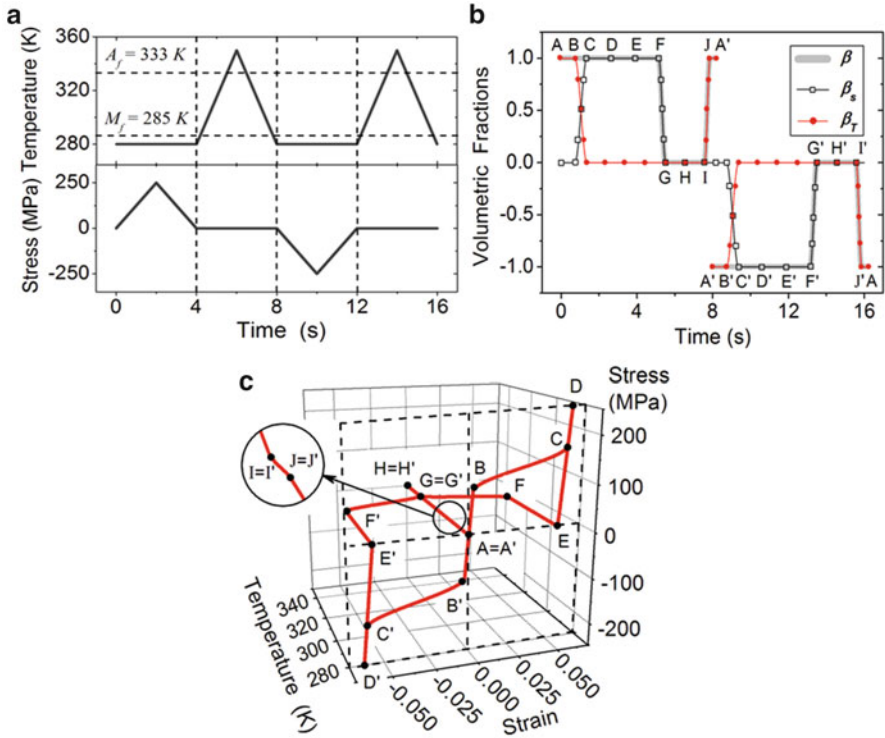


Fig. 28 Shape memory effect for $T = 280 \text{ K} < M_f$. (a) Thermomechanical loading; (b) volume fractions' evolution; (c) stress–strain–temperature diagram

the material reaches $T = A_s$ (point F). After that, an austenitic transformation $M+ \Rightarrow A$ is responsible for the complete residual strain (ϵ_R) recovery (between points F and G). After the transformation is complete, the continuous heating induces a new linear thermal expansion (between points G and H), but this time, as an austenitic phase. The subsequent cooling process ($6 \text{ s} < t < 8 \text{ s}$) brings the sample back to the former temperature ($T = 280 \text{ K} < M_f$). During cooling, the material, initially, exhibits a linear austenitic thermal contraction, until it reaches $T = M_s$ (point I). Then, it undergoes a martensitic transformation $A \Rightarrow M$ (that lasts from point I to point J depicted in the detail of Fig. 28c, finally inducing the original phase of the test: twinned martensite ($\beta_T = 1$ for $T = 285 \text{ K} = M_f$ at point J). The material exhibits a linear martensitic thermal contraction, until it recovers its original shape at $T = 280 \text{ K}$ (point A'). An analogous process occurs for the compressive behavior.

Figure 28c presents the stress–strain–temperature diagram, demonstrating the model capability for describing the SME.

4.2 Final Remarks

This section discussed the constitutive modeling of SMAs based on macroscopic thermomechanical behavior. After a brief revision about the main constitutive models of the literature, the model due to Brinson (1993) is discussed. Some numerical simulations are carried out showing its general capability to describe the general thermomechanical behavior of SMAs.

References

- R.A.A. Aguiar, M.A. Savi, P.M.C.L. Pacheco, Experimental investigation of vibration reduction using shape memory alloys. *J. Intell. Mater. Syst. Struct.* **24**(2), 247–261 (2013)
- F. Ahlhelm, R. Kaufmann, D. Ahlhelm, M.F. Ong, C. Roth, W. Reith, Carotid artery stenting using a novel self-expanding braided, nickel–titanium stent: feasibility and safety porcine trial. *Cardiovasc. Intervent. Radiol.* **32**, 1019–1027 (2009)
- V. Birman, Effect of SMA dampers on nonlinear vibrations of elastic structures, in *SPIE Proceedings, Smart Structures and Materials 1997: Mathematics and Control in Smart Structures*, vol. 3039, 1997, 9pp
- J.G. Boyd, D.C. Lagoudas, Thermodynamic constitutive model for the shape memory materials. Part I: the monolithic shape memory alloys. *Int. J. Plast.* **12**(6), 805–842 (1996)
- L.C. Brinson, One dimensional constitutive behavior of shape memory alloys: thermomechanical derivation with non-constant material functions and redefined martensite internal variable. *J. Intell. Mater. Syst. Struct.* **4**, 229–242 (1993)
- B. Carpenter, J. Lyons, EO-1 technology validation report: lightweight flexible solar array experiment, Tech. report, NASA Goddard Space Flight Center, Greenbelt, 2001
- S.B. Choi, Y.M. Han, J.H. Kim, C.C. Cheong, Force tracking of a flexible gripper featuring shape memory alloys actuators. *Mechatronics* **11**, 677–690 (2001)
- A. Czechowicz, On the functional characteristics of pseudoelastic adaptive resetting of shape memory actuators in the field of automotive applications. *J. Intell. Mater. Syst. Struct.* **24**(13), 1539–1545 (2013)
- S. Dilibal, H. Dilibal, Ituhand Robot el ve Mayin Temizleme Alanında Kullanılabilirliği, in *Savunma Teknolojileri Kongresi*, ODTÜ, Ankara, 24–25 Ekim, 2002
- T.W. Duerig, K.N. Melton, D. Stöckel, C.M. Wayman, *Engineering Aspects of Shape Memory Alloys* (Butterworth-Heinemann, London, 1990). 499p
- T.M. Duerig, A. Pelton, D. Stöckel, An overview of nitinol medical applications. *Mater. Sci. Eng. A* **273–275**, 149–160 (1999)
- A.C. Eringen, *Mechanics of Continua* (Wiley, New York, 1967)
- M.E. Gurtin, E. Fried, L. Anand, *The Mechanics and Thermodynamics of Continua* (Cambridge University Press, Cambridge, 2010)
- D.J. Hartl, D.C. Lagoudas, Aerospace applications of shape memory alloys. *Proc. Inst. Mech. Eng. Part G J. Aerosp. Eng.* **221**(4), 535–552 (2007)
- D.E. Hodgson, J.W. Brown, *Using Nitinol Alloys* (Shape Memory Applications Inc., San Jose, 2000). 44 pp
- H.Y. Jun, O.K. Rediniotis, D.C. Lagoudas, Development of a fuel-powered shape memory alloy actuator system: II. Fabrication and testing. *Smart Mater. Struct.* **16**, S95–S107 (2007)
- J.N. Kudva, C.A. Matin, L.B. Scherer, A.P. Jardine, A.R. McGowan, R.C. Lake, G. Sendechyj, B. Sander, Overview of the DARPA/AFRL/NASA smart wing program. *Smart Struct. Mater.* **3674**, 230–236 (1999)

- C.A.P.L. La Cava, E.P. Silva, L.G. Machado, P.M.C.L. Pacheco, M.A. Savi, Modeling of a shape memory preload device for bolted joints, in *Proceedings of National Congress of Mechanical Engineering (CONEM 2000—ABCM)*, Brazil (in Portuguese), 2000
- D.C. Lagoudas, *Shape Memory Alloys: Modeling and Engineering Applications* (Springer, New York, 2008)
- C. Liang, C.A. Rogers, One-dimensional thermomechanical constitutive relations for shape memory materials. *J. Intell. Mater. Syst. Struct.* **1**, 207–234 (1990)
- L.G. Machado, M.A. Savi, Odontological applications of shape memory alloys. *Rev. Bras. Odontol.* **59**(5), 302–306 (2002) (in Portuguese)
- L.G. Machado, M.A. Savi, Medical applications of shape memory alloys. *Braz. J. Med. Biol. Res.* **36**(6), 683–691 (2003)
- G.E. Mase, G.T. Mase, *Continuum Mechanics for Engineers*, 2nd edn. (CRC Press, Boca Raton, 1999)
- J. McCormick, D. Fugazza, F. Auricchio, R. DesRoches, Seismic vibration control of structures using superelastic shape memory alloy. *J. Eng. Mater. Technol.* **128**(3), 294–301 (2006)
- M. Mosley, C. Mavroidis, C. Pfeiffer, Design and dynamics of a shape memory alloy wire bundle, in *Proceedings of the ANS, 8th Topical Meeting on Robotics and Remote Systems*, Pittsburgh, April 1999
- T. Nagnuma, M. Kyo, T. Ueki, K. Takeda, J. Ishibashi, A new, automatic hydrothermal fluid sampler using a shape-memory alloy. *J. Oceanogr.* **54**(3), 241–246 (1998)
- M. Nakatani, H. Kajimoto, D. Sekiguchi, N. Kawakami, S. Tachi, 3D form display with shape memory alloy, in *13th International Conference on Artificial Reality and Telexistence*, 2003
- E.R. Oberaigner, F.D. Fischer, K. Tanaka, On the optimal damping of a vibration shape memory alloy rod. *Eng. Mater. Technol. ASME* **124**, 97–102 (2002)
- A. Paiva, M.A. Savi, An overview of constitutive models for shape memory alloys. *Math. Probl. Eng.* **2006**, 1–30 (2006). Article ID 56876
- RAYCHEM—TYCO ELECTRONIC CORPORATION, www.raychem.com captured on 04/29/2001
- O.K. Rediniotis, L.N. Wilson, D.C. Lagoudas, M.M. Khan, Development of a shape-memory-alloy actuated biomimetic hydrofoil. *J. Intell. Mater. Syst. Struct.* **13**(1), 35–49 (2002)
- D. Reynaerls, J. Peirs, H.V. Brussel, An implantable drug-deliver system based on shape memory alloy micro-actuation. *Sens. Actuators A Phys.* **61**(1–3), 455–462 (1997)
- C.A. Rogers, Intelligent materials, *Scientific American*, 1995, pp. 122–127
- K.K. Safak, G.G. Adams, Modeling and simulation of an artificial muscle and its application to biomimetic robot posture control. *Robot. Auton. Syst.* **41**, 225–243 (2002)
- M.A. Savi, A.S. De Paula, D. Lagoudas, Numerical investigation of an adaptive vibration absorber using shape memory alloys. *J. Intell. Mater. Syst. Struct.* **22**(1), 67–80 (2011)
- SINTEF, Shape memory alloys in oil well applications, <http://iku.sintef.no/Borebronn/Brosjyre/SMA/SMA.htm>, 1999
- E. Sitnikova, E. Pavlovskaja, M. Wiercigroch, M.A. Savi, Vibration reduction of the impact system by an SMA restrain: numerical studies. *Int. J. Non Linear Mech.* **45**(9), 837–849 (2009)
- K. Tanaka, S. Nagaki, Thermomechanical description of materials with internal variables in the process of phase transformation. *Ing. Archiv.* **51**, 287–299 (1982)
- B. Tiseo, A. Concilio, S. Ameduri, A. Gianvito, A shape memory alloys based tuneable dynamic vibration absorber for vibration tonal control. *J. Theor. Appl. Mech.* **48**(1), 135–153 (2010)
- H. Tobushi, N. Iwanaga, K. Tanaka, T. Hori, T. Sawada, Deformation behavior of Ni-Ti shape memory alloy subjected to variable stress and temperature. *Contin. Mech. Thermodyn.* **3**, 79–93 (1991)
- A. Tuissi, P. Bassani, R. Casati, M. Boccione, A. Collina, M. Carnevale, B. Previtali, Application of SMA composites in the collectors of the railway pantograph for the Italian high-speed train. *J. Mater. Eng. Perform.* **18**(5–6), 612–619 (2009)
- R. Vaidyanathan, H.J. Chiel, R.D. Quinn, A hydrostatic robot for marine applications. *Robot. Auton. Syst.* **30**, 103–113 (2000)

- J. van Humbeeck, Non-medical applications of shape memory alloys. *Mater. Sci. Eng. A* **273–275**, 134–148 (1999)
- K. Williams, G. Chiu, R. Bernhard, Adaptive-passive absorbers using shape-memory alloys. *J. Sound Vib.* **249**(5), 835–848 (2002)
- K. Williams, G. Chiu, R. Bernhard, Dynamic modelling of a shape memory alloy adaptive tuned vibration absorber. *J. Sound Vib.* **280**, 211–234 (2005)
- X.D. Zhang, C.A. Rogers, C. Liang, Modeling of two-way shape memory effect. *Smart Struct. Mater. ASME* **24**, 79–90 (1991)

Electro- and Magneto-Rheological Materials

**Gustavo Luiz Chagas Manhães de Abreu, Flávio Donizeti Marques,
Fabrício César Lobato de Almeida, Amarildo Tabone Paschoalini,
and Felipe Silva Bellucci**

Abstract Novel materials suitable for engineering applications are under development in a number of research centers. Among them, fluids and gels that can change their rheological properties start to grow in importance for smart structures applications. Such materials usually present changes in their properties due to action of an external field, such as electric or magnetic. It has been observed that changes may occur very fast, allowing applications in active control, for instance. There are two main classes of the so-called smart fluids, one exploiting the electro-rheological (ER) effect, and the other exploiting the magneto-rheological (MR) effect. These variable rheology fluids can have their mechanical properties modeled in terms of different behaviors of the field-dependent stress–strain curve. For the pre-yield region of the stress–strain curve the fluid behaves like a viscoelastic material, then as plastic in the post-yield region, and as viscoelastic-plastic in the transition through yield region. Considering that smart fluids exhibit linear shear behavior at small strain levels, similar to many viscoelastic materials, it is convenient to model variable rheology fluids with the same approaches developed for viscoelastically damped structures. As a study case, a sandwich beam with ER fluid core is modeled with finite element method. The dynamical behavior is assessed with the Golla-Hughes-McTavish (GHM) method to incorporate the frequency dependence properties of the ER fluid in a structural time domain model, admitting its behavior as viscoelastic and dependent on an electric field. The results are compared with analytical models and experimental data available in literature, aiming to illustrate the potential of variable rheology fluids in further smart structures concepts.

G.L.C.M. de Abreu (✉) • F.C.L. de Almeida • A.T. Paschoalini
Department of Mechanical Engineering, Faculty of Engineering of Ilha Solteira,
São Paulo State University (FEIS/UNESP), Av. Brasil, 56, Ilha Solteira, SP 15385-000, Brazil
e-mail: gustavo@dem.feis.unesp.br

F.D. Marques
Engineering School of São Carlos, University of São Paulo (EESC/USP),
São Carlos, SP, Brazil

F.S. Bellucci
University of Brasília (MCTI/UNB), Brasília, DF, Brazil

Keywords ER/MR fluids • Intelligent materials • GHM method • Viscoelastic materials

1 Introduction

To keep the dynamical responses of structures in acceptable levels some possible strategies can be used, such as adopting new materials, passive and active control techniques, and advanced design methods. Vibration suppression has been recently assessed by using the so-called concept of *smart structures*. This approach combines active materials and controllers to the structure, and it has been mainly related to advanced materials with increasing developments since the 1980s. Shape memory alloys, piezoelectric, electro- and magnetostrictive materials, optic fiber, and *variable rheology fluids/gels* are successful examples that have furnished reasonable results in a broad range of engineering applications.

The aforementioned *variable rheology fluids* are those that can change their rheological properties with growing importance for active control applications. Such materials present changes in their properties due to the action of an external field, for instance, electric or magnetic. It has been observed that these changes may occur very fast, thereby allowing applications to control systems. There are two main classes of variable rheology fluids, that is, those exploiting the electro-rheological (ER) effect, and the others exploiting the magneto-rheological (MR) effect. ER or MR fluids provide three possible arrangements: (1) flow mode, (2) shear mode, and (3) squeeze flow mode (Sims et al. 2000), although most of the demands for variable rheology fluids adopt the flow mode. This approach is particularly used for semi-active suspensions. The shear mode is more indicated to use in smart structures because it is easily integrated into the structural elements and being lesser intrusive. A natural design to get the benefits of ER/MR fluids in shear mode is employing the concept of sandwich structural elements (e.g., beam, shell, and plates). Therefore, this technique can admit ER/MR fluids restrained by layers of another elastic material (e.g., metals), which results in a more compact structural element.

The aim of this chapter is to present the basics of variable rheology materials, in particular, to the electro-rheological and magneto-rheological fluids. To extend the possibilities of such fluids in smart structures applications, a model of sandwich beam composed of two layers of isotropic material confining an ER/MR fluid is presented. The finite element method is used to develop the beam element, while the behavior of the ER/MR fluid is supposed to have equivalent properties of a viscoelastic material and modeled by *Golla-Hughes-McTavish* (GHM) approach. A study of MR elastomer characterization is also presented.

1.1 Variable Rheology Fluids

The electro- and magneto-rheological fluids are those that change their primary rheological properties and their characteristics, such as viscosity, elasticity, and plasticity, due to an electric and magnetic field applied, respectively. These materials consist of a compound of sensitive particles dispersed in a fluid (or gel) inert to the applied field. Under the application of a field (electric or magnetic), the dispersed particles align in the direction of the field, creating chains with the strength proportional to the intensity of the applied field. Those chain arrangements handle changing the material rheological properties. Figure 1 illustrates the changes in the material components due to changes in electric field.

The MR fluid was discovered in 1951 by Rabinow and consists of magnetic particles dispersed in a non-magnetic liquid. There are a wide variety of materials that may be used as the base for MR fluids, the most popular being water, silicone oil, and hydrocarbon oils. The magnetic particles are usually derived from metals like iron (Yalcintas and Dai 1999; Lord Corporation 2001).

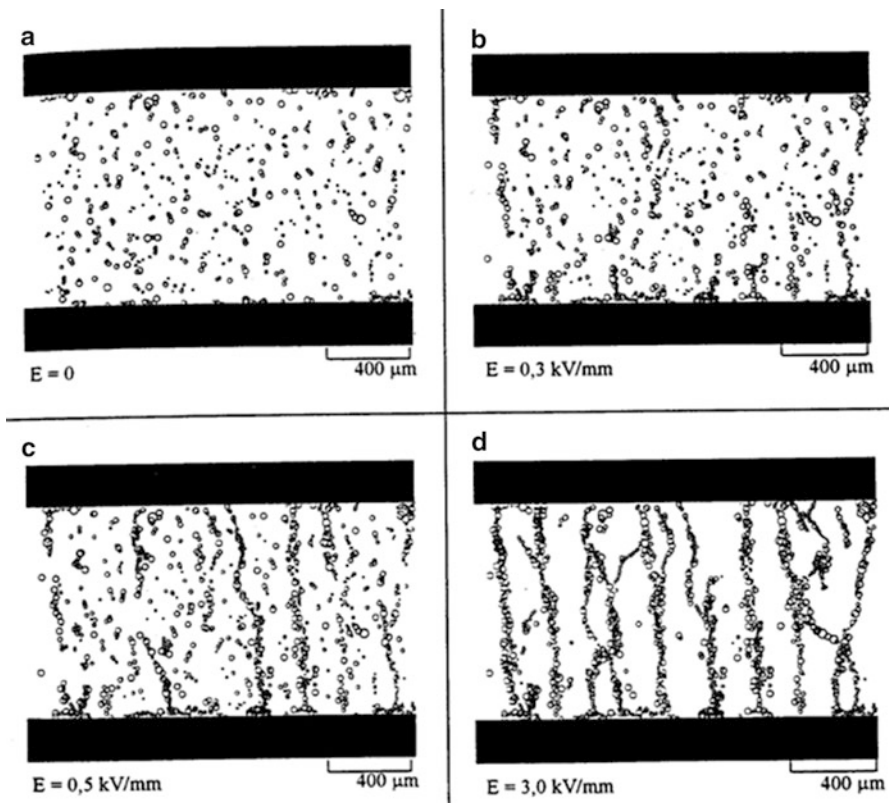


Fig. 1 Chain arrangements due to changes in electric field (Conrad et al. 1987)

ER fluids are analogous to the MR ones being first observed in 1949 by Winslow. The ER fluid comprises dielectric particles suspended in a liquid with low dielectric constant and non-conductive. These particles may be graphite, limestone, iron fillings, silica gel, and alumina, among others. The liquid base may also be a mineral oil, e.g., silicone, kerosene, and castor oil, among others (Yalcintas and Dai 1999; Li et al. 1999; Chen and Liu 1999; Vieira 1996).

Both ER/MR fluids are very similar. However, the MR fluid generates a maximum shear 20–50 times greater than ER fluids. MR fluids are also able to operate directly with small power sources, and are less sensitive to contaminants and temperature extremes. In contrast, the ER fluids have high response speed and fast relaxation (since there is residual magnetization in MR fluids). In addition to all the equipment needed for the generation of the electric field for ER applications are smaller and lighter than those used to generate the magnetic field (Lord Corporation 2001; Vieira 1996).

In the absence of a field, ER and MR fluids behave initially as liquids. When subjected to a field, both resemble as a gel. During this transformation, rheological properties also vary. ER and MR materials have different levels of stresses and deformations in particular response to various levels of electric or magnetic fields applied. These fluids follow the same type of pattern in their rheological behavior (Yalcintas and Dai 1999). Figure 2 depicts in the stress–strain plot, how typical ER/MR fluids behave with respect to the applied field. Three different types of behavior with increasing deformation of the material are: (1) the pre-yield region, (2) the yield region, and (3) the post-yield region. From the first region, it is that small deformations lead to some elasticity.

To achieve an ER/MR fluid, the first item to be considered is the type of base to be used (water, hydrocarbon oils, silicone oil, for example). If the fluid operates in a sealed environment, water is recommended, beyond what it can be doped with a variety of semiconductor particles. If the system is not sealed, and the evaporation of the liquid may be a problem, hydrocarbon oil is an adequate solution. Moreover, such oils are not hazardous materials, but they are not easy to handle. If the

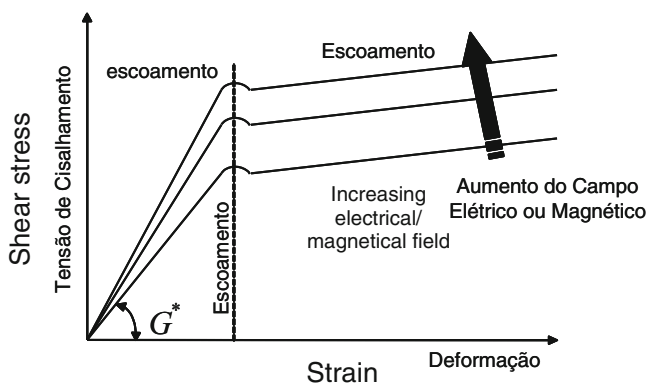


Fig. 2 Stress–strain behavior of ER/MR fluids with an applied field

operating temperature is below 40 °C and above 100 °C, the use of silicone-based fluid is indicated. However, this type of liquid is difficult to seal. The silicone-based oil operates in a temperature range between –40 and 150 °C, whereas water has an operating range between 0 and 70 °C. Also common is the use of substances surfactants to allow greater variations in the rheological properties, as well as to stabilize the material minimizing sedimentation. Typically, slightly soluble non-ionic surfactants are used (Lord Corporation 2001).

According to Leng and Asundi (1999), ER/MR can be manufactured in a variety of mixtures (fluids and solids). The following characteristics are ideally expected: (a) high boiling point, low freezing point; (b) low viscosity to maintain the fluidity when solid particles are added; (c) high dielectric constant to reduce the loss of power; (d) the overall density should be similar to the density of the particles; (e) suitable chemical stability, and cannot decompose under the conditions of operation; (f) nontoxic; (g) high point of combustion; (h) low power required; (i) non-corrosive; (j) nonabrasive; and (k) low cost.

There are three ways of applying the ER/MR fluids, as illustrated in Fig. 3. The first and most common is the *flow* mode, in which the working fluid flows through two stationary electrodes. Among possible applications using flow mode are shock absorbers, brakes, and hydraulic systems. Another way to use is known as *squeeze flow*, where the electrodes are free to move in the direction of the applied field. In this case, the fluid is subjected to tension and compression, with small displacements and large forces in a tiny space. The squeeze flow arrangement has a potential application in vibration isolation. The latter method is called as *shear* mode operation where a relative motion between the electrodes (translation or rotation) is allowed, which generates shear in the ER/MR fluid. An adequate application of this type of operation arrangement is a sandwich structure, where ER/MR fluid could be restricted by two elastic layers (Sims et al. 2000).

Research involving variable rheology fluids began to attract attention from the second half of the 1980s and early 1990s. Initially, these studies were based on modeling of rheological properties, characterization of new compounds, and seeking for materials with stable and sufficiently powerful rheological fluid properties. There have also been studies to identify applications, such as brakes, clutches, shock absorbers, and dampers. Much of the research involving ER/MR fluids has focused on active dampers (Wu and Griffin 1997; Sims et al. 2000; Choi and Kim

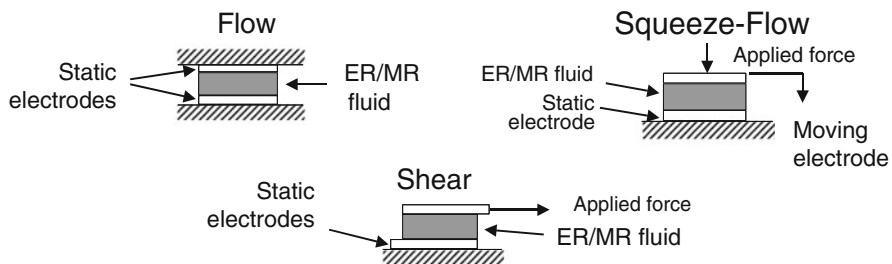


Fig. 3 Operating arrangements for ER/MR fluids

2000; Yao et al. 1999; Chen and Liu 1999; Wang et al. 1994), with some studies on beams for active control (Yalcintas and Dai 1999; Aboudi 1999; Leng and Asundi 1999; Yalcintas et al. 1995; Yalcintas and Coulter 1998; Leng et al. 1997; Choi et al. 1995; Rahn and Joshi 1998). Although admitting similar principles, these two study trends require different mathematical models, which implies the proper characterization of the materials used in each case.

ER/MR fluids are a good alternative when the question concerns actuators. Their employment as sensors proves to be impracticable, only possible by applying the joint use of other active elements such as PVDF films or optical fibers. From the evidence shown in the applications in dampers and active beams, the ER/MR fluids can be used to control the structural response by varying the respective field (electric or magnetic).

1.2 Sandwich Beams of ER/MR Fluids

Sandwich beams comprise layers of different materials. The most typical sandwich arrangement is done by two external layers of elastic materials with a core of viscoelastic material in between. The use of these devices in structural systems to reduce the effects of vibration and noise is well known and its mechanism of attenuation is based on energy dissipation by cyclic shear in the core layer. The great benefit of these beams is to reduce the resonance peaks (damping effect) without significantly altering the mass or structural rigidity (Balamurugan and Narayanan 2002).

In the late 1980s and early 1990s research began to emerge suggesting the use of sandwich beams with ER fluids in the core (Gandhi et al. 1989; Coulter and Duclos 1989; Choi et al. 1990, 1992). These early studies attempted to demonstrate with experiments that by changing the applied electric field, a change in the structural damping and natural frequencies is observed. In these experiments, a number of ER fluids, beam geometries, and excitation conditions were tried, and the effect of varying field on the beams dynamics were confirmed.

Earlier investigated as a passive solution in reducing the vibrational response of structures, the sandwich beams were first studied in the 1950s. These studies resulted in an analytical model that became known as RKU model (as a reference for the developers *Ross-Kerwin-Ungar*) (Kerwin 1959; Ross et al. 1959; Ungar and Kerwin 1962). This model considers a simply supported beam with its intermediate layer having a negligible stiffness compared to the outer layers and damping due to shear in this core layer. This modeling involves fourth-order differential equations for a simple Euler-Bernoulli beam and introduces the concept of complex damped flexural modulus for composite structures. Later, Ditaranto (1965) has extended the RKU model for various boundary conditions for free vibrations. Mead and Markus (1969) have presented a new development for the RKU model, where a sixth-order differential equation was admitted to encompass the vibration analysis for various boundary conditions. The work by Mead and Markus (1969) has served as the

starting point for the mathematical modeling of fluid sandwich beams with ER/MR fluid core conducted by Yalcintas et al. (1995) and Yalcintas and Coulter (1998). Another way of expressing the dynamic behavior of sandwich beams is using the energy method based on the principle of Hamilton. This type of modeling can be found in works by Rahn and Joshi (1998) and Yalcintas and Dai (1999). Nonetheless, these sandwich beam models are not able to incorporate the dependency of the ER/MR materials to the frequency, temperature, amplitude, and excitation type. In the works by Lee (1995) and Lee and Cheng (1998), the dependence of the amplitude has been incorporated to the sandwich beams with ER/MR fluid core.

Some other works present frequency dependence. However, these do not allow the modeling of more complex dynamic behaviors. The need for models that incorporate viscoelastic hysteresis or frequency dependence have motivated a considerable number of research work. The first works presented in the 1980s bring the idea of a complex modulus. Previous approaches consider only the real part as variable, and then the investigations extended to both varying real and imaginary parts (storage modulus and dissipation module, respectively). The complex modulus is associated with the concept of Modal Strain Energy (MSE) establishing the mode to mode dissipation factors approach. This method is well known for acceptable approximation of small viscoelastic damping (Trindade and Benjeddou 2002).

Several ways in the time domain have been explored to represent the frequency dependence of the linear viscoelastic theory. Lesieutre and colleagues (Lesieutre 1992; Lesieutre and Mingori 1990) have proposed a method denoted as Augmenting Thermodynamic Fields (ATF) that have introduced dissipation coordinates. Initially limited to one-dimensional case, the approach has been extended to the three-dimensional case (Lesieutre and Bianchini 1995; Lesieutre and Lee 1996) which has been named Anelastic Displacement Field (ADF) method.

Another method developed with very similar characteristics to the ADF model is the so-called Golla-Hughes-McTavish (GHM) model (Golla and Hughes 1985; McTavish and Hughes 1993) which also uses dissipative coordinates.

Both the GHM and the ATF/ADF models have advantages over the MSE model since they are in the time domain formulation. For them, the elastic and dissipative structural behaviors are represented in a system of fixed matrices. Damping factors are calculated with modal frequencies without iteration, and the resulting modes reflect the relative phase at various points. The modal orthogonality is preserved (Lesieutre and Bianchini 1995). Therefore, these models may allow accurate modeling of a structure with viscoelastic behavior, such as the ER/MR materials. Other studies on the identification of viscoelastic characteristics that can be used to ER/MR fluids modeling are referred to Mahjoob et al. (1995). They have used an analysis of the inverse problem. Choi and Park (1994) and Phani and Venkatraman (2003) have designed controllers based on experimental data within the same context.

2 Mathematical Model

The mathematical modeling of a sandwich beam with an ER fluid core via the finite element method is considered. As a starting point the following assumptions are considered: (1) the beam geometry is constant along the length of the beam, (2) the core material is isotropic and of much greater thickness than the face sheets, (3) the shear strain is constant through the core and negligible in the face sheets, (4) the longitudinal displacements of the face sheets are uniform through the thickness of the face sheets, and (5) the transverse displacement does not vary through the thickness of core material and is small relative to the beam length.

Admitting the application of the principle of Hamilton, that is,

$$\delta \int_{t_1}^{t_2} (T - V) dt + \int_{t_1}^{t_2} \delta W dt = 0, \quad (1)$$

where T , V , and δW are, respectively, the kinetic, potential (electro-mechanical coupling) energies and the virtual work of non-conservative loads.

The kinetic energy T for a beam can be expressed as:

$$T = \frac{1}{2} \int_V \{ (\rho_1 A_1 + \rho_2 A_2 + \rho_3 A_3) \dot{w}^2 + \rho_1 A_1 \dot{u}_1^2 + \rho_3 A_3 \dot{u}_3^2 \} dx, \quad (2)$$

where the subscript indicates the layer, ρ is mass density, w is the transverse displacement along the y -axis, and u is the translation of the neutral axis along the x -axis direction.

The potential energy formulation includes the bending in the faces, the shear in the ER material, and the extensional energy.

$$V_b = \frac{1}{2} (E_1 I_1 + E_3 I_3) \int_0^L \left(\frac{\partial^2 w}{\partial x^2} \right)^2 dx, \quad (3)$$

$$V_a = \frac{1}{2} E_1 A_1 \int_0^L \left(\frac{\partial u_1}{\partial x} \right)^2 dx + \frac{1}{2} E_3 A_3 \int_0^L \left(\frac{\partial u_3}{\partial x} \right)^2 dx, \quad (4)$$

$$V_s = \frac{1}{2} G^* A_2 \int_0^L \gamma^2 dx, \quad (5)$$

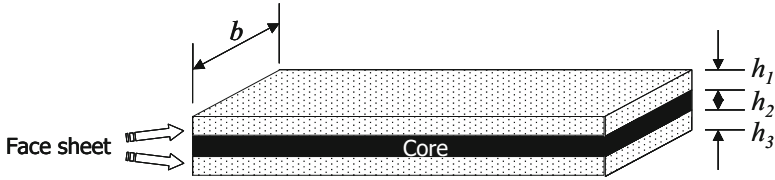
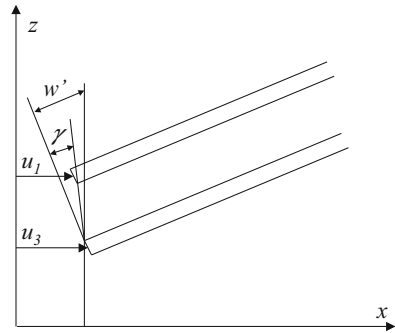


Fig. 4 Schematics of a sandwich beam

Fig. 5 Geometry and deformation of the sandwich beam



where E , G^* , γ , I , and A are, respectively, the Young’s modulus of the face sheets, the shear modulus of the ER material, the shear strain of the viscoelastic shear layer, the moment of inertia, and the area of the cross section.

Axial displacements are assumed to be linear through the thickness, whereas transverse ones are supposed constant. The geometry and deformation of the sandwich beam are shown in Figs. 4 and 5.

The relation for the shear strain is based on the axial and transverse displacements, that is,

$$\gamma = \frac{1}{h_2} \left[u_1 - u_3 + \left(\frac{h_1 + 2h_2 + h_3}{2} \right) \frac{\partial w}{\partial x} \right], \tag{6}$$

where h_i is the thickness of the i th layer.

2.1 Finite Element Discretization

The finite element (FE) method is essentially a process through which a continuum with infinite degrees of freedom can be approximated by an assemblage of sub-regions (or elements) each with a specified but now finite number of unknowns.

Further, each such element interconnects with others in a way familiar to engineers dealing with discrete structural or electrical assemblies. The assumed mechanical degrees of freedom $[u_j u_3 w \theta]^T$ are, respectively, the axial and vertical displacements, and the rotation around the y -axis. The model developed here is based on Nagamine et al. (2005) and Nagamine (2006).

For the k th element the corresponding generalized displacement vector $\{\mathbf{q}_k\}$ can be assembled, which allows the determination of the discrete form of the displacements and rotation at the node i and j , that is:

$$\mathbf{q}_k = [u_{1i} \quad u_{3i} \quad w_i \quad \theta_i \quad u_{1j} \quad u_{3j} \quad w_j \quad \theta_j]^T. \quad (7)$$

This discretization procedure is achieved by using the shape functions \mathbf{N}_{u_1} , \mathbf{N}_{u_3} , \mathbf{N}_w , and \mathbf{B}_w , which relates the continuum displacements to discrete ones

$$\begin{aligned} u_{1i} &= \mathbf{N}_{u_1} \mathbf{q}_i \\ u_{3i} &= \mathbf{N}_{u_3} \mathbf{q}_i \\ w_i &= \mathbf{N}_w \mathbf{q}_i \\ \theta_i &= \frac{dw_i}{dx} = \frac{d\mathbf{N}_w}{dx} = \mathbf{B}_w \mathbf{q}_i. \end{aligned} \quad (8)$$

Taking into account the Lagrange linear shape functions for the axial displacement and a cubic Hermitian functions for the transverse displacement, then,

$$\mathbf{N}_{u_1} = [1 - x/L \quad 0 \quad 0 \quad 0 \quad x/L \quad 0 \quad 0 \quad 0], \quad (9)$$

$$\mathbf{N}_{u_3} = [0 \quad 1 - x/L \quad 0 \quad 0 \quad 0 \quad x/L \quad 0 \quad 0], \quad (10)$$

$$\mathbf{N}_w = \left[0 \quad 0 \quad 1 - \frac{3x^2}{L^2} + \frac{2x^3}{L^3} \quad x\left(1 - \frac{x}{L}\right)^2 \quad 0 \quad 0 \quad \frac{x^2}{L^2} \left(3 - \frac{2x}{L}\right) \frac{x^2}{L} \left(\frac{x}{L} - 1\right) \right]. \quad (11)$$

Rewriting Eqs. (2), (3), (4), and (5) into variational formulation and taking into account the generalized coordinate shown in Eq. (8) and a relation for γ in Eq. (6):

$$\begin{aligned} \delta T &= \rho_1 A_1 \int_0^L \delta \ddot{\mathbf{q}}^T \mathbf{N}_{u_1}^T \mathbf{N}_{u_1} \ddot{\mathbf{q}} dx + \rho_3 A_3 \int_0^L \delta \ddot{\mathbf{q}}^T \mathbf{N}_{u_3}^T \mathbf{N}_{u_3} \ddot{\mathbf{q}} dx \rho_3 A_3 + \dots \\ &+ (\rho_1 A_1 + \rho_2 A_2 + \rho_3 A_3) \int_0^L \delta \ddot{\mathbf{q}}^T \mathbf{N}_w^T \mathbf{N}_w \ddot{\mathbf{q}} dx, \end{aligned} \quad (12)$$

$$\delta V_b = (E_1 I_1 + E_3 I_3) \int_0^L \delta \mathbf{q}^T \mathbf{B}'_w{}^T \mathbf{B}'_w \mathbf{q} dx, \quad (13)$$

$$\delta V_a = E_1 A_1 \int_0^L \delta \mathbf{q}^T \mathbf{B}'_{u1}{}^T \mathbf{B}'_{u1} \mathbf{q} dx + E_3 A_3 \int_0^L \delta \mathbf{q}^T \mathbf{B}'_{u3}{}^T \mathbf{B}'_{u3} \mathbf{q} dx, \quad (14)$$

$$\delta V_s = G^* A_2 \int_0^L \delta \mathbf{q}^T \mathbf{B}'_\gamma{}^T \mathbf{B}'_\gamma \mathbf{q} dx. \quad (15)$$

The kinetic energy in a variational form can be written as:

$$\delta T = \delta \ddot{\mathbf{q}}^T (\mathbf{M}_b + \mathbf{M}_a) \ddot{\mathbf{q}}, \quad (16)$$

where \mathbf{M} is the mass matrix and the subscripts a and b are related to a axial and transverse movement, respectively,

$$\mathbf{M}_a = \rho_1 A_1 \int_0^L \mathbf{N}_{u1}{}^T \mathbf{N}_{u1} dx + \rho_3 A_3 \int_0^L \mathbf{N}_{u3}{}^T \mathbf{N}_{u3} dx, \quad (17)$$

$$\mathbf{M}_b = (\rho_1 A_1 + \rho_2 A_2 + \rho_3 A_3) \int_0^L \mathbf{N}_w{}^T \mathbf{N}_w dx. \quad (18)$$

Similarly the potential energy can be expressed in a variational form like,

$$\delta V = \delta \mathbf{q}^T (\mathbf{K}_b + \mathbf{K}_a + \mathbf{K}_s) \mathbf{q}, \quad (19)$$

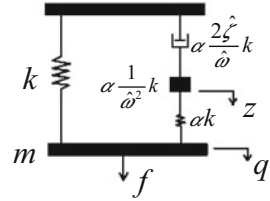
where \mathbf{K} is the stiffness matrix, and the subscript s is related to shear energy, that is,

$$\mathbf{K}_b = (E_1 I_1 + E_3 I_3) \int_0^L \mathbf{B}'_w{}^T \mathbf{B}'_w dx, \quad (20)$$

$$\mathbf{K}_a = E_1 A_1 \int_0^L \mathbf{B}'_{u1}{}^T \mathbf{B}'_{u1} dx + E_3 A_3 \int_0^L \mathbf{B}'_{u3}{}^T \mathbf{B}'_{u3} dx, \quad (21)$$

$$\mathbf{K}_s = G^* A_2 \int_0^L \mathbf{B}'_\gamma{}^T \mathbf{B}'_\gamma dx. \quad (22)$$

Fig. 6 Mini-oscillator



2.2 The GHM Model of Material Properties

In the theory of linear viscoelasticity for one-dimensional structures the constitutive relation stress–strain can be represented by:

$$\sigma(t) = G(t)\epsilon(0) + \int_0^t G(t - \tau) \frac{d\epsilon(\tau)}{d\tau} d\tau, \tag{23}$$

where $G(t)$ is the relaxation function of the viscoelastic material (the stress response to a unit step input).

This stress relaxation related to $G(t)$ represents the energy loss from the material. Hence it is associated with damping (Balamurugan and Narayanan 2002).

The Golla-Hughes-McTavish (GHM) method (McTavish and Hughes 1993; Golla and Hughes 1985) represents the material modulus as a series of mini-oscillator terms or internal variables as illustrated in Fig. 6.

The GHM method was developed to allow its incorporation into the finite element representation. The material complex modulus can be written in the Laplace domain in the form,

$$s\tilde{G}(s) = G^\infty \left[1 + \sum_k \alpha_k \frac{s^2 + 2\hat{\zeta}_k \hat{\omega}_k s}{s^2 + 2\hat{\zeta}_k \hat{\omega}_k s + \hat{\omega}_k^2} \right], \tag{24}$$

where the factor G^∞ corresponds to the equilibrium value of the modulus (the final value of the relaxation function $G(t)$), each mini-oscillator term is a second-order rational function involving three positive constants ($\alpha_k, \hat{\zeta}_k, \hat{\omega}_k$).

These constants govern the shape of the modulus function over the complex s -plane. Depending on the nature of the material modulus function and the range of s over which it is to be modeled, any number of mini-oscillator terms may be used in the GHM expression. Considering the elementary mass-spring system with an applied force, with an elastic spring the motion of the system is described by the second-order equation of motion,

$$m\ddot{q}(t) + kq(t) = f(t). \tag{25}$$

Now, if the spring behaves as viscoelastic, described by relaxation function $k(t)$, then,

$$m\ddot{q}(t) + \int_0^t k(t-\tau)\dot{q}(\tau)d\tau = f(t). \quad (26)$$

Initial conditions have been assumed to be zero for convenience. The material modulus function of $k(t)$ is now modeled by a single-term GHM expression, leading to,

$$s^2 m\tilde{q}(s) + k \left[1 + \alpha \frac{s^2 + 2\hat{\zeta}\hat{\omega}s}{s^2 + 2\hat{\zeta}\hat{\omega}s + \hat{\omega}^2} \right] \tilde{q}(s) = \tilde{f}(s). \quad (27)$$

Now, an auxiliary coordinate z is introduced, so that,

$$\tilde{z}(s) \frac{\hat{\omega}^2}{s^2 + 2\hat{\zeta}\hat{\omega}s + \hat{\omega}^2} \tilde{q}(s). \quad (28)$$

Using this new dissipation coordinate, the Laplace transformed equation of motion may be written as two coupled second-order equations:

$$\begin{aligned} s^2 m\tilde{q} + (k + \alpha k)\tilde{q} - \alpha k\tilde{z} &= \tilde{f} \\ s^2 \tilde{z} + 2\hat{\zeta}\hat{\omega}s\tilde{z} - \alpha k\tilde{z} - \hat{\omega}\tilde{q} + \hat{\omega}^2 \tilde{z} &= 0. \end{aligned} \quad (29)$$

2.3 GHM Viscoelastic Finite Element Matrices

Multiplying the second equation from Eq. (29) by $\alpha k/\hat{\omega}^2$, the resulting system of equations has a symmetric matrix second-order time-domain realization, that is,

$$\begin{bmatrix} \mathbf{M} & 0 \\ 0 & \alpha \frac{1}{\hat{\omega}^2} \mathbf{K} \end{bmatrix} \begin{bmatrix} \ddot{\mathbf{q}} \\ \ddot{\mathbf{z}} \end{bmatrix} + \begin{bmatrix} 0 & 0 \\ 0 & \alpha \frac{2\hat{\zeta}}{\hat{\omega}} \mathbf{K} \end{bmatrix} \begin{bmatrix} \dot{\mathbf{q}} \\ \dot{\mathbf{z}} \end{bmatrix} + \begin{bmatrix} \mathbf{K}(1 + \alpha) & -\alpha \mathbf{K} \\ -\alpha \mathbf{K} & \alpha \mathbf{K} \end{bmatrix} \begin{bmatrix} \mathbf{q} \\ \mathbf{z} \end{bmatrix} = \begin{bmatrix} \mathbf{f} \\ 0 \end{bmatrix}. \quad (30)$$

Since the elastic element stiffness matrix \mathbf{K} is usually positive semi-definite (one or more eigenvalues representing rigid body motion), the mass matrix in this formulation will not usually be positive definite. To overcome this situation, spectral decomposition of the elastic stiffness matrix \mathbf{K} is used, therefore,

$$\mathbf{K} = G^\infty \bar{\mathbf{K}} = G^\infty \bar{\mathbf{R}} \bar{\Lambda} \bar{\mathbf{R}}^T, \quad (31)$$

where $\bar{\Lambda}$ is a diagonal matrix of the nonzero (necessarily positive) eigenvalues k_p , and the corresponding orthonormalized eigenvectors \mathbf{r}_p form the columns of the matrix \mathbf{R} , therefore,

$$\bar{\Lambda} = \text{diag}\{k_p\}, \quad \bar{\mathbf{R}} = \text{row}(\mathbf{r}_p), \quad \bar{\mathbf{R}}^T \bar{\mathbf{R}} = \mathbf{1}, \quad (32)$$

such that,

$$\bar{\mathbf{K}}\mathbf{r}_p = \mathbf{r}_p k_p, \quad k_p > 0. \quad (33)$$

To achieve the objective of fewest dissipation coordinates as possible and a positive definite viscoelastic mass matrix, the equilibrium modulus G can be associated into the diagonal eigenvalue matrix $\bar{\Lambda}$, i.e., $\Lambda = G^\infty \bar{\Lambda}$, which results in,

$$\mathbf{z} = \mathbf{R}^T \hat{\mathbf{z}} \quad \text{and} \quad \mathbf{R} = \bar{\mathbf{R}}\Lambda. \quad (34)$$

The final set of equations of motion results in,

$$\mathbf{M}_v \begin{bmatrix} \ddot{\mathbf{q}} \\ \ddot{\mathbf{z}} \end{bmatrix} + \mathbf{D}_v + \begin{bmatrix} \dot{\mathbf{q}} \\ \dot{\mathbf{z}} \end{bmatrix} + \mathbf{K}_v \begin{bmatrix} \mathbf{q} \\ \mathbf{z} \end{bmatrix} = \begin{bmatrix} \mathbf{f} \\ 0 \end{bmatrix}, \quad (35)$$

where the viscoelastic matrices are

$$\mathbf{M}_v = \begin{bmatrix} \mathbf{M} & 0 \\ 0 & \alpha \frac{1}{\hat{\omega}^2} \Lambda \end{bmatrix} \quad \mathbf{D}_v = \begin{bmatrix} 0 & 0 \\ 0 & \alpha \frac{2\hat{\zeta}}{\hat{\omega}} \Lambda \end{bmatrix} \quad \mathbf{K}_v = \begin{bmatrix} \mathbf{K}(1 + \alpha) & -\alpha \mathbf{R} \\ -\alpha \mathbf{R} & \alpha \Lambda \end{bmatrix}. \quad (36)$$

These finite element matrices have the symmetry and definiteness properties desired for a standard second-order structural dynamics model,

$$\mathbf{M}_v^T = \mathbf{M}_v > 0, \quad \mathbf{D}_v^T = \mathbf{D}_v, \quad \mathbf{K}_v^T = \mathbf{K}_v. \quad (37)$$

3 GHM Fe Model of a Sandwich Beam

To verify the performance of the GHM FE model for a sandwich beam with ER fluid, comparisons with experimental and numerical results found in the literature are presented. The first verification has been carried out in terms of verifying the current/GHM FE model for the case of a free rod in a longitudinal vibration and a cantilever rod according to Golla and Hughes (1985). The viscoelastic properties of the rod have been modeled with four mini-oscillator, and the non-dimensionalized parameters are presented in Table 1 and the results obtained for a longitudinal vibration in Table 2 and for transverse vibration in Table 3.

Table 1 Mini-oscillator non-dimensionalized properties

<i>Mini oscillator</i>	α	$2\hat{\zeta}\hat{\omega}$	$\hat{\omega}^2$
1	3.0×10^{-2}	4.16×10^{-1}	3.16×10^{-2}
2	3.0×10^{-2}	4.16	3.16
3	3.0×10^{-2}	4.16×10^1	3.16×10^2
4	3.0×10^{-2}	4.16×10^2	3.16×10^4

Table 2 Non-dimensionalized frequency and damping for elastic and viscoelastic FEM in a longitudinal vibration

<i>Mode</i>			Viscoelastic FEM			
	Elastic PDE	Elastic FEM	Frequency	Damping	Frequency	Damping
	(Golla and Hughes 1985)	(Golla and Hughes 1985)	(Golla and Hughes 1985)	(Golla and Hughes 1985)	Present	Present
1	0	0	0	0	0	0
2	3.14	3.22	3.33	8.55×10^{-3}	3.33	8.55×10^{-3}
3	6.28	6.93	7.19	1.01×10^{-2}	7.19	1.01×10^{-2}
4	9.42	11.26	11.73	1.02×10^{-2}	11.73	1.02×10^{-2}
5	12.57	13.85	14.46	9.71×10^{-3}	14.46	9.71×10^{-3}

Table 3 Non-dimensionalized frequency and damping for elastic and viscoelastic FEM in a transverse vibration

<i>Mode</i>			Viscoelastic FEM			
	Elastic PDE	Elastic FEM	Frequency	Damping	Frequency	Damping
	(Golla and Hughes 1985)	(Golla and Hughes 1985)	(Golla and Hughes 1985)	(Golla and Hughes 1985)	Present	Present
1	3.52	3.52	3.63	8.60×10^{-3}	3.63	8.60×10^{-3}
2	2.20×10^1	2.21×10^1	2.31×10^1	8.27×10^{-3}	2.31×10^1	8.27×10^{-3}
3	6.17×10^1	6.22×10^1	6.53×10^1	8.42×10^{-3}	6.53×10^1	8.42×10^{-3}
4	1.21×10^2	1.23×10^2	1.30×10^2	7.46×10^{-3}	1.30×10^2	7.46×10^{-3}
5	2.00×10^2	2.28×10^2	2.42×10^2	3.94×10^{-3}	2.42×10^2	3.94×10^{-3}

A second verification has been performed based on experimental results published by Lam (1997). In this experiment a free-free sandwich beam with aluminum face sheets constraining the core of ISD 112 viscoelastic material. Sheets have dimensions of 0.381 m in length, 0.0381 m in wide, and 0.0032 m in thick. The physical properties are assumed as 70 GPa for stiffness and 2700 kg/m³ for mass density. The core is made from the viscoelastic ISD 112 10 mil (0.381 × 0.0381 × 0.000254 m and G[∞] = 5 × 10⁴), which leads to GHM model parameters as those in Table 4.

The sandwich beam dynamics is assessed through an impact hammer and accelerometer. The measurement and impact points are located at the beam. Figure 7 presents an illustration of the test performed by Lam (1997).

Table 4 Parameters for ISD 112 GHM FE model

<i>Mini oscillator</i>	$\hat{\alpha}$	$\hat{\zeta}$	$\hat{\omega}$
1	9.6	73.4	1×10^4
2	99.1	1.1	5×10^4
3	26.2	3.28	0.5×10^4

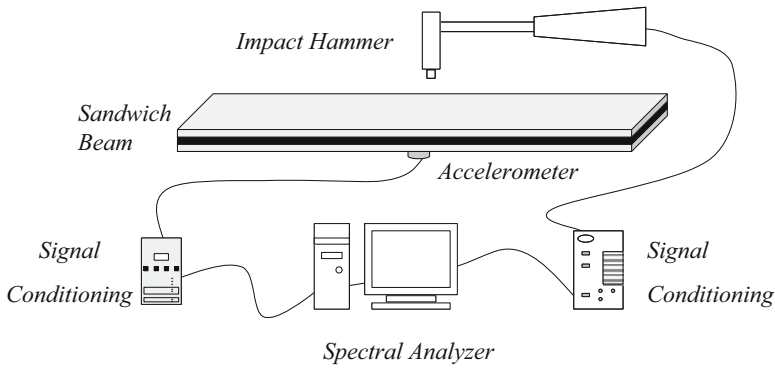


Fig. 7 Setup for the experiment (Lam 1997)

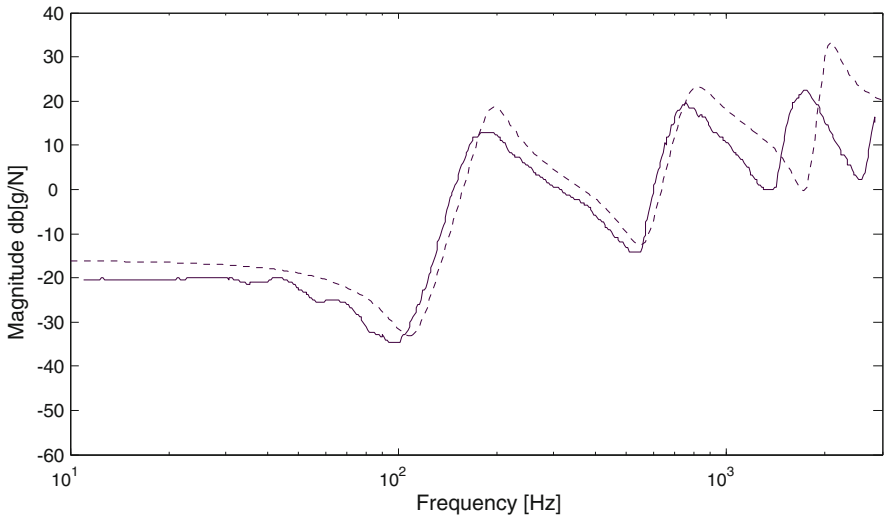
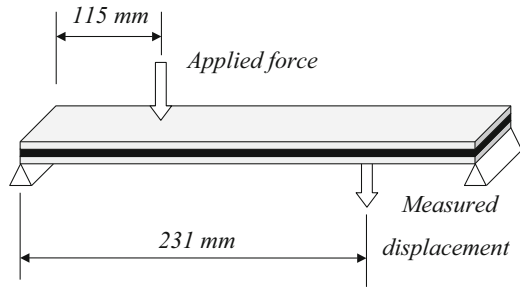


Fig. 8 Lam (1997) experiment (*solid line*) and the present GHM FE model (*dashed line*)

Lam (1997) experimental results comprise frequency response functions. The present GHM FE model has been used to predict the frequency response function (FRF) in the same conditions as in the work by Lam (1997). Figure 8 shows a comparison between Lam (1997) and the present GHM FE model FRFs. The result

Fig. 9 Experimental setup for sandwiched beam with ER fluid core (Yalcintas and Dai 1999)



indicates how adequate is the current GHM FE model in assessing the dynamic characteristics of the sandwich beam. The measurement and excitation points are in a modal node of the beam. Therefore the even modes have been lost from both experimental and numerical prediction.

After verifying the effectiveness of the GHM FE model for typical sandwich beam with conventional viscoelastic cores, now a sandwich beam with an ER fluid is considered. The experimental data from Yalcintas and Dai (1999) has been used to verify the GHM FE model. Figure 9 depicts the experimental setup under consideration. The test sandwich beam has 381 mm in length and 25.4 mm in width and mass density of 2700 kg m^{-3} and stiffness of 70 GPa . The elastic upper and lower plate material is aluminum at a thickness of 0.79 mm and the ER fluid layer has been confined to a 0.50 mm thickness, with mass density of 1700 kg m^{-3} . The test has been done using a simple support configuration and applied voltage of 3.5 kV mm^{-1} . The excitation force is applied at 115 mm from a reference support, and the transverse vibration response is measured at 231 mm from the same reference. The GHM FE model has the following parameters: $\alpha = 1$, $\hat{\zeta} = 5000$, $\hat{\omega} = 4$, and $G^\infty = 0.4 \times 10^6$.

The results have been obtained using ten elements, four physical variables, and three dissipation coordinates per node. Figure 10 presents the comparison between FRFs from experimental and GHM FE model. They present adequate agreement, which allows inferring that the numerical model represents a real potential to model sandwich beams with variable rheology fluids core. This result has been carried out considering only one mini-oscillator for the GHM FE model, which is a good feature towards a reduced number of extra dissipation coordinates. Modeling with GHM FE still needs better representation of the ER/MR fluids behavior. This issue is one of the major challenges in the development of this kind of active material.

4 Variable Magnetorheological Elastomers: Application and Characterization

Magnetorheological materials (MR) are smart materials that consist of micron-sized or nano-sized magnetizable particles embedded in a non-magnetic medium. Furthermore, different types of MRs are available, such as fluids, elastomers, foam,

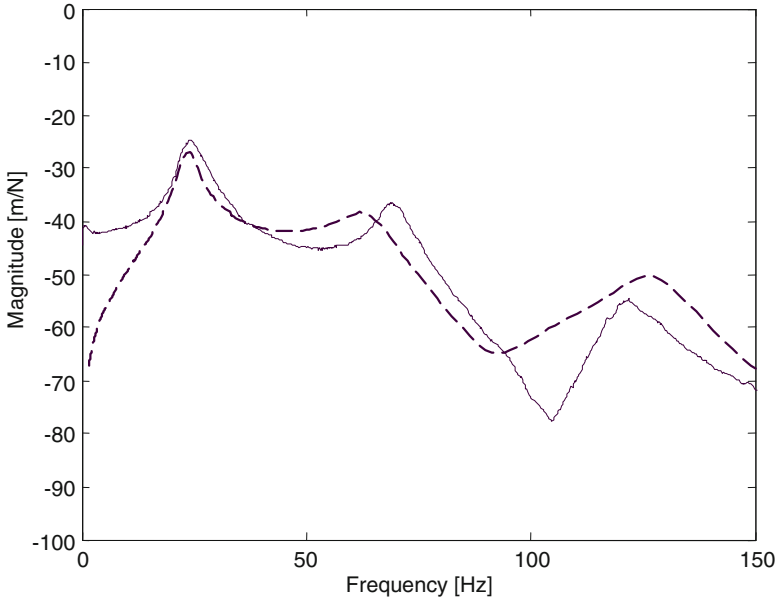


Fig. 10 Yalcintas and Dai (1999) experiment (*solid line*) and the GHM FE model (*dashed line*) FRFs comparison

and gel. An introduction to magnetorheological fluids (MRF) was covered in the previous sections. However, in this section a brief introduction to magnetorheological elastomers (MRE) and its application will be made. Although the modeling approach is not concerned in this section, information about this topic can be found in Jolly et al. (1996), Davis (1999), and Li and Sun (2014).

Magnetorheological elastomers (MRE) are a type of smart materials that consist of a non-magnetic elastomer matrix, such as rubber, mixed with micron-sized or nano-sized magnetizable particles. The elastomer is cured in a magnetic field causing the magnetic particles to align in chains and remain aligned after the magnetic field is removed. A continuous and reversible change of the mechanical properties of the elastomer can be achieved by applying an external magnetic field (Carlson and Jolly 2000; Shiga et al. 1995; Fuchs et al. 2004). These materials have been developed from magneto-rheological fluids (MRF) that were initially developed by Jacob Rabinow (Carlson and Jolly 2000) in the 1940s. Although MRFs have been used in several application including clutches, dampers, and vibration absorbers (Li and Du 2003; Jung et al. 2003; Brigley et al. 2007; Hirunyapruk et al. 2010), they have some disadvantages in that the particles in the fluid tend to collect as sediment, which means that the fluids require agitation to prevent this phenomenon. Moreover, the MRFs need to be storage and well sealed to avoid leakage, so that the effectiveness of the device is not affected by its application (Behrooz et al. 2014). MREs do not suffer from these problems as the magnetizable

particles are fixed within a solid non-magnetic matrix (elastomer). These materials can be anisotropic or isotropic, depending on whether the iron particles within the rubber have been aligned by a magnetic field during vulcanization. Although anisotropic MREs usually display higher MR effects, they are more difficult and expensive to manufacture (Fuchs et al. 2004).

MREs are useful as vibration control elements as they have a variable stiffness that can be changed in real time. There are two main applications in this field that is the adaptive tuned vibration absorbers (TVAs), and the stiffness tuneable mounts or suspensions (Ginder et al. 2001; Albanese and Cunefare 2003; Deng et al. 2006; Sun et al. 2007; Hoang et al. 2009). Silicon and rubber are used as a matrix for MREs. However, the mechanical properties of silicon are affected by heat and are approximately one-tenth of those of natural rubber (Jeong et al. 2013). Hence, rubber-based RMEs are extensively used in mechanical applications, such as automotive industry, where the temperature is an issue of concern. In this field, Jeong et al. (2013) developed a magnetorheological elastomer-based stiffness-variable differential mount to reduce the vibration propagated from the engine to the body of the car via the propeller shaft. Hoang et al. (2009) developed a torsional adaptive tunable vibration absorber (ATVA) using MRE for vibration attenuation of a power train test rig. Lee (2014) designed and developed an active damping system based on MRE for reducing vibration and noise in washing machines.

As observed MREs have been applied to some practical problems in the engineering field. However, before using such materials in practice, they have to be developed and characterized first. This procedure ensures that MREs can achieve required characteristics, for instance, the amount of change in the mechanical properties when an external magnetic field is applied to it. The manufacturing process together with how the mechanical and dynamic properties can be measured will be covered in the next two sections.

4.1 Morphological Magnetic and Mechanical Characterizations of Magnetic Particles and MRE

Magnetic materials are widely used in the industrial sector. The aims are innovative applications (e.g., magnetic composites based on natural rubber), and also the enhancement of already consolidated applications (e.g., the use of magnetic particles in cores of transformers and electronic devices). The preparation of structured materials, powders, and ceramic particles in micrometric and nanometric scales needs refined forms of processing to obtain materials on an adequate dimensional scale and desired magnetic properties. Currently, it is known that it is possible to architect, design, estimate, and add specific characteristics or properties to materials through the use of specific preparation routes. The preparation methods of magnetic ceramic materials are classified in physical and chemical routes.

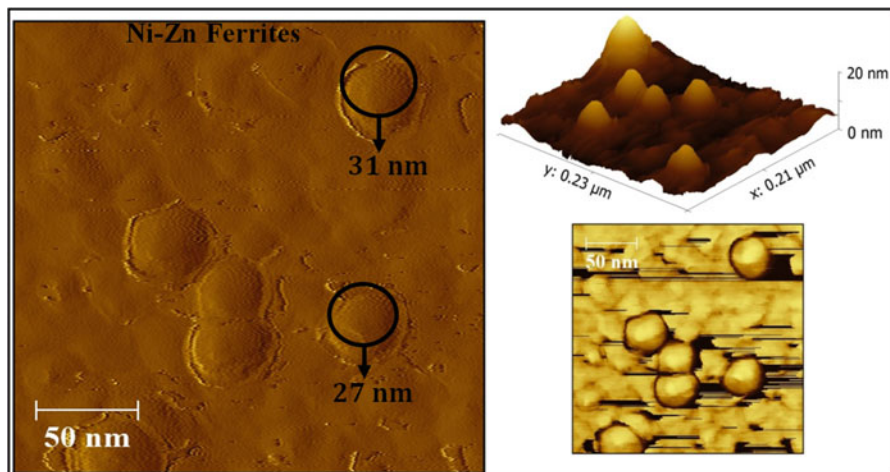


Fig. 11 Ni-Zn ferrite nanoparticles calcined at 450 °C viewing from AFM photomicrograph. On the right-hand side, details about the geometry and profile of the nanoparticles

In the context of magnetic ceramics, Ni-Zn ferrite (NZF) awakens much interest of the scientific community for its high permeability and high resistivity. Figure 11 shows the morphological characterization of the Ni-Zn ferrite nanopowders, calcined at 450 °C, by Atomic Force Microscopy (AFM). From AFM photograph, the geometry of primary particles is approximately spherical due to the growth mechanism, in this case, nucleation and coalescence to reach a minimum in the surface energy. The average particle size for the KSN is close to 30 nm while the size of aggregates is at around 100 nm. The formation of small aggregates of nanoparticles is typical for material processing by chemical routes.

About the magnetic characterization of the nanoparticles and nanocomposites, the Vibrating Sample Magnetometry (VSM) is a very versatile and widely used technique. This approach provides the main magnetic properties and relevant magnetic parameters of the sample with acceptable accuracy in a relatively fast way. The hysteresis loop between ± 15 kOe at room temperature, details of the low magnetic field region between ± 1 kOe and the main magnetic parameters like M_S , M_R , H_C , and μ_i for Ni-Zn ferrite nanopowders and magnetic nanocomposite with 50 phr of nanoparticles are shown in Fig. 12.

As it can be seen in Fig. 12, both hysteresis loops exhibit a characteristic profile of soft magnetic material at temperatures above the blocking temperature. Soft magnetic materials or materials with low coercivity are systems used in technological applications whose magnetization/demagnetizing process should be easy. For example, in transformer and motor cores to minimize the energy dissipation with the alternating fields and vibration absorption systems that use alternating magnetic field.

As a form to aggregate economic value to the polymeric and ceramic materials, composites and nanocomposites formed by inserting particles or magnetic

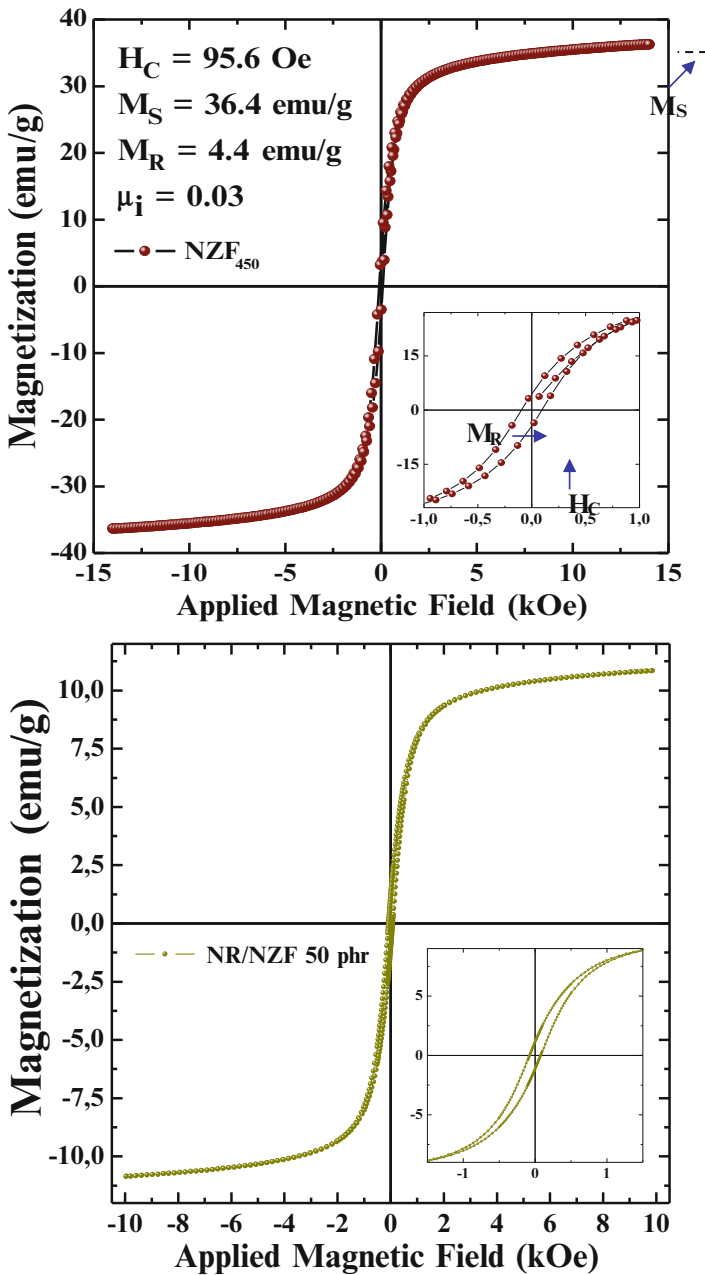


Fig. 12 Hysteresis loop at room temperature for Ni-Zinc ferrite nanopowders with calcined at 450 °C (a) and for the magnetic nanocomposites NR/NZF with a concentration of 50 phr of nanoparticles. In more detail, the region of low magnetic fields and indications of M_S , M_R , H_C , and μ_i

nanoparticles in a matrix of vulcanized natural rubber can be used in intelligent, high-performance systems for the absorption or damping of impacts, by having the ability to amplify or reduce the mechanical response of the system when subjected to a magnetic field. Such variations are proportional to the amount of magnetic material inserted in natural rubber and the intensity of externally applied magnetic field. Technological applications as more efficient damping systems for footwear and high-performance damping systems for intensive vehicles already have the potential for industrial use.

To illustrate this type of utilization, compression tests between 0 and 75 % assisted by magnetic field in accordance with international standard ISO 7743:1989 were performed in vulcanized natural rubber nanocomposites with ferrite magnetic nanoparticles (NR/NZF). The qualitative results are shown in Fig. 13.

In according to Fig. 13, the adding of magnetic nanoparticles in the polymeric matrix in the presence of the magnetic field alters the values of the compression module in up to 40 %. For all investigated samples, depending on the concentration of NZF nanoparticles, compression amount, and presence of a constant magnetic field, it is possible to modulate the values of resistance to compression. Hence, with proper manipulation of the composition of the magnetic composites and the magnetic field applied, it is possible to modulate the mechanical response of the system conveniently.

4.2 *Measuring the Dynamic Properties of MREs*

Young's and Shear Modulus are the mechanical properties of MREs measured as a function of the magnetic field. This feature allows determining how much these properties can change when the material is subject to a magnetic field. Some rubber-based MREs can change their Young's modulus by up to 60 % (Gong et al. 2005). In vibrating systems, it is more convenient to measure the dynamic stiffness instead. The dynamic stiffness is the frequency-dependent ratio between an input force and the output displacement under dynamic conditions. There are many methods to measure dynamic stiffness, and more information can be found in BS ISO 10446. The dynamic driving point stiffness k_d and the dynamic transfer stiffness k_t are the methods presented here to measure the dynamic stiffness. This fact justifies why these methods are widely used in mounts characterization. Figure 14a, b shows a schematic of the setup used to measure dynamic stiffness by using driving point and transfer stiffness methods, respectively. Figure 14c shows the equivalent system for these methods, where m is the mass, c is the damping, k is the stiffness, x is the displacement, f is force applied to the system, and f_t is the so-called blocked force.

Observing Fig. 14c the dynamic driving point stiffness can be used to represent the vibratory response of a single degree of freedom (SDOF) system. Considering a hysteretic damping, the vibratory response of the MRE shown in Fig. 14a can be given as

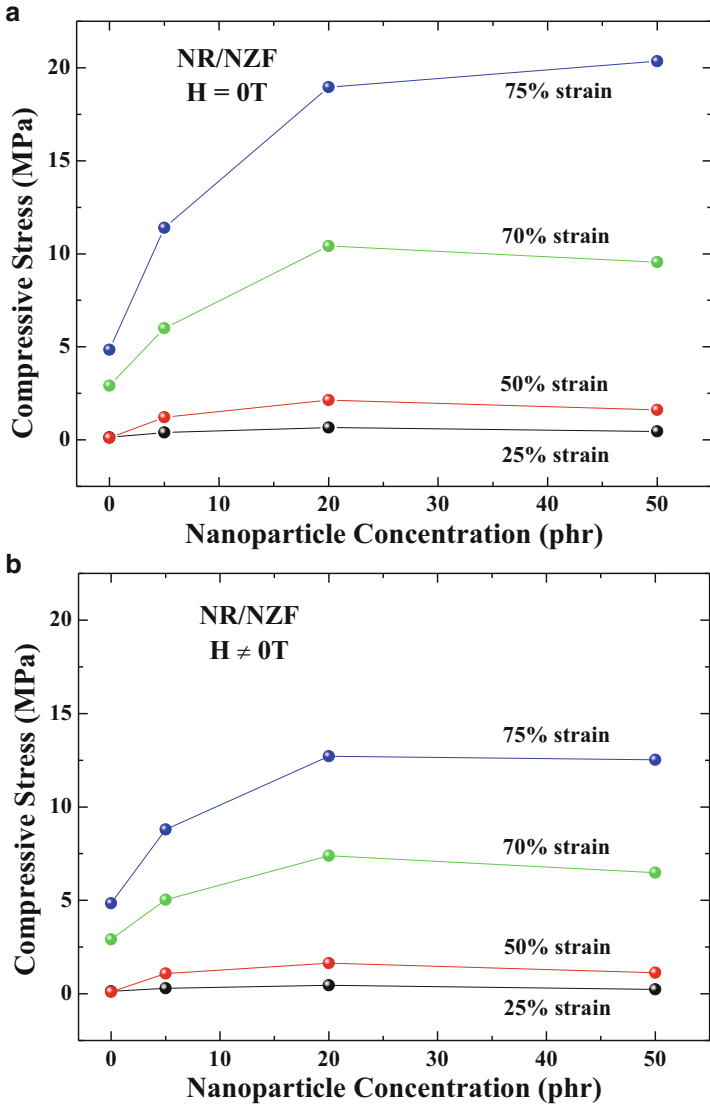


Fig. 13 Stress/compression curves for magnetic nanocomposites (NR/NZF) with 5, 20, and 50 phr of nanoparticles. (a) Tests carried out without magnetic field. (b) Test carried out with a constant magnetic field

$$\frac{F}{X} = k_d = (-m\omega^2 + k'), \tag{38}$$

where $k' = k(1 + j\eta)$ is the complex stiffness, $\eta = c/k$ is the loss factor of the system, F is the frequency-dependent force applied to the system, X is the

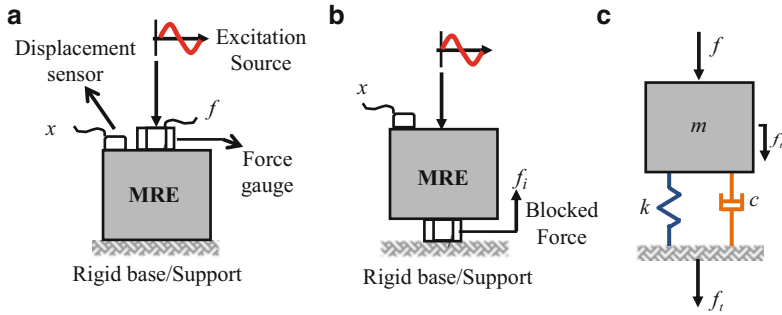


Fig. 14 Schematic of how to measure the dynamic stiffness using: (a) dynamic driving point stiffness method; (b) dynamic transfer stiffness method. (c) Schematic of the equivalent system for the dynamic driving point stiffness and dynamic transfer stiffness methods

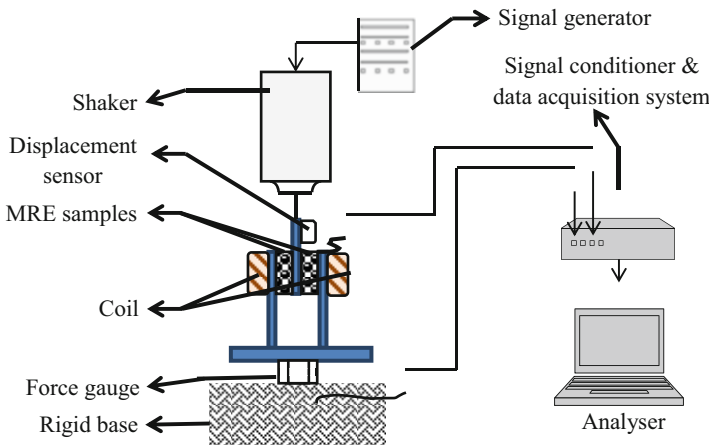


Fig. 15 Schematic of a rig used to measure the dynamic stiffness by using the dynamic transfer stiffness method

frequency-dependent output displacement, and $j = \sqrt{-1}$. For the transfer stiffness method shown in Fig. 14b, the dynamic stiffness is given by

$$\frac{F_t}{X} = k_t = k' = k(1 + j\eta), \tag{39}$$

where F_t is the frequency-dependent blocked force. The advantage of using the transfer stiffness method is that the mass of the MRE sample is not taking into account, so that the complex stiffness can be calculated directly. However, in some practical situations it is not easy to obtain a rigid base (blocked force) or to attach the force gauge underneath the MRE, such as mounts supporting a car engine. Despite that, in controlled situations the transfer stiffness method (cf. Eq. (39)) is applied. In this case, the stiffness and the loss factor are given by the real part $\text{Re}\{k_t\}$ and the phase $\text{Im}\{k_t\}/\text{Re}\{k_t\}$ of the dynamic stiffness, respectively. Figure 15

shows a schematic rig used to measure the dynamic stiffness by applying the transfer stiffness method.

The signal generator is the device that provides a certain type of signal to the shaker, which is an electro-mechanical actuator responsible for delivering the excitation to the MRE. The two coils located on the side of the MRE samples are responsible for supplying a tunable magnetic field. Hence, the input displacement and the output force (blocked force) can be measured, so that the dynamic stiffness can be estimated as a function of the supplied magnetic field.

References

- J. Aboudi, Effective behaviour and dynamic response modeling of electro-rheological and magneto-rheological fluid composites. *Smart Mater. Struct.* **8**, 106–115 (1999)
- A.M. Albanese, K.A. Cunefare, Properties of a magnetorheological semi-active vibration absorber, in *Proceedings of SPIE Conference on Smart Structures and Materials 2003: Damping and Isolation*, vol. 5052 (2003), pp. 36–43
- V. Balamurugan, S. Narayanan, Finite element formulation and active vibration control study on beams using smart constrained layer damping (SCLD) treatment. *J. Sound Vib.* **249**(2), 227–250 (2002)
- M. Behrooz, W. Xiaojie, G. Faramarz, Performance of a new magnetorheological elastomer isolation system. *Smart Mater. Struct.* **23**, 045014 (2014)
- M. Brigley, Y.T. Choi, N.M. Wereley, S.B. Choi, Magnetorheological isolators using multiple fluid modes. *J. Intel. Mater. Syst. Struct.* **18**, 1143–1148 (2007)
- J.D. Carlson, M.R. Jolly, MR fluid, foam and elastomer devices. *Mechatronics* **10**, 555–569 (2000)
- S. Chen, X. Liu, Spectral analysis for response dynamic damping force and phenomenological modeling of electro-rheological fluid. *Smart Mater. Struct.* **8**, 499–503 (1999)
- S.B. Choi, W.K. Kim, Vibration control of a semi-active suspension featuring electrorheological fluid dampers. *J. Sound Vib.* **234**(3), 537–546 (2000)
- S.B. Choi, Y.K. Park, Active vibration control of a cantilevered beam containing an electro-rheological fluid. *J. Sound Vib.* **172**(3), 428–432 (1994)
- Y. Choi, F. Sprecher, H. Conrad, Vibration characteristics of a composite beam containing an electrorheological fluid. *J. Intel. Mater. Syst. Struct.* **1**, 91–104 (1990)
- Y. Choi, F. Sprecher, H. Conrad, Response of electrorheological fluid-filled laminate composites to forced vibration. *J. Intel. Mater. Syst. Struct.* **3**, 17–29 (1992)
- S.B. Choi, B.S. Thompson, M.V. Gandhi, Experimental control of a single-link flexible arm incorporating electrorheological fluids. *J. Guid. Control Dynam.* **18**(4), 916–919 (1995)
- H. Conrad, A.R. Shamala, A.F. Sprecher, Characteristics of silica/silicone oil electrorheological fluid at small strains and strain rates, in *International Symposium on Electrorheological fluids*, Raleigh, 1987, pp. 47–62
- J.P. Coulter, T.G. Duclos, Applications of electrorheological materials in vibration control, in *International Conference on ER fluids, Proceedings*, 1989, pp. 300–325
- L.C. Davis, Model of magnetorheological elastomers. *J. Appl. Phys.* **85**, 3348–3351 (1999)
- H.X. Deng, X.L. Gong, L.H. Wang, Development of an adaptive tuned vibration absorber with magnetorheological elastomer. *Smart Mater. Struct.* **15**, N111–N116 (2006)
- R.A. Ditaranto, Theory of vibratory bending of elastic and viscoelastic layered finite-length beams. *J. Appl. Mech.* **32**, 881–886 (1965)
- A. Fuchs, M. Xin, F. Gordaninejad, X.J. Wang, G.H. Hitchcock, H. Gecol, C. Evrensel, G. Korol, Development and characterization of hydrocarbon polyol polyurethane and silicone magnetorheological polymeric gels. *J. Appl. Polym. Sci.* **92**, 1176–1182 (2004)

- M.V. Gandhi, B.S. Thompson, S.B. Choi, A new generation of revolutionary ultra-advanced intelligent composite materials featuring electro-rheological fluids: an experimental investigation. *J. Compos. Mater.* **23**(12), 1232–1255 (1989)
- J.M. Ginder, W.F. Schlotter, M.E. Nichols, Magnetorheological elastomers in tunable vibration absorber, in *Proceedings of SPIE Conference on Smart Structures and Materials 2001: Damping and Isolation*, vol. 4331 (2001), pp.103–110
- D.F. Golla, P.C. Hughes, Dynamics of viscoelastic structures—a time-domain, finite element formulation. *J. Appl. Mech.* **52**(4), 897–906 (1985)
- X.L. Gong, X.Z. Zhang, P.Q. Zhang, Fabrication and characterization of isotropic magnetorheological elastomers. *Polym. Test.* **24**, 669–676 (2005)
- C. Hirunyapruk, M.J. Brennan, B.R. Mace, W.H. Li, A tuneable magneto-rheological fluid-filled beam-like vibration absorber. *Smart Mater. Struct.* **19**, 055020 (2010)
- N. Hoang, N. Zhang, H. Du, A dynamic absorber with a soft magnetorheological elastomer for powertrain vibration suppression. *Smart Mater. Struct.* **18**, 074009 (2009)
- U.C. Jeong, J.H. Yoon, I.H. Yang, J.E. Jeong, J.S. Kim, K.H. Chung, J.E. Oh, Magnetorheological elastomer with stiffness-variable characteristics based on induced current applied to differential mount of vehicles. *Smart Mater. Struct.* **22**, 115007 (2013)
- M.R. Jolly, J.D. Carlson, B.C. Muñoz, A model of the behavior of magnetorheological materials. *Smart Mater. Struct.* **5**, 607–614 (1996)
- H.J. Jung, B.F. Spencer, I.W. Lee, Control of seismically excited cable-stayed bridge employing magnetorheological fluid dampers. *J. Struct. Eng.* **129**, 873–883 (2003)
- E.M. Kerwin, Damping of flexural waves by constrained layer. *J. Acoust. Soc. Am.* **31**, 952–962 (1959)
- M.J. Lam, *Hybrid active/passive models with frequency dependent damping*, Thesis (Doctor of Philosophy), Virginia Polytechnic Institute and State University, Blacksburg, 145p, 1997
- C.H. Lee, Active type damper for washing machine, has piston rod arranged in magnetic field production device, and magnetorheological elastomer adhered into cylinder, where penetration holes are formed in ends of cylinder and piston rod (Kor), Korea Patent KR1375695-B1, 2014
- C.Y. Lee, Finite element formulation of a sandwich beam with embedded electro-rheological fluids. *J. Intel. Mater. Syst. Struct.* **6**, 718–728 (1995)
- C.Y. Lee, C.C. Cheng, Dynamic characteristics of a sandwich beam with embedded electro-rheological fluid. *J. Intel. Mater. Syst. Struct.* **9**, 60–68 (1998)
- J. Leng, A. Asundi, Active vibration control system of smart structures based on FOS and ER actuator. *Smart Mater. Struct.* **8**, 252–256 (1999)
- J.S. Leng, Y.J. Liu, S.Y. Du, Y. Deng, D.F. Wang, Dynamic characteristics of a beam specimen featuring electrorheological fluids. *Exp. Mech.* **37**(1), 1–4 (1997)
- G.A. Lesieutre, Finite elements for dynamic modeling of uniaxial rods with frequency-dependent material properties. *Int. J. Solids Struct.* **29**(12), 1567–1579 (1992)
- G.A. Lesieutre, E. Bianchini, Time domain modeling of linear viscoelasticity using anelastic displacement fields. *J. Vib. Acoust.* **117**(4), 424–430 (1995)
- G.A. Lesieutre, U. Lee, A finite element for beams having segmented active constrained layers with frequency-dependent viscoelasticity. *Smart Mater. Struct.* **5**(5), 615–627 (1996)
- G.A. Lesieutre, D.L. Mingori, Finite element modeling of frequency-dependent material damping using augmenting thermodynamic fields. *J. Guid. Control Dynam.* **13**(6), 1040–1050 (1990)
- W.H. Li, H. Du, Design and experimental evaluation of a magnetorheological brake. *Int. J. Adv. Manuf. Tech.* **21**, 508–515 (2003)
- R. Li, L.Z. Sun, Dynamic viscoelastic modeling of magnetorheological elastomers. *Acta Mech.* **225**, 1347–1359 (2014)
- W.H. Li, G. Chen, S.H. Yeo, Viscoelastic properties of MR fluids. *Smart Mater. Struct.* **8**, 460–468 (1999)
- Lord Corporation, *Rheonetic magnetic fluids and systems—purchasing* (2001), <http://www.mrfuid.com/purchasing.htm>. Accessed 9 Apr 2001

- M.J. Mahjoob, H.R. Martin, F. Ismail, Identification of damping and stiffness of smart structures incorporating ER fluids. *Appl. Acoust.* **45**, 211–226 (1995)
- D.J. McTavish, P.C. Hughes, Modeling of linear viscoelastic space structures. *J. Vib. Acoust.* **115**, 103–110 (1993)
- D.J. Mead, S. Markus, The forced vibration of a three-layer, damped sandwich beam with arbitrary boundary conditions. *J. Sound Vib.* **10**(2), 163–175 (1969)
- Nagamine, R.K., Amortecimento ativo para redução da resposta aeroelástica via fluidos reológicos, Thesis (Doctorate), Universidade de São Paulo (in Portuguese), 2006
- R.K. Nagamine, F. Nitzsche, F.D. Marques, Flutter analysis of ER/MR actuated wing, in *International Conference on Adaptive Structures and Technologies, Paris, France, 2005*
- A.S. Phani, K. Venkatraman, Vibration control of sandwich beams using electro-rheological fluids. *Mech. Syst. Signal Process* **17**(5), 1083–1095 (2003)
- C.D. Rahn, S. Joshi, Modeling and control of an electrorheological sandwich beam. *J. Vib. Acoust.* **120**, 221–227 (1998)
- D. Ross, E.E. Ungar, E.M. Kerwin, Damping of plate flexural vibrations by means of viscoelastic laminae, in *Structural Damping: Colloquium on Structural Damping, ASME Annual Meeting*, 1959
- T. Shiga, A. Okada, T. Kurauchi, Magnetroviscoelastic behavior of composite gels. *J. Appl. Polym. Sci.* **58**, 787–792 (1995)
- N.D. Sims, D.J. Peel, R. Stanway, A.R. Johnson, W.A. Bullough, The electrorheological long-stroke damper: a new modelling technique with experimental validation. *J. Sound Vib.* **229**(2), 207–227 (2000)
- H.L. Sun, P.Q. Zhang, X.L. Gong, H.B. Chen, A novel kind of active resonator absorber and the simulation on its control effort. *J. Sound Vib.* **300**, 117–125 (2007)
- M.A. Trindade, A. Benjeddou, Hybrid active-passive damping treatments using viscoelastic and piezoelectric materials: review and assessment. *J. Vib. Contr.* **8**, 699–745 (2002)
- E.E. Ungar, E.M. Kerwin, Loss factors of viscoelastic systems in terms of energy concepts. *J. Acoust. Soc. Am.* **34**, 954–958 (1962)
- S.L. Vieira, Caracterização das Propriedades Mecânicas e Reológicas de Fluidos Eletro-Reológicos (FER), Thesis (Doctorate), University of Campinas (Unicamp), Campinas, 195p, in Portuguese, 1996
- K.W. Wang, T.S. Kim, D. Shea, Structural vibration control via electrorheological fluid based actuators with adaptive viscous and frictional damping. *J. Sound Vib.* **177**(2), 227–237 (1994)
- X. Wu, J. Griffin, A semi active control policy to reduce the occurrence and severity of end-stop impacts in a suspension seat with an electrorheological fluid damper. *J. Sound Vib.* **203**(5), 781–793 (1997)
- M. Yalcintas, J.P. Coulter, Electrorheological material based non-homogeneous adaptive beams. *Smart Mater. Struct.* **7**, 128–143 (1998)
- M. Yalcintas, H. Dai, Magnetroreological and electrorheological materials in adaptive structures and their performance comparison. *Smart Mater. Struct.* **8**, 560–573 (1999)
- M. Yalcintas, J.P. Coulter, D. Don, Structural modeling and optimal control of electrorheological material based adaptive structures. *Smart Mater. Struct.* **4**, 207–214 (1995)
- G.Z. Yao, Y. Qiu, G. Meng, T. Fang, Y.B. Fan, Vibration control of a rotor system by disk type electrorheological damper. *J. Sound Vib.* **219**(1), 189–192 (1999)

Composite Structures Design and Analysis

Volnei Tita

Abstract Recent improvements in manufacturing processes and materials properties associated with excellent mechanical characteristics and low weight have become composite materials very attractive for application on different types of structures. However, even new designs are still very conservative, because the composite structure failure phenomena are very complex. This chapter shows the principal fundamentals to design and analyze composite structures. In the introduction, there is a definition and a classification of composite materials, as well as motivation, considering advantages and challenges to design by using this type of material. Thus, it is presented a methodology to design composite structures in order to overcome the main challenges related to this task. In this methodology, it is found three important analyses: micromechanical, macromechanical, and failure analyses. In order to perform micromechanical analysis, it is necessary to know more about matrix, reinforcements, and interfaces. For example, in this chapter, it is addressed only polymeric matrix and long fibers as reinforcements, which are combined to create an orthotropic ply. Then, different plies can stack with fibers oriented in different directions, creating an anisotropic or orthotropic laminate. The material properties of the ply can be obtained by Rule of Mixture or via mechanical testing. Hence, it is commented some difficulties to carry out experiments on composite materials and how is complicated to obtain allowable values for laminates. Based on the material properties, it is possible to calculate strain in the laminate, as well as strain and stress distribution in each ply. To perform the macromechanical analysis, it is possible to use Classical Laminate Theory (CLT). Thus, it is shown all hypothesis adopted for that theory and the implications generated by these ones. Finally, based on the actuating stress or strain values in each ply and allowable values of the used composite material, it is calculated the margin of safety for the plies by applying a failure criterion. In fact, for laminate structures, failure phenomena include intralaminar damages and interlaminar failures (delaminations), which are very complicated to be predicted via any failure

V. Tita, M.Sc., Ph.D. (✉)

Department of Aeronautical Engineering, University of São Paulo, São Carlos
School of Engineering, Av. João Dagnone, 1100—Jardim Santa Angelina,
13573-12 São Carlos, São Paulo, Brazil
e-mail: voltita@sc.usp.br

theory. Therefore, even nowadays, many researchers have developed different failure theories to improve the design and analysis of composite structures.

Keywords Composite materials • Composite structures • Composite design • Composite analysis • Design methodology

1 Introduction

The usage of composite materials is a reality nowadays, mainly in the aeronautical and aerospace engineering. During several years, it has been observed different designs, which were developed considering high performance provided by this type of material, such as F-111, Vought A-7, F-18, F-22, Lockheed L-1011, Rutan Voyager, Boeing 777, Airbus 380, Boeing 787, and others. A composite can be defined as a multiphase material, which has properties better than if each phase were used alone (Callister 1985).

According to this synergistic effect in composite materials, the engineers have tried to design very carefully the combination of the phases in order to obtain materials with very high performance. The phases, which form the composite material, can be classified as matrix, reinforcements, and interface. The matrix has the function to maintain the reinforcements together, transmitting the loadings applied on the structure by the interface. Then the reinforcements have the function to support these loadings (Matthews and Rawlings 1994). Due to the different types of composite materials, Callister (1985) classified them as composite reinforced by particles; composite reinforced by fibers; and structural composites. In this chapter, it will be addressed the laminate composite materials, which has polymer matrix and long fibers as reinforcements stacked in plies. Each ply has fibers in one specific direction and the stacked plies generate a composite structure as shown by Fig. 1a.

The natural anisotropy related to the laminate composite materials provides a unique way to design the material properties with the geometric characteristics in order to reach the performance required by the project. The combination of high



Fig. 1 Composite material: (a) fuselage made of laminate composite; (b) damage and failure in laminate composite materials

strength and stiffness, as well as the low volumetric mass density, become the composite materials very strategic for structural applications, mainly in aeronautical and aerospace designs. Regarding the strength and the stiffness of the structure, it is possible to design both characteristics, considering the project requirements. In other words, the material can be developed in function of the loadings, which actuate in the structure. In fact, the stiffness and strength can be improved without increasing weight of the structure. Thus, for automobiles and airplanes, the performance of the product can be improved, reducing the fuel usage. In addition, the ratio between weight of green material and weight of the final product is very low for composites (1.2–1.3) compared to metals (15–25) (Jones 1999). This shows that manufacturing processes for composite structures are more efficient than manufacturing processes for metals.

However, the anisotropy and heterogeneity in the composite structures could be seen as a positive or a negative aspect. By one side, it is feasible not only to select the materials of the phases, but also to select the orientation of the fibers in each ply. By the other side, it is very complicated to predict the failure modes in the structure (Fig. 1b). This challenge is related directly to the reliability of the structure and this is more critical for products, which suffer fatigue or damage by impact loadings. Thus, it is necessary to apply high safety factors during the design process, which reduce the potentialities of composite materials and increase the cost of the final product (Tita 2003). Therefore, this scenario motivates to understand better how to design and to analyze with more accuracy composite structures.

1.1 Composite Materials: Definition and Classification

As commented earlier, a composite can be defined as a multiphase material, which has properties better than if each phase were used alone (Callister 1985). And, the phases, which form the composite material, can be classified as matrix, reinforcements, and interface. According to Vinson and Sierakowski (1986), the laminate composite can be addressed by two different analyses: micromechanics and macromechanics approaches (Fig. 2).

In the micromechanics approach, it is considered each phase in the analysis. Although the phases are frequently heterogeneous and non-isotropic, it is normally assumed the hypotheses of isotropy and homogeneity. This approach can be used to determine the elastic properties of the ply or to estimate the local damage in each phase when the ply is loaded.

In the macromechanics approach, it is considered that each ply is homogenous, and the orientation of the fibers in the plies is very important in the analysis, as well. In addition, the plies are frequently non-isotropic, so they are assumed to be orthotropic. This approach can be used to predict the stiffness of the laminate, as well as its mechanical behavior when the laminate structure is loaded.

Nowadays, many researchers have combined both approaches in order to analyze the composite structures, and this new approach is called multi-scale analysis.

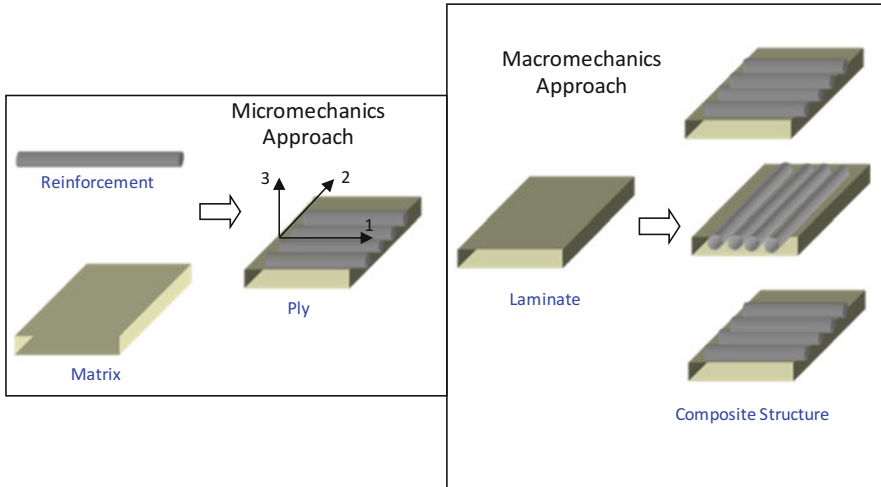


Fig. 2 Micro and macromechanics approaches (Vinson and Sierakowski 1986)

1.2 Motivation: Advantages and Challenges

For a long time, the man has combined different materials in order to obtain other materials. For example, in 4000 BC, Sumerians added straw in the mud in order to built better bricks. Although the benefits of composite materials are known for a long time, only recently, there was the development of manufacturing processes, which produce structures with high quality and high structural efficiency.

The structural efficiency is associated directly to the material used in the manufacturing process. This parameter is high when strength/density or stiffness/density is high and vice-versa. According to the literature, composite materials with 70 % of epoxy volume fraction and 30 % of carbon fiber volume fraction, or 40 % of epoxy volume fraction and 60 % of glass fiber volume fraction show stiffness close to aluminum, which is more density than both composite materials. In the same way, a composite with 40 % of epoxy volume fraction and 60 % of carbon fiber volume fraction shows stiffness close to steel (Magagnin Filho 1996) (Fig. 3).

Beyond high specific strength (strength/density), composite materials show good performance under dynamic loadings (Tita 1999). For example, in some products, it is necessary to avoid damage caused by vibrations. Thus, the plies can be stacked in order to obtain a laminate with natural frequencies different to the excitation frequencies (Tita et al. 2001). In the last years, the composite materials are not only used to guarantee high structural efficiency, but also the safety of passenger under impact loadings. Thus, the laminate is designed in order to absorb the maximum impact energy, controlling the collapse of the structure and reducing the accelerations after impact.

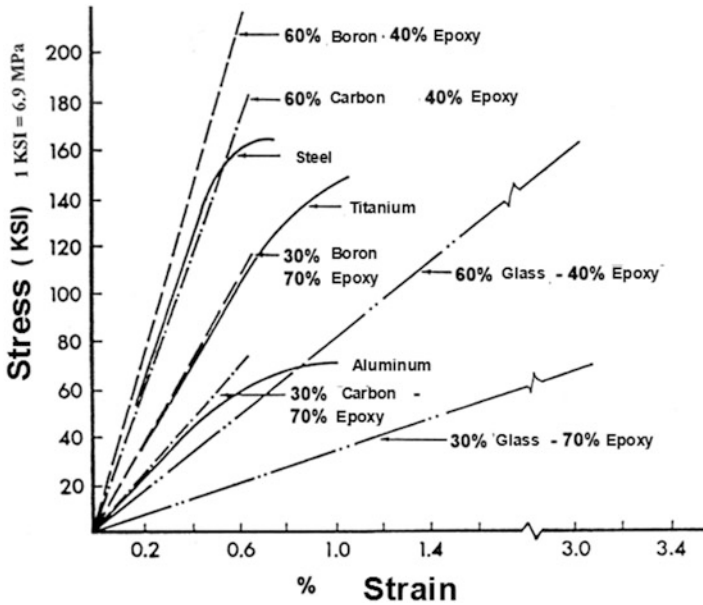


Fig. 3 Stress–strain curves: metals vs. composite materials (Adapted from Magagnin Filho 1996)

As commented earlier, the anisotropy related to the laminate composite materials provides a unique way to design the material properties with the geometric characteristics in order to reach the performance required. However, this inherent anisotropy and heterogeneity of the composite materials promote complex failure modes in the structures, which are very complicated to predict. Then, in the next section, it is shown a methodology to design composite structures in order to help engineers to overcome this challenge.

1.3 Methodology to Design Composite Structures

Figure 4 shows a procedure proposal to design laminate composite structures. It is verified that the procedure starts with the selection of the type of fibers and polymer matrix. Normally, the manufacturers of the fibers and the polymer provide the data sheet for each material. Then, by using the Rule of Mixture, which is based on *Micromechanics Analysis*, mechanical properties of each ply can be evaluated. However, it is recommended to perform experimental tests for determining not only the elastic properties of the plies, but also the allowable values (strength and strain limits) and the damage/failure modes of the composite material. In fact, the mechanical tests are very important, because the mechanical behavior of the real ply, which was manufactured by using specific values for process parameters (pressure, temperature, and time), can be investigated in details.

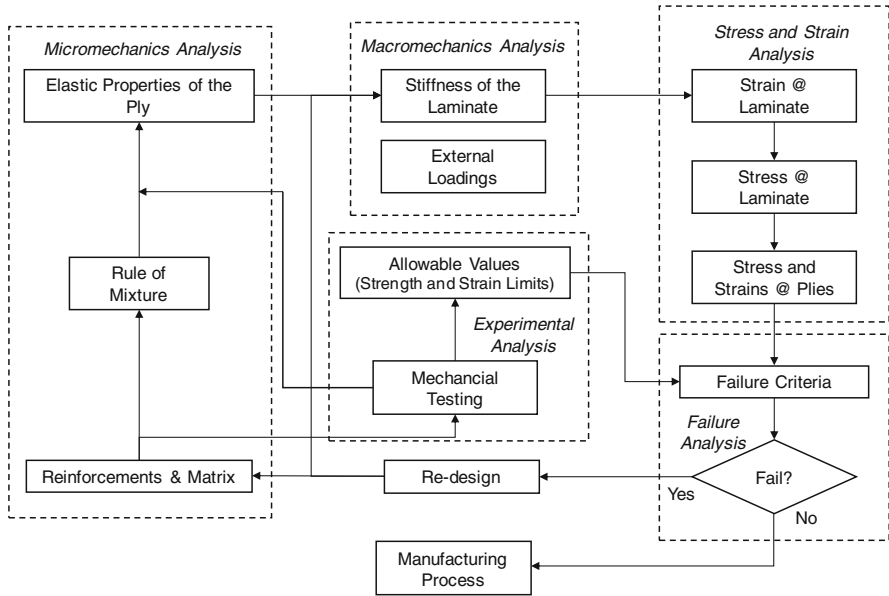


Fig. 4 Procedure proposal to design and analyze composite structures

Based on the elastic properties of each ply, it can be calculated the stiffness of the laminate via Classical Laminate Theory (CLT), for example. By using the stiffness and the external loadings applied in the laminate, it is calculated the strain components and curvatures for the Global Coordinate System for the laminate. This calculus can be named as *Macromechanics Analysis*, and based on the constitutive relations, the stress components for each ply for the Global Coordinate System can be determined. By using the transformation of coordinate systems, it is calculated not only the strain components, but also the stress components for the Local Coordinate System.

The next step in the procedure consists on carrying out *Failure Analysis*. Hence, the values of the strain or stress components for the Local Coordinate System and the allowable values determined via mechanical testing are used in the failure criterion, which is selected considering the mechanical behavior of the composite material shown during the tests. In case of failure, it is necessary to redesign the composite structure. Thus, there are many options to do this, such as changing the stacking sequence of the plies; changing the fibers and/or the polymer matrix; and increasing the fiber volume fraction. Finally, if the composite structure does not fail, then it can be manufactured.

2 Micromechanical Analysis and Testing

Micromechanical analysis can be used for evaluating the mechanical properties for “one single ply” (stacked plies with the same fiber orientations), which is formed by the reinforcements (fibers), matrix (polymeric resin), and interface fiber-matrix.

2.1 *Matrix, Reinforcements, and Interfaces*

The matrix is the first phase in the composition of the composite materials. One of the most important functions of the matrix is to join the reinforcements. This guarantees the adequate position and orientation of the fibers such as the loads in the structure can be transferred to the reinforcements. Moreover, the matrix protects the fibers against environment effects and damages caused by hand contacts. In some cases, greater values of flexibility and damping can be obtained due to the polymeric resin. Then, this is good for attenuation of mechanical vibrations amplitudes.

The reinforcements are the second phase in the composition of the composite materials. They have an important mission, which consists on supporting the loads transferred by the matrix. In the case of long fibers, it is very important the orientation of the fibers in relation to applied design loadings. The final mechanical properties of the ply strongly depend on the fiber volume fraction and the polymer matrix processing, i.e., temperature, time, and pressures used during the manufacturing process of the composite material. Besides, it must consider the type of the fibers such as continuous (long) or discontinuous (short) and oriented or random.

The interface fiber-matrix is the third phase in the composition of the composite material. This phase is produced during the composite material processing and it is very important, because it quantifies the degree of interaction between reinforcements and matrix. Thus, in order to have a satisfactory performance by the composite material, it is necessary that there is a strong adhesion between fibers and matrix. According to Callister (1985), it is essential to have adhesive forces in the interface fiber-matrix, because the strength of the composite depends on these forces, as well.

2.1.1 **Polymeric Matrix**

Physics and chemical properties of the polymers influence a lot on the properties of the composite materials. For example, the maximum temperature in service of the composite material depends on the polymer used as matrix. Therefore, variations in the chemical formulations can affect the performance of the final composite

Table 1 Comparison between properties of thermoset and thermoplastic polymers

Property	Thermosetting polymer	Thermoplastic polymer
Young’s modulus (GPa)	1.3–6.0	1.0–4.8
Tensile strength value (GPa)	0.02–0.18	0.04–0.19
Maximum temperature in service (°C)	50–450	25–230

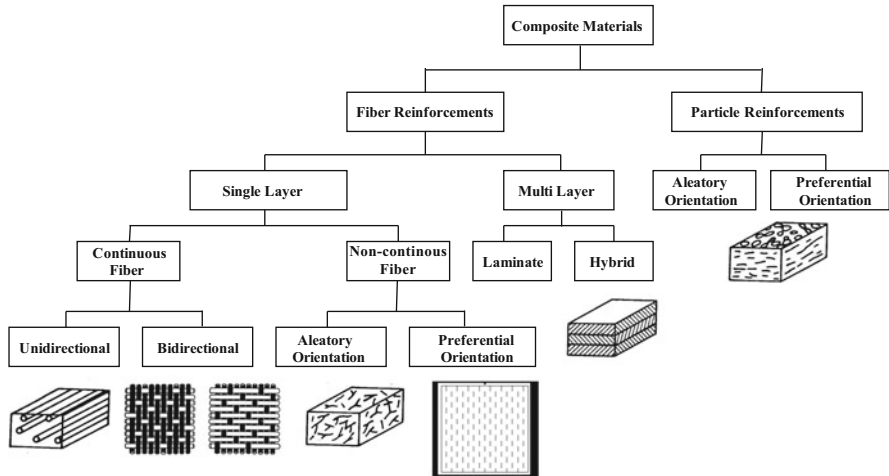


Fig. 5 Types of reinforcements

material. It is important to be careful to keep polymers, avoiding, for example, exposition to UV light.

In general, polymers can be classified as thermosetting or thermoplastic. In fact, one of the most important differences between both polymers consists on showing different behavior under heating. Thermoplastic polymers, such as PE, PP, and nylon, can suffer fusion (physic process) under heating, and the composite structure can be molded and solidified in a required geometry. Thermosetting polymers, such as epoxy and phenol resins, suffer cure (chemical process), creating cross-link between the polymer chains. Table 1 shows a comparison between properties of thermosetting and thermoplastic polymers.

Nowadays, thermosetting polymers are often applied on composite structures. However, due to reduced time to manufacture, the usage of thermoplastic polymers has been increased.

2.1.2 Reinforcements

Figure 5 shows different forms that can be used for reinforcements in the composite materials. In general, it is verified two relevant categories: fibers and particles. However, as commented earlier, this chapter is focused on the unidirectional (ply) and multidirectional (laminate) composite material.

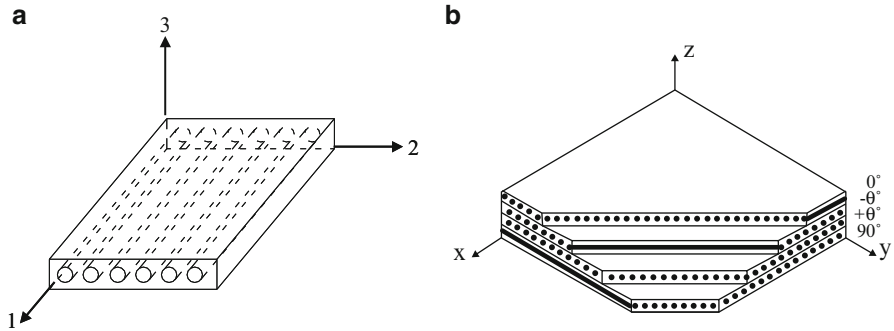


Fig. 6 (a) Unidirectional fibers: orthotropic material (ply); (b) multidirectional fibers: anisotropic material (laminate)

Table 2 Mechanical properties of fibers

Fiber	Density [10^6 g/m^3]	Young's modulus [GPa]	Tensile strength [MPa]
E-glass	2.54	70	2200
Kevlar 49	1.45	130	2900
SiC	2.60	250	2200
Alumina	3.90	380	1400
Boron	2.65	420	3500
Carbon	1.86	380	2700

In Fig. 6a, the unidirectional arrangement creates 3 (three) planes of symmetry, which are orthogonal each other (planes 1-2, 1-3, and 2-3). Hence, in this case (for the ply), it is assumed to have an orthotropic material. By other side, in Fig. 6b, it is observed multidirectional arrangement, which does not create any plane of symmetry. Thus, in this case (for the laminate), it is assumed to have an anisotropic material in the most of cases.

Table 2 shows some typical data about fibers, which can be found in the literature and data sheet of fiber manufacturers.

2.2 Rule of Mixture

The mechanical properties of the composite materials strongly depend on the properties and proportions of the 3 (three) phases (fiber, matrix, and interface) as well as the conditions of the manufacturing process (temperature, pressure, and time). The principal objective of the Rule of Mixture is the determination of the mechanical or thermal properties of the composite material by using micromechanical analysis. Indeed, this is the simplest analytical approach to homogenize a ply, which is formed by the 3 (three) phases as shown by Fig. 7a.

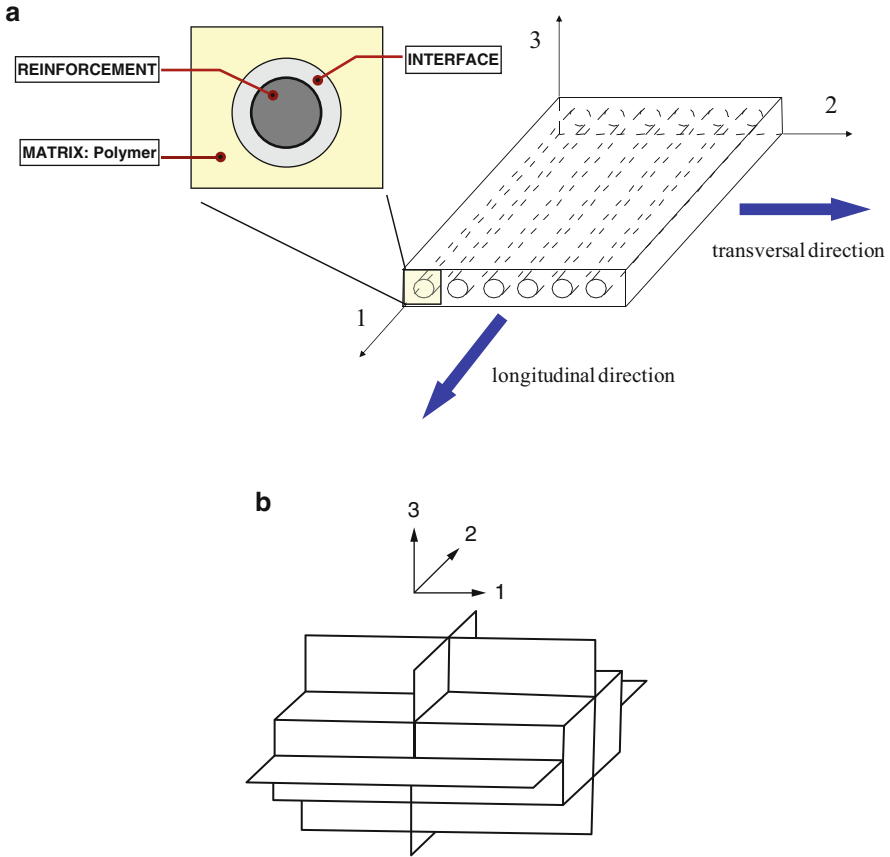


Fig. 7 (a) Ply: longitudinal and transversal directions; (b) orthotropy planes

And, this homogenized ply is assumed to be an orthotropic material with 3 (three) planes of symmetry as shown by Fig. 7b.

As the ply is assumed to be an orthotropic material, then it is necessary to determine 9 (nine) elastic constants:

- E_{11} = Young's modulus in the longitudinal direction
- E_{22} = Young's modulus in the transversal direction (in-plane of the ply)
- E_{33} = Young's modulus in the transversal direction (out-of-plane of the ply)
- G_{12} = shear modulus in plane 1-2
- G_{13} = shear modulus in plane 1-3
- G_{23} = shear modulus in plane 2-3
- ν_{12} = Poisson's ratio in plane 1-2
- ν_{13} = Poisson's ratio in plane 1-3
- ν_{23} = Poisson's ratio in plane 2-3

However, the orthotropic unidirectional ply is also transversely isotropic in the plane 2-3, so: $E_{22} = E_{33}$; $G_{12} = G_{13}$; and $\nu_{12} = \nu_{13}$. Thus, now, it is necessary to determine 6 (six) elastic constants.

The elastic properties obtained via Rule of Mixture are calculated in function of the fiber and matrix properties as well as their respective volume fractions and considering following hypotheses:

- The response of ply is linear elastic and there are not residual and thermal internal stresses.
- Fibers are uniform, homogenous, same diameter, continuous, parallels, and regularly spaced.
- The matrix is homogenous, isotropic, showing linear elastic response.
- There is a perfect interface fiber-matrix and there are not voids in the material.
- The interface is infinitely fine, being disregard in the calculus.

Considering the volume of the composite V_c and mass of the composite M_c with fiber volume V_f and fiber mass M_f , matrix volume V_m and matrix mass M_m , and voids volume V_v , it is written:

$$M_e = M_f + M_m \quad (1)$$

$$V_c = V_f + V_m + V_v \quad (2)$$

Dividing Eqs. (1) and (2) by M_c and V_c , respectively:

$$1 = \frac{M_f}{M_c} + \frac{M_m}{M_c} \quad (3)$$

$$1 = \frac{V_f}{V_c} + \frac{V_m}{V_c} + \frac{V_v}{V_c} \quad (4)$$

The mass and volume fraction can be defined as:

$$m_f = \frac{M_f}{M_c}; \quad m_m = \frac{M_m}{M_c} \quad (5)$$

$$v_f = \frac{V_f}{V_c}; \quad v_m = \frac{V_m}{V_c}; \quad v_v = \frac{V_v}{V_c} \quad (6)$$

Thus, rewriting (3) and (4):

$$\begin{aligned} m_f + m_m = 1 \quad \text{or} \quad \frac{\sum M_i}{M_c} = \sum m_i = 1 \\ v_f + v_m + v_v = 1 \quad \text{or} \quad \frac{\sum V_i}{V_c} = \sum v_i = 1 \end{aligned} \quad (7)$$

In order to calculate the mass and volume fractions, it is necessary to determine the composite density ρ_c . Based in the Eq. (1) or in the Eq. (2), it is written:

$$\rho_c = \frac{M_c}{V_c} = \frac{1}{\frac{V_c}{M_c}} = \frac{1}{\frac{V_f}{M_c} + \frac{V_m}{M_c} + \frac{V_v}{M_c}} \quad (8)$$

$$\rho_c = \frac{1}{\frac{M_f}{\rho_f M_c} + \frac{M_m}{\rho_m M_c} + \frac{v_v}{\rho_c V_c}} = \frac{1}{\frac{m_f}{\rho_f} + \frac{m_m}{\rho_m} + \frac{v_v}{\rho_c}}$$

or:

$$\rho_c = \frac{M_c}{V_c} = \frac{M_f + M_m}{V_c} = \frac{\rho_f V_f + \rho_m V_m}{V_c} \quad (9)$$

$$\rho_c = \rho_f v_f + \rho_m v_m$$

The voids volume fraction v_v is given by:

$$v_v = 1 - (v_f + v_m) \quad (10)$$

or, by using Eq. (8), it is obtained:

$$v_v = 1 - \left(\frac{m_f}{\rho_f} + \frac{m_m}{\rho_m} \right) \rho_{c(\text{experimental})} \quad (11)$$

Besides, the theoretical density is calculated via:

$$\rho_{c(\text{theoretical})} = \frac{1}{\frac{m_f}{\rho_f} + \frac{m_m}{\rho_m}} \quad (12)$$

Therefore, Eq. (12) can be written as:

$$v_v = 1 - \frac{\rho_{c(\text{experimental})}}{\rho_{c(\text{theoretical})}} \quad (13)$$

After determining the matrix and fiber volume fractions, it is necessary to have the matrix and fiber properties, such as Young's moduli of the matrix (E_m) and fiber (E_f), Poisson's ratios of the matrix (ν_m) and the fiber (ν_f). Frequently, these properties are provided by the manufacturers of the polymers and fibers. Otherwise, it should be carried out experimental tests in order to obtain these data.

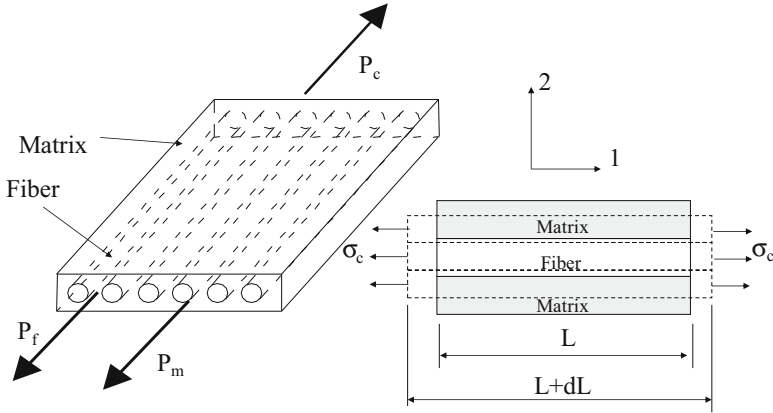


Fig. 8 Ply loaded in the longitudinal direction

2.2.1 Longitudinal Young’s Modulus

Considering a loading P_c applied in the direction of the fiber, the strains in the fibers, matrix, and composite are assumed to be equals (Fig. 8):

$$\epsilon_c = \epsilon_f = \epsilon_m \tag{14}$$

Considering elastic response, stresses can be calculated by Hooke’s Law:

$$\sigma_f = E_f \epsilon_f \quad \text{and} \quad \sigma_m = E_m \epsilon_m \tag{15}$$

Stresses σ_f and σ_m actuate on the A_f and A_m , respectively. Based on Fig. 8, the loading P_c can be calculated as follows:

$$P_c = P_f + P_m \tag{16}$$

Moreover:

$$P_f = \sigma_f A_f = E_f \epsilon_f A_f \quad \text{and} \quad P_m = \sigma_m A_m = E_m \epsilon_m A_m \tag{17}$$

Applying (17) into (16):

$$P_c = \sigma_c A_c = \sigma_f A_f + \sigma_m A_m \quad \text{or} \quad \sigma_c = \sigma_f \frac{A_f}{A_c} + \sigma_m \frac{A_m}{A_c} \tag{18}$$

The volume of the fiber can be calculated as follows:

$$V_f = A_f L_f \tag{19}$$

By using the same way, it is calculated matrix and composite volume. Thus, based on Fig. 8:

$$L_f = L_m = L_c \tag{20}$$

Replacing (19) into (18) and considering (20):

$$\sigma_c = \sigma_f v_f + \sigma_m v_m \tag{21}$$

Since the ply has an elastic behavior, then $\sigma_c = E_c \varepsilon_c$ and $\varepsilon_c = \varepsilon_f = \varepsilon_m$, so:

$$\begin{aligned} \sigma_c &= E_c \varepsilon_c = E_f \varepsilon_f v_f + E_m \varepsilon_m v_m \\ E_c &= E_f v_f + E_m v_m \quad \text{or} \quad E_{11} = E_f v_f + E_m v_m \end{aligned} \tag{22}$$

Finally, Eqs. (21) and (22) can be rewritten:

$$\sigma_{11} = \sum_{i=1}^n \sigma_i v_i \quad \text{and} \quad E_{11} = \sum_{i=1}^n E_i v_i \tag{23}$$

It is important to notice that the Rule of Mixture calculates de elastic properties of the ply by using the weighted average of the volume fractions for n constituents of the composite material.

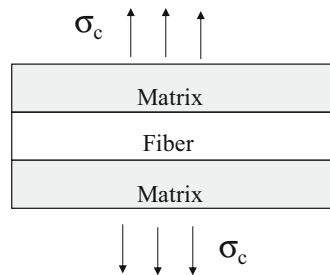
2.2.2 Transversal Young’s Modulus

Considering the hypotheses used by Rule of Mixture, if a transversal loading P_c is applied in the transversal direction, then the actuating stresses in the fibers, matrix, and composite are assumed to be the same in this direction (Fig. 9):

$$\sigma_c = \sigma_f = \sigma_m \tag{24}$$

Thus, the transversal elongation in the ply δ_c is given by the sum of elongations of the fibers δ_f and the matrix δ_m :

Fig. 9 Ply loaded in the transversal direction



$$\delta_c = \delta_f + \delta_m \quad (25)$$

As $\varepsilon = \delta/t$, where t is thickness of the phase or the composite, then:

$$\varepsilon_c t_c = \varepsilon_f t_f + \varepsilon_m t_m \quad (26)$$

Since the matrix and fibers volume fraction can be written as:

$$v_f = \frac{t_f}{t_c} \quad \text{and} \quad v_m = \frac{t_m}{t_c} \quad (27)$$

Replacing (27) into (26):

$$\varepsilon_c = \varepsilon_f v_f + \varepsilon_m v_m \quad (28)$$

As the actuating transversal stresses in the fibers are equal in the matrix, then:

$$\varepsilon_f = \frac{\sigma_c}{E_f} \quad \text{and} \quad \varepsilon_m = \frac{\sigma_c}{E_m} \quad (29)$$

Replacing (29) into (28):

$$\frac{1}{E_c} = \frac{1}{E_f} v_f + \frac{1}{E_m} v_m \quad (30)$$

Finally, Eqs. (28) and (30) can be rewritten:

$$\varepsilon_{22} = \sum_{i=1}^n \varepsilon_i v_i \quad \text{and} \quad E_{22} = \frac{1}{\sum_{i=1}^n \frac{1}{E_i} v_i} \quad (31)$$

Due to the transversal isotropy of the ply, the Transversal Young Modulus in the ply plane (E_{22}) is equal to the Transversal Young Modulus out of the ply plane (E_{33}).

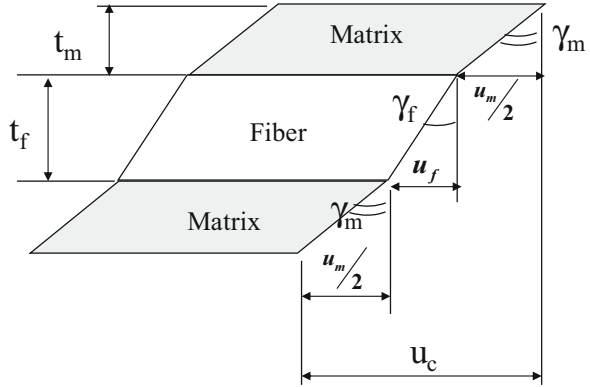
2.2.3 Shear Modulus

For the determination of the shear modulus of the ply, it is assumed that the shear strains are linear and the actuating stresses are the same in the fibers and matrix (Fig. 10).

The total displacement of the ply u_c is calculated by the sum of the displacements of the fibers u_f and the matrix u_m , thus:

$$u_c = u_f + u_m \quad \text{or} \quad u_c = t_f \gamma_f + t_m \gamma_m \quad (32)$$

Fig. 10 Ply deformed due to shear loading



where γ_f is the angle for fibers and γ_m is the angle for the matrix. Applying (27) into (32):

$$u_c = v_f t_c \gamma_f + v_m t_c \gamma_m \tag{33}$$

γ_{12} for the ply can be calculated as follows:

$$\gamma_{12} = \frac{u_c}{t_c} \tag{34}$$

Applying (34) into (33):

$$\gamma_{12} = v_f \gamma_f + v_m \gamma_m \tag{35}$$

Based on the linear hypotheses, then:

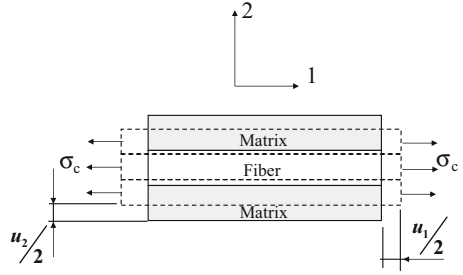
$$\gamma_f = \frac{\tau_f}{G_f}, \quad \gamma_m = \frac{\tau_m}{G_m} \quad \text{and} \quad \gamma_{12} = \frac{\tau_{12}}{G_{12}} \tag{36}$$

Considering that the actuating shear stresses in the fibers, matrix, and composite are equal and replacing Eq. (36) into Eq. (35), it is calculated the shear modulus of the ply in the plane 1-2:

$$\frac{1}{G_{12}} = v_f \frac{1}{G_f} + v_m \frac{1}{G_m} = \sum_{i=1}^n \frac{v_i}{G_i} \tag{37}$$

Due to the transversal isotropy of the ply, it is assumed that G_{12} is equal to G_{13} (shear modulus of the ply in the plane 1-3). However, G_{23} (shear modulus of the ply in the plane 2-3) is much more complicated to calculate, and, normally, it is required experimental tests.

Fig. 11 Poisson's effect in the ply



2.2.4 Poisson's Coefficient

If a normal stress σ_c is applied in the longitudinal direction of the fibers, there will be a contraction of the ply in the transversal direction (Fig. 11), which is calculated by:

$$u_2^c = u_2^f + u_2^m \tag{38}$$

Contractions of the fibers and matrix can be calculated via Poisson's ratios:

$$\begin{aligned} \nu_m &= -\frac{\epsilon_2^m}{\epsilon_1^m} = -\frac{u_2^m/t_m}{\epsilon_1^m} \quad \text{or} \quad u_2^m = -\nu_m \epsilon_1^m t_m \\ \nu_f &= -\frac{\epsilon_2^f}{\epsilon_1^f} = -\frac{u_2^f/t_f}{\epsilon_1^f} \quad \text{or} \quad u_2^f = -\nu_f \epsilon_1^f t_f \end{aligned} \tag{39}$$

where ν_m and ν_f are Poisson's ratio for fibers and matrix, respectively. And, t_f and t_m are thickness of the fibers and matrix, respectively.

Replacing (39) into (38):

$$u_2^c = -\nu_m u_1^m - \nu_f u_1^f = -(\nu_m \epsilon_1^m t_m + \nu_f \epsilon_1^f t_f) \tag{40}$$

Considering that the strains in the fibers, matrix, and composite are equal, then:

$$\epsilon_1^m = \epsilon_1^f = \epsilon_1^c = \epsilon_{11} \tag{41}$$

Applying (41) into (40) and operating t_c (thickness of the ply) in the both sides of the equation:

$$t_c u_2^c = -(\nu_m t_m + \nu_f t_f) t_c \epsilon_{11} \tag{42}$$

or:

$$u_2^c = -\left(\nu_m \frac{t_m}{t_c} + \nu_f \frac{t_f}{t_c}\right) t_c \epsilon_{11} \tag{43}$$

Since the fiber and matrix volume fraction can be written as:

$$v_f = \frac{t_f}{t_c} \quad \text{and} \quad v_m = \frac{t_m}{t_c} \quad (44)$$

Thus, Eq. (43) can be rewritten:

$$\frac{u_2^c}{t_c} = -(\nu_m v_m + \nu_f v_f) \varepsilon_{11} = \varepsilon_{22} \quad (45)$$

The Poisson's ratio ν_{12} calculated in the ply plane (plane 1-2) is given by:

$$\nu_{12} = -\frac{\varepsilon_{22}}{\varepsilon_{11}} = \nu_m v_m + \nu_f v_f = \sum_{i=1}^n \nu_i v_i \quad (46)$$

Due to the transversal isotropy of the ply, it is assumed that ν_{12} is equal to ν_{13} (Poisson's ratio of the ply in the plane 1-3). However, ν_{23} (Poisson's ratio of the ply in the plane 2-3) is much more complicated to calculate, and, normally, it is required experimental tests.

2.3 Mechanical Testing

Regarding the hypothesis used in the Rule of Mixture, sometimes, the values of mechanical properties obtained by this approach are very different when compared to the experimental values. This occurs because different effects influence on the final properties of composite materials. For example, parameters of material processing (time, pressure and temperature) are very important, because, a composite plate made of a kind of fiber, matrix, and volume fractions can show totally different properties than other composite plate with the same fiber, matrix, and volume fractions of phases manufactured on different conditions. Therefore, it is almost impossible to avoid experimental tests for determination of elastic properties, strength and strain limit values of composite materials.

For an isotropic material, a tensile test in one direction can provide: Young Modulus, Poisson's ratio, strength values, and strain limits. However, for orthotropic materials, it is necessary 6 (six) experimental tests as shown by Table 3.

Moreover, the experimental tests provide the stress-strain curves, which helps to identify different mechanisms in the ply, such as micro-damages or macro-failures (delamination). This will be very important to select a failure criterion for designing a composite structure. However, to carry out experimental tests on composite materials is a hard task, because there are many particularities:

1. The experimental tests are based on the concepts of the basic mechanic theory, which are applied for isotropic, elastic, homogeneous materials. However, composite materials are anisotropic, heterogeneous, and inelastic. Thus, the application of these concepts is not direct.

Table 3 Experimental testing for orthotropic materials

Mechanical testing	Elastic properties	Strength value	Strain limit
(1) <i>Tension 0°</i> : tension in the longitudinal direction	$E_{11}; \nu_{12} (= \nu_{13})$	X_T	X'_T
(2) <i>Tension 90°</i> : tension in the normal direction.	$E_{22} (= E_{33})$	Y_T	Y'_T
(3) <i>Compression 0°</i> : compression in the longitudinal direction	–	X_C	X'_C
(4) <i>Compression 90°</i> : compression in the normal direction	–	Y_C	Y'_C
(5) <i>Shear in plane 1-2</i> : shear loading in the plane 1-2	$G_{12} (= G_{13})$	S_{12}	S'_{12}
(6) <i>Shear in plane 2-3</i> : shear loading in the plane 2-3	G_{23}	–	–

2. During the tests, many difficulties can take place, such as:

- Influence of end-effects, which produces regions with stress concentration close to the edges of the specimen
- How to apply acceptable load levels without creating premature fails in the material
- How to determine the correct dimensions of the specimen (mainly thickness), regarding the heterogeneity

3. Problems caused by the anisotropy:

- Increase the problem related to the end-effects
- Promote premature fails in regions close to the clamps
- Promote premature delaminations close to the edge of the specimen

4. Experimental tests of composite materials are expensive and take long time, mainly the manufacturing of the specimens.

5. For some cases, traditional standards (ASTM, ISO, DIN, etc.) work, but for others, these standards are completely inappropriate.

In fact, in the literature, different standards to perform experimental tests in composite materials can be found (Whitney et al. 1984). However, it is better to use these standards as a guide to carry out the tests, because, for some composite materials, it is necessary to change some parameters specified in the standard, such as the dimensions and/or test speed.

3 Macromechanical Analysis

In the macromechanical analysis, it is considered not only the ply properties, but also the stacking sequence of the laminate.

3.1 Classical Laminate Theory

First, it is important to assume a code to identify the stacking sequence used in the laminate. In this chapter, it is used the SLC (*Standard Laminate Code*), which requires:

- Orientation of each ply, considering the global coordinate system ($x-y-z$).
- Number of the plies for a given orientation.
- Stacking sequence of the plies to obtain the laminate.

For example, a laminate with orientation angles for fibers equal 0° , 90° , 90° , and 0° can be represented by different ways: $[0/90/90/0]$; $[0/90_2/0]$; $[0/90]_s$; $[0/90/90/0]_T$. The subscripts of the angles specify the number of the plies with fibers oriented in that direction. The subscript S indicates symmetry of the laminate, and T shows that the laminate has the total number of the plies used to manufacture the structure.

The composite structure $[0/90/90/0]$ is a symmetric laminate, because the plane, which split the thickness in two parts is like a mirror, i.e., the laminate is symmetric in relation to its medium plane. Other example is the laminate in Fig. 12, which is represented by $[0_3/90_2/45/-45_3/-45_3/45/90_2/0_3]_T$ or $[0_3/90_2/45/-45_3]_s$.

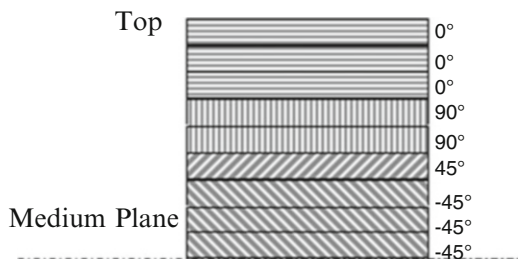
Beyond symmetric laminates, there are the antisymmetric laminates and the asymmetric laminates. However, in the literature, it can be found a large number of classifications for laminates. Regarding antisymmetric laminates, the plies are stacked in order to create antisymmetry in relation of medium plane. By one side, a laminate with orientation angles of fibers in 0° , 90° , 0° , and 90° can be considered antisymmetric. By the other side, an asymmetric laminate has a random stacking sequence, and there is none rule of stacking related to the medium plane.

At this moment, there is a question: How to determine the laminate stiffness considering the plies stacked in different directions?

One approach to do this consists on using the CLT, which is based on Theory of Elasticity. Therefore, considering a solid (continuous media) loaded, this body produces internal stresses in order to equilibrate the applied loadings (Fig. 13).

A point in the body has the 3D stress state represented by the following stress tensor:

Fig. 12 Symmetric laminate



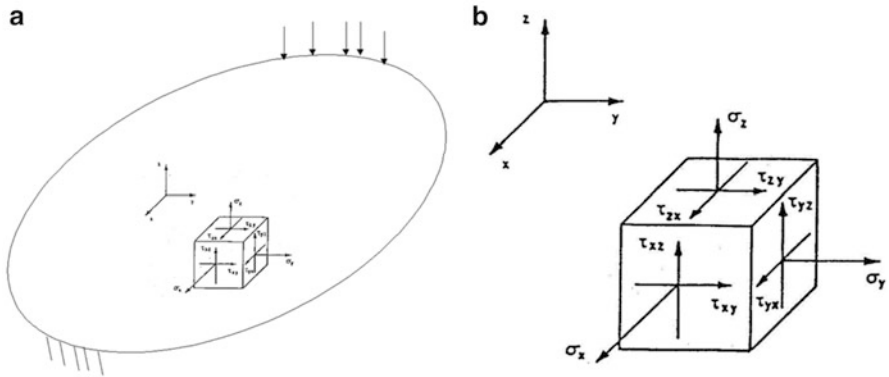


Fig. 13 (a) Solid loaded; (b) 3D stress state

$$\sigma = \begin{bmatrix} \sigma_{xx} & \tau_{xy} & \tau_{xz} \\ \tau_{yx} & \sigma_{yy} & \tau_{yz} \\ \tau_{zx} & \tau_{zy} & \sigma_{zz} \end{bmatrix} \tag{47}$$

By using the equilibrium equations of momentum, it is obtained:

$$\tau_{xy} = \tau_{yx} \quad \text{and} \quad \tau_{xz} = \tau_{zx} \quad \text{and} \quad \tau_{yz} = \tau_{zy} \tag{48}$$

Thus, the stress tensor is symmetric and it can be represented mathematically by a vector with 6 (six) positions:

$$\sigma = \begin{bmatrix} \sigma_x \\ \sigma_y \\ \sigma_z \\ \tau_{yz} \\ \tau_{zx} \\ \tau_{xy} \end{bmatrix} \quad \text{or} \quad \sigma = \begin{bmatrix} \sigma_1 \\ \sigma_2 \\ \sigma_3 \\ \sigma_{23} \\ \sigma_{31} \\ \sigma_{12} \end{bmatrix} \quad \text{or} \quad \sigma = \begin{bmatrix} \sigma_1 \\ \sigma_2 \\ \sigma_3 \\ \sigma_4 \\ \sigma_5 \\ \sigma_6 \end{bmatrix} \tag{49}$$

An analog approach can be used for the strain tensor:

$$\varepsilon = \begin{bmatrix} \varepsilon_{xx} & \frac{\gamma_{xy}}{2} & \frac{\gamma_{xz}}{2} \\ \frac{\gamma_{yx}}{2} & \varepsilon_{yy} & \frac{\gamma_{yz}}{2} \\ \frac{\gamma_{zx}}{2} & \frac{\gamma_{zy}}{2} & \varepsilon_{zz} \end{bmatrix} \tag{50}$$

Thus, the strain tensor is also symmetric and it can be represented mathematically by a vector with 6 (six) positions:

$$\varepsilon = \begin{bmatrix} \varepsilon_{xx} \\ \varepsilon_{yy} \\ \varepsilon_{zz} \\ \gamma_{yz}/2 \\ \gamma_{zx}/2 \\ \gamma_{xy}/2 \end{bmatrix} \quad \text{or} \quad \varepsilon = \begin{bmatrix} \varepsilon_x \\ \varepsilon_y \\ \varepsilon_z \\ \varepsilon_{yz} \\ \varepsilon_{zx} \\ \varepsilon_{xy} \end{bmatrix} \quad \text{or} \quad \varepsilon = \begin{bmatrix} \varepsilon_1 \\ \varepsilon_2 \\ \varepsilon_3 \\ \varepsilon_{23} \\ \varepsilon_{31} \\ \varepsilon_{12} \end{bmatrix} \quad \text{or} \quad \varepsilon = \begin{bmatrix} \varepsilon_1 \\ \varepsilon_2 \\ \varepsilon_3 \\ \varepsilon_4 \\ \varepsilon_5 \\ \varepsilon_6 \end{bmatrix} \quad (51)$$

The constitutive equation relates the stress and strain vectors. For anisotropic materials, this relation is given by the Hooke’s Law Generalized as follows (for index notation):

$$\sigma_i = D_{ij}\varepsilon_j \quad i, j = 1, 2, \dots, 6$$

For matrix notation, it is observed the constitutive tensor D with 36 (thirty six) components:

$$\begin{bmatrix} \sigma_1 \\ \sigma_2 \\ \sigma_3 \\ \sigma_4 \\ \sigma_5 \\ \sigma_6 \end{bmatrix} = \begin{bmatrix} D_{11} & D_{12} & D_{13} & D_{14} & D_{15} & D_{16} \\ D_{21} & D_{22} & D_{23} & D_{24} & D_{25} & D_{26} \\ D_{31} & D_{32} & D_{33} & D_{34} & D_{35} & D_{36} \\ D_{41} & D_{42} & D_{43} & D_{44} & D_{45} & D_{46} \\ D_{51} & D_{52} & D_{53} & D_{54} & D_{55} & D_{56} \\ D_{61} & D_{62} & D_{63} & D_{64} & D_{65} & D_{66} \end{bmatrix} \begin{bmatrix} \varepsilon_1 \\ \varepsilon_2 \\ \varepsilon_3 \\ \gamma_4 \\ \gamma_5 \\ \gamma_6 \end{bmatrix} \quad (52)$$

However, it is shown that the constitutive tensor D is symmetric ($D_{ij} = D_{ji}$) and, in fact, the number of components is equal to 21 (twenty-one). Moreover, D represents the stiffness of the material and D^{-1} represents the compliance. Thus, D can be written in function of the material properties of composite phases (matrix, reinforcements, and interface).

As commented earlier, a ply of the laminate is assumed to be orthotropic material. Then, this ply has 3 (three) planes of symmetry. Also, an orthotropic material does not show coupling between normal stresses and shear strains (γ), as well as between shear stresses and normal strains (ε). Thus, the tensor D for this type of material has only 9 (nine) components:

$$D = \begin{bmatrix} D_{11} & D_{12} & D_{13} & 0 & 0 & 0 \\ D_{12} & D_{22} & D_{23} & 0 & 0 & 0 \\ D_{13} & D_{23} & D_{33} & 0 & 0 & 0 \\ 0 & 0 & 0 & D_{44} & 0 & 0 \\ 0 & 0 & 0 & 0 & D_{55} & 0 \\ 0 & 0 & 0 & 0 & 0 & D_{66} \end{bmatrix} \quad (53)$$

By analogy, the tensor C has 9 (nine) components:

$$\begin{bmatrix} \varepsilon_1 \\ \varepsilon_2 \\ \varepsilon_3 \\ \gamma_4 \\ \gamma_5 \\ \gamma_6 \end{bmatrix} = \begin{bmatrix} C_{11} & C_{12} & C_{13} & 0 & 0 & 0 \\ C_{21} & C_{22} & C_{23} & 0 & 0 & 0 \\ C_{31} & C_{32} & C_{33} & 0 & 0 & 0 \\ 0 & 0 & 0 & C_{44} & 0 & 0 \\ 0 & 0 & 0 & 0 & C_{55} & 0 \\ 0 & 0 & 0 & 0 & 0 & C_{66} \end{bmatrix} \begin{bmatrix} \sigma_1 \\ \sigma_2 \\ \sigma_3 \\ \sigma_4 \\ \sigma_5 \\ \sigma_6 \end{bmatrix} \tag{54}$$

$$C_{11} = \frac{1}{E_{11}}; \quad C_{21} = \frac{-\nu_{12}}{E_{11}}; \quad C_{31} = \frac{-\nu_{13}}{E_{11}}$$

$$C_{12} = \frac{-\nu_{21}}{E_{22}}; \quad C_{22} = \frac{1}{E_{22}}; \quad C_{32} = \frac{-\nu_{23}}{E_{22}}$$

$$C_{13} = \frac{-\nu_{31}}{E_{33}}; \quad C_{23} = \frac{-\nu_{32}}{E_{33}}; \quad C_{33} = \frac{1}{E_{33}}$$

$$C_{44} = \frac{1}{G_{23}}; \quad C_{55} = \frac{1}{G_{31}}; \quad C_{66} = \frac{1}{G_{12}}$$

Considering the symmetry of the tensor C , then:

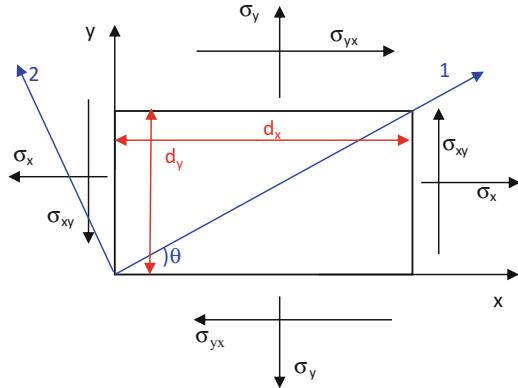
$$\frac{\nu_{ij}}{E_i} = \frac{\nu_{ji}}{E_j} \tag{55}$$

The matrix inverse of compliance is the stiffness, and for composites, this matrix will be named by Q :

$$\begin{bmatrix} \sigma_1 \\ \sigma_2 \\ \sigma_3 \\ \sigma_4 \\ \sigma_5 \\ \sigma_6 \end{bmatrix} = \begin{bmatrix} Q_{11} & Q_{12} & Q_{13} & 0 & 0 & 0 \\ Q_{21} & Q_{22} & Q_{23} & 0 & 0 & 0 \\ Q_{31} & Q_{32} & Q_{33} & 0 & 0 & 0 \\ 0 & 0 & 0 & Q_{44} & 0 & 0 \\ 0 & 0 & 0 & 0 & Q_{55} & 0 \\ 0 & 0 & 0 & 0 & 0 & Q_{66} \end{bmatrix} \begin{bmatrix} \varepsilon_1 \\ \varepsilon_2 \\ \varepsilon_3 \\ \gamma_4 \\ \gamma_5 \\ \gamma_6 \end{bmatrix} \tag{56}$$

where:

Fig. 14 Thin ply of composite material: plane stress state. Local coordinate system (1-2) and Global coordinate system ($x-y$)



$$Q_{11} = \frac{E_{11}(1 - \nu_{23}\nu_{32})}{\Delta}$$

$$Q_{22} = \frac{E_{22}(1 - \nu_{31}\nu_{13})}{\Delta}$$

$$Q_{33} = \frac{E_{33}(1 - \nu_{12}\nu_{21})}{\Delta}$$

$$Q_{44} = G_{23}$$

$$Q_{55} = G_{13}$$

$$Q_{66} = G_{12}$$

$$Q_{12} = \frac{E_{11}(\nu_{21} + \nu_{31}\nu_{23})}{\Delta} = \frac{E_{22}(\nu_{12} + \nu_{32}\nu_{13})}{\Delta}$$

$$Q_{13} = \frac{E_{11}(\nu_{31} + \nu_{21}\nu_{32})}{\Delta} = \frac{E_{22}(\nu_{13} + \nu_{12}\nu_{23})}{\Delta}$$

$$Q_{23} = \frac{E_{22}(\nu_{32} + \nu_{12}\nu_{31})}{\Delta} = \frac{E_{33}(\nu_{23} + \nu_{21}\nu_{13})}{\Delta}$$

$$\Delta = 1 - \nu_{12}\nu_{21} - \nu_{23}\nu_{32} - \nu_{31}\nu_{13} - 2\nu_{21}\nu_{32}\nu_{13}$$

However, for a ply reinforced by fibers in one direction, it is considered a transversally isotropic material, so: $E_{22} = E_{33}$; $G_{13} = G_{23}$ and $\nu_{12} = \nu_{13}$. Besides, the thickness of the ply is very thin compared to the length and the width, then it is assumed plane stress state (Fig. 14).

Thus, the Hooke's Law can be written by using the Reduced Stiffness Stress:

$$\begin{bmatrix} \sigma_1 \\ \sigma_2 \\ \sigma_6 \end{bmatrix} = \begin{bmatrix} Q_{11} & Q_{12} & 0 \\ Q_{21} & Q_{22} & 0 \\ 0 & 0 & Q_{66} \end{bmatrix} \begin{bmatrix} \varepsilon_1 \\ \varepsilon_2 \\ \gamma_6 \end{bmatrix} \quad (57)$$

where:

$$Q_{11} = \frac{E_{11}}{1 - \nu_{12}\nu_{21}} = \frac{E_{11}^2}{E_{11} - \nu_{12}^2 E_{22}} \quad Q_{12} = Q_{21} = \frac{\nu_{12} E_{22}}{1 - \nu_{12}\nu_{21}} = \frac{\nu_{12} E_{11} E_{22}}{E_{11} - \nu_{12}^2 E_{22}}$$

$$Q_{22} = \frac{E_{22}}{1 - \nu_{12}\nu_{21}} = \frac{E_{11} E_{22}}{E_{11} - \nu_{12}^2 E_{22}} \quad \frac{\nu_{12}}{E_{11}} = \frac{\nu_{21}}{E_{22}}$$

$$Q_{66} = G_{12}$$

Considering the axes 1 and 2 and that 1 is aligned to the fibers and 2 is normal to the fibers, it can be used the transformation matrix of coordinates in order to write the stress components in Local or Global coordinate systems:

$$\begin{bmatrix} \sigma_1 \\ \sigma_2 \\ \sigma_{12} \end{bmatrix}_{\text{Local}} = [T] \begin{bmatrix} \sigma_x \\ \sigma_y \\ \sigma_{xy} \end{bmatrix}_{\text{Global}} \quad \text{or} \quad \begin{bmatrix} \sigma_x \\ \sigma_y \\ \sigma_{xy} \end{bmatrix}_{\text{Global}} = [T]^{-1} \begin{bmatrix} \sigma_1 \\ \sigma_2 \\ \sigma_{12} \end{bmatrix}_{\text{Local}} \quad (58)$$

where:

$$[T] = \begin{bmatrix} m^2 & n^2 & 2mn \\ n^2 & m^2 & -2mn \\ -mn & mn & (m^2 - n^2) \end{bmatrix}; \quad m = \cos(\theta) \quad \text{and} \quad n = \sin(\theta)$$

By analogy, the strain relations can be given by:

$$\begin{bmatrix} \varepsilon_1 \\ \varepsilon_2 \\ \gamma_6/2 \end{bmatrix}_{\text{Local}} = [T] \begin{bmatrix} \varepsilon_x \\ \varepsilon_y \\ \gamma_{xy}/2 \end{bmatrix}_{\text{Global}} \quad \text{or} \quad \begin{bmatrix} \varepsilon_x \\ \varepsilon_y \\ \gamma_{xy}/2 \end{bmatrix}_{\text{Global}} = [T]^{-1} \begin{bmatrix} \varepsilon_1 \\ \varepsilon_2 \\ \gamma_6/2 \end{bmatrix}_{\text{Local}} \quad (59a)$$

Replacing (58) and (59a) into (57), it is obtained the constitutive equation for the Global coordinate system by using the Transformed Reduced Stiffness Matrix:

$$\begin{bmatrix} \sigma_x \\ \sigma_y \\ \sigma_{xy} \end{bmatrix}_{\text{Global}} = \begin{bmatrix} \bar{Q}_{11} & \bar{Q}_{12} & \bar{Q}_{16} \\ \bar{Q}_{12} & \bar{Q}_{22} & \bar{Q}_{26} \\ \bar{Q}_{16} & \bar{Q}_{26} & \bar{Q}_{66} \end{bmatrix} \begin{bmatrix} \varepsilon_x \\ \varepsilon_y \\ \gamma_{xy} \end{bmatrix}_{\text{Global}} \quad (59b)$$

or:

$$\begin{bmatrix} \bar{Q}_{11} & \bar{Q}_{12} & \bar{Q}_{16} \\ \bar{Q}_{12} & \bar{Q}_{22} & \bar{Q}_{26} \\ \bar{Q}_{16} & \bar{Q}_{26} & \bar{Q}_{66} \end{bmatrix} = [T]^{-1} \begin{bmatrix} Q_{11} & Q_{12} & Q_{16} \\ Q_{12} & Q_{22} & Q_{26} \\ Q_{16} & Q_{26} & Q_{66} \end{bmatrix} [T] \quad (59c)$$

Thus, the matrix components $[\bar{Q}]$ are given by:

$$\begin{aligned} \bar{Q}_{11} &= Q_{11}m^4 + 2m^2n^2(Q_{12} + 2Q_{66}) + Q_{22}n^4 \\ \bar{Q}_{12} &= (Q_{11} + Q_{22} - 4Q_{66})n^2m^2 + Q_{12}(n^4 + m^4) \\ \bar{Q}_{22} &= Q_{11}n^4 + 2(Q_{12} + 2Q_{66})n^2m^2 + Q_{22}m^4 \\ \bar{Q}_{16} &= (Q_{11} - Q_{12})nm^3 + (Q_{12} - Q_{22})n^3m - 2mn(m^2 - n^2)Q_{66} \\ \bar{Q}_{26} &= (Q_{11} - Q_{12})n^3m + (Q_{12} - Q_{22})nm^3 + 2mn(m^2 - n^2)Q_{66} \\ \bar{Q}_{66} &= (Q_{11} + Q_{22} - 2Q_{12} - 2Q_{66})n^2m^2 + Q_{66}(n^4 + m^4) \end{aligned} \quad (60)$$

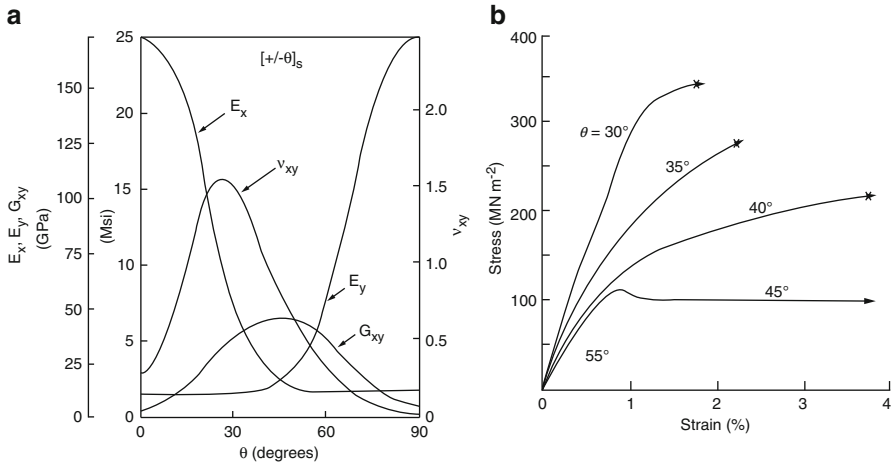


Fig. 15 Influence of the fiber orientation: (a) in the elastic properties (Jang 1994); (b) in the ply stiffness (Hull 1981)

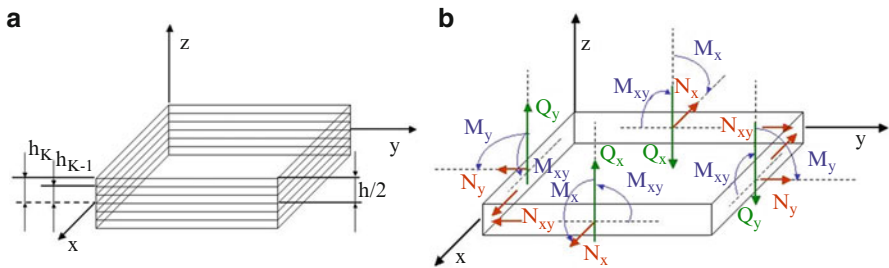


Fig. 16 (a) Laminate structure; (b) membrane loadings, shear forces, and bending moments

Therefore, \bar{Q} has the influence of the orientation of the fiber in the ply (Fig. 15). It is verified that the orientation of the fiber influences in the mechanical properties and, consequently, in the ply stiffness, which will influence in the laminate stiffness.

Considering a laminate with h thickness and N plies, where the top of each k ply is distant h_k from the medium plane of the laminate as show by Fig. 16a, it will be calculated its stiffness by using CLT.

In this laminate, Membrane Loadings (N_x ; N_y ; and N_{xy}), Shear Forces (Q_x and Q_y), Bending Moments (M_x and M_y), and Torsion Moments (M_{xy}) can actuate as shown by Fig. 16b. These loadings can be calculated in function of the intern stresses of the laminate as follows:

$$\begin{bmatrix} N_x \\ N_y \\ N_{xy} \\ Q_x \\ Q_y \end{bmatrix} = \int_{-h/2}^{h/2} \begin{bmatrix} \sigma_x \\ \sigma_y \\ \sigma_{xy} \\ \sigma_{xz} \\ \sigma_{xy} \end{bmatrix} dz [N/m] \tag{61}$$

$$\begin{bmatrix} M_x \\ M_y \\ M_{xy} \end{bmatrix} = \int_{-h/2}^{h/2} \begin{bmatrix} \sigma_x \\ \sigma_y \\ \sigma_{xy} \end{bmatrix} z dz \text{ [Nm/m]} \tag{62}$$

Therefore, it is necessary to obtain the intern stresses of the laminate, which can be calculated by using CLT. And, this theory is based on the Kirchhoff's and other hypotheses, as well.

- The laminate is considered plane (as a plate) and the medium plane (medium surface), which split the laminate, is in the middle of the laminate and contains the plane $x-y$.
- The plies are perfectly linked and there is not relative displacement between plies, so the displacements are continuous.
- The matrix, which is between two plies, is very thin and it is not deformed by shear stress.
- The laminate is thin and Kirchhoff's kinematic hypotheses are applied. Therefore, these promotes $\epsilon_{xz} = \epsilon_{yz} = \epsilon_z = 0$ and $\sigma_{xz}, \sigma_{yz}, \sigma_z \ll \sigma_{xy}, \sigma_y, \sigma_x$.

It is important to highlight that the Kirchhoff's kinematic hypotheses do not make account the transversal shear stress (Fig. 17). Hence, the transversal sections of the medium plane, which were plane and normal to the medium plane, remain plane and normal to the medium plane after the applied loading. Therefore:

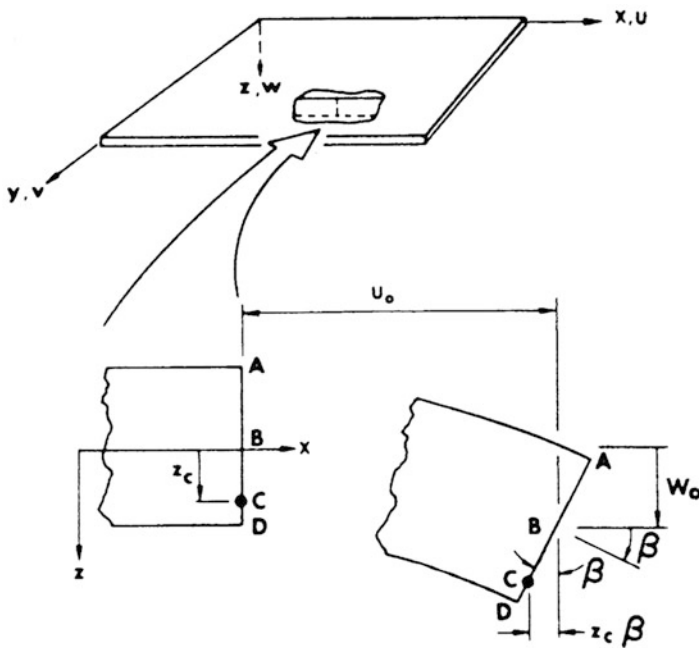


Fig. 17 Kirchhoff's kinematic hypotheses (Keunings 1992)

$\varepsilon_{xz} = \varepsilon_{yz} = \varepsilon_z = 0$. However, the stresses σ_{xz} , σ_{yz} , and σ_z are very important for delamination analyses. Moreover, if the structure is thick, the structural analyses should be affected in case of the transversal shears are not considered. Thus, for thick laminates or delamination analyses, it is necessary to use other kinematic hypotheses such as Mindlin-Reissner or Higher-order Shear deformation Theory—HST. However, in this chapter, it is considered mainly thin laminates, i.e., the relation length (or width) per thickness is minimum higher than 10.

Considering Fig. 17, for the point C with distance equal to z_c from the medium plane, the displacement u_c in the x direction is given by:

$$u_c = u_0 - z_c \beta \quad (63)$$

Thus:

$$\beta = \frac{\partial w_0}{\partial x} \quad (64)$$

Therefore, the displacements u and v in the directions x and y , respectively, are given by:

$$u(x, y, z) = u_0(x, y) - z \frac{\partial w_0(x, y)}{\partial x} \quad (65)$$

$$v(x, y, z) = v_0(x, y) - z \frac{\partial w_0(x, y)}{\partial y} \quad (66)$$

where:

u_0 and v_0 are displacements measured in the medium plane.
 w is the displacement in z direction:

$$w(x, y, z) = w_0(x, y) \quad (67)$$

Thus, the strain for k ply can be calculated as follows:

$$\varepsilon_x(x, y, z) = \frac{\partial u_0}{\partial x} - z \frac{\partial^2 w_0}{\partial x^2} = \varepsilon_{x0} + zK_x \quad (68)$$

$$\varepsilon_y(x, y, z) = \frac{\partial v_0}{\partial y} - z \frac{\partial^2 w_0}{\partial y^2} = \varepsilon_{y0} + zK_y \quad (69)$$

$$2\varepsilon_{xy}(x, y, z) = \frac{\partial u_0}{\partial y} + \frac{\partial v_0}{\partial x} - 2z \frac{\partial^2 w_0}{\partial x \partial y} = 2\varepsilon_{xy0} + zK_{xy} \quad (70)$$

$$\text{or} \quad \gamma_{xy} = \gamma_{xy0} + zK_{xy}$$

where:

ϵ_{x0} , ϵ_{y0} , and ϵ_{xy0} are strains related to extensional and distortional deformation in plane $x-y$.

It is observed that Kirchhoff’s kinematic hypotheses results on a linear variation of the displacements and strains along the thickness. Hence, for a laminate, the strain vector can be written for the Global Coordinate System ($x-y$) as follows:

$$[\epsilon]_{Global} = [\epsilon_0]_{Global} + z[K]_{Global} \tag{71}$$

Therefore, the stress distribution varies from one ply to another along the thickness. Replacing (71) into (59b), it is calculated the stress vector for each k ply for the Global Coordinate System:

$$\begin{bmatrix} \sigma_x \\ \sigma_y \\ \sigma_{xy} \end{bmatrix}_{Global}^k = \begin{bmatrix} \bar{Q}_{11} & \bar{Q}_{12} & \bar{Q}_{16} \\ \bar{Q}_{12} & \bar{Q}_{22} & \bar{Q}_{26} \\ \bar{Q}_{16} & \bar{Q}_{26} & \bar{Q}_{66} \end{bmatrix}^k \begin{bmatrix} \epsilon_{x0} \\ \epsilon_{y0} \\ \gamma_{xy0} \end{bmatrix}_{Global} + z \begin{bmatrix} \bar{Q}_{11} & \bar{Q}_{12} & \bar{Q}_{16} \\ \bar{Q}_{12} & \bar{Q}_{22} & \bar{Q}_{26} \\ \bar{Q}_{16} & \bar{Q}_{26} & \bar{Q}_{66} \end{bmatrix}^k \begin{bmatrix} K_x \\ K_y \\ K_{xy} \end{bmatrix}_{Global} \tag{72}$$

Considering the compact form:

$$[\sigma]_{Global}^k = [\bar{Q}]_{Global}^k [[\epsilon_0]_{Global} + z[K]_{Global}] \tag{73}$$

where:

$[\epsilon_0]$ = strains

$[K]$ = curvatures

k = ply in the k position.

Replacing (73) into (61) and into (62):

$$\begin{bmatrix} N_X \\ N_Y \\ N_{XY} \end{bmatrix} = \sum_{K=1}^n \left\{ \int_{h_{K-1}}^{h_K} [\bar{Q}]_K \begin{bmatrix} \epsilon_{x0} \\ \epsilon_{y0} \\ \gamma_{xy0} \end{bmatrix} dz + \int_{h_{K-1}}^{h_K} [\bar{Q}]_K \begin{bmatrix} K_x \\ K_y \\ K_{xy} \end{bmatrix} z dz \right\} \tag{74}$$

$$\begin{bmatrix} M_X \\ M_Y \\ M_{XY} \end{bmatrix} = \sum_{K=1}^n \left\{ \int_{h_{K-1}}^{h_K} [\bar{Q}]_K \begin{bmatrix} \epsilon_{x0} \\ \epsilon_{y0} \\ \gamma_{xy0} \end{bmatrix} z dz + \int_{h_{K-1}}^{h_K} [\bar{Q}]_K \begin{bmatrix} K_x \\ K_y \\ K_{xy} \end{bmatrix} z^2 dz \right\} \tag{75}$$

The matrix $[\bar{Q}]$ remains constant for each ply, because it is only function of the elastic properties of plies and fiber orientation in each ply. The strain components $[\epsilon_0]$ and the curvature $[K]$ of the laminate remains constant for each ply, also. Therefore, Eqs. (74) and (75) can be written as follows:

$$[N] = [A][\varepsilon_0] + [B][K] \quad (76a)$$

$$[M] = [B][\varepsilon_0] + [D][K] \quad (76b)$$

where:

$$[A] = \sum_{k=1}^n \int_{h_{k-1}}^{h_k} [\bar{Q}]_K dz = \text{membrane stiffness matrix.}$$

$$[B] = \sum_{k=1}^n \int_{h_{k-1}}^{h_k} [\bar{Q}]_K z dz = \text{coupling stiffness matrix.}$$

$$[D] = \sum_{k=1}^n \int_{h_{k-1}}^{h_k} [\bar{Q}]_K z^2 dz = \text{bending/torsion stiffness matrix.}$$

or:

$$\begin{bmatrix} [N] \\ [M] \end{bmatrix} = \begin{bmatrix} [A] & [B] \\ [B] & [D] \end{bmatrix} \begin{bmatrix} [\varepsilon_0] \\ [K] \end{bmatrix} \quad (77)$$

If the coupling matrix $[B]$ is not null, then membrane loadings can cause not only normal and shear strains, but also curvatures K_x , K_y , and K_{xy} . By analogy, moments loadings can cause not only curvatures K_x , K_y , and K_{xy} , but also normal and shear strains. By the other side, if the coupling matrix $[B]$ is null, these effects cannot occur. In fact, matrix $[B]$ is null for symmetric laminates, and this is easily proved by verifying that stiffness part related to z positive values are canceled by stiffness part related to z negative values.

In case of thick laminate analysis, it is necessary to consider the shear forces (Q_x and Q_y). Thus, one simple approach consists on assuming parabolic distribution along of the laminate thickness:

$$f(z) = \frac{5}{4} \left[1 - \left(\frac{z}{h/2} \right)^2 \right] \quad (78)$$

Integrating this equation, it is obtained:

$$Q_x = (A_{55}\gamma_{xz} + A_{45}\gamma_{yz}) \quad (79)$$

$$Q_y = (A_{45}\gamma_{xz} + A_{44}\gamma_{yz}) \quad (80)$$

where:

$$A_{ij} = \frac{5}{4} \sum_{k=1}^n (\bar{Q}_{ij})_k \left[h_k - h_{k-1} - \frac{4}{3}(h_k^3 - h_{k-1}^3) \frac{1}{h^2} \right]$$

Therefore:

$$\begin{bmatrix} N_x \\ N_y \\ N_{xy} \\ M_x \\ M_y \\ M_{xy} \end{bmatrix} = \begin{bmatrix} A_{11} & A_{12} & A_{16} & B_{11} & B_{12} & B_{16} \\ A_{12} & A_{22} & A_{26} & B_{12} & B_{22} & B_{26} \\ A_{16} & A_{26} & A_{66} & B_{16} & B_{26} & B_{66} \\ B_{11} & B_{12} & B_{16} & D_{11} & D_{12} & D_{16} \\ B_{12} & B_{22} & B_{26} & D_{12} & D_{22} & D_{26} \\ B_{16} & B_{26} & B_{66} & D_{16} & D_{26} & D_{66} \end{bmatrix} \begin{bmatrix} \varepsilon_{x_0} \\ \varepsilon_{y_0} \\ \gamma_{xy_0} \\ K_x \\ K_y \\ K_{xy} \end{bmatrix} \quad (81)$$

$$\begin{bmatrix} Q_y \\ Q_x \end{bmatrix} = \begin{bmatrix} A_{44} & A_{45} \\ A_{45} & A_{55} \end{bmatrix} \begin{bmatrix} \gamma_{yz} \\ \gamma_{xz} \end{bmatrix} \quad (82)$$

It is concluded that for thin laminates, it should be used only Eq. (81), and, for thick laminates, it is necessary to use at least Eq. (82), as well.

In terms of design, the equations above should be written in inverse format, because, normally, the loadings are provided and it is required to calculate the strains and curvatures. However, these values are obtained for each ply, considering the Global Coordinate System, and, now, it is necessary to calculate these values for Local Coordinate System.

3.2 Strain and Stress Analyses in the Ply

The determination of stress and strain components for each ply for the Local Coordinate System is very important to evaluate the failure or not of a laminate, considering a load case.

The failure mechanisms and failure criteria will be addressed in the next section, but the criteria are normally verified in each ply of the laminate considering the stress and strain components for the Local Coordinate System (1-2). Thus, in order to obtain these values, it is initially written Eq. (76a) in the following format:

$$[\varepsilon_0] = [A]^{-1}[N] - [A]^{-1}[B][K] \quad (83)$$

Replacing (83) into (76b), there is:

$$[M] = [B][A]^{-1}[N] - \left\{ [B][A]^{-1}[B] - [D] \right\} [K] \quad (84)$$

Equations (83) and (84) can be combined:

$$\begin{bmatrix} [\varepsilon_0] \\ [M] \end{bmatrix} = \begin{bmatrix} [A^*] & [B^*] \\ [C^*] & [D^*] \end{bmatrix} \begin{bmatrix} [N] \\ [K] \end{bmatrix} \quad (85)$$

where:

$$\begin{aligned}
[A^*] &= [A^{-1}] \\
[B^*] &= -[A^{-1}][B] \\
[C^*] &= [B][A^{-1}] = -[B^*]^T \\
[D^*] &= [D] - [B][A^{-1}][B]
\end{aligned}$$

Thus, Eqs. (83) and (84) can be written as follows:

$$[\varepsilon_0] = [A^*][N] + [B^*][K] \quad (86)$$

$$[M] = [C^*][N] + [D^*][K] \quad (87)$$

Solving the system above for the curvatures K :

$$[K] = [D^*]^{-1}[M] - [D^*]^{-1}[C^*][N] \quad (88)$$

Replacing Eq. (88) into (86):

$$[\varepsilon_0] = \left\{ [A^*] - [B^*][D^*]^{-1}[C^*] \right\} [N] + [B^*][D^*]^{-1}[M] \quad (89)$$

Combining Eqs. (88) and (89), it is obtained the system of equation completely inverted:

$$\begin{bmatrix} [\varepsilon_0] \\ [K] \end{bmatrix} = \begin{bmatrix} [A'] & [B'] \\ [C'] & [D'] \end{bmatrix} \begin{bmatrix} [N] \\ [M] \end{bmatrix} \quad (90)$$

where:

$$\begin{aligned}
[A'] &= [A^*] - [B^*][D^*]^{-1}[C^*] = [A^*] + [B^*][D^*]^{-1}[B^*]^T \\
[B'] &= [B^*][D^*]^{-1} \\
[C'] &= -[D^*]^{-1}[C^*] = [B']^T = [B'] \\
[D'] &= [D^*]^{-1}
\end{aligned}$$

Hence, it is calculated the strain components $[\varepsilon_0]$ and the curvatures $[K]$ of the laminate for the Global Coordinate System, considering a loading state. Based on these values, it is calculated the stress components for each k ply for the Global Coordinate System (Fig. 18):

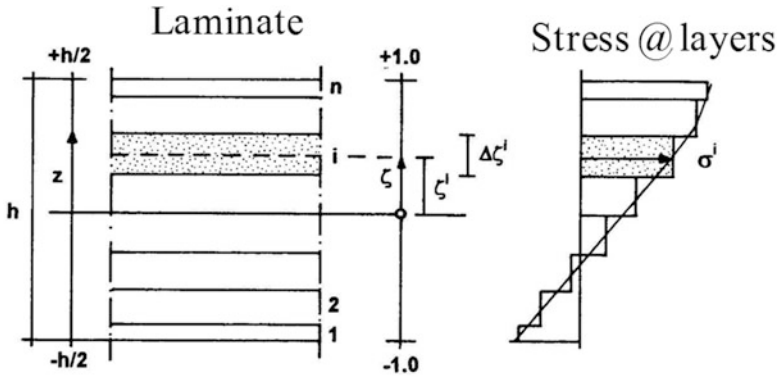


Fig. 18 Distribution of stress along of thickness

$$[\sigma]_{Global}^k = [\bar{Q}]_{Global}^k [[\epsilon_0]_{Global} + z[K]_{Global}] \tag{91}$$

By using the equations for coordinate transformation, it is determined the stress and strain components for the Local Coordinate System:

$$\begin{bmatrix} \sigma_1 \\ \sigma_2 \\ \sigma_{12} \end{bmatrix}_{Local}^k = [T] \begin{bmatrix} \sigma_x \\ \sigma_y \\ \sigma_{xy} \end{bmatrix}_{Global}^k \quad \text{and} \quad \begin{bmatrix} \epsilon_1 \\ \epsilon_2 \\ \gamma_{6/2} \end{bmatrix}_{Local}^k = [T] \begin{bmatrix} \epsilon_x \\ \epsilon_y \\ \gamma_{xy/2} \end{bmatrix}_{Global}^k \tag{92}$$

where:

$$[T] = \begin{bmatrix} m^2 & n^2 & 2mn \\ n^2 & m^2 & -2mn \\ -mn & mn & (m^2 - n^2) \end{bmatrix}; \quad m = \cos(\theta) \quad \text{and} \quad n = \sin(\theta)$$

Hence, the calculation of the stress and strain components for the Local Coordinate System can be summarized in 7 (seven) steps:

Step 1: Determine the elastic properties of each ply (E_{11} ; E_{22} ; G_{12} ; and ν_{12}).

Step 2: Calculate the Reduced Stiffness Matrix for each ply in relation of Local Coordinate System.

$$[Q]_{Local} = \begin{bmatrix} Q_{11} & Q_{12} & 0 \\ Q_{21} & Q_{22} & 0 \\ 0 & 0 & Q_{66} \end{bmatrix}$$

where:

$$\begin{aligned}
Q_{11} &= \frac{E_{11}}{1 - \nu_{12}\nu_{21}} = \frac{E_{11}^2}{E_{11} - \nu_{12}^2 E_{22}} \\
Q_{22} &= \frac{E_{22}}{1 - \nu_{12}\nu_{21}} = \frac{E_{11}E_{22}}{E_{11} - \nu_{12}^2 E_{22}} \\
Q_{66} &= G_{12} \\
Q_{12} = Q_{21} &= \frac{\nu_{12}E_{22}}{1 - \nu_{12}\nu_{21}} = \frac{\nu_{12}E_{11}E_{22}}{E_{11} - \nu_{12}^2 E_{22}} \\
\frac{\nu_{12}}{E_{11}} &= \frac{\nu_{21}}{E_{22}}
\end{aligned}$$

Step 3: Calculate the Transformed Reduced Stiffness Matrix for each ply in relation of Local Coordinate System.

$$[\bar{Q}]_k = \begin{bmatrix} \bar{Q}_{11} & \bar{Q}_{12} & \bar{Q}_{16} \\ \bar{Q}_{12} & \bar{Q}_{22} & \bar{Q}_{26} \\ \bar{Q}_{16} & \bar{Q}_{26} & \bar{Q}_{66} \end{bmatrix}$$

where:

$$\begin{aligned}
\bar{Q}_{11} &= Q_{11}m^4 + 2m^2n^2(Q_{12} + 2Q_{66}) + Q_{22}n^4 \\
\bar{Q}_{12} &= (Q_{11} + Q_{22} - 4Q_{66})n^2m^2 + Q_{12}(n^4 + m^4) \\
\bar{Q}_{22} &= Q_{11}n^4 + 2(Q_{12} + 2Q_{66})n^2m^2 + Q_{22}m^4 \\
\bar{Q}_{16} &= (Q_{11} - Q_{12})nm^3 + (Q_{12} - Q_{22})n^3m - 2mn(m^2 - n^2)Q_{66} \\
\bar{Q}_{26} &= (Q_{11} - Q_{12})n^3m + (Q_{12} - Q_{22})nm^3 + 2mn(m^2 - n^2)Q_{66} \\
\bar{Q}_{66} &= (Q_{11} + Q_{22} - 2Q_{12} - 2Q_{66})n^2m^2 + Q_{66}(n^4 + m^4) \\
m &= \cos(\theta) \quad \text{and} \quad n = \sin(\theta)
\end{aligned}$$

Step 4: Calculate matrixes A, B, and D in relation of Global Coordinate System.

$$\begin{aligned}
[A] &= \sum_{k=1}^n [\bar{Q}]_k (h_k - h_{k-1}) \\
[B] &= \frac{1}{2} \sum_{k=1}^n [\bar{Q}]_k (h_k^2 - h_{k-1}^2) \\
[D] &= \frac{1}{3} \sum_{k=1}^n [\bar{Q}]_k (h_k^3 - h_{k-1}^3)
\end{aligned}$$

Step 5: Calculate the strain components $[\varepsilon_0]$ and the curvatures $[K]$ of the laminate for the Global Coordinate System.

$$\begin{bmatrix} [\varepsilon_0] \\ [K] \end{bmatrix}_{\text{Global}} = \begin{bmatrix} [A'] & [B'] \\ [C'] & [D'] \end{bmatrix} \begin{bmatrix} [N] \\ [M] \end{bmatrix}$$

where:

$$\begin{aligned} [A'] &= [A^*] - [B^*][D^*]^{-1}[C^*] = [A^*] + [B^*][D^*]^{-1}[B^*]^T \\ [B'] &= [B^*][D^*]^{-1} \\ [C'] &= -[D^*]^{-1}[C^*] = [B']^T = [B'] \\ [D'] &= [D^*]^{-1} \end{aligned}$$

Step 6: Calculate the stress components for each k ply for the Global Coordinate System.

$$[\sigma]_{\text{Global}}^k = [\overline{Q}]_{\text{Global}}^k [[\varepsilon_0]_{\text{Global}} + z[K]_{\text{Global}}]$$

Step 7: Calculate the stress components for each k ply for the Local Coordinate System.

$$\begin{bmatrix} \sigma_1 \\ \sigma_2 \\ \sigma_{12} \end{bmatrix}_{\text{Local}} = [T] \begin{bmatrix} \sigma_x \\ \sigma_y \\ \sigma_{xy} \end{bmatrix}_{\text{Global}}$$

where:

$$[T] = \begin{bmatrix} m^2 & n^2 & 2mn \\ n^2 & m^2 & -2mn \\ -mn & mn & (m^2 - n^2) \end{bmatrix}$$

These stress or strain components will be used in the Failure Criteria, and the engineer will be able to evaluate if the composite structure will fail or not under a specific load case.

4 Failure Analysis

Based on the stress or strain components values for each ply for the Local Coordinate System, it is carried out the failure analysis of the laminate. However, it is necessary to know previously the different failure modes, which can be found in the composite structures. Thus, based on the failure modes, which can occur, the failure criterion should be selected.

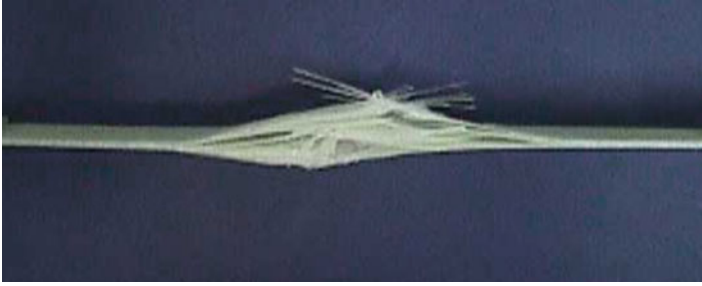


Fig. 19 Damage and failure mechanisms

4.1 Laminate Failure Modes

In this chapter, the failure/damage mechanisms are classified in two types:

- *Intralaminar damage*: occur inside the ply;
- *Interlaminar failure*: occur between plies.

The intralaminar damages correspond to the damage in the matrix, fibers, or interface fiber-matrix. The interlaminar failures correspond to the delaminations between plies, which consists on the separation of plies (Fig. 19).

4.1.1 Intralaminar Damage

The intralaminar damages can be divided in three different mechanisms:

- Mechanism of fiber damage.
- Mechanism of damage damage.
- Mechanism of interface matrix-fiber damage.

The mechanism of fiber damage depends on different aspects, such as diameter and length of fibers, volume fraction of fibers, and orientation of fibers. However, the damage modes are also related to the applied loadings. For examples, compression loading can produce fails in the fibers through micro-buckling or shearing (Fig. 20).

Tension loading can promote the rupture of the fibers and depends on the level of the adhesion between fibers and polymer matrix. In other words, if the loading, which acts in the matrix, is transferred to the fibers in an efficient way, then the fibers can fracture, depending on the level of load.

The matrix damage modes depend on the physic-chemical properties of the polymer, which can be fragile or ductile and have linear elastic or viscoelastic response. Moreover, this behavior depends on the environment temperature. However, in general way, the rupture of the matrix occurs close to a fractured fiber or close to a void created during the material processing. These regions show stress

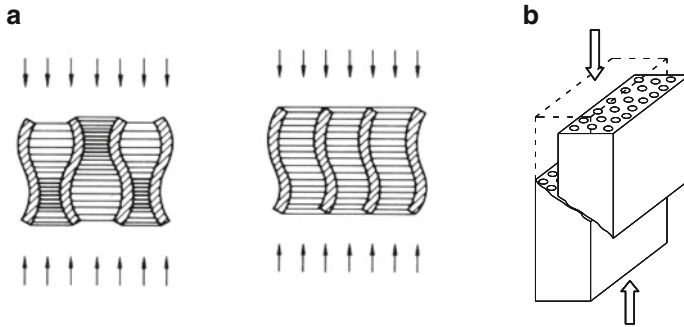


Fig. 20 Fiber damage mode under compression: (a) micro-buckling (Agarwal and Broutman 1990); (b) shearing (Adapted from Agarwal and Broutman 1990)

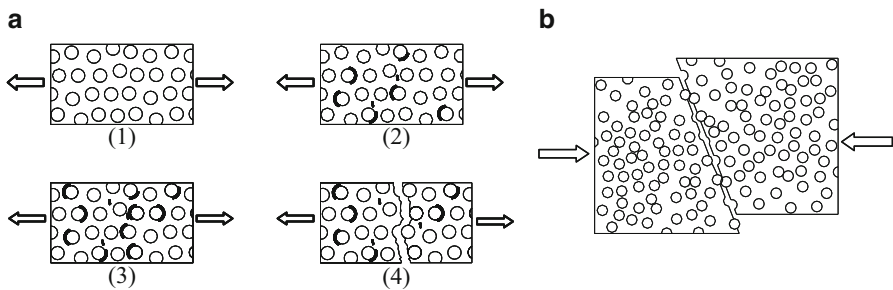


Fig. 21 Damage process in the matrix: (a) under tension; (b) under compression (adapted from Agarwal and Broutman 1990)

concentration, which causes failure of the matrix. Therefore, under tension loading, the damage process in the matrix, as shown by Fig. 21a, starts close to micro-failures (1), then propagates (2) and, finally, coalesces (3) until creating a catastrophic macro-failure (4). By the other side, under compression loading, the matrix can fail by shearing (Fig. 21b).

For the ply under shear loading, the damage mode will occur as shown by Fig. 22a. As it is observed, this damage mode depends mainly on the polymer matrix behavior, which can be non-linear due to inelastic strains.

The damage process of the ply is strongly influenced by the orientation of the fibers. For example, the ply can show a linear response when the loading is applied in the direction 1 (0°) or in the direction 2 (90°) due to the relevance of normal stresses. However, for the loadings applied close to the angle 15° , it is observed a non-linear response, because there is an important contribution of the shear stresses as shown by Fig. 22b.

Regarding the damage modes of the interface, it is confirmed that these modes depend on physic-chemical interaction between fiber and matrix. In fact, the quality of the interface is a parameter that it is used to evaluate the toughness of the

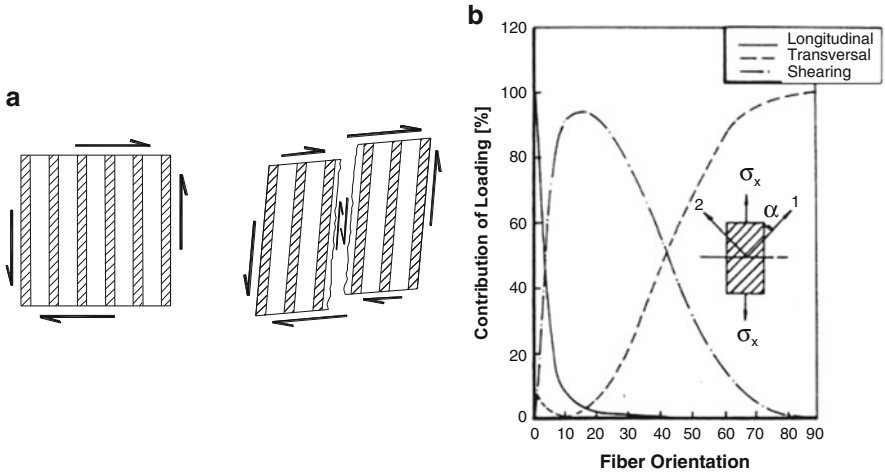


Fig. 22 (a) Damage of matrix under shear loadings (adapted from Agarwal and Broutman 1990); (b) influence of the fiber orientation in the damage process (Hahn and Tsai 1973)

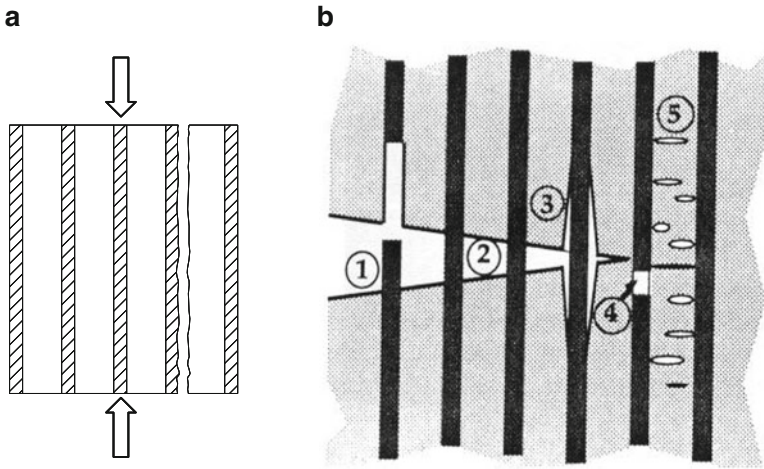


Fig. 23 (a) Debonding due to weak interface; (b) damage mechanisms in the ply (Anderson 1995)

composite material. Thus, if there is a weak interaction between fiber and matrix, then it occurs “*debonding*” as shown by Fig. 23a.

Figure 23b shows different damage mechanisms in the ply. If there is a weak interface, after the fiber failure, “*Pull-Out*” (mechanism 1) can take place. Before this mechanism, it is possible to occur “*Fiber Bridging*” (mechanism 2), since the composite has fragile fibers, ductile matrix, and strong interface. Thus, the crack propagation creates like bridges by using the fibers. As commented earlier, if the interface is weak, then “*debonding*” (mechanism 3) can occur. By the other side, if

the interface is strong, then failure of the fiber (mechanism 4) and the damage process of the matrix (mechanism 5) are verified. However, these all damage mechanisms are random and depend on several aspects:

- Physic-chemical properties of the fibers and polymer matrix.
- Alignment and strength of the fibers.
- Orientation and volume fraction of the fibers.
- Type of loading: tension, compression, shear, or combined.
- Environment effects: temperature, humidity, corrosion, etc.

4.1.2 Interlaminar Failure (Delaminations)

In composite materials, the failure starts with micromechanisms (intralaminar damages) and, after that, it is observed the macromechanisms like delaminations. In general, the damage evolution starts in the plies with fiber orientation close to 90° in relation to the loading. After the first damage, stresses are redistributed in the laminated and new failure mechanisms can occur in the same ply or in other plies. This failure process evolves until the damage to reach the interface between two plies, creating a discrete crack. In fact, the frontiers of the cracks, which were created in one ply, propagate until to find adjacent ply with fiber oriented in other direction (Fig. 24a). At this moment, the interlaminar shear stresses increase abruptly and the laminate suffers the delamination as shown by Fig. 24b. Considering the increment of the loadings, the delaminations increase (initiation) and evolve (propagation).

Researchers proved that the interlaminar failure is promoted by the interlaminar shear stress and normal stress in direction z as shown by Fig. 25a.

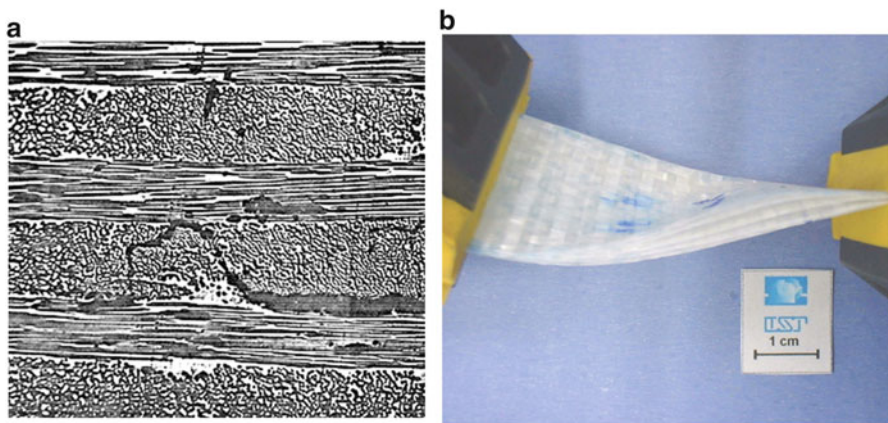


Fig. 24 Mechanisms of damage and failure in the plies: (a) evolution of the failure process (Hull 1981); (b) laminate with delaminations

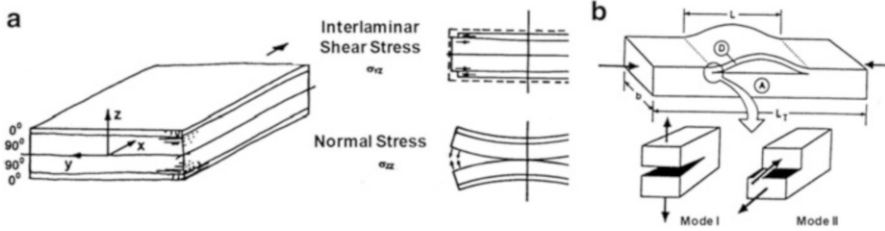


Fig. 25 (a) Delamination: interlaminar shear stress and normal stress; (b) modes of delamination (adapted from Magagnin Filho 1996)

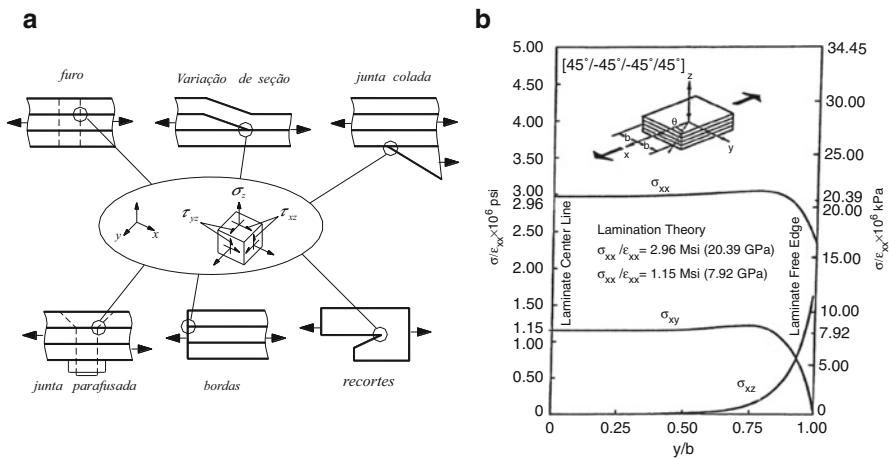


Fig. 26 (a) candidate regions of delamination (adapted from Jang 1994). (b) stress distribution along the ply length—edge effects (Keunings 1992)

According to the Fracture Mechanics, laminate material composites, normally, show two classic modes of delamination: Mode I and Mode II (Fig. 25b). The Mode I is created by tension loadings and Mode II is created by shear loadings. Thus, during the delamination process is common to observe the Mixed Mode, i.e., Mode I and Mode II are coupled.

In practical terms, the engineer should be pay attention, mainly in the geometrical discontinuities in the composite structures, such as holes and ply drop. In these regions, there is a 3D stress state, which promotes delamination (Fig. 26a). Another important region consists of the edge of the laminate. In fact, in this portion of the laminate, edge-effects can increase the transversal shear stress close to the edges (Fig. 26b).

4.2 Procedure to Analyze Failure in Laminates

It is considered that a structure fails when this one cannot satisfy the design criteria. Thus, failure criterion goals to provide an interpretation of the damages promoted by the loadings, showing if there is a local or a global failure in the structure. However, for laminate composite structures, there is a large number of damage and failure mechanisms, which occur in a random way. Thus, different approaches can be applied to design composite structures. One approach consists on carrying out micromechanics analyses in order to identify the local failure of fibers, matrix, or interface. By the other side, there is the macromechanics analysis, which consists on using a failure criterion in order to identify the failure of the ply.

The failure criterion can be written by using mathematical expressions (the criterion function), considering the stress or strain components for the Local Coordinate System (1-2) and allowable values for the ply:

$$\begin{aligned} \text{If } f(\sigma_1, \sigma_2, \sigma_3) \geq 0 & \text{ then the ply fails.} \\ \text{If } f(\sigma_1, \sigma_2, \sigma_3) < 0 & \text{ then the ply does not fail} \end{aligned} \quad (93)$$

Associated to the failure criterion, there are two methods of approaching the problem:

- *FPF Method (First Ply Failure)*: the laminate fails when the first ply fails.
- *LPF Method (Last Ply Failure)*: the laminate fails when the last ply fails.

LPF Method can be summarized in 9 (nine) steps (Fig. 27):

1. *Stress analyses*: calculate the stress components in each ply.
2. *Failure criterion selection*: select the most adequate criterion, considering the failure modes observed during the experimental tests for determination of allowable values and elastic properties.
3. *Calculate the criterion function*: use the stress components and allowable values to calculate the value for the criterion function.
4. *Verify the failure plies*: identify the plies, which fail.
5. *If there is not failure—increase the loading*: increase the loading in order to re-calculate the stress components in each ply.
6. *If there is failure—reduce the mechanical properties*: before increasing the loading, the mechanical properties of the plies, which failed, should be reduced.
7. *Total failure?*: check if all plies fail.
8. *If there is not total failure—re-calculate the stress distribution*: re-calculate the stress components in each ply, considering the reduction of laminate stiffness.
9. *If there is total failure—THE END*: finalize the analyses.

The FPF Method is strongly safety, because the failure of only single ply implies in the failure of the entire laminate. By the other side, the LPF Method over-estimates the strength of the laminate. Therefore, the engineer must be careful when choosing the method, mainly the failure criterion. However, due to the

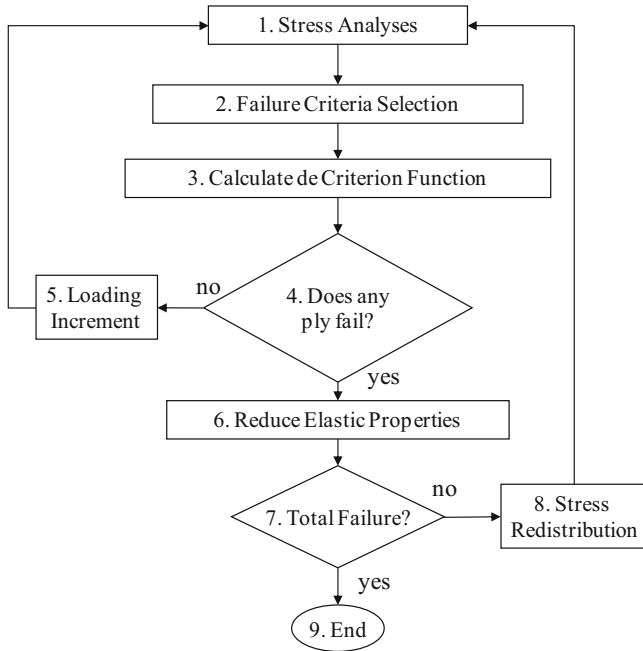


Fig. 27 Procedure to perform failure analyses by using Last Ply Failure Method

complexity to predict the failure mechanisms on composite structures, there is a large number of failure criteria to address this problem. In the next sub-items, it will be shown 3 (three) different failure criteria.

4.2.1 Maximum Stress Criterion

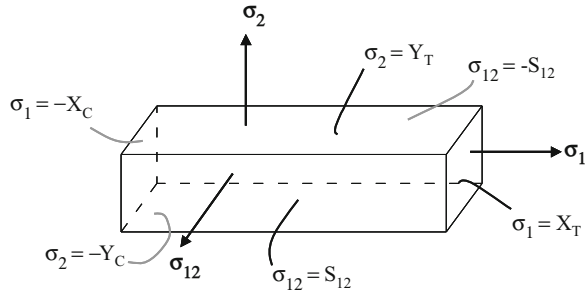
This failure criterion consists of 5 (five) sub-criteria and each one corresponds to the 5 (five) fundamental damage mode of the ply. If, at least, one allowable stress limit is exceeded, then the ply fails:

$$\sigma_1 \geq X_T \text{ or } \sigma_1 \leq -X_C \text{ or } \sigma_2 \geq Y_T \text{ or } \sigma_2 \leq -Y_C \text{ or } |\sigma_{12}| \geq S_{12} \tag{94}$$

where:

- σ_1 : normal stress component in direction 1.
- σ_2 : normal stress component in direction 2.
- σ_{12} : shear stress component in the plane 1-2.
- $X_{T,C}$: strength value for tension or compression in direction 1.
- $Y_{T,C}$: strength value for tension or compression in direction 2.
- S_{12} : strength value for shear in plane 1-2.

Fig. 28 Failure surface of maximum stress criterion



The failure surface for this criterion is a parallelepiped in the space of stresses (Fig. 28). Due to the difference between strength values for tension and compression, the geometric center of the parallelepiped does not coincide to the origin of space of stresses.

4.2.2 Maximum Strain Criterion

This failure criterion also consists of 5 (five) sub-criteria and each one corresponds to the 5 (five) fundamental damage mode of the ply. However, in this case, the criterion is written in terms of strains. Thus, if, at least, one allowable strain limit is exceeded, then the ply fails:

$$\epsilon_1 \geq X'_T \quad \text{or} \quad \epsilon_1 \leq -X'_C \quad \text{or} \quad \epsilon_2 \geq Y'_T \quad \text{or} \quad \epsilon_2 \leq -Y'_C \quad \text{or} \quad |\gamma_{12}| \geq S'_{12} \quad (95)$$

where:

ϵ_1 = normal strain component in direction 1.

ϵ_2 = normal strain component in direction 2.

ϵ_{12} = shear strain component in plane 1-2.

$X'_{T,C}$ = strain limit value for tension or compression in direction 1.

$Y'_{T,C}$ = strain limit value for tension or compression in direction 2.

S'_{12} = strain limit value for shear in plane 1-2.

In general, the Maximum Stress Criterion and Maximum Strain Criterion provide similar predictions, but when the composite material shows non-linear behavior, it is better to use the second one. Also, these criteria are not interactive, i.e., the stress component in one direction does not influence the failure mode caused by a stress component in other direction and vice-versa, but the mode failure of the ply can be identified.

4.2.3 TSAI-HILL Criterion

Based on HILL criterion, Tsai proposed a failure criterion for composite materials, especially for laminates with orthotropic plies. Thus, TSAI-HILL criterion for plane stress state can be written as follows:

$$f(\sigma) = \left(\frac{\sigma_1}{X}\right)^2 + \left(\frac{\sigma_2}{Y}\right)^2 - \left(\frac{\sigma_1\sigma_2}{X^2}\right) + \left(\frac{\sigma_{12}}{S_{12}}\right)^2 = 1 \quad (96)$$

where σ_1 and σ_2 are the normal stress components in the ply. Besides, in this criterion, it is necessary to use different values for compression and tension, not only for actuating stresses, but also for allowable values. Thus, re-organizing the equation above, it is obtained 4 (four) different equations in the space of stresses ($\sigma_1 - \sigma_2$):

1. For the First Quadrant ($\sigma_1, \sigma_2 > 0$):

$$\frac{\sigma_1^2}{X_T^2} + \frac{\sigma_2^2}{Y_T^2} - \frac{\sigma_1\sigma_2}{X_T^2} = 1 - \frac{\sigma_{12}^2}{S_{12}^2} \quad (96a)$$

2. For the Second Quadrant ($\sigma_1 < 0, \sigma_2 > 0$):

$$\frac{\sigma_1^2}{X_C^2} + \frac{\sigma_2^2}{Y_T^2} + \frac{\sigma_1\sigma_2}{X_C^2} = 1 - \frac{\sigma_{12}^2}{S_{12}^2} \quad (96b)$$

3. For the Third Quadrant ($\sigma_1, \sigma_2 < 0$):

$$\frac{\sigma_1^2}{X_C^2} + \frac{\sigma_2^2}{Y_C^2} - \frac{\sigma_1\sigma_2}{X_C^2} = 1 - \frac{\sigma_{12}^2}{S_{12}^2} \quad (96c)$$

4. For the Fourth Quadrant ($\sigma_1 > 0, \sigma_2 < 0$):

$$\frac{\sigma_1^2}{X_T^2} + \frac{\sigma_2^2}{Y_C^2} + \frac{\sigma_1\sigma_2}{X_T^2} = 1 - \frac{\sigma_{12}^2}{S_{12}^2} \quad (96d)$$

Based on the equations above, it is obtained the failure surface for TSAI-HILL criterion as shown by Fig. 29. It is verified that the increase of shear stress causes the contraction of the failure surface, becoming the failure process easier to occur for lower values of normal stresses.

In practical, it is used the definitions of Factor of Safety (FS) and Margin of Safety (MS) to determine if a ply fails or not by using TSAI-HILL criterion:

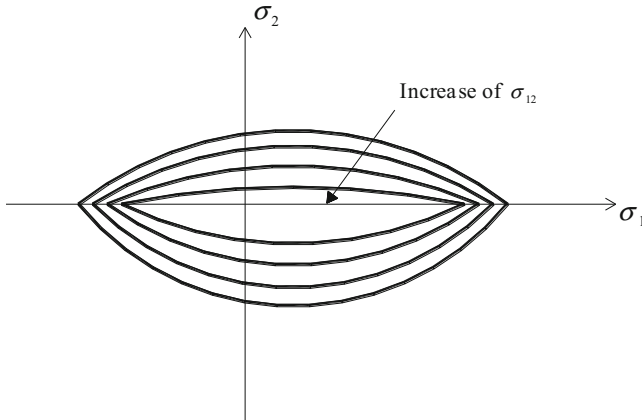


Fig. 29 Failure surface of TSAI-HILL criterion

$$FS = \sqrt{f(\sigma)} = \sqrt{\left(\frac{\sigma_1}{X}\right)^2 + \left(\frac{\sigma_2}{Y}\right)^2 - \left(\frac{\sigma_1\sigma_2}{X^2}\right) + \left(\frac{\sigma_{12}}{S_{12}}\right)^2} \tag{97}$$

$$MS = \frac{1}{FS} - 1 \tag{98}$$

If MS is lower than zero then the ply fails. By the other side, if the MS is much greater than zero, then it is concluded that the laminate should be optimized. This criterion is used a lot by the engineers, but it is important to highlight that it is not recommended for laminates with non-linear behavior. However, it is an interactive criterion; so a stress component in one direction can influence the failure mode caused by a stress component in other direction and vice-versa, but it is not possible to identify the failure mode for the ply.

In fact, advances in procedure to analyze failure in laminates have been performed by different research groups in the World for a long time. The research group coordinate by Professor Volnei Tita at University of São Paulo has worked in this way, as well. Therefore, some scientific contributions can be found in the literature, such as Tita and Carvalho (2001), Tita et al. (2002, 2008, 2012), Angelo et al. (2012, 2015), Sartorato et al. (2012), and Ribeiro et al. (2012a, b, 2013a, b, 2015).

Finally, if a failure occurs, then the engineer can redesign the laminate composite structure as shown by Fig. 4. Thus, the stacking sequence of the laminate should be modified in order to change the stiffness, or it is necessary to change the type of polymer matrix or the fibers, or to increase the volume fraction of the fibers.

References

- B.D. Agarwal, L.J. Broutman, *Analysis and Performance of Fiber Composites* (Wiley, New York, 1990)
- T.L. Anderson, *Fracture Mechanics—Fundamentals and Applications*, 2nd edn. (CRC Press, New York, 1995)
- M.V. Angelo, A.C. Galucio, V. Tita, Parametric analysis of Puck-Matzenmiller theory based damage model for composite structures. *Int. J. Vehicle Struct. Syst.* **4**, 152–157 (2012)
- M.V. Angelo, J.P. Charles, V. Tita, A new progressive failure analyses model: development, implementation, parametric study and validation. *Int. J. Autom. Compos.* **1**, 223–243 (2015)
- W.D. Callister Jr., *Materials Science and Engineering* (Wiley, New York, 1985)
- H.T. Hahn, S.W. Tsai, Nonlinear elastic behavior of unidirectional composite laminae. *J. Compos. Mater.* **7**, 102–118 (1973)
- D. Hull, *An Introduction to Composite Materials* (Cambridge University Press, London, 1981)
- B.Z. Jang, *Advanced Polymer Composites* (ASM International, Metals Park, 1994)
- R.M. Jones, *Mechanics of Composite Materials*, 2nd edn. (Taylor & Francis Inc, Philadelphia, 1999)
- R. Keunings, in *Macromechanics of Composites* (European Postgraduate Education in Polymer and Composites Engineering (EUPOCO), Leuven, 1992), K. U. Leuven. v.2, Module 4
- N. Magagnin Filho, Composite laminated plates of long fibers: constituents thermoelastic properties; lamina equivalent properties; rupture criteria and finite element analysis. Master Dissertation, São Carlos School of Engineering, University of São Paulo, São Carlos, 1996, p. 147 (in Portuguese)
- F.L. Matthews, R.D. Rawlings, *Composite Materials: Engineering and Science* (Chapman-Hall, New York, 1994)
- M.L. Ribeiro, T.H.P. Martins, M. Sartorato, G.F.O. Ferreira, V. Tita, D. Vandepitte, Analysis of low energy impact on filament-wound composite cylinders. *Int. J. Vehicle Struct. Syst.* **4**, 118–122 (2012a)
- M.L. Ribeiro, V. Tita, D. Vandepitte, A new damage model for composite laminates. *Compos. Struct.* **94**, 635–642 (2012b)
- M.L. Ribeiro, R.A. Angelico, R. Medeiros, V. Tita, Finite element analyses of low velocity impact on thin composite disks. *Int. J. Compos. Mater.* **3**, 59–70 (2013a)
- M.L. Ribeiro, D. Vandepitte, V. Tita, Damage model and progressive failure analyses for filament wound composite laminates. *Appl. Compos. Mater.* **20**, 975–992 (2013b)
- M.L. Ribeiro, D. Vandepitte, V. Tita, Experimental analysis of transverse impact loading on composite cylinders. *Compos. Struct.* **133**, 547–563 (2015)
- M. Sartorato, R. Medeiros, M.L. Ribeiro, V. Tita, Representative volume element based transverse shear characterization of laminated composites. *Int. J. Vehicle Struct. Syst.* **4**, 136–140 (2012)
- V. Tita, Theoretical and experimental dynamic analysis of beams manufactured from polymer reinforced composites, Master Dissertation, São Carlos School of Engineering, University of São Paulo, São Carlos, 1999, p. 119 (in Portuguese)
- V. Tita, Contribution to the study of damage and progressive failure on composite structures, Ph.D. Thesis, São Carlos School of Engineering, University of São Paulo, São Carlos, 2003, p. 193 (in Portuguese)
- V. Tita, J. Carvalho, Impact study on composite materials using finite element method, in *International Conference on Composite Materials*, vol. 13 (Beijing, 2001)
- V. Tita, J. Carvalho, J. Lirani, A procedure to estimate the dynamic damped behavior of fiber reinforced composite beams submitted to flexural vibrations. *Mater. Res.* **4**(4), 315–321 (2001)
- V. Tita, J. Carvalho, N.C. Santos, Modelagem do comportamento mecânico de materiais compósitos utilizando o método dos elementos finitos, in *Congresso Nacional de Engenharia Mecânica*, vol. 2, (João Pessoa, 2002) (in Portuguese)
- V. Tita, J. De Carvalho, D. Vandepitte, Failure analysis of low velocity impact on thin composite laminates: experimental and numerical approaches. *Compos. Struct.* **83**, 413–428 (2008)

- V. Tita, M.F. Caliri Jr., E. Massaroppi Jr., Theoretical models to predict the mechanical behavior of thick composite tubes. *Mater. Res.* **15**, 70–80 (2012)
- J.R. Vinson, R.L. Sierakowski, *Behavior of Structures Composed of Composite Materials* (Martins Nijhoff, Dordrecht, 1986)
- J.M. Whitney, I.M. Daniel, R.B. Pipes, *Experimental Mechanics of Fiber Reinforced Composite Materials* (Prentice-Hall, New Jersey, 1984)

Part III

Applications

Piezoelectric Energy Harvesting

Carlos De Marqui Jr.

Abstract This chapter reports on the modeling of electromechanically coupled beams with uniform and varying cross-sectional areas for energy harvesting. The governing equations are formulated by using the Rayleigh-Ritz method and Euler-Bernoulli assumptions. A resistive electrical load is considered in the electrical domain. Electromechanic frequency response functions (FRFs) are presented and the electroelastic behavior is discussed for a wide range of load resistances. The model is verified against the experimental results of a tapered bimorph with tip mass and issues related to the determination of the optimum load resistance for maximum power output is also addressed.

Keywords Piezoelectricity • Energy harvesting • Electroelastic behavior

1 Introduction

The research interest in converting ambient vibration energy to usable electrical energy has increased in the last years (Sodano et al. 2004a, b; Beeby et al. 2006; Priya 2007; Anton and Sodano 2007; Cook-Chennault et al. 2008). The concept of energy harvesting is particularly useful for wireless sensors powered by batteries and remotely operated systems with limited energy source. Different transduction mechanisms such as the piezoelectric one (Roundy et al. 2003; Sodano et al. 2004a, b; Du Toit and Wardle 2007; Erturk et al. 2008), the electromagnetic (Williams and Yates 1996; Arnold 2007; Glynne-Jones et al. 2004; Beeby et al. 2007; Manna and Sims 2009), and the electrostatic (Roundy et al. 2002; Mitcheson et al. 2004) can be used for converting vibrations to electricity. However, the recent literature shows that piezoelectric transduction has received the most attention for vibration-based energy harvesting and several review articles directly focusing on piezoelectric energy harvesting can be found in the literature (Sodano et al. 2004a, b; Priya 2007; Anton and Sodano 2007; Cook-Chennault et al. 2008).

C. De Marqui Jr., Dr. Ing. Habil. (✉)

Escola de Engenharia de São Carlos, University of São Paulo, Av Trabalhador
Sancarlense 400, São Carlos 13566-590, São Paulo, Brazil
e-mail: demarqui@sc.usp.br

Piezoelectric power generators can harvest electrical energy from mechanical vibrations based on the direct piezoelectric effect. These generators have been extensively studied as a low-cost and efficient alternative for low-level energy harvesting. Researchers have proposed various models to represent the electromechanical behavior of piezoelectric energy harvesters, which range from lumped parameter models (Roundy et al. 2003; Du Toit et al. 2005) to Rayleigh-Ritz type approximate distributed parameter models (Sodano et al. 2004a, b; Du Toit and Wardle 2007; Du Toit et al. 2005) as well as analytical distributed parameter solution attempts (Chen et al. 2006; Lin et al. 2007). Recently, certain issues observed in some lumped parameter and distributed parameter piezoelectric energy harvester models have been clarified in the literature (Erturk and Inman 2008a, b). More recently, the analytical distributed parameter solutions for unimorph (Erturk and Inman 2008a, b; Erturk et al. 2008) and bimorph (Erturk and Inman 2009) piezoelectric energy harvester configurations with closed-form expressions have been presented. Convergence of the Rayleigh-Ritz type electromechanical solution (Sodano et al. 2004a, b; Du Toit and Wardle 2007; Du Toit et al. 2005) to the analytical solution given by Erturk and Inman (2008a, b) was observed by Elvin and Elvin (2009) when sufficient number of admissible functions were used. The lumped parameter solution (Du Toit et al. 2005) has been found useful for a fundamental understanding of the problem and to investigate the optimization of system parameters for better electrical outputs (Stephen 2006; Renno et al. 2009). However, accurate prediction of the electromechanical behavior of piezoelectric energy harvesters requires using distributed parameter solutions. Experimental verifications and validations were also reported for the approximate (Erturk et al. 2008) and analytical (Erturk et al. 2008; Erturk and Inman 2009) (beam-type) distributed parameter electromechanical solutions.

The investigation into alternative configurations of electromechanically beams has also been reported in the literature. (Erturk et al. 2009) presented a linear distributed parameter model for predicting the electromechanical behavior of an L-shaped piezoelectric energy harvester configuration. A broadband harvester can be obtained when the first two natural frequencies of the L-shaped are properly tuned. The use of tapered cantilevers in order to improve the electromechanical behavior of piezoelectric energy harvesters has also been investigated (Matova et al. 2013; Roundy et al. 2005; Goldschmidtboeing and Woias 2008; Mateu and Moll 2005; Benasciutti et al. 2010; Dietl and Garcia 2010; Lu et al. 2004). The shape is changed from the basic rectangular configuration towards a tapered or reversed tapered geometry and the main motivation is to increase the electrical power output. The modeling of electromechanically coupled beams with non-uniform width is presented in Dietl and Garcia (2010). An optimal beam shape is determined by an optimization code. In the cited paper (Dietl and Garcia 2010), the expression $1/\omega C_p$ (where ω is the excitation frequency and C_p is the equivalent capacitance of piezoceramic layers) is employed for the optimum load resistance (which gives maximum power output) of a piezoelectric energy harvester. In general, the authors approximate the eigenvalues and eigenvector of electromechanically coupled beams with non-uniform width to the ones

corresponding to rectangular shape beams (Goldschmidtboeing and Woias 2008; Mateu and Moll 2005; Benasciutti et al. 2010). Recently, the solution of eigenvalue problem of non-uniform width beams by using the differential quadrature method has been presented and the effects of beam shape on the structural natural frequencies and mode shapes are discussed (Ayed et al. 2014). An important aspect, the effect of load resistance on the electroelastic behavior of variable-shaped harvesters, is only considered in Ayed et al. (2014).

This chapter reports on the modeling of electromechanically coupled beams for energy harvesting. The governing equations are formulated by the Rayleigh-Ritz method and Euler-Bernoulli assumptions. A resistive electrical load is considered in the electrical domain, in agreement with the simplified analyses followed by others (Roundy et al. 2003; Sodano et al. 2004a, b; Du Toit and Wardle 2007; Erturk et al. 2008; Du Toit et al. 2005; Chen et al. 2006; Lin et al. 2007; Elvin and Elvin 2009). Electrical circuitry-based work dealing with AC-to-DC (alternating current-to-direct current) converters can be found in the literature (Ottman et al. 2002; Guyomar et al. 2005; Shu and Lien 2006; Guan and Liao 2007). Voltage, current, power, and relative tip motion frequency response functions (FRFs) are presented for a wide range of load resistance, and the electroelastic behavior discussed.

2 Approximate Distributed Parameter Model of a Piezoelectric Energy Harvester

2.1 Generalized Hamilton's Principle for a Piezoelectric Energy Harvester

In the absence of magnetic effects, the generalized Hamilton's principle for an electroelastic body is (Crandall et al. 1968)

$$\int_{t_1}^{t_2} [\delta(T - U + W_e) + \delta W] dt = 0 \quad (1)$$

where the total kinetic energy (T), the total potential energy (U), and the electrical energy (W_e) terms are defined as

$$T = \int_{V_s} \frac{1}{2} \rho_s \dot{\mathbf{u}}^t \dot{\mathbf{u}} dV_s + \int_{V_p} \frac{1}{2} \rho_p \dot{\mathbf{u}}^t \dot{\mathbf{u}} dV_p \quad (2a)$$

$$U = \int_{V_s} \frac{1}{2} \mathbf{S}^t \mathbf{T} dV_s + \int_{V_p} \frac{1}{2} \mathbf{S}^t \mathbf{T} dV_p \quad (2b)$$

$$W_e = \int_{V_p} \frac{1}{2} \mathbf{E}^t \mathbf{D} dV_p \quad (2c)$$

where \mathbf{u} is the vector of mechanical displacements, \mathbf{S} is the vector of mechanical strain components, \mathbf{T} is the vector of mechanical stress components, \mathbf{D} is the vector of electric displacement components, \mathbf{E} is the vector of electric field components, ρ is the mass density, V is the volume, t denotes transpose when it is used as a superscript (otherwise it stands for the time), and an over-dot represents differentiation with respect to time. Here and hereafter, subscripts s and p stand for the substructure and piezoceramic layers, respectively.

For a set of discrete mechanical forces \mathbf{f} applied at locations (x_i, y_i) and for a set of discrete electric charge outputs q extracted at locations (x_j, y_j) , one can express the variation of the *mechanically applied* and *electrically extracted* work as follows:

$$\delta W = \sum_{i=1}^{nf} \delta \mathbf{u}(x_i, y_i, t) \cdot \mathbf{f}(x_i, y_i, t) + \sum_{j=1}^{nq} \delta \varphi(x_j, y_j, t) q(x_j, y_j, t) \quad (3)$$

where nf is the number of discrete mechanical forces, φ_j is the scalar electrical potential, and nq is the number of discrete electrode pairs.

The generalized Hamilton's principle for electroelastic bodies (Crandall et al. 1968) described by the foregoing equations was previously employed by Hagood et al. (1990) where they combined the Rayleigh-Ritz method and Euler-Bernoulli beam theory for active structural control. The Rayleigh-Ritz formulation given by Hagood et al. (1990) was also implemented by Sodano et al. (2004a, b), Du Toit and Wardle (2007), and Du Toit et al. (2005) for predicting the electrical power output of cantilevered Euler-Bernoulli beams in energy harvesting. It should be mentioned that, as oppose to the energy harvesting problem, the electric charge is the input in the structural actuation problem, and therefore the second term in Eq. (3) has a minus sign in Hagood et al. (1990). Note that the energy dissipation due to mechanical damping is excluded at this point and it will be introduced later in the form of proportional damping.

The linear-elastic constitutive relation for the substructure material can be written as

$$\mathbf{T} = \mathbf{c}_s \mathbf{S} \quad (4a)$$

and the linear electroelastic constitutive relation for the piezoceramic material is (IEEE Standard on Piezoelectricity 1978)

$$\begin{Bmatrix} \mathbf{T} \\ \mathbf{D} \end{Bmatrix} = \begin{bmatrix} \mathbf{c}_p^E & -\mathbf{e}^t \\ \mathbf{e} & \boldsymbol{\epsilon}^S \end{bmatrix} \begin{Bmatrix} \mathbf{S} \\ \mathbf{E} \end{Bmatrix} \quad (4b)$$

where \mathbf{c} is the elastic stiffness matrix, \mathbf{e} is the matrix of piezoelectric constants, $\boldsymbol{\varepsilon}$ is the matrix of permittivity components, superscript E and S denote that the parameters are measured at constant electric field and constant strain, respectively. The expanded form of Eq. (4b) is

$$\begin{Bmatrix} S_1 \\ S_2 \\ S_3 \\ S_4 \\ S_5 \\ S_6 \\ D_1 \\ D_2 \\ D_3 \end{Bmatrix} = \begin{bmatrix} s_{11}^E & s_{12}^E & s_{13}^E & 0 & 0 & 0 & 0 & 0 & d_{31} \\ s_{12}^E & s_{11}^E & s_{13}^E & 0 & 0 & 0 & 0 & 0 & d_{31} \\ s_{13}^E & s_{13}^E & s_{33}^E & 0 & 0 & 0 & 0 & 0 & d_{33} \\ 0 & 0 & 0 & s_{55}^E & 0 & 0 & 0 & d_{15} & 0 \\ 0 & 0 & 0 & 0 & s_{55}^E & 0 & d_{15} & 0 & 0 \\ 0 & 0 & 0 & 0 & 0 & s_{66}^E & 0 & 0 & 0 \\ 0 & 0 & 0 & 0 & 0 & 0 & \varepsilon_{11}^T & 0 & 0 \\ 0 & 0 & 0 & 0 & 0 & 0 & 0 & \varepsilon_{11}^T & 0 \\ d_{31} & d_{31} & d_{33} & 0 & 0 & 0 & 0 & 0 & \varepsilon_{33}^T \end{bmatrix} \begin{Bmatrix} T_1 \\ T_2 \\ T_3 \\ T_4 \\ T_5 \\ T_6 \\ D_1 \\ D_2 \\ D_3 \end{Bmatrix} \quad (5)$$

which is the reduced (2D) form of Eq. (4b). Note that the elastic, piezoelectric, and dielectric components in Eq. (25) are given in the contracted notation (i.e., Voigt's notation: $11 \rightarrow 1$, $22 \rightarrow 2$, $33 \rightarrow 3$, $23 \rightarrow 4$, $31 \rightarrow 5$, and $12 \rightarrow 6$) where 1, 2, and 3 directions are coincident with x , y , and z directions.

If the behavior of the piezoceramic is to be as a thin beam (the case of this chapter) based on Euler-Bernoulli beam theory, the non-zero stress component is T_1 . Assuming that an electrode pair is covering the faces perpendicular to three direction, Eq. (5) is simplified to

$$\begin{Bmatrix} S_1 \\ D_3 \end{Bmatrix} = \begin{bmatrix} s_{11}^E & d_{31} \\ d_{31} & \varepsilon_{33}^T \end{bmatrix} \begin{Bmatrix} T_1 \\ E_3 \end{Bmatrix} \quad (6)$$

which can be written in the stress-electric displacement form for a thin beam

$$\begin{Bmatrix} T_1 \\ D_3 \end{Bmatrix} = \begin{bmatrix} \bar{c}_{11}^E & -\bar{e}_{31} \\ -\bar{e}_{31} & \bar{\varepsilon}_{33}^S \end{bmatrix} \begin{Bmatrix} S_1 \\ E_3 \end{Bmatrix} \quad (7)$$

and the overbar denotes a constant in the reduced form for a plane-stress condition,

$$\bar{c}_{11}^E = \frac{1}{s_{11}^E}, \quad \bar{e}_{31} = \frac{d_{31}}{s_{11}^E}, \quad \bar{\varepsilon}_{33}^S = \varepsilon_{33}^T - \frac{d_{31}^2}{s_{11}^E} \quad (8)$$

where superscript S denotes a constant evaluated at constant strain. One should note that different non-zero stress components will be obtained when the piezoceramic is modeled based on Timoshenko beam theory or plate theory and, therefore, different expressions for the reduced elastic, piezoelectric, and permittivity constants.

Using the constitutive relations given by Eqs. (4a) and (4b) (or a simplified version) in Eq. (1), the generalized Hamilton’s principle for a piezoelectric energy harvester becomes

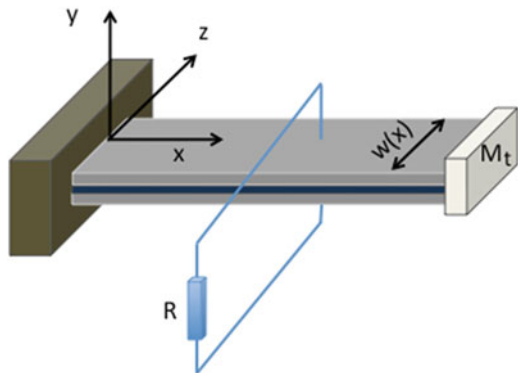
$$\begin{aligned}
 & \int_{t_1}^{t_2} \left[\int_{V_s} \rho_s \delta \dot{\mathbf{u}}^t \dot{\mathbf{u}} \, dV_s + \int_{V_p} \rho_p \delta \dot{\mathbf{u}}^t \dot{\mathbf{u}} \, dV_p - \int_{V_s} \delta \mathbf{S}^t \mathbf{c}_s \mathbf{S} \, dV_s - \int_{V_p} \delta \mathbf{S}^t \mathbf{c}_p^E \mathbf{S} \, dV_p \right. \\
 & + \int_{V_p} \delta \mathbf{S}^t \mathbf{e}^t \mathbf{E} \, dV_p + \int_{V_p} \delta \mathbf{E}^t \mathbf{e} \mathbf{S} \, dV_p + \int_{V_p} \delta \mathbf{E}^t \theta^S \mathbf{E} \, dV_p \quad (9) \\
 & \left. + \sum_{i=1}^{nf} \delta \mathbf{u}(x_i, y_i, t) \cdot \mathbf{f}(x_i, y_i, t) + \sum_{j=1}^{nq} \delta \varphi(x_j, y_j, t) q(x_j, y_j, t) \right] dt = 0
 \end{aligned}$$

2.2 Mathematical Model of a Piezoelectric Energy Harvester

The derivation provided in this section is for a bimorph piezoelectric beam of uniform width along its length (rectangular) or non-uniform width along its length (tapered or reversed tapered). The bimorph harvester has a brass substructure bracketed by two piezoceramic layers as shown in Fig. 1 (for the rectangular beam). Each piezoelectric layer is covered by continuous conductive electrodes that can be connected either in series (when piezoceramic layers are poled in the opposite direction) or in parallel (poled in the same direction) to an external load resistance. In this work, the pairs of electrodes covering each piezoceramic layer are connected in series. In Fig. 1, R is the resistive load, $w(x)$ is the width of the beam along the length (x), and M_t is the tip mass attached to the free end of the harvester.

The combination of Hamilton’s principle (Crandall et al. 1968) and the Rayleigh-Ritz method based on the Euler-Bernoulli beam assumptions are used in

Fig. 1 A bimorph piezoelectric energy harvester with tip mass under clamped-free boundary conditions



the modeling approach of this paper. The generalized Hamilton's principle was applied by Hagood et al. (1990), who combined the Rayleigh-Ritz method to the Euler-Bernoulli beam theory for active structural control. The Rayleigh-Ritz formulation used by Hagood et al. (1990) was also implemented by Du Toit and Wardle (2007) and Sodano et al. (2004a, b) for predicting the electric power output of electromechanically coupled Euler-Bernoulli beams in energy harvesting problems. Dietl and Garcia (2010) combined the Rayleigh-Ritz method with the Euler-Bernoulli beam theory to model electromechanically coupled beams with a varying cross-sectional area in energy harvesting problems.

In the Euler-Bernoulli beam theory the motion is restricted to the transverse direction and the only non-zero component of the displacement field \mathbf{u} is $y(x, t)$. Furthermore, the beam strain is given by $y(x, t)$ and its partial derivatives. In the Rayleigh-Ritz procedure the displacement $y(x, t)$ of the beam can be written as the summation of the modes and the temporal coordinate of the displacement as

$$y(x, t) = \mathbf{\Phi}(x)^T \mathbf{r}(t) \quad (10)$$

where $\mathbf{\Phi}(x)$ is a matrix of assumed mode shapes and $\mathbf{r}(t)$ is the temporal coordinate of displacement. Here, the mode shapes are assumed to be an acceptable solution to an Euler-Bernoulli beam under a clamped-free condition,

$$\tilde{\Phi}_k(x) = \cos \lambda_k \frac{x}{L} - \cosh \lambda_k \frac{x}{L} - \sigma_k \left(\sin \lambda_k \frac{x}{L} - \sinh \lambda_k \frac{x}{L} \right) \quad (11)$$

where L is the length of the beam and λ_k is the natural frequency of the k th mode obtained from the equation given by

$$\frac{1}{a} (\cos \lambda \cosh \lambda + 1) + \lambda (\cos \lambda \sinh \lambda - \sin \lambda \cosh \lambda) = 0 \quad (12)$$

where a is the ratio of the tip mass to the mass of the beam (substructure and piezoceramic layers) and σ_k is expressed as

$$\sigma_k = \frac{\sin \lambda_k - \sinh \lambda_k + \lambda_k r (\cos \lambda_k - \cosh \lambda_k)}{\cos \lambda_k + \cosh \lambda_k - \lambda_k r (\sin \lambda_k - \sinh \lambda_k)} \quad (13)$$

the general form for the k th mode shape must satisfy the following equation

$$\int_0^L \phi_k^2(x) \rho_1 w(x) dx + M_T \phi_k^2(L) = 1 \quad (14)$$

where ρ_1 is the equivalent mass density given by

$$\rho_1 = \rho_s h_s + 2\rho_p h_p \quad (15)$$

where ρ is the mass density, h is the thickness of the layer, and the subscripts s and p represent, respectively, the substructure and the piezoceramic layers. The mode shape is obtained as

$$\phi_k(x) = \frac{\tilde{\phi}_k(x)}{\sqrt{\int_0^L \tilde{\phi}_k^2(x) dx + a \tilde{\phi}_k^2(L)}} \quad (16)$$

and since piezoceramic layers are poled in the thickness direction, the non-zero electric field component (E), which is assumed to be uniform along the thickness direction, is expressed as

$$E = -\frac{\partial \psi}{\partial z} = -\frac{V}{2h_p} \quad (17)$$

where the electric potential (ψ) is assumed to vary linearly across the electrodes and V is the voltage across the electrodes.

The previous definitions for mechanical and electrical variables should be used to define the terms in Hamilton's principle (please check Dietl and Garcia 2010 and De Marqui et al. 2009) for details) to provide the electromechanically coupled equations governing the beam,

$$\mathbf{M}\ddot{\mathbf{r}}(t) + \mathbf{C}\dot{\mathbf{r}}(t) + \mathbf{K}\mathbf{r}(t) - \mathbf{\Theta}V(t) = \mathbf{F} \quad (18)$$

$$C_p \dot{V}(t) + \frac{V(t)}{R} + \mathbf{\Theta}^T \dot{\mathbf{r}}(t) = 0 \quad (19)$$

where \mathbf{M} is the mass matrix, \mathbf{C} is the damping matrix, \mathbf{K} is the stiffness matrix, $\mathbf{\Theta}$ is the electromechanical coupling matrix, \mathbf{F} is the vector of mechanical forces (where $\mathbf{F} = \mathbf{m}^* a_b(t)$, where $a_b(t)$ is the base acceleration in function of time and \mathbf{m}^* is the input matrix to be defined later), T represents the matrix transpose when superscripted, an over-dot represents the time derivative, R is the load resistance, \mathbf{q} is the vector of modal mechanical displacements, $V(t)$ is the voltage in function of the time, and C_p is the effective capacitance.

The mass matrix is defined as

$$\mathbf{M} = \int_0^L \rho_1 w(x) \boldsymbol{\Phi}(x) \boldsymbol{\Phi}^T(x) dx + M_T \boldsymbol{\Phi}(L) \boldsymbol{\Phi}^T(L) \quad (20)$$

and the stiffness matrix is defined as

$$\mathbf{K} = \frac{I}{s_p^E} \left[\int_0^L w(x) \boldsymbol{\Phi}''(x) \boldsymbol{\Phi}''^T(x) dx \right] \quad (21)$$

where s_p^E is the compliance measured in a constant electric field, (\prime) represents the space derivative, and I is given by

$$I = \frac{I_z(x)}{w(x)} \quad (22)$$

where $I_z(x)$ is the moment of inertia.

The damping matrix is assumed to be proportional to the mass and stiffness matrices

$$\mathbf{C} = \alpha\mathbf{M} + \beta\mathbf{K} \quad (23)$$

where α and β are the constants of proportionality.

The capacitance for a bimorph harvester in series connection case is given by

$$C_p = \frac{\epsilon_{33}^S}{2h_p} \int_0^L w(x) dx \quad (24)$$

where ϵ_{33}^S is the dielectric constant evaluated at constant strain for an Euler-Bernoulli beam as

$$\epsilon_{33}^S = 1730 \epsilon_0 - \frac{d_{31}}{E_p} \quad (25)$$

and ϵ_0 is the permittivity in free space, d_{31} is the piezoelectric coupling coefficient, and E_p is the Young's modulus of the piezoceramic.

The electromechanical coupling matrix is given as

$$\Theta = -\left(h_s h_p + h_p^2\right) \frac{d_{31}}{2s_p^E h_p} \int_0^L w(x) \phi''(x) dx \quad (26)$$

and the input matrix is

$$\mathbf{m}^* = \int_0^L \rho_1 w(x) \boldsymbol{\phi}(x) dx + M_T \boldsymbol{\phi}(L) \quad (27)$$

Expressions for the electromechanical FRFs, voltage across the resistive load, current passing through the resistive load, electrical power output, and relative tip motion can be obtained from the equations of motion (Eqs. (9) and (10)). The excitation is due to the harmonic motion of the base in the transverse direction, $w_B = Y_0 e^{j\omega t}$ (where $w_B(t)$ is the base displacement, Y_0 is its amplitude, ω is the excitation frequency, and j is the unit imaginary number), and the voltage output-to-base acceleration FRF can be obtained from Eqs. (9) and (10) as

$$\begin{aligned} \frac{V(t)}{a(t)} &= \frac{V(t)}{-\omega^2 Y_0 e^{j\omega t}} = j\omega \left(\frac{1}{R} + j\omega C_p \right)^{-1} \Theta^T \\ &\times \left[-\omega^2 \mathbf{M} + j\omega \mathbf{C} + \mathbf{K} + j\omega \left(\frac{1}{R} + j\omega C_p \right)^{-1} \Theta \Theta^T \right]^{-1} \mathbf{p}^* \end{aligned} \quad (28)$$

the electric current FRF is obtained by dividing the voltage FRF by the load resistance of the electrical circuit and the electrical peak power FRF (since the voltage FRF is the peak voltage FRF) is the product of the voltage and current FRFs.

The relative tip motion FRF is defined as the ratio of the amplitude of the displacement at the tip of the beam (relative to the base) to the amplitude of the base displacement input and it is obtained from Eqs. (9) and (10) as

$$\frac{w_{\text{rel}}}{Y_0 e^{j\omega t}} = \omega^2 \left[-\omega^2 \mathbf{M} + j\omega \mathbf{C} + \mathbf{K} + j\omega \left(\frac{1}{R} + j\omega C_p \right)^{-1} \Theta \Theta^T \right]^{-1} \mathbf{p}^* \quad (29)$$

The tip velocity FRF is defined as the ratio of the amplitude of velocity at the tip of the beam (relative to the fixed frame) to the gravitational acceleration. This FRF is easily obtained from the expression of the relative tip motion FRF by using

$$v_{\text{rel}} = -\frac{jg}{\omega} \left(1 + \frac{w_{\text{rel}}(L, t)}{Y_0} \right) \quad (30)$$

where g is the gravitational acceleration.

3 Theoretical Case Study

This section presents theoretical case studies using the linear model described in this chapter. The electroelastic behavior of a bimorph harvester with tip mass under harmonic base excitation is discussed for a set of load resistances ranging from open circuit condition to short circuit condition (1, 6.7, 11.8, 22, 33, 47, 100, 470 k Ω). The previously presented expressions for the electromechanical FRFs (voltage, current, and power output FRFs as well as tip velocity FRF) are employed. The bimorph harvester configuration has a brass substructure bracketed by two PZT-5A layers. The piezoceramic layers are poled in the opposite directions and therefore the combination of the layers to the electrical load results in the series connection case. The numerical input data of the bimorph is shown in Table 1.

The voltage FRF is defined here as the voltage output per gravitational acceleration ($g = 9.81 \text{ m/s}^2$). Equation (19) is easily modified to provide voltage output per g . The modulus of the voltage FRF for a range of excitation frequencies around

Table 1 Geometric and material properties of the bimorph harvester

Length of the beam (mm)	50.8
Width of the beam on the clamped end (mm)	31.8
Thickness of the substructure (mm)	0.14 (each)
Thickness of the PZT (mm)	0.26 (each)
Young’s modulus of the substructure (GPa)	105
Young’s modulus of the PZT-5A (GPa)	66
Mass density of the substructure (kg/m ³)	9000
Mass density of the PZT (kg/m ³)	7800
Tip mass (kg)	0.012
Proportional constant α (rad/s)	14.65
Proportional constant β (s/rad)	10 ⁻⁵
Piezoelectric coupling coefficient d_{31} (pm/V)	-190
Permittivity of free space (pF/m)	8.854

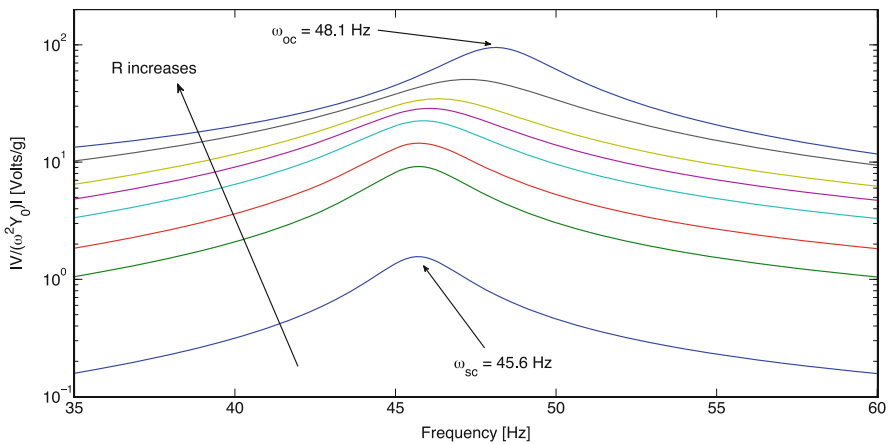


Fig. 2 Voltage FRFs for eight different values of load resistance

the first mode of the bimorph harvester is displayed in Fig. 2 for eight different values of load resistance (1, 6.7, 11.8, 22, 33, 47, 100, 470 kΩ). The voltage output increases monotonically with increasing load resistance for all excitation frequencies. One should note that the compliance of the piezoelectric material decreases from short circuit condition to open circuit condition. Therefore, a short circuit resonance frequency and an open circuit resonance frequency can be defined for the electromechanically coupled system. This way, the resonance frequency of the first mode of the bimorph harvester (Fig. 2) increases from the short circuit resonance frequency ($\omega_{sc} = 45.6$ Hz) to the open circuit resonance frequency ($\omega_{oc} = 48.1$ Hz) with increasing load resistance.

The variation of voltage output with increasing load resistance when the bimorph harvester is excited at the short circuit resonance frequency and at the open circuit resonance frequency is shown in Fig. 3. In both cases, voltage increases

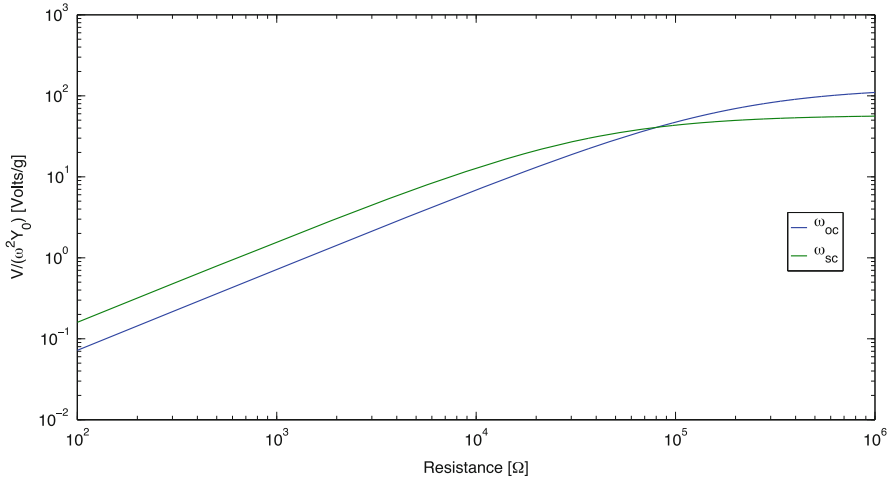


Fig. 3 Voltage output with increasing load resistance for excitations at the short circuit resonance frequency and open circuit resonance frequency

with increasing load resistance and is less sensitive to the variation of load resistance around the open circuit condition. For load resistances smaller than $79 \text{ k}\Omega$ (intersection of short circuit and open circuit curves) the voltage output at the short circuit resonance frequency is higher than at the open circuit resonance frequency. For load resistances larger than the intersection point, the voltage output at the open circuit resonance frequency is higher than the voltage output obtained from the system excited at the short circuit resonance frequency. Larger voltages are obtained when the system is excited at the short circuit resonance frequency and the load resistances are smaller than one of the intersection points.

The modulus of the electric current FRF is displayed in Fig. 2 for the same set of load resistances. The electric current FRF is obtained by dividing the voltage FRF to the load resistance of the energy harvesting circuit. Electric current decreases monotonically with increasing load resistance for all excitation frequencies. The resonance frequency of the first mode of the bimorph harvester (Fig. 4) increases from the short circuit resonance frequency of 45.6 Hz to the open circuit resonance frequency of 48.1 Hz with increasing load resistance.

The variation of electric current with load resistance when the bimorph harvester is excited at the short circuit resonance frequency and at the open circuit resonance frequency is shown in Fig. 5. Electric current is insensitive to the variation of load resistance around the short circuit condition. For load resistances smaller than $79 \text{ k}\Omega$ (intersection point) the current at the short circuit resonance frequency is higher than at the open circuit resonance frequency. For load resistances larger than the intersection point the current at the open circuit resonance frequency is higher than at short circuit resonance frequency since the electromechanical systems is close to open circuit condition.

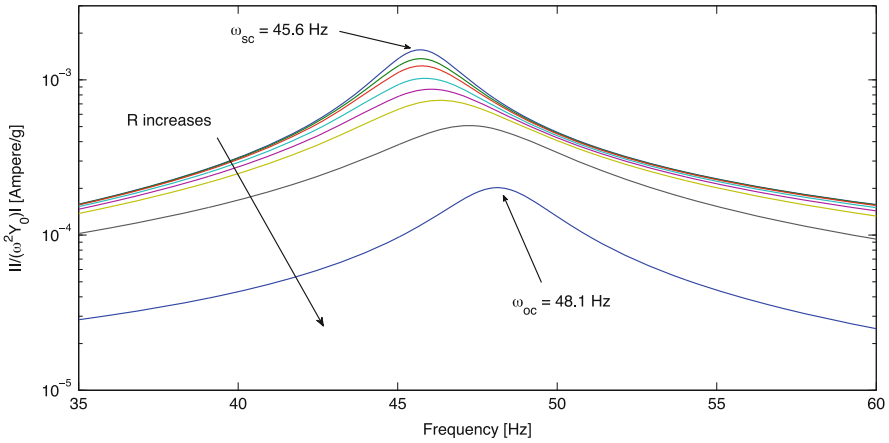


Fig. 4 Current FRFs for eight different values of load resistance

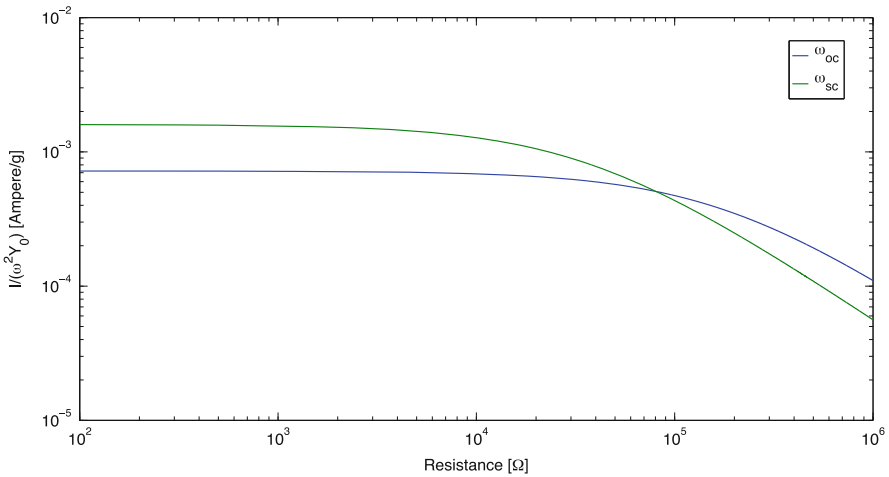


Fig. 5 Electric current with increasing load resistance for excitations at the short circuit resonance frequency and open circuit resonance frequency

The electrical power FRF is the product of voltage and current FRFs and it is defined as the ratio of electrical power output to square of the base acceleration. Note that the modulus form of Eq. (19) is the peak voltage FRF. As previously discussed, the voltage FRF has a monotonic behavior with increasing load resistance for every excitation frequency since the voltage across the resistive load increases with increasing load resistance and the frequency of maximum voltage output moves from short circuit to open circuit resonance frequency. The electrical current FRF exhibits an opposite behavior since current passing through the electrical load decreases with increasing load resistance for every excitation frequency (Erturk and Inman 2008a, b). Since the product of these two FRFs gives the

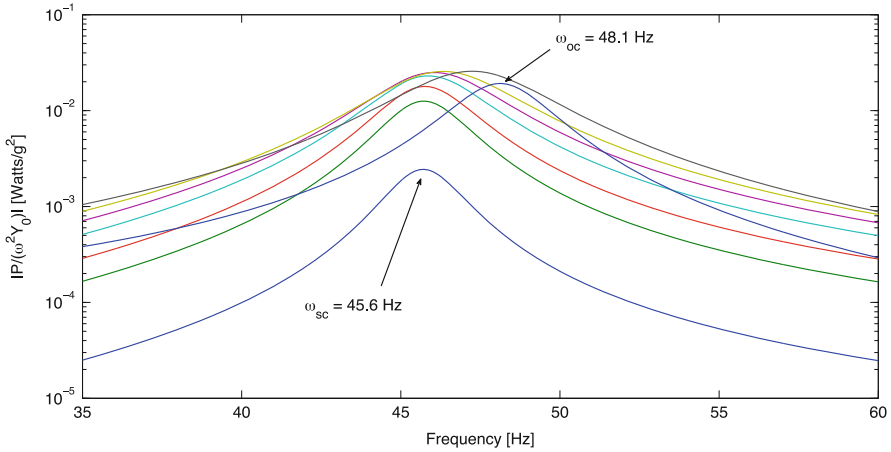


Fig. 6 Power FRFs for eight different values of load resistance

electrical power FRF, Fig. 6 shows intersections between the power curves of different electrical load resistances. Therefore, at a fixed frequency, the variation of peak power output with load resistance is not monotonic as can be seen for the first mode of the electromechanically coupled beam plotted in Fig. 6. Consequently the short circuit resonance frequency (45.6 Hz) and the open circuit resonance frequency (48.1 Hz) have considerably different optimum load values (Erturk and Inman 2008a, b) although the difference between these two frequencies is small (2.5 Hz).

The variation of power output with load resistance when the bimorph harvester is excited at the short circuit resonance frequency of the first mode and at the open circuit resonance frequency of the first mode is shown in Fig. 5. The intersection point is again verified around the load resistance of 79 k Ω . The power output at the short circuit resonance frequency is higher than the power output at the open circuit resonance frequency for load resistances smaller than the value of load resistance at the intersection point after which the opposite is valid. Each power curve of Fig. 7 has peak values corresponding to the optimum load resistance at each resonance frequency (short and open circuit). Although different optimum load resistances are observed for each electrical boundary condition, both of them deliver the same power output. One should note that voltage and current are not identical at the optimum load resistance of for the short circuit and open circuit resonance frequencies. However, the products of voltage and current are the same for both cases.

The mechanical vibration FRFs of the bimorph piezoelectric energy harvester are presented in Fig. 8. The tip velocity FRF is defined as the ratio of the amplitude of velocity at the tip of the beam (relative to the fixed frame) to the gravitational acceleration. The vibration amplitude at the short circuit resonance frequency is attenuated as the load resistance is increased up to 100 k Ω . Approximately after this value of load resistance, increasing load resistance amplifies the vibration

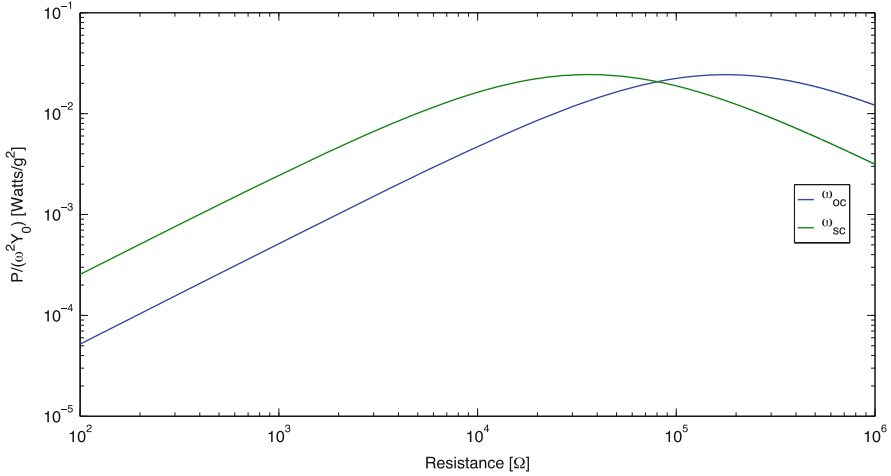


Fig. 7 Variation of power output with increasing load resistance for excitations at the short circuit resonance frequency and open circuit resonance frequency

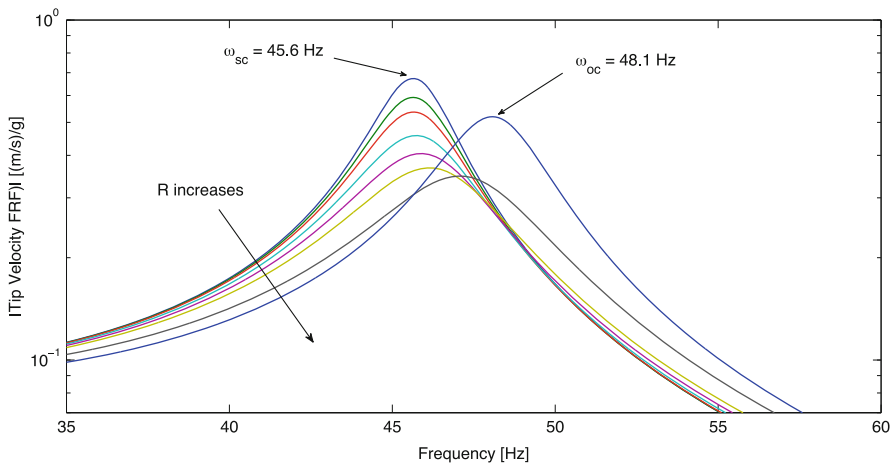


Fig. 8 Power FRFs for eight different values of load resistance

amplitude at the open circuit resonance frequency and the vibration amplitude at the short circuit resonance frequency is no longer attenuated.

Figure 9 shows the variation of relative tip displacement amplitude with load resistance. The relative tip vibration is insensitive to variations of load resistance for low values of load resistance. The vibration amplitude at the short circuit resonance frequency is higher than at open circuit resonance frequency for this same region. As the load resistance is further increased the vibration amplitude at the short circuit resonance frequency is attenuated. This is the expected behavior

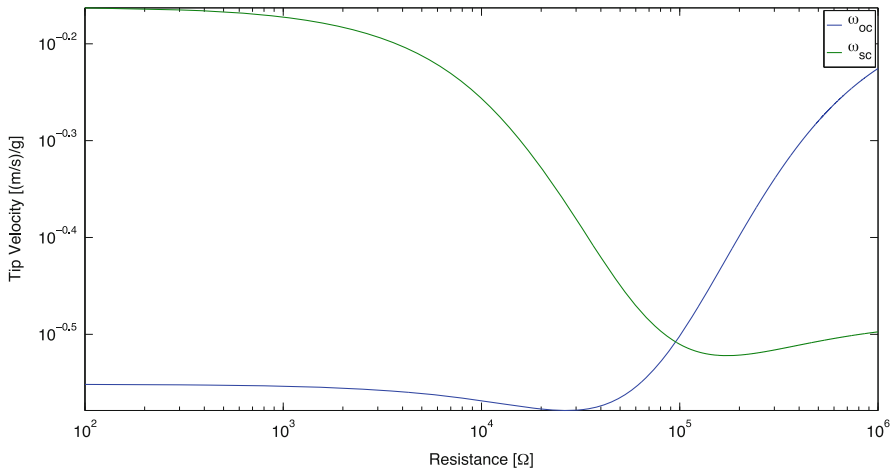


Fig. 9 Variation of tip velocity with increasing load resistance for excitations at the short circuit resonance frequency and open circuit resonance frequency

since in Fig. 8 the peak moves from the short circuit resonance frequency to the open circuit resonance frequency. Therefore, in this case, the attenuation is more related to stiffness variation than to damping. As the load resistance is increased, the tip velocity at the open circuit resonance frequency also increases (since the electromechanical system is excited at its resonance frequency).

4 Numerical and Experimental Results for a Tapered Bimorph with Tip Mass

In this second case study, the results from our approximate model for a tapered piezoelectric energy harvester are verified against experimental results. The bimorph harvester configuration has a brass substructure bracketed by two PZT-5A layers. The piezoceramic layers are poled in the opposite directions and therefore the series connection case is studied. The geometric and material properties for the tapered beam are given in Table 2. The width of the beam at the clamped end is larger than the width at the free end as well as it is assumed to vary linearly along the length of the harvester.

Small magnets were attached at the free end of the tapered harvester as a tip mass in the experiments. The base acceleration was measured at the clamped end (Accelerometer Model 352C22—PCB Piezotronics), which is connected to a shaker (Model 4810—Brüel & Kjær). A digital laser vibrometer (Model PDV-100—Polytec) measures the tip velocity at the free end. The electromechanical behavior is investigated by using three different resistive loads (1 k Ω , 50 k Ω , and 1 M Ω) and the electromechanical FRF were acquired through a Data

Table 2 Geometric and material properties of the bimorph harvester

Length of the beam (mm)	50.8
Width of the beam on the clamped end (mm)	31.8
Width of the beam at the free end (mm)	7.25
Thickness of the substructure (mm)	0.14 (each)
Thickness of the PZT (mm)	0.26 (each)
Young’s modulus of the substructure (GPa)	105
Young’s modulus of the PZT-5A (GPa)	66
Mass density of the substructure (kg/m ³)	9000
Mass density of the PZT (kg/m ³)	7800
Tip mass (kg)	0.012
Proportional constant α (rad/s)	8.79
Proportional constant β (s/rad)	6×10^{-6}
Piezoelectric coupling coefficient d_{31} (pm/V)	-190
Permittivity of free space (pF/m)	8.854

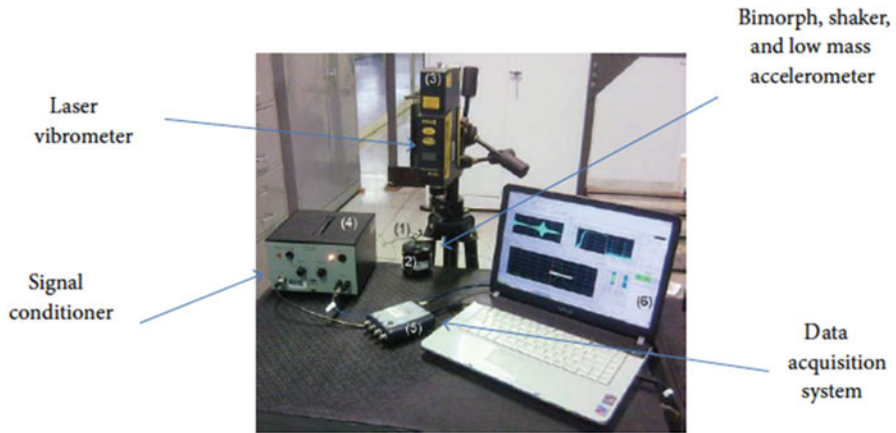


Fig. 10 Experimental setup used for the verification of relations for a tapered beam

Acquisition System (Photon II All in One System—LDS Dactron). Figure 10 shows the experimental setup.

The voltage FRFs for the first mode of the tapered harvester obtained from our model and the experimental results are plotted in Fig. 11a. The experimental short circuit and open circuit resonance frequencies for the tapered harvester are 179.1 and 189.1 Hz, respectively. The present model has predicted such frequencies as 178.8 and 188.9 Hz, respectively. The tip velocity FRFs are in agreement with those of the experimental results, as shown in Fig. 11b. The electromechanical vibration and voltage FRFs obtained from the presented model for a tapered electromechanically coupled beam are in very good agreement with those obtained from the experiments.

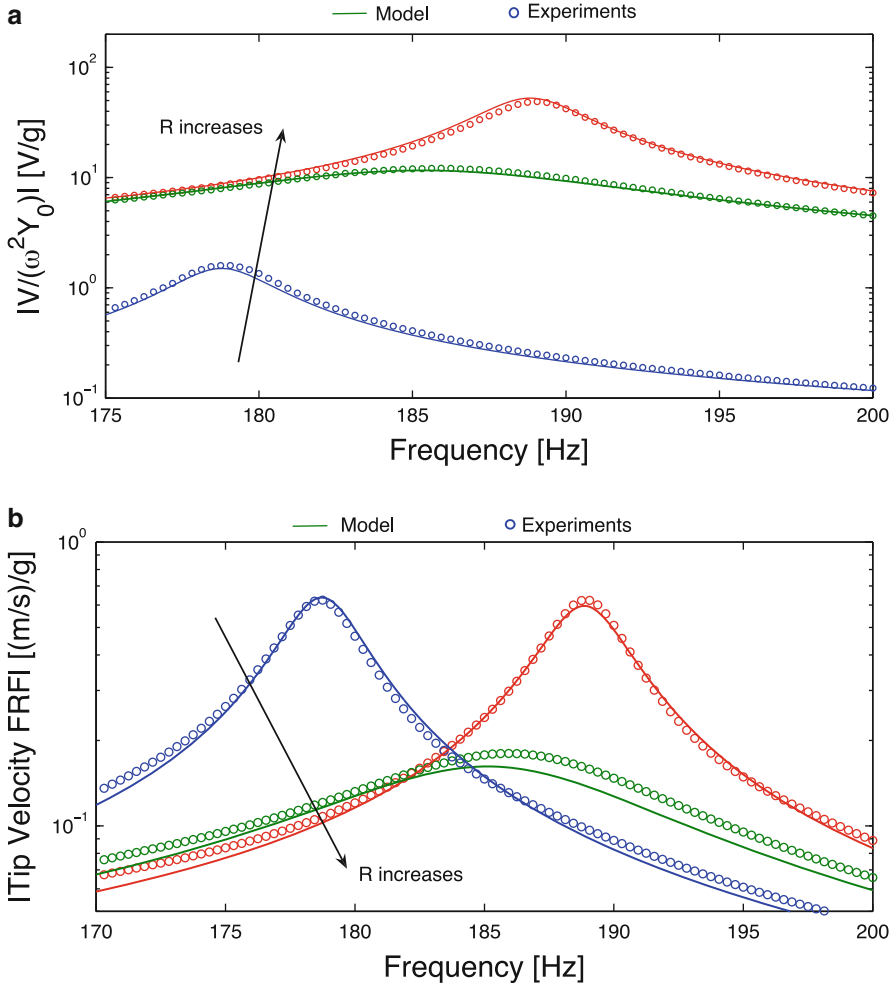


Fig. 11 Model and experimental voltage FRFs (a) and tip velocity FRFs (b) for three values of load resistance

The expression $1/\omega C_p$ (where ω is the excitation frequency and C_p is the equivalent capacitance of piezoceramic layers) is usually employed by some authors in order to calculate the optimum load resistance (which gives maximum power output, as discussed in the previous section) of a piezoelectric energy harvester. An issue related to the estimate of the optimum load from the equation $1/\omega C_p$ was previously discussed (Erturk 2009) for a rectangular (or squared) energy harvester configuration. The piezoceramic layer of a piezoelectric energy harvester can be represented as a current source in parallel with its internal capacitance (Norton representation) or as a voltage source in series with its internal capacitance (Thévenin representation). In Norton representation $R_{opt} = 1/\omega C_p$ is obtained only

if a constant current amplitude oscillating at a frequency ω is assumed. However, regarding the electromechanical behavior of a piezoelectric energy harvesting discussed in the previous section of this chapter, the current source in Norton representation is not constant, but it depends on the load resistance since the vibration response also depends on the load resistance. The expression $R_{\text{opt}} = 1/\omega C_p$ could be obtained from the coupled equations that govern a piezoelectric energy harvester only if the electromechanical coupling term were artificially removed from the mechanical equation (Erturk 2009).

By considering the electromechanically coupled equations (Eqs. (18) and (19)) one should obtain the expression for the optimum load as (Erturk 2009),

$$R_{\text{opt}} = \frac{1}{\omega_k C_p \left[1 + \left(\frac{\gamma_k}{2\zeta_k} \right)^2 \right]} \tag{31}$$

where $\gamma_k = \frac{\Theta_k}{C_p \omega_k}$ and ω_k are the short-circuit resonance frequency of the desired mode, ζ_k is the damping ratio of the same mode, and Θ_k is the modal electromechanical coupling of the mode. The optimum load resistance can also be searched by the calculation of the power output for a wide range of load resistance until the optimal one is reached when the system is excited at a target frequency.

Figure 12 shows the variation of the optimum load resistance for several different tip widths (the width at the tip is $w(L) = Pw(0)$ and the width along the body is assumed linearly modified along the span) for a piezoelectric energy harvester with tip mass (basic data given in Table 2) excited at the short circuit resonance frequency. The same load resistance is obtained by searching for the optimum one and by using Eq. (23). However, inaccurate predictions are obtained from Eq. (31).

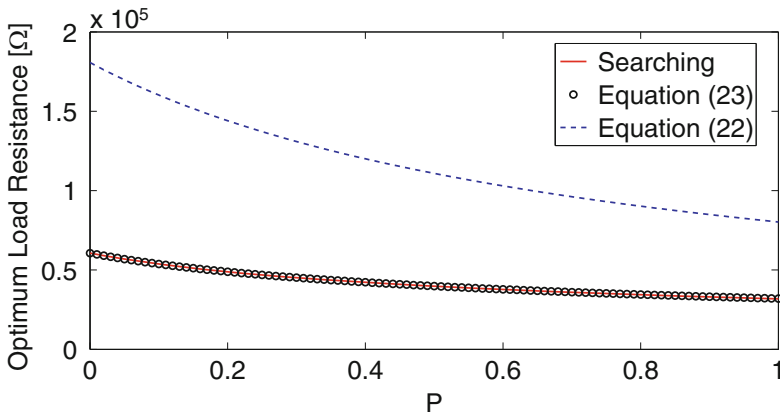


Fig. 12 Variation of optimum load resistance with parameter P

5 Summary

The modeling of electromechanically coupled beams with uniform and varying cross-sectional areas was reported for energy harvesting. The combination of Hamilton's principle and the Rayleigh-Ritz method based on the Euler-Bernoulli beam assumptions was used in the modeling approach. The model accounts for the presence of a pair of conductive electrodes covering the entire piezoceramic layer and a resistive electrical load was considered in the electrical domain of the problem. Derivations are given for predicting the coupled mechanical vibration and electrical response of the birmorph harvester beam with tip mass due to base excitation.

Frequency domain electroelastic analysis of the rectangular birmorph harvester was presented. Electromechanically coupled FRFs were defined and the magnitude of the electrical outputs (voltage, current, and power) and the magnitude of mechanical variables could be investigated at different electrical conditions (a set of load resistances ranging from short circuit to open circuit condition). Moreover, the behavior of the electroelastic beam with varying load resistance at two excitation frequencies (short circuit resonance frequency and open circuit resonance circuit) was discussed. In the second study case, the model was successfully verified against the experimental results of a tapered birmorph with tip mass. Issues related to the determination of the optimum load resistance have also been addressed.

References

- S.R. Anton, H.A. Sodano, A review of power harvesting using piezoelectric materials (2003–2006). *Smart Mater. Struct.* **16**, R1–R21 (2007)
- D. Arnold, Review of microscale magnetic power generation. *IEEE Trans. Magn.* **43**, 3940–3951 (2007)
- S.B. Ayed, A. Abdelkefi, F. Najar, M.R. Hajj, Design and performance of variable-shaped piezoelectric energy harvesters. *J. Intel. Mater. Syst. Struct.* **25**, 174–186 (2014)
- S.P. Beeby, M.J. Tudor, N.M. White, Energy harvesting vibration sources for microsystems applications. *Meas. Sci. Technol.* **13**, R175–R195 (2006)
- S.P. Beeby, R.N. Torah, M.J. Tudor, P. Glynn-Jones, T. O'Donnell, C.R. Saha, S. Roy, A micro electromagnetic generator for vibration energy harvesting. *J. Micromech. Microeng.* **17**, 1257–1265 (2007)
- D. Benasciutti et al., Vibration energy scavenging via piezoelectric birmorphs of optimized shapes. *Microsyst. Technol.* **16**, 657–668 (2010)
- S.N. Chen, G.J. Wang, M.C. Chien, Analytical modeling of piezoelectric vibration-induced micro power generator. *Mechatronics* **16**, 379–387 (2006)
- K.A. Cook-Chennault, N. Thambi, A.M. Sastry, Powering MEMS portable devices—a review of non-regenerative and regenerative power supply systems with emphasis on piezoelectric energy harvesting systems. *Smart Mater. Struct.* **17**, 043001 (2008) (33pp)
- S.H. Crandall, D.C. Karnopp, E.F. Kurtz Jr., D.C. Pridmore-Brown, *Dynamics of Mechanical and Electromechanical Systems* (McGraw-Hill, New York, 1968)
- C. De Marqui Jr., A. Erturk, D.J. Inman, An electromechanical finite element model for piezoelectric energy harvester plates. *J. Sound Vib.* **327**, 9–25 (2009)

- J.M. Dietl, E. Garcia, Beam shape optimization for power harvesting. *J. Intel. Mater. Syst. Struct.* **21**, 633–646 (2010)
- N.E. Du Toit, B.L. Wardle, Experimental verification of models for microfabricated piezoelectric vibration energy harvesters. *AIAA J.* **45**, 1126–1137 (2007)
- N.E. Du Toit, B.L. Wardle, S.G. Kim, Design considerations for MEMS-scale piezoelectric mechanical vibration energy harvesters. *Integr. Ferroelectr.* **71**, 121–160 (2005)
- N. Elvin, A. Elvin, A general equivalent circuit model for piezoelectric generators. *J. Intel. Mater. Syst. Struct.* **20**(2009), 3–9 (2009)
- A. Erturk, *Electromechanical Modeling of Piezoelectric Energy Harvesters*, Ph.D. Dissertation, (xxviii + 291pp), November 2009, Department of Engineering Science and Mechanics, Virginia Polytechnic Institute and State University, Blacksburg, 2009
- A. Erturk, D.J. Inman, A distributed parameter electromechanical model for cantilevered piezoelectric energy harvesters. *J. Vib. Acoust.* **130**, 041002 (2008a) (15pp)
- A. Erturk, D.J. Inman, Issues in mathematical modeling of piezoelectric energy harvesters. *Smart Mater. Struct.* **17**, 065016 (2008b) (14pp)
- A. Erturk, D.J. Inman, An experimentally validated bimorph cantilever model for piezoelectric energy harvesting from base excitations. *Smart Mater. Struct.* **18**, 025009 (2009)
- A. Erturk, O. Bilgen, D.J. Inman, Power generation and shunt damping performance of a single crystal lead magnesium niobate—lead zirconate titanate unimorph: analysis and experiment. *Appl. Phys. Lett.* **93**, 224102 (2008) (3pp)
- A. Erturk, J.M. Renno, D.J. Inman, Modeling of piezoelectric energy harvesting from an L-shaped beam-mass structure with an application to UAVs. *J. Intel. Mater. Syst. Struct.* **20**(5), 529–544 (2009b)
- P. Glynn-Jones, M.J. Tudor, S.P. Beeby, N.M. White, An electromagnetic, vibration-powered generator for intelligent sensor systems. *Sens. Actuators A* **110**, 344–349 (2004)
- F. Goldschmidtboeing, P. Woias, Characterization of different beam shapes for piezoelectric energy harvesting. *J. Micromech. Microeng.* **18**, 104013 (2008)
- M.J. Guan, W.H. Liao, On the efficiencies of piezoelectric energy harvesting circuits towards storage device voltages. *Smart Mater. Struct.* **16**, 498–505 (2007)
- D. Guyomar, A. Badel, E. Lefeuvre, Toward energy harvesting using active materials and conversion improvement by nonlinear processing. *IEEE Trans. Ultrason. Ferroelec. Freq. Contr.* **52**, 584–595 (2005)
- N.W. Hagood, W.H. Chung, A. Von Flotow, Modelling of piezoelectric actuator dynamics for active structural control. *J. Intel. Mater. Syst. Struct.* **1**, 327–354 (1990)
- IEEE Group on Sonics and Ultrasonics, *IEEE Standard on Piezoelectricity* (Institute of Electrical and Electronics Engineers, New York, 1978)
- J.H. Lin, X.M. Wu, T.L. Ren, L.T. Liu, Modeling and simulation of piezoelectric MEMS energy harvesting device. *Integr. Ferroelectr.* **95**, 128–141 (2007)
- F. Lu, H.P. Lee, S.P. Lim, Modeling and analysis of micro piezoelectric power generators for micro-electromechanical-systems applications. *Smart Mater. Struct.* **13**, 57–63 (2004)
- B.P. Manna, N.D. Sims, Energy harvesting from the nonlinear oscillations of magnetic levitation. *J. Sound Vib.* **319**, 515–530 (2009)
- L. Mateu, F. Moll, Optimum piezoelectric bending beam structures for energy harvesting using shoe inserts. *J. Intell. Mater. Syst. Struct.* **16**, 835–844 (2005)
- S.P. Matova, M. Renaoud, M. Jambunathan, M. Goedbloed, R. Van Schaijk, Effect of length/width ratio of tapered beams on the performance of piezoelectric energy harvesters. *Smart Mater. Struct.* **22**, 075015 (2013) (8pp)
- P. Mitcheson, P. Miao, B. Start, E. Yeatman, A. Holmes, T. Green, MEMS electrostatic micro-power generator for low frequency operation. *Sens. Actuators A* **115**, 523–529 (2004)
- G.K. Ottman, H.F. Hofmann, A.C. Bhatt, G.A. Lesieutre, Adaptive piezoelectric energy harvesting circuit for wireless remote power supply. *IEEE Trans. Power Electr.* **17**, 669–676 (2002)

- S. Priya, Advances in energy harvesting using low profile piezoelectric transducers. *J. Electroceram.* **19**, 167–184 (2007)
- J.M. Renno, M.F. Daqaq, D.J. Inman, On the optimal energy harvesting from a vibration source. *J. Sound Vib.* **320**, 386–405 (2009)
- S. Roundy, P.K. Wright, J. Rabaey, Micro-electrostatic vibration-to-electricity converters, in *Proceedings of the ASME 2002 International Mechanical Engineering Congress and Exposition*, 2002
- S. Roundy, P.K. Wright, J. Rabaey, A study of low level vibrations as a power source for wireless sensor nodes. *Comput. Commun.* **26**, 1131–1144 (2003)
- S. Roundy, E.S. Leland, J. Baker, E. Carleton, E. Reilly, E. Lai, B. Otis, J.M. Rabaey, P.K. Wright, V. Sundararajan, Improving power output for vibration-based energy scavengers. *IEEE Perv. Comput.* **4**(1), 28–36 (2005)
- Y.C. Shu, I.C. Lien, Analysis of power output for piezoelectric energy harvesting systems. *Smart Mater. Struct.* **15**, 1499–1512 (2006)
- H.A. Sodano, D.J. Inman, G. Park, A review of power harvesting from vibration using piezoelectric materials. *Shock Vib. Dig.* **36**, 197–205 (2004a)
- H.A. Sodano, G. Park, D.J. Inman, Estimation of electric charge output for piezoelectric energy harvesting. *Strain* **40**, 49–58 (2004b)
- N.G. Stephen, On energy harvesting from ambient vibration. *J. Sound Vib.* **293**, 409–425 (2006)
- C.B. Williams, R.B. Yates, Analysis of a micro-electric generator for Microsystems. *Sens. Actuators A* **52**, 8–11 (1996)

Piezoelectric Structural Vibration Control

Marcelo A. Trindade

Abstract Over the last two decades, piezoelectric materials have been extensively used as components in active and passive structural vibration control solutions. The most frequent applications consider piezoceramic thin patches bonded to thin structures subjected to bending. For active vibration control solutions, the piezoceramic patches can be used as strain sensors and/or bending actuators when connected to properly designed signal conditioning, processing, and amplification. For passive vibration control solutions, they can be used as vibration dampers and/or absorbers when connected to properly designed electronic shunt circuits. The objective of this chapter is to present some examples of the use of piezoelectric materials, as distributed sensors and actuators, for the development and implementation of passive and active vibration control solutions.

Keywords Piezoelectric structures • Electromechanical coupling • Piezoelectric sensors and actuators • Piezoelectric shunted damping • Piezoelectric active control

1 Introduction

Over the last two decades, piezoelectric materials have been extensively used as components in active and passive structural vibration control solutions. The most frequent applications consider piezoceramic thin patches bonded to thin structures subjected to bending. For active vibration control solutions, the piezoceramic patches can be used as strain sensors and/or bending actuators when connected to properly designed signal conditioning, processing, and amplification. For passive vibration control solutions, they can be used as vibration dampers and/or absorbers when connected to properly designed electronic shunt circuits. The objective of this chapter is to present some examples of the use of piezoelectric materials,

M.A. Trindade (✉)

Department of Mechanical Engineering, São Carlos School of Engineering, University of São Paulo, Av. Trabalhador São-Carlense, 400, São Carlos, SP 13566-590, Brazil
e-mail: trindade@sc.usp.br

as distributed sensors and actuators, for the development and implementation of passive and active vibration control solutions. Other textbooks discussing some of the topics presented in this chapter can be recommended (Meirovitch 1990; Preumont 1997, 2006; Reza Moheimani and Fleming 2006; Leo 2007).

2 Passive Vibration Control Using Piezoelectric Materials

For thin flexible structures, such as beams, plates, shells, and panels, most part of the vibrating energy is in bending motion and, thus, it seems worthwhile to make use of patches and/or layers of functional materials that can bend (deform) together with the structure and are capable of extracting (converting) this deformation energy from the host structure. To this end, piezoelectric materials are an interesting choice since they are quite effective in converting deformation energy into electrical energy. If connected to properly designed electric circuits, this electrical energy could then be extracted from the piezoelectric material. The seminal work of Hagood and von Flotow (1991) proposed the use of piezoelectric patches connected to resistive shunt circuits, leading to an equivalent vibration damper (in which the electrical energy is dissipated in the circuit resistance), or to resonant (resistive-inductive) shunt circuits, leading to an equivalent vibration absorber (in which the electrical energy is absorbed by the circuit within a narrow frequency range).

Later, studies focused mainly on the optimization of the shunt circuits by including resistances, inductances, capacitances, and switches in series and/or parallel (Lesieutre 1998; Clark 2000; Reza Moheimani 2003; Viana and Steffen 2006; Lallart et al. 2008). Other studies focused on the optimization of the electromechanical coupling between the piezoelectric materials and host structure (Trindade and Maio 2008; Trindade and Benjeddou 2009; Godoy and Trindade 2011).

2.1 *Coupled Formulation for Structure, Piezoelectric Patches, and Shunt Circuits*

In this section, a general methodology for the variational formulation of coupled equations of motion for structures with piezoelectric materials is presented. Equations are written in terms of both electric potential and electric charge in the piezoelectric elements. Equipotentiality over each piezoelectric element electrodes is accounted for in both formulations. Finally, a methodology for coupling the piezoelectric elements with electric circuits is presented.

2.1.1 Electric Potential Formulation

First, a formulation considering structure's generalized displacements and electric potential in the piezoelectric elements as variables is proposed. The virtual work done by internal forces can be found from the virtual variation of the electromechanical potential energy. In this first formulation, it is chosen to write the potential energy as the electric Gibbs energy, written in terms of mechanical strains $\boldsymbol{\varepsilon}$ and electric fields \mathbf{E} , such that its variation reads

$$\delta U(\boldsymbol{\varepsilon}, \mathbf{E}) = \int_{\Omega} (\delta \mathbf{e}^t \mathbf{c}^E \boldsymbol{\varepsilon} - \delta \mathbf{e}^t \mathbf{e} \mathbf{E} - \delta \mathbf{E}^t \mathbf{e}^t \boldsymbol{\varepsilon} - \delta \mathbf{E}^t \boldsymbol{\varepsilon}^E \mathbf{E}) d\Omega, \quad (1)$$

where \mathbf{c}^E , \mathbf{e} , and $\boldsymbol{\varepsilon}^E$ are the matrices of elastic (for constant electric field), piezoelectric, and dielectric (for constant mechanical strain) constants of the material.

Using appropriate kinematic assumptions for the piezoelectric structure to be studied and performing any form of spatial discretization, the coupled equations of motion can be derived in the form

$$\begin{bmatrix} \mathbf{M}_s + \mathbf{M}_p & 0 \\ 0 & 0 \end{bmatrix} \begin{Bmatrix} \ddot{\mathbf{u}} \\ \ddot{\mathbf{V}} \end{Bmatrix} + \begin{bmatrix} \mathbf{K}_{us} + \mathbf{K}_{up}^E & -\mathbf{K}_{uv} \\ -\mathbf{K}_{uv}^t & -\mathbf{K}_v \end{bmatrix} \begin{Bmatrix} \mathbf{u} \\ \mathbf{V} \end{Bmatrix} = \begin{Bmatrix} \mathbf{F}_m \\ 0 \end{Bmatrix}, \quad (2)$$

where \mathbf{M}_s and \mathbf{K}_{us} are the mass and elastic stiffness matrices of the structure (without piezoelectric elements) and \mathbf{M}_p and \mathbf{K}_{up}^E are the mass and elastic (for constant electric fields) stiffness matrices of the piezoelectric elements. \mathbf{K}_{uv} and \mathbf{K}_v are the piezoelectric and dielectric stiffnesses of the piezoelectric elements. \mathbf{F}_m is a vector of the mechanical loads applied to the structure. The degrees of freedom (dofs) \mathbf{u} are the generalized displacements and \mathbf{V} are the generalized differences of electric potentials (voltages) on the piezoelectric material.

To account for the equipotential condition on the electrodes of each piezoelectric element, let us define the vectors of differences of electric potentials \mathbf{V}_p induced or applied to the electrodes of the piezoelectric elements, such that

$$\mathbf{V} = \mathbf{L}_p \mathbf{V}_p. \quad (3)$$

The boolean matrix \mathbf{L}_p has dimension $N \times N_p$, where N is the number of spatial (nodal) points and N_p is the number of independent piezoelectric elements. \mathbf{L}_p allows to set an equal value to selected nodal differences of electric potentials.

Substituting Eq. (3) into Eq. (2) and pre-multiplying the second line of the resulting equation by \mathbf{L}_p^t leads to

$$\begin{bmatrix} \mathbf{M}_s + \mathbf{M}_p & 0 \\ 0 & 0 \end{bmatrix} \begin{Bmatrix} \ddot{\mathbf{u}} \\ \ddot{\mathbf{V}}_p \end{Bmatrix} + \begin{bmatrix} \mathbf{K}_{us} + \mathbf{K}_{up}^E & -\bar{\mathbf{K}}_{uv} \\ -\bar{\mathbf{K}}_{uv}^t & -\bar{\mathbf{K}}_v \end{bmatrix} \begin{Bmatrix} \mathbf{u} \\ \mathbf{V}_p \end{Bmatrix} = \begin{Bmatrix} \mathbf{F}_m \\ 0 \end{Bmatrix}, \quad (4)$$

where

$$\bar{\mathbf{K}}_{uv} = \mathbf{K}_{uv} \mathbf{L}_p, \quad \bar{\mathbf{K}}_v = \mathbf{L}_p^t \mathbf{K}_v \mathbf{L}_p. \quad (5)$$

2.1.2 Electric Charge Formulation

An electric charge formulation can be obtained by using the Helmholtz free energy, written in terms of mechanical strains $\boldsymbol{\varepsilon}$ and electric displacements \mathbf{D} , as potential energy instead of the electric Gibbs energy, such that the virtual variation of the potential energy is

$$\delta U(\boldsymbol{\varepsilon}, \mathbf{D}) = \int_{\Omega} (\delta \boldsymbol{\varepsilon}^t \mathbf{c}^D \boldsymbol{\varepsilon} - \delta \boldsymbol{\varepsilon}^t \mathbf{h} \mathbf{D} - \delta \mathbf{D}^t \mathbf{h}^t \boldsymbol{\varepsilon} + \delta \mathbf{D}^t \boldsymbol{\beta}^e \mathbf{D}) d\Omega, \quad (6)$$

where \mathbf{c}^D , \mathbf{h} , and $\boldsymbol{\beta}^e$ are the matrices of elastic (for constant electric displacement), piezoelectric, and dielectric (for constant mechanical strain) constants of the material.

In this case, the equations of motion are now written in terms of the generalized displacements \mathbf{u} and electric displacements \mathbf{D}_n , such that

$$\begin{bmatrix} \mathbf{M}_s + \mathbf{M}_p & 0 \\ 0 & 0 \end{bmatrix} \begin{Bmatrix} \ddot{\mathbf{u}} \\ \ddot{\mathbf{D}}_n \end{Bmatrix} + \begin{bmatrix} \mathbf{K}_{us} + \mathbf{K}_{up}^D & -\mathbf{K}_{ud} \\ -\mathbf{K}_{ud}^t & \mathbf{K}_d \end{bmatrix} \begin{Bmatrix} \mathbf{u} \\ \mathbf{D}_n \end{Bmatrix} = \begin{Bmatrix} \mathbf{F}_m \\ 0 \end{Bmatrix}, \quad (7)$$

where, as in the previous case, \mathbf{M}_s and \mathbf{K}_{us} are the mass and elastic stiffness matrices of the structure (without piezoelectric elements) and \mathbf{M}_p and \mathbf{K}_{up}^D are the mass and elastic (for constant electric displacements) stiffness matrices of the piezoelectric elements. \mathbf{K}_{ud} and \mathbf{K}_d are the piezoelectric and dielectric stiffnesses of the piezoelectric elements.

To account for the equipotential condition on the electrodes of each piezoelectric element, let us define the vectors of electric charges \mathbf{q}_p on the electrodes of piezoelectric elements (with uniform and equal material properties and thickness), such that

$$\mathbf{D}_n = \mathbf{B}_p \mathbf{q}_p, \quad \mathbf{B}_p = \mathbf{L}_p \mathbf{A}_p^{-1}. \quad (8)$$

The boolean matrix \mathbf{L}_p has dimension $N \times N_p$, where N is the number of spatial (nodal) points and N_p is the number of independent piezoelectric elements. \mathbf{L}_p allows to set an equal value to selected nodal electric displacements. \mathbf{A}_p is a diagonal matrix with the surface area of the electrodes of the piezoelectric elements.

Substituting Eq. (8) in Eq. (7) and pre-multiplying the second line of the resulting equation by \mathbf{B}_p^t leads to

$$\begin{bmatrix} \mathbf{M}_s + \mathbf{M}_p & 0 \\ 0 & 0 \end{bmatrix} \begin{Bmatrix} \ddot{\mathbf{u}} \\ \ddot{\mathbf{q}}_p \end{Bmatrix} + \begin{bmatrix} \mathbf{K}_{us} + \mathbf{K}_{up}^D & -\mathbf{K}_{uq} \\ -\mathbf{K}_{uq}^t & \mathbf{K}_q \end{bmatrix} \begin{Bmatrix} \mathbf{u} \\ \mathbf{q}_p \end{Bmatrix} = \begin{Bmatrix} \mathbf{F}_m \\ 0 \end{Bmatrix}, \quad (9)$$

where

$$\mathbf{K}_{uq} = \mathbf{K}_{ud}\mathbf{B}_p, \quad \mathbf{K}_q = \mathbf{B}_p^t\mathbf{K}_d\mathbf{B}_p. \quad (10)$$

2.2 Connection to Electric Circuits

It is worthwhile to analyze the connection of piezoelectric elements to electric circuits, specially when shunt circuits are considered for passive vibration control. To this end, it seems that an electric charge formulation is more appropriate since it is possible to relate the electric charges flowing between the piezoelectric elements electrodes with the electric charges flowing through the electric circuit. First, let us consider a set of simple but quite general electric circuits composed of an inductor, a resistor, and a voltage source. The equations of motion for such circuits can be found using d'Alembert's principle, such that the virtual work done by the inductors δT_{Lj} , resistors, δW_{Rj} , and voltage sources, δW_{Vj} , of the j -th electric circuit are

$$\delta T_{Lj} = -\delta q_{cj}L_{cj}\ddot{q}_{cj}, \quad \delta W_{Rj} = -\delta q_{cj}R_{cj}\dot{q}_{cj}, \quad \delta W_{Vj} = \delta q_{cj}V_{cj}, \quad (11)$$

where L_{cj} , R_{cj} , and V_{cj} are the inductance, resistance, and applied voltage of the j -th electric circuit. q_{cj} is the electric charge flowing through the j -th electric circuit. Combining the virtual work done by all circuits leads to

$$\begin{aligned} \delta T_L &= \sum_j \delta T_{Lj} = -\delta \mathbf{q}_c^t \mathbf{L}_c \ddot{\mathbf{q}}_c, & \delta W_R &= \sum_j \delta W_{Rj} = -\delta \mathbf{q}_c^t \mathbf{R}_c \dot{\mathbf{q}}_c, \\ \delta W_V &= \sum_j \delta W_{Vj} = \delta \mathbf{q}_c^t \mathbf{V}_c, \end{aligned} \quad (12)$$

where \mathbf{q}_c is the vector of electric charges, \mathbf{L}_c and \mathbf{R}_c are diagonal matrices with the inductances and resistances of each circuit, and \mathbf{V}_c is the vector of applied voltages.

Adding these virtual works to the electromechanical virtual works of previous section, such that

$$\delta T - \delta U + \delta W + \delta T_L + \delta W_R + \delta W_V = 0, \quad (13)$$

or, in terms of the generalized displacements,

$$\begin{aligned} \delta \mathbf{u}^t \left[(\mathbf{M}_s + \mathbf{M}_p) \ddot{\mathbf{u}} + (\mathbf{K}_{us} + \mathbf{K}_{up}^D) \mathbf{u} - \mathbf{K}_{uq} \mathbf{q}_p - \mathbf{F}_m \right] \\ + \delta \mathbf{q}_p^t \left(-\mathbf{K}_{uq}^t \mathbf{u} + \mathbf{K}_q \mathbf{q}_p \right) + \delta \mathbf{q}_c^t (\mathbf{L}_c \ddot{\mathbf{q}}_c + \mathbf{R}_c \dot{\mathbf{q}}_c - \mathbf{V}_c) = 0. \end{aligned} \quad (14)$$

Then, the connection between each piezoelectric element and a corresponding electric circuit is done by stating that the electric charges flowing from the piezoelectric element enter the circuit and vice-versa, such that

$$\mathbf{q}_c = \mathbf{q}_p. \quad (15)$$

Thus, replacing \mathbf{q}_c by \mathbf{q}_p in Eq. (14) leads to the following coupled equations of motion

$$\begin{aligned} \begin{bmatrix} \mathbf{M}_s + \mathbf{M}_p & 0 \\ 0 & \mathbf{L}_c \end{bmatrix} \begin{Bmatrix} \ddot{\mathbf{u}} \\ \ddot{\mathbf{q}}_p \end{Bmatrix} + \begin{bmatrix} 0 & 0 \\ 0 & \mathbf{R}_c \end{bmatrix} \begin{Bmatrix} \dot{\mathbf{u}} \\ \dot{\mathbf{q}}_p \end{Bmatrix} \\ + \begin{bmatrix} \mathbf{K}_{us} + \mathbf{K}_{up}^D & -\mathbf{K}_{uq} \\ -\mathbf{K}_{uq}^t & \mathbf{K}_q \end{bmatrix} \begin{Bmatrix} \mathbf{u} \\ \mathbf{q}_p \end{Bmatrix} = \begin{Bmatrix} \mathbf{F}_m \\ \mathbf{V}_c \end{Bmatrix}. \end{aligned} \quad (16)$$

In this case, the solution for \mathbf{u} and \mathbf{q}_p must be simultaneous, that is accounting for the electromechanical and circuit equations of motion. Notice that the passive components of the electric circuit \mathbf{L}_c and \mathbf{R}_c affect the equivalent piezoelectric force applied to the structure when an actuator with applied voltage is considered. For a simple actuator with applied voltage, that is with only a voltage source in the circuit ($\mathbf{L}_c = \mathbf{R}_c = 0$), the second equation in Eq. (16) can be solved for \mathbf{q}_p leading to

$$\mathbf{q}_p = \mathbf{K}_q^{-1} \mathbf{V}_c + \mathbf{K}_q^{-1} \mathbf{K}_{uq}^t \mathbf{u}, \quad (17)$$

which can be substituted in Eq. (16) such that it reduces to

$$(\mathbf{M}_s + \mathbf{M}_p) \ddot{\mathbf{u}} + \left[\mathbf{K}_{us} + \left(\mathbf{K}_{up}^D - \mathbf{K}_{uq} \mathbf{K}_q^{-1} \mathbf{K}_{uq}^t \right) \right] \mathbf{u} = \mathbf{F}_m + \mathbf{F}_p, \quad (18)$$

where the equivalent piezoelectric force \mathbf{F}_p applied to the structure by the piezoelectric actuators is

$$\mathbf{F}_p = \mathbf{K}_{uq} \mathbf{K}_q^{-1} \mathbf{V}_c. \quad (19)$$

From Eq. (18), the generalized displacements \mathbf{u} induced by mechanical and piezoelectric equivalent forces can be evaluated. Then, the electric charges \mathbf{q}_p flowing between electrodes of the piezoelectric elements can be found using Eq. (17).

2.3 Design of Passive Resistive Shunt Circuits

In this section, the equations of motion (16) are reduced to the case of purely resistive shunt circuit by considering $\mathbf{L}_c = 0$ and $\mathbf{V}_c = 0$. It is then desired to use these equations to properly tune the values of electric resistance of the shunt circuits in order to maximize the added damping provided to a given vibration mode of interest.

For the sake of simplicity, only one piezoelectric patch connected to one resistive shunt circuit is considered. The structural response is represented only by the contribution of the vibration mode of interest, such that

$$\mathbf{u}(t) = \boldsymbol{\phi}_n \alpha_n(t), \quad (20)$$

where $\boldsymbol{\phi}_n$ is the n -th structural vibration mode, mass normalized, and α_n is the corresponding modal displacement. Then, the equations of motion (16) can be rewritten as

$$\ddot{\alpha}_n + \omega_n^2 \alpha_n - k_p q = F_n, \quad (21)$$

$$R_c \dot{q} + k_e q - k_p \alpha_n = 0, \quad (22)$$

where $k_p = \boldsymbol{\phi}_n^T \mathbf{K}_{uq}$, $k_e = K_q$, and $F_n = \boldsymbol{\phi}_n^T \mathbf{F}_m$. It is interesting to notice that ω_n is the n -th natural frequency for the structure considering an open circuit electric boundary condition for the piezoelectric patch ($R_c \rightarrow \infty$).

The computation of R_c is performed considering that the resistive shunt circuit behaves as a simple energy dissipation element and, thus, may modify (increase) the structural damping factor. Therefore, let us consider the free vibration case ($F_m = 0$) and quantify the effect of the shunt circuit on the dynamic behavior of the structure. Supposing a harmonic response $\alpha_n = \tilde{\alpha}_n e^{j\omega t}$ and $q = \tilde{q} e^{j\omega t}$,

$$(-\omega^2 + \omega_n^2) \tilde{\alpha}_n - k_p \tilde{q} = 0, \quad (23)$$

$$(j\omega R_c + k_e) \tilde{q} - k_p \tilde{\alpha}_n = 0. \quad (24)$$

Solving Eq. (24) for \tilde{q} and substituting in Eq. (23) yields

$$\left[-\omega^2 + \left(\omega_n^2 - \frac{k_p^2}{jR_c \omega + k_e} \right) \right] \tilde{\alpha}_n = 0. \quad (25)$$

Hence, the resistive shunt circuit leads to a complex natural frequency ω_n^* defined by

$$\omega_n^{*2} = \omega_n^2 - \frac{k_p^2}{jR_c \omega + k_e}. \quad (26)$$

From this equation, it is possible to obtain relevant information about the electromechanical coupling and its effects. For instance, it is clear that the larger the electromechanical coupling coefficient (EMCC) between patch and structure for the vibration mode of interest, represented by k_p , the larger is the effect of the circuit on the structure. Besides, the cases of open circuit (oc) and short-circuit (sc) may be derived such that

$$\begin{aligned}\omega_n^{\text{oc}2} &= \lim_{R_c \rightarrow \infty} \omega_n^{*2} = \omega_n^2, \\ \omega_n^{\text{sc}2} &= \lim_{R_c \rightarrow 0} \omega_n^{*2} = \omega_n^2 - \frac{k_p^2}{k_e},\end{aligned}\quad (27)$$

where the effect of stiffness increase due to the induced potential is clear. One may also derive the following expression for the effective EMCC using

$$K_n^2 = \frac{\omega_n^{\text{oc}2} - \omega_n^{\text{sc}2}}{\omega_n^{\text{oc}2}} = \frac{k_p^2}{\omega_n^2 k_e}. \quad (28)$$

Introducing the nondimensional frequency ρ , it is possible to obtain

$$\rho = \frac{R_c \omega}{k_e} = R_c \omega C_p^\varepsilon. \quad (29)$$

where C_p^ε is the piezoelectric patch electric capacitance for constant strain. Then, the complex natural frequency ω_n^* may be rewritten as function of the EMCC K_n^2 and nondimensional natural frequency ρ as

$$\omega_n^{*2} = \omega_n^2 \left(1 - \frac{K_n^2}{1 + j\rho} \right), \quad (30)$$

which, after some algebraic manipulations, may be written as

$$\omega_n^{*2} = \omega_{nr}^2 (1 + j\eta_n), \quad (31)$$

where ω_{nr} and η_n are defined as the real part of the natural frequency and the loss factor, respectively, which are

$$\omega_{nr}^2 = \omega_n^2 \left(1 - \frac{K_n^2}{1 + \rho^2} \right), \quad (32)$$

$$\eta_n = \frac{\rho K_n^2}{(1 - K_n^2) + \rho^2}. \quad (33)$$

Notice that the loss factor and the real part of the complex natural frequency are functions of the nondimensional frequency ρ . Therefore, it is desired to search for the value ρ_{op} that maximizes η_n . Making $d\eta_n/d\rho = 0$, the following solution is obtained

$$\rho_{op} = \sqrt{1 - K_n^2}, \tag{34}$$

such that the maximum loss factor is given by

$$\eta_n^{max} = \frac{K_n^2}{2\sqrt{1 - K_n^2}}. \tag{35}$$

Combining Eqs. (29) and (34), an expression for the value of the electric resistance R_{op} that maximizes the loss factor at the natural frequency ω_n reads

$$R_{op} = \frac{k_e \sqrt{1 - K_n^2}}{\omega_n}. \tag{36}$$

Figure 1 shows theoretically attainable levels of material loss factor for standard piezoceramic materials in operation modes k_{33} , k_{15} , and k_{31} .

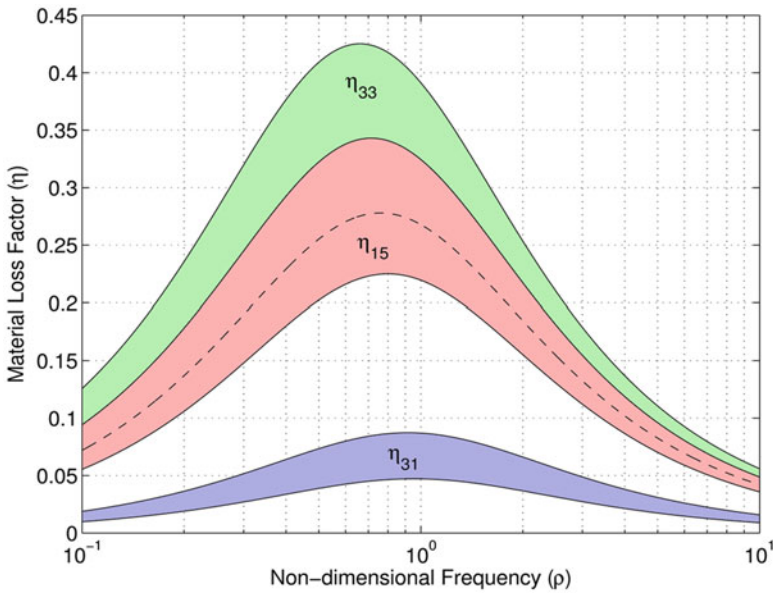


Fig. 1 Loss factor for standard piezoceramic materials using operation modes k_{33} , k_{15} , and k_{31} combined to resistive shunt circuits

2.4 Design of Passive Resonant Shunt Circuits

In the case of piezoelectric patches connected to resonant, or resistive-inductive (RL), shunt circuits, the circuit is no longer a simple energy dissipation element since the combination of circuit inductance and piezoelectric patch capacitance leads to an electrical resonance. On the other hand, this fact may be used in such a way that the circuit may absorb part of the energy generated by the piezoelectric material and, thus, behave as a dynamic vibration absorber. Therefore, the theory of dynamic vibration absorbers (Den Hartog 1985) is used.

To this end, the equations of motion (16) could be reduced to two degrees-of-freedom, one mechanical and one electrical. Thus, as in the previous section, the structural response is approximated by only the contribution of the vibration mode of interest. In the present case, the decomposition Eq. (20) is applied to Eq. (16) but maintaining both passive circuit elements ($R_c \neq 0$ and $L_c \neq 0$) while the voltage source is removed ($V = 0$). The equations of motion (16) are then reduced to

$$\ddot{\alpha}_n + \omega_n^2 \alpha_n - k_p q = b_n p, \quad (37)$$

$$L_c \ddot{q} + R_c \dot{q} + k_e q - k_p \alpha_n = 0. \quad (38)$$

The design of L_c and R_c aims to minimize the structure's frequency response amplitude. For that, let us suppose a mechanical excitation $p = \tilde{p} e^{j\omega t}$, such that $\alpha_n = \tilde{\alpha}_n e^{j\omega t}$ and $q = \tilde{q} e^{j\omega t}$. It is also considered that the structural response will be measured by a displacement sensor that provides the output $y = \mathbf{c}_y \mathbf{u}$, where \mathbf{c}_y is a vector that describes the output in terms of the contributions of the mechanical dof \mathbf{u} . Due to the harmonic excitation, the output is also in the form $y = \tilde{y} e^{j\omega t}$, with $\tilde{y} = c_n \tilde{\alpha}_n$ and $c_n = \mathbf{c}_y \boldsymbol{\phi}_n$. The equations of motion (37) and (38) may be written as

$$(\omega_n^2 - \omega^2) \tilde{\alpha}_n - k_p \tilde{q} = b_n \tilde{f}, \quad (39)$$

$$(-\omega^2 L_c + j\omega R_c + k_e) \tilde{q} - k_p \tilde{\alpha}_n = 0. \quad (40)$$

Solving Eq. (40) for \tilde{q} , it is possible to write $\tilde{\alpha}_n$ and, thus \tilde{y} , as functions of the excitation amplitude \tilde{f} , where $\tilde{y} = H(\omega) \tilde{f}$,

$$H(\omega) = c_n b_n \frac{-\omega^2 L_c + k_e + j\omega R_c}{\omega^4 L_c - \omega^2 (k_e + \omega_n^2 L_c) + \omega_n^2 k_e - k_p^2 + j\omega R_c (\omega_n^2 - \omega^2)}. \quad (41)$$

The frequency response amplitude is defined as

$$|H(\omega)| = c_n b_n \left\{ \frac{(-\omega^2 L_c + k_e)^2 + (\omega R_c)^2}{\left[\omega^4 L_c - \omega^2 (k_e + \omega_n^2 L_c) + \omega_n^2 k_e - k_p^2 \right]^2 + \omega R_c (\omega_n^2 - \omega^2)^2} \right\}^{1/2}, \quad (42)$$

and, for limited values of R_c , there is an anti-resonance at a frequency that is equal to the one of the electric circuit resonances, defined as $\omega_c = (k_e/L_c)^{1/2}$. One of the possible strategies to minimize the structural response amplitude at one of its resonance frequencies consists of designing the resonance frequency of the sub-system so that it coincides with the structure's resonance frequency of interest.

In this case, although both k_e and L_c may be designed, k_e is considered as a fixed parameter since it depends on physical and geometric properties of the piezoelectric patch. Therefore, it is desired to design a circuit that minimizes the structural response. This can be achieved by considering $\omega_c = \omega_n$, that allows us to compute the circuit inductance directly by

$$L_c = \frac{k_e}{\omega_n^2}. \quad (43)$$

The anti-resonance placed at ω_n is accompanied by two resonances, before and after ω_n , that must have their amplitudes controlled in order to minimize the amplification of the structural response in the case of frequency detuning. This can be achieved using the shunt circuit resistance to provide an equivalent damping to the two resonances. One possible methodology is to search for the resistance value that makes the amplitude at anti-resonance to be approximately equal to the one at two invariant frequencies, for which the amplitude is limited and independent on the resistance (Den Hartog 1985). These invariant frequencies can be evaluated through the following expression

$$\lim_{R_c \rightarrow 0} |H(\omega)|^2 = \lim_{R_c \rightarrow \infty} |H(\omega)|^2, \quad (44)$$

which, by substituting Eq. (42), leads to

$$\omega_{1,2}^2 = \frac{1}{2} \left[\omega_c^2 + \omega_n^2 \pm \sqrt{(\omega_c^2 - \omega_n^2)^2 + 2\omega_c^2 (k_p^2/k_e)} \right]. \quad (45)$$

The response amplitude at these invariant frequencies ω_1 and ω_2 and at the anti-resonance frequency ω_n are

$$|H(\omega_1)|^2 = \frac{R_c^2 \omega_n^2}{k_p^4} \quad \text{and} \quad |H(\omega_n)|^2 = \frac{2k_e}{k_p^2 \omega_n^2}. \quad (46)$$

By equalizing the two amplitudes, it is possible to find an expression for the shunt circuit resistance, such that

$$R_c = \frac{k_p \sqrt{2k_e}}{\omega_n^2}. \quad (47)$$

Notice that it is written in terms of the equivalent coupling stiffness k_p , equivalent dielectric stiffness k_e , and structure's resonance frequency of interest ω_n .

2.5 Piezoelectric Shunted Damping Example

In this section, a case study of passive vibration control using piezoelectric patches connected to resistive and resonant shunt circuits is presented. The host structure is an Aluminum cantilever beam as shown in Fig. 2. The beam is lightly damped and this is accounted for using a constant modal damping factor of 0.5 %. The material properties of the Aluminum are: Young’s modulus 70 GPa, Poisson ratio 0.35, and mass density 2700 kg m^{-3} . It is then desired to increase the structural damping of the host structure by using a passive control solution. Two piezoceramic patches (PZT5A) perfectly bonded to the host structure are connected to a shunt circuit, consisting of a resistance and an inductance. The width of both host structure and piezoceramic patches, not shown in the figure, is 25 mm. The material properties of the PZT5A piezoceramic are: $\bar{c}_{11}^D = c_{22}^D = 96.39 \text{ GPa}$, $\bar{c}_{12}^D = 51.22 \text{ GPa}$, $\bar{c}_{44}^D = \bar{c}_{55}^D = 39.63 \text{ GPa}$, $\bar{c}_{66}^D = 22.57 \text{ GPa}$, $\bar{h}_{31} = \bar{h}_{32} = -1.677 \times 10^9 \text{ NC}^{-1}$, $\bar{\beta}_{33}^e = 104.5 \times 10^6 \text{ mF}^{-1}$, and $\rho^{\text{pzt}} = 7750 \text{ kg m}^{-3}$. The piezoceramic patches are fully covered by electrodes on the upper and lower surfaces. Electrodes at the interface with the host structure are considered to be grounded.

Figures 3 and 4 show the frequency response of the structure (between tip velocity and tip force) for three cases depending on the connection of the piezoelectric patches: (i) open-circuit, (ii) resistive shunt, (iii) resonant (resistive-inductive) shunt. The optimal value for the resistance in the resistive circuit was obtained using Eq. (36) leading to $R_c = 103 \text{ k}\Omega$. In the case of the resonant circuit, the optimal values for resistance and inductance were obtained using Eqs. (47) and (43), respectively, leading to $R_c = 18 \text{ k}\Omega$ and $L_c = 514 \text{ H}$. Notice that the resistance values were rounded in $\text{k}\Omega$ and the inductance value was manually fine tuned from 514 to 503 H.

It is possible to observe in Fig. 3 that both resistive and resonant shunt circuits allow to reduce the vibration amplitude only around a single resonance frequency with no modification of other resonances. In terms of vibration amplitude reduction performance, it is clear from Fig. 4 that the resonant shunt circuit, which may reduce the vibration amplitude in about 20 dB, is much more effective than the resistive one, which reduces amplitude in about 5 dB.

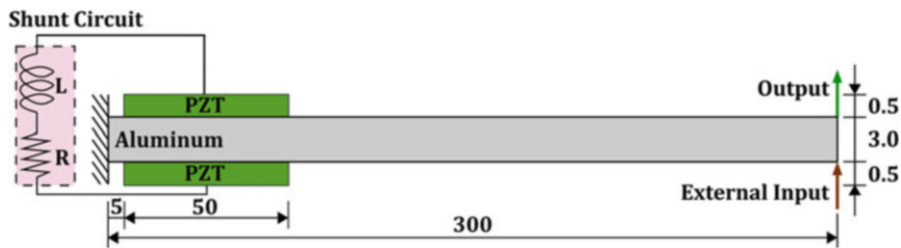


Fig. 2 Schematic representation of a cantilever beam with two piezoelectric patches connected to a resonant shunt circuit (dimensions in mm)

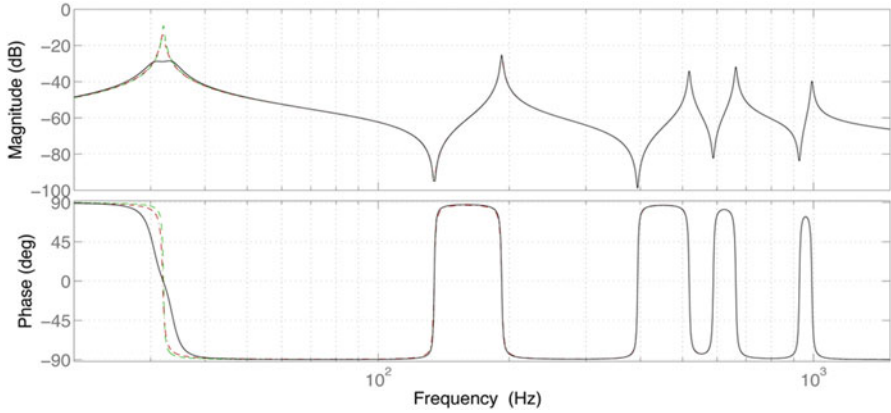


Fig. 3 Frequency response (*dashed*: open-circuit, *dash-dotted*: R shunt, *solid*: RL shunt) of the cantilever beam with piezoceramic patches connected to shunt circuit

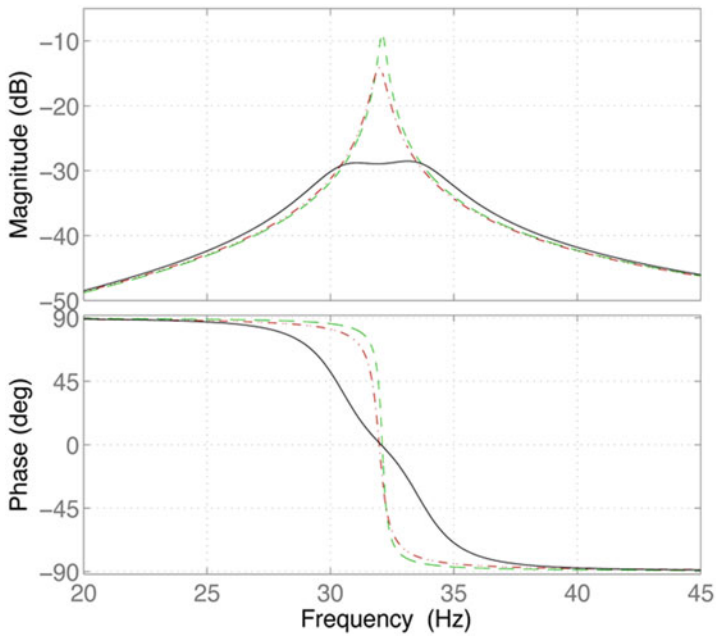


Fig. 4 Frequency response (*dashed*: open-circuit, *dash-dotted*: R shunt, *solid*: RL shunt) of the cantilever beam with piezoceramic patches connected to shunt circuit zoomed at the first resonance

3 Active Vibration Control Using Piezoelectric Materials

Since the mid-1980s, several studies focused on the use of distributed piezoelectric patches for the active vibration and noise control of thin plate-like structures (Bailey and Hubbard 1985). The main goal was to obtain a so-called adaptive structure with very integrated sensors and actuators so that adaptive/reconfigurable vibration mitigation solutions could be part of the structural design phase. Since then, several advances were observed in terms of predictive models, control design and optimization, experimental implementation and required power reduction with main focus on aeronautic and aerospace applications (Ahmadian and DeGuilio 2001; Reza Moheimani and Fleming 2006; Leo 2007). Some researchers also proposed combined active-passive vibration control strategies using piezoelectric patches (Tang et al. 2000; Santos and Trindade 2011).

In this section, a case study of active vibration control using piezoelectric patches as sensors and actuators is presented. The host structure is an Aluminum cantilever beam as shown in Fig. 5. The beam is lightly damped and this is accounted for using a constant modal damping factor of 0.5 %. The material properties of the Aluminum are: Young’s modulus 70 GPa, Poisson ratio 0.35, and mass density 2700 kg m^{-3} . It is then desired to increase the structural damping of the host structure by using an active control solution. Two piezoceramic patches (PZT5A) perfectly bonded to the host structure are considered as sensor and actuator and these are connected by an active controller, consisting of a control unit and a power amplifier. The width of both host structure and piezoceramic patches, not shown in the figure, is 25 mm. The material properties of the PZT5A piezoceramic are: $\bar{c}_{11}^D = c_{22}^D = 96.39 \text{ GPa}$, $\bar{c}_{12}^D = 51.22 \text{ GPa}$, $\bar{c}_{44}^D = \bar{c}_{55}^D = 39.63 \text{ GPa}$, $\bar{c}_{66}^D = 22.57 \text{ GPa}$, $\bar{h}_{31} = \bar{h}_{32} = -1.677 \times 10^9 \text{ NC}^{-1}$, $\bar{\beta}_{33}^e = 104.5 \times 10^6 \text{ mF}^{-1}$, and $\rho^{\text{pzt}} = 7750 \text{ kgm}^{-3}$. The piezoceramic patches are fully covered by electrodes on the upper and lower surfaces. Electrodes at the interface with the host structure are considered to be grounded. The piezoceramic sensor is considered to be connected to the control unit through a high impedance input such that it provides a voltage (electric potential) signal. The control voltage is imposed to the upper electrode of the piezoceramic actuator.

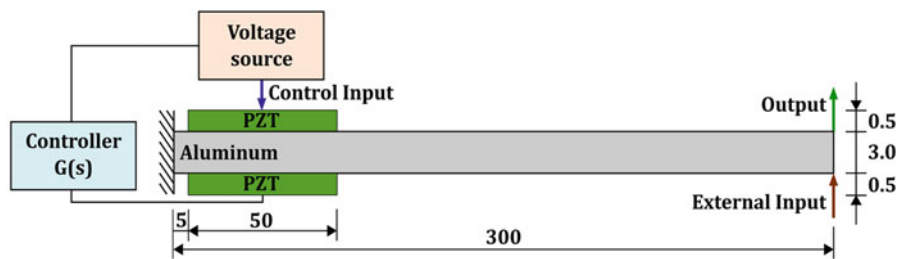


Fig. 5 Schematic representation of a cantilever beam with two piezoelectric patches serving as sensor and actuator connected to an active controller (dimensions in mm)

A coupled second-order model is constructed for the host structure with piezoelectric patches using the finite element method leading to

$$\begin{bmatrix} \mathbf{M}_t & \mathbf{0} & \mathbf{0} \\ \mathbf{0} & 0 & 0 \\ \mathbf{0} & 0 & 0 \end{bmatrix} \begin{Bmatrix} \ddot{\mathbf{u}} \\ \ddot{V}_s \\ \ddot{V}_a \end{Bmatrix} + \begin{bmatrix} \mathbf{K}_{us} + \mathbf{K}_{ups}^E + \mathbf{K}_{upa}^E & -\bar{\mathbf{K}}_{uvs} & -\bar{\mathbf{K}}_{uva} \\ -\bar{\mathbf{K}}_{uvs}^t & -\bar{\mathbf{K}}_{vs} & 0 \\ -\bar{\mathbf{K}}_{uva}^t & 0 & -\bar{\mathbf{K}}_{va} \end{bmatrix} \begin{Bmatrix} \mathbf{u} \\ V_s \\ V_a \end{Bmatrix} = \begin{Bmatrix} \mathbf{F}_m \\ 0 \\ 0 \end{Bmatrix}. \quad (48)$$

The control voltage applied to the actuator V_a is prescribed and thus the third line of Eq. (48) is automatically satisfied and the terms containing V_a in the first line can be moved to the right side. As for the sensor voltage V_s , it may be written in terms of the structure's displacements vector as

$$V_s = -\bar{\mathbf{K}}_{vs}^{-1} \bar{\mathbf{K}}_{uvs}^t \mathbf{u}, \quad (49)$$

and then substituted in the first equation such that

$$\mathbf{M}_t \ddot{\mathbf{u}} + \mathbf{D} \dot{\mathbf{u}} + \mathbf{K}_{ut} \mathbf{u} = \mathbf{F}_m + \bar{\mathbf{K}}_{uva} V_a, \quad (50)$$

where $\mathbf{K}_{ut} = \mathbf{K}_{us} + \mathbf{K}_{ups}^E + \mathbf{K}_{upa}^E + \bar{\mathbf{K}}_{uvs} \bar{\mathbf{K}}_{vs}^{-1} \bar{\mathbf{K}}_{uvs}^t$ and a damping matrix \mathbf{D} is included a posteriori.

Applying the methodology presented previously, the mechanical force is considered as a perturbation input such that $\mathbf{F}_m = \mathbf{b}_p p$, the voltage induced in the piezoceramic sensor is considered as the measurement output such that $y = V_s = \mathbf{c}_y \mathbf{u}$, with $\mathbf{c}_y = -\bar{\mathbf{K}}_{vs}^{-1} \bar{\mathbf{K}}_{uvs}^t$, and the voltage applied to the piezoceramic actuator V_a is considered as the control input, such that $\mathbf{b}_f = \bar{\mathbf{K}}_{uva}$.

In order to simplify the control design, a model reduction is performed using projection onto a reduced undamped modal basis, truncated to the vibration modes of interest $\boldsymbol{\phi}_j$, solution of $(-\omega_j^2 \mathbf{M}_t + \mathbf{K}_{ut}) \boldsymbol{\phi}_j = \mathbf{0}$. As discussed previously, it is very important to well represent the anti-resonance frequencies (or system zeros) in the control design. The low-frequency response of the neglected higher-frequencies vibration modes may have an important contribution to the location of the system zeros. Therefore, it is advisable to keep some vibration modes outside the frequency range of interest. The modal basis can also be enriched using the static contribution of the neglected vibration modes $\boldsymbol{\phi}_s = \mathbf{K}_{ut}^{-1} \bar{\mathbf{K}}_{uva}$. The structure's displacements are then approximated as $\mathbf{u} \approx \sum_j \boldsymbol{\phi}_j \alpha_j$ and, thus, the reduced equations of motion are written as

$$\begin{cases} \ddot{\boldsymbol{\alpha}} + \boldsymbol{\Lambda} \dot{\boldsymbol{\alpha}} + \boldsymbol{\Omega}^2 \boldsymbol{\alpha} = \boldsymbol{\Phi}^t \mathbf{F}_m + \boldsymbol{\Phi}^t \bar{\mathbf{K}}_{uva} V_a, \\ V_s = -\bar{\mathbf{K}}_{vs}^{-1} \bar{\mathbf{K}}_{uvs}^t \boldsymbol{\Phi} \boldsymbol{\alpha}. \end{cases} \quad (51)$$

For the sake of simplicity, in the present case, only the first six vibration modes (bending modes for all but the third and fifth ones that correspond to torsion modes) are kept in the reduced-order model.

Then, in order to make use of standard control system tools, the second-order reduced system Eq. (51) is rewritten in the following state-space form

$$\begin{cases} \dot{\mathbf{z}} = \mathbf{A}\mathbf{z} + \mathbf{B}_p p + \mathbf{B}_c V_a, \\ V_s = \mathbf{C}_y \mathbf{z}, \end{cases} \quad (52)$$

where

$$\mathbf{z} = \begin{bmatrix} \boldsymbol{\alpha} \\ \dot{\boldsymbol{\alpha}} \end{bmatrix}, \quad \mathbf{A} = \begin{bmatrix} \mathbf{0} & \mathbf{I} \\ -\boldsymbol{\Omega}^2 & -\boldsymbol{\Lambda} \end{bmatrix}, \quad \mathbf{B}_p = \begin{bmatrix} \mathbf{0} \\ \boldsymbol{\Phi}^t \mathbf{b}_p \end{bmatrix}, \quad \mathbf{B}_c = \begin{bmatrix} \mathbf{0} \\ \boldsymbol{\Phi}^t \bar{\mathbf{K}}_{uva} \end{bmatrix}, \quad (53)$$

$$\mathbf{C}_y = \begin{bmatrix} -\bar{\mathbf{K}}_{vs}^{-1} \bar{\mathbf{K}}_{uvs}^t \boldsymbol{\Phi} & \mathbf{0} \end{bmatrix}.$$

Then, the transfer function between sensor and actuator used in the control system reads $H_c(s) = \mathbf{C}_y (s\mathbf{I} - \mathbf{A})^{-1} \mathbf{B}_c$. In what follows, two simple control laws are designed based on this information: (i) Direct Velocity Feedback (DVF) and (ii) Positive Position Feedback (PPF). The control design is performed here with the aid of *rltool* Graphical User Interface of Control System Toolbox of MATLAB(R). For the DVF control, a real zero at $s = 0$ is added leading to a simple differentiator. For the PPF control, two complex conjugate poles near the open-loop poles corresponding to the vibration mode to be controlled are added.

Figure 6a shows the root locus of the closed-loop system. From the root locus, one may conclude that very large damping values could be obtained, in particular for the second and fourth modes (which are the second and third bending modes). However, it is important to notice that large values of control gains may not be realistic since they would require large control voltages that may not be feasible due to the maximum electric field supported by the piezoelectric patches and also the voltage and power demanded to the power amplifier (Trindade, Benjeddou, and Ohayon 2001). In the present case, it is assumed that the control voltage should not exceed 250 V (which leads to an applied electric field of 500 V/mm in the 0.5 mm thick piezoelectric patches). Commercial power amplifiers allow the application of such voltages for a limited frequency range and patches capacitance. For some applications, the energy consumption could also be used to design and analysis of control strategies (Wang and Inman 2011). There are also alternatives to reduce the maximum voltage required for a given performance (Tang et al. 2000; Sirohi and Chopra 2001; Santos and Trindade 2011).

Considering the maximum voltage limitation, the maximum feasible control gain is approximately $g = 5000 \text{ Vs/V}$. Then, the control performance is much weaker than the ones allowed by the control law alone. Nevertheless, a feasible DVF control still yields reasonable performance in terms of added structural

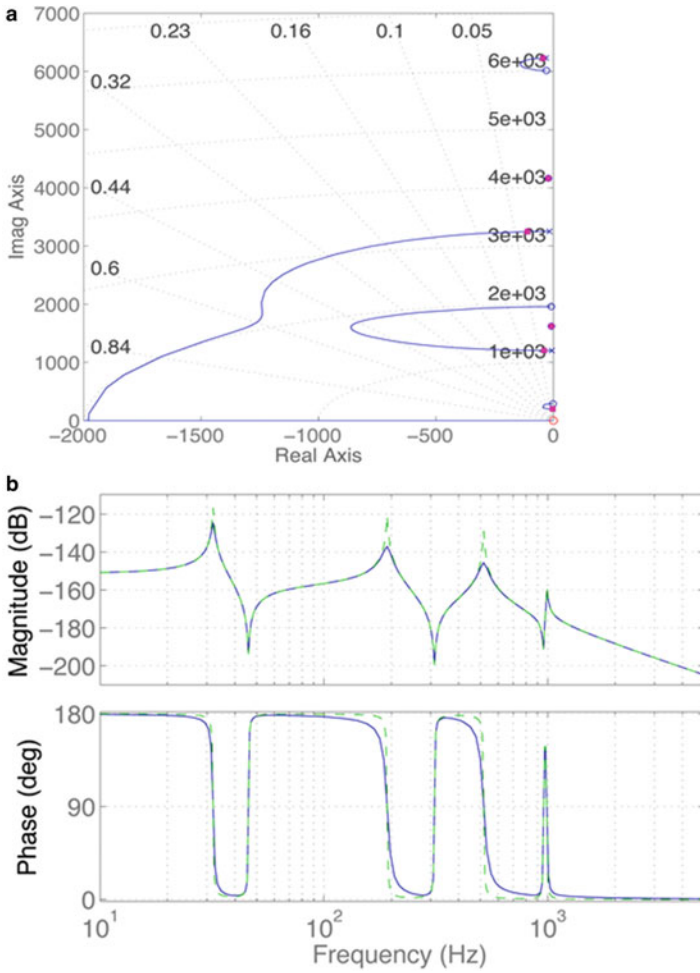


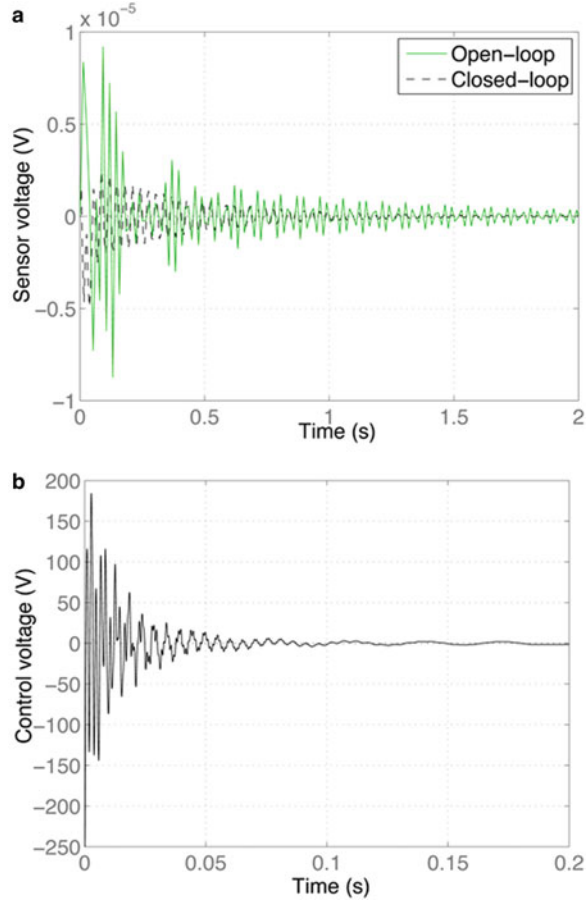
Fig. 6 (a) Root locus and (b) frequency response (*solid*: open loop, *dashed*: closed-loop) of the cantilever beam with piezoceramic patches and DVF control law

damping. Indeed, the modal damping factors of first three bending modes are increased from 0.5 to 1.2 %, 3.3 %, and 3.4 %, respectively. This also leads to a reduction in the vibration amplitude as shown in Fig. 6b.

Figure 7a, b shows, respectively, the impulsive time responses of the open-loop and closed-loop sensor voltages and the control voltage applied to the actuator.

As discussed previously a simple output feedback law, as DVF, is not able to focus on given vibration modes. The selection/prioritization of the modes that are better controlled depends mainly on the positioning of sensor and actuator and its relation with the mode shapes. This is one of the reasons why the Positive Position Feedback (PPF) may be very useful for structural vibration control. Provided that

Fig. 7 Impulse responses of (a) sensor voltage (*solid*: open loop, *dashed*: closed-loop) and (b) control voltage of the cantilever beam with piezoceramic patches and DVF control law



the natural frequencies (in fact, the open-loop poles) are known and available for proper tuning of the control parameters ω_f and ξ_f , the PPF control should allow to focus on a given vibration mode and, thus, to minimize the modification of other modes and optimize the use of the control energy.

As an example, a PPF control law focusing on the first vibration mode is considered for the cantilever beam with piezoelectric patches. The first vibration mode natural frequency is approximately 32 Hz (201 rad/s). Based on this information and with the aid of simulations in *rltool*, the PPF parameters are set to $\omega_f = 205$ rad/s and $\xi_f = 0.2$. Figure 8a shows the root locus of the closed-loop system in which it is possible to notice that the PPF does allow to completely modify the path of the closed-loop poles such that the first vibration mode can now be substantially damped while the second and third bending modes are much less modified. For a PPF control gain of $g = 38$ V/V, the vibration amplitude at the first natural frequency is greatly reduced as shown in Fig. 8b.

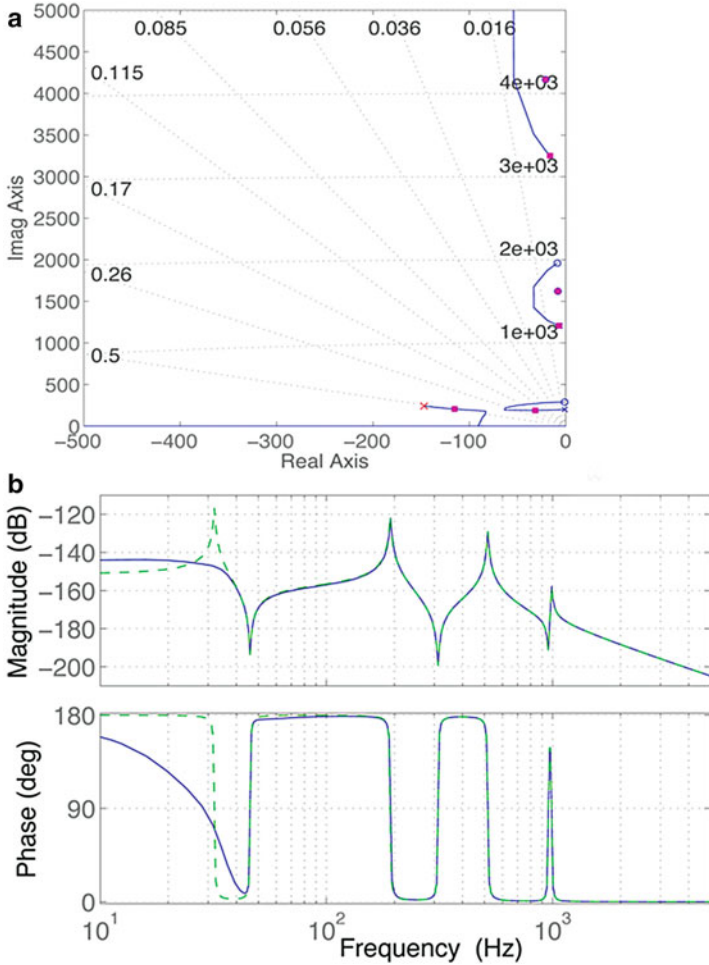
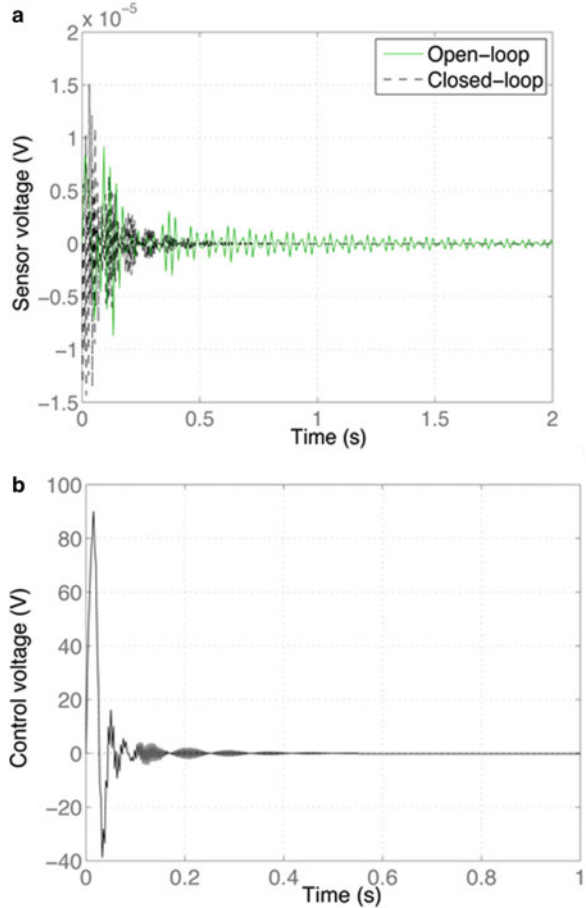


Fig. 8 (a) Root locus and (b) frequency response (*solid*: open loop, *dashed*: closed-loop) of the cantilever beam with piezoceramic patches and PPF control law

It is possible to observe in Fig. 9a, however, that the overshoot of the impulsive time response is increased in closed-loop although the settling time is reduced. Figure 9b also shows the control voltage required for such performance.

It is worthwhile to notice that, as discussed briefly in previous section, the obtained closed-loop control performance for both DVF and PPF control laws depend on the perturbation level of the system. Although theoretically these control performances are attainable, for higher excitation levels, the sensor output is also increased and so is the control voltage required to achieve such performances. In the present case, a perturbation force leading to a displacement amplitude of the order of the host structure thickness was used. To avoid saturation of the control voltage and its unpredictable effects, the control gain should be diminished as the perturbation level increases, leading to less performing vibration control.

Fig. 9 Impulse responses of (a) sensor voltage (*solid*: open loop, *dashed*: closed-loop) and (b) control voltage of the cantilever beam with piezoceramic patches and PPF control law



References

- M. Ahmadian, A.P. DeGiulio, Recent advances in the use of piezoceramics for vibration suppression. *Shock Vib. Dig.* **33**(1), 15–22 (2001)
- T. Bailey, J.E. Hubbard Jr., Distributed piezoelectric-polymer active vibration control of a cantilever beam. *AIAA J.* **8**(5), 605–611 (1985)
- W.W. Clark, Vibration control with state-switched piezoelectric materials. *J. Intel. Mater. Syst. Struct.* **11**(4), 263–271 (2000)
- J.P. Den Hartog, *Mechanical Vibrations*, 4th edn. (Dover, New York, 1985)
- T.C. Godoy, M.A. Trindade, Modeling and analysis of laminate composite plates with embedded active-passive piezoelectric networks. *J. Sound Vib.* **330**(2), 194–216 (2011)
- N.W. Hagood, A. von Flotow, Damping of structural vibrations with piezoelectric materials and passive electrical networks. *J. Sound Vib.* **146**(2), 243–268 (1991)
- M. Lallart, E. Lefeuvre, C. Richard, D. Guyomar, Self-powered circuit for broadband, multimodal piezoelectric vibration control. *Sens. Actuators A* **143**, 377–382 (2008)
- D.J. Leo, *Engineering Analysis of Smart Material Systems* (Wiley, New York, 2007)

- G.A. Lesieutre, Vibration damping and control using shunted piezoelectric materials. *Shock Vib. Dig.* **30**(3), 187–195 (1998)
- L. Meirovitch, *Dynamics and Control of Structures* (Wiley, New York, 1990)
- A. Preumont, *Vibration Control of Active Structures: An Introduction* (Kluwer Academic, Dordrecht, 1997)
- A. Preumont, *Mechatronics: Dynamics of Electromechanical and Piezoelectric Systems* (Springer, Dordrecht, 2006)
- S.O. Reza Moheimani, A survey of recent innovations in vibration damping and control using shunted piezoelectric transducers. *IEEE Trans. Contr. Syst. Technol.* **11**(4), 482–494 (2003)
- S.O. Reza Moheimani, A.J. Fleming, *Piezoelectric Transducers for Vibration Control and Damping* (Springer, London, 2006)
- H.F.L. Santos, M.A. Trindade, Structural vibration control using extension and shear active–passive piezoelectric networks including sensitivity to electrical uncertainties. *J. Braz. Soc. Mech. Sci. Eng.* **33**(3), 287–301 (2011)
- J. Sirohi, I. Chopra, Actuator power reduction using L-C oscillator circuits. *J. Intel. Mater. Syst. Struct.* **12**(12), 867–877 (2001)
- J. Tang, Y. Liu, K.W. Wang, Semiactive and active–passive hybrid structural damping treatments via piezoelectric materials. *Shock Vib. Dig.* **32**(3), 189–200 (2000)
- M.A. Trindade, A. Benjeddou, Effective electromechanical coupling coefficients of piezoelectric adaptive structures: critical evaluation and optimization. *Mech. Adv. Mater. Struct.* **16**(3), 210–223 (2009)
- M.A. Trindade, C.E.B. Maio, Multimodal passive vibration control of sandwich beams with shunted shear piezoelectric materials. *Smart Mater. Struct.* **17**(5), 055015 (2008)
- M.A. Trindade, A. Benjeddou, R. Ohayon, Piezoelectric active vibration control of damped sandwich beams. *J. Sound Vib.* **246**(4), 653–677 (2001)
- F.A.C. Viana, V. Steffen Jr., Multimodal vibration damping through piezoelectric patches and optimal resonant shunt circuits. *J. Braz. Soc. Mech. Sci.* **28**(3), 293–310 (2006)
- Y. Wang, D.J. Inman, Comparison of control laws for vibration suppression based on energy consumption. *J. Intel. Mater. Syst. Struct.* **22**(8), 795–809 (2011)

Impedance-Based Structural Health Monitoring

Valder Steffen Jr. and Domingos Alves Rade

Abstract Structural Health Monitoring—SHM—is known as the nondestructive process of online, in service, allowing the systems and structures to monitor their own integrity all along their useful lives. The most important goals in this context are to prevent failures, to increase security, and to reduce maintenance costs. One of the most important available techniques is the so-called impedance-based structural health monitoring, which is the focus of the present chapter. Practical implementations of the technique are described for illustration purposes.

Keywords Structural health monitoring • Impedance-based technique • Electromechanical coupling • Smart material • Piezoceramic material

1 Introduction

Failures occurring in industrial equipment and structures in general are mostly associated to friction, fatigue, impact, corrosion, and crack growth. For an appropriate functioning of the system, failure should be localized and repaired timely. In general terms, the problem of damage monitoring consists in localizing and measuring the fault and estimating the remaining life of the system (damage prognosis). One of the most important ambitions of modern engineering is to perform structural health monitoring in real time of structural components of high cost and considerable responsibility. Thus, the creation or improvement of techniques that enhance the accuracy and reliability of the damage tracking process is highly desirable and is the subject of several studies both in industry and academic environments (Farrar et al. 2005).

There are several techniques for monitoring the occurrence and propagation of structural damage. One of these techniques is the so-called impedance-based

V. Steffen Jr. (✉)

School of Mechanical Engineering, Federal University of Uberlândia,

Uberlândia, MG, Brazil

e-mail: vsteffen@ufu.br

D.A. Rade

Division of Mechanical Engineering, Technological Institute of Aeronautics,

São José dos Campos, SP, Brazil

e-mail: rade@ita.br

structural health monitoring (Park and Inman 2005). This technique is based on the electromechanical coupling that results from a piezoelectric transducer installed on the monitored structure (bonded on or incorporated into). Then, by measuring the electrical impedance, which depends on both the electrical characteristics of the transducer and the physical or mechanical characteristics of the structure (Liang et al. 1994), incipient damage can be detected from the variations found in the impedance curves (impedance signatures). Specific damage metrics can be used to quantify the damage. These damage metrics are calculated from the measurement comparisons between the cases without damage (healthy) and with damage, by using numerical and statistical tools as described in the literature (Palomino and Steffen 2009). In many applications, particularly those related to aeronautical structures, detecting incipient damage is an important issue, both from maintenance and security viewpoints. Another important point is that the use of statistical pattern recognition techniques to different problems of structural health monitoring (SHM) represents the best alternative available (Farrar and Worden 2013).

The determination of mechanical properties of materials is made by performing various tests, which are usually destructive. The most widely performed tests are the following: tensile tests, bending tests, torsion tests, fatigue tests, impact tests, and compression tests. The tensile test consists of subjecting the specimen to a stretching effort, while the fatigue test is an experimental procedure that produces a permanent, progressive, and localized structural change. Fatigue test process occurs while the material is subjected to conditions that produce dynamic tensions in one or more points that can form cracks or, in some cases, cause complete failure after a sufficient number of load cycles (Branco 1994). In order to evaluate the sensitivity of the impedance-based structural health monitoring method, impedance signals were measured along tensile and fatigue testing. The impedance signatures were used to create meta-models designed to predict the state of the structure (Palomino et al. 2011). It is worth mentioning that fatigue tests have a major importance in the aerospace industry. The life of components together with the life of the entire aircraft structure is of great importance for design and operation processes.

2 Impedance-Based Structural Health Monitoring: A Review

The technique known as impedance-based structural health monitoring utilizes the piezoelectric properties of the PZT patch (PZT stands for lead–zirconate–titanate, an intermetallic inorganic compound) that is installed in the structure being tested and is considered as a nondestructive damage evaluation method (Park et al. 2003). The basic idea behind this technique is monitoring the changes in the structure's mechanical impedance as caused by the presence of damage. Since the direct measurement of the mechanical impedance of the structure is a difficult task, the method uses piezoelectric materials (PZT) bonded to or incorporated into the

structure, allowing the measurement of the electrical impedance. This measure is related to the structure mechanical impedance, which is affected by the presence of damage. Evidently, it is considered that the piezoelectric sensor–actuator used in the monitoring procedure remains intact along the test. The PZT patches use a low voltage (< 1 V) and generate high frequency excitation at given points along the structure (Park et al. 2003).

The impedance-based SHM technique was first proposed by Liang et al. (1994) and, subsequently, the method was extended by Chaudhry et al. (1995, 1996), Sun et al. (1995), Park et al. (1999, 2000, 2001, 2003), Giurgiutiu and Zagari (2000), Giurgiutiu et al. (2000, 2002), Soh et al. (2000), Bhalla et al. (2002), Moura and Steffen (2004, 2006), Peairs et al. (2004), and Palomino and Steffen (2009). As mentioned above, this health monitoring technique utilizes impedance sensors to monitor changes in the structural stiffness, damping, and mass. The impedance sensors consist of small piezoelectric patches, usually smaller than $25 \times 25 \times 0.1$ mm, which are used to measure directly the local dynamic response.

The piezoelectric material acts directly producing an electric voltage when a mechanical stress is applied on the material. Conversely, mechanical strains are produced when an electric field is applied. The impedance-based monitoring method uses simultaneously both versions, direct and inverse, of the piezoelectric effect (Park et al. 2003).

When the PZT patch is bonded to the structure and a very low electric voltage is applied, generally 1 V (Raju 1997), a strain is produced in the PZT patch. Using a high frequency of excitation (in terms of typical modal analysis testing), the dynamic response of the structure represents only the local area of the sensor and is not affected by the boundary conditions. Then, the response of the mechanical vibrations is transmitted to the sensor in the form of an electrical response. When an incipient damage leads to changes in the dynamic response (given by the impedance signal), this is observed in the electric response of the PZT patch.

The electromechanical model that quantifies and describes the measurement process is illustrated in Fig. 1 for a single-degree-of-freedom system.

For this 1 d.o.f. system, Liang et al. (1994) demonstrated that the admittance, $Y(\omega)$, of the PZT patch can be written as a function of the combined actuator PZT’s and structure’s mechanical impedance, as given by Eq. (1):

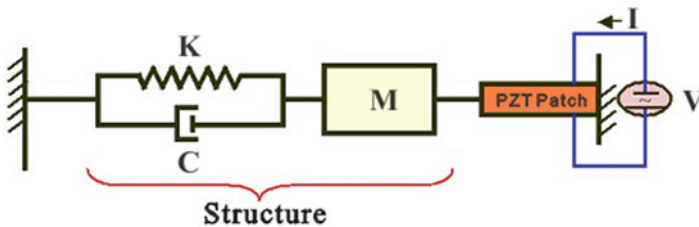


Fig. 1 Model used to represent a 1 d.o.f. PZT-driven dynamic structural system (Liang et al. 1994)

$$Y(\omega) = i\omega a \left(\bar{\epsilon}_{33}^T (1 - i\delta) - \frac{Z_s(\omega)}{Z_s(\omega) + Z_a(\omega)} d_{3x}^2 \hat{Y}_{xx}^E \right) \quad (1)$$

where $Y(\omega)$ is the electrical admittance (inverse of the impedance), $Z_a(\omega)$ and $Z_s(\omega)$ are the PZT's and structure's mechanical impedances, respectively. \hat{Y}_{xx}^E is the complex Young's modulus of the PZT at zero electric field, d_{3x} is the piezoelectric coupling constant in the arbitrary x direction at zero electric field, $\bar{\epsilon}_{33}^T$ is the dielectric constant at zero stress, δ is the dielectric loss tangent of the PZT, and a is a geometric constant of the PZT. Assuming that the mechanical properties of the PZT do not vary over time used for monitoring, Eq. (2) shows that the electrical impedance of the PZT patch is directly related to the structure's impedance. Damage causes changes in the structure's mechanical impedance, thus changing local dynamic features. Hence, the electrical impedance is used to monitor the structure health as represented by the structure's mechanical impedance.

Impedance is a complex quantity represented by Eq. (2), given in ohm. In general, the real part of the impedance is used for structural health monitoring purposes since it is less sensitive to temperature variation. However, the imaginary part and the magnitude values of the impedance are used in various applications.

$$Z = R + jX \quad (2)$$

where R is the resistance and X is the reactance.

The sensitivity of the technique to detect structural damage is related to the frequency range selected. A very small damage in the structure does not cause significant change in the structure's stiffness, mass, and damping properties. Hence, it is necessary for the excitation wavelength to be smaller than the characteristic length of the damage to be detected. According to the literature, the frequency range typically used in the impedance-based method is 30–250 kHz. The range for a given structure is usually determined by trial and error methods. However, Moura and Steffen (2004) presented a statistical procedure that can be used to obtain the best settings for tests of electromechanical impedance; however, the proposed procedure is rather time-consuming. In the impedance-based method, frequency ranges that contain 20–30 peaks are usually chosen, because the higher number of peaks provides a better dynamic response over the frequency range. A band around a high frequency (150 kHz) is favorable to detect the location, while a lower range, around 70 kHz, covers more sensing areas (Sun et al. 1995). In relation to the sensitive region to identify changes, Park et al. (2003) claim that for a single PZT patch damage located at a radial distance of up to 0.4 m can be identified in composite materials, and up to 2 m in bars consisting of a single metal.

Figure 2 presents an example of a simple riveted beam-like structure (Fig. 2a) for which the impedance responses are shown for two different conditions, namely the pristine condition (blue), and the case in which the rivet was lost, i.e., the damaged condition (red). The tests were performed by using the Agilent 4294A impedance analyzer shown in Fig. 3. It can be easily observed that the impedance curves are

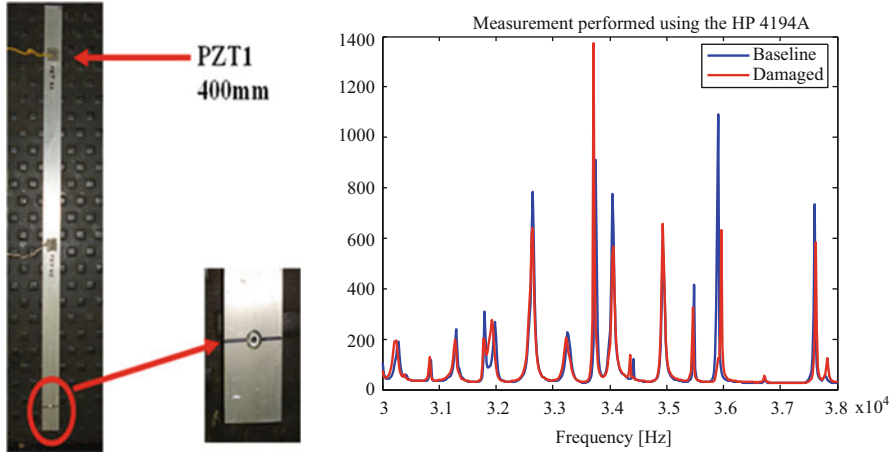


Fig. 2 Impedance-based structural health monitoring. (a) Riveted beam-like structure, (b) impedance responses

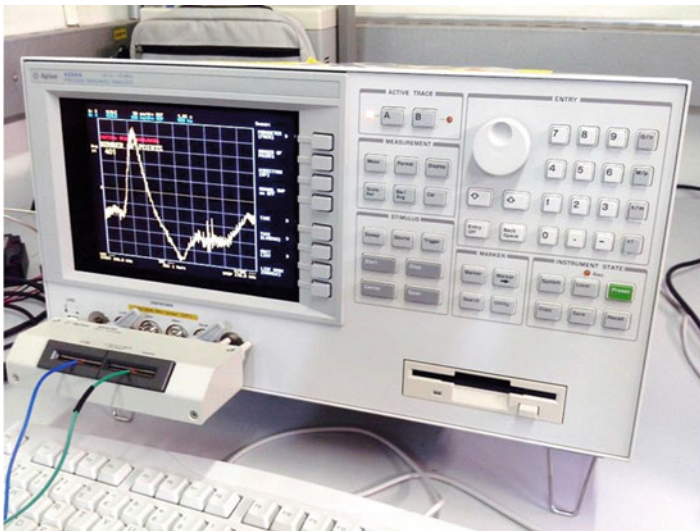


Fig. 3 Agilent 4294A Impedance Analyzer

qualitatively different. However, for making the analysis easier, it is more appropriate to quantify the influence of damage, which can be performed by the so-called damage metrics.

As mentioned above, the frequency ranges containing about 20–30 peaks are chosen, since that high number of peaks is related to rich dynamic responses. As an example, Fig. 4 shows the dynamic response between 10 and 250 kHz of an AI

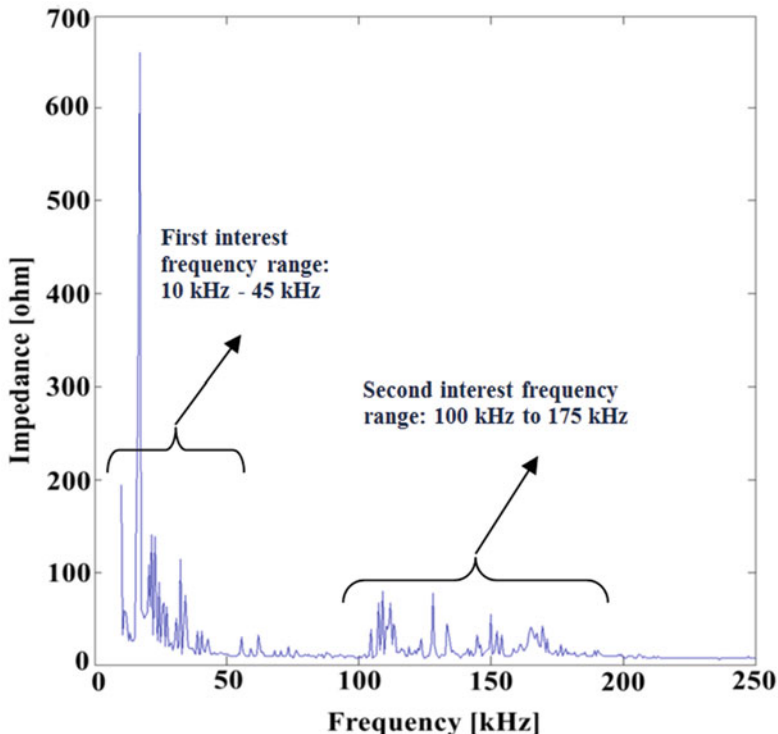


Fig. 4 Frequency ranges of interest

beam, in which two frequency ranges are highlighted, namely 10–45 kHz and 100–175 kHz.

In addition, it has been observed that the influence of the initial conditions is minimal since the PZT patch will excite the structure locally along the frequency test band.

2.1 Damage Metrics

To establish a methodology able to quantify structural changes, a reference to the damage metric (baseline) should be defined, corresponding to the structure without damage. Thus, comparisons can be made involving the metric values of the pristine condition and the damaged structure. These comparisons should be able to indicate the presence of damage in the structure. Palomino and Steffen (2009) studied the most significant damage metrics found in the literature. These damage metrics are briefly reviewed in the following.

The most used statistical model in the literature is the root mean square deviation (RMSD) as given by Eq. (3)

$$\text{RMSD} = \sqrt{\sum_{i=1}^n \left(\frac{(\text{Re}(Z_{1,i}) - \text{Re}(Z_{2,i}))^2}{n} \right)} \quad (3)$$

where $\text{Re}(Z_{1,i})$ is the impedance of the PZT measured under healthy condition, $\text{Re}(Z_{2,i})$ is the impedance for the comparison with the baseline measurement at frequency interval i , and n is the total number of frequency points adopted. This calculation is done within a predefined frequency range.

As a first alternative to this metrics, it is proposed to replace the denominator by the impedance measured under healthy condition (baseline) (Grisso 2005; Peairs 2006).

$$\text{RMSD1} = \sqrt{\sum_{i=1}^n \left(\frac{(\text{Re}(Z_{1,i}) - \text{Re}(Z_{2,i}))^2}{\text{Re}(Z_{1,i})^2} \right)} \quad (4)$$

The root mean square deviation defined by Eq. (4) is called RMSD1. In this case, the level of impedance measurement does not affect qualitatively the damage metrics, although the points taken in the comparison change the result obtained.

Giurgiutiu and Rogers (1998) describe another definition of the root mean square deviation, RMSD2, as represented by Eq. (5). It is possible to observe in this equation that the sum is made independently in the numerator and the denominator.

$$\text{RMSD2} = \sqrt{\frac{\sum_{i=1}^n (\text{Re}(Z_{1,i}) - \text{Re}(Z_{2,i}))^2}{\sum_{i=1}^n \text{Re}(Z_{1,i})^2}} \quad (5)$$

The damage metric described by Eq. (5) was used in other studies where comparisons were made between different metrics (Tseng and Naidu 2002; Giurgiutiu and Zagrai 2005).

Another possibility to use the root mean square deviation, RMSD3, is provided by Park et al. (2003).

$$\text{RMSD3} = \sum_{i=1}^n \sqrt{\frac{(\text{Re}(Z_{1,i}) - \text{Re}(Z_{2,i}))^2}{\text{Re}(Z_{1,i})^2}} \quad (6)$$

In Eq. (6) the sum is outside the root mean square sign, unlike the definitions previously given.

Peairs (2006) presents yet another change in the root mean square deviation, RMSD4, as shown by the following equation:

$$\text{RMSD4} = \sqrt{\sum_{i=1}^n \left(\frac{((\text{Re}(Z_{1,i}) - \text{Re}(\bar{Z}_1)) - (\text{Re}(Z_{2,i}) - \text{Re}(\bar{Z}_2)))^2}{n} \right)} \quad (7)$$

where $\text{Re}(\bar{Z}_1)$ and $\text{Re}(\bar{Z}_2)$ are the averages of measurements for the two conditions analyzed. These averages are included in Eq. (7) to minimize the effect of small variations on the metric value, resulting from possible changes in temperature or electrical resistance of the cables connecting the sensor to the impedance analyzer.

The variations mentioned above appear quite frequently. Then, to determine the baseline, the average of several measurements for the structure in healthy state should be used.

Using the mean value and the standard deviation calculated for each point, Peairs (2006) presents Eq. (8) as a new definition of the root mean square deviation:

$$\text{RMSD5} = \sqrt{\sum_{i=1}^n \left(\frac{\left(\frac{\text{Re}(\bar{Z}_{1,i}) - \text{Re}(Z_{2,i})}{S_{Z_{1,i}}} \right)^2}{n} \right)} \quad (8)$$

where the standard deviation of each point of the baseline, $S_{Z_{1,i}}$, is included in order to make the metric less sensitive to changes in the impedance signal due to changes in the environment (not linked to any damage in the structure).

Another alternative is the correlation coefficient deviation damage metric, which is used to quantify and interpret information from two data sets. The mathematical formulation, Eq. (9), involves the difference between one and the correlation coefficient between the measurement and the reference (Giurgiutiu and Zagrai 2005).

$$\text{CCD} = 1 - \text{CC} \quad (9)$$

where CCD is the correlation coefficient deviation and CC is the correlation coefficient that it is given by Eq. (10).

$$\text{CC} = \frac{1}{n} \sum_{i=1}^n \frac{(\text{Re}(Z_{1,i}) - \text{Re}(\bar{Z}_1))(\text{Re}(Z_{2,i}) - \text{Re}(\bar{Z}_2))}{S_{Z_1} S_{Z_2}} \quad (10)$$

where S_{Z_1} is the standard deviation of the baseline and S_{Z_2} is the standard deviation of the impedance signal to be compared. When the correlation coefficient is equal to one, it means that the signals are fully correlated. When the difference between the signals is large the CC value is small. The CC value is also used to compare and quantify the admittance signals (Naidu and Soh 2004).

The average square difference is another metric used by the electromechanical impedance method to quantify the damage (Raju 1997), and its mathematical formulation is given by Eq. (11):

$$\text{ASD} = \sum_{i=1}^n [\text{Re}(Z_{1,i}) - (\text{Re}(Z_{2,i}) - \delta)]^2 \quad (11)$$

where δ is the difference of the averages of each signal, as represented by Eq. (12)

$$\delta = \text{Re}(\bar{Z}_1) - \text{Re}(\bar{Z}_2) \quad (12)$$

This damage metric is also used to remove the effect of variations in the amplitude due to changes in the environment.

Another metric used by the electromechanical impedance method is the so-called mean absolute percentage deviation (Tseng and Naidu 2002):

$$\text{MAPD} = \sum_{i=1}^n \left| \frac{(\text{Re}(Z_{1,i}) - \text{Re}(Z_{2,i}))}{\text{Re}(Z_{1,i})} \right| \quad (13)$$

It is observed that the MAPD, Eq. (13), is similar to the root mean square deviation defined by RMSD3, (Eq. (5)).





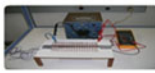



Finally, one has the metric given by the simple sum of the average difference between the signals (Peairs 2002). This damage metric does not use any relation between the values considered and is calculated as shown by Eq. (14):

$$M = \sum_{i=1}^n (\text{Re}(Z_{1,i}) - \text{Re}(Z_{2,i}))^2 \quad (14)$$

2.2 Environmental Influence on Impedance-Based SHM

For the success of the monitoring procedure, the measurement system should be robust enough with respect to environmental influences from different sources, in such a way that correct and reliable decisions can be made from the measurements. The environmental influences become more critical under certain circumstances, especially in aerospace applications, in which extreme conditions are frequently encountered. Palomino et al. (2012) examined the influence of electromagnetic radiation, temperature and pressure variations, and ionic environment under laboratory conditions. In this context, the major concern was to determine if the impedance responses are affected by these influences. In addition, the sensitivity of the method with respect to the shape of the PZT patches was also evaluated. For this aim, two shapes of piezoelectric patches of the same size, namely circular and

Table 1 Sensor shape and environmental influences

Sensor Geometry		Ionic Environment	
Squared PZT Patch	Circular PZT Patch	Without shielded PZT patch	With shielded PZT patch
	= 	 YES	 NO
Electromagnetic Radiation	Temperature		Pressure
 NO	Low	High	 NO
	 NO	 YES	

squared, have been tested in the laboratory. They were bonded to two different types of structures, namely a plate and a beam, so that the impedance response was measured both for pristine and damaged conditions. Similar results were obtained for the two shapes of PZT patches tested. The results are summarized in Table 1, in which it can be observed that temperature is a major environment issue in the context of impedance-based SHM.

3 Case Studies

To illustrate the application of the impedance-based structural health monitoring technique, two case studies are presented. The first is dedicated to a beam-like structure in which both the influence of the position of a small mass (representing a structural modification) and the influence of the size of holes in the structure are evaluated. The second case study is related to the influence of cumulative damage on the impedance responses in a typical fatigue test.

3.1 Impedance-Based SHM Applied to a Beam-Like Structure

Figure 5 shows a schematic representation of a cantilever Al beam to which a PZT patch was bonded to, aiming at monitoring structural changes that have been introduced to the system through the addition of a small mass, so that a structural modification results. The structural modifications obtained intend to represent damage.

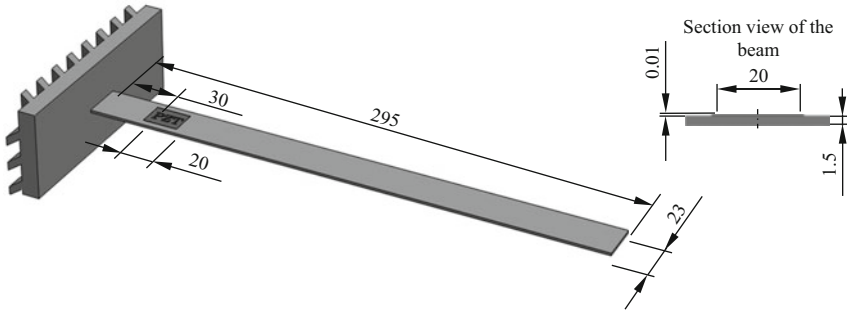


Fig. 5 Geometry of the beam

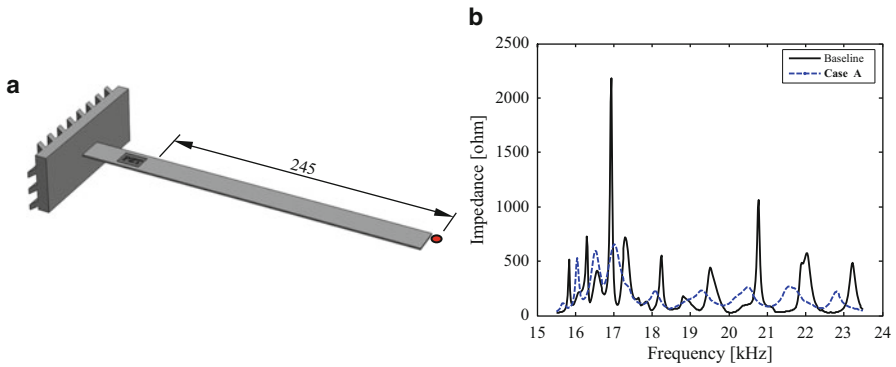


Fig. 6 Case A: (a) “damage” position; (b) impedance responses

The thickness of the beam is 1.5 mm and the thickness of the PZT patch is 0.01 mm. For the pristine condition, the baseline is shown in Fig. 6. Two frequency bands have been selected for the analysis, namely 15.5–23.5 kHz and 108–116 kHz. At this point a mass of 8.5 g was added to the system at different locations as explained in the following:

- Case A: the mass is placed 245 mm from the PZT patch (at the right end of the beam).
Figure 6 shows the position of the mass (a) and the impedance response in the frequency band of 15.5–23.5 kHz.
- Case B: the same mass is placed at a position 195 mm from the PZT patch.
Figure 7 shows the position of the mass (a) and the impedance responses (b) obtained.
- Similar tests were made by changing the distance of the mass (8.5 g), as follows:
Case C (distance = 195 mm); Case D (distance = 145 mm); Case E (distance = 95 mm). Following, a second frequency band was investigated (108–116 kHz).

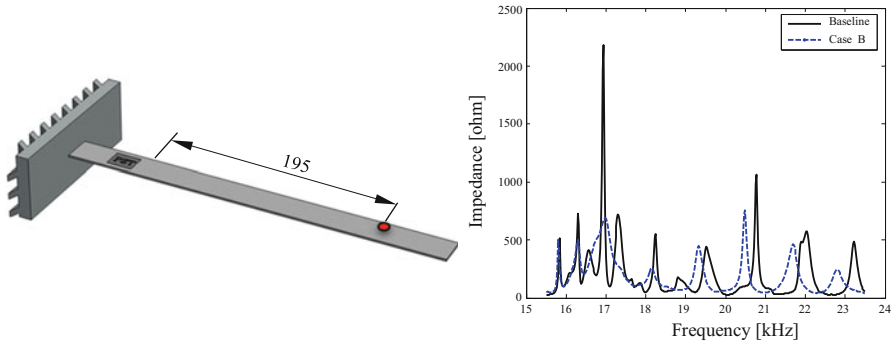


Fig. 7 Case B: (a) “damage” position; (b) impedance responses

Table 2 Damage metrics

Test cases	15.5–23.5 kHz			108–116 kHz		
	M_R	M_I	M_Z	M_R	M_I	M_Z
A	495.23	137.35	95.83	81.03	72.76	30.60
B	503.32	146.98	102.72	102.09	89.94	56.11
C	515.77	146.98	103.01	157.7	133.34	81.30
D	535.48	161.37	106.23	220.17	163.77	39.54
E	466.28	161.59	100.14	268.09	237.72	98.95

Then, the damage matrix was calculated as based on Eq. (3), namely the RMSD1. As impedance is a complex quantity, three different metrics were determined, as follows: by taking into account the real part of the impedance (resistance); by taking into account the imaginary part of the impedance (reactance); and by taking into account the magnitude of the impedance. The corresponding expressions are given by Eq. (15).

$$\begin{aligned}
 M_R &= \sum_{i=1}^n \sqrt{\frac{[\text{Re}(Z_{i,1}) - \text{Re}(Z_{i,2})]^2}{[\text{Re}(Z_{i,1})]^2}} & M_I &= \sum_{i=1}^n \sqrt{\frac{[\text{Im}(Z_{i,1}) - \text{Im}(Z_{i,2})]^2}{[\text{Im}(Z_{i,1})]^2}} \\
 M_Z &= \sum_{i=1}^n \sqrt{\frac{[(Z_{i,1}) - (Z_{i,2})]^2}{[(Z_{i,1})]^2}} & & & & & (15)
 \end{aligned}$$

Table 2 presents the results for the test cases above.

For illustration purposes, the damage metrics given by M_R are shown in Fig. 8 for the frequency band of 108–116 kHz. It can be observed that the closer the added mass, the larger the damage metrics. The same trend is kept for the other damage metrics.

Next, different masses were added to the beam at the same position. The goal is to observe the variation of the damage metrics when increasing the mass, keeping

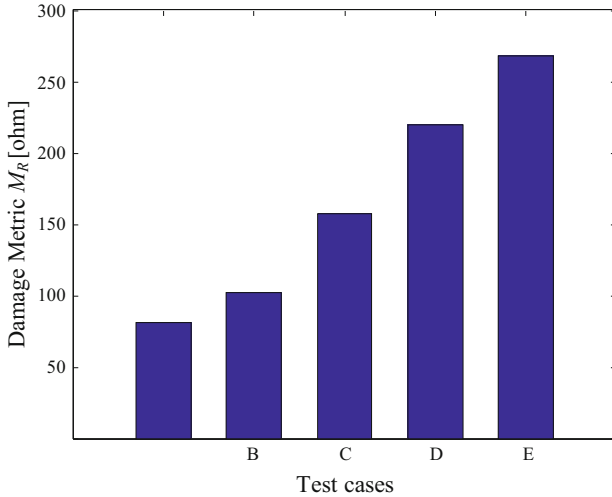
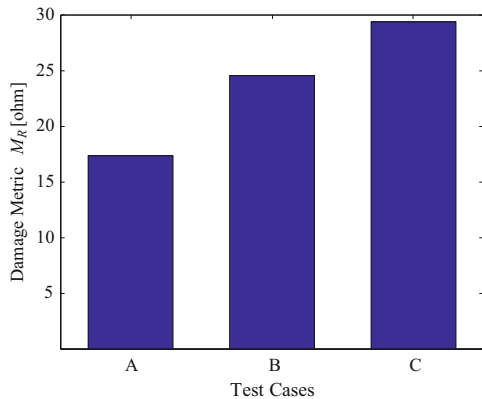


Fig. 8 Damage metric M_R (108–116 kHz)

Fig. 9 Damage metric M_R (108–116 kHz)



however the same position along the beam (195 mm from the PZT patch), for the two frequency bands considered. The following masses were considered sequentially: A—1.76 g; B—3.45 g; C—5.16 g. Figure 9 shows the damage metric M_R for the frequency band given by 108–116 kHz. It can be observed that the larger the added mass, the larger the damage metrics. The same trend is kept for the other damage metrics. Similar results are obtained for the lower frequency band.

Finally, holes with different diameters were made sequentially in the beam, all at the same position. The goal is to observe the variation of the damage metrics when increasing the diameter, keeping however the same position of the center of the holes along the beam (195 mm from the PZT patch), for the two frequency bands considered. The following diameters were considered sequentially: A—1.0 mm; B—2.0 mm; C—4.0 mm; D—8.0 mm. Figure 10 shows the damage metric M_R for the frequency band represented by 108–116 kHz. It can be observed that the larger

Fig. 10 Damage metric M_R (108–116 kHz)

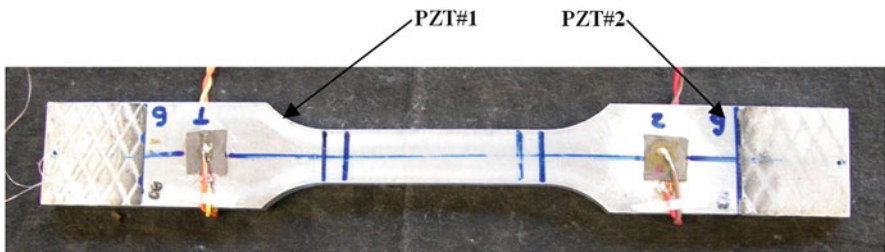
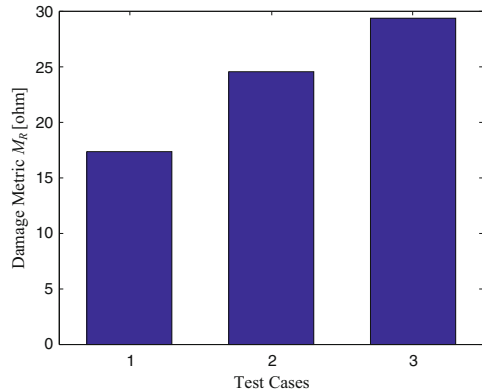


Fig. 11 PZT patches bonded on the surface of the test sample

the diameter, the larger the damage metrics. The same trend is kept for the other damage metrics. Similar results are obtained for the lower frequency band considered.

3.2 Fatigue Test

To determine the value of the stress amplitude that should be applied in the fatigue test so that no plastic deformation results, preliminary tensile tests were performed to obtain the stress–strain curve for the material used (Al). After determining the stress amplitude (corresponding to a force peak value of 9324 N), defining the frequency to be used in the fatigue tests (10 Hz) and selecting the number of cycles, two $10 \times 10 \times 0.1$ mm PZT patches were bonded to the test sample. The PZT patches were bonded outside the area of critical stress concentration, as shown in Fig. 11.

The test sample presented a visible crack after 50,636 cycles. Six impedance measurements were taken at each 8000 cycles until reaching 48,000 cycles. One additional measurement was taken after the crack became visible—50,636 cycles—shown in Fig. 12.

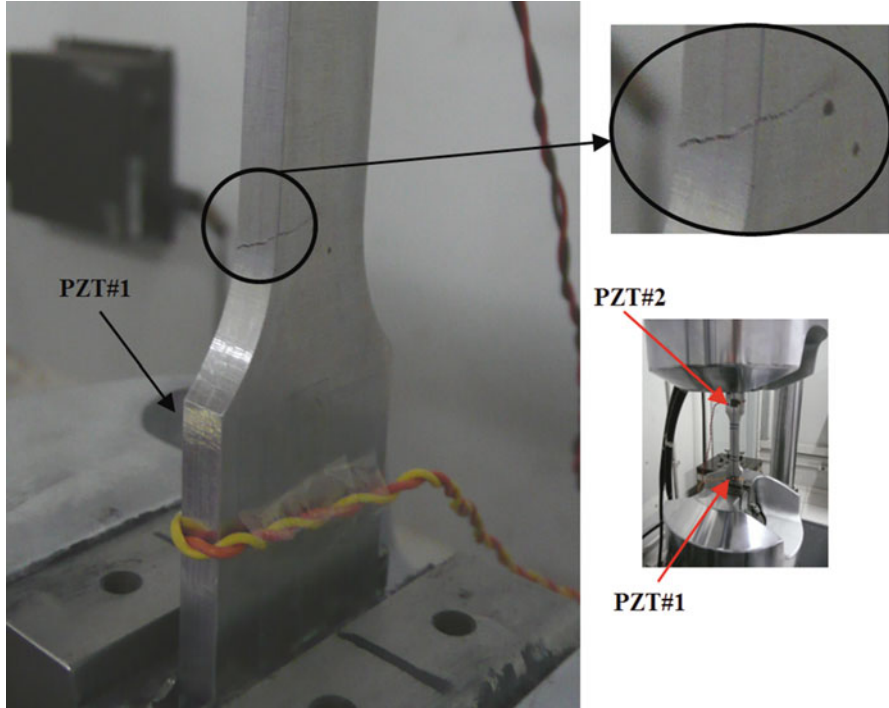


Fig. 12 Crack in the test sample (fatigue testing for the impedance-based technique)

In summary, the procedure was the following (as illustrated in Fig. 13):

- (a) First, measurements were taken to determine the soundness state of the structure (before starting the fatigue test);
- (b) Then, the test sample was placed in the fatigue testing machine and 8000 force cycles were performed;
- (c) Impedance measurements were made;
- (d) Another 8000 cycles were applied to the specimen;
- (e) The sequence above was repeated until the specimen exhibited a visible crack.

As the frequency range of 30–50 kHz is commonly used for the electromechanical impedance method (Moura, 2008), the range used in the present case was 39–46 kHz. The real part of the impedance was measured for the PZT1 and PZT2 patches as shown in Fig. 14. In this figure it is possible to observe how the impedance responses change after a given number of cycles, demonstrating that the technique is sensitive to the damage accumulation associated with the cyclic load. This means that a clear correlation exists between the number of cycles applied to the test samples and the impedance signals. It is worth mentioning that the experimental procedure can be simplified by using a portable impedance meter.

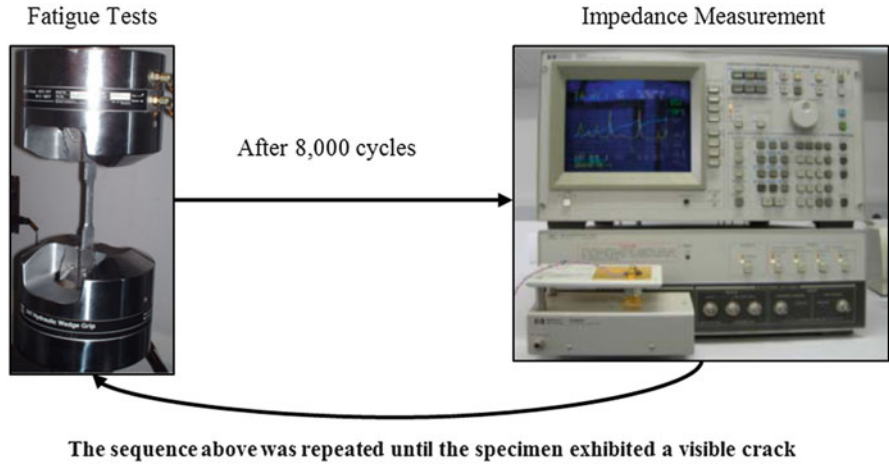


Fig. 13 The fatigue test procedure

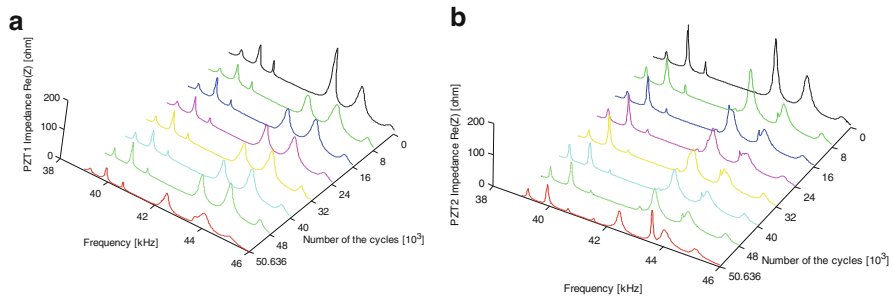


Fig. 14 Impedance signatures for the fatigue tests. (a) Signatures of the PZT patch #1; (b) signatures of the PZT patch #2

4 Conclusion

The basic aspects of impedance-based structural health monitoring have been presented in this chapter. We have also included two case studies to illustrate the application of the technique conveyed.

It is worth mentioning that for many applications the use of a commercial impedance analyzer is not appropriate due to its weight and cost. It is well known that on board real time monitoring requires low weight, high performance equipment, particularly for aerospace applications. Consequently, different groups on SHM research around the world have designed low weight/low cost impedance analyzers even for the case in which several monitoring channels are necessary.

Another important point is temperature compensation. Impedance-based structural health monitoring is sensitive to temperature. In general, the compensation is done in the software used to manage the impedance responses.

Finally, damage classification is an issue to be taken into account. In the same structure various types of damage may occur simultaneously: corrosion, rivet loss, cracks. Additionally, in the case of composite structures, delamination should be carefully monitored. For damage classification purposes a number of artificial intelligence methods are available.

All the points above will be addressed in further developments.

References

- S. Bhalla, A.S.K. Naidu, C.W. Ong, C.K. Soh, Practical issues in the implementation of electro-mechanical impedance technique for NDE, in *Proceedings of the SPIE International Symposium on Smart Materials, Nano-, and Micro-Smart System*, Melbourne, Australia, December 2002
- C.A.G.M. Branco, *Mecânica dos Materiais*, 2nd edn. (Fundação Calouste Guelbenkian, Lisboa, 1994)
- Z. Chaudhry, T. Joseph, F. Sun, C. Rogers, Local-area health monitoring of aircraft via piezoelectric actuator/sensor patches, in *Proceedings of the Smart Structures and Integrated Systems*, San Diego, March 1995
- Z. Chaudhry, F. Lalande, A. Ganino, C. Rogers, Monitoring the integrity of composite patch structural repair via piezoelectric actuators/sensors, AIAA-1996-1074-CP, 1996
- C.R. Farrar, K. Worden, *Structural Health Monitoring, A Machine Learning Perspective* (Wiley, Chichester, 2013)
- C.R. Farrar, N.A.J. Lieven, M.T. Bement, *Damage Prognosis for Aerospace, Civil and Mechanical System* (Wiley, Chichester, 2005) (Chapter 1)
- V. Giurgiutiu, A. Zagrai, Characterization of piezoelectric wafer active sensors. *J. Intel. Mater. Syst. Struct.* **11**, 959–976 (2000)
- V. Giurgiutiu, A. Zagrai, Damage detection in thin plates and aerospace structure with the electro-mechanical impedance method. *Struct. Health Monit.* **4**(2), 99–118 (2005)
- V. Giurgiutiu, J. Redmond, D. Roach, K. Rackow, Active sensors for health monitoring of aging aerospace structures, in *Proceedings of SPIE'S 7th International Symposium on Smart Structures and Materials and 5th International Symposium on nondestructive Evaluation and Health Monitoring of Aging Infrastructure*, Newport Beach, Canada, March 2000
- V. Giurgiutiu and C.A. Rogers, Recent Advancements in the Eletro-Mechanical (E/M) Impedance Method for Structural Health Monitoring and NDE. In: 5th Annual International Symposium on Structures and Materials, San Diego. *Proc. SPIE* 3329 536–47 (1998)
- V. Giurgiutiu, A. Zagrai, J.J. Bao, Piezoelectric wafer embedded active sensors for aging aircraft structural health monitoring. *Int. J. Struct. Health Monit.* **1**(1), 41–61 (2002)
- B.L. Grisso, Tailoring the impedance-based structural health monitoring technique to composites and wireless systems, in *13th March 2005-CMISS*, 2005
- C. Liang, F.P. Sun, C.A. Rogers, Coupled electromechanical analysis of adaptive material systems—determination of the actuator power consumption and system energy transfer. *J. Intel. Mater. Syst. Struct.* **5**, 12–20 (1994)
- J.R.V. Moura Jr, A Contribution to Structural Health Monitoring Systems Applied to Aeronautical and Space Structures, PhD Thesis, Federal Univ. of Uberlandia, Brazil (in portuguese) (2008)
- J.R.V. Moura, V. Steffen, Impedance-based health monitoring: frequency band evaluation, in *Proceedings of XXII IMAC International Modal Analysis Conference*, Dearborn, January 2004
- J.R.V. Moura, V. Steffen, Impedance-based health monitoring for aeronautic structures using statistical meta-modeling. *J. Intel. Mater. Syst. Struct.* **17**, 1023–1036 (2006)

- A.S.K. Naidu, C.K. Soh, Damage severity and propagation characterization with admittance. *Smart Mater. Struct.* **13**, 393–403 (2004)
- L.V. Palomino, V. Steffen Jr., Damage metrics associated with electromechanical impedance technique for SHM applied to a riveted structure, in *Proceedings of the 20th International Congress of Mechanical Engineering*, Gramado, Brazil, 15–20 November 2009
- L.V. Palomino, J.R.V. Moura Jr., K.M. Tsuruta, D.A. Rade, V. Steffen Jr., Impedance-based health monitoring and mechanical testing of structures. *Smart Struct. Syst.* **7**, 15–25 (2011)
- L.V. Palomino, K.M. Tsuruta, J.R.V. Moura Jr., D.A. Rade, V. Steffen Jr., D.J. Inman, Evaluation of the influence of sensor geometry and physical parameters on impedance-based structural health monitoring. *Shock Vib.* **9**(5), 811–823 (2012). doi:[10.3233/SAV-2012-0690](https://doi.org/10.3233/SAV-2012-0690)
- G. Park, D.J. Inman, *Damage Prognosis for Aerospace, Civil and Mechanical System* (Wiley, Chichester, 2005) (Chapter 13)
- G. Park, K. Kabeya, H.H. Cudney, D.J. Inman, Impedance-based structural health monitoring for temperature varying applications. *JSME International Journal Series A Solid Mechanics and Material Eng.* **42**(2), 249–258 (1999)
- G. Park, H. Cudney, D.J. Inman, An integrated health monitoring technique using structural impedance sensors. *J. Intel. Mater. Syst. Struct.* **11**(6), 448–455 (2000)
- G. Park, H. Cudney, D.J. Inman, Feasibility of using impedance-based damage assessment for pipeline systems. *Earthquake Engng. Struct. Dyn.* **30**, 1463–1474 (2001)
- G. Park, H. Sohn, C.R. Farrar, D.J. Inman, Overview of piezoelectric impedance-based health monitoring and path forward. *Shock Vib. Dig.* **35**(6), 85–92 (2003)
- D.M. Peairs, Development of a self-sensing and self-healing bolted joint, M.Sc. Dissertation, Faculty of Virginia Polytechnic Institute and State University, 2002
- D.M. Peairs, High frequency modeling and experimental analysis for implementation of impedance-based structural health monitoring, Ph.D. Thesis, Virginia Polytechnic Institute and State University, Virginia, 2006, p. 150
- D.M. Peairs, G. Park, D.J. Inman, Improving accessibility of the impedance-based structural health monitoring. *J. Intel. Mater. Syst. Struct.* **15**, 129–139 (2004)
- V. Raju, Implementing impedance—based health monitoring. Ph.D. Thesis, Virginia Polytechnic Institute and State University, Virginia, 1997, p. 224
- C.K. Soh, K. Tseng, S. Bhalla, A. Gupta, Performance of smart piezoceramic patches in health monitoring of a RC bridge. *Smart Mater. Struct.* **9**, 533–542 (2000)
- F.P. Sun, Z. Chaudhy, C. Liang, C.A. Rogers, Truss structure integrity identification using PZT sensor–actuator. *J. Intel. Mater. Syst. Struct.* **6**, 134–139 (1995)
- K.K.-H. Tseng, A.S.K. Naidu, Non-parametric damage detection and characterization using smart piezoceramic material. *Smart Mater. Struct.* **11**, 317–329 (2002)

Damage Detection Systems for Commercial Aviation

Ricardo Pinheiro Rulli, Camila Gianini Gonzalez Bueno, Fernando Dotta,
and Paulo Anchieta da Silva

Abstract Damage detection systems based on various technologies—such as Comparative Vacuum Monitoring, Electro-Mechanical Impedance, Acoustic Emission, and Lamb Waves—have been investigated by the major aircraft manufacturers over the last decade. The main focus of the investigations is to determine the possible application scenarios for these technologies, anticipating potential benefits for the commercial aircraft scheduled maintenance programs. Structural Health Monitoring (SHM) damage detection solutions have the potential to reduce aircraft operators direct maintenance costs and fleet downtime. In order to provide a common understanding, scope, and key elements for SHM it was produced by an SAE technical committee the ARP6461 document, encompassing guidelines for the implementation of Structural Health Monitoring for civil aviation. The document includes guidelines for development, validation, verification, and certification of damage detection systems. Although not being implemented as current inspection tools, the SHM damage detection systems have demonstrated progress for finding damages in different types of structures. Embraer is one of these major commercial aircraft manufacturers which have extensively tested different technologies, from coupons to aircraft test beds.

Keywords Structural health monitoring • SHM • Damage detection systems • Commercial aviation • Aircraft manufacturers • MSG-3 • ARP6461

1 Introduction

Over the years, aircraft manufacturers have investigated damage detection systems applied to aeronautical structures for commercial, executive, and defense aviation fleets. This concern is directly related to opportunities to reduce maintenance costs for customers, to increase competitiveness, and to improve the safety of airplanes—because automated inspections can minimize the risks associated to

R.P. Rulli (✉) • C.G.G. Bueno • F. Dotta (✉) • P.A. da Silva
Smart Structures & Structural Health Monitoring, Department for Technological
Development, Embraer S.A., São José dos Campos, SP, Brazil
e-mail: rulli@embraer.com.br; fernando.dotta@embraer.com.br

“human-factors”—and also to reduce redundancy in metallic structures designs (Schmidt et al. 2004).

Regarding the benefits of introducing Structural Health Monitoring (SHM) into commercial aviation, Kent and Murphy (2000) provided cost benefit analysis for three different structures (trailing edge, vertical stabilizer, and engine mount) showing that a significant reduction in the life-cycle costs could result in a realistic return on investments. According to this study, considering a replacement of 30–40 % of traditional maintenance requirements by SHM solutions, the time to recover the cost of the initial investment for both the engine mount and the trailing edge structure would be 2 to 3 years (Santos 2013).

Various initiatives of system’s development and for the construction of a robust implementation process are in progress, but with no application into an aircraft maintenance program so far—something that can be changed in the near future. This scenario shows that some additional understanding about this type of solutions is still required, such as determining implications derived from changes related to damage detection systems in Airlines for America (A4A) Maintenance Steering Group 3 (MSG-3) methodology that is used for the development of aircraft scheduled maintenance programs; and, exploring the potential effects on the maintenance review board process, on the aircraft maintenance manuals and on the operators maintenance programs (Santos 2011).

2 Maintenance of Commercial Aircraft

A4A Maintenance Steering Group 3 (MSG-3) is the pillar methodology for all structural scheduled inspections that assure the continued airworthiness of an aircraft. The process starts much before an aircraft goes into service. The aircraft manufacturers (such as Embraer, Boeing, and Airbus), operators (Airlines), and Regulatory Agencies (ANAC—Brazilian National Civil Aviation Agency, FAA—United States Federal Aviation Administration, EASA—European Aviation Safety Agency, and others) allocate a lot of efforts on A4A MSG-3 in almost the entire development of a new aircraft and further after the aircraft starts to operate.

This is the method used by aircraft manufacturers, operators, and regulatory agencies to develop the initial maintenance schedule, as part of the work towards aircraft certification. It is often a multi-year process, involving the application of rigorous logic (process), the analysis of lots of data, and the interaction of multiple administrative bodies (Adams 2009).

According to the MSG-3 methodology (A4A/ATA MSG-3 2009), which continues to stand the test of time for almost 40 years past, the aircraft maintenance programs are defined by air carriers in accordance with the Aviation Regulations from a number of source documents. These documents include the manufacturer’s Maintenance Review Board Report (MRBR), the Certification Maintenance Requirements (CMR), the Airworthiness Limitations Items (ALI), the

manufacturer's Maintenance Planning Document (MPD), unique national regulatory requirements, and others (Wenk 2010).

The final output of the Industry Steering Committee for a new aircraft is the Maintenance Review Board Report (MRBR), which outlines the recommended minimum initial maintenance requirements. This document is then, for instance, approved by the FAA, as the MRB chairman (considering an US aircraft). The MSG-3 process provides tasks, such as lubrication, visual inspections, operational or functional checks, restoration, and discard (Adams 2009).

2.1 Economics in Aircraft Maintenance

Nowadays, a large portion of an aircraft operation cost is in the maintenance program and economics is an important consideration in the aircraft design.

In the A4A MSG-3 approach the sequence of intervention follows an order from the least to the most expensive in order to minimize the costs without affecting safety. An example of this methodology is a structural inspection task analysis that starts with a visual inspection as the first choice to be considered, followed by a detailed inspection and then by Special Detailed Inspection/Non-destructive Inspection.

2.2 Changes in MSG-3 and SHM

The MSG-3 methodology (A4A/ATA MSG-3 2009) has been adapted to new technologies such as Structural Health Monitoring (SHM) and continues to produce safe, reliable, predictable, and cost-effective aircraft maintenance task/interval packages (Wenk 2010).

Maintenance guidelines for creation of aircraft scheduled maintenance programs contained in the A4A MSG-3 document (A4A/ATA MSG-3 2009) have been updated to allow for the use of SHM. The 2009 revision of MSG-3 document introduced the definition of Scheduled Structural Health Monitoring (S-SHM) that means the act to use/run/read out a SHM device at an interval set at a fixed schedule (Wenk 2010).

SHM application will play a significant role in the future of aircraft maintenance. SHM may allow damage detection in areas with restricted access, where current visual and non-destructive testing (NDT) technique inspections are difficult or can not be performed, avoiding the disassembly processes (which may undesirably cause damages to the structure). Less time-consuming and less complex procedures enabled by SHM (compared to current NDT techniques) will lead to reduction of inspection time and burden, and as a consequence SHM can minimize "human-factor" effects (for instance, automated data analysis has the potential to reduce human errors induced by fatigue and repetitive tasks). Another potential benefit is

the early detection of structural damages, which can aid the implementation of less costly repairs.

In addition, avoiding disassembly processes and promoting less time-consuming inspections, allied to the labor costs reduction (less complex procedures), indicate that SHM damage detection systems have a strong potential to reduce aircraft structures operating and maintenance costs.

In the future, SHM damage detection systems will be capable of providing means for the replacement of the current time-based maintenance practices by the so-called Condition-Based Maintenance (CBM) philosophy. A first step towards CBM has already been performed in the scope of the A4A MSG-3 methodology (A4A/ATA MSG-3 2009). During the International Maintenance Review Board Policy Board (IMRBPB) meeting held in Singapore in April 2010, the Automated Structural Health Monitoring (A-SHM) concept was accepted by the members (including the Aviation Regulation Authorities) to become a new Issue Paper for future revision of the MSG-3 document. The A-SHM concept focuses on SHM technology that relies on a system to inform maintenance personnel that an action must take place—there is no pre-determined interval at which the action must be performed (Wenk 2010).

3 Commercial Aviation Efforts

Over the last years, the major aircraft manufacturers and some commercial aircraft operators have investigated various technologies for structural damage detection. Progress has been made in the development of such technologies. Questions related to reliability, the accurate operation of those systems, and about the ability of components to survive during regular aircraft operation—and operational environment—have begun to get answers after the installation of sensors on-board aircraft for testing.

Seeking for potential benefits, such as the implementation of less time-consuming and less complex aircraft maintenance procedures, and for the reduction of aircraft structural maintenance costs, the commercial aviation industry demonstrated interest in SHM damage detection systems proposing developments with different technologies. The most common technologies that can be identified in those developments are Comparative Vacuum Monitoring, Electro-Mechanical Impedance, Acoustic Emission, and Lamb Waves. However, many others can be found: Fiber Bragg Gratings, Meandering Winding Magnetometer, Advanced Phased Array, and others.

Each of the technologies has its own particular characteristics and may have a preferred application. The commercial aviation industry is seeking for solutions to detect damages in metallic and composite structures, with an application cost that could justify the investments.

3.1 Comparative Vacuum Monitoring

One of the promising technologies for inspecting metallic material parts is the so-called Comparative Vacuum Monitoring (CVM™), from Structural Monitoring Systems plc. It is based on the principle that vacuum maintained inside a small constant volume is extremely sensitive to any leakage (Doherty et al. 2003). The system designed for metallic structures uses elastomeric polymer sensors that are self-adhesive, passive, inert, and lightweight, and can conform to the material surface contours. When those sensors are adhered to the monitored structure, fine channels on the adhesive face of the sensor form a manifold of galleries with the structure itself. The galleries alternate, one containing the steady state vacuum and the other having air at atmospheric pressure (Fig. 1).

If a surface crack develops, it will form a leakage path, air will flow through the passage created from the atmospheric to the vacuum galleries, the vacuum level in the sensors will decrease, indicating the presence of damage. CVM™ offers an easy way to monitor “hot spot” areas.

Among the many efforts for developing damage detection technologies, it is worth mentioning Boeing’s agreement to include Comparative Vacuum Monitoring crack-detection technology in its Common Methods Non-destructive Inspection manual after completing laboratory tests with CVM™ sensors and flight tests in commercial aircraft, in 2005 (Flightglobal News Website 2005). This test validation program was conducted by Sandia National Laboratories in cooperation with the Federal Aviation Administration (FAA) (Roach et al. 2006).

Airbus, another major aircraft manufacturer, has also investigated CVM. Various tests were performed, including those with sensors installed in coupons and in a barrel test (full-scale) (Stehmeier and Speckmann 2004). Among the variety of tests, it is important to highlight that Airbus has tested Comparative Vacuum Monitoring in its A380 Full-Scale Fatigue Test (Berger 2012; Paget et al. 2009).

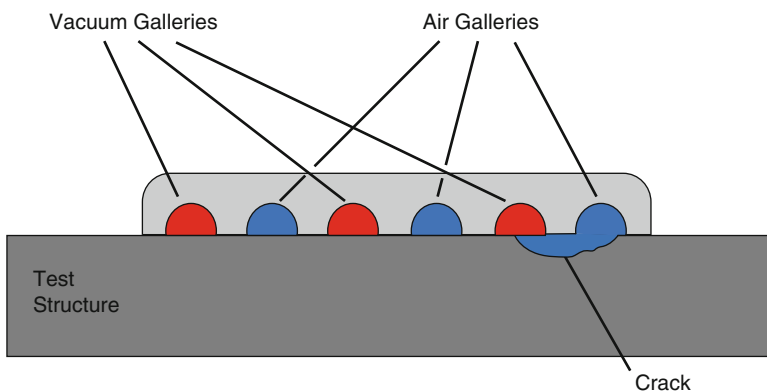


Fig. 1 Schematic of an installed CVM™ sensor

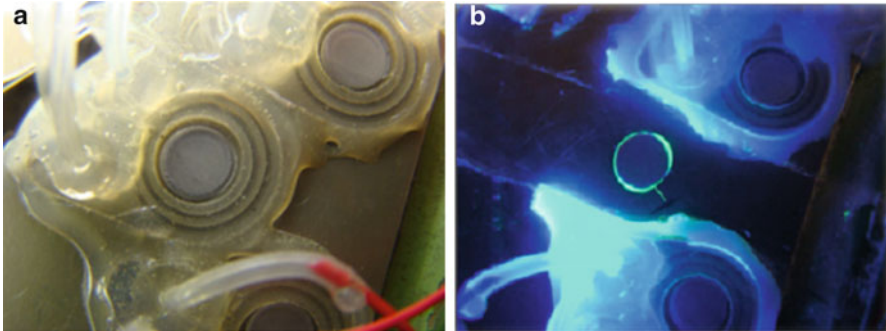


Fig. 2 Crack detected by a CVM™ sensor in a metallic barrel test. (a) CVM™ sensors installed around rivets; (b) one of the sensors was removed and dye penetrant testing confirmed the presence of a crack

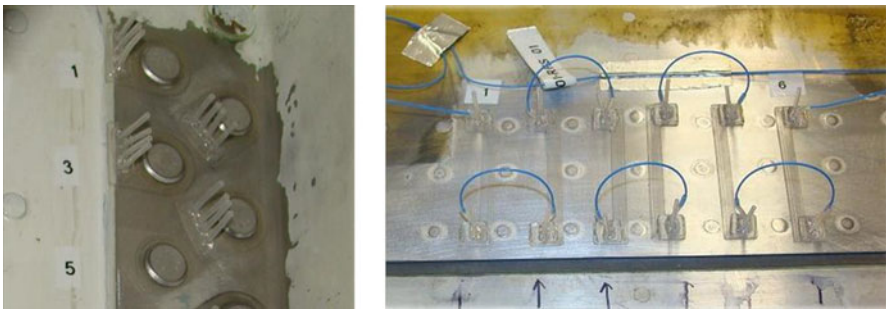


Fig. 3 CVM™ sensors in different regions of the E-Jets Full-Scale Fatigue Test

Embraer has performed laboratory tests with CVM™, applying the technology in a metallic barrel test and in its E-Jets Full-Scale Fatigue Test (Rulli and Silva 2011). An example of a crack detected in a metallic barrel test is shown in Fig. 2.

In parallel, Embraer installed more than 250 CVM™ sensors in the Full-Scale Fatigue Test of the company's E-Jets aircraft in 2008. Figure 3 shows examples of CVM™ sensors installed in the Full-Scale Fatigue Test where different regions and components—such as shear clips, splice joints, windows frames, and joint holes—have been periodically monitored.

Another test performed by Embraer is related to the installation of CVM™ sensors in a flight test aircraft in order to verify if the technology was capable of withstanding the real aircraft in-flight conditions, shown by Fig. 4. Since 2010, the company has performed periodic monitoring of these on-board sensors using CVM™ ground equipment.

Bombardier has studied Comparative Vacuum Monitoring in conjunction with the Airworthiness Assurance Nondestructive Inspection Center at Sandia National Labs for crack detection on its aircraft (Roach and Pinsonnault 2009).

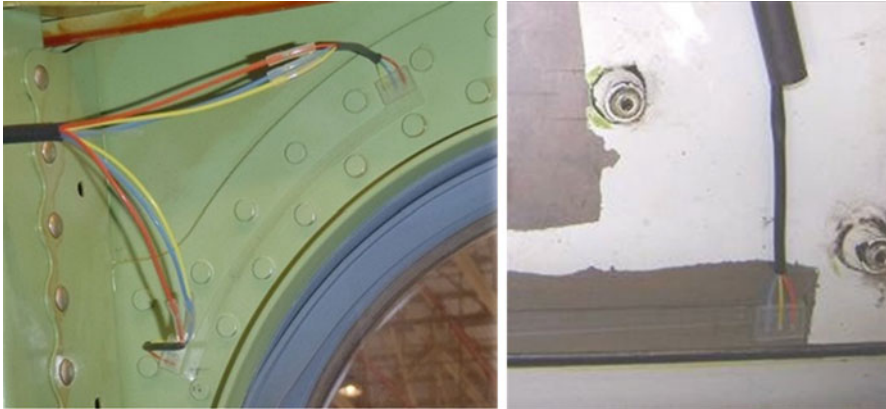


Fig. 4 CVM™ sensors installed on-board a flight test aircraft

Delta Air Lines has partnered with Sandia National Labs, FAA, Boeing, Anodyne Electronics Manufacturing Corp., and Structural Monitoring Systems, on a program applying CVM™ sensors to seven B737-700s. The objective is to produce the data package within 12–18 months of monitoring, consisting of periodic data acquisition. Some of the program’s main goals are to determine obstacles, solutions, and new processes for wide-spread industry adoption of SHM (Piotrowski et al. 2015).

3.2 *Electro-Mechanical Impedance*

Electro-Mechanical Impedance (EMI) is another technology considered by the commercial aviation players. It has been shown that the electrical impedance from patches of Piezoelectric materials (PZT) can be directly associated with the mechanical impedance of the structure to which the PZT is attached (Park et al. 2003). By using the same piezoelectric element for both actuation and sensing, results in a simpler testing device containing a smaller number of components and cables, when compared with techniques using transducers functions separated. The impedance-based method uses high-frequencies excitations that are applied to the PZT transducer attached to the surface of the structure and consider an auxiliary circuit to obtain the EMI curves. In other words, the PZT patches generate high frequency excitation at given points of the structure (Moura and Steffen 2005). Basically the EMI curves are frequency response functions of the structure. A modification in the EMI curves would indicate the presence of damage.

The EMI method begins with the work of Liang (Liang and Rogers 1994) not applied to SHM but after this study several authors reported the use of EMI method for SHM. In Brazil, the technique has been studied and developed by Federal

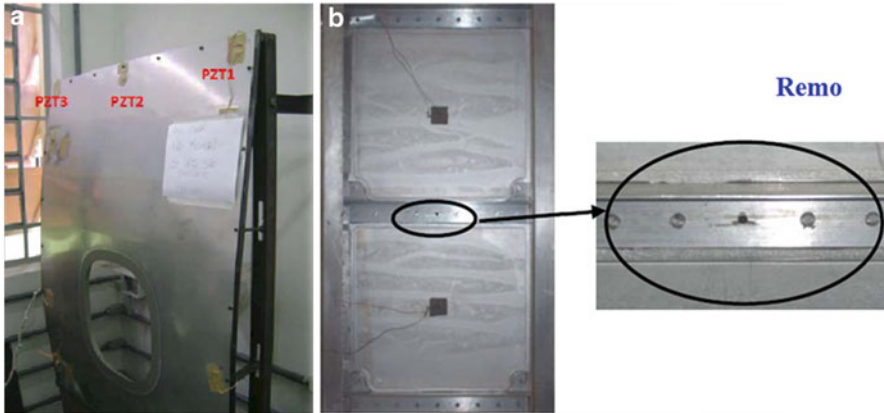


Fig. 5 Aluminum panels tested; (a) aircraft window panel; (b) details of a removed rivet simulating the damage

University of Uberlândia and São Paulo State University (UNESP—Ilha Solteira) in a partnership with Embraer (Rulli and Silva 2010). Figure 5 presents some example of aircraft structures using EMI to detect damage. The panel showed in Fig. 5b had a rivet removed in order to simulate damage. The results demonstrated that the system is sensitive enough to detect the absence of the rivet (Aeronautical Structures Tests Report 2009).

In fact, the EMI technique is useful to detect incipient damages present in monitored structures (Jalloh 2004) and is a promising technique to be applied for improving commercial aviation maintenance. In the other hand, as showed by Jalloh (2004) there are several factors that could affect the performance of the PZT transducers, among them the quality of the bond between the sensor and the host structure, sensor geometry and the characteristics of the structure monitored (such as its geometry and material properties).

Currently, the EMI technique has been studied for self-diagnosis of piezoelectric transducers. Airbus investigated Electro-Mechanical Impedance for self-diagnosis of piezoelectric transducers (Bach et al. 2007), focusing on the ability to detect degraded bond-lines as well as degraded sensors. According to the results, the company considered EMI a practicable technology for self-testing PZT sensors.

3.3 *Lamb Waves*

Airbus, Boeing, and Embraer have extensively investigated another promising technology for damage detection called Lamb Waves (LW). Lamb Waves represents two-dimensional wave propagation in thin plates, shells, or membranes, which are described by known mathematical equations originally formulated by Horace Lamb in 1917 (Viktrov 1967).

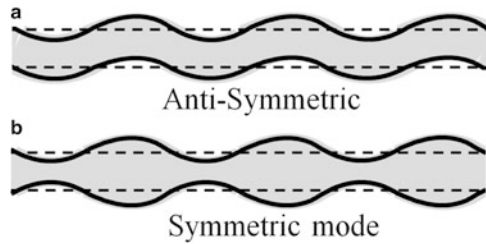


Fig. 6 Wave modes: (a) anti-symmetric, where a peak at one surface corresponds to a trough at the other surface; (b) symmetric, where the wave peaks or troughs occur simultaneously at the same in-plane location

The LW approach for damage detection uses the changes in the structural dynamic responses (acoustics) between the undamaged and damaged condition for the same structure. The fundamental of this technique is based on the assumption that structural damage changes the physical dynamic response of the structure, such as natural frequencies, mode shapes and damping, and frequency response (Doebbling et al. 1996). However, a structure with a damage like fatigue crack or thickness reduction (corrosion) exhibits non-linear vibrations due to the stiffness change under load variation (Matveev and Bovsunovsky 2002). The accuracy of relating changes in modal parameters to flaws such as cracks becomes quite poor when the aspect ratio between the size of the structure and the size of the flaw is larger than ten (Matveev and Bovsunovsky 2002; Ihn and Chang 2004).

There are two groups of LW propagation, the symmetric waves and the anti-symmetric waves that satisfy the wave equation and the boundary conditions. The general solutions can then be split into two modes: symmetric (S_i) and anti-symmetric (A_i) (Giurgiutiu 2005). For symmetric wave modes, each plate surface has a peak or trough at the same in-plane location. For anti-symmetric wave modes, a peak at one surface corresponds to a trough at the other surface, as shown in Fig. 6. The Lamb wave modes are considered to be sensitive to cracks. The presence of damages can be verified by comparing the changes in the signal to a baseline.

Embraer evaluated Lamb Waves technology for detecting damages—such as cracks and corrosion in metallic materials, and delamination in composite materials (2008)—obtaining valuable results (Dotta et al. 2011; Rulli et al. 2013). The company has performed laboratory tests with LW applying it in a wide range of specimens, such as coupons, Full-Scale Fatigue Test, barrel tests, and others. Figure 7 shows two examples of the tests performed.

Besides the laboratory tests, Lamb Waves sensors were installed in the Embraer-190 flight test aircraft (Fig. 8) in 2010. In this study, only the sensors (Fig. 9) and the cables were installed in the aircraft and the inspections were performed periodically using a ground support equipment (Rulli et al. 2013).

Airbus has been involved with Acellent Technologies Inc. in a joint development about Lamb Waves for several years (Zhang et al. 2011; Eckstein et al. 2013). One of the tests performed was related to the installation of sensors on a Carbon

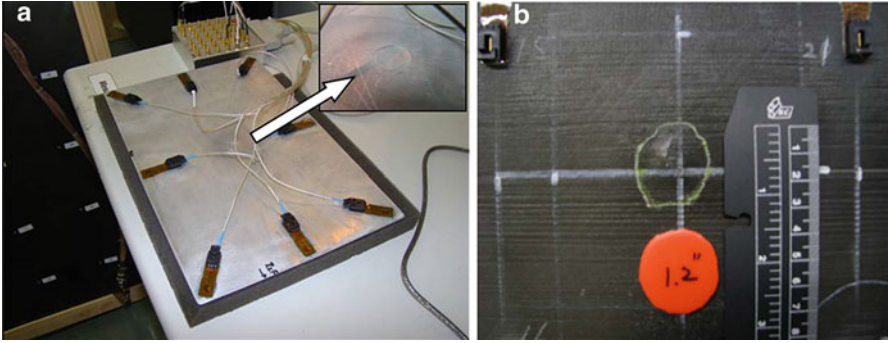


Fig. 7 Tests performed in different coupons: (a) thickness reduction in aeronautical aluminum; (b) delamination detection in carbon fiber reinforced polymer



Fig. 8 Flight Test Aircraft where CVM™ and LW sensors were installed

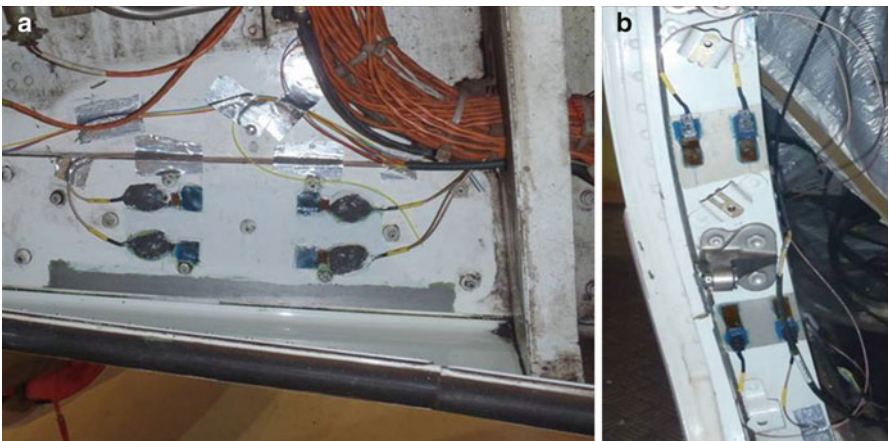


Fig. 9 LW sensors applied to the Embraer-190 flight test aircraft

Fiber Reinforced Plastics (CFRP) fuselage panel (about 15 m² size) in 2010. This panel was inserted in the fuselage of an A340 flight test aircraft. Data has been obtained periodically when the aircraft is on ground.

Boeing Research and Technology investigated techniques that use elastic waves in various structural configurations, including a composite wing structure (Brown et al. 2009) and a metallic lug component (utilizing a SHM system design framework developed by Boeing and Air Force Research Laboratory) (Ihn et al. 2011).

3.4 Acoustic Emission

Commercial Aviation has also demonstrated interest on another SHM damage detection technology known as Acoustic Emission (AE). Acoustic Emission based structural health monitoring is one of the methods which originally began as a non-destructive testing technique. In the AE method a solid structure begins to deform elastically when a load is applied to it (for instance, by internal pressure or by external mechanical means) (Boller et al. 2009). Changes in the structure's stress distribution and storage of elastic strain energy are associated with this elastic deformation. Some permanent deformation and cracking may occur during the load increment, which is accompanied by a release of stored energy. Part of the stored energy that was released is in the form of propagating elastic waves termed Acoustic Emissions. Emissions are detected by sensitive piezoelectric transducers attached to the surface of the monitored structure and, above a certain threshold level, are converted and saved as an event.

Airbus developed tests with Acoustic Emission for both metallic and composite structures. Composite plates were used for the development of an analytical triangulation algorithm to determine damage location (Paget et al. 2003). Investigations were performed with AE in a full-scale metal wing loaded in fatigue. Airbus reported that the system located all simulated and artificial damages placed in the wing and, in addition, it was capable to locate real damage (Paget et al. 2004).

Acoustic Emission systems have been tested by Embraer in test specimens and in the Full-Scale Fatigue Test of the E-Jets aircraft. These tests have the objective to provide enough information about Acoustic Emission technology regarding capabilities, installation, operation and maintenance of sensors and systems (Rulli and Silva 2010). Damages, including simulated and real, were satisfactorily detected by the AE systems in different test articles (Figs. 10 and 11).

3.5 Guidelines for SHM

In addition to the SHM damage detection systems initiatives around the world, Society of Automotive Engineers (SAE International) has created the document



Fig. 10 Fuselage panel in the E-Jets FSFT monitored by acoustic emission

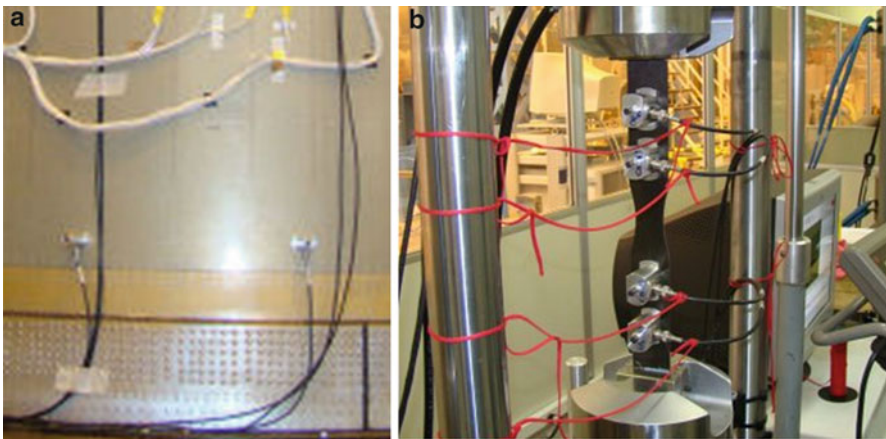


Fig. 11 Examples of acoustic emission monitoring: (a) Barrel test; (b) Coupon test

Aerospace Recommended Practice “ARP6461: Guidelines for Implementation of Structural Health Monitoring on Fixed Wing Aircraft” focusing on the commercial aviation (SAE International 2013). The document was published in September 2013.

Launched by the Aerospace Industry Steering Committee for SHM, the document was generated by an SAE technical committee (encompassing the world’s leading aircraft manufacturers, systems and equipment integrators, Regulatory Agencies, and technical experts) (SAE International 2013).

These guidelines present details related to the application of sensors for monitoring aircraft operational conditions, and also for determining the occurrence and the extent of a structural damage. The purpose of ARP6461 is to establish the basics of SHM for commercial aviation maintenance applications, including its scope and its essential elements, discussing about requirements and describing approaches for SHM systems verification, validation, and qualification.

References

- A4A/ATA MSG-3 (2009), Operator/Manufacturer Scheduled Maintenance Development; Revision 2009.1, Air Transport Association (ATA) of America, Inc., available from ATA <http://www.airlines.org>. MSG-3 reference and extracted details are provided courtesy of Air Transport Association of America, Inc. Copyright (c) 2009 by ATA of America, Inc
- C. Adams, Understanding MSG-3. Aviation today (2009), http://www.aviationtoday.com/am/repairstations/Understanding-MSG-3_33062.html
- Aeronautical Structures Tests Report*. Federal University of Uberlândia, Uberlândia, Minas Gerais
- M. Bach et al., Self-diagnostic capabilities of piezoelectric transducers using the electromechanical impedance, in *6th International Workshop on SHM*, 2007
- U. Berger, Onboard—SHM for life time prediction and damage detection on aircraft structure using fibre optical sensor and Lamb Wave technology, in *6th European Workshop on SHM*, 2012.
- C. Boller et al., History of SHM for commercial transport aircraft, in *Encyclopedia of Structural Health Monitoring* (Wiley, New York, 2009), Chapter 96, pp. 1–2
- K.S. Brown et al., Hot spot monitoring of a composite wing, in *7th International Workshop on SHM*, 2009
- S.W. Doebling, C.R. Farrar, M.B. Prime, D.W. Shevitz, Damage identification and health monitoring of structural and mechanical systems from changes in their vibration characteristics: a literature review. *Technical Report*, No. LA-13070-MS, Los Alamos National Laboratory, 1996
- C.M. Doherty, M. Lindroos, D.P. Barton, Structural health monitoring of aircraft using CVM, in *4th Australian Pacific Vertiflite Conference on Helicopter Technology*, 2003
- F. Dotta et al., Early results of Lamb waves approach to assess corrosion damage using direct image path in an aeronautical aluminum alloy, in *8th International Workshop on SHM*, 2011
- B. Eckstein et al., Large scale monitoring of CFRP structures by acousto-ultrasonics—a flight test experience, in *9th International Workshop on SHM*, 2013
- Flightglobal News Website, Boeing opts for vacuum crack sensor (2005), <http://www.flightglobal.com/news/articles/boeing-opts-for-vacuum-crack-sensor-212710/>
- V. Giurgiutiu, Tuned lamb wave excitation and detection with piezoelectric wafer active sensors for structural health monitoring. *J. Intel. Mater. Syst. Struct.* **16**(2), 291–305 (2005)
- J.-B. Ihn, F.-K. Chang, Detection and monitoring of hidden fatigue crack growth using a built-in piezoelectric sensor/actuator network: I. Diagnostics. *Smart Mater. Struct.* **13**, 609–620 (2004)
- J.-B. Ihn et al., Development and performance quantification of an ultrasonic structural health monitoring system for monitoring fatigue cracks on a complex aircraft structure, in *8th International Workshop on SHM*, 2011
- A. Jalloh, Effects of piezoelectric (PZT) sensor bonding and the characteristics of the host structure on impedance based structural health monitoring. *Nasa Faculty Fellowship Program*, Mechanical Engineering Department Alabama A&M University, Normal, 2004
- R.M. Kent, D.A. Murphy, Health monitoring system technology assessments—cost benefits analysis, *NASA/CR-2000209848*, 2000

- C. Liang, F.P. Sun, C.A. Rogers, Coupled electromechanical analysis of adaptive material system—determination of actuator power consumption and system energy transfer. *J. Intel. Mater. Syst. Struct.* **5**, 12–20 (1994)
- V.V. Matveev, A.P. Bovsunovsky, Vibration-based diagnostics of fatigue damage of beam-like structures. *J. Sound Vib.* **249**, 23–40 (2002)
- J.R.V. Moura Jr., V. Steffen Jr., Damage detection techniques for aeronautic structures. *XXIII IMAC*, 2005
- C. Paget et al., Triangulation algorithm for damage location in aeronautical composite structures. in *4th International Workshop on SHM*, 2003
- C. Paget et al., Damage assessment in a full-scale aircraft wing by modified acoustic emission, in *2nd European Workshop on SHM*, 2004
- C. Paget et al., Validation of SHM sensors in Airbus A380 full-scale fatigue test, in *Encyclopedia of Structural Health Monitoring* (Wiley, New York, 2009), Chapter 92, pp. 1839–1848
- G. Park et al., Overview of piezoelectric impedance-based health monitoring and path forward. *Shock Vib. Dig.* **35**(6), 451–463 (2003)
- D. Piotrowski et al., Implementation of structural health monitoring (SHM) into an Airline Maintenance Program, in *10th International Workshop on SHM*, 2015
- D. Roach, J. Pinsonnault, Use of mountable sensors to address periodic inspections for cracks on regional aircraft, in *7th International Workshop on SHM*, 2009
- D. Roach et al., Application and certification of comparative vacuum monitoring sensors for in-situ crack detection. *Air Transport Association Nondestructive Testing Forum*, 2006
- R.P. Rulli, P.A. Silva, Embraer perspective for maintenance plan improvements by using SHM, in *3rd Asia-Pacific Workshop on SHM*, 2010
- R.P. Rulli, P.A. Silva, Overview of CVM technology tests performed by Embraer, in *8th International Workshop on SHM*, 2011
- R.P. Rulli et al., Flight tests performed by EMBRAER with SHM Systems, in *Key Engineering Materials*, vol. 558 (Trans Tech Publications, Switzerland, 2013), pp. 305–313. doi:[10.4028/www.scientific.net/KEM.558.305](https://doi.org/10.4028/www.scientific.net/KEM.558.305)
- SAE International, Press Release: SAE International Creates First-Ever Guidelines for Structural Health Monitoring of Commercial Aircraft, 2013
- L.G. dos Santos, Embraer perspective on the introduction of SHM into current and future commercial aviation programs, in *8th International Workshop on SHM*, 2011
- L.G. dos Santos, Embraer perspective on the challenges for the introduction of scheduled SHM (S-SHM) applications into commercial aviation maintenance programs, in *Key Engineering Materials*, vol. 558 (Trans Tech Publications, Switzerland, 2013), pp. 323–330. doi:[10.4028/www.scientific.net/KEM.558.323](https://doi.org/10.4028/www.scientific.net/KEM.558.323)
- H.-J. Schmidt et al., Application of structural health monitoring to improve efficiency of aircraft structure, in *2nd European Workshop on SHM*, 2004
- H. Stehmeier, H. Speckmann, Comparative vacuum monitoring (CVM): monitoring of fatigue cracking in aircraft structures, in *2nd European Workshop on SHM*, 2004
- I.A. Viktorov, *Rayleigh and Lamb Waves: Physical Theory and Applications* (Plenum, New York, 1967)
- L. Wenk, MSG-3 (Maintenance Steering Group 3) guidance update on using SHM for continued airworthiness of aero structures, in *5th European Workshop on SHM*, 2010
- D.C. Zhang et al., Large sensor network architectures for monitoring large-scale structures, in *8th International Workshop on SHM*, 2011